

The neural basis of motor control and learning in the vestibulocerebellar system

De neurale basis van motor controle en motorisch leren in het
vestibulocerebellaire systeem

Proefschrift

ter verkrijging van de graad van doctor aan de
Erasmus Universiteit Rotterdam
op gezag van rector magnificus

Prof. Dr. H.A.P. Pols

en volgens besluit van het College voor Promoties

De openbare verdediging zal plaatsvinden op

Dinsdag 2 July 2019
om 15:30 uur

Bin Wu

geboren te Qingdao, Shandong, China



Promotiecommissie

Promotor: Prof. Dr. C.I. de Zeeuw

Overige leden: Dr. T.J.H. Ruigrok
Prof. S.A. Kushner
Prof. F.E.Hoebeek

Co-promotor: Dr. M. Schonewille

Table of contents

Chapter 1	Introduction	5
51.1	The neuronal machine of the cerebellum	6
1.2	A new perspective on vestibulo-ocular reflex adaptation	18
1.3	Scope of the thesis	32
Chapter 2	Methodology	39
	Targeted electrophysiological recordings in vivo in the mouse cerebellum	
Chapter 3	Cerebellar modules and heterogeneity	54
	TRPC3 is essential for functional heterogeneity of cerebellar Purkinje cells	
Chapter 4	Anatomical advance	90
	The basal interstitial nucleus of the cerebellum provides diffuse ascending inhibitory input to the floccular granule cell layer	
Chapter 5	Physiology of Purkinje cell during motor control and learning	
5.1	Modulating Modulation: Purkinje cell activity in impaired and enhanced compensatory eye movement adaptation	118
5.2	Mechanisms underlying vestibulo-cerebellar motor learning in mice depend on movement direction	131
Chapter 6	Development, motor learning and associated synaptic proteins	
6.1	Cerebellar development contributes to compensatory eye movement behavioral and adaptive functionality	164
6.2	Interactions of protein phosphatase 2B with PSD-proteins support synaptic integrity and cerebellar learning earning	184
6.3	AMPA protein Shisa6 is essential for Purkinje cell synaptic potentiation and motor learning	211
Chapter 7	Beyond motor control	242
	Dysfunctional cerebellar Purkinje cells contribute to autism-like behavior in Shank2-deficient mice	
Chapter 8	Discussion	265
Appendices		
	Summary / Samenvatting	281
	Curriculum Vitae	285
	PhD Portfolio	286
	List of Publications	287
	Acknowledgement	288

CHAPTER

1

Introduction

The human brain has 100 billion neurons, each neuron connected to 10,000 other neurons.
 Sitting on your shoulders is the most complicated object in the known universe.

— Michio Kaku (American physicist)

The brain, the most complex and important organ in the nervous system, gives rise to our ability to sense, think, remember, and act. It consists of billions of neurons communicating with one another by means of axons, which carry trains of action potentials and convey either sensory or motor information to other parts of the body. A fundamental challenge nowadays in neuroscience is to understand how our brain processes sensory information in order to generate accurate perception and guide appropriate behavioral responses.

Intriguingly, although the mammalian cerebellum accounts for only approximately 10% of the total brain weight and volume, it contains at least 50% of all neurons¹⁻³, which robustly outnumbers all other brain areas combined. With this thesis, I pay attentions on multiple aspects of the neural activities within the cerebellum, including the development, anatomy, physiology and function. By using the vestibulocerebellar system, I try to understand how the cerebellum process sensory information to drive motor behaviors and learning.

1.1 The neuronal machine of the cerebellum

Anatomy and structure

The cerebellum, meaning “little brain” in Latin, is a highly organized brain area located dorsally to the pons and medulla of the brainstem (**Fig.1**).

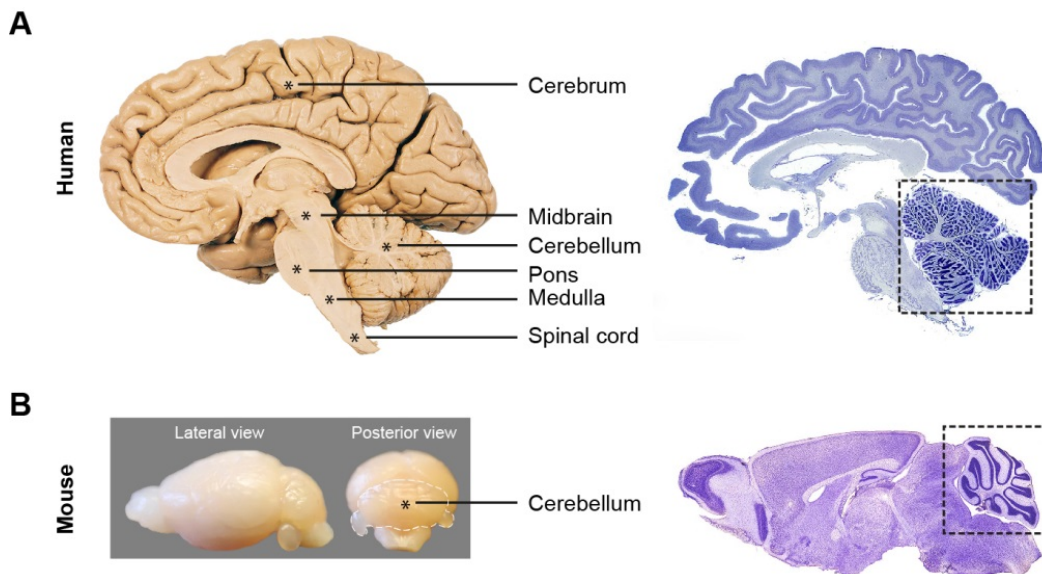


Figure 1. Location of the cerebellum in the human (A) and mouse (B) brain. Nissl staining of sagittal sections are shown on the right, with highlighted cerebellum in the black squares, adapted from the Human Brain Atlas (Brain Biodiversity Bank, Michigan state university) and Paxinos Mouse Atlas (Academic Press,2001).

It is symmetrically connected with the rest of the brain through three peduncles: superior, middle, and inferior. The superior peduncle contains most of cerebellar output fibers, projecting to the brain stem, red nucleus, hypothalamus, and thalamus; the middle peduncle contains exclusively afferents from the contralateral pontine nuclei; and the inferior cerebellar peduncle contains afferent fibers from the brain stem and the spinal cord, as well as cerebellar efferent fibers to the vestibular nuclei.

Longitudinally, the cerebellum is composed of three regions from medial to lateral: the vermis, the paravermis and the hemisphere, which are further foliated into 10 lobules (**Fig. 2A**). In sagittal plane, the vermis of cerebellum is further divided into 4 zones: anterior, central, posterior and the nodular zone (**Fig. 2B**). There are three pairs of nuclei embedded in the white matter: the fastigial, interpose (consisting of globose and emboliform nucleus in primates) and dentate nucleus.

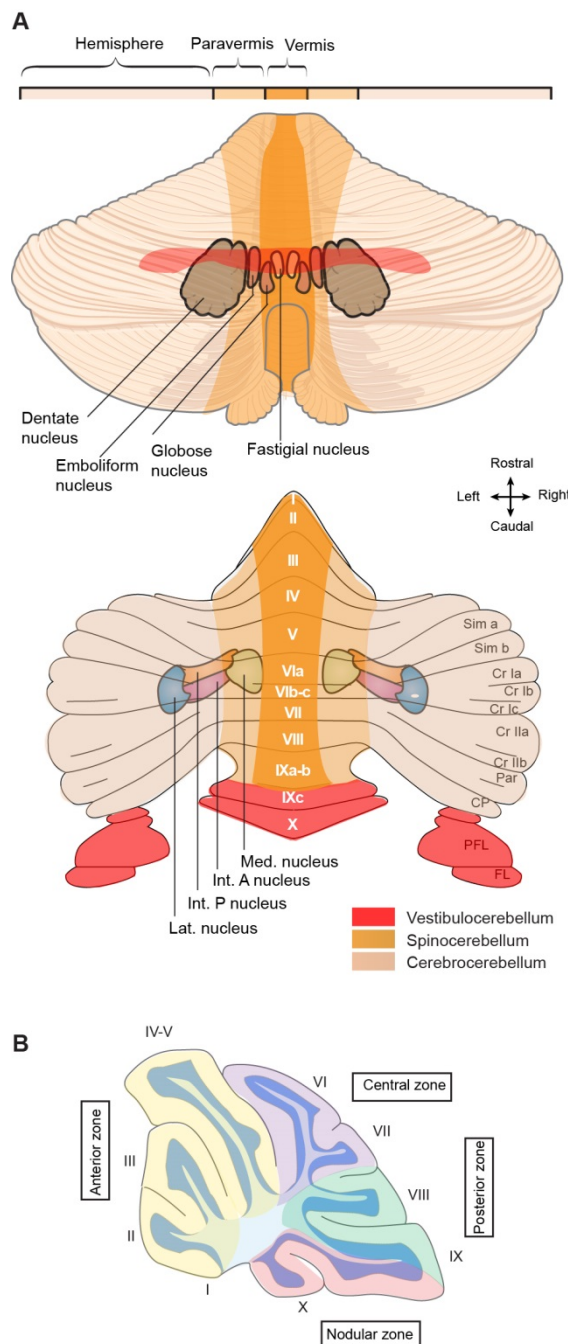


Figure 2. Gross anatomical segmentation of the cerebellum. **A**, Schematic representation of dorsal view of the human cerebellum (top) and unfolded mouse (bottom) cerebellum, as well as the superimposed deep cerebellar nuclei. The functional regions, named vestibulocerebellum, spinocerebellum and cerebrocerebellum, are indicated in three different colors. Note that the widest folia are found in the lateral part (hemispheres). The hemispheres spread overtly more widely than that in the mice, while the flocculonodular lobe (vestibulocerebellum) is relatively larger in the latter. Adapted from *Principles of Neural Science* (Kandel et al. 2012) and reference (Sugihara et al. 2007)⁴. **B**, Sagittal view of the mouse cerebellum revealing 10 different lobules (I-X), which can be classified into 4 zones: the anterior zone (lobules I-V), the central zone (lobule VI-VII), the posterior zone (lobules VIII to dorsal IX), and the nodular zone (ventral lobule IX and lobule X).

The most primitive and phylogenetically preserved part of the cerebellum is the flocculonodular lobe. The nodulus receives input directly from vestibular projections and the flocculonodular lobe sends its output primarily to the vestibular nuclei. It is generally believed that the flocculonodular region is involved exclusively in controlling body balance and eye movement in high vertebrates. The anatomy and connectivity

of flocculonodular cerebellum is one of the most extensively studied cerebellar regions, and is also one of the regions of interest in this thesis.

Cyto-architecture and neural circuitry

The cerebellum as a whole consists of three functional regions: the outermost is the cerebellar cortex, which contains most of the cerebellar neurons and connections; the middle is the white matter that consists of the input and output fibers; and the innermost cerebellar nuclei.

Cerebellar cortex

Despite some anatomical variations, the cerebellar cortex consists of a well-organized homogenous neuronal circuitry that can be divided in three layers: the molecular layer, the granular layer and the Purkinje cell layer^{5,6} (**Fig. 3**). The molecular layer is the outermost layer, containing two types of inhibitory interneurons including the stellate cells (SC) and basket cells (BC), collectively referred to as molecular layer interneurons (MLIs). The inner layer contains an abundance of small excitatory granule cells (GrC) and fewer inhibitory Golgi cells (GoC). Two less well known cell types in the granular layer, the unipolar brush cell (UBC), which are mostly found in the vermis and vestibulocerebellum. The intermediate layer, so-called Purkinje cells (PC) layer, is composed of PCs only, forming the only output of the cerebellar cortex. PCs are the largest cells in the cerebellum with extensive dendritic trees extending far into the molecular layer.

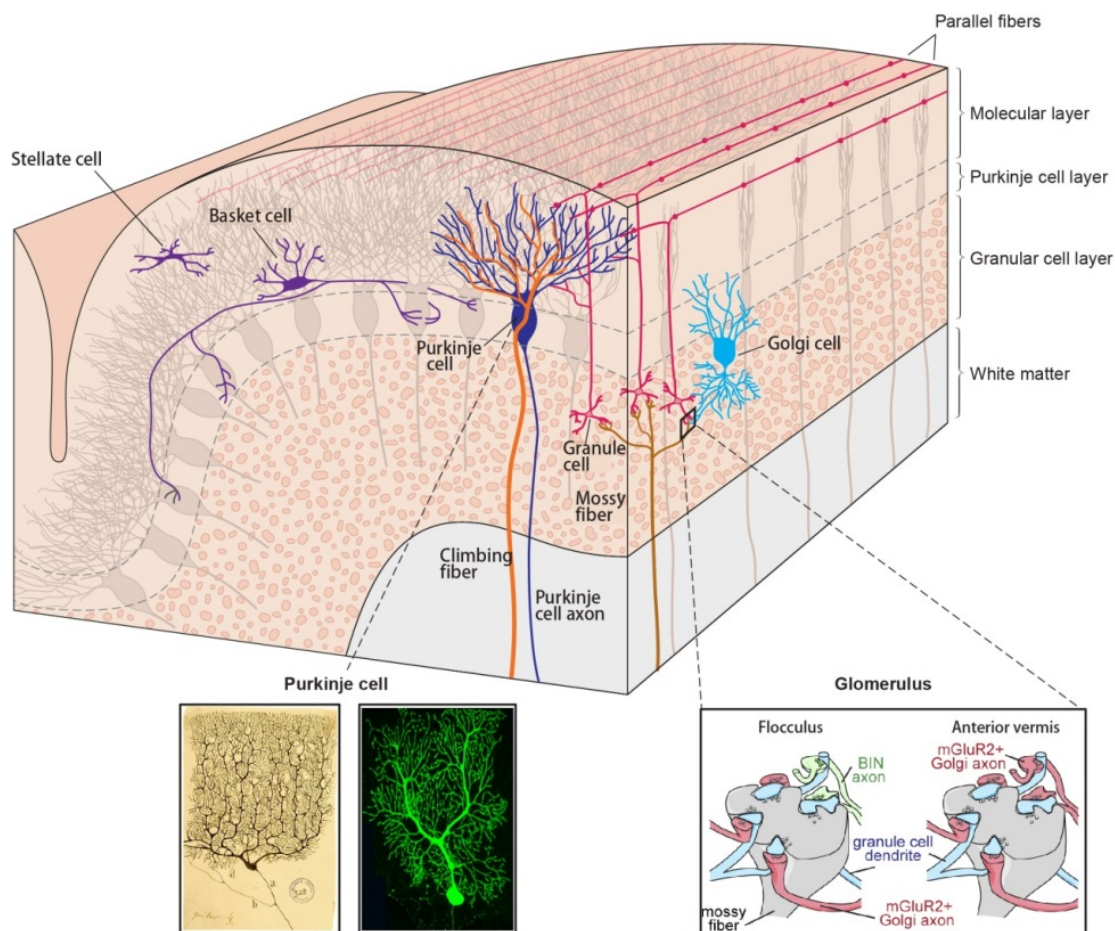


Figure 3. Scheme of cerebellar cortex with most important neurons organized into three layers, which are from outside to inside: molecular layer, Purkinje cell layer, granule cell layer. The biggest cells are Purkinje cells (PC) forming the sole output of the cerebellum. They are innervated by bundles of parallel fibers that run transversely to PCs innervating them and molecular layer interneurons at the same time. Note that Purkinje cell dendrites are prone to spread out in the parasagittal plane than in the transverse plane. Inhibitory stellate cells make connections on distal parts of dendritic tree. Basket cell axons form a basket-like synapse on the PC soma. Granule cells are inhibited by Golgi cells and make contacts with PCs through their ascending axons and parallel fibers. Mossy fibers originate in the deeper layers (not shown) and form end terminals with granule and Golgi cells called glomerulus. Climbing fibers rising from inferior olive (not shown) innervate PC with a one-on-one relationship. They also make synaptic contacts with Golgi cells and indirectly with molecular layer interneurons. Inset on the left show Purkinje cell morphology drawn by Santiago Ramón y Cajal (1852-1934) and a mouse Purkinje cell stained with biocytin (Middle inset). Right inset show the detail of glomeruli in the granular layer that contains a mossy fiber terminal as well as granule cell and Golgi cell or BIN cell (see Chapter 4) terminals is also shown. (Adapted from Kandel et al. 2012).

There are predominantly two types of inputs in the cerebellar cortex: one is mossy fibers (MF), conveying sensorimotor and motor command information, and the other is climbing fibers (CF), mainly relaying information about motor errors (Fig. 4). MFs arise from various sources in the brainstem and spinal cord and mainly provide excitatory inputs to GrCs, UBCs and GoCs. The ascending GrC axons bifurcate in the molecular layer and together form a network of fibers perpendicular to the orientation of PC dendrites but parallel to each other, so-called parallel fibers (PF). PFs, providing glutamatergic neurotransmission⁷, innervate PCs, GoCs, SCs and BCs. The other major input, the CF, originating from the contralateral inferior olive (IO), runs through the granule cell layer and terminates on Purkinje dendrites. They also make synaptic contacts with Golgi cells and indirectly with molecular layer interneurons.

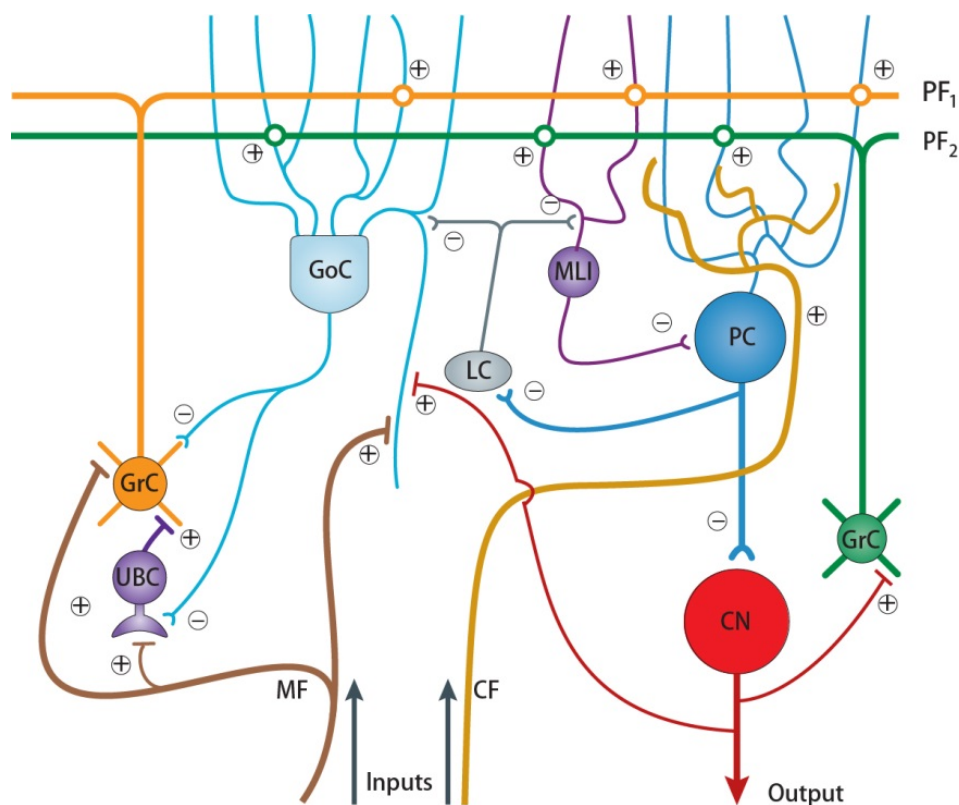


Figure 4. Synaptic connectivity of the cerebellar microcircuit. The excitatory mossy fiber (MF) and climbing fiber (CF) pathways are the two inputs into the cerebellum. Granule cells (GrC) with their parallel fibers (PF) and Purkinje cells (PC) form the major input-output pathway in the cerebellar cortex, whereas stellate and basket cells (collectively called MLI), receiving excitatory inputs from parallel fibers, make inhibitory contacts with the Purkinje cell. Golgi cells (GoC) also receive excitatory inputs from parallel fibers and provide inhibitory feedback to the granule cell dendrites within the glomerulus. PCs inhibit neurons in the cerebellar nuclei (CN), which in turn excite GoC and GrC through an internal feedback pathway. In addition, excitatory unipolar brush cells (UBCs) and inhibitory Lugaro cells (LC) are superimposed into the networks. The excitatory and inhibitory synaptic connections are indicated by “+” and “-” respectively. Adapted from (Gao et al. 2012)⁶.

Cerebellar Nuclei

Cerebellar nuclei (CN) are embedded into the white matter core on each side of the midline, specifically, the medial cerebellar nuclei (MCN) (fastigial nuclei in human), the anterior and posterior interposed nuclei (AIN and PIN) (globose and emboliform nuclei in human) and the lateral nuclei (LCN) (dentate nuclei in human) cover almost the whole mediolateral cerebellar axis⁸ (Fig. 2). Each nucleus targets different areas: In addition, CN neurons receive excitatory inputs from both MFs and CFs collaterals^{9,10}. More interestingly, typically CN neurons are innervated by PCs that receive CF input from the same area in the IO as the CN neuron projects to¹¹ (Fig. 6). CN neurons, together with and vestibular nuclei (VN, see details in Chapter 1.2), are the ultimate output of the cerebellum; however, the exact circuitry and how the input convergence happens are still under debate¹².

Physiology in the cerebellar cortex

PCs are featured with a striking pace-making activity, which is presumably driven by a specific mixture of transient, persistent and resurgent Na⁺-currents counterbalanced by voltage-gated K⁺-current¹³. This property of PCs is so robust that it will generate spontaneous action potentials even in dissociated cells. Purkinje cells are also unique because they elicit two very distinctive forms of action potential: simple spikes and complex spikes (SS and CS respectively) (Fig. 5). This specific pattern of spiking, makes PCs easy to identify in single unit extracellular recordings¹⁴ (see Chapter 2 for detailed methodology).

Simple spikes

Simple spikes are mainly mediated by sodium, calcium and potassium currents¹⁵ and can be triggered by PF stimulation even in slice without synaptic input^{13,16,17}. The most common view is that the interplay between transient, persistent, and resurgent Na currents, and voltage gated K currents mediates PCs' pace-making activity^{18,19}, while the excitatory and inhibitory synaptic inputs drive the firing rate and influence the regularity of PC intrinsic activity in vivo, respectively^{20,21}. Neurotransmitter release from PF is followed by activation of AMPA receptors and metabotropic glutamate type 1 receptors (mGluR1), which leads respectively to fast sodium-mediated EPSCs and delayed slow ones sustained by IP3-mediated calcium release from internal calcium stores²². The subsequent increase in the intracellular calcium concentration can activate the VGCC located in dendritic spines. These depolarizing dendritic currents spread towards the soma and if they are temporally and/or spatially summed up to

threshold levels they cause the opening of voltage-gated sodium channels in the axon hillock and, consequently, generation of a simple spike^{23,24}.

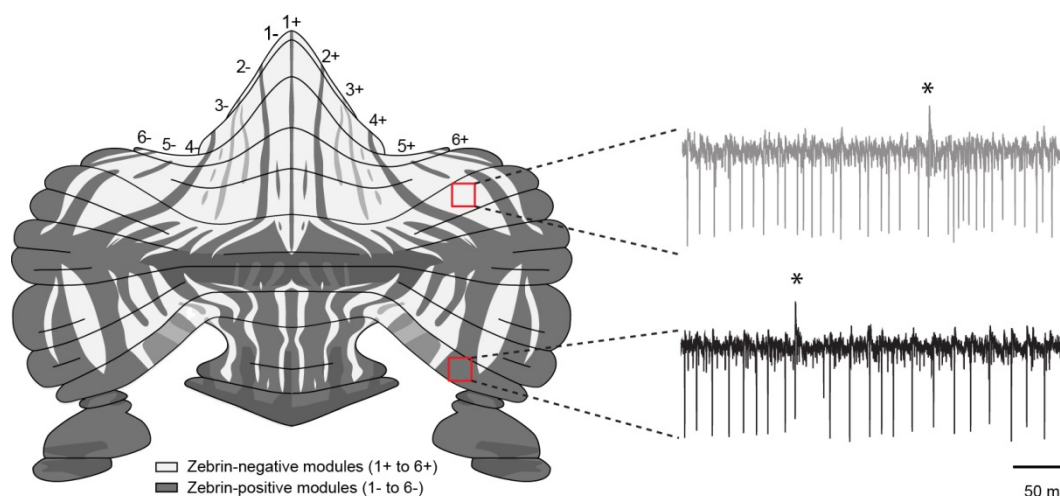


Figure 5. Purkinje cell activity differs based on zebrin identity. The alternation of zebrin-positive (gray) and zebrin-negative (white) zones gives rise to the cerebellum cortex a striped pattern. Right showing example traces of single unit Purkinje cells from extracellular recording in zebrin-positive and negative zones respectively. Asterisks indicate complex spikes.

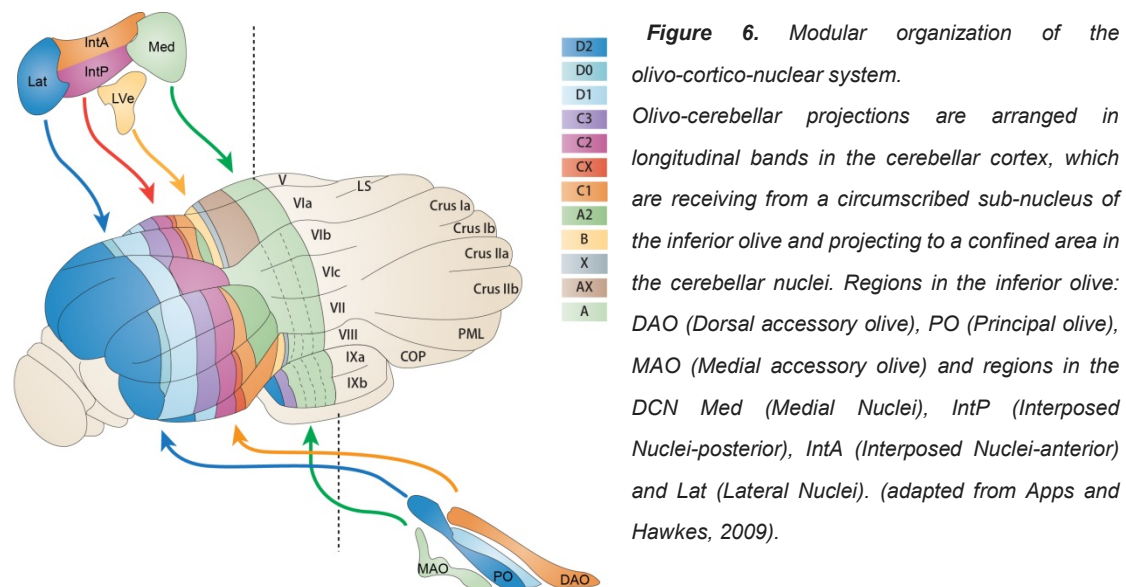
Complex spikes

The complex spike (CS), evoked through CFs activation, is characterized as a somatic sodium spike and a few spikelets ride on a depolarization plateau²⁵. The average spontaneous CS firing frequency is about 1 Hz, but can overshoot to 10 Hz for very short periods due to specific conductances in the olivary membranes²⁶. PCs that are contacted by the same olivary neuron can be activated synchronously due to the gap-junction mediated electrotonic coupling in the inferior olive (IO)²⁷. In vivo, each CS is followed by a pause, known as “climbing fiber pause”, in the simple spike activity, and of still unclear origin²⁸.

The CS is initiated by glutamate release from numerous CF contact sites on a single PC, thus leading to a large postsynaptic depolarization²⁹. Fast excitatory postsynaptic current at CF-PC synapses is mainly mediated by AMPAR, and to a much less extent involves kainate and NMDA receptors^{30,31}. Subsequently, dendritic P/Q and T-type voltage gated calcium channels (VGCC) are activated³². Calcium influx from NMDA receptors and released from the internal stores also participates in the postsynaptic response. Since large (BK) and small (SK2) voltage-gated potassium channels are reported to co-localize with VGCCs, calcium activated potassium channels are of particular importance in regulating the amount of calcium influx during CS³³. When it spreads to the axon hillock, fast sodium conductance generates the initial spike in the CS waveform³⁴. The plateau phase recorded from PC soma probably attributes to the dendritic calcium channels and the de-inactivation of somatic resurgent sodium channels.

Following this initial fast spike and the sodium channels de-inactivation, two slow components constitute the rest of the CS waveform, namely a first VGCC-mediated phase with spikelet's sitting on a voltage plateau and a second potassium channel-mediated repolarization and slow after-hyperpolarization phase. The membrane repolarization is likely to

be mediated by large-conductance calcium-dependent potassium channels and resurgent sodium currents, while the slow after-hyperpolarization is likely to be mediated by the small-conductance potassium channels and non-inactivating sodium currents^{17,32}.



Zebrin-identity

The apparent homogeneity of the cerebellum's crystalline cortical structure and the absence of clear structure-function relationships have long nourished the assumption that the cerebellar cortex was, for all practical purposes, physiologically uniform. This concept of a homogenous cortex existed despite accumulating evidence for the presence of a sub-organization in the cerebellar cortex. However, recently emerging data show that cerebellar modules can be further divided into smaller compartments in the sagittal plane by the expression of a molecular marker called zebrin II, a glycolytic enzyme aldolase C which is selectively expressed in PCs^{4,11,35,36}. In particular, zebrin II is differentially expressed by symmetric bands of zebrin-positive (Z+) and alternative zebrin-negative (Z-) PCs (Fig. 5), and this kind of striped-organization is highly conserved in all vertebrate classes, varying from birds and mice up to primates including humans³⁷⁻⁴⁰. The CF input, restricting afferent input to either Z+ or Z- PCs, adheres to the zebrin-identified modules, and in turn, PCs with the same zebrin identity converge to designated parts of the cerebellar nuclei^{4,41} (Fig. 6). Moreover, both the firing rate of simple spikes and complex spikes of cerebellar PCs were recently found to be selectively higher in Z- modules, which was proved subsequently to be the result of the intrinsic properties of PCs⁴². Given these features, it is becoming increasingly clear that zebrin-identified modules as more fundamental architecture not only differ in their input and output relations but also differ in operational capabilities and may play differential roles in distinct cerebellar function. Yet, how these well-defined cerebellar modules can give rise to differential forms of cerebellar learning remains to be elucidated. Recent technical developments that are available to tackle this question (see Chapter 3 for detailed description).

Behavioral paradigms of motor control and learning

The cerebellum has mainly been implicated in various forms of motor behaviors and learning. Disruptions of cerebellar functioning, e.g. through stroke or neurodegenerative disorders, affect coordination and adaption of many types of behaviors such as gait, eye movements and even speech^{43,44}. Thus, the key function of the cerebellum is sensorimotor control.

Compensatory eye movements

One of the most investigated motor functions is the compensatory eye movement. Compensatory eye movements and their adaptation is used study the cerebellum because: a) the same test can be applied in human patients facilitating translational research, b) the brain areas involved and their anatomical connectivity is described in detail, allowing for targeted (cell- or area-specific) manipulations, but also recordings and c) the behavior is very reproducible due to the nature of the movement (reflex), meaning that less animals are needed to identify differences. Hence, compensatory eye movements are one of the most suitable model systems to understand the neural code and locations of learning, which is an important goal in itself (see details in Chapter 1.2).

Species with a retinal fovea (area of retina with increased density of specialized cells) are equipped with other types of eye movements, like smooth pursuit, that are related to compensatory eye movements. In species that lack a fovea, like rodents, the basic performance of compensatory eye movements are optokinetic reflex (OKR), vestibulo-ocular reflex (VOR) and visually-enhanced VOR (VVOR) (**Fig. 7A**). OKR is driven by movement of the visual field - the eyes follow the surrounding. VOR is driven by movement of the animal in darkness - the eyes move in the opposite direction as the head. VVOR is performed when the animal is rotated in an illuminated surrounding - the eyes follow the surrounding and compensate for the movement of the head. The neuronal circuit of these responses centers on the vestibulocerebellar system, e.g., flocculus as well as vestibular nucleus.

The flocculus is subdivided in several zones; vertical axis zones and horizontal axis zones. These zones are functionally different in that the neurons of each zone predominantly encode eye movement around the vertical axis and a horizontal axis⁴⁵. The orientation of these axes is related to the position of the vestibular sensory organs, e.g., the semicircular canals in the inner ear. The anterior and posterior semicircular canals innervate superior and inferior rectus and oblique eye muscles to evoke eye movements in the vertical plane around horizontal axes. The horizontal canals innervate the medial and lateral rectus muscles and thereby evoke eye movements in the horizontal plane around the vertical axis. Whereas the vertical axis is predefined, the horizontal axis can be rotated. Rotations of the head around horizontal axes that are perpendicular to the orientation of the anterior (45° ipsilateral azimuth) and posterior (135° ipsilateral azimuth) semicircular canal will evoke an eye movement. The floccular PCs in the horizontal axes zones (HA PCs) respond with modulation of spiking frequency most sensitively to eye movements around a horizontal axis 135° ipsilateral azimuth. Similarly, rotations of the eye around a vertical axis also evoke a response in PCs within vertical axes zones (VA PCs). As natural eye movements will be a mixture of horizontal and vertical axes, both HA and VA PCs will be involved in the coordination of such complex movements. Notably, sensorimotor information transmitted by the parallel fibers and signals coming from the inferior olive through climbing fibers modulate the firing frequency and temporal patterns of both simple and complex spikes resulting in reciprocal firing configuration. For example, during

OKR, complex spike and simple spike activities in Purkinje cells of the vestibulocerebellum modulate out of phase with respect to each other over a wide range of frequencies (**Fig. 7B**).

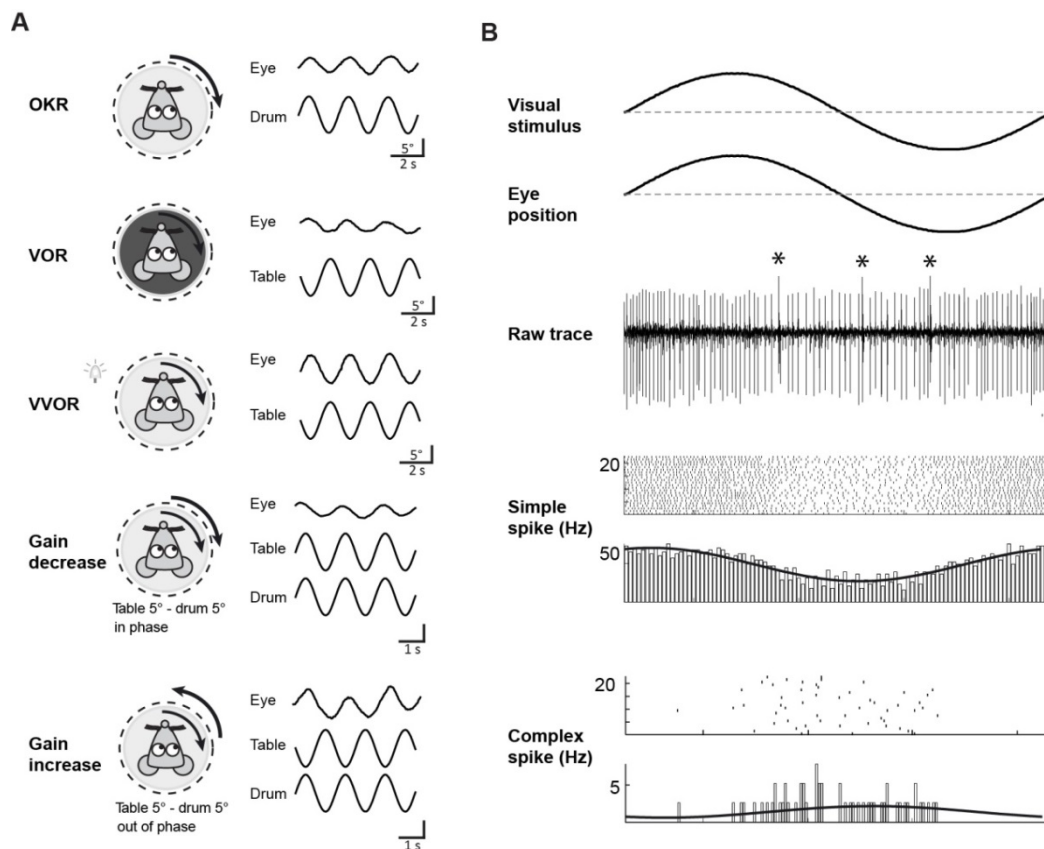


Figure 7. Compensatory eye movement behavioral paradigm. **A**, The recording mouse is placed in the center of a turntable (vestibular stimulus) and surrounded with a random dotted drum (visual stimulus). Compensatory eye movements were induced by sinusoidal rotation of the drum in light (OKR), rotation of the table in the dark (VOR) or the rotation of the table in the light (visually enhanced VOR, VVOR) with an amplitude of 5° at 0.1-1 Hz. Motor learning was studied by subjecting mice to mismatched visual and vestibular input. Rotating the drum and table simultaneously, in phase or out of phase (at 0.6 Hz, both with an amplitude of 5°) in the light will induce an decrease or increase of the gain of the VOR, respectively. **B**, Recording of a floccular Purkinje cell (VA cell) during sinusoidal optokinetic stimulation, shows modulation of both simple and complex spikes (asterisks). Ipsilateral rotation (here: down slope of the sine curve) is related to a decrease in simple spike firing rate, whereas an increase in complex spike. Histograms and raster plots further demonstrate this reciprocal relationship.

Eyeblink conditioning

The other most extensively studied forms of motor learning is eyeblink conditioning. In a typical eyeblink conditioning experiment, a conditioned stimulus (CS), which usually consists of an auditory tone or light stimulus, precedes the unconditioned stimulus (US), typically peri-ocular stimulation, like an air puff or electrical stimulation. The interval between the CS and US usually is a couple of hundreds of milliseconds. Repeated pairings of CS and US will gradually lead an eyelid closure in response to the CS only, which is called the conditioned response or CR (**Fig. 8A-B**).

Importantly, eyeblink CR is not just a matter of all or nothing, but rather is a optimally

timed motor response.. In well-trained subjects the eyeblink CR starts just prior to and peaks at the onset of the US^{46,47}. This finding motivated scientists to use eyeblink conditioning not only as an example for associative learning but also as a paradigm to study motor learning. Of course the eye movements and eyelid movement are extremely simple compared to for instance limb movements. Still, they share the same properties, like timing (onset, peak), amplitude (strength), duration, and velocity of the movement. All these parameters can be relatively easy and reliably measured by monitoring the eye.

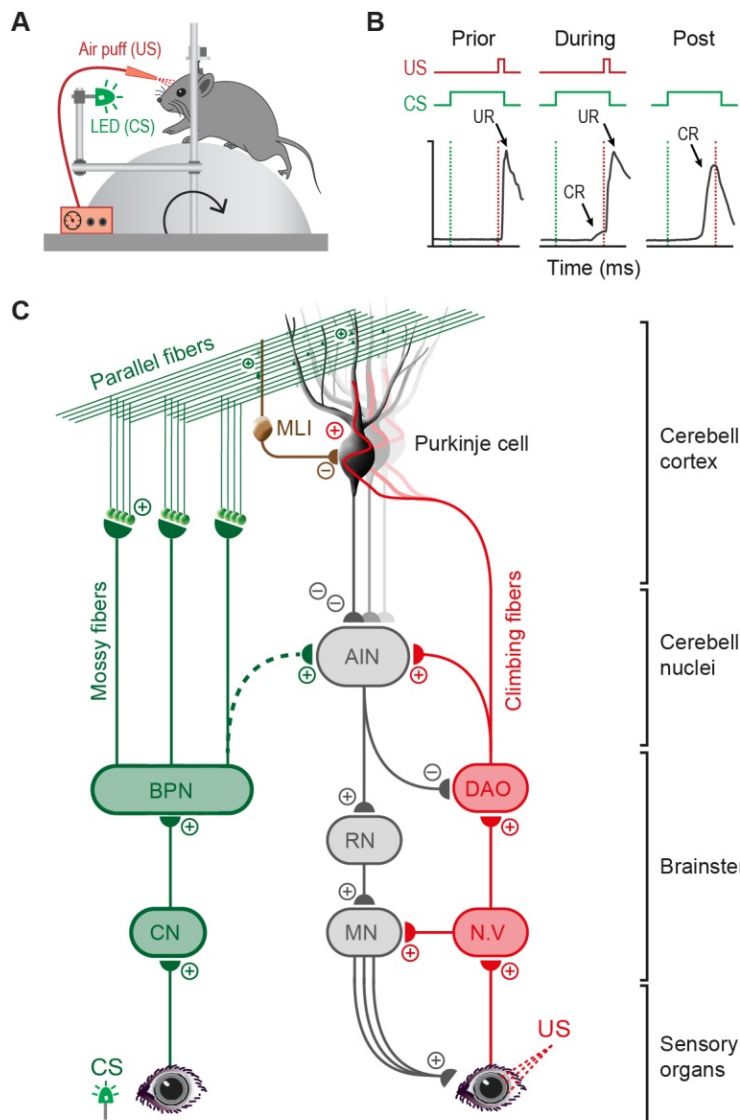


Figure 8. Eyeblink conditioning behavioral paradigm. **A**, Two stimuli, the unconditioned stimulus (US, here is an air puff) and the conditioned stimulus (CS, here is a beam of light) are presented to the recording mouse. CS and US are presented in a delay paradigm, which means that the onset of the CS precedes the onset of the US but both stimuli co-terminate. **B**, Before training the CS will not elicit an eyelid closure. At the very beginning of training the CS will not elicit a conditioned response (CR), whereas the US elicits a reflexive eyelid closure (unconditioned response; UR). After training, the CS will elicit a perfectly timed eyeblink CR, which peaks exactly at the point where the US would be delivered. Note that the shape of the timed CR differs from the reflexive UR. **C**, Neuronal circuits involved in eyeblink conditioning. Purkinje cells in eyeblink controlling microzones in the C3 and D0 zone of cerebellar lobule

HVI receive climbing fiber input from the dorsal accessory olive (DAO), which relays sensory information from the peri-orbital facial region (US pathway in red). Additionally, the same Purkinje cells receive a continuous stream of virtually all sensory information from some two hundred thousand parallel fibers, originating from mossy fibers from various brainstem nuclei including the basilar pontine nuclei (CS pathway in green). These Purkinje cells project to the anterior interposed nucleus (AIN), which in turn innervates, via the red nucleus (RN), the motor neurons that control the eyeblink (CR pathway in gray). CN, Cochlear Nucleus, MLI, Molecular Layer Interneuron, MN, Motor Neurons innervating the eyeblink muscles, including oculomotor nucleus (III), accessory nucleus (VI), and facial nucleus (VII), N.V. Trigeminal nucleus (V).

Molecular pathway and mechanisms for motor learning

The most fascinating property unique to neurons is their ability to adapt their structure or function in response to previous experience. The changes can take place in the morphology of dendrites and boutons, the neuronal excitability, and the synaptic plasticity. This latter type of plasticity, postulated by Donald Hebb, consists of two forms: long term potentiation (LTP) and long term depression (LTD), which have been extensively studied during the last decades for their involvement in variety of learning and memory.

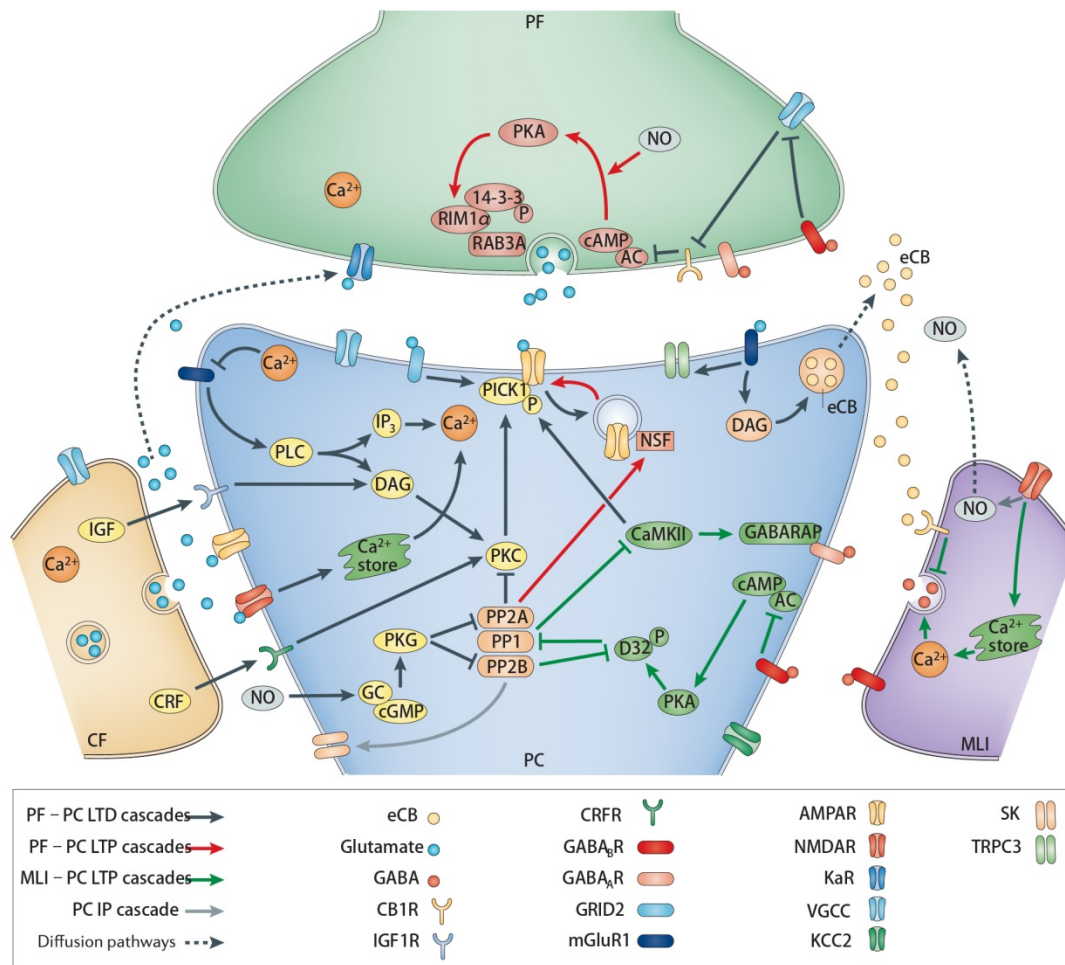


Figure 9. Molecular pathways involved in multiple forms of synaptic plasticity that can occur at synapses between PFs, CFs or MLIs and PCs. Pathways involved in long-term depression (LTD) at PF–PC synapses are marked in black, and pathways involved in long-term potentiation (LTP) at PF–PC synapses are marked in red. Green arrows indicate pathways involved in LTP at MLI–PC synapses and the grey arrow indicates the molecular cascade for intrinsic plasticity (IP). Freely diffusing messenger pathways are marked in dashed arrows. Figure from (Gao et al. 2012).

PCs have the necessary molecular machinery to support those synaptic strength changes and indeed many studies have shown that they express both types of synaptic plasticity (**Figure 9**). Throughout the decades studies were focused on the parallel fiber to Purkinje cell synapse (PF-PC). The PF-PC synapse has been considered the core of cerebellar dependent learning, due to its location within the circuit and its high input convergence. In the 70s the

historical triad composed by David Marr, James Albus and Masao Ito independently proposed that depression in the strength of the PF-PC synapses under the control of CFs activation underlie cerebellar learning⁴⁸⁻⁵⁰. Various mechanisms underlying LTD have been since demonstrated, and the plasticity has been shown to be bidirectional, i.e. LTP, is achievable by high-frequency PF stimulation in absence of CF activation^{51,52}. Both LTD and LTP induction strictly correlates with the increase in intracellular calcium caused by the afferent fibers activation, and contrary to what happens in any other glutamatergic synapse equipped with both AMPA and NMDA receptors, low calcium correlates with LTP and PF activation alone (no NMDAR activation, mGluR1-IP3 mediated Ca²⁺ rise), while high calcium induced by conjunctive CF and PF stimulation provokes LTD (NMDAR activation at the CF synapses, strong depolarization which opens VGCC)^{6,53}. Downstream of calcium, the signaling cascade supporting the plastic synaptic changes involves a delicate balance between calcium-activated kinases and phosphatases such as PKC, CaMKII, PP2B, which eventually will trigger the insertion/removal/phosphorylation of ligand-gated receptors and control the direction of synaptic plasticity⁵⁴⁻⁵⁶.

1.2 A new perspective on vestibulo-ocular reflex adaptation

Bin Wu, Chris de Zeeuw and Martijn Schonewille

Department of Neuroscience, Erasmus Medical Center, 3015 GE Rotterdam, The Netherlands

Abstract

The gain adaptation of vestibulo-ocular reflex (VOR), generated in order to compensate the consequences of head movements whilst stabilize the images of visual scenes on the retina, is a long-standing experimental model of cerebellar reflexive movement. This compensatory eye movement requires a direct transformation of sensory input into appropriate motor output without immediate sensory feedback, and learning occurs during this process at the same time. However, how and where the adaptation in association with motor learning undergoes, has been long debated. In this review, we recapitulate the anatomical and physiological characteristics of the components of the VOR circuit, and illustrate how it provides precise adjustments in response to multisensory information by adaptively increasing or decreasing the speed and amplitude of eye movement. Moreover, we present evidence showing that these two types of VOR adaptation are mediated via different pathways and encoded at different loci: gain-increase learning is accomplished in the floccular complex whereas gain-decrease learning is induced in the vestibular nucleus. Finally, we summarize plausible cellular mechanisms for VOR learning in both structures of cerebellar cortex and vestibular nucleus. This review, by using the VOR, sheds light on the question that where and how specific form of motor learning emerges in response to the outside world.

In preparation

Introduction

Skilled movements, such as riding a bike or playing the piano, are all acquired and improved through learning^{21,57}. Although motor learning plausibly involves the multiple processes of sensorimotor integration, phenomena observed in laboratory-based tasks tend to be conceptualized in terms of one single process: adaptation⁵⁸. The adaptive process in association with motor learning is commonly considered as a reciprocal change of one behavior for another, or the reciprocal modification of motor output in response to gain changes in sensory input⁵⁹, thereby is essential for the optimal adjustment of motor behaviors in a particular environment. Several simple behavioral models have been developed in laboratory in attempts to unravel the underlying neural principles of motor learning, among which vestibulo-ocular reflex (VOR) is likely to be the best-studied one.

The VOR is a reflexive compensatory eye movement that stabilizes the image on the retina, by moving the eyes in the opposite direction to the head; its tremendous performance throughout life is maintained by experience-dependent learning, which relies on the cerebellum^{48,49,56,60-63}. The gain of the rotational VOR, defined as the ratio of head velocity to eye velocity, is desired to be 1.0 under physiological conditions, as the eye moves equally to the head, thus leading to perfect image stabilization⁶⁴. The gain of VOR can either increase or decrease by experimental manipulating the relationship between the vestibular head movement and visual stimulus movement, and this capacity of VOR is referred to as the so-called adaptation^{65,66}. For example, if the head moves in phase with the visual stimulus (gain-decrease), the VOR is adaptively decreased to elicit eye movements with lower velocity (gain < 1.0), ideally capable to keep the target stable on the retina. On the other hand, if the head moves out of phase with the visual stimulus (gain-increase), then an adaptive increase in eye velocity ensues (gain > 1.0).

Adaptation, a prime form of motor learning, facilitates a gradual decrease of the motor error and makes the realized movement more akin to the desired movement^{67,68}. VOR adaptation occurs whenever images move persistently during head movement, wherein it is indispensable for ensuring a clear vision in an ever-changing environment. In humans, during the first few years after birth, the VOR must be continuously adjusted to compensate for larger changes in the size of the head⁶⁹; for mature individuals, it becomes even more important whenever in the face of changes within the motor system (fatigue, injury to vestibular organs, eye-muscle weakness, or aging) and varying visual requirement (wearing corrective lenses).

The adaptation of the VOR, enabling sensitive, quantitative assessment of experience-dependent plasticity, has been elaborated extensively. Ever-emerging evidence shows significantly molecular physiological and functional changes in the vestibulocerebellar system during VOR adaptive process. Meanwhile, considerable controversy has arisen concerning where and how these plastic changes occur. Thus, we reviewed recent findings of behavioral, electrophysiological, pharmacological, and lesion studies of VOR adaptation, in order to advance our understanding of the adaptation of VOR as well as motor learning.

Anatomical circuitry of vestibulo-ocular reflex

To acquire clear vision, the VOR needs to correspond fast to compensate head movement. By using a three-neuron-arc⁷⁰, signals from the semicircular canals are sent as directly as

possible to the eye muscles, thus eye movements only lag the head movements by only 5-6 ms in the primate⁷¹.

The three-neuron-arc pathway mediating the VOR and its adaptation has been extensively investigated since it was first described by Lorente de No' in 1933⁷². It starts from the vestibular system in the inner ear, where semicircular canals (SCC) get excited by head rotation and send their impulses via the primary vestibular afferent (cranial nerve VIII) through the vestibular ganglion (VG). VG then relays sensory information to the ipsilateral secondary vestibular nuclei (VN) that in turn projects bilaterally to the third order - extraocular premotor neurons incorporating oculomotor nucleus (OMN) and abducens nucleus (ABN). OMN and ABN drive medial rectus (MR) muscle and lateral rectus (LR) muscle respectively.

Besides, the cerebellum plays an important role in the control of compensatory eye movements⁷³. The major cerebellar substrates in this context are the flocculus and the adjacent ventral paraflocculus, which are together referred to as floccular complex (FC), situated in the ventrolateral cerebellum. FC and VN send projections reciprocally to each other, forming an essential side loop or indirectly pathway for eye movements. Nevertheless, some VN interneurons that are devoid of Purkinje cell inputs, are presumed to be indispensable in VOR adaption. For instance, flocculus projecting neurons (FPNs), carrying vestibular information, extend their axonal projections into FC and form mossy fibers that project to the granule cell (GrC) layer⁷⁴. Each Purkinje cells in FC is also contacted by a single climbing fiber originating from the contralateral inferior olive, which is thought to offer an "error" signal for VOR learning.

The anatomy of the VN has been well characterized, and four major parts are found: the medial vestibular nucleus (MVN), the superior vestibular nucleus (SVN), the lateral (or Dieters) vestibular nucleus (LVN), and the inferior (or descending) vestibular nucleus (IVN). Neurons that are sensitive to horizontal rotations are found primarily in the rostral MVN and the ventro-LVN⁷⁵⁻⁷⁷; while neurons that are responsive to vertical rotations primarily locate in the SVN, MVN, and group Y^{78,79}. Consistently, floccular zones that are responsible for horizontal eye movements largely project to MVN and LVN, while zones reflecting vertical eye movements target primarily SVN and group Y in mouse⁴⁵. These targeting interneurons within the VN are termed flocculus target neurons (FTNs)⁸⁰⁻⁸³. Here, as we only pay attention on the horizontal eye movement, the VN mentioned in the following section is mainly referred to MVN and LVN, unless state otherwise.

In VN, many different types of interneurons have been identified based on their behavioral responses and their synaptic connections. Among them, mostly two classes participate in the horizontal VOR pathway. The first class is so-called position-vestibular pause (PVP) neurons, concentrated in the ventro-LVN. PVPs project to and excite the contralateral ABN which in turn activates ipsilateral OMN via medial longitudinal fasciculus (MLF)^{84,85}, and ultimately innerve the ipsilateral medial rectus (MR) muscle. PVPs robustly encode head velocity signals as well as eye position signals, and especially feature in pause during saccades^{76,86}. The second class is FTN neurons mentioned above. FTNs receive inhibitory afferents from the flocculus and excitatory inputs from the vestibular nerve⁸⁷⁻⁹⁰. In addition, FTNs project to and inhibit the ipsilateral ABN which project to the ipsilateral lateral rectus (LR) muscle and the contralateral OMN that innerve contralateral MR muscle⁹⁰. Notably, FTNs also send excitatory efferent to the ipsilateral OMN which projects to ipsilateral MR muscle, thus generating the horizontal eye

Figure 1 / Circuitry of the horizontal vestibulo-ocular reflex

Schematic illustration of neural pathways and relevant firing responses involved in the control of the horizontal VOR during clockwise head rotation. The semicircular canals (SCC) first detect head rotation signals, and then vestibular information is transferred by vestibular ganglion (VG) to the ipsilateral vestibular nuclei (VN). These excitatory inputs drive flocculus projecting neurons (FPN), flocculus target neurons (FTN) and position-vestibular pause neurons (PVP) within the VN. The Purkinje cells (PC) in the floccular complex (FC), receive their inputs either through mossy fibers (MF) originating from FPN or via climbing fibers (CF) deriving from contralateral inferior olive (IO), and provide an inhibitory input to FTN. The FTN inhibits the ipsilateral abducens nucleus (ABN) which innervates lateral rectus (LR) muscle, meanwhile stimulates the ipsilateral oculomotor nucleus (OMN) which drives medial rectus (MR) muscle. Also note that PVP projects to cross the midline and excites the contralateral ABN which in turn activates ipsilateral OMN via medial longitudinal fasciculus (MLF) and ultimately innervates the ipsilateral MR. In this case shown in the figure, rightward head rotation cause hyperpolarization in the left SCC whereas depolarization in the right one, which is followed by inhibition in the left VN, and excitation in the right VN. In addition to the inhibitory inputs from PCs in the FC to FTN, the left ABN is expected to be activated through an ipsilateral process of disinhibition as well as excitation from contralateral FTN inputs, and eventually facilitates the contraction of the left LR. The left OMN, however, receives inhibitory commands from both sides, thus leading relaxation of the left MR. In the end, the left eye moves leftwards. The same head movement resulting in an increased signal in the right SCC, has similar connections and effects on the right eye (not shown).

Masao Ito first proposed a widespread belief of “flocculus hypothesis”⁶⁰, on the basis of the classic Marr-Albus theory^{48,49}. In his framework, Ito postulated that the parallel fiber-Purkinje cell synapse in the flocculus is the site of VOR adaption, and the underlying mechanism is cerebellar dependent LTD. Climbing fibers from the inferior olive also participate in this process as “teachers”, relaying an error signal of visual motion. The error signal, reflecting either too big or too small motion of images on the retina (referred to as retinal slip), guides the adjustment of synaptic efficacy between the parallel fibers and the Purkinje cells, thus inducing a compensation in the gain of eye movement. According to Ito, whenever that gaze consistently moves in space while the head moves, learning occurs and continues until the retinal slip signal encoded by the climbing fibers becomes zero.

Many lines of experimental evidence support this hypothesis. Lesions of the flocculus or flocculus complex in rabbits⁹⁶⁻⁹⁸, cats⁹⁹, or in primates^{95,100}, lead to a complete inability in learning new VOR gains. Temporary inactivation of the flocculus using lidocaine, a sodium channel blocker, just after learning appears to prevent VOR learning^{101,102}. Blockade of excitatory synapses in the flocculus has the similar effect¹⁰³.

Extracellular single unit recordings of flocculus Purkinje cells in rabbits showed an in-phase as well as out of phase discharge pattern relative to head velocity induced by sinusoidal rotation¹⁰⁴. Dufossé and colleagues¹⁰⁵ further showed that this differential discharge modulation of floccular Purkinje cells could decrease or increase the VOR gain, respectively. Similarly, other in vivo recordings consistently suggest an indispensable role of the flocculus during VOR adaption^{106,107}. Consistently, Watanabe identified a specific zone in the FC, with PCs whose simple spike discharge was modulated in conjunction with the horizontal VOR¹⁰⁶. Schonewille and colleagues mapped the flocculus topography in more details in mouse, and showed that zone 2 and 4 responded best to the optokinetic stimulation of the vertical axis (VA zones)⁴⁵. They also found that both simple spike and complex spike

activity of Purkinje cells exhibited clear changes in the strength of their discharge modulation during horizontal visual stimulation.

Furthermore, the dorsal cap of the inferior olive, receiving direct projections that relay the visual signal from the accessory optic system and the nucleus of the optic tract^{108,109}, projects climbing fibers to the flocculus. These climbing fiber inputs serve as a performance error signal and fire in response to image motion^{104,110-112}. Without the visual error signal, rotation in the dark by itself could not alter the gain of the VOR¹¹³. Similarly, impairment of the inferior olive or the optic tract abolishes the ability to change the gain of the VOR¹¹⁴⁻¹¹⁷.

Together, these results suggest that flocculus and climbing fibers are required for the VOR learning.

In 1981, however, Miles and Lisberger¹¹⁸ proposed a different view - “vestibular nuclei hypothesis”. This hypothesis proposes that when there is a visual-vestibular mismatch, floccular Purkinje cells outputs encoding the error signal, induce plastic changes in the level of FTNs in the vestibular nuclei, so that the vestibular nuclei instead of the flocculus, is the exclusive locus for VOR adaptive modifications. This theory is upheld because, according to Miles and Lisberger, Purkinje cells modify their discharge in the wrong direction, conflicting the changes to drive the expected motor learning¹¹⁹; in addition, after the onset of head motion, the latency of changes in the Purkinje cells (about 100 ms) are too long to induce the firing changes in the FTNs whose latency is about 13 ms in the cat, therefore, the response of Purkinje cells could be a secondary reflection of adaptation-related neuronal changes occurring downstream in the brainstem by way of the feedback loop from vestibular nuclei to the flocculus^{86,120}. The delay of latency between climbing fiber and vestibular signals is considered to be an essential requirement for VOR learning, as it is thought to indicate Purkinje cells how to process these signals.

Since the FTNs receive both vestibular and Purkinje cell efferent directly, plasticity is possibly induced at the primary FTN synapses, guided by Purkinje cell inputs⁸⁸. In support of this model, Luebke and Robinson assume that the site of learning must be the brainstem, as silencing the flocculus by high-frequency stimulation of climbing fibers prevented the gain of the VOR from returning to its pre-adaptive value¹²¹. Indeed, if climbing fiber signaling is eliminated, which means abolished error signals to the flocculus, the VOR can still perform a gain-decrease learning¹²².

Over the years, as more evidence of electrophysiological experiments showing up, Lisberger further modified “vestibular nuclei hypothesis” to “multisite hypothesis” that VOR motor learning lie in both the flocculus as well as the brain stem¹²⁰. On one hand, investigators have continued to gather evidence in support of Ito's hypothesis. During the VOR in darkness, Purkinje cell responses are shown to be modified in a way that is appropriate to support motor learning in monkeys¹²³ and in rabbits¹⁰⁷. Lisberger and colleagues also found that the discharge modulation of Purkinje cells was actually changed in a correct direction compatible with the associated changes which were responsible for the adapted behavior^{86,95}. On the other hand, recordings from FTNs in conjunction with VOR learning reveal pronounced changes in their firing responses in both horizontal⁹⁵ and vertical eye movement^{78,124,125}, indicating a contribution of FTNs to the plasticity. Specifically, it has been shown that silencing or removal of the flocculus after chronic VOR adaptation leads to a partial loss of learned VOR changes⁸⁵; even in some acute testing following learning, only partial changes in VOR gain

are found to be affected by inactivation of the floccular complex^{101,126}. In this schema, the modifiable synaptic weights in either Purkinje cells in the flocculus or the FTNs in the vestibular nuclei initially generate the adapted motor learning, but the long-term storage occurs downstream of Purkinje cells in the brainstem^{93,125}.

Accumulating studies have been in efforts to delineate a simple picture to unravel the sites of the adaptive changes of the VOR; nevertheless, the complexity of the multi-sensory circuitry prevents the specification of causality among the changes in the neuronal activities and the assignment of each component in the process of the adaptation of the VOR. We argue that none of the three models aforementioned can accurately fit all the actual results, and each one has more or less criticisms. First, many studies are based on lesion experiment. Actually, specific lesions are usually hard to acquire and often result in damage to the surrounding structures which may cause secondary effects. For instance, the ablation of the flocculus may result in retrograde degeneration in the olivocerebellar neurons in the dorsal cap of the inferior olive^{127,128}. Next, some studies focus on interrupting the chronic learning or long-term learning, which may not be the same as initial adaptive period, due to the transformation of memory storage. Therefore, we will rule out those studies on the long-term learning and merely emphasize on the studies about the short-term of learning or so-called memory engram. Lastly, it has also been shown that motor learning is featured with direction-selectivity^{110,111,129-131}. A big challenge to the majority of previous studies is to preferentially select Purkinje cells based on their directional sensitivity by using sinusoidal stimuli. Therefore, the absence of clear correlation between Purkinje cell simple spike activity and VOR adaptation may be a population analysis artifact, thus hampering the interpretation of directional preference as well as selectivity of learning locus.

A modified viewpoint of multisite hypothesis

Recently, Voges and colleagues designed an ingenious experiment by using a sigmoidal, rather than sinusoidal, combination of visual and vestibular stimuli which could optimally isolate the responses of Purkinje cells to a specific direction (**Figure 2A**). They provided convincing evidence showing that adaptation to the visual stimulus is more pronounced during contraversive head movements with respect to the recording side, which coincides with the preferred naso-temporal direction of eye movements driven visually; and the learned changes in gain-increase VOR adaptation were quantitatively reflected in the potentiated activity of Purkinje cell simple spike. They also asserted that the locus of neural correlates for VOR adaptation is paradigm specific. In other words, to make learning possible, the instructive signals that each learning site receives must be able to distinguish different stimulating conditions: whether it is gain-increase training or gain-decrease training. Hence, the question comes to what are the differences between gain-increase learning and gain-decrease learning in terms of the behavioral consequences as well as the underlying plasticity mechanisms.

Simultaneously, rapid advances in genetics and optogenetic technology have provided powerful tools that help us better understand the dichotomy between gain-increase and gain-decrease. Primarily, emerging studies on specific mutants in which various forms of plasticity and/or parts of the network from cerebellar cortical to vestibular nucleus are affected, show that gain-increase and gain-decrease exhibit a different vulnerability to a specific interference (see details in **Table 1**). Gain decreases do not require nitric oxide¹³², mGluR1

receptors¹³³, both of which are thought to be important to long-term depression (LTD), or directly cerebellar parallel-fiber long-term potentiation (LTP) or LTD^{54,134}. In other words, either

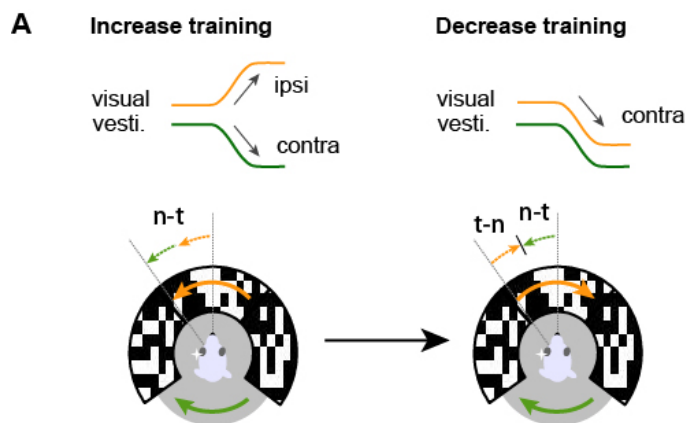
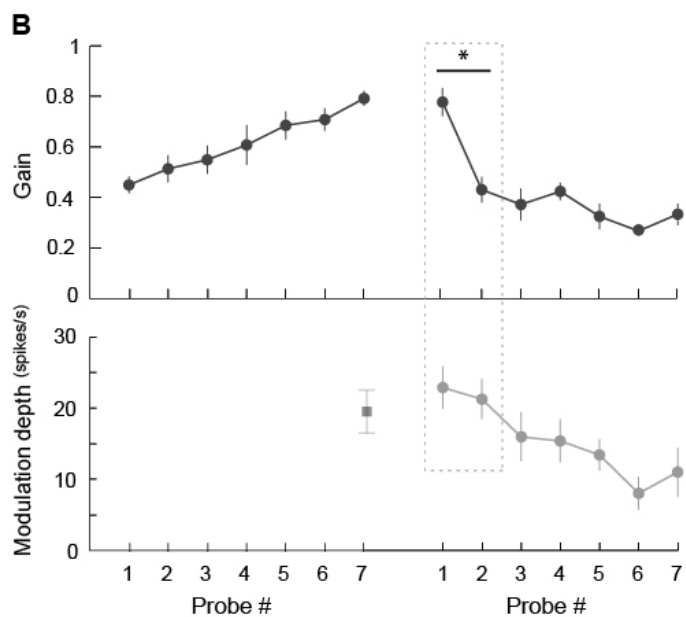


Figure 2 / Neuronal correlates for VOR gain-increase and gain-decrease adaptation

A, scheme depicts the sigmoidal stimulations in the preferred direction during gain-increase training (left) induced by ipsiversive visual (orange) and contraversive vestibular (green) stimulations and gain-decrease training (right) induced by contraversive visual and contraversive vestibular stimulations.

Note that both ipsiversive visual and contraversive vestibular stimulations can induce naso-temporal (n-t) eye movement in the gain-increase paradigm, which results in a larger gain of VOR; in the gain-decrease paradigm, the eye movement would be restricted due to the conflicting supposed directions of eye movement induced by contraversive visual and vestibular stimulations. B, given that gain-decrease training is conducted following gain-increase training immediately, the adapted changes in eye movement gain as a result of increase training can be reversed (top), and the increase in



simple spike firing after gain-increase training would return to near baseline levels during decrease training. However, eye movement gains decrease with an initial sharp drop after the first decrease training block followed by a slower decrease, whereas the depth of simple spike modulation (bottom) returned more gradually to baseline levels (shown in the frame), indicating that gain-decrease adaptation and changes in Purkinje cell simple spike activity follow different dynamics. (Modified from Voges et al. 2017 with permission)

mGluR1 blockade, or selective disabling of cerebellar LTP and intrinsic plasticity, will actually cause the gain to decrease in the paradigm that is supposed to cause increases^{54,133}. Gain increases are still possible if only LTD is impaired, underwent by LTP probably¹³⁴. In contrast, mutants lacking Ca²⁺/calmodulin-dependent protein kinase IV (CaMKIV), in which LTD is abolished, display impaired adaptation to VOR gain increases, whereas the adaptation to VOR gain decreases is normal¹³⁵. Furthermore, mutant mice lacking GABA γ 2 receptor subunits at the synapses of molecular layer interneuron to PC or mutants lacking PC-specific potassium chloride transporter (KCC2), both of which suffer from impaired inhibition onto their PC, show virtually normal gain-decrease learning, whereas gain-increase learning are strongly

affected^{6,21,136}. Similarly, transgenic mutants, in which the majority of granule cell output is impaired and both LTD and LTP are impaired, can still successfully complete the gain-decrease but not the gain-increase paradigm²⁰.

Hence, although there is a large variability among these studies, at least they illustrate two important points that the neuronal circuits engaging gain-increase and gain-decrease are different, and different mechanisms can come into play for different adjustments of gain.

Furthermore, VOR gain-increase adaptation shows a faster decay or less stable after elimination of the mismatch stimulation when compared to gain-decrease^{137,138}. This is in line with the observations that gain-decrease learning is not only easier to learn but also more easily generalized to a different context than gain-increase^{139,140}. These results suggest that the plasticity mechanisms supporting gain-decrease must be less synapse-specific, thus making it more broadly tuned for head rotation frequency, compared to that of gain-increase.

Last but not least, combined experiments that reciprocally pair gain-increase with gain-decrease have shown that VOR adaptations are reversible^{68,141} but in an asymmetric manner^{131,142}. In naive animals without prior learning experience, gain-decrease learning appears to be more potent and not easily reversed by following gain-increase learning which is saturated at a lower value¹³⁹. Similarly, Broussard and colleagues found that a cat wearing magnifying prisms for two hours was still not able to completely overcome one hour of prior experience with miniaturizing prisms. On the contrary, if gain-increase training precedes gain-decrease training when induced with sigmoidal stimulation, the animal is able to reverse its VOR gain completely to a level comparable to gain-decrease learning alone. Intriguingly, although the gain has already dropped to baseline levels after one training session, Purkinje cell simple spike modulation depth gradually declines over several training sessions but never dropped below baseline (**Figure 2B**). This mismatched pace between behavior and neuronal signal strongly suggests that gain-decrease adaptation and changes in Purkinje cell simple spike activity follow different dynamics, once more indicating that the locus for gain-decrease learning resides somewhere downstream of Purkinje cell output.

Taken together, with so many discrepancies that reflect the differential processes between gain-increase and gain-decrease, we propose a modified viewpoint of multisite hypothesis that both cerebellar cortex and vestibular nucleus are sites of VOR adaptation, more specifically, gain-increase learning lies in flocculus whereas gain-decrease learning locates in vestibular nucleus.

Thereby, the concomitant question comes: how does each component of the VOR circuitry in the two learning sites contribute for the differential adaptive consequences?

During gain-increase training, visual stimulus is rotated out of phase with vestibular stimulus, which is expected to cause a larger retinal slip. Note that there are two feedback loops to the flocculus: the visual error signal from climbing fibers via inferior olive, and the vestibular signal from the floccular projecting neurons (FPN) in the VN via the primary vestibular. These two excitatory feedbacks reach the very same PC, providing information about the discrepancy between the actual eye movement and the intended eye movement. Therefore, a larger retinal slip induces a stronger feedback, thus leading a higher gain of VOR. After gain-increase training, although the vestibular inputs from primary vestibular afferents to the vestibular nucleus is uniform, Purkinje cells become significantly more sensitive to head velocity signals than the baseline in normal conditions¹³⁷, which results in the potentiation of

their simple spike firing (herein referred to as potentiation), and thus an increase in their downstream target of vestibular nucleus. The increasing responses of PCs actually decrease the responses of FTNs in the vestibular nucleus, thus disinhibiting the inhibitory afferent to ABN and decreasing the excitatory afferent to OMN, eventually leading to an increase in the VOR gain (**Figure 3**).

If there is a larger retinal slip or error signal, one would expect an increased complex spike firing activity. However, experimental results are not congruent with this assumption. The changes in complex spike firing response are not correlated with the size of the retinal error¹⁴³, more specifically, corresponding to an increased simple spike firing rate, the complex spike firing rate is significantly decreased in the gain-increase learning¹³¹. Thus, complex spike, probably reflects changes in the adaptive state, rather than an error signal, consistent with a recent finding that climbing fiber provides predictive instructional input but not motor errors¹⁴⁴.

In contrast, in gain-decrease training, visual stimulus and vestibular stimulus are rotated in phase with each other with an identical velocity, thus leading to the minimized or under ideal conditions nullified retinal slip. As a result, no net drive would be encoded by climbing fibers, and no extra instructive signal would be sent to FTNs through Purkinje cells. Concurrently, persistent extra vestibular signals are conveyed to VN by vestibular nerve, and as a result, the homeostatic plasticity of FTNs, induced by PCs and vestibular nerve afferent, is broken. Hence, after gain-decrease training, we postulate that floccular Purkinje cells are still set in the default state same as baseline, however, the vestibular nucleus interneurons receiving vestibular inputs from vestibular ganglion, become less sensitive to head velocity signals¹⁴⁵. Given that vestibular nerve afferents are excitatory, and drive postsynaptic vestibular nucleus neurons firing tonically at high rates in quiescence¹⁴⁶, the decreased responses to the decreasing afferents induce an increased output of VN (herein referred to as attenuation), thus leading to an increased inhibitory input to ABN as well as an increased excitatory input to OMN, which results in a smaller VOR gain (**Figure 3**).

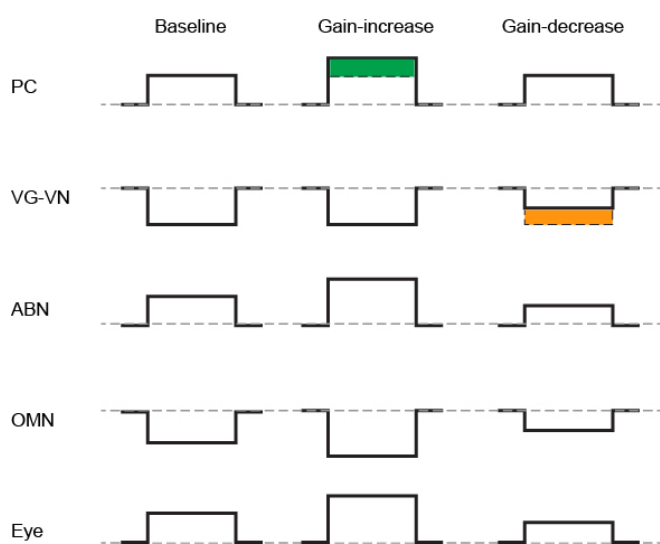


Figure 3 / Expected neuronal firing responses and eye movements to the stimulation in the learning direction. Schematic illustration shows the supposed neuronal firing changes of each synaptic component, compared to their corresponding default setting in a rest state (dash lines), when performing VOR baseline (left), gain-increase (middle) and gain-decrease (right) in the learning direction which is contraversive head movement with respect to the recording site. Upwards, potentiated firing response or ipsilateral eye movement; downwards, suppressed firing response or contralateral eye movement.

Note that Purkinje cell (PC) activity is potentiated exclusively in gain-increase learning (green area) whereas the activity of vestibular ganglion targeting neurons in the vestibular nucleus (VG-VN) is depressed exclusively in gain-decrease learning (orange area). ABN, abducens nucleus; OMN, oculomotor nucleus.

It should be kept in mind that, since flocculus is an indispensable component for VOR performance, it is also required for VOR gain-decrease adaptation by supporting a defaulted inhibition to VN, but presumably no significant modification taking place within itself. If the default setting of PC was altered, for example, by specific knocking out PP2B protein in PC⁵⁴, the basic VOR performance would be affected, as a result, the gain-decrease learning would be impaired too. Alternatively, instantaneous complementary adaptive changes might also be generated in flocculus, which work to offset the reduced sensitivity of VN neurons and contribute to the maintenance of plastic equilibrium. This could be the reason why Purkinje cell simple spike modulation depth declines but never drops below baseline (**Figure 2B**), and significant changes in complex spike activity, in the gain-decrease training preceded by the gain-increase training.

Plausible cellular mechanisms underlying VOR adaptation in differential sites

As discussed above, there is general agreement that VOR adaption takes place in multiple sites, and we further extend this prevailing model with more details: FC and VN are the sites responsible for gain-increase and gain-decrease respectively. Subsequently, a more fundamental question comes up: what cellular mechanisms are involved in the VOR adaptation in each locus?

In this regard, substantial studies have provided insight into the plasticity of cerebellar-dependent motor learning, and several forms of cellular mechanisms that have been proposed, including Hebbian (synaptic efficacy is strengthened after coincident activation of presynaptic and postsynaptic neurons) and non-Hebbian synaptic plasticity, as well as intrinsic excitability.

Hereinto, the most best-documented type of synaptic plasticity in the VOR adaptation is cerebellar parallel-fiber LTD. Ito and colleagues first demonstrated that climbing fiber activation could trigger LTD at conjunctively activated parallel-fiber synapses⁵⁰. Since then, the idea that the cerebellum learns by sculpting away synapses that cause errors through this non-Hebbian form of synaptic plasticity has had a prevailing influence on the cerebellar field. It has been found that parallel fiber inputs activate glutamate receptors including AMPA receptors and metabotropic receptors (mGluRs), whereas climbing fiber activation causes an increase in calcium influx into the Purkinje cell dendrite through voltage-gated channels¹⁴⁷. Considerable additional evidence has accumulated in support of the theory that cerebellar LTD plays a critical role in VOR motor learning. Pharmacological studies using blockers of parallel-fiber LTD of parallel fiber-Purkinje cell synapses^{132,148} as well as gene-manipulated mice lacking LTD^{56,135,149,150} suggest the unique role of cerebellar LTD in the VOR adaptation^{151,152}.

On the other hand, accumulating evident argues that LTD is not the only mechanism for the motor learning of VOR. As reviewed above, motor learning deficits are not complete in transgenic mice with impaired cerebellar LTD¹³⁵. Selectively disabling parallel-fiber LTD, by blocking internalization of AMPA receptors in PCs, does not affect VOR motor learning¹³⁴. Moreover, optogenetically driven floccular Purkinje cells simple spike activity during contraversive (but not ipsiversive) vestibular input indeed resulted in a higher VOR gain¹⁵³, providing direct evidence that Potentiation of Purkinje cell is required for VOR motor learning. More recently, Voges and colleagues provided further evidence that VOR gain-increase, rather

than gain-decrease, correlated with Purkinje cell simple spike potentiation¹³¹. Taken together, the results of these studies provide support for the notion that it might be the Purkinje cell simple spike potentiation that brought VOR gain-increase learning into play.

But how can both cerebellar LTD and LTP participate in increasing the gain of the VOR? One possibility is that during learning, LTP first comes into play to increase the active synapses and the number of signals available, and then LTD prunes these into an optimal configuration⁶.

Other sites, such as the glomeruli of the granular layer, also could contribute to learning in the absence of complex-spike error signals. In situations where the climbing fibers do signal errors, they are not restricted to causing learning at P-cell inputs, but may also trigger learning in the vestibular nuclei and at the synaptic inputs to the molecular-layer interneurons.

Arguably, even within the cerebellar cortex, other forms of plasticity may also influence the firing activity of PCs and thereby gain-increase learning. Such as the molecular layer interneurons, which directly control the rate and regularity of simple spike activity¹⁵⁴, and the glomeruli of the granule cell layer, which also could contribute to learning in the absence of complex spike error signals. Plasticity in the molecular layer and plasticity at the glomeruli may interact synergistically to adjust the response amplitudes for Purkinje cells with various on-directions⁶.

As reviewed above, the cellular characteristics of VN has been well described. There are five different cell types in the medial vestibular nucleus that receive Purkinje cell GABAergic innervation from the floccular complex¹⁵⁵. Among them, glycinergic and glutamatergic FTNs, with somata densely surrounded by Purkinje cell terminals, project axons to the ipsilateral abducens and oculomotor nuclei, respectively. FTNs that are sparsely innervated by Purkinje cells, are glutamatergic and glycinergic, projecting to the contralateral and ipsilateral abducens, respectively¹⁵⁶. GABAergic FTNs project to contralateral vestibular nuclei. Concurrently, these FTNs are expected to be innervated by glutamatergic axons from the primary vestibular afferents. The plasticity homeostasis of FTNs receiving multiple signals makes it possible for the site of adaptation.

Given the complicated anatomical topography, the cellular mechanisms underlying VOR adaptation in the VN is still enigmatic. Multiple forms and sites of synaptic plasticity described here provide the gain-decrease learning in the VN with several potential regulatory mechanisms.

It has been demonstrated that LTP presumably arises from the excitatory synapse between primary afferents and secondary vestibular neurons, which depends on NMDA receptor activation¹⁵⁷ and can be reversed by low-frequency stimulation¹⁵⁸. Furthermore, a striking study done by McElvain and colleagues who argued that the synapses in the short reflex pathway of the VOR exhibited both LTP and LTD⁹². Specifically, repetitive stimulation of the vestibular nerve can evoke LTD at the afferent vestibular nuclei neuron synapse when paired with postsynaptic depolarization, by a mechanism that involves calcium-permeable AMPA receptors; or LTP when paired with postsynaptic hyperpolarization through NMDA receptors. Similarly, a subsequent study showed that either LTD or LTP could be evoked at the afferent FTNs synapse using repetitive stimulation of vestibular afferents depending on the pattern of pulse trains that are being delivered¹⁵⁹. Besides, Local inhibition in the MVN includes feedforward¹⁶⁰ and commissural connections^{161,162}, may also play roles in signal

processing and circuit throughput during VOR adaptation ¹⁶³.

We propose that plasticity of the primary excitatory vestibular drive onto interneurons could regulate VOR gain-decrease adaptation by attenuating the sensitivity of FTNs to head velocity. Note that vestibular nerve afferents are excitatory, the firing rate of postsynaptic interneurons can still be increased, regardless the attenuated responses, thus the LTP is possibly evoked. In support of this assumption, Mitchell and colleagues found that stimulation of the vestibular nerve resulted in a decreased efficacy of the synapse between vestibular afferents and postsynaptic interneurons, which ultimately caused a reduction in VOR eye movements.

In addition to synaptic plasticity, changes in the intrinsic excitability of neurons provide additional possible mechanisms for altering the gain of the VOR pathway ¹⁶⁴. Target neurons including PCs and FTNs, can modify their intrinsic input-output functions, so that a synaptic input of a given size that once elicited a modest response (as evaluated by postsynaptic spiking) now elicits a strong one, or vice versa ¹⁶⁵. This type of plasticity might be useful for generalized changes of gains of the VOR. A sustained increase in excitability of deep cerebellar nuclear neurons has been reported following tetanization of afferent pathways ¹⁶⁶, and an analogous mechanism could operate in the vestibular nuclei. Both SK and BK-type calcium-dependent potassium channels have been implicated as sites for changes in excitability in the vestibular nuclei ¹⁶⁷.

It should be kept in mind that the plasticity, in terms of LTP and LTD, are usually observed in intracellular recording undertaken in tissue culture and slice preparations; it does not accurately mimic what takes place during motor learning in vivo which is usually tested by measuring changes in an awake-behaving animal under natural conditions. Therefore, we start to use potentiation and attenuation of neuronal firing responses, instead of LTP and LTD respectively, to simulate the outcome changes in the synaptic connection weights within the network of VOR adaptation.

In summary, significant synaptic plasticity can occur within the Purkinje cells of floccular complex in a potentiation manner, alongside synaptic modifications within the vestibular nuclei in an attenuation fashion, likely play a role in guiding VOR adaptation in a specific condition.

Conclusions and perspectives

The VOR, operating on basis of the vestibulocerebellum, is an adaptive control system that self-calibrates motor commands to achieve compensatory eye movements. Its adaptive capability has been extensively investigated as a model of neural plasticity and considerable controversy has arisen concerning the specific neural site at which plastic modifications take place. In this scenario, a prevailing hypothesis of multiple sites in both the cerebellum and brain stem as the primary locus has been proposed. But there is still significant paradox. In this review, we extend this theory to better account for the substantial divergent experimental studies. We hypothesize that floccular complex (flocculus and ventral paraflocculus) and medial vestibular nucleus (for horizontal VOR), both acting as adaptive valves capable of distinguishing different external conditions, are the sites for VOR adaptation. Specifically, VOR gain-increase learning is accomplished in the floccular complex by potentiation of Purkinje cell

simple spike firing, whereas gain-decrease learning is induced by attenuation of the synaptic efficacy between primary vestibular afferents and their postsynaptic interneurons in the medial vestibular nuclei (**Figure 4**). In addition, we postulate that gain-increase learning is a feedback loop represented by the eye velocity signal originating from the inferior olive, whereas gain-decrease learning is likely to be a feedforward loop, both of which occur probably through an ever-updating internal model.

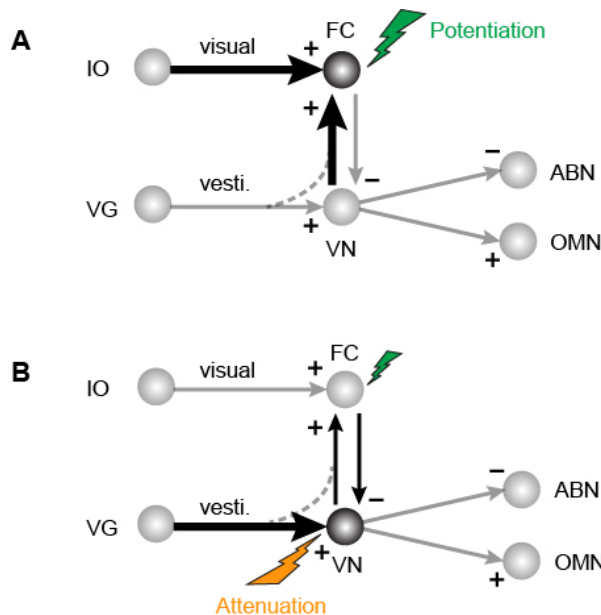


Figure 4 / A new viewpoint of multisite hypothesis for vestibulo-ocular reflex adaptation. Schematic illustrates the plausible adaptive sites (dark circles) that floccular complex (FC) for VOR gain-increase learning (A) by a putative potentiation mechanism (green flash) and vestibular nucleus (VN) for gain-decrease learning (B) via presumable attenuation mechanism (orange flash), respectively. The neural circuits, conveying instructive signals (either visual or vestibular) that are involved in the adaptive process in each paradigm, are indicated by thick-dark arrows. IO, inferior olive; VG, vestibular ganglion; ABN, abducens nucleus; OMN, oculomotor nucleus; + and -, excitatory and inhibitory input respectively.

There are still several anatomical and physiological questions to answer in order to connect activity at the cellular level and behavioral learning. Remarkably, although the VOR is mediated by as few as two muscles, Purkinje cells in the flocculus project onto at least five different cell types in the vestibular nucleus¹⁵⁵. The relative contribution of plasticity in the flocculus versus these vestibular nucleus neurons to motor learning in the VOR remains to be elucidated. Thus, the cellular mechanisms underlying VOR adaptation is still open for debate. For example, the neuronal responses of VN, ABN and OMN, are extrapolated, further *in vivo* physiological research is required. In addition, given the anatomical limitations of the VN, it is difficult to selectively record one certain subset of floccular targeting interneuron; it is also impossible to investigate using destructive lesions, temporary inactivation, or GABA antagonists, because these manipulations would prevent the VOR from working. New tools for activating or inhibiting subsets of neurons will be of great use in the future. For example, cell-specific transgenic mice, and/or virus specific expression of channelrhodopsin (a light-responsive channel) in the subset of glutamatergic neurons in the MVN, would offer help to investigate the role of NMDA or AMPA receptors during the VOR gain-decrease learning *in vivo*.

In a nutshell, it is clear that VOR adaptation is distributed in either cerebellum or brain stem, depending on different learning conditions. Remarkably, the VOR is an excellent model, by which we are able to get closer to achieving a full mechanistic understanding of where and how the brain adapts and perfects movements to an ever-changing environment.

1.3 Scope of the thesis

The goal of the research in this thesis is to elucidate the fundamental neural basis of the motor control and motor learning. More specifically, revolving the vestibulocerebellar system, we make use of in vitro and in vivo electrophysiological, imaging, optogenetic, and specific behavioral techniques combined with mouse genetic and molecular methods, to probe how the unitary architectures and functional modules of the cerebellum process information and give rise to the pluriformity of behavioral features.

Chapter 2 describes a targeted approach of recording electrophysiological activity in the cerebellum, particular that of Purkinje cells, in vivo in the awake, active animal.

Chapter 3 we set out to address the question that how homogeneous cyto-architecture of the cerebellar cortex gives rise to variety of behavioral consequences, where does the zebrin-related differentiation come from at the cellular level? Our results show that TRPC3 is essential for the cellular heterogeneity that introduces distinct physiological properties in an otherwise homogeneous population of Purkinje cells, conjuring functional heterogeneity in cerebellar sensorimotor integration.

Chapter 4 we clarify the characteristics of the basal interstitial nucleus in the vestibulocerebellum, which may contribute to controlling the compensatory and smooth pursuit eye movements.

Chapter 5 we lay emphasis on the electrophysiological investigation of spike responses in individual Purkinje cell in the context of compensatory eye movement performance and adaptation. **Chapter 5.1** we identify that modulation depths might be a form of neural code underlying the process of motor learning; **Chapter 5.2** we use direction-specific visuo-vestibular mismatch training to evoke VOR gain adaptation in relation to movement direction, and show that asymmetries in the magnitude of adaptation depends on movement direction.

Chapter 6 we investigate the role of several synaptic proteins during motor learning and cerebellar development. **Chapter 6.1** through genetic manipulation of PP2B, we come up with the idea that cerebellar development plays a crucial role in the emergence of motor behaviors and learning. **Chapter 6.2** we demonstrate that PP2B plays a crucial role in controlling the PSD structure at the parallel fiber to Purkinje cell synapse and this function contributes to behavioral learning. **Chapter 6.3** we report that Shisa6 is crucial for Purkinje cell AMPA-receptor function, synaptic plasticity, and cerebellar motor learning.

Chapter 7 we expand the argument for the role of cerebellum in autism by presenting evidence on cerebellar malfunction due to the deletion of shank2 gene.

Chapter 8 we discuss the results described in this thesis.

References

- 1 Herculano-Houzel, S. The human brain in numbers: a linearly scaled-up primate brain. *Front Hum Neurosci.* 2009; 3, 31.
- 2 Williams, R. W. & Herrup, K. The control of neuron number. *Annu Rev Neurosci.* 1988; 11, 423-53.
- 3 Herculano-Houzel, S. Coordinated scaling of cortical and cerebellar numbers of neurons. *Front Neuroanat.* 2010; 4, 12.
- 4 Sugihara, I. & Quy, P. N. Identification of aldolase C compartments in the mouse cerebellar cortex by olivocerebellar labeling. *J Comp Neurol.* 2007; 500, 1076-92.
- 5 De Zeeuw, C. I., Hoebeek, F. E., Bosman, L. W. *et al.* Spatiotemporal firing patterns in the cerebellum. *Nat Rev Neurosci.* 2011; 12, 327-44.
- 6 Gao, Z., van Beugen, B. J. & De Zeeuw, C. I. Distributed synergistic plasticity and cerebellar learning. *Nat Rev Neurosci.* 2012; 13, 619-35.
- 7 Chadderton, P., Margrie, T. W. & Hausser, M. Integration of quanta in cerebellar granule cells during sensory processing. *Nature.* 2004; 428, 856-60.
- 8 Apps, R. & Garwicz, M. Anatomical and physiological foundations of cerebellar information processing. *Nat Rev Neurosci.* 2005; 6, 297-311.
- 9 Ruigrok, T. J. & Voogd, J. Organization of projections from the inferior olive to the cerebellar nuclei in the rat. *J Comp Neurol.* 2000; 426, 209-28.
- 10 Wu, H. S., Sugihara, I. & Shinoda, Y. Projection patterns of single mossy fibers originating from the lateral reticular nucleus in the rat cerebellar cortex and nuclei. *J Comp Neurol.* 1999; 411, 97-118.
- 11 Sugihara, I., Fujita, H., Na, J. *et al.* Projection of reconstructed single Purkinje cell axons in relation to the cortical and nuclear aldolase C compartments of the rat cerebellum. *J Comp Neurol.* 2009; 512, 282-304.
- 12 Person, A. L. & Raman, I. M. Synchrony and neural coding in cerebellar circuits. *Front Neural Circuits.* 2012; 6, 97.
- 13 Raman, I. M. & Bean, B. P. Ionic currents underlying spontaneous action potentials in isolated cerebellar Purkinje neurons. *J Neurosci.* 1999; 19, 1663-74.
- 14 Wu, B. & Schonewille, M. (2018). Targeted Electrophysiological Recordings In Vivo in the Mouse Cerebellum. *Extracellular Recording Approaches, Roy Sillitoe, ed. (New York: Humana Press), pp. 19-37.*
- 15 Llinas, R. & Sugimori, M. Electrophysiological properties of in vitro Purkinje cell somata in mammalian cerebellar slices. *J Physiol.* 1980; 305, 171-95.
- 16 Häusser, M. & Clark, B. A. Tonic synaptic inhibition modulates neuronal output pattern and spatiotemporal synaptic integration. *Neuron.* 1997; 19, 665-78.
- 17 Raman, I. M. & Bean, B. P. Resurgent sodium current and action potential formation in dissociated cerebellar Purkinje neurons. *J Neurosci.* 1997; 17, 4517-26.
- 18 Edgerton, J. R. & Reinhart, P. H. Distinct contributions of small and large conductance Ca²⁺-activated K⁺ channels to rat Purkinje neuron function. *J Physiol.* 2003; 548, 53-69.
- 19 Womack, M. D., Chevez, C. & Khodakhah, K. Calcium-activated potassium channels are selectively coupled to P/Q-type calcium channels in cerebellar Purkinje neurons. *J Neurosci.* 2004; 24, 8818-22.
- 20 Galliano, E., Gao, Z., Schonewille, M. *et al.* Silencing the majority of cerebellar granule cells uncovers their essential role in motor learning and consolidation. *Cell Rep.* 2013; 3, 1239-51.
- 21 Wulff, P., Schonewille, M., Renzi, M. *et al.* Synaptic inhibition of Purkinje cells mediates consolidation of vestibulo-cerebellar motor learning. *Nat Neurosci.* 2009; 12, 1042-9.
- 22 Finch, E. A. & Augustine, G. J. Local calcium signalling by inositol-1,4,5-trisphosphate in Purkinje cell dendrites. *Nature.* 1998; 396, 753-6.
- 23 Callaway, J. C. & Ross, W. N. Spatial distribution of synaptically activated sodium concentration changes in cerebellar Purkinje neurons. *J Neurophysiol.* 1997; 77, 145-52.
- 24 Kuruma, A., Inoue, T. & Mikoshiba, K. Dynamics of Ca²⁺ and Na⁺ in the dendrites of mouse cerebellar Purkinje cells evoked by parallel fibre stimulation. *Eur J Neurosci.* 2003; 18, 2677-89.
- 25 Eccles, J. C., Llinas, R. & Sasaki, K. The excitatory synaptic action of climbing fibres on the purinje cells of the cerebellum. *J Physiol.* 1966; 182, 268-96.
- 26 Llinas, R. & Yarom, Y. Properties and distribution of ionic conductances generating electroresponsiveness of mammalian inferior olivary neurones in vitro. *J Physiol.* 1981; 315, 569-84.
- 27 Llinas, R., Baker, R. & Sotelo, C. Electrotonic coupling between neurons in cat inferior olive. *J Neurophysiol.* 1974; 37, 560-71.
- 28 Simpson, J. I., Wylie, D.R., and DeZeeuw, C.I. in *Behavioral and brain sciences* Ch. 19, 384-98 (Cambridge University Press, 1996).
- 29 Sugihara, I., Wu, H. & Shinoda, Y. Morphology of single olivocerebellar axons labeled with biotinylated dextran amine

in the rat. *J Comp Neurol*. 1999; 414, 131-48.

30 Perkel, D. J., Hestrin, S., Sah, P. *et al.* Excitatory synaptic currents in Purkinje cells. *Proc Biol Sci*. 1990; 241, 116-21.

31 Piochon, C., Levenes, C., Ohtsuki, G. *et al.* Purkinje cell NMDA receptors assume a key role in synaptic gain control in the mature cerebellum. *J Neurosci*. 2010; 30, 15330-5.

32 Schmolesky, M. T., Weber, J. T., De Zeeuw, C. I. *et al.* The making of a complex spike: ionic composition and plasticity. *Ann N Y Acad Sci*. 2002; 978, 359-90.

33 Indriati, D. W., Kamasawa, N., Matsui, K. *et al.* Quantitative localization of Cav2.1 (P/Q-type) voltage-dependent calcium channels in Purkinje cells: somatodendritic gradient and distinct somatic coclustering with calcium-activated potassium channels. *J Neurosci*. 2013; 33, 3668-78.

34 Stuart, G. & Hausser, M. Initiation and spread of sodium action potentials in cerebellar Purkinje cells. *Neuron*. 1994; 13, 703-12.

35 Brochu, G., Maler, L. & Hawkes, R. Zebrin II: a polypeptide antigen expressed selectively by Purkinje cells reveals compartments in rat and fish cerebellum. *J Comp Neurol*. 1990; 291, 538-52.

36 Sugihara, I. & Shinoda, Y. Molecular, topographic, and functional organization of the cerebellar cortex: a study with combined aldolase C and olivocerebellar labeling. *J Neurosci*. 2004; 24, 8771-85.

37 Graham, D. J. & Wylie, D. R. Zebrin-immunopositive and -immunonegative stripe pairs represent functional units in the pigeon vestibulocerebellum. *J Neurosci*. 2012; 32, 12769-79.

38 Marzban, H. & Hawkes, R. On the architecture of the posterior zone of the cerebellum. *Cerebellum*. 2011; 10, 422-34.

39 Caffè, A. R., Von Schantz, M., Szel, A. *et al.* Distribution of Purkinje cell-specific Zebrin-II/aldolase C immunoreactivity in the mouse, rat, rabbit, and human retina. *J Comp Neurol*. 1994; 348, 291-7.

40 Apps, R. & Hawkes, R. Cerebellar cortical organization: a one-map hypothesis. *Nat Rev Neurosci*. 2009; 10, 670-81.

41 Ruigrok, T. J. Ins and outs of cerebellar modules. *Cerebellum*. 2011; 10, 464-74.

42 Zhou, H., Lin, Z., Voges, K. *et al.* Cerebellar modules operate at different frequencies. *Elife*. 2014; 3, e02536.

43 Bodranghien, F., Bastian, A., Casali, C. *et al.* Consensus Paper: Revisiting the Symptoms and Signs of Cerebellar Syndrome. *Cerebellum*. 2016; 15, 369-91.

44 Ackermann, H., Vogel, M., Petersen, D. *et al.* Speech deficits in ischaemic cerebellar lesions. *J Neurol*. 1992; 239, 223-7.

45 Schonewille, M., Luo, C., Ruigrok, T. J. *et al.* Zonal organization of the mouse flocculus: physiology, input, and output. *J Comp Neurol*. 2006; 497, 670-82.

46 Gormezano, I., Schneiderman, N., Deaux, E. *et al.* Nictitating membrane: classical conditioning and extinction in the albino rabbit. *Science*. 1962; 138, 33-4.

47 Ivarsson, M. & Svensson, P. Conditioned eyeblink response consists of two distinct components. *J Neurophysiol*. 2000; 83, 796-807.

48 Marr, D. A theory of cerebellar cortex. *J Physiol*. 1969; 202, 437-70.

49 Albus, J. S. A theory of cerebellar function. *Math. Biosci*. 1971; 10, 25-61.

50 Ito, M., Jastreboff, P. J. & Miyashita, Y. Specific effects of unilateral lesions in the flocculus upon eye movements in albino rabbits. *Exp Brain Res*. 1982; 45, 233-42.

51 Lev-Ram, V., Wong, S. T., Storm, D. R. *et al.* A new form of cerebellar long-term potentiation is postsynaptic and depends on nitric oxide but not cAMP. *Proc Natl Acad Sci U S A*. 2002; 99, 8389-93.

52 Salin, P. A., Malenka, R. C. & Nicoll, R. A. Cyclic AMP mediates a presynaptic form of LTP at cerebellar parallel fiber synapses. *Neuron*. 1996; 16, 797-803.

53 Coesmans, M., Weber, J. T., De Zeeuw, C. I. *et al.* Bidirectional parallel fiber plasticity in the cerebellum under climbing fiber control. *Neuron*. 2004; 44, 691-700.

54 Schonewille, M., Belmeguenai, A., Koekkoek, S. K. *et al.* Purkinje cell-specific knockout of the protein phosphatase PP2B impairs potentiation and cerebellar motor learning. *Neuron*. 2010; 67, 618-28.

55 van Woerden, G. M., Hoebeek, F. E., Gao, Z. *et al.* betaCaMKII controls the direction of plasticity at parallel fiber-Purkinje cell synapses. *Nat Neurosci*. 2009; 12, 823-5.

56 De Zeeuw, C. I., Hansel, C., Bian, F. *et al.* Expression of a protein kinase C inhibitor in Purkinje cells blocks cerebellar LTD and adaptation of the vestibulo-ocular reflex. *Neuron*. 1998; 20, 495-508.

57 Yarrow, K., Brown, P. & Krakauer, J. W. Inside the brain of an elite athlete: the neural processes that support high achievement in sports. *Nat Rev Neurosci*. 2009; 10, 585-96.

58 Huang, V. S., Haith, A., Mazzoni, P. *et al.* Rethinking motor learning and savings in adaptation paradigms: model-free memory for successful actions combines with internal models. *Neuron*. 2011; 70, 787-801.

59 Hess, G. & Donoghue, J. P. Long-term depression of horizontal connections in rat motor cortex. *Eur J Neurosci*. 1996; 8, 658-65.

60 Ito, M. Neural design of the cerebellar motor control system. *Brain Res*. 1972; 40, 81-4.

61 Shutoh, F., Katoh, A., Ohki, M. *et al.* Role of protein kinase C family in the cerebellum-dependent adaptive learning of

horizontal optokinetic response eye movements in mice. *Eur J Neurosci.* 2003; 18, 134-42.

62 De Zeeuw, C. I. & Yeo, C. H. Time and tide in cerebellar memory formation. *Curr Opin Neurobiol.* 2005; 15, 667-74.

63 Highstein, S. M. & Holstein, G. R. The anatomy of the vestibular nuclei. *Prog Brain Res.* 2006; 151, 157-203.

64 Ito, M. The modifiable neuronal network of the cerebellum. *Jpn J Physiol.* 1984; 34, 781-92.

65 Dash, S., Yan, X., Wang, H. *et al.* Continuous updating of visuospatial memory in superior colliculus during slow eye movements. *Curr Biol.* 2015; 25, 267-74.

66 Miles, F. A. & Lisberger, S. G. The "error" signals subserving adaptive gain control in the primate vestibulo-ocular reflex. *Ann N Y Acad Sci.* 1981; 374, 513-25.

67 Blazquez, P. M., Hirata, Y. & Highstein, S. M. The vestibulo-ocular reflex as a model system for motor learning: what is the role of the cerebellum? *Cerebellum.* 2004; 3, 188-92.

68 Boyden, E. S., Katoh, A. & Raymond, J. L. Cerebellum-dependent learning: the role of multiple plasticity mechanisms. *Annu Rev Neurosci.* 2004; 27, 581-609.

69 Mitchell, D. E., Della Santina, C. C. & Cullen, K. E. Plasticity within excitatory and inhibitory pathways of the vestibulo-spinal circuitry guides changes in motor performance. *Sci Rep.* 2017; 7, 853.

70 Szentágothai, J. The elementary vestibulo-ocular reflex arc. *J Neurophysiol.* 1950; 13, 395-407.

71 Huterer, M. & Cullen, K. E. Vestibuloocular reflex dynamics during high-frequency and high-acceleration rotations of the head on body in rhesus monkey. *J Neurophysiol.* 2002; 88, 13-28.

72 Lorente de Nó, R. Vestibulo-ocular reflex arc. *Arch. Neurol. Psychiat.* 1933; 30, 245-91.

73 De Zeeuw, C. I., Koekkoek, S. K., van Alphen, A. M. *et al.* in *Handbook of auditory research* 375-422 (Springer Verlag, 2003).

74 Barmack, N. H., Baughman, R. W., Eckenstein, F. P. *et al.* Secondary vestibular cholinergic projection to the cerebellum of rabbit and rat as revealed by choline acetyltransferase immunohistochemistry, retrograde and orthograde tracers. *J Comp Neurol.* 1992; 317, 250-70.

75 Chubb, M. C., Fuchs, A. F. & Scudder, C. A. Neuron activity in monkey vestibular nuclei during vertical vestibular stimulation and eye movements. *J Neurophysiol.* 1984; 52, 724-42.

76 Scudder, C. A. & Fuchs, A. F. Physiological and behavioral identification of vestibular nucleus neurons mediating the horizontal vestibuloocular reflex in trained rhesus monkeys. *J Neurophysiol.* 1992; 68, 244-64.

77 Cullen, K. E. & McCrea, R. A. Firing behavior of brain stem neurons during voluntary cancellation of the horizontal vestibuloocular reflex. I. Secondary vestibular neurons. *J Neurophysiol.* 1993; 70, 828-43.

78 Partsalis, A. M., Zhang, Y. & Highstein, S. M. Dorsal Y group in the squirrel monkey. II. Contribution of the cerebellar flocculus to neuronal responses in normal and adapted animals. *J Neurophysiol.* 1995; 73, 632-50.

79 Dickman, J. D. & Angelaki, D. E. Dynamics of vestibular neurons during rotational motion in alert rhesus monkeys. *Exp Brain Res.* 2004; 155, 91-101.

80 Ito, M., Nisimaru, N. & Yamamoto, M. Specific patterns of neuronal connections involved in the control of the rabbit's vestibulo-ocular reflexes by the cerebellar flocculus. *J Physiol.* 1977; 265, 833-54.

81 du Lac, S. & Lisberger, S. G. Eye movements and brainstem neuronal responses evoked by cerebellar and vestibular stimulation in chicks. *J Comp Physiol [A].* 1992; 171, 629-38.

82 Sekirnjak, C., Vissel, B., Bollinger, J. *et al.* Purkinje cell synapses target physiologically unique brainstem neurons. *J Neurosci.* 2003; 23, 6392-8.

83 Ramachandran, R. & Lisberger, S. G. Neural substrate of modified and unmodified pathways for learning in monkey vestibuloocular reflex. *J Neurophysiol.* 2008; 100, 1868-78.

84 McCrea, R. A., Strassman, A., May, E. *et al.* Anatomical and physiological characteristics of vestibular neurons mediating the horizontal vestibulo-ocular reflex of the squirrel monkey. *J Comp Neurol.* 1987; 264, 547-70.

85 Broussard, D. M., DeCharms, R. C. & Lisberger, S. G. Inputs from the ipsilateral and contralateral vestibular apparatus to behaviorally characterized abducens neurons in rhesus monkeys. *J Neurophysiol.* 1995; 74, 2445-59.

86 Lisberger, S. G., Pavelko, T. A., Bronte-Stewart, H. M. *et al.* Neural basis for motor learning in the vestibuloocular reflex of primates. II. Changes in the responses of horizontal gaze velocity Purkinje cells in the cerebellar flocculus and ventral paraflocculus. *J Neurophysiol.* 1994; 72, 954-73.

87 Langer, T., Fuchs, A. F., Chubb, M. C. *et al.* Floccular efferents in the rhesus macaque as revealed by autoradiography and horseradish peroxidase. *J Comp Neurol.* 1985; 235, 26-37.

88 Broussard, D. M. & Lisberger, S. G. Vestibular inputs to brain stem neurons that participate in motor learning in the primate vestibuloocular reflex. *J Neurophysiol.* 1992; 68, 1906-9.

89 Lisberger, S. G. & Pavelko, T. A. Brain stem neurons in modified pathways for motor learning in the primate vestibulo-ocular reflex. *Science.* 1988; 242, 771-3.

90 Sato, Y., Kanda, K. & Kawasaki, T. Target neurons of floccular middle zone inhibition in medial vestibular nucleus. *Brain Res.* 1988; 446, 225-35.

91 Stahl, J. S. & Simpson, J. I. Dynamics of abducens nucleus neurons in the awake rabbit. *J Neurophysiol.* 1995; 73, 1383-95.

92 McElvain, L. E., Bagnall, M. W., Sakatos, A. *et al.* Bidirectional plasticity gated by hyperpolarization controls the gain
of postsynaptic firing responses at central vestibular nerve synapses. *Neuron*. 2010; 68, 763-75.

93 Broussard, D. M. & Kassardjian, C. D. Learning in a simple motor system. *Learn Mem*. 2004; 11, 127-36.

94 Medina, J. F. The multiple roles of Purkinje cells in sensori-motor calibration: to predict, teach and command. *Curr
Opin Neurobiol*. 2011; 21, 616-22.

95 Lisberger, S. G. & Sejnowski, T. J. Motor learning in a recurrent network model based on the vestibulo-ocular reflex
[see comments]. *Nature*. 1992; 360, 159-61.

96 Ito, M., Shida, T., Yagi, N. *et al.* The cerebellar modification of rabbit's horizontal vestibulo-ocular reflex induced by
sustained head rotation combined with visual stimulation. *Proc Jpn Acad*. 1974; 50, 85-9.

97 Zee, D. S., Yamazaki, A., Butler, P. H. *et al.* Effects of ablation of flocculus and paraflocculus of eye movements in
primate. *J Neurophysiol*. 1981; 46, 878-99.

98 Nagao, S. Effects of vestibulocerebellar lesions upon dynamic characteristics and adaptation of vestibulo-ocular and
optokinetic responses in pigmented rabbits. *Exp Brain Res*. 1983; 53, 36-46.

99 Torte, M. P., Courjon, J. H., Flandrin, J. M. *et al.* Anatomical segregation of different adaptative processes within the
vestibulocerebellum of the cat. *Exp Brain Res*. 1994; 99, 441-54.

100 Rambold, H., Churchland, A., Selig, Y. *et al.* Partial Ablations of the Flocculus and Ventral Paraflocculus in Monkeys
Cause Linked Deficits in Smooth Pursuit Eye Movements and Adaptive Modification of the VOR. *J Neurophysiol*. 2002;
87, 912-24.

101 McElligott, J. G., Beeton, P. & Polk, J. Effect of cerebellar inactivation by lidocaine microdialysis on the vestibuloocular
reflex in goldfish. *J Neurophysiol*. 1998; 79, 1286-94.

102 Anzai, M., Kitazawa, H. & Nagao, S. Effects of reversible pharmacological shutdown of cerebellar flocculus on the
memory of long-term horizontal vestibulo-ocular reflex adaptation in monkeys. *Neurosci Res*. 2010; 68, 191-8.

103 Kassardjian, C. D., Tan, Y. F., Chung, J. Y. *et al.* The site of a motor memory shifts with consolidation. *J Neurosci*. 2005;
25, 7979-85.

104 Ghelarducci, B., Ito, M. & Yagi, N. Impulse discharges from flocculus Purkinje cells of alert rabbits during visual
stimulation combined with horizontal head rotation. *Brain Res*. 1975; 87, 66-72.

105 Dufosse, M., Ito, M., Jastreboff, P. J. *et al.* A neuronal correlate in rabbit's cerebellum to adaptive modification of the
vestibulo-ocular reflex. *Brain Res*. 1978; 150, 611-6.

106 Watanabe, E. Role of the primate flocculus in adaptation of the vestibulo-ocular reflex. *Neurosci Res*. 1985; 3, 20-38.

107 Nagao, S. Role of cerebellar flocculus in adaptive interaction between optokinetic eye movement response and
vestibulo-ocular reflex in pigmented rabbits. *Exp Brain Res*. 1989; 77, 541-51.

108 Maekawa, K. & Takeda, T. Electrophysiological identification of the climbing and mossy fiber pathways from the
rabbit's retina to the contralateral cerebellar flocculus. *Brain Res*. 1976; 109, 169-74.

109 Maekawa, K. & Takeda, T. Origin of descending afferents to the rostral part of dorsal cap of inferior olive which
transfers contralateral optic activities to the flocculus. A horseradish peroxidase study. *Brain Res*. 1979; 172, 393-405.

110 Simpson, J. I. & Alley, K. E. Visual climbing fiber input to rabbit vestibulo-cerebellum: a source of direction-specific
information. *Brain Res*. 1974; 82, 302-8.

111 Graf, W., Simpson, J. I. & Leonard, C. S. Spatial organization of visual messages of the rabbit's cerebellar flocculus. II.
Complex and simple spike responses of Purkinje cells. *J Neurophysiol*. 1988; 60, 2091-121.

112 Stone, L. S. & Lisberger, S. G. Visual responses of Purkinje cells in the cerebellar flocculus during smooth-pursuit eye
movements in monkeys. II. Complex spikes. *J Neurophysiol*. 1990; 63, 1262-75.

113 Gonshor, A. & Jones, G. M. Extreme vestibulo-ocular adaptation induced by prolonged optical reversal of vision. *J
Physiol*. 1976; 256, 381-414.

114 Ito, M. The vestibulo--cerebellar relationships: vestibulo-ocular reflex arc and flocculus. pp 129-46. *In: Naunton RF,
ed. The vestibular system. New York, Academic Press. 1975; 255.*

115 Haddad, G. M., Demer, J. L. & Robinson, D. A. The effect of lesions of the dorsal cap of the inferior olive on the
vestibulo-ocular and optokinetic systems of the cat. *Brain Res*. 1980; 185, 265-75.

116 Tempia, F., Dieringer, N. & Strata, P. Adaptation and habituation of the vestibulo-ocular reflex in intact and inferior
olive-lesioned rats. *Exp Brain Res*. 1991; 86, 568-78.

117 Yakushin, S. B., Reisine, H., Buttner-Ennever, J. *et al.* Functions of the nucleus of the optic tract (NOT). I. Adaptation
of the gain of the horizontal vestibulo-ocular reflex. *Exp Brain Res*. 2000; 131, 416-32.

118 Miles, F. A. & Lisberger, S. G. Plasticity in the vestibulo-ocular reflex: a new hypothesis. *Annu Rev Neurosci*. 1981; 4,
273-99.

119 Miles, F. A., Braitman, D. J. & Dow, B. M. Long-term adaptive changes in primate vestibuloocular reflex. IV.
Electrophysiological observations in flocculus of adapted monkeys. *J Neurophysiol*. 1980; 43, 1477-93.

120 Lisberger, S. G., Pavelko, T. A. & Broussard, D. M. Neural basis for motor learning in the vestibuloocular reflex of
primates. I. Changes in the responses of brain stem neurons. *J Neurophysiol*. 1994; 72, 928-53.

121 Luebke, A. E. & Robinson, D. A. Gain changes of the cat's vestibulo-ocular reflex after flocculus deactivation. *Exp*

Brain Res. 1994; 98, 379-90.

122 Ke, M. C., Guo, C. C. & Raymond, J. L. Elimination of climbing fiber instructive signals during motor learning. *Nat Neurosci.* 2009; 12, 1171-9.

123 Watanabe, E. Neuronal events correlated with long-term adaptation of the horizontal vestibulo-ocular reflex in the primate flocculus. *Brain Res.* 1984; 297, 169-74.

124 Blazquez, P. M., Hirata, Y., Heiney, S. A. *et al.* Cerebellar signatures of vestibulo-ocular reflex motor learning. *J Neurosci.* 2003; 23, 9742-51.

125 Hirata, Y. & Highstein, S. M. Acute adaptation of the vestibuloocular reflex: signal processing by floccular and ventral parafloccular purkinje cells. *J Neurophysiol.* 2001; 85, 2267-88.

126 Nagao, S. & Kitazawa, H. Effects of reversible shutdown of the monkey flocculus on the retention of adaptation of the horizontal vestibulo-ocular reflex. *Neuroscience.* 2003; 118, 563-70.

127 Barmack, N. H. & Simpson, J. I. Effects of microlesions of dorsal cap of inferior olive of rabbits on optokinetic and vestibuloocular reflexes. *J Neurophysiol.* 1980; 43, 182-206.

128 Ito, M., Jastreboff, P. J. & Miyashita, Y. Retrograde influence of surgical and chemical flocculectomy upon dorsal cap neurons of the inferior olive. *Neurosci Lett.* 1980; 20, 45-8.

129 Wylie, D. R., De Zeeuw, C. I., DiGiorgi, P. L. *et al.* Projections of individual Purkinje cells of identified zones in the ventral nodulus to the vestibular and cerebellar nuclei in the rabbit. *J Comp Neurol.* 1994; 349, 448-63.

130 De Zeeuw, C. I., Wylie, D. R., Stahl, J. S. *et al.* Phase Relations of Purkinje Cells in the Rabbit Flocculus During Compensatory Eye Movements. *J of Neurophysiol.* 1995; 74, 2051-63.

131 Voges, K., Wu, B., Post, L. *et al.* Mechanisms underlying vestibulo-cerebellar motor learning in mice depend on movement direction. *J Physiol.* 2017; 595, 5301-26.

132 Li, J., Smith, S. S. & McElligott, J. G. Cerebellar nitric oxide is necessary for vestibulo-ocular reflex adaptation, a sensorimotor model of learning. *J Neurophysiol.* 1995; 74, 489-94.

133 Titley, H. K., Heskin-Sweezie, R. & Broussard, D. M. The bidirectionality of motor learning in the vestibulo-ocular reflex is a function of cerebellar mGluR1 receptors. *J Neurophysiol.* 2010; 104, 3657-66.

134 Schonewille, M., Gao, Z., Boele, H. J. *et al.* Reevaluating the role of LTD in cerebellar motor learning. *Neuron.* 2011; 70, 43-50.

135 Boyden, E. S., Katoh, A., Pyle, J. L. *et al.* Selective engagement of plasticity mechanisms for motor memory storage. *Neuron.* 2006; 51, 823-34.

136 Seja, P., Schonewille, M., Spitzmaul, G. *et al.* Raising cytosolic Cl⁻ in cerebellar granule cells affects their excitability and vestibulo-ocular learning. *EMBO J.* 2012; 31, 1217-30.

137 Miles, F. A. & Eighmy, B. B. Long-term adaptive changes in primate vestibuloocular reflex. I. Behavioral observations. *J Neurophysiol.* 1980; 43, 1406-25.

138 Kuki, Y., Hirata, Y., Blazquez, P. M. *et al.* Memory retention of vestibuloocular reflex motor learning in squirrel monkeys. *Neuroreport.* 2004; 15, 1007-11.

139 Boyden, E. S. & Raymond, J. L. Active reversal of motor memories reveals rules governing memory encoding. *Neuron.* 2003; 39, 1031-42.

140 Kimpo, R. R., Boyden, E. S., Katoh, A. *et al.* Distinct patterns of stimulus generalization of increases and decreases in VOR gain. *J Neurophysiol.* 2005; 94, 3092-100.

141 Broussard, D. M., Titley, H. K., Antflick, J. *et al.* Motor learning in the VOR: the cerebellar component. *Exp Brain Res.* 2011; 210, 451-63.

142 Titley, H. K. & Hansel, C. Asymmetries in Cerebellar Plasticity and Motor Learning. *Cerebellum.* 2016; 15, 87-92.

143 Dash, S., Catz, N., Dicke, P. W. *et al.* Specific vermal complex spike responses build up during the course of smooth-pursuit adaptation, paralleling the decrease of performance error. *Exp Brain Res.* 2010; 205, 41-55.

144 Heffley, W., Song, E. Y., Xu, Z. *et al.* Coordinated cerebellar climbing fiber activity signals learned sensorimotor predictions. *Nat Neurosci.* 2018; 21, 1431-41.

145 Mitchell, D. E., Della Santina, C. C. & Cullen, K. E. Plasticity within non-cerebellar pathways rapidly shapes motor performance in vivo. *Nat Commun.* 2016; 7, 11238.

146 Bagnall, M. W., McElvain, L. E., Faulstich, M. *et al.* Frequency-independent synaptic transmission supports a linear vestibular behavior. *Neuron.* 2008; 60, 343-52.

147 Hansel, C., Linden, D. J. & D'Angelo, E. Beyond parallel fiber LTD: the diversity of synaptic and non-synaptic plasticity in the cerebellum. *Nat Neurosci.* 2001; 4, 467-75.

148 Nagao, S. & Ito, M. Subdural application of hemoglobin to the cerebellum blocks vestibuloocular reflex adaptation. *Neuroreport.* 1991; 2, 193-6.

149 Hansel, C., de Jeu, M., Belmeguenai, A. *et al.* alphaCaMKII Is essential for cerebellar LTD and motor learning. *Neuron.* 2006; 51, 835-43.

150 Kakegawa, W., Katoh, A., Narumi, S. *et al.* Optogenetic Control of Synaptic AMPA Receptor Endocytosis Reveals Roles of LTD in Motor Learning. *Neuron.* 2018; 99, 985-98 e6.

151 Ito, M. Cerebellar learning in the vestibulo-ocular reflex. *Trends Cogn Sci.* 1998; 1998, 305-71.
152 Ito, M. Long-term depression. *Annu Rev Neurosci.* 1989; 12, 85-102.
153 Nguyen-Vu, T. D., Kimpo, R. R., Rinaldi, J. M. *et al.* Cerebellar Purkinje cell activity drives motor learning. *Nat Neurosci.*
2013; 16, 1734-6.
154 Miyashita, Y. & Nagao, S. Contribution of cerebellar intracortical inhibition to Purkinje cell response during
vestibulo-ocular reflex of alert rabbits. *J Physiol.* 1984; 351, 251-62.
155 Shin, M., Moghadam, S. H., Sekirnjak, C. *et al.* Multiple types of cerebellar target neurons and their circuitry in the
vestibulo-ocular reflex. *J Neurosci.* 2011; 31, 10776-86.
156 Spencer, R. F., Wenthold, R. J. & Baker, R. Evidence for glycine as an inhibitory neurotransmitter of vestibular, reticular,
and prepositus hypoglossi neurons that project to the cat abducens nucleus. *J Neurosci.* 1989; 9, 2718-36.
157 Capocchi, G., Della Torre, G., Grassi, S. *et al.* NMDA receptor-mediated long term modulation of electrically evoked
field potentials in the rat medial vestibular nuclei. *Exp Brain Res.* 1992; 90, 546-50.
158 Grassi, S., Pettorossi, V. E. & Zampolini, M. Low-frequency stimulation cancels the high-frequency-induced long-
lasting effects in the rat medial vestibular nuclei. *J Neurosci.* 1996; 16, 3373-80.
159 Scarduzio, M., Panichi, R., Pettorossi, V. E. *et al.* The repetition timing of high frequency afferent stimulation drives
the bidirectional plasticity at central synapses in the rat medial vestibular nuclei. *Neuroscience.* 2012; 223, 1-11.
160 Straka, H., Biesdorf, S. & Dieringer, N. Canal-specific excitation and inhibition of frog second-order vestibular neurons.
J Neurophysiol. 1997; 78, 1363-72.
161 Bagnall, M. W., Stevens, R. J. & du Lac, S. Transgenic mouse lines subdivide medial vestibular nucleus neurons into
discrete, neurochemically distinct populations. *J Neurosci.* 2007; 27, 2318-30.
162 Malinvaud, D., Vassias, I., Reichenberger, I. *et al.* Functional organization of vestibular commissural connections in
frog. *J Neurosci.* 2010; 30, 3310-25.
163 Cullen, K. E. & Roy, J. E. Signal processing in the vestibular system during active versus passive head movements. *J*
Neurophysiol. 2004; 91, 1919-33.
164 du Lac, S. Candidate cellular mechanisms of vestibulo-ocular reflex plasticity. *Ann N Y Acad Sci.* 1996; 781, 489-98.
165 Zhang, W. & Linden, D. J. The other side of the engram: experience-driven changes in neuronal intrinsic excitability.
Nat Rev Neurosci. 2003; 4, 885-900.
166 Aizenman, C. D. & Linden, D. J. Rapid, synaptically driven increases in the intrinsic excitability of cerebellar deep
nuclear neurons. *Nat Neurosci.* 2000; 3, 109-11.
167 Nelson, A. B., Krispel, C. M., Sekirnjak, C. *et al.* Long-lasting increases in intrinsic excitability triggered by inhibition.
Neuron. 2003; 40, 609-20.

CHAPTER 2

Targeted electrophysiological recordings in vivo in the mouse cerebellum

Bin Wu and Martijn Schonewille

Department of Neuroscience, Erasmus Medical Center, 3015 GE Rotterdam, The Netherlands

Published in Extracellular Recording Approaches (2018), Ch.2

Abstract

Single unit recordings *in vivo* are the unitary elements in the processing of the brain, and as such essential in systems physiology to understand brain functioning. In the cerebellum, a structure with high levels of intrinsic activity, studying these elements *in vivo* in an awake animal is imperative to obtain information regarding the processing features of these units in action. In this chapter we address the rationale and the approach of recording electrophysiological activity in the cerebellum, particular that of Purkinje cells, *in vivo* in the awake, active animal. In line with the developing appreciation for the diversity within populations of the cells of the same type, there is a growing interest in the differentiation within the population of Purkinje cells. Here we describe a successful approach to analyzing the activity of two populations of Purkinje cells, which differ in connectivity and the expression of several genes. By driving the expression of a fluorescent marker with the promotor of one of the differentiating genes, the presence of a fluorescence signal could be used to recognize and approach Purkinje cells, while the strength of the signal can be used as a marker to identify the two subpopulations. Finally, the drawbacks and the advantages of this technique are discussed, and placed into a future perspective.

Single unit recordings in vivo

Understanding what goes on in the most studied black box we know, the brain, is the essence of neuroscience. Brain physiology traditionally has been studied at several levels, varying from broad view approaches using EEGs or fMRI to that of individual cell structures such as axons, dendrites or even synapses using patch clamp recordings. Analysis at this level of detail has provided a wealth of knowledge regarding the cellular activity underlying concepts such as sensory processing, motor coding and learning. Top down, non-invasive approaches have taught us about functionalities, somatotopy, or about temporal aspects of activity and about the connectivity between areas. To bridge the gap between molecular processes occurring at the (sub)cellular level and the activity observed using non-invasive techniques, several electrophysiological approaches are used. Local field potential recordings indicate activity in a particular volume of recording area, while imaging -at the expense of temporal resolution- adds or increases spatial resolution. These forms of recording population code will help us understand the information passing through and processed by the ensemble, but are less informative regarding the individual units. For detailed information on the specific activity of individual units, the neurons, single unit recordings are required. Neuronal activity presents itself predominantly in the form of rapid fluctuation of the electrical membrane potential, also known as action potentials. Whereas the membrane potential can only be recorded inside the cell with patch clamp recordings or voltage sensitive dyes, the currents underlying the action potential are significantly large enough to reliably be recorded in the extracellular space. The potential of this technique has been known and used for a long time, including, for instance, in the landmark scientific discovery of the direction selectivity of neurons in the cat striatum ¹. But even today the technique is still used in many key studies^{2,3}, in part driven by the revival of systems physiology. New technical developments such as optogenetic manipulations of cellular activity require, to assure appropriate manipulation, a cell-specific read-out of the change in the firing rate induced by the light.

Targeted recordings in vivo: why and how?

Although the local environment of neurons in slice preparations is thought to remain intact, features such as sensory input, extracellular chemical configuration and axons of projecting neurons are typically disrupted. Switching to recording *in vivo* circumvents these issues, but at the expense of the possibility to use visual information for guidance. In many instances recordings can be somewhat directed based on neuroanatomy or known cellular activity patterns, or is simply not needed. If information on cell-type is essential but not needed to direct sampling, cells can also be labeled and classified post mortem. In all other situations, whether it is to minimize variation or to zoom in on the properties of specific cell types, the ability to target recordings can be essential. This technique was pioneered by Margrie and colleagues, who performed *in vivo* electrophysiological recordings based on images generated by two-photon excitation laser-scanning microscopy ⁴, a technique they named two-photon targeted patching, or TPTP ⁵. Transgenic mice expressing enhanced green fluorescent protein (eGFP) under control of the parvalbumin promoter to label cortical interneurons were anesthetized and placed under a two-photon microscope. With the cells labeled in green, and with the pipette filled with red Alexa594 the approach could be visualized and directed, and the success rate of patching was >50% per animal and over >10% per penetration ⁴. Following the TPTP approach describe above an alternative, inverse method was developed. Kitamura and colleagues demonstrated that by labeling the extracellular space with a fluorescent dye, the neurons can be 'visualized' as a negative image ⁶. By perfusing the extracellular space with the same Alexa594, which is not taken up by neurons, the authors were able to identify neurons as shadows and either electroporate or recorded from them. The success rate of obtaining a giga-seal and whole cell configuration was >60% for pyramidal cells and interneurons per attempt. Despite promising success rates both approaches are, however, used quite rarely, as whole cell recordings *in vivo* remain labor intensive with relatively low success rates and hence their use in today's neuroscience is limited.

Cerebellar wiring and physiology

The cerebellum holds a special place in neuroscience, not in the least due to its electrophysiological properties. The 'little brain' presents a combination of central nuclei surrounded by a highly organized, crystalline cortical structure (**Fig. 1**), with a sole principal output neuron, the Purkinje cell, that uses GABA as a neurotransmitter and has an immense, two-dimensional dendritic tree ⁷. Information enters the cerebellum predominantly via two sources: mossy fibers and climbing fibers. Mossy fibers carry information about sensory stimulation and ongoing motor activities in the form of efference

copies, or corollary discharges⁸, and contact excitatory granule cells and inhibitory Golgi cells^{9,10}. In contrast, a single climbing fibers provide excitatory input to each Purkinje cells resulting in a complex spike^{11,12} and are commonly thought to carry error signals^{13,14}, but other potential functions have also been described^{15,16}. Granule cells send their axon into the molecular layer, where they bifurcate and provide a direct excitatory drive to the Purkinje cell's extensive dendritic tree via parallel fibers and an indirect inhibitory input via the molecular layer interneurons, stellate cells and basket cells, which predominantly contact the Purkinje cell's dendrite and the soma, respectively¹⁷. Granule cells typically fire action potentials in bursts¹⁸. Purkinje cells are intrinsically active and integrate excitatory and inhibitory input into a GABAergic output onto cerebellar nuclear neurons. Most inhibitory interneurons have an intermediate firing rate, with less pronounced differences amongst them¹⁹. Together the mossy fiber and climbing fiber system create a matrix-like configuration. Parallel fibers run horizontally for millimeters, contacting spines on the dendrites of numerous Purkinje cells in the coronal plane. In contrast, the Purkinje cell dendrite is oriented sagittally and the inferior olive with its climbing fibers connects to multiple Purkinje cells in a sagittal plane, with each Purkinje cell receiving hundreds of inputs from only a single climbing fiber in the adult stage (**Fig. 1c**). This typical configuration sparked the interest of computational neuroscientists to generate a theory for cerebellar learning^{20,21}, which is still the topic of discussion today²²⁻²⁷.

Electrophysiological recordings in the cerebellum in vivo

The cerebellum is characterized by several features that facilitate convenient, reliable *in vivo* electrophysiological recordings. First there is the location; as the cerebellum is situated in the back of the skull there is ample space to place an immobilizing construct on the more frontal parts, assuring a preparation that is solid enough for chronic experiments. Secondly, the layered, cyto-architectural organization, due to its predictable pattern, allows for online reconstructions of the trajectory and thereby makes it possible to determine in which lobules recordings are made, even without post mortem analysis (**Fig. 3a**). Moreover, due to the two types of inputs, parallel fibers and climbing fibers, the cells that integrate all inputs and form the only output of the cerebellar cortex, the Purkinje cells, can be readily identified by their two types of action potentials. Activation of the hundreds of synapses from a single climbing fiber onto a Purkinje cell results in a massive, prolonged depolarization, also known as the 'complex' spike¹². This signature response can also be observed in extracellular recordings, here too as a complex shape (**Fig. 3a**), and as such forms a landmark feature to identify cerebellar Purkinje cells. Hence it has been possible for decades, and thus since long before two-photon imaging became available, to perform cell-type specific targeted recordings of Purkinje cells. The 'visualization' here, however, comes in the form of recorded electrical signal, which is commonly converted into an auditory signal that allows the experimenter to 'hear' Purkinje cells, rather than see them. Finally, combining the advantages elements described above, the ability to record cell-specific activity at relatively deep locations in the cerebellum with long tapered pipettes brings the advantage of increased stability due to the intimate and extended contact between pipette and brain. The relevance of the technique in neuroscience is substantiated by the list of animal types (and labs) that have been used to perform cerebellar extracellular recordings *in vivo*. Originally technical limitation prohibited the use of smaller animals, and experiments were done in larger mammals, e.g. in monkeys²⁸⁻³¹, cats³²⁻³⁵, rabbits³⁶⁻³⁹ and less conventional animal models including fish^{40,41}, birds⁴² and amphibians⁴³. More recent work has been done on rats^{19,44,45} and ferrets^{46,47}, but the mouse has rapidly move into the spot of the most popular animal for extracellular recordings *in vivo*, also in the cerebellum^{3,13,48-51}.

Cerebellar genetics and connectivity

With its crystalline architecture, the cerebellum has attracted the attention from neuroanatomists since the early days of neuroscience^{52,53}. Particularly the cerebellar cortex attracted attention, with its apparent highly homogenously present layered organization (**Fig. 1c**). Over the years, or even decades, this image of a homogeneous structure has been contested at different levels. The first evidence against the uniform nature is the description of a patterned expression of 5'-nucleotidase, more than half a century ago⁵⁴. Since then, numerous protein have been found to expressed in particular patterns, with the most well-known example being , identified in rats, the zebrins: zebrin I and II^{55,56}. Zebrins owe their name to the peculiar pattern of expression, consisting of sagittal stripes of stained, 'positive' and non-stained, 'negative' Purkinje cells (**Fig. 1b**). This pattern of stripes of varying width is not unique to rats, but has been observed in various species of different classes

ranging from pigeons⁵⁷, via e.g. hedgehogs⁵⁸ to humans. It has been observed for numerous proteins since, including for instance: mGluR1b⁵⁹, EAAT4⁶⁰, PLCβ3 and β4⁶¹, PKCδ⁶², NCS-1⁶³, IP3R1⁶⁴ and Neuroplastin⁶⁵ (**Fig. 1b**). Interestingly, the differentiation does not only exist in the genetic profile, but also in morphology and connectivity. For instance, Altman and Bayer in 1977 described cell-type that is abundantly present, but almost only in the granule cell layer of vestibule-cerebellum⁶⁶, later to be recognized and named by its peculiar shape as the unipolar brush cell (UBC)⁶⁷. This discovery signifies the more general notion that despite its homogeneous appearance, the cerebellar cortex has regional variations in composition.

Apart from the variations, cumulative research indicates that the connectivity of the cerebellum adheres to particular patterns as well. PCs with the same zebrin II-identity form a cerebellar module, in that they receive CF inputs from a the same subnucleus of the inferior olive, and send their output to the parts of the cerebellar nuclei (**Fig. 1c**)⁶⁸⁻⁷³. In fact, even mossy fibers can adhere to the zebrin signature⁶⁸, although there is integration of different modalities at the input stage already⁷⁴. Hence, one could argue that zebrin is a marker identifying cerebellar cortical regions, or modules, that form a functional unit that integrates particular mossy and climbing information^{68,70,75}.

Differential cerebellar physiology

The presence of differential gene expression profiles between distinct Purkinje cell populations could implicate that there are related differences in physiology as well. The first evidence supporting this concept came from Wadiche and Jahr, who demonstrated that the presence of EAAT4, which has an expression pattern very similar to that of Zebrin, inhibits the activation of metabotropic glutamate receptors. As a result, EAAT4-negative (and thus zebrin-negative) Purkinje cells in lobule III exhibit long-term depression of the PF-PC synapse (PF-PC LTD), while zebrin/EAAT4-positive Purkinje cells in lobule X do not⁷⁶. Similar differences between anterior and posterior lobules have been described for a depolarization-induced slow current, a current related to postsynaptic dopamine, released in an autocrine manner^{77,78}. *In vitro* experiments also revealed differences in general excitability between Purkinje cells in anterior and posterior lobules, and related them to differences in specific K⁺ and Na⁺ currents⁷⁹. Even the climbing fiber input itself has been suggested to be physiologically different between zebrin-positive and zebrin-negative Purkinje cells, although is not clear if these differences work in conjunction with or against those observed in Purkinje cells⁸⁰.

Taken together these results sparked our interest in the activity of individual zebrin-positive and zebrin-negative Purkinje cells in the awake, active mouse. This scientific question required exactly those recordings conditions, that allow insight into not only into the identity of the recorded cell in terms of cell-type, but also that in terms of genetic 'identity', a feature that can only be visualized by immunohistochemistry or genetically-encoded fluorescent markers. To determine the impact of these features or other differences in gene expression profiles, hundreds of Purkinje cells were recorded throughout the cerebellar cortex and the activity patterns were correlated to their location and zebrin-identity, either by postmortem analysis or by online identification based on two-photon imaging (**Fig. 3b-c**)^{81,82}, results that were confirmed by others⁴⁴.

Methods

By preparing mice for *in vivo* recordings in the awake animal with the option for chronic recordings over several days, one can avoid side-effects of anesthetics or analgesics (see e.g. Schonewille, et al.⁴⁸). In this section we provide a detailed protocol for the surgical preparation of a craniotomy to access the cerebellum, followed by an overview of the experimental setup and the protocol for *in vivo* electrophysiological recording in an awake mouse, and the data analysis. These methods have been successfully developed and applied in our laboratory over the last decade to record neuronal activities in an anesthetized^{19,48}, or alert^{81,83,84}, or behaving mouse^{85,86}.

Surgical procedures

Mice are commonly prepared for experiments with a preparational surgery, as also described by White, et al.⁸⁷. During the surgery a "pedestal" for immobilization of the head and a chamber for a single or

multiple electrophysiological recording session(s) will be placed as follows (see also **Fig. 2a**). Mice are anaesthetized by a mixture of isoflurane and oxygen (initial concentration: 4% V/V in O₂, maintenance concentration: 1.5-2% V/V in O₂) in a gas chamber. Once the mouse no longer has a foot pinching reflex, the mouth is opened and the tongue is pulled out with tweezers. Next, the bar of a stereotaxic apparatus (Bilaney, Germany) is gently inserted into the mouth. When in the proper position, the screw is fastened to fix the head horizontally. To assure that body temperature is maintained at 37 °C, the anal thermosensor is carefully placed and connected to a heating pad (FHC, Bowdoinham, ME). The eyes are protected by covering them with an eye ointment (duratears, Alcon, Belgium). The dorsal cranial fur is shaven with soap and a scalpel, a midline incision is made to expose the skull, and the periosteum is cleared and cleaned with cotton swabs (**Fig. 2a**). A drop of OptiBond all-in-one (Kerr, Salerno, Italy) is applied to the dorsal cranial surface of the skull from bregma to lambda and cured with light for 60 seconds. The adhesive layer is covered with a thin layer of Charisma composite (Heraeus Kulzer, Germany) and the pedestal is embedded in the composite and cured immediately. Additional layers of composite are added to surround the base of the pedestal and cured with light, to complete the pedestal placement part of the surgery (**Fig. 2a**).

From here on, the mouse can be fixed by either the pedestal or the mouth bar. The skin over the skull is opened until the foramen magnum and the three layers of medial neck muscles overlying the occipital bone and foramen magnum are removed. A craniotomy is made by drilling an opening (max. Ø < 3 mm) in the interparietal or occipital bone, overlying the cerebellar part of interest. Size and location of the craniotomy can be adapted to the experimental approach. Smaller craniotomies are preferable for reasons of stability and the dura mater should be preserved to keep the brain intact and healthy, if possible (**Fig. 2b**). A recording chamber is constructed around the craniotomy with Charisma composite again and sealed with self-curing silicone composite (Twinsil speed 22, Picodent, Germany). The mouse preferably is allowed to recover in its home cage for at least 3 days after the surgery before starting electrophysiological recordings.

Anesthesia, analgesia and anti-inflammatory drugs for experimental mice

Discomfort to the mice is limited by the use of several anesthetics, analgesics and anti-inflammatory drugs given pre-, peri- and post-surgery. A balanced combination could include isoflurane (4% induction, 1.5-2% maintenance), lidocaine (in Xylocain 10%, drop of 100mg/ml), Bupivacaine (Bupivacaine Actavis, drop of 2.5mg/ml), buprenorphine (Temgesic, 0.3 mg/ml) and rimadyl (Carprofen, 50 mg/ml). Isoflurane is given as indicated in the experimental approach, lidocaine and bupivacaine are administered locally as analgesic on the skull and buprenorphine (diluted to 0.02 mg/kg) and Rimadyl (5 mg/kg) are injected intraperitoneally for post-operative analgesia and to prevent inflammation.

The equipment and recording procedures

There is no golden standard for in vivo electrophysiological recordings. Below the method that has been developed over several years of using this technique is detailed. First, to assure that the animal is comfortable with the experimental conditions including the restraining of the head, mice are habituated by placing them in the experimental setup for 30–60 min for one or two days before the first experimental session. For habituation and experiments the mice are immobilized using a custom-made restrainer, by bolting the head holder to a head fixation post. Prior to experiments, the dental mixture should be removed to expose the craniotomy. Tissue can accumulate on top of the dura, which needs to be removed to allow a clean entrance and easy penetration for the recording and stimulation probes. Using a hypodermic needle an incision is made in the dura to facilitate the penetration of glass pipettes (only needed for sharper tips) and the exposed cortex is rinsed with saline to remove blood. During the recording, the brain surface is covered with saline in order to prevent dehydration. Glass pipettes (OD 1.5 mm, ID 0.86 mm, borosilicate, Sutter Instruments, USA; 1-2 µm tips, 4-8 MΩ) are pulled (P-1000, Sutter Instruments, USA) and filled with 2 M NaCl solution and Alcian Blue (for pressure injections) or 2–3% solution of biotin (Vector Laboratories). The pipette is lowered slowly into the cerebellar cortex by either an analogue, hydraulic Microdrive (Trent Wells, TX, USA) or a digital Microdrive (in final approach set to 2–4-µm step size, step every 2–3 s). The recorded signals are pre-amplified (custom-made preamplifier, 1000x DC), filtered and digitized (either CyberAmp320, Molecular Devices, with Power1401, CED, Cambridge, UK or Axon Multiclamp 700B with Digidata 1440A, Molecular Devices, Sunnyvale, CA, USA) and stored on disk (using Spike2, CED

or pClamp10, Molecular Devices) for offline analysis (**Figure 2c**). To mark the recording location, brief air pulses (MPPI-3, ASI, USA) or iontophoresis (custom-made device, 4-8 μ A, 7 s on – 7 s off) can be used locally deliver the Alcian Blue or biotin, respectively. After the recording session the animal will be sacrificed if the experiment is completed or the brain is covered with an ointment (Duratears, Alcon, Belgium) and the chamber is sealed using self-curing silicone composite (Twindil speed 22, Picodent, Germany) to continue the next day.

Targeted recordings using two-photon imaging

Described above is the general surgical preparation for *in vivo* recording in awake mice. For *in vivo* two-photon targeted recordings the approach is similar to these procedures, but the construction for immobilization and craniotomy is adapted to the requirements of the microscope. For these experiments a rectangular metal plate is used and placed perpendicular to the midline of the mouse, with grooves for solid fixation and a larger opening for imaging and recordings.

Images are acquired using a TriM Scope II (LaVision BioTec, Bielefeld, Germany) attached to an upright microscope with a 40x/0.8 NA water-immersion objective (Olympus, Tokyo, Japan). Laser illumination is provided by a Chameleon Ultra titanium sapphire laser (Coherent, Santa Clara, CA) and to detect fluorescent emissions, two photomultiplier tubes (Hamamatsu, Iwata City, Japan) are used. The recording pipette is filled with Alexa-594 (10 μ M in 2 M NaCl; Life Technologies, Carlsbad, CA) and visualized with an excitation wavelength of 800 nm. Images from eGFP and Alexa-594 are filtered using a Gaussian kernel, contrast-optimized and subsequently merged in Photoshop (Adobe, San Jose, CA). A typical recording sampled 40 x 200 μ M with a frame rate of approximately 25Hz⁸¹ (**Figure 2c**).

Selecting cells for recording

In contrast to *in vitro* techniques, *in vivo* approaches can be used to study neurons in physiological conditions with normal inputs and intact axon, and in their virtually natural ambience of neuronal circuits, thus resulting in more realistic characterization that can be more easily extrapolated than *in vitro* recordings. However, in an intact animal, it is not easy to determine the type and location of the neuron that is being recorded. Fortunately, there are several ways to identify the cell type and location in the cerebellum.

Spike waveform. Even when recorded extracellularly, different types of cells present distinct spike waveforms. For instance, Purkinje cells are identified by the presence of simple and complex spikes and are confirmed to be a single unit by the presence of a pause in simple spikes after each complex spike⁸⁸. Interestingly, the signal recorded when approaching a Purkinje cell depends on the location relative to the orientation of the cell. When approached from the molecular layer, the first signal that can be identified visually (and heard if the recordings signals are converted to audio) is that of the complex spikes. These large, slow spikes (lower tones) appear as negative deflections from the baseline, at ~1 Hz (**Figure 3a, top**). Continuing in the direction of the soma will slowly reveal the ~50-100 Hz firing rate (a soft hum) of the simple spikes, also as negative deflections, while the complex spike signal slowly changes into a predominantly positive signal (See **Figure 3a, middle**). Close to the soma, the spike waveform indicates the distance between the tip of pipette and neuron. In extracellular recordings, the tip of an electrode is positioned adjacent to, but outside of a neuron, as depicted in (**Figure 3a, upper middle**). With a clean tip one can, in optimal circumstances and -if needed- aided by a little negative pressure, establish a juxtacellular recording (**Figure 3a, lower middle**). The ultimate step would be to proceed to whole cell patch clamp recording configuration, the most commonly used patch-clamp mode where the membrane patch is disrupted by briefly applying strong suction to establish electrical and molecular access to the intracellular space. It is the gold standard for high-fidelity analysis of the electrical properties and functional connectivity of neurons, but its success rate is much lower than extracellular and juxtacellular recording (**Figure 3a, bottom**)^{2,3,89}.

Firing pattern. In the cerebellar cortex other cell types can be identified, apart from Purkinje cells. Separating these is more complicated, but can be done quite reliably based on wave forms and firing characteristics under anesthesia as indicated by Ruigrok, et al.¹⁹, although this is debated⁹⁰. In this manner, granule cells can be identified by their high irregularity and low average firing rate; unipolar brush cells have a signature low CV2 (see “data analysis”); molecular layer interneurons typically

stand out by their irregularity and intermediate to high firing rate, while Golgi cells have an intermediate firing rate and are more regular¹⁹. Due to the poor level of somatotopy in the cerebellar cortex, the potential to identify the recording area based on responses to sensory input is limited⁹¹. Nonetheless there are several exceptions of well-studied areas including: the (para)floculus, which responds with reciprocal modulation of simple and complex spikes to visual and vestibular input^{28,85}, the saccade-related area in lobule VI and VII in which Purkinje cells respond to saccadic eye movements²⁹ and a designated area in the transitions between the vermis and the hemispheres and (the hemispherical parts of) lobules IV-V and lobule VI - simple lobule^{24,35}.

Labeling. To know the exact recording location when recording deeper in the brain, it is imperative to label the cell individually after completing the recording. The two most common forms of labeling with glass pipettes are iontophoresis and pressure injections, whereas with metal electrodes often lesions are placed to mark recording location. Iontophoresis results in minimal tissue damage, but requires a charged tracer or dye and has limited control over injection volume or concentration. Several tracers are very suitable for iontophoresis, including biotinylated dextran amines (i.e., BDA-3000), as they can be used for visualization of long-range axonal projections and hence require intact structures and up to a few days of survival after labeling^{92,93}. Alternatively, an uncharged dye can be injected with controlled back-pressure on the glass pipette, such as Alcian Blue (0.1 - 2 % solution in saline, Sigma-Aldrich, USA) by air pressure^{81,94}. Ideal for these injections are double barrel or septum borosilicate glass pipettes (e.g. theta septum, 1.5 OD, 1.02 ID, USA), one half of the pipette is filled with 2 M NaCl for recording, the other half barrel is filled with a blue dye for labeling. Although the immunohistological procedures are time-consuming, iontophoresis-based injections allow for the most controlled small injections that, by controlling the amount of current and duration, ideally label only one cell.

Imaging. With the growing understanding of the complexity of the brain, there is also a growing appreciation for the diversity present, even within populations of a particular cell-type. To be able to characterize this diversity *in vivo*, tools are required to identify this subdivision within cell-types, either offline with immunohistochemistry, or online with fluorescent markers. Hence, to be able to identify the different cerebellar modules, based on the expression of zebrin, we used EAAT4-promotor driven eGFP expressing, or EAAT4-eGFP, mice⁹⁵. EAAT4, or Excitatory Amino Acid Transporter 4, is expressed in a pattern similar to that of zebrin⁹⁶. Alternatively, one could also use a zebrin (aldolase c) promotor driven expression of a fluorescent marker⁹⁷. The strong expression of eGFP in both the dendrite and the soma readily identifies zebrin / EAAT4 positive Purkinje cells, but the weak expression in zebrin / EAAT4 negative cells helps localizing also those, and thus facilitates targeted recordings of both types, with a single genetic manipulation⁸¹. By visualizing also the recording pipette with Alexa-594 both the pipette and the preferred area can be made visible, allowing for selection of and careful, precise approaches to the chosen cells.

Data analysis

Several commercial software packages are available to analyze the recorded traces. Off-line analysis is performed here using SpikeTrain (Neurasmus B.V., Rotterdam, The Netherlands, www.neurasmus.com), running under Matlab (Mathworks, MA, USA). SpikeTrain is an object oriented program code that can use either superparamagnetic clustering⁹⁸ or on principal component analysis. After automated SS and CS detection and discrimination of simple spike and complex spike the assigned codes can be manually checked and corrected, if needed. Histograms of SS trigger on the occurrence of a CS (bin width 1 ms) can be used to verify that each isolated Purkinje cell shows a clean climbing fiber pause (i.e. no simple spikes for the duration of each complex spike, see also **Fig. 3a**). The absence of a climbing fiber pause, the minimum duration between a complex spike and the following simple spike, is taken to indicate that the isolation is imperfect and there is a second unit present. For each cell several parameters for simple and complex spikes can be calculated, including: firing rate, CV and mean CV2, as well as the climbing fiber pause⁸⁴. CV is the standard deviation of inter-spike intervals (ISI) divided by the mean, the mean CV2 is calculated as the mean of $2 \cdot (|ISI|_{n+1} - |ISI|_n) / (|ISI|_{n+1} + |ISI|_n)$ ⁹⁹. Both are measures for the regularity of the firing, also referred to as precision⁵⁰, with CV reflecting that of the entire recording and mean CV2 that of adjacent intervals, making the latter a measure of regularity on small timescales. In addition to auto-correlograms, which also illustrates the regularity, the presence of complex spikes also allows for cross-correlograms¹⁰⁰, of which the shape correlates with the cerebellar region^{81,82}.

Technical considerations

Several aspects need to be taken into account when performing recordings *in vivo* and when using fluorescent signals. First, when experimental procedures and ethical considerations allow to do so, recording in awake animals is preferable. Generalize anesthesia significantly reduces the discomfort of the animal and enhances the stability of the preparation, especially if the slower and deeper breathing can be properly controlled to avoid movement of the brain. However, anesthesia significantly impacts for instance Purkinje cells, and changes various properties of its firing activity, depending also on the type of anesthetic⁴⁸. The effects of anesthetics are comprehensible, as the cerebellum is a sensorimotor integrator¹⁰¹ and under anesthesia at least the motor part is disrupted. Isoflurane had a more pronounced effect on Purkinje cell activity than ketamine/xylazine in that it increased the pausing time and other parameters related to inter-spike intervals more severely⁴⁸.

Moreover, both in anesthetized and in awake animals it is essential to consider the role of temperature. It is common knowledge that in *in vitro* experiments temperature has a substantial influence on activity and plasticity. Similar effects can be predicted *in vivo*, but it is less clear to what extent they are present¹⁰². Using a miniature probe *in vivo* we found that the temperature drops dramatically at the surface of the craniotomy in the absence of any form of heating. In fact, we observed a temperature difference of up to 5°C compared to deeper parts of the cerebellum that correlated with a lower Purkinje cell simple spike firing rate in the first 0.5 to 1 mm of tissue⁸². Two-photon imaging only reaches to first couple of hundred micrometers, implicating that recordings under these conditions can be affected (compare **Fig. 3b vs. 3c**). A perfusion system, similar to that used in *in vitro* recordings, could potentially solve the issue, which is of particular relevance in studies that also include a behavioral component¹⁰³. Conversely, during two-photon imaging photo-stimulation can hamper the success rate of obtaining patch recordings *in vivo*, possibly due to photo-damage or interactions with the pipette solution⁴.

Conclusions

In this chapter we describe the use of extracellular recordings in mice during quiet wakefulness combined with methods to target specific subpopulations. We focus on cerebellar Purkinje cells and describe the approach to targeted recordings from specific sub-types of Purkinje cells. In addition to post-mortem labelling we detailed the approach to imaging based recordings of specific Purkinje cells. In mice expressing a fluorescent protein under a cell sub-type specific promoter (so-called zebrin-positive or negative neurons), we used two-photon imaging to identify the target neurons and subdivide them based on the intensity of fluorescence. By visualizing the pipette tip with a fluorescent dye we assure an optimal approach to the identified neuron and create the potential to even do dual or multiple, side-by-side recordings. In this time of increasing appreciation for the heterogeneity within particular cell-types, the ability to make targeted recordings of specific sub-types will become more and more relevant.

References

- 1 Hubel, D. H. & Wiesel, T. N. Receptive fields of single neurones in the cat's striate cortex. *J Physiol.* 1959; 148, 574-91.
- 2 van Welie, I., Roth, A., Ho, S. S. *et al.* Conditional Spike Transmission Mediated by Electrical Coupling Ensures Millisecond Precision-Correlated Activity among Interneurons *In Vivo*. *Neuron.* 2016; 90, 810-23.
- 3 Chen, S., Augustine, G. J. & Chadderton, P. The cerebellum linearly encodes whisker position during voluntary movement. *Elife.* 2016; 5, e10509.
- 4 Margrie, T. W., Meyer, A. H., Caputi, A. *et al.* Targeted whole-cell recordings in the mammalian brain *in vivo*. *Neuron.* 2003; 39, 911-8.
- 5 Komai, S., Denk, W., Osten, P. *et al.* Two-photon targeted patching (TPTP) *in vivo*. *Nat Protoc.* 2006; 1, 647-52.
- 6 Kitamura, K., Judkewitz, B., Kano, M. *et al.* Targeted patch-clamp recordings and single-cell electroporation of unlabeled neurons *in vivo*. *Nat Methods.* 2008; 5, 61-7.
- 7 Palay, S. L. & Chan-Palay, V. *Cerebellar cortex: cytology and organization.* 180-336 (Springer Verlag, 1974).
- 8 Kennedy, A., Wayne, G., Kaifosh, P. *et al.* A temporal basis for predicting the sensory consequences of motor commands in an electric fish. *Nat Neurosci.* 2014; 17, 416-22.
- 9 Eccles, J., Llinas, R. & Sasaki, K. Golgi Cell Inhibition in the Cerebellar Cortex. *Nature.* 1964; 204, 1265-6.
- 10 Eccles, J. C., Llinas, R. & Sasaki, K. The mossy fibre-granule cell relay of the cerebellum and its inhibitory control by Golgi cells. *Exp Brain Res.* 1966; 1, 82-101.

- 11 Eccles, J. C., Llinas, R. & Sasaki, K. The excitatory synaptic action of climbing fibres on the Purkinje cells of the cerebellum. *J Physiol.* 1966; 182, 268-96.
- 12 Schmolesky, M. T., Weber, J. T., De Zeeuw, C. I. *et al.* The making of a complex spike: ionic composition and plasticity. *Ann N Y Acad Sci.* 2002; 978, 359-90.
- 13 Najafi, F. & Medina, J. F. Beyond "all-or-nothing" climbing fibers: graded representation of teaching signals in Purkinje cells. *Front Neural Circuits.* 2013; 7, 115.
- 14 Ito, M. Cerebellar long-term depression: characterization, signal transduction, and functional roles. *Physiol Rev.* 2001; 81, 1143-95.
- 15 Winkelman, B. & Frens, M. Motor coding in floccular climbing fibers. *J Neurophysiol.* 2006; 95, 2342-51.
- 16 Yarom, Y. & Cohen, D. The olivocerebellar system as a generator of temporal patterns. *Ann N Y Acad Sci.* 2002; 978, 122-34.
- 17 Andersen, P., Eccles, J. & Voorhoeve, P. E. Inhibitory Synapses on Somas of Purkinje Cells in the Cerebellum. *Nature.* 1963; 199, 655-6.
- 18 van Beugen, B. J., Gao, Z., Boele, H. J. *et al.* High frequency burst firing of granule cells ensures transmission at the parallel fiber to purkinje cell synapse at the cost of temporal coding. *Front Neural Circuits.* 2013; 7, 95.
- 19 Ruigrok, T. J., Hensbroek, R. A. & Simpson, J. I. Spontaneous activity signatures of morphologically identified interneurons in the vestibulocerebellum. *J Neurosci.* 2011; 31, 712-24.
- 20 Albus, J. S. A theory of cerebellar function. *Math. Biosci.* 1971; 10, 25-61.
- 21 Marr, D. A theory of cerebellar cortex. *J Physiol.* 1969; 202, 437-70.
- 22 Ito, M., Sakurai, M. & Tongroach, P. Climbing fibre induced depression of both mossy fibre responsiveness and glutamate sensitivity of cerebellar Purkinje cells. *J Physiol.* 1982; 324, 113-34.
- 23 Schonewille, M., Gao, Z., Boele, H. J. *et al.* Reevaluating the role of LTD in cerebellar motor learning. *Neuron.* 2011; 70, 43-50.
- 24 ten Brinke, M. M., Boele, H. J., Spanke, J. K. *et al.* Evolving Models of Pavlovian Conditioning: Cerebellar Cortical Dynamics in Awake Behaving Mice. *Cell Rep.* 2015; 13, 1977-88.
- 25 Boyden, E. S., Katoh, A. & Raymond, J. L. Cerebellum-dependent learning: the role of multiple plasticity mechanisms. *Annu Rev Neurosci.* 2004; 27, 581-609.
- 26 Gao, Z., van Beugen, B. J. & De Zeeuw, C. I. Distributed synergistic plasticity and cerebellar learning. *Nat Rev Neurosci.* 2012; 13, 619-35.
- 27 Ito, M., Yamaguchi, K., Nagao, S. *et al.* Long-term depression as a model of cerebellar plasticity. *Prog Brain Res.* 2014; 210, 1-30.
- 28 Lisberger, S. G. & Fuchs, A. F. Response of flocculus Purkinje cells to adequate vestibular stimulation in the alert monkey: fixation vs. compensatory eye movements. *Brain Res.* 1974; 69, 347-53.
- 29 Thier, P., Dicke, P. W., Haas, R. *et al.* Encoding of movement time by populations of cerebellar Purkinje cells. *Nature.* 2000; 405, 72-6.
- 30 Pasalar, S., Roitman, A. V., Durfee, W. K. *et al.* Force field effects on cerebellar Purkinje cell discharge with implications for internal models. *Nat Neurosci.* 2006; 9, 1404-11.
- 31 Roy, J. E. & Cullen, K. E. A neural correlate for vestibulo-ocular reflex suppression during voluntary eye-head gaze shifts. *Nat Neurosci.* 1998; 1, 404-10.
- 32 Sato, Y., Miura, A., Fushiki, H. *et al.* Complex spike responses of cerebellar Purkinje cells to constant velocity optokinetic stimuli in the cat flocculus. *Acta Otolaryngol Suppl.* 1993; 504, 13-6.
- 33 Jorntell, H. & Ekerot, C. F. Reciprocal bidirectional plasticity of parallel fiber receptive fields in cerebellar Purkinje cells and their afferent interneurons. *Neuron.* 2002; 34, 797-806.
- 34 Yartsev, M. M., Givon-Mayo, R., Maller, M. *et al.* Pausing purkinje cells in the cerebellum of the awake cat. *Front Syst Neurosci.* 2009; 3, 2.
- 35 Hesslow, G. Inhibition of classically conditioned eyeblink responses by stimulation of the cerebellar cortex in the decerebrate cat. *J Physiol (Lond).* 1994; 476, 245-56.
- 36 Ekerot, C. F. & Kano, M. Stimulation parameters influencing climbing fibre induced long-term depression of parallel fibre synapses. *Neurosci Res.* 1989; 6, 264-8.
- 37 Simpson, J. I. & Alley, K. E. Visual climbing fiber input to rabbit vestibulo-cerebellum: a source of direction-specific information. *Brain Res.* 1974; 82, 302-8.
- 38 Yagi, N., Chikamori, Y. & Matsuoka, I. Response of single Purkinje neurons in the flocculus of albino rabbits to caloric stimulation. *Acta Otolaryngol.* 1977; 84, 98-104.
- 39 Miyashita, Y. Eye velocity responsiveness and its proprioceptive component in the floccular Purkinje cells of the alert pigmented rabbit. *Exp Brain Res.* 1984; 55, 81-90.
- 40 Yoshida, M. & Kondo, H. Fear conditioning-related changes in cerebellar Purkinje cell activities in goldfish. *Behav Brain Funct.* 2012; 8, 52.
- 41 Sawtell, N. B., Williams, A. & Bell, C. C. Central control of dendritic spikes shapes the responses of Purkinje-like cells through spike timing-dependent synaptic plasticity. *J Neurosci.* 2007; 27, 1552-65.
- 42 Wylie, D. R. & Frost, B. J. Purkinje cells in the vestibulocerebellum of the pigeon respond best to either translational or rotational wholefield visual motion. *Exp Brain Res.* 1991; 86, 229-32.
- 43 Llinas, R., Bloedel, J. R. & Hillman, D. E. Functional characterization of neuronal circuitry of frog cerebellar cortex. *J Neurophysiol.* 1969; 32, 847-70.
- 44 Xiao, J., Cerminara, N. L., Kotsurovskyy, Y. *et al.* Systematic regional variations in Purkinje cell spiking patterns. *PLoS One.* 2014; 9, e105633.
- 45 Shin, S. L., Hoebeek, F. E., Schonewille, M. *et al.* Regular patterns in cerebellar Purkinje cell simple spike trains. *PLoS ONE.* 2007; 2, e485.
- 46 Hesslow, G. & Ivarsson, M. Suppression of cerebellar Purkinje cells during conditioned responses in ferrets. *Neuroreport.* 1994; 5, 649-52.
- 47 Lou, J. S. & Bloedel, J. R. The responses of simultaneously recorded Purkinje cells to the perturbations of the step cycle in the walking ferret: a study using a new analytical method--the real-time postsynaptic response (RTPR). *Brain Res.* 1986; 365, 340-4.
- 48 Schonewille, M., Khosrovani, S., Winkelman, B. H. *et al.* Purkinje cells in awake behaving animals operate at the upstate membrane potential. *Nat Neurosci.* 2006; 9, 459-61; author reply 61.

49 Arancillo, M., White, J. J., Lin, T. *et al.* In vivo analysis of Purkinje cell firing properties during postnatal mouse development. *J Neurophysiol.* 2015; 113, 578-91.

50 Walter, J. T., Alvina, K., Womack, M. D. *et al.* Decreases in the precision of Purkinje cell pacemaking cause cerebellar dysfunction and ataxia. *Nat Neurosci.* 2006; 9, 389-97.

51 Barmack, N. H. & Yakhnitsa, V. Functions of interneurons in mouse cerebellum. *J Neurosci.* 2008; 28, 1140-52.

52 Cajal, S. R. y. *Histologie du Système Nerveux de l'Homme et des Vertébrés.* Vol. I-II (1911).

53 Henle, J. *Handbuch der Nervenlehre des Menschen.* (Fachbuchverlag Dresden, 1879).

54 Scott, T. G. A Unique Pattern of Localization within the Cerebellum. *Nature.* 1963; 200, 793.

55 Leclerc, N., Dore, L., Parent, A. *et al.* The compartmentalization of the monkey and rat cerebellar cortex: zebrin I and cytochrome oxidase. *Brain Res.* 1990; 506, 70-8.

56 Brochu, G., Maler, L. & Hawkes, R. Zebrin II: a polypeptide antigen expressed selectively by Purkinje cells reveals compartments in rat and fish cerebellum. *J Comp Neurol.* 1990; 291, 538-52.

57 Graham, D. J. & Wylie, D. R. Zebrin-immunopositive and -immunonegative stripe pairs represent functional units in the pigeon vestibulocerebellum. *J Neurosci.* 2012; 32, 12769-79.

58 Sillitoe, R. V., Kunzle, H. & Hawkes, R. Zebrin II compartmentation of the cerebellum in a basal insectivore, the Madagascan hedgehog tenrec *Echinops telfairi*. *J Anat.* 2003; 203, 283-96.

59 Grandes, P., Mateos, J. M., Ruegg, D. *et al.* Differential cellular localization of three splice variants of the mGluR1 metabotropic glutamate receptor in rat cerebellum. *Neuroreport.* 1994; 5, 2249-52.

60 Nagao, S., Kwak, S. & Kanazawa, I. EAAT4, a glutamate transporter with properties of a chloride channel, is predominantly localized in Purkinje cell dendrites, and forms parasagittal compartments in rat cerebellum. *Neuroscience.* 1997; 78, 929-33.

61 Sarna, J. R., Marzban, H., Watanabe, M. *et al.* Complementary stripes of phospholipase Cbeta3 and Cbeta4 expression by Purkinje cell subsets in the mouse cerebellum. *J Comp Neurol.* 2006; 496, 303-13.

62 Barmack, N. H., Qian, Z. & Yoshimura, J. Regional and cellular distribution of protein kinase C in rat cerebellar purkinje cells [In Process Citation]. *J Comp Neurol.* 2000; 427, 235-54.

63 Jinno, S., Jeromin, A., Roder, J. *et al.* Compartmentation of the mouse cerebellar cortex by neuronal calcium sensor-1. *J Comp Neurol.* 2003; 458, 412-24.

64 Furutama, D., Morita, N., Takano, R. *et al.* Expression of the IP3R1 promoter-driven nls-lacZ transgene in Purkinje cell parasagittal arrays of developing mouse cerebellum. *J Neurosci Res.* 2010; 88, 2810-25.

65 Marzban, H., Khanzada, U., Shabir, S. *et al.* Expression of the immunoglobulin superfamily neuroplastin adhesion molecules in adult and developing mouse cerebellum and their localisation to parasagittal stripes. *J Comp Neurol.* 2003; 462, 286-301.

66 Altman, J. & Bayer, S. A. Time of origin and distribution of a new cell type in the rat cerebellar cortex. *Exp Brain Res.* 1977; 29, 265-74.

67 Harris, J., Moreno, S., Shaw, G. *et al.* Unusual neurofilament composition in cerebellar unipolar brush neurons. *J Neurocytol.* 1993; 22, 1039-59.

68 Pijpers, A., Apps, R., Pardoe, J. *et al.* Precise spatial relationships between mossy fibers and climbing fibers in rat cerebellar cortical zones. *J Neurosci.* 2006; 26, 12067-80.

69 Sugihara, I. & Shinoda, Y. Molecular, topographic, and functional organization of the cerebellar nuclei: analysis by three-dimensional mapping of the olivonuclear projection and aldolase C labeling. *J Neurosci.* 2007; 27, 9696-710.

70 Voogd, J. & Ruigrok, T. J. The organization of the corticonuclear and olivocerebellar climbing fiber projections to the rat cerebellar vermis: the congruence of projection zones and the zebrin pattern. *J Neurocytol.* 2004; 33, 5-21.

71 Apps, R. & Hawkes, R. Cerebellar cortical organization: a one-map hypothesis. *Nat Rev Neurosci.* 2009; 10, 670-81.

72 Sugihara, I. Compartmentalization of the deep cerebellar nuclei based on afferent projections and aldolase C expression. *Cerebellum.* 2011; 10, 449-63.

73 Sugihara, I., Fujita, H., Na, J. *et al.* Projection of reconstructed single Purkinje cell axons in relation to the cortical and nuclear aldolase C compartments of the rat cerebellum. *J Comp Neurol.* 2009; 512, 282-304.

74 Huang, C. C., Sugino, K., Shima, Y. *et al.* Convergence of pontine and proprioceptive streams onto multimodal cerebellar granule cells. *Elife.* 2013; 2, e00400.

75 Ruigrok, T. J. Ins and outs of cerebellar modules. *Cerebellum.* 2011; 10, 464-74.

76 Wadiche, J. I. & Jahr, C. E. Patterned expression of Purkinje cell glutamate transporters controls synaptic plasticity. *Nat Neurosci.* 2005; 8, 1329-34.

77 Shin, J. H., Kim, Y. S. & Linden, D. J. Dendritic glutamate release produces autocrine activation of mGluR1 in cerebellar Purkinje cells. *Proc Natl Acad Sci U S A.* 2008; 105, 746-50.

78 Kim, Y. S., Shin, J. H., Hall, F. S. *et al.* Dopamine signaling is required for depolarization-induced slow current in cerebellar Purkinje cells. *J Neurosci.* 2009; 29, 8530-8.

79 Kim, C. H., Oh, S. H., Lee, J. H. *et al.* Lobule-specific membrane excitability of cerebellar Purkinje cells. *J Physiol.* 2012; 590, 273-88.

80 Paukert, M., Huang, Y. H., Tanaka, K. *et al.* Zones of enhanced glutamate release from climbing fibers in the mammalian cerebellum. *J Neurosci.* 2010; 30, 7290-9.

81 Zhou, H., Lin, Z., Voges, K. *et al.* Cerebellar modules operate at different frequencies. *Elife.* 2014; 3, e02536.

82 Zhou, H., Voges, K., Lin, Z. *et al.* Differential Purkinje cell simple spike activity and pausing behavior related to cerebellar modules. *J Neurophysiol.* 2015; 113, 2524-36.

83 Peter, S., Ten Brinke, M. M., Stedehouder, J. *et al.* Dysfunctional cerebellar Purkinje cells contribute to autism-like behaviour in Shank2-deficient mice. *Nat Commun.* 2016; 7, 12627.

84 Goossens, J., Daniel, H., Rancillac, A. *et al.* Expression of protein kinase C inhibitor blocks cerebellar long-term depression without affecting Purkinje cell excitability in alert mice. *J Neurosci.* 2001; 21, 5813-23.

85 Schonewille, M., Luo, C., Ruigrok, T. J. *et al.* Zonal organization of the mouse flocculus: physiology, input, and output. *J Comp Neurol.* 2006; 497, 670-82.

86 Badura, A., Schonewille, M., Voges, K. *et al.* Climbing fiber input shapes reciprocity of Purkinje cell firing. *Neuron.* 2013.

87 White, J. J., Lin, T., Brown, A. M. *et al.* An optimized surgical approach for obtaining stable extracellular single-unit recordings from the cerebellum of head-fixed behaving mice. *J Neurosci Methods.* 2016; 262, 21-31.

- 88 Simpson, J. I., Wylie, D. R. & De Zeeuw, C. I. On climbing fiber signals and their consequence(s). *Beh. Brain Sciences*. 1996; 19, 380-94.
- 89 Bengtsson, F. & Jorntell, H. Specific relationship between excitatory inputs and climbing fiber receptive fields in deep cerebellar nuclear neurons. *PLoS One*. 2014; 9, e84616.
- 90 Haar, S., Givon-Mayo, R., Barmack, N. H. *et al.* Spontaneous activity does not predict morphological type in cerebellar interneurons. *J Neurosci*. 2015; 35, 1432-42.
- 91 Manni, E. & Petrosini, L. A century of cerebellar somatotopy: a debated representation. *Nat Rev Neurosci*. 2004; 5, 241-9.
- 92 Pinault, D. A novel single-cell staining procedure performed in vivo under electrophysiological control: morpho-functional features of juxtacellularly labeled thalamic cells and other central neurons with biocytin or Neurobiotin. *J Neurosci Methods*. 1996; 65, 113-36.
- 93 Boele, H. J., Koekkoek, S. K., De Zeeuw, C. I. *et al.* Axonal sprouting and formation of terminals in the adult cerebellum during associative motor learning. *J Neurosci*. 2013; 33, 17897-907.
- 94 Hoebeek, F. E., Stahl, J. S., van Alphen, A. M. *et al.* Increased noise level of purkinje cell activities minimizes impact of their modulation during sensorimotor control. *Neuron*. 2005; 45, 953-65.
- 95 Gincel, D., Regan, M. R., Jin, L. *et al.* Analysis of cerebellar Purkinje cells using EAAT4 glutamate transporter promoter reporter in mice generated via bacterial artificial chromosome-mediated transgenesis. *Exp Neurol*. 2007; 203, 205-12.
- 96 Dehnes, Y., Chaudhry, F. A., Ullensvang, K. *et al.* The glutamate transporter EAAT4 in rat cerebellar Purkinje cells: a glutamate-gated chloride channel concentrated near the synapse in parts of the dendritic membrane facing astroglia. *J Neurosci*. 1998; 18, 3606-19.
- 97 Fujita, H., Aoki, H., Ajioka, I. *et al.* Detailed expression pattern of aldolase C (Aldoc) in the cerebellum, retina and other areas of the CNS studied in Aldoc-Venus knock-in mice. *PLoS One*. 2014; 9, e86679.
- 98 Quiroga, R. Q., Nadasdy, Z. & Ben-Shaul, Y. Unsupervised spike detection and sorting with wavelets and superparamagnetic clustering. *Neural Comput*. 2004; 16, 1661-87.
- 99 Holt, G. R., Softky, W. R., Koch, C. *et al.* Comparison of discharge variability in vitro and in vivo in cat visual cortex neurons. *J Neurophysiol*. 1996; 75, 1806-14.
- 100 De Zeeuw, C. I., Wylie, D. R., Stahl, J. S. *et al.* Phase Relations of Purkinje Cells in the Rabbit Flocculus During Compensatory Eye Movements. *J of Neurophysiol*. 1995; 74, 2051-63.
- 101 De Zeeuw, C. I., Hoebeek, F. E., Bosman, L. W. *et al.* Spatiotemporal firing patterns in the cerebellum. *Nat Rev Neurosci*. 2011; 12, 327-44.
- 102 Kalmbach, A. S. & Waters, J. Brain surface temperature under a craniotomy. *J Neurophysiol*. 2012; 108, 3138-46.
- 103 Long, M. A. & Fee, M. S. Using temperature to analyse temporal dynamics in the songbird motor pathway. *Nature*. 2008; 456, 189-94.

Figure legends

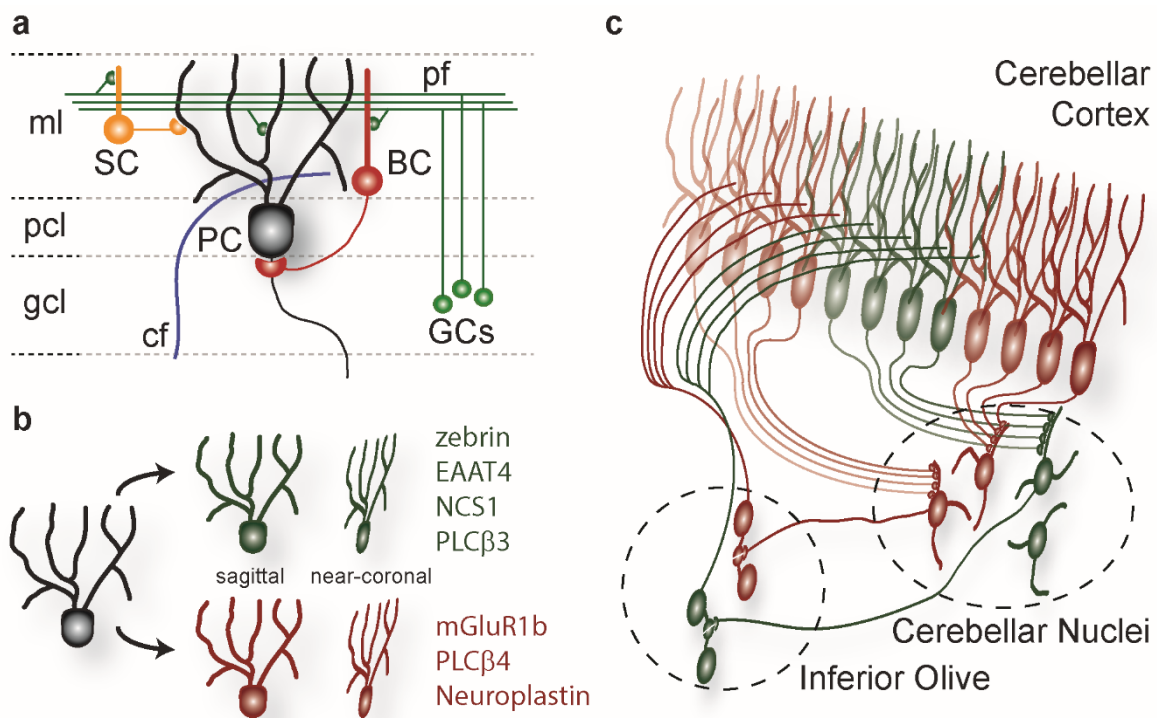


Figure 1. The olivo-cerebellar circuit is constructed of modules with distinct cytochemical signatures. *a)* Schematic drawing of the main cortical cell types, including granule (GC), stellate (SC), basket (BC) and Purkinje cells (PC) with parallel (pf) and climbing fibers (cf) in their respective layers: gcl, pcl and molecular layer. *b)* Purkinje cells can be subdivided based on the expression pattern of particular proteins, of which the most well-known is zebrin, or aldolase *c.* Purkinje cell dendritic trees are virtually two dimensional; in the vermis they can be fully visualized in a sagittal plane. *c)* Schematic representation of the three dimensional configuration and the inter-modular connectivity between the inferior olive, cerebellar cortex and cerebellar nuclei. Inferior olivary neurons typically project to Purkinje cells of the same zebrin-identity in similar modules, which in turn commonly project to the same regions in the cerebellar nuclei. As a result, the cerebellar nuclei can be divided into zebrin-positive and -negative parts too, based on zebrin stained Purkinje cell axons. In contrast to this organisation in the sagittal plane, parallel fibers (not depicted) run horizontally, i.e. perpendicular to the orientation of the virtually flat Purkinje cell dendritic tree.

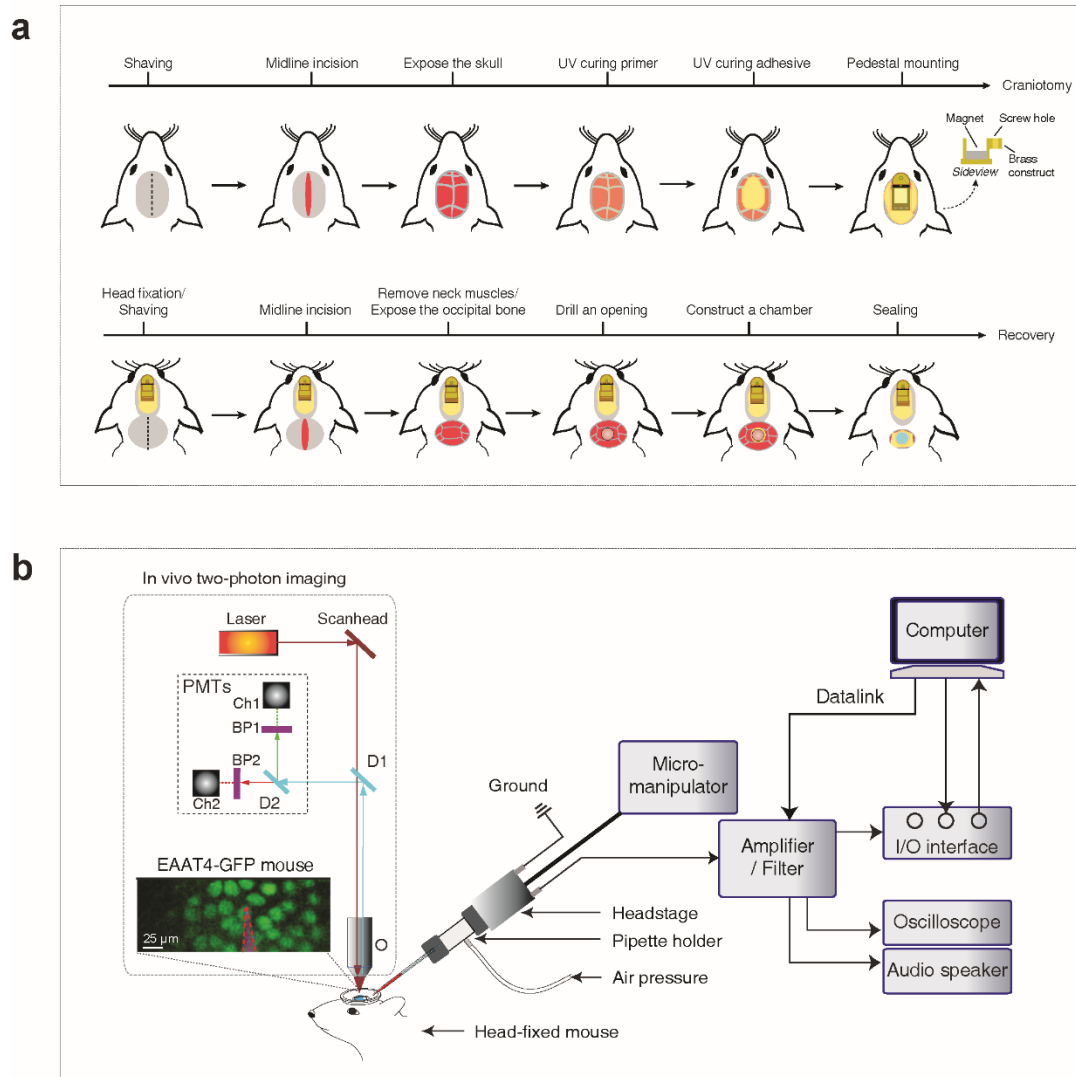


Figure 2. Outline of preparational surgery and recording setup. a) Diagram of procedures for installation of pedestal and craniotomy surgeries in anesthetized mice. b) Schematic drawing of the configuration for combined electrophysiological (right) and two-photon imaging to allow targeted recordings in vivo (left). In short, the mouse is head-fixed in the restrainer. Electrical signals are recorded by a microelectrode and amplified by the headstage, which is attached to a three-axis micromanipulator to, and forwarded to the main amplifier. The signal is then sent to a sound monitor and/or oscilloscope for rapid monitoring of the recorded signals, digitized by the I/O interface and stored on the computer controlling the recording settings and stimulations. Left, scheme of two-photon microscope for imaging the eGFP labelled neurons and the electrode. PMT, photomultiplier tube; D1, dichroic 1 (695 nm split); D2, dichroic 2 (585 nm split); BP1, band-pass filter 1 (500-550 nm); BP2, band-pass filter 2 (584-676 nm); O, water immersion objective. Inset with image: a glass pipette containing Alexa Fluor 594 (10 μ M in 2M NaCl, depicted in red) is targeted towards Purkinje cells (green circles) using the eGFP signal from the EAAT4-positive cells, and cell-population specific extracellular recordings are obtained.

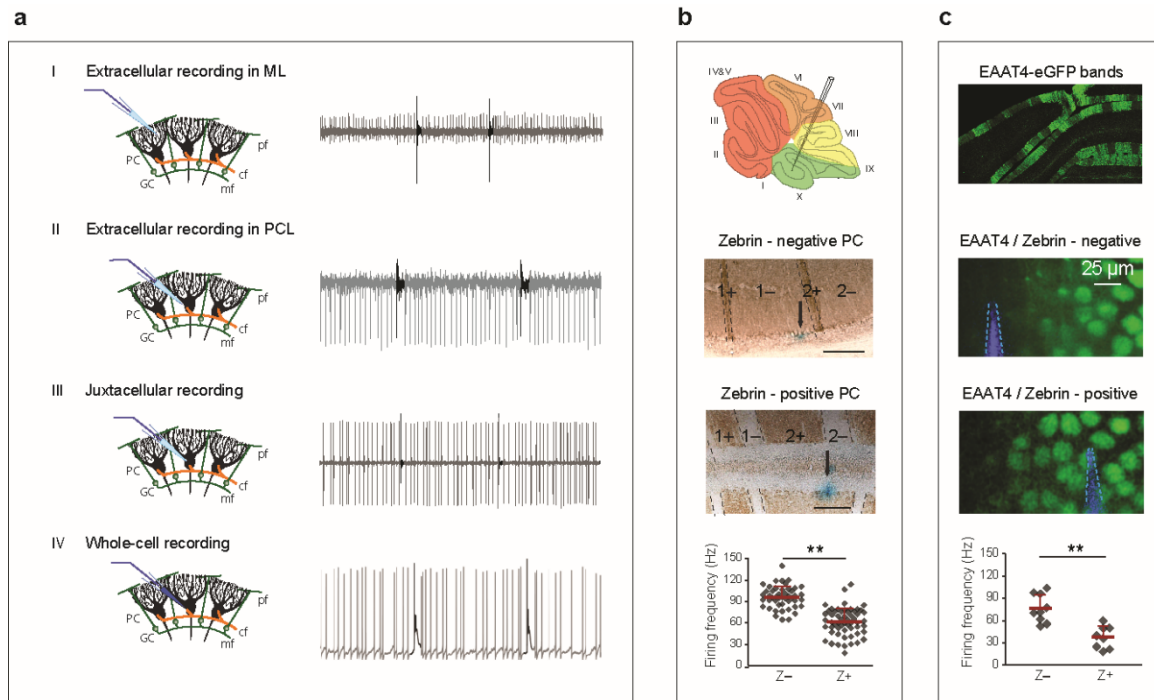


Figure 3. In vivo recording configurations and example data from labelled and targeted Purkinje cell recordings. a) The position of the recording electrode relative to the Purkinje cell determines the observed signals. Liquid filled glass pipette electrodes are used to record single cell activity from PCs. In the molecular layer only complex spikes are observed, seen as slow, negative deflections (I). Towards the soma complex spike signals become predominantly positive with slower elements, while simple spikes appear as negative or more bidirectional deflections (II). When the tip of the electrode is placed even more intimately with the soma, this is referred to as juxtacellular, a configuration that allows cell-specific labelling (III). Ultimately, using suction, followed by sealing and breaking in, the configuration can be converted into a whole-cell patch clamp recording (IV). b) Schematic representation in sagittal plane of the electrode path. Micrographs show coronal sections of recorded Purkinje cells labelled with Alcian blue after staining against zebryn; top: zebryn-negative Purkinje cell in the anterior cerebellum, bottom: zebryn-positive in the posterior cerebellum. The bottom graph depicts the difference in simple spike firing rate between modules observed using this technique. c) Confocal image of a coronal section of an EAAT4-eGFP brain, showing the typical EAAT4 / zebryn pattern. Two-photon images (approx. the same location, shifted about 25 μm) with the pipette recording a negative (top) and a positive (bottom) Purkinje cell. The bottom graph shows how the targeted recordings confirmed the difference observed in b, with a lower number of cells. Results in b and c are adapted from Zhou et al., 2014. PC, Purkinje cell. GC, granule cell. PF, parallel fiber. CF, climbing fiber. MF, mossy fiber.

CHAPTER

3

TRPC3 is essential for functional heterogeneity of cerebellar Purkinje cells

Bin Wu¹, Francois G.C. Blot¹, Aaron B. Wong¹, Catarina Osório¹, Youri Adolfs², R. Jeroen Pasterkamp², Jana Hartmann³, Esther B. E. Becker⁴, Henk-Jan Boele¹, Chris I. De Zeeuw^{1,5} and Martijn Schonewille^{1*}

¹ Department of Neuroscience, Erasmus Medical Center, 3015CN, Rotterdam, the Netherlands

² Department of Translational Neuroscience, University Medical Center Utrecht, Utrecht University, 3584 CG, Utrecht, the Netherlands

³ Institute of Neuroscience, Technical University Munich, Munich, Germany

⁴ Department of Physiology, Anatomy and Genetics, University of Oxford, Oxford, UK

⁵ Netherlands Institute for Neuroscience, Royal Dutch Academy for Arts and Sciences, 1105 CA, Amsterdam, the Netherlands

* Correspondence: Martijn Schonewille

Under review in Elife

Abstract

Despite the canonical homogenous character of its organization, the cerebellum plays differential computational roles in distinct sensorimotor behaviors. In a previous study (Zhou et al., 2014), we showed that Purkinje cell activity differs between zebrin-negative (Z⁻) and zebrin-positive (Z⁺) modules. Here, using gain-of-function and loss-of-function mouse models, we show that transient receptor potential cation channel type C3 (TRPC3) controls the simple spike activity of Z⁻, but not Z⁺ Purkinje cells. Moreover, *in vivo* TRPC3 also regulated complex spike rate and their interaction with simple spikes, exclusively in Z⁻ Purkinje cells. Finally, we found that eyeblink conditioning, related to Z⁻ modules, but not compensatory eye movement adaptation, linked to Z⁺ modules, was affected in TRPC3 loss-of-function mice. Together, our results indicate that TRPC3 is essential for the cellular heterogeneity that introduces distinct physiological properties in the homogeneous population of Purkinje cells, conjuring functional heterogeneity in cerebellar sensorimotor integration.

Introduction

Maintaining correct sensorimotor integration relies on rapid modifications of activity. The cerebellum is instrumental herein, evidenced by the fact that disruptions of cerebellar functioning, e.g. through stroke or neurodegenerative disorders, affect coordination and adaption of many types of behaviors such as gait, eye movements and speech^{1,2}. The palette of behavioral parameters controlled by the cerebellum is also broad and includes features like timing³⁻⁵, strength^{6,7}, as well as coordination^{8,9} of muscle activity. However, the pluriformity of behavioral features does not match with the homogeneity of the structure and cyto-architecture of the cerebellar cortex.

Recently, it has been uncovered that the sole output neurons of the cerebellar cortex, the Purkinje cells (PCs), can be divided into two main groups with a distinct firing behavior^{10,11}. One group, consisting of PCs that are positive for the glycolytic enzyme aldolase C, also referred to as zebrin II^{12,13}, shows relatively low simple spike firing rates, whereas the PCs in the other group that form zebrin-negative zones, fire at higher rates¹⁰. Zebrin II demarcates olivocerebellar modules, anatomically defined operational units each consisting of a closed loop between the inferior olive, parasagittal bands of the cerebellar cortex and the cerebellar nuclei^{14,15}. Given that different motor domains are controlled by specific olivocerebellar modules^{14,16}, the differential intrinsic firing frequencies may be tuned to the specific neuronal demands downstream of the cerebellum¹⁷. Thus, dependent on the specific behavior controlled by the module involved, the PCs engaged may show low or high intrinsic firing as well as related plasticity rules to adjust these behaviors.

Cellular heterogeneity can drive differentiation in the activity and plasticity of individual cells that operate within a larger ensemble¹⁸. The molecular and cellular determinants of differential electrophysiological processing in the cerebellar PC modules are just starting to be identified^{19,20}. For example, while the impact of zebrin II itself is still unclear¹⁰, excitatory amino acid transporter 4 (EAAT4) and GLAST/EAAT1 can directly modulate simple spike activity of PCs as well as plasticity of their parallel fiber inputs in a zone specific manner^{21,22}. Likewise, phospholipase C subtype $\beta 4$ (PLC $\beta 4$) is required for climbing fiber elimination and PF-PC LTD through mGluR1 activation by spill-over glutamate and is only expressed in zebrin-negative modules²³⁻²⁵. The alpha isoform of mGluR1 (mGluR1a) is responsible for PLC $\beta 4$ activation and is uniformly expressed in cerebellar PCs²⁶. Conversely, the mGluR1b receptor is expressed in a pattern complementary to that of zebrin²⁷, but it is less clear to what extent mGluR1b may affect PCs.

Given that mGluR1b interacts with TRPC3 to drive mGluR1-dependent currents²⁸, we set out to test the hypothesis that TRPC3 is a key player in the molecular machinery responsible for differential control over PC activity and function. We demonstrate that TRPC3 in the brain has particularly strong expression in the cerebellum, in a pattern complementary to zebrin in the vermis and more uniform in the hemispheres. We examined the impact of TRPC3 gain-of-function and loss-of-function mutations and found effects on the spiking rate of Z- but not Z+ PCs *in vitro*. *In vivo* recordings during quiet wakefulness in the same mutants revealed that the level of TRPC3 influences both simple spike and complex spike rates, and the interaction between the two, also selectively in Z- modules. Finally, we show that adaptation of compensatory eye movements, which is controlled by Z+-modules in the vestibulocerebellum^{10,29}, is not affected by the loss of TRPC3 function, whereas the learning rate during eyeblink conditioning, which is linked to the Z- modules^{30,31}, is decreased after PC-specific ablation of TRPC3, highlighting the behavioral relevance of firing rate modulation by TRPC3.

Results

Specific expression pattern and subcellular localization of TRPC3 in the mouse brain

The expression of TRPC3 and how it relates to that of zebrin in the adult mammalian brain is unclear, in part due to poor antibody quality. Using a novel TRPC3-specific antibody (Cell signaling, #77934), we examined the immunohistochemistry of TRPC3. We found that in the mouse brain TRPC3 is most prominently expressed in the cerebellum (**Figure 1A**), specifically in PCs and unipolar brush cells (UBCs) (**Figure 1B**). However, upon further scrutiny, it is clear that, although expressed in all PCs, endogenous TRPC3 does not distribute homogeneously. TRPC3 expresses in a pattern that in the vermis complements that of zebrin,

while in the hemispheres it appears more uniform (**Figure 1B** and **Figure S1**). Specifically, the TRPC3 level, in the anterior cerebellum (referred to as lobules I-III), where the PCs are predominantly Z-, is quite intense; while less so in the posterior PCs (referred to as lobule X), which are primarily Z+ (**Figure S1B-C**). Although clearly observable in our standard immunohistochemistry, this pattern was visualized in a more comprehensive manner using whole-mount brain light sheet imaging. The antibody staining appears to be of better quality in the iDISCO protocol. The lens and resolution of the light sheet also circumvent stitching artefacts resulting from a tile scanning of the confocal microscope by imaging the full cerebellum in one single scanning window (**Figure 1C** and **Movie S1**). The anterior and posterior differences of the protein amount were confirmed by western blot analysis (**Figure S2A-B**).

Our immunohistochemical imaging reveals that TRPC3 is present in the soma and dendritic arbor of PCs (**Figure 1B** and **Figure S1B-C**), to further examine the subcellular localization of TRPC3 in the cerebellum, we performed immunoblots of isolated fractions following a synaptic protein extraction procedure (**Figure S2C**). As expected, TRPC3, a channel protein, is abundantly present in the membrane and almost completely absent in the cytosol (**Figure S2D-F**). Moreover, TRPC3 is enriched in synapstosomes (**Figure S2D**), in line with the common conception of mGluR1b-dependent activation^{26,28}. Together, these results indicate that, within the brain, strong TRPC3 expression is restricted to the cerebellum, where it is present in all PCs and UBCs, but at particularly high levels in Z- PCs.

TRPC3 differentially controls the physiological properties of PCs in vitro

Next, we investigated the contribution of TRPC3 to cerebellar function in Z+ and Z- PCs using both loss-of-function and gain-of-function mouse models (**Figure 2A**). TRPC3-Moonwalker (TRPC3^{Mwk}) mice harbor a point mutation resulting in TRPC3 gain-of-function through increased Ca²⁺ influx upon activation³². Inversely, TRPC3 was selectively ablated from cerebellar PCs by crossing mice carrying loxP-flanked TRPC3 alleles²⁸ with L7-Cre (*Pcp2-Cre*)³³ mice, generating L7-TRPC3^{KO} mice. Western blotting and immunostaining of the anterior (Z-) and the posterior (Z+) cerebellar cortex of L7-TRPC3^{KO} mice confirmed that protein levels are reduced (**Figure S2**). The loss of TRPC3 was specific for cerebellar PCs, as TRPC3 expression in UBCs was not affected (**Figure S2G**, white arrow heads).

PCs are intrinsically active pace-making neurons, which fire regular action potentials even when deprived of synaptic inputs^{34,35}. To determine the contribution of TRPC3 to the activity of Z+ and Z- PCs, we performed *in vitro* electrophysiological recordings on sagittal sections of adult mice of both mutants (**Figure 2B**), taking lobules X and I-III as proxies for Z+ and Z- PC modules, respectively (see ref.^{10,15}). In littermate controls, the intrinsic firing rate of Z- PCs is higher than that of Z+ PCs, confirming previous results¹⁰. Gain-of-function TRPC3^{Mwk} mice showed a decrease in inter spike intervals (ISI) and an increase in PC simple spike firing rate selectively in Z- PCs, without affecting Z+ PCs (**Figure 2C**). Inversely, ablating TRPC3 from PCs caused an increase in ISI and decrease in firing rate in Z- PCs, again without affecting Z+ PCs (**Figure 2D**). We also assessed the regularity of firing activities by measuring the coefficient of variation (CV) and the coefficient of variation of adjacent intervals (CV2) of ISI. Both the CV and CV2 of Z- PCs in lobules I-III declined significantly in L7-TRPC3^{KO} mice, while remaining unchanged in TRPC3^{Mwk} mice; in contrast, in Z+ lobule X, none of these parameters were altered in either TRPC3^{Mwk} or L7-TRPC3^{KO} mice (**Figure S3 A-F**).

To verify the effect of TRPC3 deletion on other cell physiological properties of PCs, we performed whole-cell patch-clamp recordings in a subset of PCs. Injections of current steps into PCs evoked increasing numbers of action potential, in the presence of blockers for both excitatory and inhibitory synaptic inputs. In line with the cell-attached recordings, in loss-of-function L7-TRPC3^{KO} mice, PC intrinsic excitability, quantified by the slope of firing rate versus current injection curve, was significantly reduced in lobules I-III, but unchanged in lobule X, compared with those of littermate controls (**Figure 2E**). Other physiological parameters in terms of holding current, amplitudes, half-widths and after-hyperpolarization amplitudes, were not significantly affected in either lobules I-III or lobule X (**Figure S3G**).

Together, our *in vitro* recordings from gain- and loss-of-function mutants indicate that TRPC3 selectively controls the activity in Z- PCs, without affecting excitability or other cell intrinsic properties. Thus, at least *in vitro*, TRPC3 contributes to the difference in intrinsic firing activity between Z+ and Z- PCs, by directly controlling the intrinsic excitability of Z- PCs.

TRPC3 regulates the activity of simple spikes selectively in Z- PCs in vivo

To examine the role of TRPC3 in the closed loop, intact cerebellar module, we next performed PC recordings *in vivo* in adult mice during quiet wakefulness (**Figure 3A**). PCs could be identified during extracellular recordings by the presence of complex spikes, while the consistent presence of a pause in simple spikes following each complex spike confirmed that the recording was obtained from a single unit³⁶. PC recording locations in either Z- lobules I-III or Z+ lobule X were confirmed with iontophoretic injections of biotinylated dextran amine (BDA), which could be identified by immunostaining (**Figure 3B**). As we showed before^{10,37}, PCs in Z- modules fired simple spikes at a higher rate than those in Z+ modules (**Figure 3D and F**).

In vivo, in the presence of physiological inputs the PCs in Z- lobules I-III of TRPC3^{Mwk} mutants showed a decreased ISI and increased simple spike firing rate, whereas the Z+ PCs were unaffected. Conversely, Z- PCs in L7-TRPC3^{KO} mutants featured an increased ISI and decreased simple spike firing rate, but again without changes in PCs of the Z+ lobule X, all compared to those of their littermate controls (**Figure 3C-F**). Unlike *in vitro*, PCs in the L7-TRPC3^{KO} mice showed comparable CV and CV2 to controls for both Z- and Z+ modules (**Figure S4G-I**). The CV of simple spike ISI was, however, prominently elevated in both Z- and Z+ modules in TRPC3^{Mwk} mutants (**Figure S4B**). It should be noted that PC regularity *in vivo* is largely determined by external inputs (compared **Figure S3 to S4**), which thereby can offset those intrinsic variations induced by the mutation of TRPC3. The irregular firing activity of PCs in TRPC3^{Mwk} mutants, at least for Z+ PCs, may be attributed to impaired function or degeneration of UBCs, while the physiological synaptic input *in vivo* in L7-TRPC3^{KO} mice could obscure the regularity changes observed *in vitro* in these mice.

In short, even *in vivo*, in the presence of all physiological inputs both gain-of-function and loss-of-function mutations of TRPC3 exclusively affects Z- PCs, with the most pronounced, persistent effect being the mutation-selective influence on simple spike firing rate.

TRPC3-related effects correlate with zebrin expression and are independent of development

Our results so far have identified selective TRPC3-related effects by comparing lobules I-III and X, as proxies for Z- and Z+ modules. Immunohistochemical analysis indicated that the TRPC3 expression differs substantially between these lobules (**Figure S1 and Movie S1**), suggesting that the effects of gain- and loss-of-function mutations could be directly related to protein levels. Alternatively, other differences in molecular machinery could underlie or further enhance this cellular differentiation, for instance through mGluR1b-related effects. As the difference in TRPC3 expression is minimal or absent in the more lateral parts of the cerebellum (**Figure S1**), recording the activity of adjacent Z- and Z+ PCs there would solve this question. To this end, we crossed L7-TRPC3^{KO} mice with EAAT4^{eGFP} mice that express eGFP in Z+ PCs to generate L7-TRPC3^{KO}-EAAT4^{eGFP} mice. Using two-photon microscopy, we identified Z+ and Z- modules on the dorsal surface (lobules IV-VI and simplex) of the cerebellum and recorded PC activity (**Figure 4A-B**). Here, the absence of TRPC3 attenuated the firing rate and enhanced the irregularity of Z- PCs even more robustly, without an effect on Z+ PCs (**Figure 4C-D, Figure S5A-C, cf Figure 3F**). These results argue against a direct link between simple spike firing rate and TRPC3 levels and support the concept that other proteins, e.g. mGluR1b, influence TRPC3 activity and thereby control the spiking activity of PCs.

To test the possibility that developmental effects influenced PC activity in the adult mice we tested (L7^{Cre} begins to be expressed in postnatal week 1-2), we crossed the *loxP*-flanked TRPC3 mice with tamoxifen-dependent L7^{Cre-ERT2} to generate L7-TRPC3^{CKO} mice (**Figure 4E**). If the divergent effects of TRPC3 on Z- and Z+ PCs are completely or in part of developmental origin, we should observe no or less changes in L7-TRPC3^{CKO} adult mice after tamoxifen injections (injected after maturation). Four weeks after tamoxifen treatment, L7-TRPC3^{CKO} mice showed a virtually complete ablation of TRPC3 in PCs (**Figure 4F**). Again, simple spike regularity and firing rate were affected in Z-, but not Z+ PCs of tamoxifen injected adult L7-TRPC3^{CKO} mice (**Figure 4G-H and Figure S5G-I**), in a manner similar to that in L7-TRPC3^{KO}.

Taken together and combined with L7-TRPC3^{KO} data, these results indicate that the TRPC3-dependent effects in zebrin-identified PCs are independent of cerebellar development or developmental compensation. Moreover, the larger effect of TRPC3 ablation on Z- PCs in areas where its expression is similar to that in Z+ PCs suggests that other proteins contribute to the state of increased excitability in Z- PCs.

TRPC3 mutations selectively affect the activity in Z– olivocerebellar modules

PCs in the cerebellar cortex, form a closed loop with the cerebellar nuclei neurons they innervate by their axon output and the olivary neurons from which they receive their climbing fiber input¹⁴. If TRPC3 contributes to the output of this loop, one could hypothesize that other elements in the loop should be affected by the mutations^{7,38}. To test this hypothesis, we examined complex spikes activity in PCs, as the complex spike directly reflects the activity of the climbing fiber and thereby that of the inferior olivary neuron it originates from³⁸. We identified complex spikes based on their characteristic shape in our *in vivo* recordings from Z– lobules I-III or Z+ lobule X (**Figure 5A**). Complex spike firing rates were, similar to simple spike rates, higher in Z– than in Z+ PCs (**Figure 5B**), as shown previously¹⁰. Chronic manipulations of TRPC3 activity, gain- and loss-of-function, in PCs predominantly affected complex spike firing rate in Z–, but not Z+ PCs (**Figure 5B**). Intriguingly, acute ablation of TRPC3 in L7-TRPC3^{CKO} mice did not affect complex spike activity in terms of firing rate, CV, CV2 or pause in simple spikes following climbing fiber activation (CF-pause) in Z– PCs (**Figure 5B** bottom panel, **Figure S5J-L**). In line with the lower simple spike firing rates in loss-of-function TRPC3 mutants, the CF-pause of L7-TRPC3^{CKO} and L7-TRPC3^{CKO}-EAAT4^{eGFP} mice were longer, selectively in Z– PCs (**Figure S4L** and **S5F**). Except for the CV value, other complex spike parameter changes in TRPC3^{Mwk} mice were not affected (**Figure S4D-F**). Together, *in vivo* experiments indicate that TRPC3 also selectively affects the activity in the inferior olive in that the Z– modules are most prominently affected, and this influence has a developmental component.

Complex spikes are known to have a direct influence on simple spike activity (CS-SS)^{10,39}. Based on the peri-complex spike time histograms, we could categorize four different types of simple spike responses following the CF-pause (see also ref.¹⁰), including no change in rate (normal), increased simple spike activity (facilitation), decreased simple spike activity (suppression), and a superimposed oscillatory pattern (oscillation) (**Figure 5C**). Our data confirmed our previous finding¹⁰ that the CS-SS interaction pattern among the Z+ and Z– PCs is different in that the facilitation prevails in the Z– PCs, whereas the suppression and oscillation types occur predominantly in the Z+ PCs (**Figure 5D**). In addition, we found that manipulation of TRPC3 activity changed the types of CS-SS responses most frequently in Z– PCs (**Figure 5D**). Interestingly, Z– PCs exhibited much more suppression in gain-of-function TRPC3^{Mwk} mutants and vice versa more facilitation in loss-of-function L7-TRPC3^{CKO}-EAAT4^{eGFP} mice, compared to those in their littermate controls (**Figure 5D**), suggesting that Z– PCs partly compensate for the effects of TRPC3 manipulation.

Together, these results indicate that TRPC3 controls not only the activity of PCs, but also that of the inferior olivary neurons, another element in the olivocerebellar loop. Moreover, manipulation of TRPC3 activity alters the interaction between complex spikes and simple spikes.

Functional heterogeneity of TRPC3 is reflected in differential effects on motor behaviors

The ultimate question is: does cellular heterogeneity of PCs also differentially affect their contribution to specific cerebellar functions? As the TRPC3^{Mwk} mutation is not cell-specific and affects for instance also UBCs, we focused on the behavioral effects in L7-TPRC3^{CKO} mice. Before testing specific functions, we first evaluated the consequences of the manipulations of TRPC3 on locomotion, a type of behavior that by nature requires the entire body and as such can be linked to many sub-regions of the cerebellar cortex, from the Z+ vestibular zones to the Z– anterior lobules. We first investigated whether these mutant mice showed any obvious deficits in locomotion using the Erasmus Ladder⁹. L7-TPRC3^{CKO} mice could not be discriminated from control littermates by the percentage of different types of steps, including lower steps, also known as missteps (**Figure S6**). The apparent discrepancy with earlier evidence in stride width in the global TRPC3 knockout²⁸ could be due to the different methods or the fact that UBCs, particularly important in the vestibular zone, are also affected in that mouse model⁴⁰.

Next, we subjected L7-TPRC3^{CKO} mice to two specific, but intrinsically distinct types of cerebellum-dependent learning tasks, i.e., vestibulo-ocular reflex (VOR) adaptation and eyeblink conditioning. VOR adaptation is the adjustment of the amplitude and/or direction of compensatory eye movements controlled by the vestibulocerebellum (**Figure 6A-C**), which is predominantly Z+ (**Figure S7A**). Eyeblink conditioning requires the animal to generate a

well-timed movement following a previously unrelated sensory input and is linked to more anterior regions that are largely Z– (**Figure 7A** and **Figure S7B**). Note that the difference in zebrin labeling is pronounced between the two related regions; while the difference in TRPC3 staining is less clear (**Figure S7A-B**). Nonetheless, given the electrophysiological changes described above, we hypothesized that altered TRPC3 function should impair Z– linked eyeblink conditioning, whereas VOR adaptation would be unaffected.

Before examining adaptation, we first tested if the basal eye movement reflexes, the optokinetic reflex driven by visual input (OKR) and the vestibular input-driven VOR (in the dark) and visually-enhanced VOR (VVOR, in the light), were affected. Neither the gain (the ratio of eye movement to stimulus amplitude), nor the phase (timing of the response relative to input), differed significantly between L7-TPRC3^{KO} mutants and littermate controls (**Figure S7C**). Next, using mismatched visual and vestibular stimulation, we tested the ability of mutant mice to adapt their compensatory eye movements. When L7-TPRC3^{KO} mice were subjected to both out-of-phase and in-phase training paradigms, we did not observe any significant deficit in the VOR gain increase and VOR gain decrease, respectively (**Figure 6D-E**). To evaluate the ability of the mice to perform a long-term, more demanding adaptation, we subjected the mice for three more days, following the gain decrease training, to a training stimulus aimed at reversing the direction of their VOR, referred to as VOR phase reversal (**Figure 6G**). Again, no difference was found between L7-TPRC3^{KO} and control littermate mice: neither in the VOR phase over the training (**Figure 6H**), nor in the increased OKR gain following the phase reversal training (**Figure 6F**, compare to **Figure S7C**).

To determine whether the differential activity of TRPC3 ultimately also affects the behavior of the animal, we subjected mice to a task linked to Z– modules, i.e. delay eyeblink conditioning. Mice were trained using a light pulse with 250 ms duration as the conditioned stimulus (CS) and a puff to the cornea as a short unconditioned stimulus (US) at the end of the CS, which over the period of several days evoked conditioned responses (CR, preventative eyelid closure) in the absence of the US (**Figure 7B**). In contrast to VOR adaptation, the L7-TPRC3^{KO} mice showed significant deficits in eyeblink conditioning during the first week of training (**Figure 7C**). However, when we subjected them to longer periods, they reached similar CR percentages, amplitudes and timing (**Figure 7D** and **Figure S7D-E**).

Thus, although TRPC3 is expressed in both regions underlying the cerebellum-dependent behavioral experiments tested here, TRPC3 activity is selectively required to optimize the cerebellum-dependent learning behavior that is processed in a Z– module¹⁷. This indicates that the cellular heterogeneity and consequential differentiation in cellular activity also affects the behavior of the animals.

Discussion

The cerebellum offers a rich repertoire of electrophysiological properties that allows us to coordinate a wide variety of sensorimotor and cognitive behaviors. We recently uncovered that there are probably two main heterogeneous types of cerebellar modules with different intrinsic profiles and plasticity rules¹⁰. This organization is highly preserved throughout phylogeny and characterized by a series of molecular markers such as zebrin that are distributed in a complementary fashion across the cerebellar cortex^{16,41,42}. Here, we demonstrated that zebrin-negative PCs show a relatively high expression of TRPC3, which has a dominant impact on its electrophysiological features (**Table S1**). Indeed, gain-of-function and loss-of-function mutations in the gene encoding for TRPC3 selectively affected activity in the zebrin-negative modules and the motor behavior that is controlled by these modules.

TRPC channels, which are calcium-permeable upon activation by phospholipase C or diacylglycerol, are widely expressed in the brain and critically involved in the development and maintenance of synaptic transmission^{28,43-45}. TRPC1 and TRPC3 are both prominently expressed in the cerebellum, but in PCs TRPC3 is most abundant²⁸. In addition to its contribution to intrinsic activity, TRPC3 currents also mediate the slow excitatory postsynaptic potential following activation of mGluR1b, which is expressed in a pattern complementary to that of zebrin^{26,27,45}. The finding that TRPC3 can be detected in all PCs, but that effects of ablation are restricted to zebrin-negative PCs suggests that it is in fact the ‘molecular machinery’ involving mGluR1b activation that drives the differential effects of TRPC3 activation.

In contrast to mGluR1b, mGluR1a is expressed by all PCs (estimated ratio 2:1 to

mGluR1b)²⁷. The metabotropic receptor mGluR1a is important for IP3-mediated calcium release, climbing fiber elimination as well as PF-PC LTD²⁶. Intriguingly, and in line with the concept of modular differentiation, mGluR1-dependent processes are hampered in zebrin-positive PCs by the expression of EAAT4²¹, whereas zebrin-negative PCs selectively express PLC β 4 that works in concert with mGluR1a²⁶. The differences in expression patterns may enhance the probability of PF-PC LTD in zebrin-negative PCs over that in zebrin-positive PCs, which is supported by experiments performed in P21 mice²¹. The consequences of EAAT4 or PLC β 4 deletion on PC physiology have been evaluated *in vitro* in several studies²¹⁻²⁴, but what the consequences *in vivo* on circuit physiology and on the behaviors tested here are, is unclear. Our results here demonstrate that changes that occur at the cell physiological level, i.e. reduced simple spike rate and altered CS-SS interaction, lead to a more complex pattern of changes in the intact system. The additional effects are particularly striking in the L7-TPRC3^{KO} mice, where the reduced simple spike rate in zebrin-negative PCs leads to a lower complex spike rate. In principle, this could have been a direct effect, as lower simple spike rate results in reduced inhibition of the also inhibitory projection from the cerebellar nuclei to the inferior olive^{7,46}. However, the unaltered complex spike rate of L7-TPRC3^{KO} mice suggests that the changes occur during development.

To test the functional consequences of the loss of TRPC3 and the modular specificity of these effects, we tested the impact on behavioral experiments that can be linked to specific modules. Eyeblink conditioning and VOR adaptation are controlled by different modules in the cerebellum and they are distinctly different by nature. Eyeblink conditioning requires a novel, well-timed eyelid movement to a previously unrelated, neutral stimulus, and has been linked to largely or completely zebrin-negative modules in the anterior cerebellum^{30,31}. The activity of the putative zebrin-negative PCs in this area is relatively high at rest, in line with their zebrin identity, and a decrease in this high firing rate correlates to the eyeblink response⁴⁷⁻⁴⁹. Conversely, VOR adaptation adjusts the amplitude of an existing reflex to optimize sensory processing using visual feedback and is controlled by the vestibulocerebellum, the flocculus in particular, which is classically considered to be zebrin-positive^{10,29} (cf ref. ^{15,50}). There are more variations in VOR adaptation and the underlying activity patterns are less well-described. In unidirectional VOR gain increase, we recently found that the change correlating with the adapted eye movement consisted of a potentiation, an increase, of the -at rest- lower PC firing rate⁵¹. Although our current study has its main focus on the differential contribution of TRPC3 at the cell and systems physiological level, it is tempting to speculate how the loss of TRPC3 in PCs results in an eyeblink conditioning phenotype without affecting VOR adaptation. The reduction in firing rate of zebrin-negative PCs may directly contribute to the impaired conditioning. The suppression of simple spike firing that correlates with the conditioned response could be occluded by the lower resting rate in L7-TPRC3^{KO} mice. Alternatively, PF-PC LTD could play a role as it is in line with the simple spike suppression and blocking TRPC3 function completely abolishes this form of LTD⁵². However, genetically ablating PF-PC LTD did not affect the ability to perform eyeblink conditioning successfully⁵³, arguing against an exclusive role for this form of plasticity. Schreurs and colleagues demonstrated that intrinsic excitability is increased after eyeblink conditioning⁵⁴. A third option could be that TRPC3 also affects the adaptive increase of excitability, intrinsic plasticity, which is calcium-activated potassium channel function dependent⁵⁵, and thereby delays the expression of a conditioned blink response. All three options would not necessarily affect VOR adaptation and could contribute to the deficits in eyeblink conditioning, but given the relatively mild phenotype, one or two could be sufficient. Future experiments will have to unravel the cellular changes underlying eyeblink conditioning and VOR adaptation and the specific role of TRPC3 in the former.

In this study we aimed to gain insight in the mechanisms that convert molecular heterogeneity into differentiation of cell physiology and function. This mechanistic question goes hand in hand with the more conceptual question: why are there, at least, two different types of PCs? An appealing hypothesis is that zebrin-negative and zebrin-positive bands control two muscles with opposing functions, e.g. a flexor and an extensor. However, trans-synaptic retrograde tracing using rabies virus from antagonist muscles demonstrated that although 3rd order labeling can be found in different parasagittal strips of PCs, there is no apparent division in zebrin-negative and zebrin-positive strips⁵⁶. A second possibility would be that individual muscles are controlled by either only zebrin-negative or zebrin-positive strips, or a combination of both, when needed. In the vestibulocerebellum of the pigeon, each movement direction is controlled by a set of zebrin-negative and zebrin-positive bands¹⁶. In

this configuration each PC within the set, or separately, would then serve a distinct function, for which it is optimized by gene expression patterns. This dissociation of function could entail e.g. timing versus coordination⁵⁷ or moving versus holding still⁵⁸, although none of these distinctions have been linked to specific zebrin-identified modules. Alternatively, it may be the net polarity of the connectivity downstream of the cerebellar nuclei up to the motor neurons or the cerebral cortical neurons that determines the demand(s) of the module(s) involved¹⁷. Module-specific driver lines would greatly aid to answer these questions, but are currently not available.

To summarize, our results support the hypothesis that cerebellar modules control distinct behaviors based on cellular heterogeneity, with differential molecular configurations. We present the first evidence for a non-uniform expression pattern of TRPC3 in PCs, complementary to that of zebrin in the vermis but more homogeneous in the hemispheres. Nonetheless, TRPC3 effects are directly coupled to zebrin, a specificity that putatively requires mGluR1b²⁶, the activator of TRPC3 that is expressed in a pattern perfectly complementary to zebrin²⁷.

Since the discovery of protein expression patterns in the cerebellar cortex¹², numerous other proteins with patterned expression have been identified²⁰. These patterns have been linked to circuit organizations of modules⁴¹, to disease and degeneration²⁰, and more recently to electrophysiological differences^{10,21}. Altogether, this work demonstrates that proper cerebellar function is based on the presence of (at least) two *modi operandi* that have distinct molecular machineries, with a central role for TRPC3, to differentially control sensorimotor integration in downstream circuitries that require control with opposite polarity.

Materials and Methods

Animals

For all experiments, we used adult male and female mice with a C57Bl/6 background that were, unless stated otherwise, individually housed, had food ad libitum and were on a 12:12 light/dark cycle. In all experiments the experimenters were blind to mouse genotypes. All experiments were approved by the Dutch Ethical Committee for animal experiments and were in accordance with the Institutional Animal Care and Use Committee.

The generation of TRPC3^{Mwk} mice has been described previously³². Briefly, male BALB/cAnN mice carrying the *Mwk* mutation which was generated in a large-scale ENU mutagenesis program were subjected to cross with normal C3H/HeH females, and the first filial generation (F₁) progeny were screened for a variety of defects. The *Mwk* colony was maintained by repeated backcrossing to C3H/HeH. Experimental mice were generated by crossing C3H/HeH mice heterozygous for the *Mwk* mutation with C57Bl/6 mice. Offspring with the *Mwk* mutation on one allele were classified as gain-of-function TRPC3 Moonwalker mutant (referred to as TRPC3^{Mwk}) and littermate mice lacking the *Mwk* mutation were used as controls. Note that, the TRPC3^{Mwk} mutants present evident ataxic phenotype from a very early age, concomitant with progressive degeneration of UBCs and PCs⁴⁰.

Mice in which exon 7 of the *Trpc3* gene was flanked by *loxP* sites (TRPC3^{fl/fl} mice) were bred with mice that express Cre under the *Pcp2* promoter (L7^{Cre/-} mice)³³. The resulting offspring was genotyped using PCR of genomic DNA extracted from tail or toe by standard procedures. The F₁ was crossed again with the TRPC3^{fl/fl} mice. Among the second filial generation (F₂), mice homozygous for the *loxP* sites and one Cre allele were classified as PC-specific TRPC3 knockout (L7^{Cre/-};TRPC3^{fl/fl}, here referred to as L7-TRPC3^{KO}) mice and as controls when Cre was absent (L7^{-/-};TRPC3^{fl/fl}, here "littermate controls").

L7-TRPC3^{KO}-EAAT4^{eGFP} mice were generated by crossing L7^{Cre/-};TRPC3^{fl/fl} mice with heterozygous EAAT4^{eGFP/-} mice which express enhanced green fluorescent protein (eGFP) under control of *Eaat4* promoter. The F₂ offspring those who expressed TRPC3^{fl/-}, L7^{Cre/-} and EAAT4^{eGFP/-} were crossed again with the TRPC3^{fl/fl} mice. Among the F₃, mice with a homozygous expression of floxed-TRPC3, one Cre allele and one EAAT4^{eGFP} allele (L7^{Cre/-};TRPC3^{fl/fl};EAAT4^{eGFP/-}), were used and referred to as L7-TRPC3^{KO}-EAAT4^{eGFP} mutant mice and as controls when Cre was absent (L7^{-/-};TRPC3^{fl/fl};EAAT4^{eGFP/-}).

Inducible PC-specific TRPC3 knockouts (TRPC3^{CKO}) were generated by crossbreeding mice carrying the floxed TRPC3 with mice expressing the tamoxifen-sensitive Cre recombinase Cre-ERT2 under the control of the L7 promoter (obtained from the Institut Clinique de la Souris, www.ics-mci.fr) (experimental mice: L7^{Cre-ERT2/-};TRPC3^{fl/fl}). Tamoxifen was dissolved in corn oil to obtain a 20 mg/ml solution, and intraperitoneally injected into all subjects for consecutive 5 days, four weeks prior to electrophysiological recordings. Injections were performed in adults between 12-31 weeks of age. Experimental cohorts were always injected at the same time. Mice without L7^{Cre-ERT2} expression were as control in this study (experimental mice: L7^{-/-};TRPC3^{fl/fl}).

Immunohistochemistry

Anesthetized mice were perfused with 4% paraformaldehyde in 0.12M phosphate buffer (PB).

Brains were taken out and post-fixed for 1 h in 4% PFA at room temperature, then transferred in 10% sucrose overnight at 4°C. The next day, the solution was changed for 30% sucrose and left overnight at 4°C. Non-embedded brains were sectioned either sagittally or transversally at 40µm thickness with freezing microtome. Free-floating sections were rinsed with 0.1M PB and incubated 2h in 10mM sodium citrate at 80°C for 2 h, for antigen retrieval. For immuno-fluorescence, sections were rinsed with 0.1M PB, followed by 30 minutes in Phosphate Buffered saline (PBS). Sections were incubated 90 minutes at room temperature in a solution of PBS/0.5%Triton-X100/10% normal horse serum to block nonspecific protein-binding sites, and incubated 48 h at 4°C in a solution of PBS/0.4% Triton-X100/2% normal horse serum, with primary antibodies as follows: Aldolase C (1:500, goat polyclonal, SC-12065), Calbindin (1:7000, mouse monoclonal, Sigma, #C9848), and TRPC3 (1:500, rabbit polyclonal, Cell Signaling, #77934). After rinsing in PBS, sections were incubated 2 h at room temperature in PBS/0.4% Triton-X100/2% normal horse serum solution with secondary antibodies coupled with Alexa488, Cy3 or Cy5 (Jackson ImmunoResearch), at a concentration of 1:200. Sections were mounted on coverslip in chrome alum (gelatin/chromate) and covered with Mowiol (Polysciences Inc.). For Light Microscopy section were pre-treated for endogenous peroxidase activity blocking with 3% H_2O_2 in PBS, then rinsed for 30 minutes in PBS, incubated 90 minutes in a solution of PBS/0.5%Triton-X100/10% normal horse serum to block nonspecific protein-binding sites, followed by the primary antibody incubation as described before. After 48 h, sections were rinsed in PBS and incubated 2h at room temperature in PBS/0.4% Triton-X100/10% normal horse serum solution with HRP coupled secondary antibodies (Jackson ImmunoResearch), at a concentration of 1:200. Sections were rinsed with 0.1M PB and incubated in diaminobenzidine (DAB, 75 mg/100ml) for 10 minutes. Sections were mounted on glasses in chrome alum (gelatin/chromate), dried with successive Ethanol steps, incubated in Xylene and covered with Permount mounting medium (Fisher Chemical). Images were acquired with an upright LSM 700 confocal microscope (Zeiss) for fluorescent microscopy, and Nanozoomer (Hamamatsu) for light microscopy.

iDISCO and light sheet imaging

This protocol has been adapted from a previous study⁵⁹. After normal perfusion and post-fixation, brains were washed successively in PBS (1.5 h), 20% methanol/ H_2O (1 h), 50% methanol/ H_2O (1 h), 80% methanol/ H_2O (1 h), and 100% methanol (1 h) twice. To increase clearance, samples were treated with a solution of dichloromethane (DCM) and 100% methanol (2:1) for another hour. Brains were then bleached with 5% H_2O_2 in 90% methanol (ice cold) at 4°C overnight. After bleaching, samples successively washed in 80% methanol/ H_2O , 50% methanol/ H_2O , 40% methanol/PBS, and 20% methanol/PBS, for 1 h each, and finally in PBS/0.2% Triton X-100 for 1 h twice. After rehydration, samples were pre-treated in a solution of PBS/0.2% Triton X-100/20% DMSO/0.3 M glycine at 37°C for 36 h, then blocked in a mixture of PBS/0.2% Triton X-100/10% DMSO/6% donkey serum at 37°C for 48 h. Brains were incubated in primary antibody in PTwH solution (PBS/0.2% Tween-20/5% DMSO/3% donkey serum with 10 mg/ml heparin) for 7 days at 37°C with primary antibody: TRPC3 rabbit polyclonal, 1:500 (Cell Signaling, #77934). Amphotericin was added once every two days at 1µg/ml to avoid bacterial growth. Samples were then washed in 24 h in PTwH for six times (1h for each, after the fourth wash, leave it at room temperature overnight), followed

by the second round of 7-day incubation with primary antibody. Brains were then washed in PTwH, 6 washes in 24 h, as described before, then incubated in secondary antibody in PTwH/3% donkey serum at 37°C for 7 days with secondary anti-Rabbit Cy3 (Jackson ImmunoResearch) at 1:750. Brains were then washed in PTwH, 6 washes in 24 h, again, followed by successive washes in 20% methanol/H₂O, 40% methanol/H₂O, 60% methanol/H₂O, 80% methanol/H₂O, and 100% methanol twice, for 1 h each, and finally incubation overnight in a solution of DCM and 100% methanol. For tissue clearing, brains were incubated 20 mins in DCM, twice, and conserved in Benzyl ether at room temperature.

Ready samples were imaged in horizontal orientation with an UltraMicroscope II (LaVision BioTec) light sheet microscope equipped with Imspector (version 5.0285.0) software (LaVision BioTec). Images were taken with a Neo sCMOS camera (Andor) (2560x2160 pixels. Pixel size: 6.5 x 6.5 µm²). Samples were scanned with double-sided illumination, a sheet NA of 0.148348 (results in a 5 µm thick sheet) and a step-size of 2.5 µm using the horizontal focusing light sheet scanning method with the optimal amount of steps and using the contrast blending algorithm. The effective magnification for all images was 1.36x (zoombody*objective + dipping lens = 0.63x*2.152x). Following laser filter combinations were used: Coherent OBIS 488-50 LX Laser with 525/50nm filter, Coherent OBIS 561-100 LS Laser with 615/40 filter, Coherent OBIS 647-120 LX with 676/29 filter.

Western blot and fractionation

Cerebellar tissue from L7-TRPC3^{KO} and control mice was dissected and immediately frozen in liquid nitrogen. Samples were homogenized with a Dounce homogenizer in lysis buffer containing 50 mM Tris-HCl pH 8, 150 mM NaCl, 1% Triton X-100, 0.5% sodium deoxycholate, 0.1% SDS and protease inhibitor cocktail. Protein concentrations were measured using Pierce BCA protein assay kit (Thermo Fisher). Samples were denatured and proteins were separated by SDS-PAGE in Criterion™ TGX Stain-Free™ Gels (Bio-Rad), and transferred onto nitrocellulose membranes with the Trans-Blot® Turbo™ Blotting System (Bio-Rad). Membranes were blocked with 5% BSA (Sigma-Aldrich) in TBST (20mM Tris-HCl pH7.5, 150mM NaCl and 0.1%, Tween20) for 1 h and probed with the following primary antibodies: rabbit anti-TRPC3 (Cell Signaling Technology, #77934; 1:1000) and mouse anti-actin (Millipore, MAB1501; 1:1000). Secondary antibodies used were IRDye 800CW Donkey anti-Rabbit IgG (LI-COR Biosciences, Cat # 925-32213; 1:20000) and IRDye 680RD Donkey anti-Mouse IgG (LI-COR Biosciences, Cat # 925-68072; 1:20000). Membranes were scanned by Odyssey Imager (LI-COR Biosciences) and quantified using Image Studio Lite (LI-COR Biosciences). For quantification, densitometry of protein bands of interest was normalized to that of actin.

For fractionation experiments, cerebellar tissues from C57/BL6 were collected and the synaptosomes were isolated using Syn-PER™ Synaptic Protein Extraction Reagent (ThermoScientific, #87793) according to the manufacturer's instructions.

In vivo extracellular recordings and analysis

We performed *in vivo* extracellular recordings in adult TRPC3^{Mwk} (aged 15-47 weeks), L7-TRPC3^{KO} (aged 22-43 weeks), L7-TRPC3^{CKO} (aged 17-28 weeks) mice, respectively, as previously described¹⁰. Briefly, an immobilizing pedestal consisting of a brass holder with a neodymium magnet (4x4x2 mm) was fixed on the skull, overlying the frontal and parietal bones,

and then a craniotomy ($\varnothing 3$ mm) was made in the interparietal or occipital bone under general anesthesia with isoflurane/O₂ (4% induction, 1.5-2% maintenance). After over 24 h of recovery, mice were head-fixed and body restrained for recordings. PCs were recorded from vermal lobules I-III and X, using a glass pipette (OD 1.5 mm, ID 0.86 mm, borosilicate, Sutter Instruments, USA; 1-2 μ m tips, 4-8 M Ω) with a downward pitch angle of 40° and 65° respectively. The pipettes were filled with 2 M NaCl-solution and mounted on a digital 3-axis drive (SM-5, Luigs Neumann, Germany). After recording, biotinylated dextran amines (BDA) was iontophoretically injected to confirm that the recordings were from Lobules I-III or X. PCs were identified by the presence of simple and complex spikes, and determined to be from a single unit by confirming that each complex spike was followed by a climbing fiber pause. All in vivo recordings were analyzed offline using Spiketrain (Neurasmus BV, Rotterdam, The Netherlands), running under MatLab (Mathworks, MA, USA). For each cell, the firing rate, CV and mean CV2 were determined for simple and complex spikes, as well as the climbing fiber pause. The CV is calculated by dividing the standard deviation, SD, by the mean of ISIs, whereas CV2 is calculated as $2 \times |ISI_{n+1} - ISI_n| / (ISI_{n+1} + ISI_n)$. Both are measures for the regularity of the firing, with CV reflecting that of the entire recording and mean CV2 that of adjacent intervals, making the latter a measure of regularity on small timescales. The climbing fiber pause is determined as the duration between a complex spike and the first following simple spike. To extend this analysis, we also plotted histograms of simple spike activity time locked on the complex spike, and labelled the shape of this time histogram as normal, facilitation, suppression, or oscillation.

In vivo two-photon targeted electrophysiology

Details on targeted electrophysiological recordings in vivo in the mouse cerebellum were described previously³⁶. PCs in lobules IV-VI were recorded in adult L7-TRPC3^{KO}-EAAT4^{eGFP} mice (aged 14-49 weeks) under two-photon microscope guidance. A custom-made head plate was fixed to the cleaned skull of each animal, under isoflurane anesthesia, with dental adhesive (Optibond; Kerr corporation, West collins, USA) and secured with dental acrylic. A craniotomy was made above the cerebellum, exposing lobules IV-VI. The craniotomy was sealed with biocompatible silicone (Kwik-Cast; World Precision Instruments) and the animal was allowed to recover from surgery before recording. The silicone seal was removed prior to recording. To keep the brain surface moist, Ringer solution containing (in mM): NaCl 135, KCl 5.4, MgCl₂ 1, CaCl₂ 1.8, HEPES 5 (pH 7.2 with NaOH; Merck, Darmstadt, Germany) was applied. Glass micropipettes with tip size of ~ 1 μ m (resistance: 6-9 M Ω) were advanced from the dorsal surface under a 25° angle into the cerebellum, allowing concurrent two-photon imaging with a long working distance objective (LUMPlanFI/IR 40 \times /0.8; Olympus) on a custom-built two-photon microscope. Pipettes were filled with the same Ringer solution with an additional 40 μ M AlexaFluor 594 hydrazide (Sigma-Aldrich, Steinheim, Germany) for visualization. GFP and AlexaFluor 594 were simultaneously excited by a MaiTai laser (Spectra Physics Lasers, Mountain View, CA, USA) operated at 860 nm. Green (GFP) and red (AlexaFluor 594) fluorescence were separated by a dichroic mirror at 560nm and emission filters centered at 510nm (Brightline Fluorescence Filter 510/84; Semrock) and 630nm (D630/60; Chroma), respectively. The brain surface was stabilized with agarose (2% in Ringer; Sigma-Aldrich) and pipette pressure was initially kept at 3 kPa while entering the brain tissue.

It was then removed for cell approach and the actual recording. Extracellular potentials were acquired with a MultiClamp 700A amplifier (Molecular Devices, Sunnyvale, CA, USA) in current-clamp mode. Signals were low-pass filtered at 10 kHz (four-pole Bessel filter) and digitized at 25 kHz (Digidata 1322A). Data were recorded with pCLAMP 9.2 (Molecular Devices). Z⁺ and Z⁻ cells were identified by comparing the relative intensity of GFP fluorescence. Whenever possible, cells of both types were recording alternately between adjacent bands Purkinje neurons with high and low GFP fluorescence.

In vitro electrophysiology and analysis

We performed *in vitro* electrophysiological recordings on TRPC3^{M^{wk}} (aged 9-21 weeks) and L7-TRPC3^{KO} (aged 20-60 weeks). As described previously⁶⁰, acute sagittal slices (250 μm thick) were prepared from the cerebellar vermis and put into ice-cold slicing medium which contained (in mM) 240 sucrose, 2.5 KCl, 1.25 Na₂HPO₄, 2 MgSO₄, 1 CaCl₂, 26 NaHCO₃ and 10 D-Glucose, carbogenated continuously with 95% O₂ and 5% CO₂. After cutting using a vibrotome (VT1200S, Leica), slices were incubated in artificial cerebrospinal fluid (ACSF) containing (in mM): 124 NaCl, 5 KCl, 1.25 Na₂HPO₄, 2 MgSO₄, 2 CaCl₂, 26 NaHCO₃ and 15 D-Glucose, equilibrated with 95% O₂ and 5% CO₂ at 33.0±1.0 °C for 30 min, and then at room temperature. NBQX (10 μM), DL-AP5 (50 μM), and picrotoxin (100 μM) were bath-applied to block AMPA-, NMDA-, and GABA subtype A (GABA_A)-receptors, respectively. PCs were identified using visual guidance by DIC video microscopy and water-immersion 40X objective (Axioskop 2 FS plus; Carl Zeiss, Jena, Germany). Recording electrodes (3-5 MΩ, 1.65 mm outside diameter and 1.11 mm interior diameter (World Precision Instruments, Sarasota, FL, USA) were prepared using a P-97 micropipette puller (Sutter Instruments, Novato, CA, USA), and filled with ACSF for cell-attached recordings, or with an intracellular solution containing (in mM): 120 K-Gluconate, 9 KCl, 10 KOH, 4 NaCl, 10 HEPES, 28.5 Sucrose, 4 Na₂ATP, 0.4 Na₃GTP (pH 7.25-7.35 with an osmolality of 295) for whole-cell recordings. We measured spontaneous firing activity of PCs in cell-attached mode (0 pA injection) and intrinsic excitability in whole-cell current-clamp mode by injection of brief (1s) depolarizing current pulses (ranging from -100 to 1100pA with 100pA increments) from a membrane holding potential of -65 mV at 33.0±1.0°C. The spike count of evoked action potential was taken as a measure of excitability. AP properties including peak amplitude, after-hyperpolarization amplitude (AHP) and half-width were evaluated using the first action potential generated by each PC. AHP indicates the amplitude of undershoot relative to the resting membrane potential. Half-width indicates the width of the signal at 50% of the maximum amplitude. PCs that required > -800 pA to maintain the holding potential at -65 mV or fired action potentials at this holding potential were discarded. The average spiking rate measured over the entire current pulse was used to construct current-frequency plots. For whole-cell Recordings, cells were excluded if the series (R_s) or input resistances (R_i) changed by >15% during the experiment, which was determined using a hyperpolarizing voltage step relative to the -65 mV holding potential. All electrophysiological recordings were acquired in lobules I-III and lobule X of the vermal cerebellum using EPC9 and EPC10-USB amplifiers (HEKA Electronics, Lambrecht, Germany) and Patchmaster software (HEKA Electronics). Data were analyzed afterwards using Clampfit (Molecular Devices).

Compensatory eye movement recordings

We subjected alert L7-TRPC3^{KO} mice (aged 12-39 weeks) to compensatory eye movement recordings which were described in detail previously⁶¹. In short, mice were equipped with a pedestal under general anesthesia with isoflurane/O₂. After a 2-3 days of recovery, mice were head-fixed with the body loosely restrained in a custom-made restrainer and placed in the center of a turntable (diameter: 63 cm) in the experimental set-up. A round screen (diameter 60 cm) with a random dotted pattern ('drum') surrounded the mouse during the experiment. Compensatory eye movements were induced by sinusoidal rotation of the drum in light (OKR), rotation of the table in the dark (VOR) or the rotation of the table in the light (visually enhanced VOR, VVOR) with an amplitude of 5° at 0.1-1 Hz. Motor performance in response to these stimulations was evaluated by calculating the gain (eye velocity/stimulus velocity) and phase (eye to stimulus in degrees) of the response. Motor learning was studied by subjecting mice to mismatched visual and vestibular input. Rotating the drum (visual) and table (vestibular) simultaneously, in phase at 0.6 Hz (both with an amplitude of 5°, 5 x 10 min) in the light will induce an increase of the gain of the VOR (in the dark). Subsequently, VOR Phase reversal was tested by continuing the next days (day 2-5, keeping mice in the dark in between experiments) with in phase stimulation, but now with drum amplitudes of 7.5° (days 2) and 10° (days 3, 4, and 5), while the amplitude of the turntable remained 5°. This resulted, over days of training, in the reversal of the VOR direction, from a normal compensatory rightward eye movement (in the dark), when the head turns left, to a reversed response with a leftward eye movement, when the head moves left. At the end of the VOR phase reversal training the OKR was probed again and compared to the OKR before training, to examine OKR gain increase. VOR gain increase was evoked by subjecting mice to out of phase drum and table stimulation at 1.0 Hz (both with an amplitude of 1.6°). A CCD camera was fixed to the turntable in order to monitor the eyes of the mice. Eye movements were recorded with eye-tracking software (ETL-200, ISCAN systems, Burlington, NA, USA). For eye illumination during the experiments, two infrared emitters (output 600 mW, dispersion angle 7°, peak wavelength 880 nm) were fixed to the table and a third emitter, which produced the tracked corneal reflection, was mounted to the camera and aligned horizontally with the optical axis of the camera. Eye movements were calibrated by moving the camera left-right (peak-to-peak 20°) during periods that the eye did not move⁶². Gain and phase values of eye movements were calculated using custom-made Matlab routines (MathWorks).

Eyeblink conditioning

For all procedures on eyeblink conditioning we refer to the study done previously⁶³. L7-TRPC3^{KO} mice, aged 16-25 weeks, were anesthetized with an isoflurane/oxygen mixture and surgically placed a so-called pedestal on the skull. After a 2-3 days' recovery, mice were head-fixed and suspended over a foam cylindrical treadmill on which they were allowed to walk freely (**Figure 7B**). Before each session starting, a minuscule magnet (1.5x0.7x0.5mm) was placed on the left lower eyelid with superglue (cyanoacrylate) and an NVE GMR magnetometer was positioned above the left upper eyelid. With this magnetic distance measurement technique (MDMT), we measured the exact positions of each individual mouse eyelid by analyzing the range from optimal closure to complete aperture. The CS was a green LED light (CS duration 280 ms, LED diameter 5 mm) placed 10 cm in front of the mouse's

head. The US consisted of a weak air-puff applied to the eye (30 psi, 30 ms duration), which was controlled by an API MPPI-3 pressure injector, and delivered via a 27.5-gauge needle that was perpendicularly positioned at 0.5-1 cm from the center of the left cornea. The training consisted of 3 daily habituation sessions, 1 baseline measurement, 3 blocks of 5 daily acquisition sessions (each block was separated by 2 days of rest). During the habituation sessions, mice were placed in the setup for 30-45 minutes, during which the air puff needle (for US delivery) and green LED (for CS delivery) were positioned properly but no stimuli were presented. On the day of acquisition session 1, each animal first received 20 CS-only trials as a baseline measure, to establish that the CS did not elicit any reflexive eyelid closure. During each daily acquisition session, every animal received in total 200 paired CS-US trials, 20 US only trials, and 20 CS only trials. These trials were presented in 20 blocks, each block consisted of 1 US only trial, 10 paired CS-US trials, and 1 CS only trial. Trials within the block were randomly distributed, but the CS only trial was always preceded by at least 2 paired CS-US trials. The interval between the onset of CS and that of US was set at 250 ms. All experiments were performed at approximately the same time of day by the same experimenter. Individual eyeblink traces were analyzed automatically with custom computer software (LabVIEW or MATLAB). Trials with significant activity in the 500 ms pre-CS period ($>7 \times \text{IQR}$) were regarded as invalid for further analysis. Valid trials were further normalized by aligning the 500 ms pre-CS baselines and calibrating the signal so that the size of a full blink was 1. In valid normalized trials, all eyelid movements larger than 0.1 and with a latency to CR onset between 50-250 ms and a latency to CR peak of 100-250 ms (both relative to CS onset) were considered as conditioned responses (CRs). For CS only trials in the probe session we used the exact same criteria except that the latency to CR peak time was set at 100-500 ms after CS onset.

Erasmus Ladder

Mice aged 11-16 weeks were subjected to the Erasmus Ladder (Noldus, Wageningen, Netherlands). As described previously ⁹, the Erasmus Ladder is a fully automated system consisting of a horizontal ladder between two shelter boxes. The ladder has 2 x 37 rungs for the left and right side. Rungs are placed 15 mm apart, with alternate rungs in a descended position, so as to create an alternating stepping pattern with 30 mm gaps. All rungs are equipped with touch sensors, which are activated when subject to a pressure corresponding to more than 4 grams. The sensors are continuously monitored to record the position and the walking pattern of the mouse. A single crossing of the Erasmus Ladder is recorded as a trial. In this study, each mouse underwent a daily session consisting of 42 trials, for five consecutive days. Motor performance was measured by counting step durations and percentages during a trial, including short steps (steps from one high rung to the next high rung), long steps (skipping one high rung), jumps (skipping two high rungs), lower steps (a step forward steps, but the paw is placed on a low rung), back steps (a step backward steps from one high rung to the previous high rung). All data were collected and processed by ErasmusLadder 2.0 software (Noldus, Wageningen, Netherlands).

Statistical Analysis

All values are shown as mean \pm s.d., unless stated otherwise. To determine means, variance

and perform statistical analysis, in the electrophysiological experiments the number of cells and in the behavioral experiment the number of mice were taken as the number of replicates. Apart from the requirements for inclusion in the final datasets as stated in the separate sections for each experimental technique above, data was excluded only when the signal to noise ratio was insufficient to warrant reliable analysis. For behavioral experiments group sizes were estimated a priori using sample size calculations based on minimal relevant differences and expected variation in control cells or mice. To study compensatory eye movements the numbers are based on the VOR phase reversal. A power analysis based on repeated measures ANOVA with $\alpha = 0.05$, $\beta = 0.20$, minimal effect size f of 0.50 ($\Delta = 30^\circ$, SD 30° , 7 measurements), indicated a minimum of 11 mice per group, which were obtained ($n=11/13$ for controls/mutants). For eyeblink conditioning, these numbers are based on the percentage of conditioned responses and were: $\alpha = 0.05$, $\beta = 0.20$, minimal effect size f of 0.42 ($\Delta = 25\%$, SD 30%, 15 repeats), resulting in a minimum of 14 mice per group, which were obtained ($n=15/15$ for controls/mutants). For electrophysiological recordings the power analysis was based on previous experiments (Zhou et al., 2014), which gave a minimum group size of 10 Purkinje cells per group ($\alpha = 0.05$, $\beta = 0.20$, $\Delta = 18.1$ Hz, SD 14.0 Hz, based on Student's t -test) for *in vitro* experiments and 6 Purkinje cells per group ($\alpha = 0.05$, $\beta = 0.20$, $\Delta = 35.3$ Hz, SD 17.8 Hz) for *in vivo* experiments, which were obtained in all experiments (all $n \geq 10$ for *in vitro*, all $n \geq 12$ for *in vivo*). Inter-group comparisons were done by two-tailed Student's t -test. ANOVA for repeated measures was used to analyze eye movement and Erasmus ladder behavioral data; linear mixed-effect model analysis⁶³ (established in R version 1.1.442) was used to analyze eyeblink conditioning data. For the complete dataset, see **Table S2-S3**. All statistical analyses were performed using SPSS 20.0 software. Data was considered statistically significant if $P < 0.05$.

Acknowledgements

We kindly thank Laura Post for mouse breeding; Nadia Khosravinia for help with behavior experiment; Joshua J. White and Dick Jaarsma for discussions and comments on the manuscript. This work was supported by an ERC starter grant (ERC-Stg #680235; MS), China Scholarship Council (#201306230130; BW), the Netherlands Organization for Scientific Research (NWO-ALW; CIDZ), the Dutch Organization for Medical Sciences (ZonMW; CIDZ), ERC-adv and ERC-POC (CIDZ), and the Center for Integrated Protein Science Munich (CIPSM; JH).

Author contributions

B.W. and M.S. designed all the experiments and wrote the manuscript; B.W. performed and analyzed the *in vivo* and *in vitro* electrophysiology experiments, analyzed the *in vivo* two-photon experiments and the eye-movement behavior experiments; F.B. performed and analyzed the immunohistochemistry and iDISCO experiments; A.B.W performed the *in vivo* two-photon experiments; C.O. conducted and analyzed the Western Blot; Y.A. and R.J.P supported for light sheet imaging; J.H. supplied the TRPC3^{fl/fl} mice; E.B. supplied the TRPC3^{Mwk} mouse; H.J.B analyzed the eyeblink conditioning data; C.I.D.Z. provided major revisions to the manuscript and guided the project. M.S. initiated the project and coordinated collaborations between groups. All authors discussed the results and implications and commented on the manuscript.

Supplemental Information

Supplemental Information includes seven figures, three tables and one movie and can be found with this article online.

Competing interests

The authors declare no competing financial interests.

References

- 1 Ackermann, H., Vogel, M., Petersen, D. & Poremba, M. Speech deficits in ischaemic cerebellar lesions. *Journal of neurology* **239**, 223-227, (1992).
- 2 Bodranghien, F. *et al.* Consensus Paper: Revisiting the Symptoms and Signs of Cerebellar Syndrome. *Cerebellum* **15**, 369-391, (2016).
- 3 Raymond, J. L., Lisberger, S. G. & Mauk, M. D. The cerebellum: a neuronal learning machine? *Science* **272**, 1126-1131, (1996).
- 4 Yang, Y. & Lisberger, S. G. Purkinje-cell plasticity and cerebellar motor learning are graded by complex-spike duration. *Nature* **510**, 529-532, (2014).
- 5 De Zeeuw, C. I. & Yeo, C. H. Time and tide in cerebellar memory formation. *Curr Opin Neurobiol* **15**, 667-674, (2005).
- 6 Hirata, Y. & Highstein, S. M. Analysis of the discharge pattern of floccular Purkinje cells in relation to vertical head and eye movement in the squirrel monkey. *Progress in brain research* **124**, 221-232, (2000).
- 7 Witter, L., Canto, C. B., Hoogland, T. M., de Gruijl, J. R. & De Zeeuw, C. I. Strength and timing of motor responses mediated by rebound firing in the cerebellar nuclei after Purkinje cell activation. *Frontiers in neural circuits* **7**, 133, (2013).
- 8 Thach, W. T., Goodkin, H. P. & Keating, J. G. The cerebellum and the adaptive coordination of movement. *Annual review of neuroscience* **15**, 403-442, (1992).
- 9 Vinueza Veloz, M. F. *et al.* Cerebellar control of gait and interlimb coordination. *Brain structure & function* **220**, 3513-3536, (2015).
- 10 Zhou, H. *et al.* Cerebellar modules operate at different frequencies. *Elife* **3**, e02536, (2014).
- 11 Xiao, J. *et al.* Systematic regional variations in Purkinje cell spiking patterns. *PLoS one* **9**, e105633, (2014).
- 12 Brochu, G., Maler, L. & Hawkes, R. Zebrin II: a polypeptide antigen expressed selectively by Purkinje cells reveals compartments in rat and fish cerebellum. *The Journal of comparative neurology* **291**, 538-552, (1990).
- 13 Ahn, A. H., Dziennis, S., Hawkes, R. & Herrup, K. The cloning of zebrin II reveals its identity with aldolase C. *Development* **120**, 2081-2090, (1994).
- 14 Ruigrok, T. J. Ins and outs of cerebellar modules. *Cerebellum* **10**, 464-474, (2011).
- 15 Sugihara, I. & Quay, P. N. Identification of aldolase C compartments in the mouse cerebellar cortex by olivocerebellar labeling. *The Journal of comparative neurology* **500**, 1076-1092, (2007).
- 16 Graham, D. J. & Wylie, D. R. Zebrin-immunopositive and -immunonegative stripe pairs represent functional units in the pigeon vestibulocerebellum. *The Journal of neuroscience : the official journal of the Society for Neuroscience* **32**, 12769-12779, (2012).
- 17 De Zeeuw, C. I. & Ten Brinke, M. M. Motor Learning and the Cerebellum. *CSHP Biol* **7**, a021683, (2015).
- 18 Altschuler, S. J. & Wu, L. F. Cellular heterogeneity: do differences make a difference? *Cell* **141**, 559-563, (2010).
- 19 Apps, R. *et al.* Cerebellar Modules and Their Role as Operational Cerebellar Processing Units. *Cerebellum*, (2018).
- 20 Cerminara, N. L., Lang, E. J., Sillitoe, R. V. & Apps, R. Redefining the cerebellar cortex as an assembly of non-uniform Purkinje cell microcircuits. *Nature reviews. Neuroscience* **16**, 79-93, (2015).
- 21 Wadiche, J. I. & Jahr, C. E. Patterned expression of Purkinje cell glutamate transporters controls synaptic plasticity. *Nat Neurosci* **8**, 1329-1334, (2005).
- 22 Perkins, E. M. *et al.* Loss of cerebellar glutamate transporters EAAT4 and GLAST differentially affects the spontaneous firing pattern and survival of Purkinje cells. *Human molecular genetics*, (2018).
- 23 Miyata, M. *et al.* Deficient long-term synaptic depression in the rostral cerebellum correlated with impaired motor learning in phospholipase C beta4 mutant mice. *The European journal of neuroscience* **13**, 1945-1954, (2001).
- 24 Hashimoto, K., Miyata, M., Watanabe, M. & Kano, M. Roles of phospholipase Cbeta4 in synapse elimination and plasticity in developing and mature cerebellum. *Molecular neurobiology* **23**, 69-82, (2001).
- 25 Sarna, J. R., Marzban, H., Watanabe, M. & Hawkes, R. Complementary stripes of phospholipase Cbeta3 and Cbeta4 expression by Purkinje cell subsets in the mouse cerebellum. *The Journal of comparative neurology* **496**, 303-313, (2006).
- 26 Ohtani, Y. *et al.* The synaptic targeting of mGluR1 by its carboxyl-terminal domain is crucial for

- cerebellar function. *The Journal of neuroscience : the official journal of the Society for Neuroscience* **34**, 2702-2712, (2014).
- 27 Mateos, J. M. *et al.* Parasagittal compartmentalization of the metabotropic glutamate receptor mGluR1b in the cerebellar cortex. *Eur J Anat.* **5**, 15-21, (2001).
- 28 Hartmann, J. *et al.* TRPC3 channels are required for synaptic transmission and motor coordination. *Neuron* **59**, 392-398, (2008).
- 29 Sanchez, M. *et al.* Compartmentation of the rabbit cerebellar cortex. *The Journal of comparative neurology* **444**, 159-173, (2002).
- 30 Mostofi, A., Holtzman, T., Grout, A. S., Yeo, C. H. & Edgley, S. A. Electrophysiological localization of eyeblink-related microzones in rabbit cerebellar cortex. *The Journal of neuroscience : the official journal of the Society for Neuroscience* **30**, 8920-8934, (2010).
- 31 Hesslow, G. Inhibition of classically conditioned eyeblink responses by stimulation of the cerebellar cortex in the decerebrate cat. *The Journal of physiology* **476**, 245-256, (1994).
- 32 Becker, E. B. *et al.* A point mutation in TRPC3 causes abnormal Purkinje cell development and cerebellar ataxia in moonwalker mice. *PNAS* **106**, 6706-6711, (2009).
- 33 Barski, J., Dethleffsen K & M, M. Cre recombinase expression in cerebellar Purkinje cells. *Genesis* **28**, 93-98, (2000).
- 34 Womack, M. & Khodakhah, K. Active contribution of dendrites to the tonic and trimodal patterns of activity in cerebellar Purkinje neurons. *The Journal of neuroscience : the official journal of the Society for Neuroscience* **22**, 10603-10612, (2002).
- 35 Raman, I. M. & Bean, B. P. Ionic currents underlying spontaneous action potentials in isolated cerebellar Purkinje neurons. *The Journal of neuroscience : the official journal of the Society for Neuroscience* **19**, 1663-1674, (1999).
- 36 Wu, B. & Schonewille, M. (2018). Targeted Electrophysiological Recordings In Vivo in the Mouse Cerebellum. *Extracellular Recording Approaches*, Roy Sillitoe, ed. (New York: Humana Press), pp. 19-37.
- 37 Zhou, H., Voges, K., Lin, Z., Ju, C. & Schonewille, M. Differential Purkinje cell simple spike activity and pausing behavior related to cerebellar modules. *Journal of neurophysiology* **113**, 2524-2536, (2015).
- 38 Chaumont, J. *et al.* Clusters of cerebellar Purkinje cells control their afferent climbing fiber discharge. *Proceedings of the National Academy of Sciences of the United States of America* **110**, 16223-16228, (2013).
- 39 Simpson, J. I., Wylie, D. R. W. & De Zeeuw, C. I. On climbing fiber signals and their consequence(s). *Behavioral and Brain Sciences* **19**, 384-398, (1996).
- 40 Sekerkova, G. *et al.* Early onset of ataxia in moonwalker mice is accompanied by complete ablation of type II unipolar brush cells and Purkinje cell dysfunction. *The Journal of neuroscience : the official journal of the Society for Neuroscience* **33**, 19689-19694, (2013).
- 41 Apps, R. & Hawkes, R. Cerebellar cortical organization: a one-map hypothesis. *Nature reviews. Neuroscience* **10**, 670-681, (2009).
- 42 Marzban, H. & Hawkes, R. On the architecture of the posterior zone of the cerebellum. *Cerebellum* **10**, 422-434, (2011).
- 43 Sun, Y., Sukumaran, P., Bandyopadhyay, B. C. & Singh, B. B. Physiological Function and Characterization of TRPCs in Neurons. *Cells* **3**, 455-475, (2014).
- 44 Becker, E. B. The Moonwalker mouse: new insights into TRPC3 function, cerebellar development, and ataxia. *Cerebellum* **13**, 628-636, (2014).
- 45 Hartmann, J., Henning, H. A. & Konnerth, A. mGluR1/TRPC3-mediated Synaptic Transmission and Calcium Signaling in Mammalian Central Neurons. *Cold Spring Harbor perspectives in biology* **3**, (2011).
- 46 Chaumont, J. *et al.* Clusters of cerebellar Purkinje cells control their afferent climbing fiber discharge. *PNAS* **110**, 16223-16228, (2013).
- 47 ten Brinke, M. M. *et al.* Evolving Models of Pavlovian Conditioning: Cerebellar Cortical Dynamics in Awake Behaving Mice. *Cell Rep* **13**, 1977-1988, (2015).
- 48 Johansson, F., Jirenhed, D. A., Rasmussen, A., Zucca, R. & Hesslow, G. Memory trace and timing mechanism localized to cerebellar Purkinje cells. *Proceedings of the National Academy of Sciences of the United States of America* **111**, 14930-14934, (2014).
- 49 Jirenhed, D. A., Bengtsson, F. & Hesslow, G. Acquisition, extinction, and reacquisition of a cerebellar cortical memory trace. *The Journal of neuroscience : the official journal of the Society for Neuroscience* **27**, 2493-2502, (2007).
- 50 Fujita, H. *et al.* Detailed expression pattern of aldolase C (Aldoc) in the cerebellum, retina and other areas of the CNS studied in Aldoc-Venus knock-in mice. *PLoS one* **9**, e86679, (2014).
- 51 Voges, K., Wu, B., Post, L., Schonewille, M. & De Zeeuw, C. I. Mechanisms underlying

- vestibulo-cerebellar motor learning in mice depend on movement direction. *The Journal of physiology* **595**, 5301-5326, (2017).
- 52 Kim, S. J. TRPC3 channel underlies cerebellar long-term depression. *Cerebellum* **12**, 334-337, (2013).
- 53 Schonewille, M. *et al.* Reevaluating the role of LTD in cerebellar motor learning. *Neuron* **70**, 43-50, (2011).
- 54 Schreurs, B. G., Tomsic, D., Gusev, P. A. & Alkon, D. L. Dendritic excitability microzones and occluded long-term depression after classical conditioning of the rabbit's nictitating membrane response. *Journal of neurophysiology* **77**, 86-92, (1997).
- 55 Ohtsuki, G., Piochon, C., Adelman, J. P. & Hansel, C. SK2 channel modulation contributes to compartment-specific dendritic plasticity in cerebellar Purkinje cells. *Neuron* **75**, 108-120, (2012).
- 56 Ruigrok, T. J., Pijpers, A., Goedknegt-Sabel, E. & Coulon, P. Multiple cerebellar zones are involved in the control of individual muscles: a retrograde transneuronal tracing study with rabies virus in the rat. *The European journal of neuroscience* **28**, 181-200, (2008).
- 57 Diedrichsen, J., Criscimagna-Hemminger, S. E. & Shadmehr, R. Dissociating timing and coordination as functions of the cerebellum. *The Journal of neuroscience : the official journal of the Society for Neuroscience* **27**, 6291-6301, (2007).
- 58 Shadmehr, R. Distinct neural circuits for control of movement vs. holding still. *Journal of neurophysiology* **117**, 1431-1460, (2017).
- 59 Renier, N. *et al.* iDISCO: a simple, rapid method to immunolabel large tissue samples for volume imaging. *Cell* **159**, 896-910, (2014).
- 60 Peter, S. *et al.* Dysfunctional cerebellar Purkinje cells contribute to autism-like behaviour in Shank2-deficient mice. *Nature communications* **7**, 12627, (2016).
- 61 Schonewille, M. *et al.* Purkinje cell-specific knockout of the protein phosphatase PP2B impairs potentiation and cerebellar motor learning. *Neuron* **67**, 618-628, (2010).
- 62 Stahl, J. S. Using eye movements to assess brain function in mice. *Vision research* **44**, 3401-3410, (2004).
- 63 Boele, H. J. *et al.* Impact of parallel fiber to Purkinje cell long-term depression is unmasked in absence of inhibitory input. *Science advances* **4**, eaas9426, (2018).

Figure legends

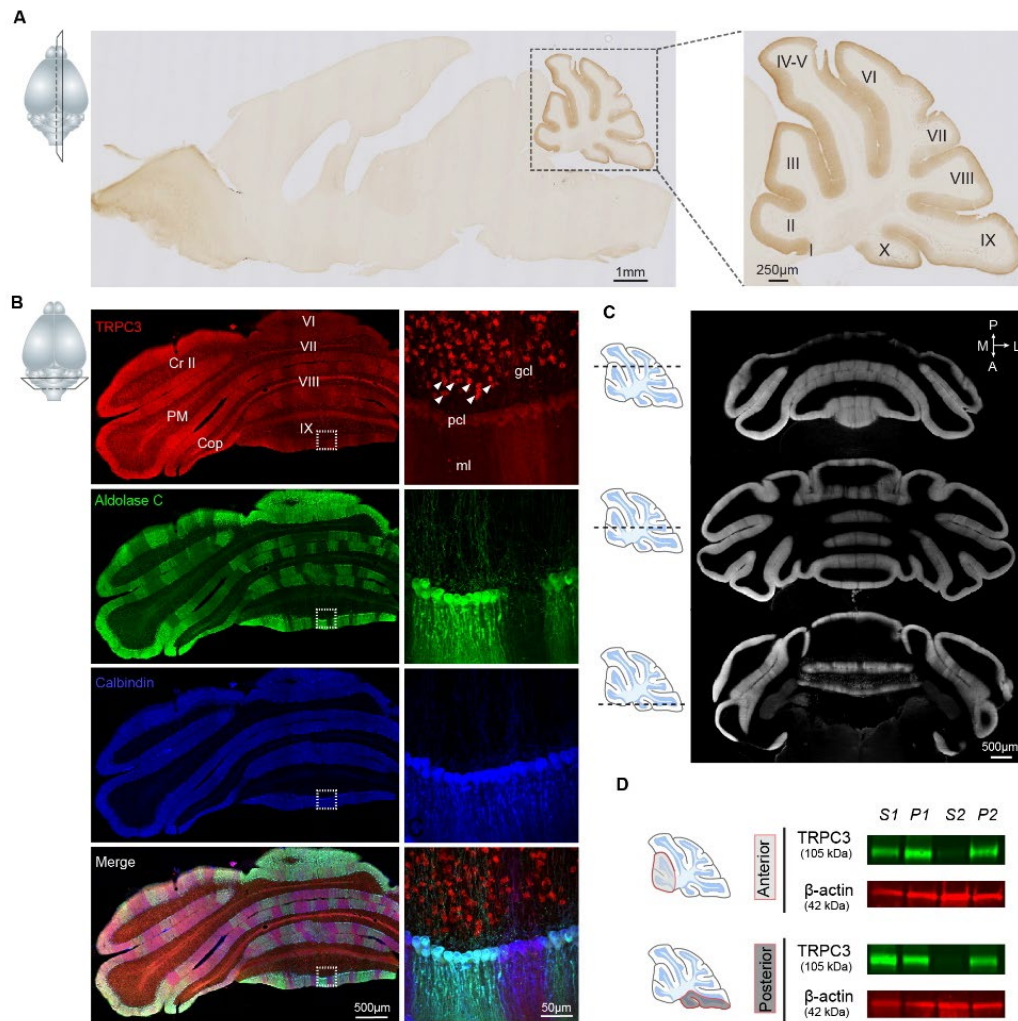


Figure 1 | TRPC3 is predominantly expressed in the cerebellum in a zebrin-related pattern. (A) Representative image and magnification (right) of sagittal cryosection of an adult mouse brain stained with anti-TRPC3. Inset, plane of section. (B) Coronal immunofluorescence images with anti-TRPC3 (red), anti-aldolase C (green) and anti-calbindin (blue) staining of the cerebellar cortex (left), with magnifications (right). TRPC3 is expressed in the cerebellar PCs and UBCs (triangles), in a pattern that in the vermis complements that of zebrin and appears more uniform in the hemispheres. Inset, plane of section. (C) Individual images of a light sheet imaging-based reconstruction of a mouse brain cleared with iDISCO and stained with anti-TRPC3. Three different planes (insets) of whole cerebellum show sagittal compartmentations across lobules. (D) Immunoblots of TRPC3 by using synaptic protein extraction protocol on the anterior (top) and posterior (bottom) cerebellum. TRPC3 is present in the homogenate (S1) and enriched in the membrane (P1) and synaptosomes (P2), but not in the cytosol (S2). I-X, cerebellar lobules I-X; Cr II, Crus II; PM, paramedian lobule; Cop, Copula Pyramidis; gcl, granule cell layer; pcl, Purkinje cell layer; ml, molecular layer; D, dorsal; V, ventral; M, medial; L, lateral.

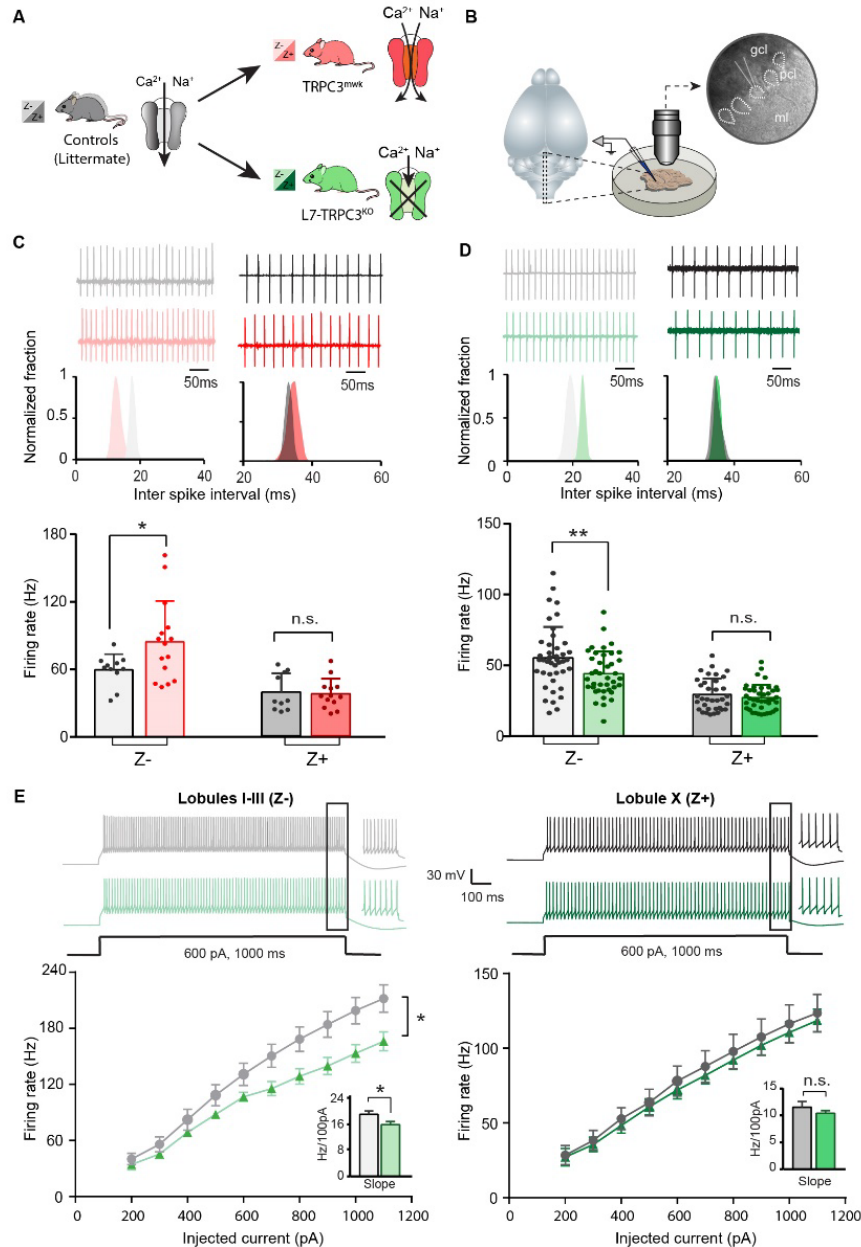


Figure 2 | Differential controls of PCs firing properties by TRPC3 in vitro. (A) Schematic drawing of TRPC3 channel function in control (black), gain-of-function ($TRPC3^{Mwk}$, red) and loss-of-function ($L7-TRPC3^{KO}$, green) mice. (B) Schematic approach illustrating of PCs (right circle, dashed lines) recording in vitro, in acute sagittal slices. (C, D) Representative traces of cell-attached PC recordings (top) and corresponding inter spike interval (ISI) distributions (middle) in a Z- PC (left) and a Z+ PC (right) of $TRPC3^{Mwk}$ (C) and $L7-TRPC3^{KO}$ (D) mice. Z- PCs were affected in $TRPC3^{Mwk}$ (C, light-red, $n=15$ cells/ $N=4$ mutant mice vs. $n=11$ cells/ $N=2$ littermate controls, $t_{19}=-2.43$, $P=0.025$ and in $L7-TRPC3^{KO}$ mice (D, light-green, $n=40$ / $N=6$ mutants vs. $n=43$ / $N=5$ controls, $t_{81}=2.69$, $P=0.009$). No differences in the firing rate of Z+ PCs in $TRPC3^{Mwk}$ (C, dark-red, $n=13$ / $N=4$ mutants vs. $n=10$ / $N=2$ controls, $t_{21}=0.242$, $P=0.811$) and $L7-TRPC3^{KO}$ mice (D, dark-green, $n=36$ / $N=10$ mutants vs. $n=35$ / $N=4$ controls, $t_{64}=0.937$, $P=0.352$). (E) Whole-cell patch-clamp recordings in slice from PCs of $L7-TRPC3^{KO}$ and control mice were used to test intrinsic excitability, by keeping cells at a holding potential of -65 mV and evoking action potentials by current steps of 100 pA (example, top). Top, exemplary traces evoked by current injection at 600 pA. Bottom, Input-output curves from whole-cell recordings of $L7-TRPC3^{KO}$ mice of Z- PCs (left, $n=17$ / $N=5$ mutants vs $n=17$ / $N=5$ controls, $t_{32}=-2.20$, $P=0.035$) and Z+ PCs (right, $n=12$ / $N=5$

mutants vs $n=12/N=4$ controls, $t_{22}=-0.95$, $P=0.354$). *gcl*, granule cell layer; *pcl*, Purkinje cell layer; *ml*, molecular layer. **C-D**, data are represented as mean \pm s.d.; **E**, data are represented as mean \pm s.e.m.. For values see **Table S2A-C**.

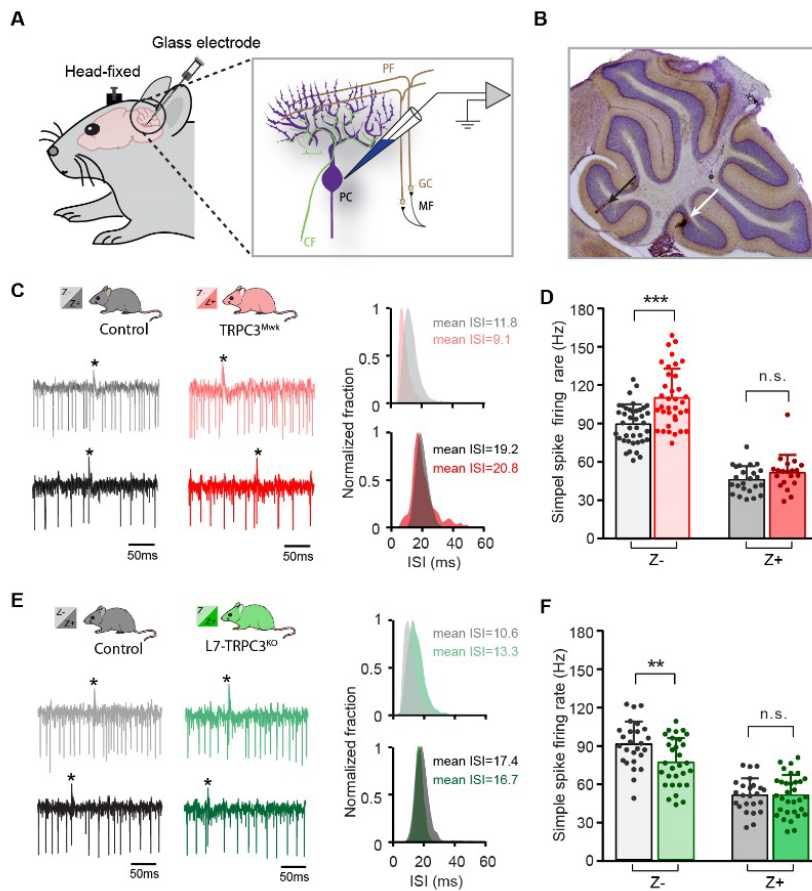


Figure 3 | In vivo simple spike firing rate of Z-, but not Z+ PCs is controlled by TRPC3. (A) Schematic illustration of extracellular recording configuration in vivo. PF, parallel fiber; CF, climbing fiber; MF, mossy fiber; GC, granule cell. (B) Representative sagittal cerebellar section with recording sites labelled by BDA injection, in lobule II (black arrow) and X (white arrow). (C) Representative example traces (left) and ISI distributions (right) of a Z- PC (top) and a Z+ PC (bottom) in gain-of-function TRPC3^{Mwk} mice. (D) PC simple spike firing rate recorded in vivo in TRPC3^{Mwk} mice compared to control littermates, for the Z- lobules I-III (light-red, $n=36/N=7$ mutants vs. $n=40/N=6$ controls, $t_{60}=-4.58$, $P<0.001$) and the Z+ lobule X (dark-red, $n=20/N=6$ mutants vs. $n=24/N=5$ controls, $t_{42}=-1.47$, $P=0.148$). (E) Representative example traces (left) and ISI distributions (right) in a Z- PC (top) and a Z+ PC (bottom) of loss-of-function L7-TRPC3^{KO} mice. (F) PC simple spike firing rate of L7-TRPC3^{KO} mice compared to controls, for Z- lobules I-III (light-green, $n=30/N=7$ mutants vs. $n=26/N=8$ controls, $t_{54}=2.88$, $P=0.006$) and in Z+ lobule X (dark-green, $n=32/N=8$ mutants vs. $n=24/N=6$ controls, $t_{54}=-0.053$, $P=0.958$). Data are represented as mean \pm s.d., for values see **Table S2D-E**.

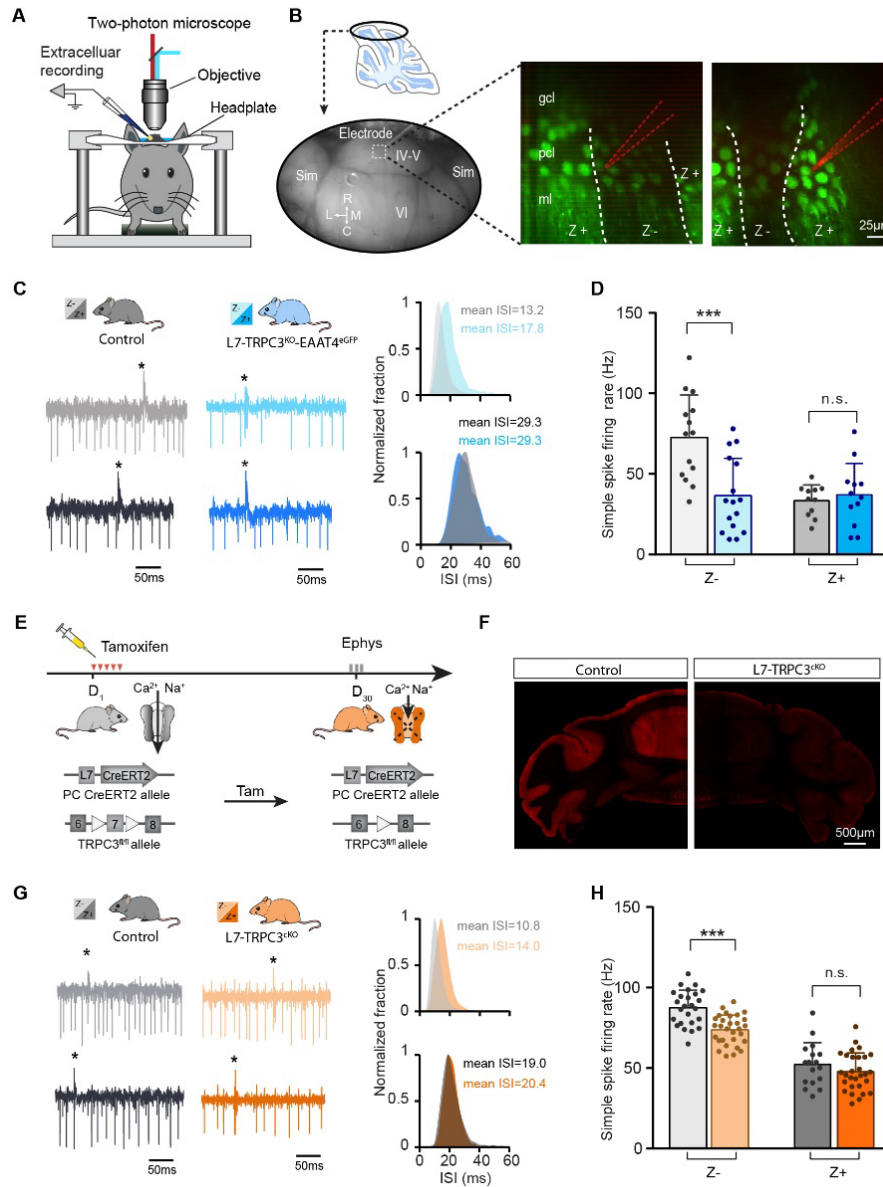


Figure 4 | TRPC3 effects follow zebrin-identity and are not developmental. (A) Schematic experimental setup for two-photon imaging-based targeted PC recordings, in vivo. (B) Sagittal view of cerebellum (schematic, top) indicating the recording region in the ellipse (bottom). Representative images (right) show the visualization of Z+ bands (strong green) in an awake L7-TRPC3^{KO}-EAAT4^{eGFP} mouse, with recording electrodes (red) positioned in Z- (left) and Z+ (right) bands. (C) Representative firing traces (left) and ISI distributions (right) in a Z- PC (top) and a Z+ PC (bottom) of loss-of-function L7-TRPC3^{KO}-EAAT4^{eGFP} mice (blue) and control littermates (no Cre; gray). (D) Average simple spike firing rate of PCs recorded from adjacent modules of L7-TRPC3^{KO}-EAAT4^{eGFP} mice and those in controls. Comparison for Z- PCs (light-blue, n=16/N=3 mutants vs. n=14/N=2 controls, $t_{28}=3.99$, $P<0.001$), and Z+ PCs (dark-blue, n=12/N=3 mutants vs. n=12/N=2 controls, $t_{21}=-0.550$, $P=0.588$). (E, F) Intraperitoneal tamoxifen injections for five days (D₁₋₅) to trigger TRPC3 gene ablation solely in PCs in adult L7^{CreERT2}-TRPC3^{fl/fl} mice. Open triangles indicate loxP sites. PC in vivo extracellular activity was recorded four weeks later (D₂₉₋₃₁) in L7-TRPC3^{cKO} mice (orange). TRPC3 deletion was confirmed after experiment by confocal image using anti-TRPC3 staining (F). (G) Representative firing traces (left) and ISI distributions (right) in a Z- PC (top) and a Z+ PC (bottom) of L7-TRPC3^{cKO} mice. (H) Simple spike firing rate in vivo in L7-TRPC3^{cKO} and control mice (no Cre). Comparison for Z- PCs (light-orange, n=30/N=4 mutants vs. n=25/N=4 controls,

$t_{53}=5.05$, $P<0.001$), and Z+ PCs (dark-orange, $n=29/N=4$ mutants vs. $n=17/N=3$ controls, $t_{44}=1.21$, $P=0.234$). Sim, simplex lobule; IV-VI, lobules IV-VI, R, rostral, C, caudal; L, lateral, M, medial. Data are represented as mean \pm s.d., for values see **Table S2F-G**.

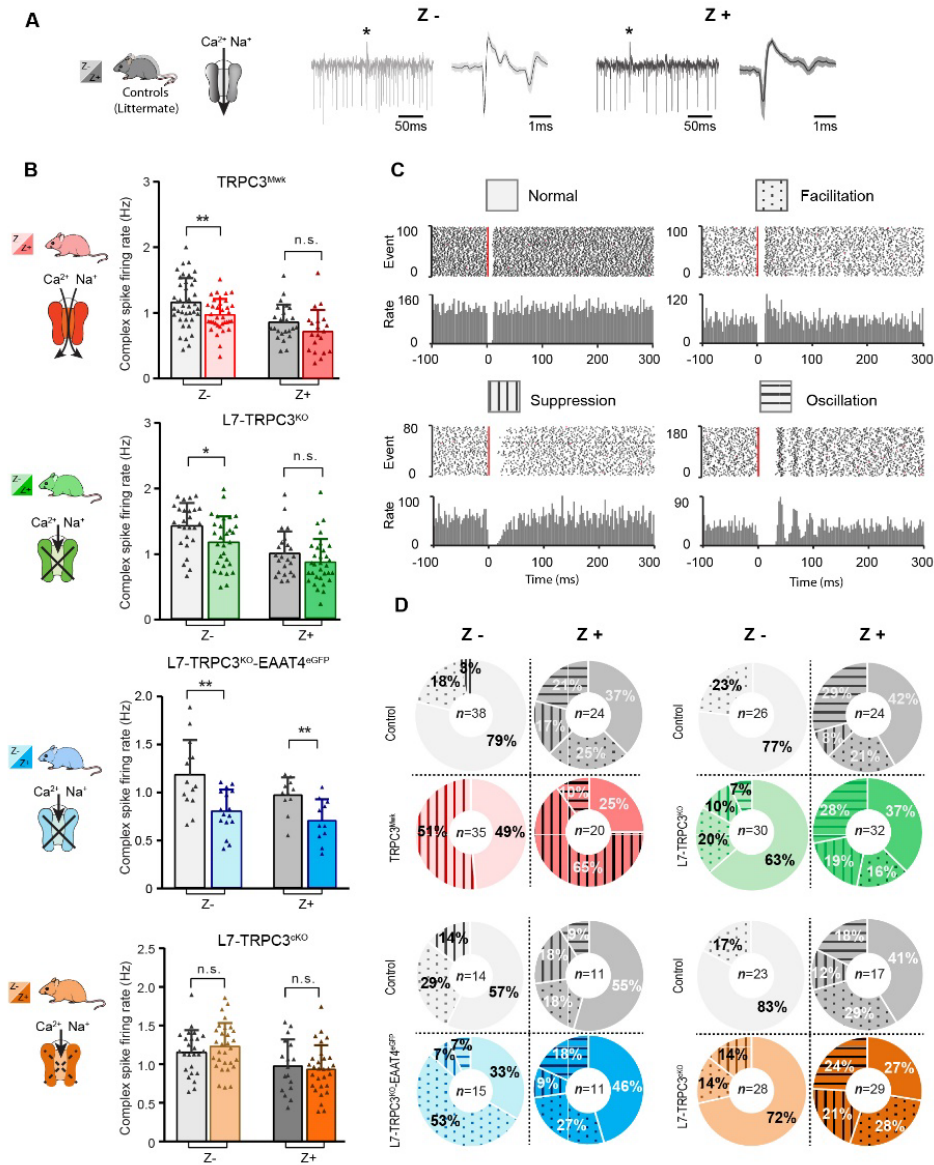


Figure 5 | Complex spikes and complex spike - simple spike interaction are affected by TRPC3 mutations. (A) Representative PC recording traces and complex spikes shape of Z- (light black) and Z+ (dark black) PCs in the control mice. (B) Top half, comparison of complex spike firing rates in $TRPC3^{Mwk}$ (red) and $L7-TRPC3^{KO}$ (green) mice versus their respective littermate controls for Z- PCs ($TRPC3^{Mwk}$: $t_{68}=2.68$, $P=0.009$; $L7-TRPC3^{KO}$: $t_{54}=2.50$, $P=0.016$) and Z+ PCs ($TRPC3^{Mwk}$: $t_{42}=1.56$, $P=0.126$; $L7-TRPC3^{KO}$: $t_{54}=1.41$, $P=0.164$). Bottom half, comparison of complex spike firing rates in $L7-TRPC3^{KO-EAAT4^{eGFP}}$ (blue) and $L7-TRPC3^{cKO}$ (orange) mice versus their respective controls for Z- PCs ($L7-TRPC3^{KO-EAAT4^{eGFP}}$: $t_{28}=3.49$, $P=0.002$; $L7-TRPC3^{cKO}$: $t_{53}=-0.940$, $P=0.352$) and Z+ PCs ($L7-TRPC3^{KO-EAAT4^{eGFP}}$: $t_{20}=3.03$, $P=0.007$; $L7-TRPC3^{cKO}$: $t_{44}=0.448$, $P=0.656$). (C) Raster plots of simple spike activity around the occurrence of each complex spike (-100 to +300 ms). These peri-complex spike time histograms can, based on post-complex spike activity, be divided into one of four types: normal (no change), facilitation, suppression and oscillation. (D) The distribution of post-complex spike response types for Z- and Z+ PCs, in $TRPC3^{Mwk}$, $L7-TRPC3^{KO}$, $L7-TRPC3^{KO-EAAT4^{eGFP}}$ and $L7-TRPC3^{cKO}$ mice. Data are represented as mean \pm s.d., for values see **Table S2**.

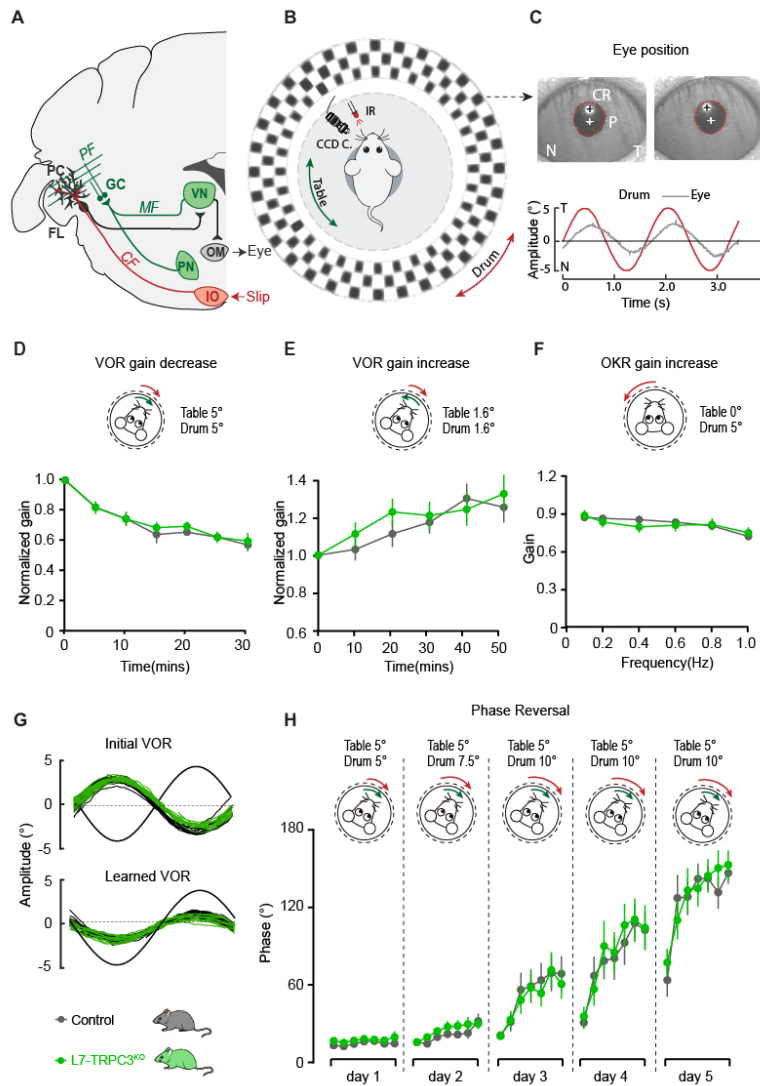


Figure 6 | PC-specific deletion of TRPC3 does not affect Z+-dependent VOR adaptation. (A)

Cerebellar circuitry controlling compensatory eye movements and their adaptation. PCs in the flocculus (FL) receive vestibular and visual input via the mossy fiber (MF) - parallel fiber (PF) system (green) and climbing fiber input (CF, red) from the inferior olive (IO), indicating retinal slip. These two inputs converge on PCs, which influence eye movements via the vestibular nuclei (VN) and the oculomotor (OM) neurons. PN, pontine nuclei; GC, granule cell. (B) Schematic illustration of eye movement recording setup. Mice are head-fixed in the center of a turntable for vestibular stimulation

and surrounded by a random dotted pattern ('drum') for visual stimulation. A CCD camera was used for infrared (IR) video-tracking of the left eye. (C) Top, examples of nasal (N) and temporal (T) eye positions. Red circles, pupil fit; black cross, corneal reflection (CR); white cross, pupil center. Bottom, example trace of eye position (grey) with drum position (red), during stimulation at an amplitude of 5° and frequency of 0.6 Hz. (D) L7-TRPC3^{KO} and control mice were subjected to six 5-min training sessions with mismatched in-phase visual and vestibular stimulation (in light, see insets), aimed at decreasing the VOR gain (probed in the dark before, between and after sessions). (E) Similar, but now mice were trained with out-of-phase stimulation, aimed at increasing VOR gain. (F) Re-recording of OKR gain following the VOR phase reversal training (see G-H) to test OKR gain increase (compare to Figure S7C, left). (G) Multiple-day training using in-phase mismatch stimulation (see inset in H) aimed at reversing the direction of the VOR (quantified as a reversal of the phase). Representative eye position recordings of VOR before (top) and after (bottom) training. (H) Results of five days of VOR phase reversal training, probed by recording VOR (in the dark before, between and after sessions) with mice kept in the dark in overnight. Data are represented as mean ± s.e.m., N=11 mutants versus N=13 controls, all P > 0.05, ANOVA for repeated measurements. See Table S3 for values.

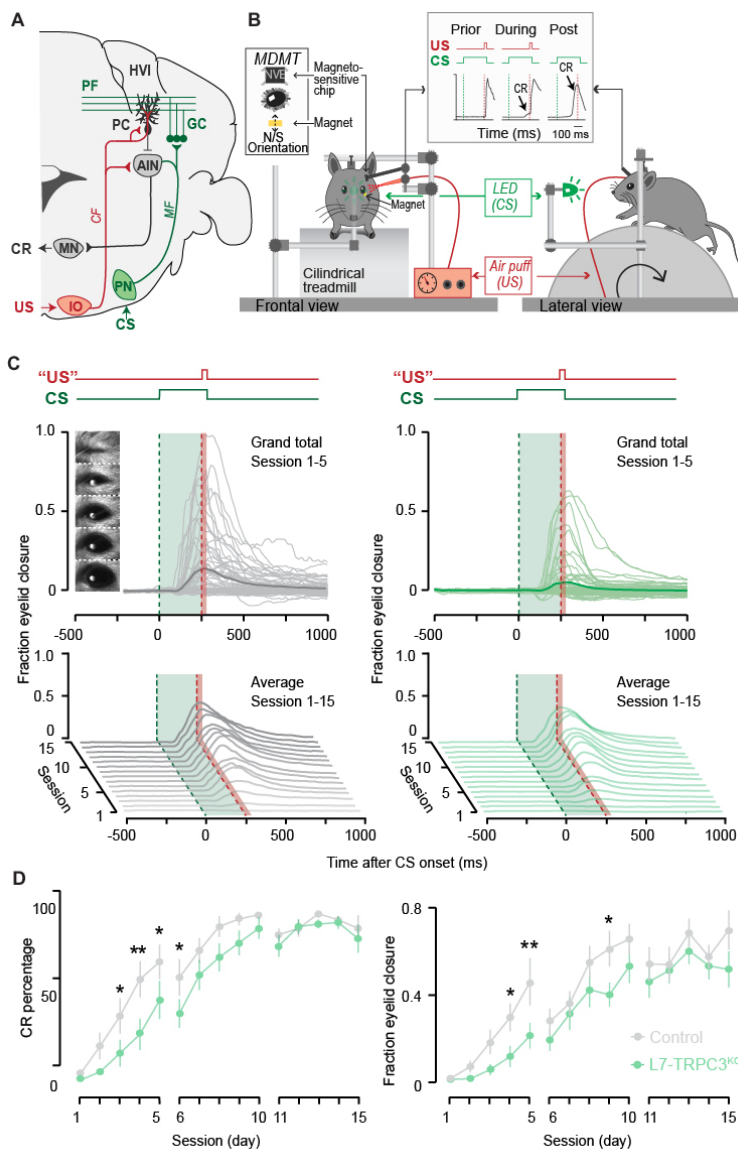


Figure 7 | Eyeblink conditioning, linked to Z-modules is delayed in $L7-TRPC3^{KO}$ mice.

(A) Cerebellar circuitry controlling eyeblink conditioning. PCs in the paravermal region around the primary fissure receive sensory information from e.g. the pontine nucleus (PN) through the MF-PF pathway and the error signal from the inferior olive (IO) through the climbing fibers (CF). These PCs in turn influence eyelid muscles via the anterior interposed nucleus (AIN) and motor nuclei (MN). (B) Schematic illustration of eyeblink conditioning setup. Head fixed mice on a freely moving treadmill, are presented a green LED light (conditional stimulus, CS) followed several hundred milliseconds later by a weak air-puff on the eye (unconditional stimulus, US). As a result of repeated CS-US pairings, mice will eventually learn to close their eye in response to the CS, which is called the conditioned response (CR). Eyelid movements were

recorded with the magnetic distance measurement technique (MDMT). (C) Comparison of fraction of eyelid closure between controls (left) and $L7-TRPC3^{KO}$ mice (right). Top, session averages (thin-lines) per mouse and overall average (thick-lines) for the first 5 days. Insets: mouse eye video captures show eyelid closure ranging from 0 (fully-open) to 1 (fully-closed). Bottom, waterfall plot of the averaged eyeblink trace during CS-only trials for the 15 daily sessions. (D) The CR percentage and CR amplitude for $L7-TRPC3^{KO}$ mice initially have a significantly slower acquisition but eventually reach the same levels as control littermates. Data are represented as mean \pm s.e.m., $N=15$ mutants versus $N=15$ controls, P values were all FDR corrected for multiple comparisons, see **Table S3** for values and statistics.

Supplemental information Legends

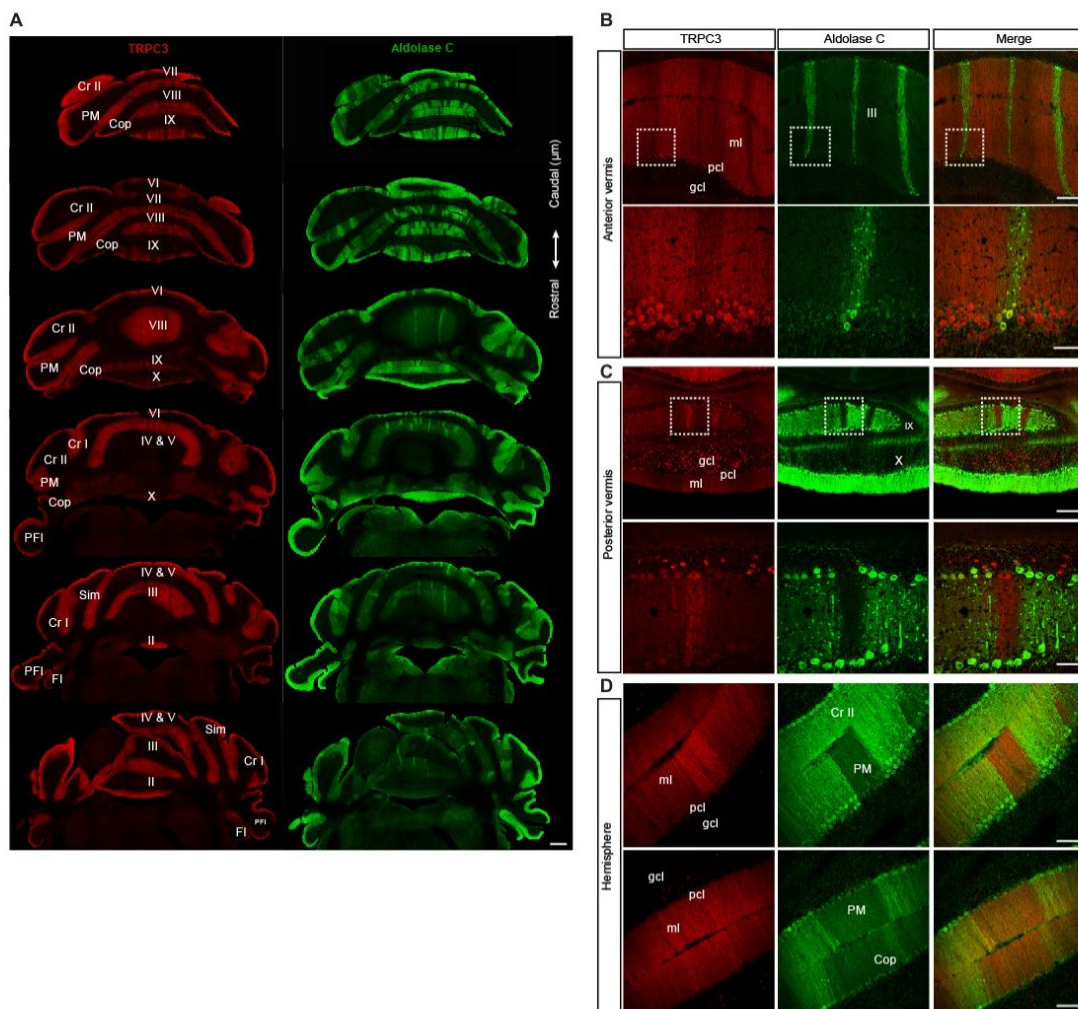


Figure S1

Figure S1 | Overview and Local patterns of TRPC3 expression, related to Figure 1
(A) Immunofluorescent images of coronal sections of wild-type mouse cerebellar cortex, from rostral to caudal, stained with anti-TRPC3 (red) and anti-aldolase C (green). TRPC3 is expressed in evident parasagittal bands which are complementary to Aldolase C (left) in the vermis, but more uniform in the hemispheres. **(B-D)** Immunofluorescent images of coronal sections of wild-type cerebellum, illustrating the distribution of TRPC3 in the anterior vermis **(B)**, posterior vermis **(C)** and hemispheres **(D)**. Demarcated areas in top row of **B** and **C** are magnified underneath. Note that TRPC3 immunoreactivity is moderately higher in the Z- PCs than that in the Z+ PCs in the vermis. In the hemispheres the TRPC3-labeled bands are less well defined and can either be complementary to **(D, top)** or indistinguishable from **(D, bottom)** zebrin bands. Cr II, Crus II; PM, paramedian lobule; Cop, copula of the pyramis; Sim, simple lobule; PFI, paraflocculus; FL, flocculus; ml, molecular layer; gcl, granule cell layer; pcl, purkinje cell layer; Scale bar: 500 µm in **(A)**; 50 µm in **(B, C)**; 100 µm in **(D)**.

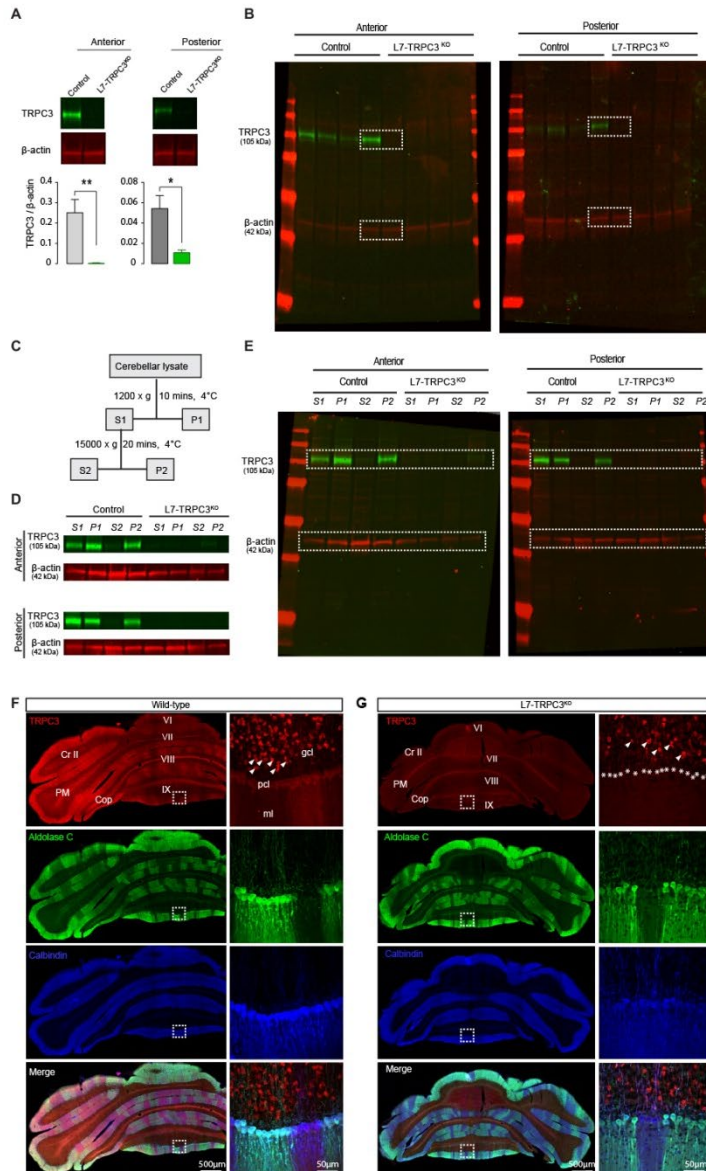


Figure S2

Figure S2 | Western blot and immunostaining of L7-TRPC3^{KO} mice, related to Figure 1

(A) Representative western blots (top) and quantification (bottom) show significantly reduced TRPC3 levels in both anterior (left) and posterior (right) cerebellum in L7-TRPC3^{KO} mice. Note the residual TRPC3 present in the posterior cerebellum, presumably due to the presence of unaffected TRPC3-expressing UBCs, which are virtually absent in the anterior cerebellum. (B) Images of full-length western blots presented in (A). (C) Schematic for synaptic protein extraction protocol. (D) Subcellular localizations by western blots in the anterior (top) and posterior (bottom) cerebellum. TRPC3 is abundantly present in the membrane (P1) and synaptosomes (P2), but less so in the cytosol (S2). L7-TRPC3^{KO} mice were devoid of TRPC3 completely in both anterior and posterior cerebellar fractionations. (E) Images of full-length western blots presented in (D). (F-G) Coronal immunofluorescence images of stainings for TRPC3 (red) and Aldolase C (green) in the posterior cerebellar cortex of L7-TRPC3^{KO} mutants (G) and normal mice (F) with a higher magnifications of the squared areas (right). In contrast to the TRPC3 staining in control mice there is no longer a banding pattern visible for TRPC3 in mutant mice, while aldolase C is still clearly present in bands. The presence of TRPC3 staining in the UBCs, see e.g. the example indicated by the arrowhead, confirms that the antibody worked and that the loss of TRPC3 is specific for PCs (marked by asterisks).

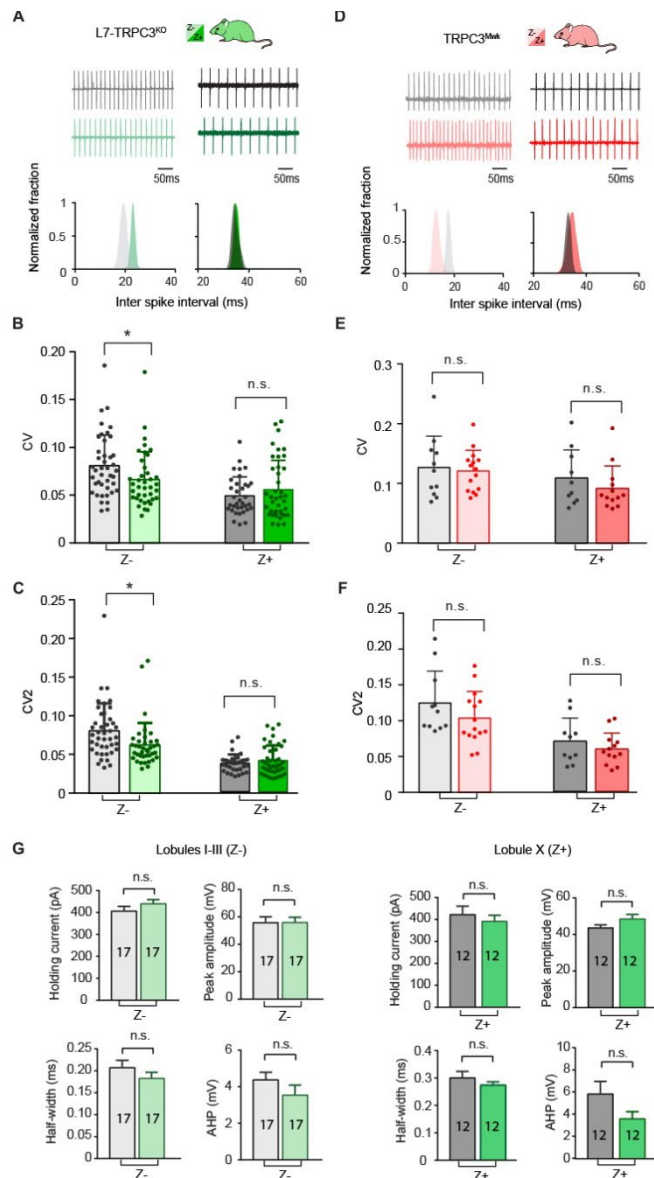


Figure S3 | PC firing activity in TRPC3 mutants in vitro, related to Figure 2

(A) Representative traces of PCs (top) and the corresponding inter spike interval (ISI) distributions of Z⁻ (left) and Z⁺ (right) PCs of L7-TRPC3^{KO} mice. **(B-C)**, The coefficient of variation (CV), measure for regularity of the entire trace, and CV2, measure of regularity on short time-scales, of ISIs were both significantly reduced in Z⁻ PCs of L7-TRPC3^{KO} mice (light-green, n=40 cells/N=6 mutants vs. n=43/N=5 controls; CV: $t_{81}=2.19$, $P=0.031$; CV2: $t_{81}=2.61$, $P=0.011$), but unaltered in Z⁺ PCs (dark-green, n=36/N=10 vs. n=35/N=4, CV: $t_{71}=-1.13$, $P=0.263$; CV2: $t_{67}=-0.977$, $P=0.332$), compared with littermate controls. **(D)** Similar to **(A)** but for TRPC3^{MwK} mice. **(E-F)** PCs of TRPC3^{MwK} mice showed no significant differences in CV and CV2, either in Z⁻ PCs (light-red, n=15/N=4 mutants vs. n=11/N=2 controls; CV: $t_{24}=0.34$, $P=0.735$; CV2: $t_{24}=1.32$, $P=0.199$), or in Z⁺ PCs (dark-red, n=13/N=4 vs. n=10/N=2 controls; CV: $t_{21}=0.985$, $P=0.336$; CV2: $t_{21}=0.960$, $P=0.348$), compared with littermate controls. **(G)** Whole-cell patch clamp recordings of PCs of L7-TRPC3^{KO} mice, revealed no significant differences in holding current or parameters of first action potential evoked by

current injection, including peak-amplitude, half-width and AHP, between mutants and controls. Error bars denote s.d. (**B-F**) or s.e.m. (**G**). Lighter colors represent Z⁻ and darker colors represent Z⁺ PCs, respectively. See **Table S2** for values and statistics.

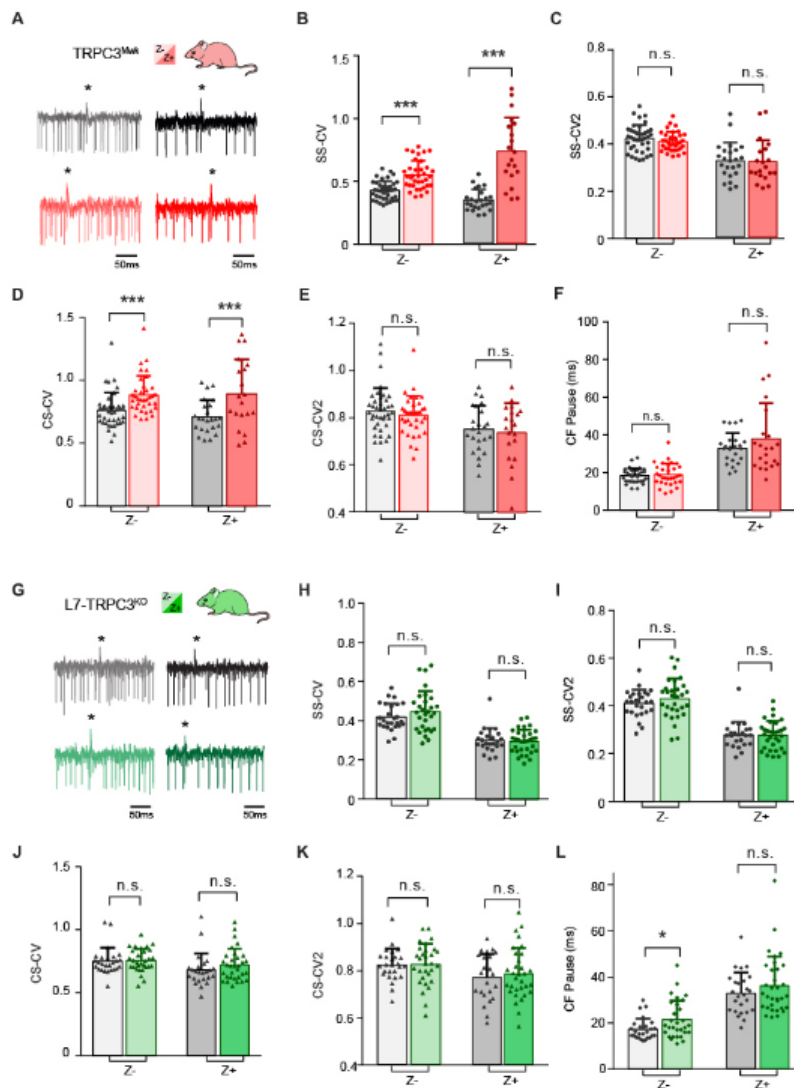


Figure S4

Figure S4 | In vivo extracellular recordings of PC activity in L7-TRPC3^{KO} and TRPC3^{Mwk} mice, related to Figure 3 and 5

(A and G) Representative PC recording traces of TRPC3^{Mwk} and L7-TRPC3^{KO} mice, respectively. Asterisks indicate complex spikes, lighter colors represent Z⁻ and darker colors represent Z⁺ PCs, respectively. (B-F) CV, a measure for regularity of the entire trace, for simple spikes (SS-CV) as well as for complex spikes (CS-CV) of PCs recorded in TRPC3^{Mwk} mice, were significantly increased in both Z⁻ and Z⁺ PCs. In Z⁻ PCs this can exclusively be attributed to TRPC3 gain-of-function, while in Z⁺ PCs the loss of the regular input from UBCs (predominantly present in Z⁺ areas) potentially contributes to the phenotype. CV2, a measure for regularity on short time-scales, for simple spikes (SS-CV2), as well as for complex spikes (CS-CV2) of PCs recorded, and CF-pause in both Z⁻ and Z⁺ PCs of TRPC3^{Mwk} mice were unaffected, compared with those of littermate controls. (H-L), In L7-TRPC3^{KO} mice, SS-CV, SS-CV2, CS-CV, CS-CV2 in both Z⁻ and Z⁺ PCs do not differ from littermate controls. However, CF-pause was significant longer Z⁻ PC (L, left), but unaffected in Z⁺ PCs. Error bars denote s.d.. See Table S2 for values and statistics.

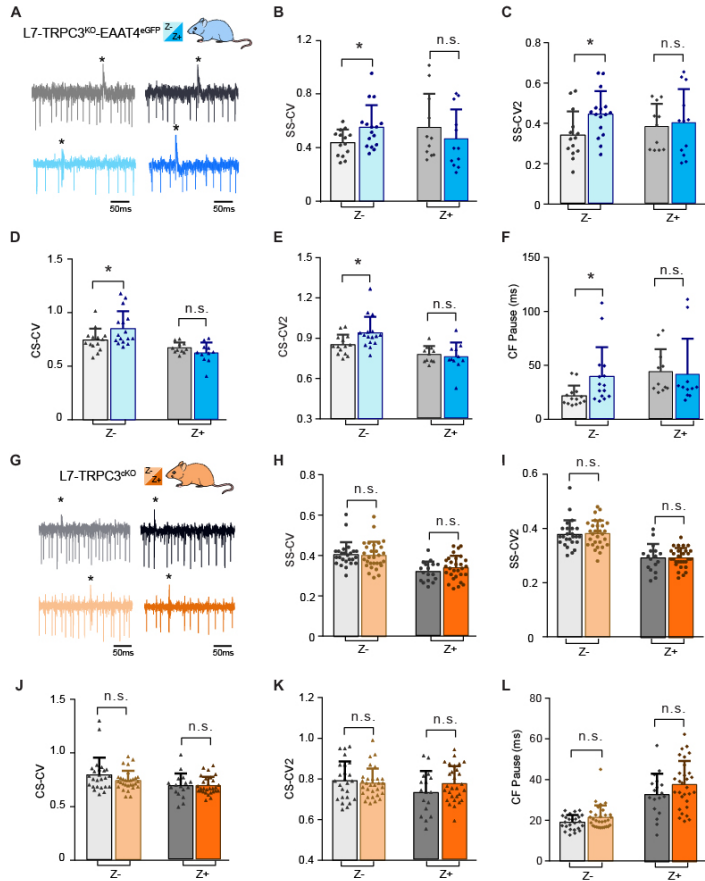


Figure S5

Figure S5 | In vivo extracellular recordings of PC activity in $L7-TRPC3^{KO}-EAAT4^{eGFP}$ and $L7-TRPC3^{cKO}$ mice, related to Figure 4 and 5

(A and G) Representative PC recording traces of $L7-TRPC3^{KO}-EAAT4^{eGFP}$ and $L7-TRPC3^{cKO}$ respectively. Asterisks indicate complex spikes, lighter colors represent Z- and darker colors represent Z+ PCs, respectively. (B-F) In $L7-TRPC3^{KO}-EAAT4^{eGFP}$ mice, all parameters for Z- PCs, including SS-CV, SS-CV2, CS-CV, CS-CV2 and CF-pause, were significantly increased compared to those of littermate controls. However, there was no change in those features of the Z+ PCs. (H-L), PCs in $L7-TRPC3^{cKO}$ mice showed, after tamoxifen-induced TRPC3 ablation, no significant differences in SS-CV, SS-CV2, CS-CV, CS-CV2 and CF-pause in Z- or Z+ PCs, as compared with those of littermate controls that were also injected with tamoxifen. Error bars denote s.d.. See **Table S2** for values and statistics.

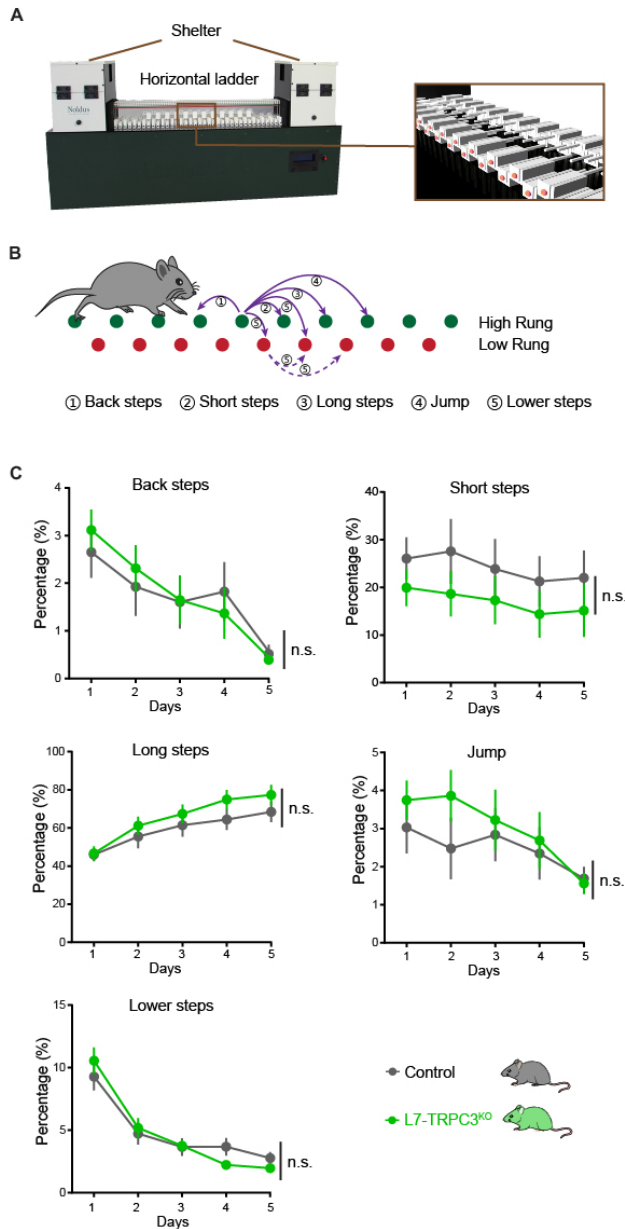


Figure S6 | L7-TRPC3^{KO} mice show normal Erasmus ladder performance, related to Figure 6 and 7

Motor coordination measured by Erasmus Ladder did not differ between L7-TRPC3^{KO} mice (N=16) and their wildtype littermates (N=16). (A) The setup of Erasmus Ladder which consists of a horizontal ladder (magnifications on the right) connecting two shelter boxes. (B) Schematic of high rungs (green) and low rungs (red) with purple arrows illustrating the five different step types: ① Back steps, ② Short steps, ③ Long steps, ④ Jumps, ⑤ Lower steps (see methods). (C) The distribution of step types in L7-TRPC3^{KO} mice did not differ from their littermate controls over the five days tested. Values are shown as mean±s.e.m., see Table S3 for values and statistics.

Figure S6

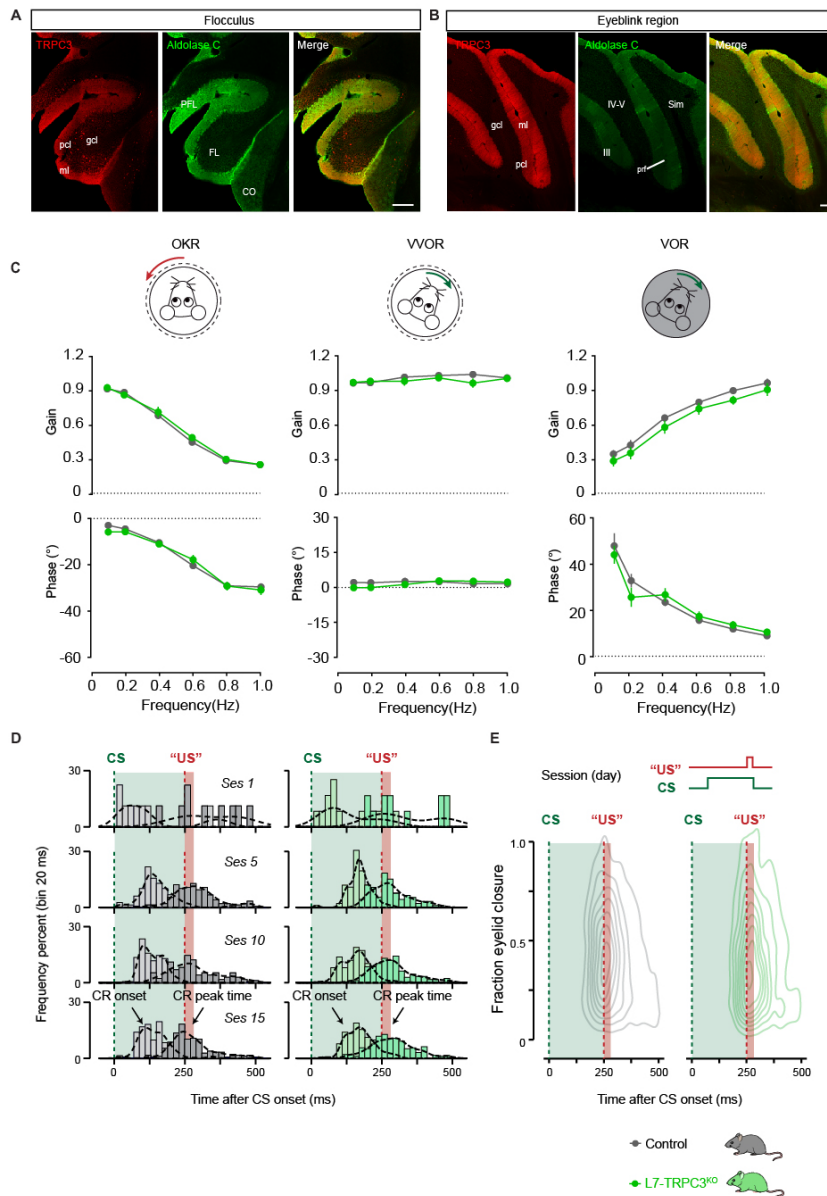


Figure S7

Figure S7 | Immunoreactivity and motor performance in flocculus-dependent compensatory eye movements and eyeblink conditioning in L7-TRPC3^{KO} mice, related to Figure 6 and 7

(A) Compensatory eye movements and their adaptation are under control of the flocculus of the cerebellum. Zebrin-staining is more positive in the flocculus (middle), while being less intense for TRPC3 (left). Note that TRPC3 staining is not absent in the flocculus and that UBCs in the granule cell layer of the flocculus also stain positive for TRPC3. (B) The region of eyeblink conditioning, locating at the sulcus between lobule IV-V and VI, is largely Z- (middle), and stained positive for TRPC3 (left). ml, molecular layer; gcl, granule cell layer; pcl, purkinje cell layer; prf, primary fissure; Sim, simple lobule; PFL, paraflocculus; FL, flocculus; CO, cochlear nucleus. Scale bars: 200 μ m. (C) Gain (top) and phase (bottom) of baseline performance of compensatory eye movements: the optokinetic reflex (OKR), the vestibulo-ocular reflex (VOR) and the visually-enhanced VOR (VVOR) were not affected in L7-TRPC3^{KO} mice, compared to littermate controls (N=13 versus N=11, all $P > 0.05$). (D) Peri-stimulus histogram plots with a Gaussian kernel density estimate (black dashed line) showing the distribution of CR onset (dark filled bars) and CR peak time (light filled bars)

relative to CS and US onset in CS only trials for session 1, 5, 10, and 15. In both groups, there is a clear development in CR onset and peak time: there are no clearly preferred times in the CS-US interval at the start of training (session 1), but during training CR onset values are centered around 100-125 ms after CS onset, and CR peak times are located around the onset of the expected US. Green dashed line is CS onset, red dashed line is US onset; light green and light red fill indicate CS and US duration, respectively. (E) Two-dimensional density plot showing latency to CR peak relative to the fraction eyelid closure over all sessions. Both groups clearly show CRs that are timed around the onset of US. Values are shown as mean \pm s.e.m., see **Table S3** for values and statistics.

Movie S1, related to Figure 1

Light sheet imaging reconstruction of whole-mount immunolabeling for TRPC3 (white signal), cleared with iDISCO protocol and scanned in the horizontal plane of an adult mouse brain from dorsal to ventral (see Methods).

CHAPTER

4

The basal interstitial nucleus (BIN) of the cerebellum provides diffuse ascending inhibitory input to the floccular granule cell layer

Dick Jaarsma^{1*}, Francois Blot¹, Bin Wu¹, Subramanian Venkatesan¹, Jan Voogd¹, Dies Meijer², Tom J.H. Ruigrok¹, Zhenyu Gao¹, Martijn Schonewille¹, and Chris I. De Zeeuw^{1,3}

1. Dept. of Neuroscience, Erasmus MC, Wytemaweg 80, 3015 CN, Rotterdam, The Netherlands

2. Centre of neuroregeneration, University of Edinburgh, Edinburgh, UK

3. Netherlands Institute for Neuroscience, Royal Netherlands Academy of Arts & Sciences, Meibergdreef 47, 1105 BA, Amsterdam, The Netherlands

Published on Journal of Comparative neurology (2018)

Abstract

The basal interstitial nucleus (BIN) in the white matter of the vestibulocerebellum has been defined more than three decades ago, but has since been largely ignored. It is still unclear which neurotransmitters are being used by BIN neurons, how these neurons are connected to the rest of the brain and what their activity patterns look like. Here, we studied BIN neurons in a range of mammals, including macaque, human, rat, mouse, rabbit and ferret, using tracing, immunohistological and electrophysiological approaches. We show that BIN neurons are GABAergic and glycinergic, that in primates they also express the marker for cholinergic neurons choline acetyl transferase (ChAT), that they project with beaded fibers to the glomeruli in the granular layer of the ipsilateral floccular complex, and that they are driven by excitation from the ipsilateral and contralateral medio-dorsal medullary gigantocellular reticular formation. Systematic analysis of co-distribution of the inhibitory synapse marker VIAAT, labeled BIN axons and Golgi cell marker mGluR2 indicate that BIN axon terminals complement Golgi cell axon terminals in glomeruli, accounting for a considerable proportion (> 20%) of the inhibitory terminals in the granule cell layer of the floccular complex. Together, these data show that BIN neurons represent a novel and relevant inhibitory input to the part of the vestibulocerebellum that controls compensatory and smooth pursuit eye movements.

Keywords: vestibulocerebellum, flocculus, GABA, Choline Acetyltransferase, Necab1, Golgi cells, gigantocellular reticular formation, human, macaque

1. INTRODUCTION

The cerebellar cortex is well known for its relatively simple stereotyped trilaminar histo-architecture and sagittally organized modules^{1,2}, and represents a powerful model system for investigating the organization and computations of complex central nervous system circuitries³⁻⁵. The cerebellar cortex receives two main types of excitatory afferent systems, the climbing fiber system and the mossy-parallel fiber system, that converge on a single output neuron, the Purkinje cell that in turn provides inhibitory control of the cerebellar and vestibular nuclei. Climbing fibers arise from the inferior olive and innervate about 8-15 Purkinje cells each, providing an exceptionally strong direct synaptic connection with well over ~1,000 release sites distributed over a large portion of the dendritic tree⁵⁻⁷. Mossy fibers originate from various sources in the brainstem and spinal cord and modulate Purkinje cell activity indirectly via the granule cells and inhibitory interneurons⁸. With about 100-200 rosettes per mossy fiber, each innervating about 10-20 granule cells that in turn may form synaptic terminals with more than 500 Purkinje cells, the mossy fibers represent a highly divergent system^{5,9-11}. One of the key questions regarding the cerebello-cortical circuitry is how mossy fiber activity is translated into granule cell activity and subsequently integrated into Purkinje cell activity¹²⁻¹⁴.

Mossy fibers are morphologically heterogeneous, encode diverse modalities and may evoke greatly distinct patterns of excitatory responses in granule cells across different parts of the cerebellar cortex¹⁵⁻¹⁸. Therefore, it is feasible that also the down-stream cerebellar cortical circuitries display modality and task-depending variabilities^{12,15,19}. For example, the activity patterns and learning mechanisms of different cerebellar modules may be dominated by Purkinje cells with different intrinsic electrophysiological and biochemical properties^{2,20,21}. In addition, the flocculus and nodulus of the vestibulocerebellum, which are involved in compensatory eye and body movements²²⁻²⁵ show a marked enrichment of unipolar brush cells (UBCs), an excitatory granular layer interneuron, which can prolong the excitatory drive of the mossy fiber system^{5,26-28}. Furthermore, there is evidence for heterogeneity of inhibitory granule cell layer interneurons across distinct lobules²⁹⁻³².

In the present study, we show that the granule cell layer of the flocculus receives an inhibitory input from a hitherto largely neglected population of neurons, the basal interstitial nucleus (BIN), which was originally identified by Langer in macaque^{33,34}. We found that BIN cells in human, rodents, ferret and rabbit are, just like in macaque, mainly located in the white matter of the lateral vestibulocerebellum, and that they are GABAergic and glycinergic. In addition, we show in rodents that BIN neurons receive a relevant and unique excitatory input from the medio-rostral medullary reticular formation. Our data indicate that the BIN represents a novel inhibitory afferent system, which may play an essential role in the proper conversion of mossy fiber activity into Purkinje cell firing in the flocculus.

2. MATERIALS AND METHODS

2.1 Animals

Mutant mouse models, primary antibodies and other key resources are summarized in Table 1. All animal experiments were performed in accordance with the guidelines the Dutch national and European legislation and were approved by the animal welfare committee for animal experiments of the Erasmus Medical Center. Male and female C57BL/6 mice, aged 2- 6 months of age, were obtained from the ErasmusMC animal core facility. BALB/c mice were from Charles River. GlyT2GFP transgenic mice (Table 1) that express enhanced green fluorescent protein under the control of the glycine transporter type 2 promoter were kindly provided by Dr. Fritschy³⁵ and maintained as hemizygotes in C57BL/6 background in the ErasmusMC animal core facility. VGluT2-ires-Cre knock-in mice, generated by Dr. Lowell³⁶, were obtained from Jackson Laboratories (JAX#016963, Table 1), and maintained as homozygotes in the Erasmus MC animal core facility. Young (3-4 weeks) and adult (3-6 months) male Wistar rats were obtained from Charles River. Animals were group housed until surgery, fed ad libitum, and kept at 12:12 light/dark cycle.

Cerebella from adult pigmented Dutch belted rabbits (n = 2), ferret (n = 2), and macaque monkey (n = 4) were derived from animals used in other studies³⁷⁻⁴⁰.

2.2 Human tissue

Human cerebella were obtained via the Dutch National body donation program. Donors gave their informed and written consent to the donation of their bodies to the Erasmus MC for research and education purposes. In this study we used cerebellar tissue from two male donors who died at 74 and

78 years of age. Cerebellar specimens were dissected within 48 h following death and fixed in formalin for 6-8 weeks.

2.3 Stereotaxic injections

For stereotaxic injections of Cholera toxin B-subunit (CTB) in rat flocculus, animals ($n = 2$) were anesthetized with an intraperitoneal injection of thiazinehydrochloride (3 mg/kg) and ketamine (100 mg/kg), placed in a stereotactic frame, and their caudal vermis was exposed by removing overlying skin and neck muscles and opening of the atlanto-occipital membrane and dura. Carprofen (Rimadyl Cattle i.p. 5 mg/kg) and lidocaine (s.c. 0,4 mg/ml) were used to reduce perisurgical pain. The flocculus was approached by a glass micropipette (tip diameter 10 - 20 μm), placed horizontally at an angle of 50 degrees with the rostrocaudal axis, and penetrating the cerebellum 6.5 mm starting from the midline at the border of lobule IX-B and -C⁴¹. 100 nl CTB (1% w/v in phosphate buffered saline, pH 7.2, 0.1 M) was injected with mechanical pressure at a speed of 10 nl/min. After injection, the pipette was left in place for >10 minutes before being slowly withdrawn. After a survival period of 5 to 7 days, rats were deeply anesthetized with an overdose of Nembutal (200 mg/kg) and transcardially perfused with an initial flush of 500 ml 0.9% saline, followed by 1 liter of 4% paraformaldehyde (PFA) in 0.12 M phosphate buffer (PB, pH 7.4).

Methods for stereotaxic injections in mice were largely as previously reported^{18,24,42}. During surgery mice were anesthetized with a mixture of isoflurane/oxygen (5% for induction, 1.5-2.0% for maintenance), while carprofen (Rimadyl Cattle i.p. 5 mg/kg), buprenorphine (Temgesic, i.p. 0.05 mg/kg), lidocaine (s.c. 0,4 mg/ml) and bupivacaine (s.c. 0,1 mg/ml) were applied to reduce perisurgical pain. Ophthalmic ointment was applied to the eyes to prevent corneal drying and damage. Body temperature was monitored and kept constant at 37°C throughout the entire surgical procedure. Mice were positioned on a custom-made mouse stereotaxic head-holding frame following the Paxinos mouse brain atlas⁴³, small craniotomies (diameter ~3 mm) were made in corresponding sites, and injections were performed using glass pipettes (tip opening 8 - 15 μm) with mechanical pressure or iontophoresis. After each injection, the pipette was left in place for >10 minutes before being slowly withdrawn. For retrograde tracing, 40-100 nl of CTB (1% w/v in phosphate buffered saline, pH 7.2) was injected with mechanical pressure (speed 10 nl/min). For anterograde tracing biotinylated dextran amine 10 kDa (BDA, 10% w/v in saline, ThermoFisher) was applied with mechanical pressure (20-100 nl) or iontophoresis (pulses of 4 μA , 10 min). Alternatively, anterograde tracing was performed using AAV viral vector expressing enhanced GFP^{44,45}: 50-100 nl purified AAV1.CAG.CI.eGFP.WPRE.rBG (AAV-GFP, 10^{12} - 10^{13} GC/ml) or AAV1.CAG.Flex.eGFP.WPRE.bGH (AAV-Flex-GFP), purchased from UPenn Vector Core (Table 1, <https://pennvectorcore.med.upenn.edu/gtp/default.php>), were pressure injected. To examine BIN axons in the flocculus, AAV-GFP was injected in C57BL/6 mice ($n=10$) using the following coordinates: 1.4 posterior of Lambda, 2.4 mm lateral and 2.6 mm ventral of the pial surface. The same coordinates were used for CTB injections in the BIN of C57BL/6 mice ($n=4$) to characterize brain stem neurons that innervate BIN neurons. This retrograde approach was complemented by an anterograde tracing approach with BDA injections made throughout the medulla oblongata and the pontine reticular formation of C57BL/6 mice ($n=20$). Coordinates of BDA injections in the medullary gigantocellular reticular nucleus that resulted in labeling of fibers innervating BIN neurons were 2,3-2,6 mm posterior of lambda, 0,2-0,4 mm lateral, 4,6 - 4,8 ventral of the pial surface. These coordinates were also used for AAV-Flex-GFP injections in VGluT2-Cre mice ($n=2$) to demonstrate that medullary gigantocellular reticular nucleus projections to BIN neurons were VGluT2+ neurons. For a subset of BDA injections ($n = 15$ mice) the squamosal part of the occipital bone was freed and the atlanto-occipital membrane and dura were opened, to approach the medulla oblongata from caudal with the pipette positioned at an angle of 45° in the rostro-caudal direction. For injection in the inferior olive, penetrations were made with reference to the obex and guided by electrophysiological recording, and injections were made using iontophoresis⁴⁶. Also injection in the medial vestibular prepositus hypoglossal nuclei were guided by electrophysiological recordings. CTB injections in the floccular cortex were performed in alert, head-fixed restrained GlyT2GFP ($n=3$) and C57BL/6 ($n=2$) mice placed on a platform in the center of a random dotted drum to enable identification of floccular zones on the basis of complex spike modulation of Purkinje cells triggered by optokinetic stimulation²⁴. In these mice, a head fixation pedestal was fixed to the skull with dental cement (Charisma, Heraeus Kulzer, NY, USA) 5 days prior to injection, and a recording chamber was made following craniotomy of the occipital bone²⁴.

Post-injection survival times for injected mice were 5-8 days (CTB, BDA) or 2-3 weeks (AAV). Mice were deeply anesthetized with an overdose of Nembutal (i.p. 200 mg/kg), transcardially perfused

with 20 ml saline followed by 100 ml 4% PFA in 0.12 M PB, and brains were removed, post-fixed for 2 h in 4% PFA, and embedded in 12% gelatin further processed for histology.

2.4 Antibody characterization

Primary antibodies used for immunohistology were from commercial sources with the exception of a rat monoclonal antibody against Lgi2 (see Table 1 for Immunogen, source, catalogue number, RRID number, and final antibody concentration of each primary antibody). The commercial primary antibodies have been well characterized in previous studies^{18,30,39,47-49}. Validation of labeling specificity in this study is based on the expected distribution pattern compared to these studies. The rat-anti Lgi2 antibody (clone Lgi2-10D6) was raised against a full length Lgi2-Fc fusion protein. Immunization of rats with antigen, and production of hybridoma cell lines was performed by Absea (<http://www.absea-antibody.com>). The labelling specificity for Lgi2 was determined using cerebellar sections from Lgi2 knockout mice, which did not show any labelling. Furthermore, the labelling pattern in the cerebellar cortex is consistent with the expected distribution based on mRNA expression in Allan Brain Atlas⁵⁰. Further details of the production and validation of the rat-anti Lgi2 antibody will be reported elsewhere.

2.5 Immunohistology

The following material was processed for immunohistology: brains from mouse and rat who received tracer injections; brains from additional transcardially 4% PFA perfused mice (n= 12; C57BL/6 or BALB/c), rats (n =4), rabbits (n=2) and macaque (n= 4), immersion (6-8 weeks) formalin-fixed brains from ferret (n=2), and formalin-fixed blocks from humans containing the flocculus, tonsils and deep nuclei. Brain samples were embedded in 11% gelatin (type B, JT Baker 2124, Fisher Scientific, CAS number: 9000-70-8), incubated overnight in 30% sucrose at 4 °C, and cut into 40 or 50 µm coronal sections on a sliding freezing microtome (Leica SM 2000R). Sections were serially collected in 8 (mouse, rat), 20 (ferret, rabbit, macaque) or 40 (human) vials with phosphate buffered saline (PBS, pH 7.2) such that each vial contained a complete series of sections. Sections were processed free-floating for diaminobenzidine (DAB, 0.05%)-immunoperoxidase histochemistry or immunofluorescence⁵¹. Following preincubation in PBS containing 0.4% Triton X-100 (PBST) and normal horse serum (NHS) and for 1 h at room temperature, sections were incubated 48-60 h at 4°C with the primary antibodies in PBST with 2% NHS. For immunoperoxidase histochemistry, sections were subsequently incubated with biotinylated secondary antibodies raised in donkey (diluted 1:400; Jackson, Burlingame, CA) for 2 h at room temperature, followed by incubation in avidin-biotin-immunoperoxidase complex (ABC; diluted 1:400; Vector Laboratories) and the reaction with DAB as described by the manufacturer. To visualize BDA in anterograde tracing experiments, sections following the preincubation step, were incubated with ABC and processed for DAB staining. Sections were mounted on glass-slides, air-dried, and counterstained with Thionin (1%) to outline cell nuclei and Nissl substance in neurons. Immunoperoxidase-stained sections were analyzed using a Leica (Nussloch, Germany) DM-RB microscope, or scanned with a Hamamatsu NanoZoomer 2 whole slide imager and analyzed with NDP.view (Hamamatsu) software. Immunoperoxidase histochemistry was performed with series of sections of BDA and CTB tracing experiments to examine injection area and map projection fibers and retrogradely labeled neurons, respectively. In addition, immunoperoxidase histochemistry was used for mapping BIN neurons using the following antibodies: goat anti-ChAT (1:500; Millipore AB144P, RRID:AB_11214092), rabbit anti-Glutamic acid decarboxylase 65 and 67 (GAD; 1:2000; Millipore AB1511, RRID:AB_90715), mouse anti-GAD67 (1:1000; Millipore MAB5406), rabbit anti-Necab1 (1:1000; Sigma, HPA023629; RRID:AB_1848014), or mouse anti-NeuN (1:2000; Millipore, MAB377; RRID:AB2298772).

For immunofluorescence, sections were incubated with multiple combinations of primary antibodies (see table 1), followed by incubation with fluorescently-labeled secondary antibodies raised in donkey, diluted 1:400 in PBST-2%NHS, and carrying Alexa Fluor 405 (A405), A488, Cy3-, or A647 as fluorophores (Jackson Immunoresearch or ThermoFisher). Typically, in triple labelling experiments A488, Cy3 and A647-labeled secondary antibodies were used, and section were counterstained with Dapi to visualize cell nuclei, while in quadruple labelling experiments A405-labeled secondary antibody was used, and Dapi was omitted. In sections from BDA tracing experiments, BDA was labeled with A488 streptavidin (ThermoFisher). Sections stained for immunofluorescence were mounted on coverslips, placed on glass slides with Vectashield mounting medium, and were examined with Zeiss LSM 510 and LSM700 confocal laser scanning microscopes.

2.6 Immuno-electron microscopy

Two mice receiving an AAV-GFP injection in the BIN were perfused with 100 ml 0.12 M PB buffered 4% PFA with 0.5% glutaraldehyde, and further processed for anti-GFP immuno-peroxidase DAB electron microscopy: the cerebellum was removed, post-fixed overnight in 4% PFA, and cut in 60 μm coronal sections on a vibratome. Sections were subjected to a freeze-thaw procedure to improve antibody penetration and incubated for 96 h at 4°C with rabbit-anti-GFP antibody (1:5000, Abcam) in Tris-buffered saline (TBS, pH7.4), followed by incubation with biotinylated-goat-anti-rabbit secondary antibody (1:200 in TBS, overnight at 4°C), and incubation with ABC (1:400 in TBS overnight at 4°C), and subsequent reaction with DAB. Subsequently, sections were rinsed and post-fixed in 1% osmium tetroxide, stained with 1% uranyl acetate, dehydrated and embedded in araldite (Durcupan ACM; Fluka, Buchs, Switzerland). Semi-thin (500 nm) and ultrathin (50-70 nm) sections were cut on an ultramicrotome (Leica, Wetzlar, Germany). Semi-thin were mounted on glass slides and stained with toluidine blue and analyzed light-microscopically. Ultrathin sections were mounted on formvar-coated grids, contrasted with 2% uranyl acetate and 1% lead citrate (Fluka), and examined using a Phillips CM100 electron microscope at 80 kV (Philips, Eindhoven, Netherlands). A subset of grids were processed for GABA immunogold labelling. The grids were rinsed in TBS with 0.1% Triton X-100, pH 7.6 (TBST), and incubated overnight at 4°C with rabbit anti-GABA (Sigma, 1:1500 in TBST) antibody. The grids were subsequently rinsed twice with TBST and incubated for 1 h at room temperature in goat anti-rabbit IgG labeled with 10 nm gold particles (Aurion) diluted 1:50 in TBST.

2.7 Slice recording

3-4 weeks old Wistar rats were decapitated under isoflurane anesthesia. 300 μm thick cerebellar coronal slices containing the flocculus were cut on a vibratome (VT1200s, Leica, Wetzlar, Germany) in icecold slicing medium containing (in mM): 240 Sucrose, 5 KCl, 1.25 Na₂HPO₄, 2 MgSO₄, 1 CaCl₂, 26 NaHCO₃ and 10 D-Glucose, bubbled with 95% O₂ and 5% CO₂. Slices were incubated at 34°C for 1 h in the oxygenated ACSF containing (in mM): 124 NaCl, 2.5 KCl, 1.25 Na₂HPO₄, 1 MgSO₄, 2 CaCl₂, 26 NaHCO₃ and 25 D-Glucose and kept at room temperature (21 \pm 1 °C) before use. Experiments were performed with a constant flow of oxygenated ACSF (1.5-2.0 ml/min) at 34 \pm 1 °C. Putative BIN neurons were identified under DIC visualization based on their distribution in the floccular white matter, and their relative large size compared to other white matter cells. Patch-clamp recordings were performed using an EPC-10 double amplifier controlled by the Patchmaster software (HEKA electronics, Lambrecht, Germany)¹⁸. All recordings were low-pass filtered at 5 kHz and digitized at 20 kHz. Borosilicate glass pipettes (WPI) were filled with intracellular solution containing the following (in mM): 120 K-gluconate, 9 KCl, 10 KOH, 3.48 MgCl₂, 4 NaCl, 10 HEPES, 4 Na₂ATP, 0.4 Na₃GTP and 17.5 sucrose (pH 7.25) and had pipette resistances of 3-5 M Ω . Spontaneous action potential firing of BIN neurons were recorded in loose cell-attached mode prior to attaining the whole-cell configuration. After obtaining stable whole-cell configuration, a series of constant depolarizing current pulses with incremental amplitudes (20 pA/step) was applied to each cell to elicit voltage action potential firing patterns. For voltage clamp recordings of spontaneous EPSCs (sEPSCs), cells were recorded for >3 mins at -65 mV. At the end of the recording, a 5 mV hyperpolarizing voltage step was applied and the cell capacitance were calculated based on the decay of capacitive current.

For morphological characterization of recorded BIN neurons, neurobiotin (1% w/v) was added to the intracellular solution. After recording, slices were fixed in 4% PFA at room temperature for 2 h, washed in PBS overnight, and processed for immunofluorescence with guinea-pig anti VGluT1, mouse anti-mGluR2, and rabbit α -GAD as primary antibodies; A405 donkey anti-guinea-pig IgG, Cy3 donkey anti-mouse, and Cy5 donkey anti-rabbit as secondary antibodies; and A488 streptavidin (1:400, ThermoFisher) to visualize neurobiotin. Slices were carefully mounted in Vectashield and examined with LSM 700 confocal microscopes (Carl Zeiss, Jena, Germany). The slices were scanned at 0.5 x 0.5 x 2 μm (xyz) resolution using a Plan-Apochromat 20x (n.a. 0.8) objective and the tile function. The confocal stacks were used to trace the dendritic and axonal arborization of biocytin filled cells using Neurolucida software (MicroBrightField, Inc., Colchester, VT).

2.8 Analyses

To map and count BIN neurons in different species, series of sections processed for bright-field microscopy were examined and plotted using an Olympus microscope fitted with a Lucivid miniature monitor and Neurolucida software (MicroBrightField, Inc., Colchester, VT), while fluorescently-labeled section selected areas were scanned at a 0.625 x 0.625 x 2.5 μm (xyz) resolution using a LSM 700 confocal microscopes (Carl Zeiss, Jena, Germany) with Plan-Apochromat 20x (n.a. 0.8) objective and the tile function, and analyzed using ImageJ. To plot and count BIN neurons in macaque cerebellum we used 1 in 5 transverse thionin-stained serial sections (section

thickness 40 μm , 160 μm interval between sections), and 1 in 10 GAD- and ChAT-immunoperoxidase stained series (360 μm between sections). Only cells with a visible nucleus were counted. In case of human cerebellum, ChAT-stained serial sections in a final frequency of 1 in 10 (section thickness 50 μm , 450 μm interval between section) were used for counting and plotting BIN neurons. For mapping the distribution of BIN neurons in rat, we used 1 in 4 CTB-immunoperoxidase/thionin stained series of transverse sections (120 μm interval) of previously documented (rat #798, rat #802, rat #836; ⁴¹ CTB experiments, and 1 in 4 CTB/GAD immunofluorescent stained series from 2 additional CTB tracing injections in rat flocculus (rat B1, rat B2). To estimate the relative size of the injection in each section, the ratio of the area of the injection occupying the floccular granule cell layer, and the area of the entire floccular granule cell layer were determined, and the means of these ratios were calculated for each experiment. To count the total number of BIN neurons in rat cerebellum, additional 1 in 4 series stained for thionin, or GAD/NeuN immunofluorescence were used. For mapping and counting BIN neurons in mouse cerebellum, we used 1 in 4 series of transverse fluorescent stained sections (120 μm interval) labeled for CTB/GlyT2GFP (n = 3 mice) or CTB/Necab1 (n = 2 mice). For mapping and counting Golgi cells in the vermis 4-5 and the flocculus we used 1 in 4 series of transverse section from GlyT2GFP mice (n=4) stained for Lgi2/Necab1 or Lgi2/neurogranin.

For mapping and counting BIN neurons in ferret, we used 40 μm GAD-immunoperoxidase stained sections at frequencies of 1 in 5 (160 μm interval). For mapping BIN neurons in rabbit, we used previously documented WGA-HRP experiments with tracer injections in the floccular cortex (K227, K244, K358, K360; ⁵²) and 40 μm GAD-immunoperoxidase stained sections at frequencies of 1 in 10 (360 μm interval between sections).

To analyze anterograde BDA tracing experiments with injections made throughout the brainstem, 1 in 4 sections were processed for ABC peroxidase-DAB staining to map the injection area, and examine the floccular white matter for the presence of BDA+ beaded fibers contacting BIN neurons. In case of the presence of BDA+ beaded fibers, adjacent series of sections were processed for triple labeling fluorescence to outline BDA+ fibers (visualized with A488 streptavidin), VGluT2+ excitatory synaptic boutons, and BIN neurons (with either anti-Muscarinic M2 or anti-Necab1 antibodies). BIN neurons were examined for the presence of BDA+VGluT2+ and BDA-VGluT2+ boutons using a LSM 700 confocal microscope with Plan-Apochromat 40x (n.a. 1.3) and 63x (n.a. 1.4) oil objectives. Only BDA+VGluT2+ and BDA-VGluT2+ boutons contacting BIN cell bodies and their proximal dendrites were analyzed.

To examine the proportion of VIAAT+ axon terminals in macaque flocculus and dorsal paraflocculus that where either ChAT+ or mGluR2+, Z-stacks of 20 x 20 x 10 μm (12 optical sections of 1,5 μm thickness) of glomeruli were collected from ChAT/VIAAT/mGluR2 stained sections using a 63x oil objective. Glomeruli were identified on the basis of a grossly circular arrangement of VIAAT+ boutons (e.g. Fig. 2g,h). A contour was drawn around the glomerular profile and VIAAT+ boutons within the contour were examined for the presence of ChAT and mGluR2 signal. To estimate the proportion of VIAAT+ axon terminals in mouse cerebellar lobules that where mGluR2+, Z-stacks of 100 x 100 x 3 μm (3 optical sections of 1,5 μm thickness) of granule cell layer 2 μm below the surface of the section were collected from GFP/VIAAT/mGluR2 triple labeled sections using the 63x oil objective. Stacks were made in lobule III of the anterior vermis, the nodulus and the flocculus of a mice showing high levels of BIN axonal labelling in the flocculus following AAV-GFP injections in the BIN (VBIN2, VBIN3, VBIN5). VIAAT, GFP and mGluR2 signals were converted to binary images using the 'internodes' thresholding function in imageJ, and the area showing VIAAT labeling, as well as showing either VIAAT-mGluR2 or VIAAT- GFP double-labeling were determined per Z-stack (= means of 3 optical sections).

2.9 Allen mouse brain atlas

We screened the Allen Mouse Brain Atlas (Allen Institute for Brain Science, Seattle, WA; available from www.brain-map.org, ⁵⁰) for genes expressed in the mouse BIN using the AGEA (Anatomic Gene Expression Atlas) viewer modus of Allen Brain Atlas with 10400, 4800, 3000 as the seed voxel coordinates and 1.0 as the expression threshold. This modus enabled efficient visual inspection of nearly 2000 genes for expression in intermediate-large cells in the floccular white matter of the anterior flocculus. The method of screening was not exhaustive and was biased towards genes with relatively low expression in the granule cell layer, facilitating the detection of gene expression in the white matter. Genes with moderate to strong expression throughout the cerebellar white and grey matter, generally representing genes expressed by glia cells, were ignored.

2.10 Statistical analyses

Statistical analyzes were performed with Graphpad Prism using Student's t-test and ANOVA. Data are expressed as Means \pm SE.

3. RESULTS

3.1 ChAT (choline acetyltransferase) immunostaining outlines the basal interstitial nucleus (BIN) in macaque cerebellum

While analyzing the distribution of immunoreactivity of choline acetyltransferase (ChAT, the terminal biosynthetic enzyme for acetylcholine) in macaque cerebellum, we identified a group of ChAT+ cells dispersed in the white matter ventrolateral of the cerebellar nuclei (Fig. 1a). The distribution and morphology of these ChAT+ neurons coincided with that of the basal interstitial nucleus (BIN), identified by Langer after retrograde tracing injections in the flocculus or the ventral paraflocculus^{33,34}. Like BIN neurons, ChAT+ cells had relatively large polymorphic cell bodies (area = $441 \pm 18 \mu\text{m}^2$, 251-720; mean \pm SE, range, n=40 cells), and formed a cluster that extended from the hilus of the ventral paraflocculus to the white matter of the most rostral folium of the nodulus, respectively, with most ChAT+ cells in the white matter medial of the stalk of the flocculus (Fig. 1a,f). While most BIN neurons had a fusiform elongated morphology with dendrites emanating from each end, other BIN neurons showed pyramidal and polygonal morphologies (Fig. 1b). Notably, ChAT+ cells were also observed in Group Y, medial of the BIN, but these cells were much smaller ($104 \pm 5 \mu\text{m}^2$, mean \pm SE, n=10 cells) and clearly distinguishable from ChAT+ BIN cells (Fig. 1c).

In accord with the notion that BIN neurons innervate the flocculus/ventral paraflocculus (also referred to as the floccular complex; see²⁵, ChAT+ fibers in the BIN were oriented towards the white matter of the floccular complex, and a high density of ChAT+ fibers occurred in the white matter and granule cell layer of the floccular complex (Fig. 1a,d). In the granule cell layer, the ChAT+ fibers provided multiple beaded branches resulting in a dense plexus of ChAT+ varicose fibers (Figs 1d). These beaded ChAT+ fibers occurred throughout the floccular complex, but were absent in other cerebellar lobules, including the dorsal paraflocculus (Fig. 1e) and the nodulus. The density of ChAT+ fibers varied across different lobules of the floccular complex: grossly, ChAT+ fibers were more frequent in the flocculus than in the ventral paraflocculus and were denser in the basal than the apical part of individual folia (Fig.1f). Together, the data indicate that BIN neurons in macaque are ChAT+ and provide dense ChAT+ innervation of the granule cell layer in the floccular complex.

3.2 BIN neurons provide GABAergic input to the granule cell layer of the flocculus/ventral paraflocculus

Further characterization of the neurochemical identity of macaque BIN neurons showed that BIN neurons also stained positive with anti-glutamic acid decarboxylase (GAD) antibody. GAD/ChAT double labeling showed that all ChAT+ BIN neurons stained positive for GAD (Fig. 2a, b), while an additional population of neurons inside the macaque BIN territory was negative for ChAT, but stained positive for GAD (Fig. 2a, b). These GAD+ChAT- BIN neurons showed the same size and morphologies as those of GAD+ChAT+ BIN neurons. Thus, the BIN in macaque may comprise 2 neurochemically distinct populations of neurons, GAD+ChAT+ and GAD+ChAT- neurons. Counting of serial ChAT and GAD immunoperoxidase stained sections indicated that there were about 1000 ($1.3 \pm 0.3 *10^3$, mean \pm SE, n= 3) ChAT+ and 2000 ($2.2 \pm 0.2 *10^3$, n= 3) GAD+ BIN cells per half macaque cerebellum.

GAD/ChAT double labelling also showed that the cell bodies and proximal dendrites of BIN neurons were only sparsely covered by GAD+ nerve terminals. In this respect, BIN neurons were distinct from cerebellar nuclear neurons, whose cell bodies and proximal dendrites are densely innervated by GAD+ synaptic terminals from Purkinje cells axons (compare Fig. 2b and e). Analysis of GAD/ChAT double labelling in the floccular complex showed that ChAT+ axons in the granule cell layer were GAD+ (Fig. 2c), supporting the notion that ChAT+ fibers in these lobes are axons from BIN neurons. Moreover, these GAD+ChAT+ labeled axonal projections were morphologically distinct from ChAT+ mossy fibers in the nodulus that were GAD-negative (Fig. 2e). In contrast to previous monkey studies suggesting that ChAT+ fibers in the flocculus represent mossy fibers from the medial vestibular and the prepositus hypoglossal nuclei^{53,54}, we found virtually no ChAT+ fibers in the macaque flocculus that showed the typical mossy fiber morphology.

ChAT+ boutons in the flocculus/ventral paraflocculus did not stain positive for the mGluR2 metabotropic glutamate receptor (Fig. 2f), which is expressed by the majority of cerebellar Golgi cells, and is present on a large proportion of the GABAergic nerve terminals in the glomeruli^{29,30,55}. Notably,

glomeruli with ChAT+ boutons always also contained mGluR2+ boutons (Fig. 2f), indicating that BIN axon terminals complement Golgi cell axonal terminals in the same glomeruli. Triple staining of ChAT and mGluR2 with antibodies against VIAAT (vesicular inhibitory amino acid transporter, also termed vesicular GABA transporter, VGAT) to outline GABAergic/glycinergic inhibitory nerve terminals, showed that ChAT+ boutons, like mGluR2+ boutons, were VIAAT+ (Fig. 2g), further indicating that ChAT+ fibers in the macaque flocculus are GABAergic. In addition to ChAT+mGluR2-VIAAT+ and ChAT-mGluR2+VIAAT+ boutons we also found ChAT-mGluR2-VIAAT+ boutons in the floccular glomeruli (Fig. 2g). Analysis of 50 floccular glomeruli in ChAT/VIAAT/mGluR2 triple-stained sections showed that about two-thirds ($64 \pm 2\%$; mean \pm SE) of the VIAAT+ boutons were ChAT-mGluR2+, while about one-third of the VIAAT+ boutons were mGluR2-, consisting of ChAT+mGluR2- ($21 \pm 1.4\%$) and ChAT-mGluR2- ($15 \pm 1.7\%$) boutons. We also performed triple staining of ChAT and VIAAT with VGluT1 to outline mossy fiber nerve endings (rosettes). This staining indicated that the distribution of ChAT+VIAAT+ boutons in floccular glomeruli resembles that of ChAT-VIAAT+ boutons (Fig. 2h). Together these data indicate that a portion of inhibitory boutons in the macaque floccular glomeruli does not arise from mGluR2+ Golgi cells, and that about half of these mGluR2- boutons represent axon terminals from ChAT+ BIN neurons. For comparison, in the dorsal paraflocculus, which is not innervated by BIN afferents, we found more than 90% ($94 \pm 1\%$) of VIAAT+ boutons in the glomeruli to be mGluR2+.

In ChAT/VIAAT/mGluR2 stained sections we also noted ChAT+VIAAT+ boutons in glomeruli with a dendritic brush of unipolar brush cells (UBCs), which also may stain positive for mGluR2⁵⁶. Double labeling for ChAT and calretinin, which outlines a subset of UBCs²⁷, showed the presence of ChAT+ boutons surrounding calretinin+ UBC brushes (Fig. 2i). However, we also found calretinin+ brushes that were not surrounded by ChAT+ boutons. This was particularly evident in a region of the ventral paraflocculus that shows a dramatic enrichment of UBCs and virtually no ChAT+ fibers (Fig. 2j). These data indicate that ChAT+ boutons do not have a simple all or none relationship with glomeruli containing UBC dendritic brushes.

3.3 ChAT-staining outlines the BIN in human cerebellum

To examine whether a BIN-like population of neurons also occurs in other species, we first examined human cerebellum. Using ChAT staining, we found a population of ChAT+ neurons in the basal white matter, reminiscent of BIN neurons in macaque (Fig. 3a,b). ChAT+ neurons were distributed in an area extending from the nodulus to the peduncles of the flocculus and the accessory paraflocculus (i.e. the human homologue of the macaque ventral paraflocculus,²⁵ ChAT+ neurons being most abundant near the base of the floccular peduncle (Fig. 3a,b). As in macaque, these ChAT+ neurons showed variable morphologies, had moderately large cell bodies (area = $533 \pm 31 \mu\text{m}^2$, 281-770; mean \pm SE, range, n=20 cells), and stained positive for GAD (Fig. 3c,d). These data indicate that also in human cerebellum the BIN can be outlined using ChAT and GAD staining. Based on analysis of 1 out of 10 sections we estimate that about 5000 ($4.6 \pm 0.7 \cdot 10^3$; Mean \pm SE, n= 2) ChAT+ BIN neurons occur on each side of the cerebellum in human. The quality of the GAD staining did not allow counting of GAD+ BIN cells in human series.

As in macaque, ChAT+ fibers emanating from the human BIN were oriented towards the white matter of the flocculus and the accessory paraflocculus, and the flocculus/accessory paraflocculus showed a correspondingly high density of ChAT+ fibers in the white matter as well as a dense network of ChAT+ beaded fibers in the granule cell layer (Fig. 3e,f). However, in contrast to macaque, the human cerebellum also showed a subset of Golgi cells that were ChAT+ (Fig. 3f,g; see also⁵⁷), and, hence, ChAT+ innervation in the human flocculus/accessory paraflocculus may also derive from Golgi cells. The overall density of granular layer ChAT+ innervation in these lobules was higher than in other lobules. A particularly high density of ChAT+ fibers occurred in the areas of the floccular granule cell layer that contained ChAT+ Golgi cells (Fig. 3f), suggesting that in these areas ChAT+ axons are from both BIN neurons and Golgi cells. We were not able to further characterize the identities of ChAT+ boutons in the human floccular complex with reliable mGluR2 and VIAAT immuno-staining, probably due to limited possibilities of fixation and antigen epitope preservation of our human brain specimen.

3.4 Retrograde tracing and GAD-staining outlines the BIN in rat cerebellum

To further examine the occurrence of BIN neurons in other species we moved to rat. No ChAT+ neurons are present in the white matter of rat cerebellum^{47,58}. However, following floccular cortical injections with cholera toxin B subunit (CTB)⁴¹, we identified retrogradely labeled neurons in the hilus and the white matter of the ipsilateral flocculus (Fig. 4a-c). These retrogradely labeled neurons occurred throughout the rostro-caudal extent of the floccular white matter (Fig. 4a), were moderately

large in size, and had multipolar and fusiform morphologies (Fig. 4b,c) reminiscent of macaque BIN neurons. Furthermore, these retrogradely labeled white matter neurons were all GAD+ (Fig. 4d). Based on their localization in the white matter and their similarities with macaque BIN neurons, we designate these neurons the rat homologues of macaque BIN neurons⁴¹. Notably, no retrogradely labeled BIN neurons occurred in an animal where the injection was centered in the ventral paraflocculus (e.g. case 902 in⁴¹).

The rat BIN neurons could also be identified in thionin and NeuN stained sections, based on their size and localization in the white matter (Fig. 4c,e). Based on CTB tracing, GAD/NeuN staining and morphological criteria we propose that the BIN area in rat is rostro-medially delimited by the medial and inferior cerebellar peduncles, and more caudo-medially by the lateral cerebellar nuclei and group Y (Fig. 4a). Ventro-medially some BIN neurons may populate the cochlear nuclear superficial granule cell layer that borders the floccular white matter (Fig. 4a,b). Based on counting of GAD/NeuN and thionin stained serial sections, we estimate that in rat there are about 600-700 ($0.66 \pm 0.06 \times 10^3$; Mean \pm SE, n= 3) BIN neurons per side. We also estimated the number of retrogradely labeled BIN neurons in three animals following CTB injections in the floccular cortex (rat #798, rat #802 and rat #836;⁴¹). Importantly, although injection areas covered less than 20% ($15 \pm 2\%$, mean \pm SE) of the floccular granule cell layer, more than 70% ($78 \pm 5\%$) of BIN neurons were retrogradely labeled. These data suggest that projections from multiple BIN neurons converge on the same portion of the granule cell layer.

3.5 Electrophysiological characterization of rat BIN neurons in acute slices

To electrophysiologically characterize the BIN cells, we performed whole cell recording in acute transverse slices of rat cerebellar cortex. After recordings, cells were filled with neurobiotin for morphological analysis (Fig. 5a,b). Consistent with immunohistological data neurobiotin-filled BIN neurons showed fusiform or polygonal cell bodies with long dendrites that extend in the white matter from opposite poles of the cell. In 3 of 7 cells dendritic branches also extended into the granule cell layer to reach the Purkinje cell layer (Fig. 5a,b). The axon extended from the cell body or a proximal dendrite and produced multiple branches, many of which left the slice. In 2 of 7 cells we could trace several axonal branches innervating a substantial portion of the granule cell layer within the slice (Fig. 5a,b). The axonal branches produced a network of fine beaded fibers with multiple ramifications (Fig. 5b-d). Co-staining for mGluR2 and VGluT1 confirmed that the neurobiotin-labeled axons do not stain for mGluR2, but co-distribute with mGluR2+ axonal profiles in glomeruli identified with VGluT1-staining of the mossy fiber rosettes (Fig. 5c,d). Typically, individual branchlets of the BIN-axon innervated 10-20 glomeruli with 2-5 boutons/per glomerulus (Fig. 5c,d). These data are consistent with the notion emerging from our tracing experiments that individual BIN neurons have diffuse widespread projections, innervating large proportions of the floccular granule cell layer.

Cell attached recordings from 7 morphologically validated BIN neurons indicated that they were silent (n=5) or fired at low frequency (8.4 and 5.6 Hz respectively). The capacitance of the cells was 48 ± 10 pF (15-88; Mean \pm SE, ranges, n = 7). We next determined their excitability in current clamp mode. Increasing depolarizing current injections with 20 pA increment triggered increased firing rates (Fig. 5e,f) with a rheobase current of 50 ± 10 pA (Mean \pm SE, n=7), action potential (AP) threshold of -43 ± 2 mV (Fig. 5g), peak AP amplitude of 93 ± 6 mV, AP rise and decay times of 0.55 ± 0.02 and 1.18 ± 0.05 ms, respectively, and afterhyperpolarization amplitude of 12 ± 1 mV. Whole-cell voltage-clamp recording uncovered spontaneous EPSC (sEPSC) in BIN cells (Fig. 5h-j), with sEPSC amplitudes of 17.69 ± 3.13 pA and frequencies of 3.93 ± 1.14 Hz. Together the data indicate that BIN neurons are readily excitable, receive excitatory input (see below), but show a low level of intrinsic firing activity in acute slices.

3.6 Necab1 outlines BIN neurons in mouse flocculus

To further characterize the BIN in rodents we performed retrograde CTB tracing in GlyT2GFP mice that express GFP under control of the GlyT2 gene promoter to label glycinergic neurons³⁵. We found that all retrogradely labeled BIN neurons were GFP+, indicating that BIN neurons are also glycinergic (Fig. 6a, b). Counting of serial GlyT2GFP sections indicated that mice have about 300 ($0.33 \pm 0.02 \times 10^3$, mean \pm SE, n = 6 flocculi from 3 animals) BIN neurons per side. Consistent with data from rat, CTB retrograde tracing in mouse showed that, while the injection areas covered less than 20%, ($12 \pm 3\%$, n = 3) of the floccular granule cell layer, more than 60% ($63 \pm 2\%$) of GFP+ BIN neurons were retrogradely labeled, indicative of widespread overlapping projection of BIN neurons. Together the data indicate that also in mice BIN neurons are distributed throughout the hilus and white matter of the flocculus.

As in macaque and rat, BIN neurons in the floccular white matter mice can be differentiated from Golgi cells in the floccular granule cell layer based on the absence of mGluR2 immunoreactivity (Fig. 6c). BIN neurons stained positive for the cholinergic muscarinic M2 receptor (Fig. 6d), which is expressed in cerebellar Golgi cells in multiple mammalian species^{39,58}. To further identify genes that are expressed by BIN neurons, we used the AGEA (Anatomic Gene Expression Atlas) viewer modus of Allen Brain Atlas that examines gene expression in user defined neuroanatomical areas. We screened nearly 2000 genes for distinct signal in intermediate-large cells in the white matter of the anterior flocculus. In accord with our immunohistological data, no visible signal occurs in the floccular white matter of *mGluR2* mRNA labeled sections, whereas sections stained for *Gad1* (*Gad67*), *Gad2* (*Gad65*), *GlyT2* (*Slc6A5*) and *ChRM2* mRNA show labelling of intermediate-sized cells in the floccular white matter, indicative of labelling of BIN neurons (Fig. 6e). Of 89 genes with distinct labelling of BIN neurons identified in our screen, the majority (85 of 89) showed similar expression in granule cell layer interneurons, while showing variable expression in other cerebello-cortical neuronal populations. Examples of genes that like *GlyT2* and *ChRM2* are expressed in both BIN neurons and granule cell layer interneurons, include acetylcholine esterase (*AChE*) and *Lgi2* (Fig. 6e). Out of the 2000 genes examined, we identified only four genes with distinct expression in BIN neurons and no apparent expression in granule cell layer interneurons in the flocculus. For one of these, *Necab1* (N-terminal EF-hand calcium Binding protein 1) expression in BIN neurons was confirmed by immunohistology (Fig. 6f,g): Analysis of *Necab1* immunostaining in GlyT2GFP mice shows that all GFP+ neurons in the floccular hilus and white matter, stain positive for *Necab1*, while other floccular cells, including GlyT2+ Golgi and Lugaro cells show no or very weak staining for *Necab1* (Fig. 6f). Accordingly, BIN neurons identified by retrograde CTB-tracing were always strongly *Necab1*+ (Fig. 6g). *Necab1* immunohistology also showed that BIN neurons may have one or more dendritic branches extending into the granule cell layer (Fig. 6f), consistent with data from rat neurobiotin-filled BIN neurons. Together, the data indicate that *Necab1* selectively outlines BIN neurons in the mouse flocculus, consistent with the idea that they represent a specific class of floccular neurons.

3.7 Absence of *Necab1*+ and *Neurogranin*+ Golgi cells in mouse flocculus

While granule cell layer interneurons in the flocculus show no or very weak *Necab1* expression, a substantial subset of granule cell layer interneurons in other cerebellar lobules stained positive for *Necab1* (Fig. 6f). The *Necab1*+ granule cell layer interneurons included both GlyT2GFP+ and GlyT2GFP- neurons (Fig. 6f). These data indicate that *Necab1* outlines one or more subclasses of granule cell layer interneurons that are absent in the flocculus. To further characterize *Necab1*+ granule cell layer interneurons, and differences between the flocculus and other cerebellar lobules we compared the distribution of *Necab1* with that of mGluR2 and neurogranin in sections from GlyT2GFP mice. A previous study focusing on lobules 4-6 of the vermis³⁰ showed that several subclasses of granule cell layer interneurons can be differentiated on the basis of differential expression of these markers, including a population of GlyT2GFP+mGluR2+neurogranin+ cells (designated type 1 Golgi cells), two populations that are GlyT2GFP+mGluR2+, but neurogranin- (type 2 and 3 Golgi cells), GlyT2GFP-GluR2-neurogranin+ cells (type 4 Golgi cells), and GlyT2GFP+ cells that are neurogranin-mGluR2- (representing Lugaro and globular cells). Consistent with this classification we found that in lobule 4-5 of the vermis (verm4/5) neurogranin occurred in GlyT2GFP+ as well as GlyT2GFP- Golgi cells (Fig. 7a), and that GlyT2GFP-/neurogranin+ cells were negative for mGluR2 (type 4 Golgi cells), while GlyT2GFP+/neurogranin+ Golgi cells were mGluR2+ (type 1 Golgi cells). However, no neurogranin+ Golgi cells occurred in the flocculus, and furthermore also BIN neurons stained negative for neurogranin (Fig. 7b). Like neurogranin, *Necab1* in verm4/5 occurred in either GlyT2GFP-/mGluR2- (potentially type 4 Golgi cells) or GlyT2GFP+/mGluR2+ (potentially type 1 Golgi cells), but not in GlyT2GFP+/mGluR2- cells (Lugaro/globular cells) (data not shown). Double labeling for *Necab1* and neurogranin showed consistent codistribution of neurogranin and *Necab1* in GlyT2GFP- (type 4) Golgi cells, but incomplete colocalization in GlyT2GFP+ Golgi cells (Fig. 7c). These data indicate that *Necab1* is expressed in type 4 Golgi cells, to variable extent is expressed by other Golgi cell subtypes, but is not expressed in Lugaro/globular cells.

We further characterized differences in Golgi cells between the flocculus and verm4/5 using an antibody against *Lgi2*. *Lgi2*-immunostaining occurred in granule cell layer interneurons as well as BIN neurons, in accord with mRNA expression data from Allan brain atlas (Fig. 6e). *Lgi2*/mGluR2 and *Lgi2*/neurogranin double labeling in GlyT2GFP mice indicated that in verm4/5 *Lgi2* is expressed in all Golgi cells, but not in Lugaro/globular cells: thus, in *Lgi2*/mGluR2 labeled sections, *Lgi2*-immunostaining outlines GlyT2GFP+mGluR2+ cells (type 1-3 Golgi cells) and GlyT2GFP-mGluR2- cells (potentially type 4 Golgi cells), but is not present in GlyT2GFP+mGluR2- cells (Lugaro/globular

cells) (data not shown). Lgi2/neurogranin staining showed that GlyT2GFP-Lgi2+ cells all stain positive for neurogranin (Fig. 7d,e) and indeed represent type 4 Golgi cells. Consistent with the notion that type 4 Golgi cells do not occur in the flocculus we found that all Lgi2+ cells in the floccular granule cell layer were GlyT2+mGluR2+, with the exception of sporadic GlyT2GFP+ cells that like BIN neurons are Necab1+ (Fig. 7f,g). Cell counts in Lgi2/Necab1/GlyT2GFP and Lgi2/neurogranin/GlyT2GFP labeled sections indicated that the density of Lgi2+ Golgi cells is slightly, but non-significantly ($p = 0.09$; unpaired 2-tailed t -test) higher in verm4/5 compared to the flocculus, with 227 ± 17 (Mean \pm SE, $n=3$ animals) Lgi2+ cells/mm² in verm4/5 and 187 ± 11 ($n=4$) Lgi2+ cells/mm² in the floccular granule cell layer, respectively. In verm4/5 87% (197 ± 15) of the Lgi2+ Golgi cells were GlyT2GFP+ representing type 1-3 Golgi cells, whereas in the flocculus all Lgi2+ cells were GlyT2+. In sum, our comparison of Golgi cells between verm4-5 and flocculus using established (mGluR2, neurogranin, GlyT2) and novel markers (Lgi2, Necab1) of (subsets of) Golgi cells, uncovered differences in the neurochemical identities of Golgi cells in the flocculus versus the anterior vermis³⁰. In particular, the absence of neurogranin+, Necab1+, and Lgi2+GlyT2GFP- Golgi cells in the flocculus indicates that type 4 Golgi cells are not present in the flocculus, all Golgi cells being mGluR2+GlyT2+.

3.8 BIN neurons innervate granule cells dendrites in floccular glomeruli

Based on analysis of BIN nerve terminals in macaque and rat, we anticipate that BIN axons provide inhibitory input to granule cell dendrites, and complement inhibitory input from Golgi cells in floccular glomeruli. To further examine the axonal projections of BIN neurons we injected AAV-GFP viral particles into the white matter and hilus of the flocculus of mice (Fig. 8a). We obtained 7 injections centered in the hilus of the flocculus infecting BIN neurons and resulting in a variable degree of axonal labelling in the ipsilateral flocculus (Fig. 8b,c). Labeled axons were morphologically distinct from mossy fibers, and form a plexus of thin fibers with multiple VIAAT-positive nerve terminals (Fig. 8c) resembling BIN fibers in macaque (Fig. 2) and rat (Fig. 5a-c). No GFP+VIAAT+ labeled axons occurred in the flocculus in case of more dorsal and medial injections that targeted the cerebellar nuclei, but did not target BIN neurons. The highest densities of labeled fibers occurred in experiments, where also BIN neurons in the floccular white matter were infected (Fig. 8b).

To characterize the post-synaptic target of AAV-GFP labeled BIN axons, we performed transmission electron microscopy of anti-GFP immunoperoxidase histochemistry with diaminobenzidine (DAB) as a substrate. Consistent with GFP fluorescence, DAB precipitate was associated with thin axonal profiles and presynaptic boutons with diameters ranging from 1 to 2 μ m. Labeled axon terminals were localized in glomeruli (Fig. 8d). Analysis of 40 labeled axon terminals, revealed multiple synaptic contacts with granule cell dendrites (Fig. 8d). Post-embedding immunogold labelling for GABA showed that DAB-labeled profiles in all occasions ($n=30$) are enriched in GABA-immunoreactivity (Fig. 8e,f) Together the data indicate that BIN axons like Golgi cell axon terminals^{6,59-61} primarily innervate granule cell dendrites.

3.9 BIN inhibitory input complements mGluR2+ Golgi axon terminals in glomeruli in the mouse flocculus

Immunostaining of AAV-GFP labeled sections for VIAAT, mGluR2 and VGluT1 showed that GFP+ BIN axon terminals always are mGluR2-negative, but co-distribute with VIAAT+mGluR2+ boutons in the same glomeruli (Fig. 8g,h). In addition, the same glomeruli also contained VIAAT+ terminals that are both mGluR2- and GFP-negative (Fig. 8g). To obtain an estimate of the proportion of mGluR2+ Golgi versus BIN axon terminals in the floccular granule cell layer we determined the proportion of VIAAT+ boutons labeled by either GFP or mGluR2 in confocal stacks from the three AAV-GFP injections that yielded the highest level of BIN axonal labelling (i.e. VBIN2, VBIN3, VBIN5). This analysis showed that 10-20% of the area labeled by VIAAT was GFP+ whereas 50-60% of the VIAAT+ area was mGluR2+ (Fig. 8i). For comparison, we analyzed the proportion of mGluR2+ VIAAT+ boutons in the nodulus and lobules 3 and 4/5 of the anterior vermis (Fig. 8j,k). In the anterior vermis, more than 90-95% of VIAAT+ area was mGluR2+ (Fig. 8j,k), consistent with the notion that inhibitory axons in the glomeruli primarily derive from mGluR2+ Golgi cells^{30,55,62}, while in the nodulus about 70% of the VIAAT+ area van mGluR2+ (Fig. 8k). The large proportion (40-50%) of VIAAT+mGluR2- boutons in the floccular granule cell layer as compared to the anterior vermis and the nodulus, can at least in part be explained by the presence of innervation from BIN neurons. In accord with data from macaque flocculus, these data indicate that BIN inhibitory input represents a significant complement of inhibitory input from Golgi cells in the floccular granule cell layer (Fig. 8l).

3.10 Rodent BIN neurons receive excitatory input from the rostro-medial medullary reticular formation

Staining for markers of inhibitory (VIAAT, GAD) and excitatory (VGluT1, VGluT2) nerve terminals, revealed that BIN neurons have a large number of VGluT2-positive boutons contacting their cell body and proximal dendrites (Fig. 9a) consistent with our electrophysiological analysis showing sEPSC in BIN neurons (Fig. 5h-j). To learn about the origin of this excitatory input, we set out tracing experiments in mouse. VGluT2 is present in climbing fibers and multiple populations of mossy fibers⁶³ raising the possibility that BIN neurons are innervated by collaterals of climbing or mossy fibers. To test this possibility, we injected anterograde tracer (biotin dextran amine 10 kDa, BDA) in the inferior olive, i.e. the source of climbing fibers, and in brainstem nuclei known to provide mossy fiber input to the flocculus, including the vestibular nuclei and the prepositus hypoglossal nucleus⁴¹. However, none of these injections resulted in labelling of fibers contacting BIN neurons, despite abundant climbing fiber and mossy fiber labelling, respectively (data not shown). Instead a systematic anterograde tracing approach with injections throughout the medulla oblongata and the pontine reticular formation, revealed that BDA injection in the rostro-medial medullary reticular formation resulted in labeling of fibers innervating BIN neurons (Fig. 9b-e). We obtained 7 BDA injections that resulted in labeling of beaded fibers contacting the cell bodies and proximal dendrites of a substantial portion (>30%) of BIN neurons. These injections all targeted the medio-dorsal aspect of the medullary gigantocellular reticular nucleus (Gi). In 4 of 7 cases injections also included the dorsal paragigantocellular reticular nucleus (DPGi) dorsal of the Gi. However, 2 injection that targeted the DPGi, but not the Gi, resulted in labeled fibers on less than 4% of BIN neurons, indicating that afferents predominantly arise in the Gi. Similarly, BDA injections in the ventral aspect of the Gi, the pontine reticular formation rostral of the Gi, or the caudal aspect of the Gi resulted in no or minimal labeling of BIN afferents, substantiating the medio-dorsal Gi as the main source of BIN afferents. Importantly, the injections restricted to the medio-dorsal Gi that resulted in substantial labelling of BIN afferents (e.g. experiments #1541, #1606 and #1536) all produced negligible mossy fiber staining, supporting the notion that fibers innervating the cell bodies of BIN neurons do not represent mossy fiber collaterals. In all experiments labeled BIN afferent fibers were observed bilaterally, even when the injection was clearly unilateral. In addition, we observed that individual afferents may innervate several BIN neurons, and typically produce multiple (5-32) consecutive swellings on the cell body and proximal dendrites of individual BIN neurons (Fig. 9c,e). Double labelling for VGluT2 indicated that these axonal swellings in all occasions were VGluT2+ (Fig. 9e). In all neurons systematically examined for codistribution of BDA and VGluT2 (30 of 30 cells) we found that BDA+VGluT2+ boutons on BIN neurons were complemented by BDA-VGluT2+ boutons (Fig. 9e). This observation indicates that individual BIN neurons are innervated by multiple excitatory axons. To further demonstrate that VGluT2+ axon terminals innervating BIN neurons arise from neurons in the medio-dorsal Gi, we injected AAV-flex-GFP viral particles in the Gi of VGluT2-Cre mice in order to express GFP selectively in VGluT2 expressing neurons. Consistent with BDA tracing these injections resulted in bilateral GFP+ beaded fibers that made multiple synaptic connections with BIN neurons (Fig. 9f).

Next, to visualize the cells of origin of the BIN afferents in the Gi, we performed retrograde tracing with cholera toxin β subunit (CTB). Comparison of CTB injections centered in the hilus of the flocculus (n=2) with injections in the floccular cortex (n=4), uncovered a population of intermediate-size (length =14 to 22 μ m) polygonal CTB-labeled neurons in the dorsal Gi following hilar, but not cortical CTB injections (Fig. 9g). Consistent with anterograde tracing experiments, retrogradely-labeled neurons occurred both ipsi- and contralateral. Large neurons, characteristic for the Gi were not retrogradely labeled. The presence of intermediately sized VGluT2+ neurons in the Gi is consistent with *VGluT2* mRNA expression data documented in Allen brain atlas⁵⁰ showing high levels of *VGluT2* mRNA staining in both very large and small-to-intermediate size neurons in the Gi. We therefore propose that BIN neurons receive bilateral excitatory input from intermediately sized neurons in the dorsal Gi. Together the data indicate that the BIN is part of a disynaptic afferent pathway to the floccular granule cell layer, consisting of glutamatergic fibers from the medullary reticular formation innervating BIN neurons that in turn provide inhibitory input to granule cells (Fig. 9h).

3.11 Variability in the distribution of BIN neurons across mammalian species.

On the basis of data from primates and rodent, the BIN can be defined as a population of GABA/glycinergic neurons in the white matter, that innervate the floccular granule cell layer. However, BIN neurons show a differential distribution in rodents and primates, i.e. a preferential localization in the floccular white matter in rodents, versus a more widespread and distant distribution in the white matter between the floccular peduncle and the cerebellar nuclei in macaque and human. This raises

questions about the presence and distribution of BIN neurons in other mammalian species. Our search for BIN neurons in rabbit cerebellum indicates that their identification in other species is not always straightforward. Thionin and GAD staining shows that in rabbit a low number of neurons is present in the white matter within and dorso-medial of the flocculus. Accordingly, analysis of sections from previous tracer experiments with small injections of the anterograde/retrograde tracer WGA-HRP in the floccular cortex (rabbits K227, K244, K358, K360; ⁵² revealed no or sporadic retrogradely labeled cells in this area. However, further analysis of these experiments revealed retrogradely labeled cells in the white matter medial of the medial cerebellar peduncle (mcp), rostral of the cerebellar nuclei (Fig. 10a,b). Retrogradely labeled cells only occurred ipsilateral. Notably, in several occasions labeled cells occurred close to the granule cell layer of the anterior vermis (Fig. 10b). Importantly, GAD staining revealed GAD+ neurons with similar size and distribution in this region of the white matter (Fig. 10c,d). The GAD+ neurons showed morphologies reminiscent of BIN neurons in primates and rodent. Based on counting of serial sections, we estimate that on each side there are about 800 ($0.8 \pm 0.2 * 10^3$, mean \pm SE, n=2) of these GAD+ neurons populating either the floccular or the anterior vermis white matter (Fig. 10c,d).

To further explore the variability in distribution of BIN neurons across mammalian species we searched for potential BIN neurons in ferret cerebellum. Analysis of thionin and GAD stained section showed that as in primates and rabbit there are only a few GAD+ neurons in the white matter of the ferret flocculus. However, a cluster of GAD+ neurons, reminiscent of BIN neurons, was present in the white matter of the transition zone between the flocculus and the ventral paraflocculus (Fig. 11). Caudo-dorsally this cluster is bordered by the lateral cerebellar nuclei. Like BIN neurons the neurons are moderately-large in size and show elongated fusiform or polygonal morphologies with dendrites emanating from two sides. With about 1000 ($1.1 \pm 0.1 * 10^3$, mean \pm SE, n=2) neurons per side, their number is compatible with BIN neurons in other species. Together the data indicate that BIN neurons also occur in rabbit and ferret cerebellum, but show different distributions than in rodent and primates.

4. DISCUSSION

The BIN has been originally identified by Langer in macaque as a population of neurons that innervate the flocculus and the ventral paraflocculus (also designated floccular complex; ²⁵, and is located in the basal white matter between the flocculus and the cerebellar nuclei ^{33,34}. Although this finding was confirmed by others ⁶⁴, the BIN has been largely neglected in the literature. In addition, in some studies ^{65,66} the term BIN has been used for a group of neurons that does not overlap with the BIN originally defined by Langer ³⁴. In these studies, 'BIN' neurons were found to project to pontine nuclei ⁶⁵ and to display saccade-related firing activity ⁶⁶. However, the cells explored in these studies were localized medial of group Y, whereas BIN neurons identified by retrograde tracing localize lateral of group Y (see Fig 1 of this study, and Fig. 3 in Langer, 1985). In a recent human brain Atlas ⁶⁷, the term BICb (basal interstitial nucleus of the cerebellum) has been assigned to a population of large neurons in the roof of the 4th ventricle neurons (see Fig. 13 in ⁶⁷. In this study, there is no reference to the study of Langer ³⁴, and it is not clear whether the BICb was intended to represent the human homologue of the macaque BIN ⁶⁷. On the basis of our data, we propose to reserve the term BIN (or BICb) for the population of neurons originally defined by Langer on the basis of retrograde tracing from the flocculus ^{33,34}. Our data indicate that these neurons represent a novel GABAergic cerebellar neuron that can be found in multiple mammalian species beyond macaque, including human, rat, mouse, rabbit and ferret (Table 2). Distinctive properties of BIN neurons are the following: they are moderately-sized GABAergic neurons localized in the white matter; they innervate floccular granule cells; and they receive excitatory input from the medullary reticular formation. BIN neurons represent a second source of inhibition of floccular granule cells, complementing inhibitory input from Golgi cells (Fig. 9h).

We found that BIN neurons in macaque stain positive for GAD and ChAT (Figs 1 and 2) and that ChAT staining can also be used to outline the BIN in human cerebellum (Fig. 3). ChAT staining did not label BIN neurons in the other species investigated, i.e. rat, mouse, rabbit and ferret, but in these species, we identified homologous populations of neurons based on the following criteria: their localization in the white matter, their size and elongated morphologies with dendrites emanating from the two ends, their retrograde labeling after tracer injection in the flocculus, and their immunoreactivity for GAD (Figs 4, 6, 10, 11). Our data indicate that the distribution of BIN neurons shows variability across species, varying from the floccular white matter in rat and mouse, to a relatively condensed

distribution in the white matter dorso-medial of the flocculus in ferret, and more widespread distributions in rabbit and primates.

A search in Allen Brain Atlas to identify molecular markers that could further aid in the identification of BIN neurons uncovered the calcium binding protein Necab1 as a marker for BIN neurons in mouse cerebellum (Fig. 6). However, Necab1 is not expressed by BIN neurons in other species. The interspecies heterogeneity of ChAT and Necab1 expression is not against our tenet that BIN neurons represent a single class of neurons across species for two reasons: First, Necab1 is also absent in rat BIN neurons, which are highly similar to mouse BIN neurons in distribution and morphology. Second, interspecies heterogeneity in the expression of neurochemical markers also occurs in other populations of cerebellar neurons, in particular Golgi cells that differentially express ChAT, neurogranin and calretinin in closely related species^{32,58,68-70}. In addition to Necab1, we found other proteins that might serve as neurochemical markers for BIN neurons, although the majority of these, like GlyT2, muscarinic M2 receptor, Lgi2, and acetylcholine esterase (AChE) are also expressed by Golgi cells (Figs 6, 7). In fact, our data show that also Necab1, while not being expressed by Golgi cells in the flocculus, is expressed in a subset of Golgi cells in most other lobules (Figs 6, 7). Instead mGluR2 is a marker that differentiates BIN neurons from Golgi cells, as it is not expressed in BIN neurons (Figs 2, 5, 6, 8) while being expressed by the majority of cerebellar Golgi cells and their nerve terminals^{29,30,55,70}. Furthermore, in mouse, we found that BIN neurons do not express neurogranin (Fig. 7), another Golgi cell marker that is expressed in at least 2 subpopulations of Golgi cells in mouse cerebellum, including a subpopulation of Golgi cells (type 4 Golgi cells) that does not express mGluR2 and GlyT2^{30,69}. Importantly, by comparing the expression of a panel of Golgi cell markers between anterior vermis and the flocculus, we found that neurogranin+GlyT2-mGluR2- Golgi cells, while constituting 10-15% of the Golgi cells in the anterior vermis³⁰, are not present in the flocculus, (Fig. 7). These findings on the one hand point to differences in neurochemical identities between Golgi cells in the flocculus compared to the anterior vermis³⁰; and on the other hand, support our notion that mGluR2 may represent a useful marker to differentiate BIN neurons from Golgi cells in the flocculus.

Recently, an ascending GABAergic/glycinergic inhibitory projection from the cerebellar nuclei to the cerebellar cortex has been reported³¹. These nucleo-cortical inhibitory neurons differ from BIN neurons in at least two aspects: They do not express Necab1 and they innervate Golgi cells rather granule cells³¹. It has been suggested that these inhibitory nucleo-cortical neurons also innervate the floccular granule cell layer (see Fig. 2A of³¹). However, we did not identify retrogradely labeled neurons in the cerebellar nuclei following CTB tracer injection in the flocculus. We, therefore, speculate that the floccular projections in the study of Ankri et al. (2015) derive from BIN neurons. The absence of inhibitory nucleo-cortical projections to the flocculus also is consistent with the absence of neurogranin+GlyT2-mGluR2- Golgi cells in the flocculus (Fig. 7), representing a major target of this projection³¹. Taken together, although BIN neurons show resemblance with either Golgi cells or inhibitory nucleo-cortical neurons and probably derive from the same lineage, they are sufficiently distinct to consider them as a novel population of cerebellar neurons.

To characterize BIN axon terminals, we took advantage of their immunoreactivity for ChAT in macaque flocculus (Fig. 2) and we used AAV-GFP anterograde tracing in mice (Fig. 8). We found that BIN axon terminals to various degrees populate glomeruli in the floccular granule cell layer and complement mGluR2+ inhibitory input from Golgi cells. Electron microscopy of anterogradely labeled BIN axons in mouse provided direct demonstration that BIN axons innervate granule cell dendrites (Fig. 8d,e). Using confocal microscopy, we found examples of ChAT+ BIN axons innervating glomeruli with UBC brushes in macaque (Fig. 2i). So far, we did not obtain ultrastructural evidence of BIN axons making synaptic contacts with UBCs. We also used confocal microscopy to examine whether AAV-GFP traced BIN axons contact Golgi cells stained with antibodies against mGluR2 or muscarinic M2 receptor, but so far, we did not find conclusive examples of BIN axons contacting the cell body or dendrites of Golgi cells. Thus, granule cell dendrites represent a major target of BIN axons, while further work is needed to establish to what extent other granule cell layer neurons receive direct BIN input.

To obtain an idea about the relative contribution of inhibition by BIN axons in the floccular granule cell layer, we determined the proportion of ChAT+ inhibitory boutons in macaque flocculus, and the proportion of GFP+ inhibitory boutons in AAV- GFP anterograde tracing experiments in mice. These analyses indicated that at least 20% of inhibitory boutons in the floccular granule cell layer represent BIN axon terminals. Thus, in macaque flocculus about 20% of VIAAT+ boutons stain positive for ChAT, while in mice AAV-GFP injections resulted in GFP labelling of up to 20% of VIAAT+ boutons. However, the proportion of BIN axon terminals is likely to be higher in both macaque and

mouse, in view of the presence of a population of ChAT- BIN neurons in macaque (Fig. 2a,b), and unlabeled BIN neurons in the AAV- GFP tracing experiments in mice. Analysis of the proportion of Golgi axon terminals on the basis of double labelling for VIAAT and mGluR2 metabotropic glutamate receptor, indicated that about 60% of VIAAT+ axon terminals in the floccular granule cell layer is from mGluR2+ Golgi cells. Instead the proportion of mGluR2+ boutons is higher in other lobules (up to 95% in the anterior vermis; Fig. 8j,k), consistent with previous data indicating that 85-90% of Golgi cells are mGluR2+^{29,30} and that toxin-mediated selective ablation of mGluR2+ Golgi cells results in almost complete loss of GABAergic boutons in the granule cell layer⁵⁵. The large proportion of mGluR2- VIAAT+ boutons in the floccular granule cell layer (about 40%) as compared to other lobules, at least in part can be explained by the presence BIN axons. mGluR2- VIAAT+ boutons also may derive from mGluR2- Golgi cells, but our data indicate that this type of Golgi cell does not occur in the flocculus (see above). Purkinje cells may represent an additional source of inhibitory boutons in the granule cell layer⁷¹ predominantly innervating Lugaro and globular cells³⁰, but double labelling for VIAAT and the Purkinje cell marker calbindin indicated that inhibitory boutons from Purkinje cells are rare in the floccular granule cell layer (<1% of VIAAT boutons). Taken together, our data indicate that about 60% of the VIAAT+ axon terminals in the floccular granule cell layer derive from mGluR2+ Golgi cells, while at least 20% and potentially up to 40% of the residual VIAAT+ axon terminals are from BIN neurons.

What could be the function of BIN neurons in the floccular circuitry? BIN axon terminals co-distribute with mGluR2+ Golgi cell axon terminals in the same glomeruli, and likely have complementary roles in controlling mossy fiber to granule cell signaling. Golgi cells receive excitatory granule cell and mossy fiber input and implement a local inhibitory feedback circuit that may control the precise timing and gain of granule cell firing^{12,60,72}. The distinctive feature of Golgi cells is their local dense axonal plexus that provides inhibitory input primarily to nearby granule cells, although some Golgi cells may have more distant projections⁶⁰. BIN neurons instead project to large portions of the flocculus, and only produce a few axon terminals per glomerulus. This wiring pattern indicates that BIN neurons have a more global inhibitory role over widely distributed granule cells (Fig. 9h). We also show that BIN neurons receive bilateral glutamatergic input from a population of neurons in the medullary gigantocellular reticular formation. These fibers innervate the cell body and proximal dendrites of BIN neurons, and likely play an important role in controlling the activity of BIN neurons. Importantly, our data also indicate that BIN neurons are not innervated by collaterals from climbing and mossy fiber collaterals that innervate the floccular cortex, although at this point we can not exclude collateral projections on distal dendrites of BIN neurons. It had been anticipated by Langer that BIN neurons receive inhibitory input from floccular Purkinje cells³⁴. However, anterograde tracing experiments in macaque have shown that BIN neurons do not receive input from the flocculus⁷³. In accord with the idea that BIN neurons do not receive Purkinje cell input, our data indicate that BIN neurons are only innervated by calbindin-negative inhibitory boutons.

Together the data indicate that BIN neurons represent a diffuse inhibitory system of floccular granule cells that is controlled by a group of neurons in the medullary formation (Fig. 9h). Understanding the information conveyed by the medullary BIN afferents, will be critical for clarifying the role of the BIN neurons in the well-established role of the flocculus in eye movement control^{22,24,25,74,75}. Importantly, future studies on the function of BIN neurons would benefit from experiments in multiple mammalian species to validate whether BIN neurons indeed represent a single class of prefloccular neurons with evolutionary conserved function.

REFERENCES

1. Voogd, J. & Glickstein, M. The anatomy of the cerebellum. *Trends Neurosci* **21**, 370-375 (1998).
2. Cerminara, N.L., Lang, E.J., Sillitoe, R.V. & Apps, R. Redefining the cerebellar cortex as an assembly of non-uniform Purkinje cell microcircuits. *Nat Rev Neurosci* **16**, 79-93 (2015).
3. Dean, P., Porrill, J., Ekerot, C.F. & Jorntell, H. The cerebellar microcircuit as an adaptive filter: experimental and computational evidence. *Nat Rev Neurosci* **11**, 30-43 (2010).
4. De Zeeuw, C.I., *et al.* Spatiotemporal firing patterns in the cerebellum. *Nat Rev Neurosci* **12**, 327-344 (2011).
5. Gao, Z., van Beugen, B.J. & De Zeeuw, C.I. Distributed synergistic plasticity and cerebellar learning. *Nat Rev Neurosci* **13**, 619-635 (2012).
6. Palay, S.L. & Chan-Palay, V.E. *Cerebellar cortex: cytology and organization*, (Springer Verlag, Berlin, 1974).
7. Davie, J.T., Clark, B.A. & Hausser, M. The origin of the complex spike in cerebellar Purkinje cells. *J Neurosci* **28**, 7599-7609 (2008).
8. Jelitai, M., *et al.* Dendritic excitation-inhibition balance shapes cerebellar output during motor behaviour. *Nat Commun* **7**, 13722 (2016).
9. Harvey, R.J. & Napper, R.M. Quantitative study of granule and Purkinje cells in the cerebellar cortex of the rat. *J Comp Neurol* **274**, 151-157 (1988).

10. Rancz, E.A., *et al.* High-fidelity transmission of sensory information by single cerebellar mossy fibre boutons. *Nature* **450**, 1245-1248 (2007).
11. Jakab, R.L. & Hamori, J. Quantitative morphology and synaptology of cerebellar glomeruli in the rat. *Anat Embryol (Berl)* **179**, 81-88 (1988).
12. Valera, A.M., *et al.* Stereotyped spatial patterns of functional synaptic connectivity in the cerebellar cortex. *Elife* **5**(2016).
13. Powell, K., Mathy, A., Duguid, I. & Hausser, M. Synaptic representation of locomotion in single cerebellar granule cells. *Elife* **4**(2015).
14. Sudhakar, S.K., *et al.* Spatiotemporal network coding of physiological mossy fiber inputs by the cerebellar granular layer. *PLoS Comput Biol* **13**, e1005754 (2017).
15. Arenz, A., Bracey, E.F. & Margrie, T.W. Sensory representations in cerebellar granule cells. *Curr Opin Neurobiol* **19**, 445-451 (2009).
16. Chabrol, F.P., *et al.* Synaptic diversity enables temporal coding of coincident multisensory inputs in single neurons. *Nat Neurosci* **18**, 718-727 (2015).
17. Huang, C.C., *et al.* Convergence of pontine and proprioceptive streams onto multimodal cerebellar granule cells. *Elife* **2**, e00400 (2013).
18. Gao, Z., *et al.* Excitatory Cerebellar Nucleocortical Circuit Provides Internal Amplification during Associative Conditioning. *Neuron* **89**, 645-657 (2016).
19. Witter, L. & De Zeeuw, C.I. Regional functionality of the cerebellum. *Curr Opin Neurobiol* **33**, 150-155 (2015).
20. Zhou, H., *et al.* Cerebellar modules operate at different frequencies. *Elife* **3**, e02536 (2014).
21. De Zeeuw, C.I. & Ten Brinke, M.M. Motor Learning and the Cerebellum. *Cold Spring Harb Perspect Biol* **7**, a021683 (2015).
22. Ito, M. Cerebellar control of the vestibulo-ocular reflex—around the flocculus hypothesis. *Annu Rev Neurosci* **5**, 275-296 (1982).
23. Lisberger, S.G. Internal models of eye movement in the floccular complex of the monkey cerebellum. *Neuroscience* **162**, 763-776 (2009).
24. Schonewille, M., *et al.* Zonal organization of the mouse flocculus: physiology, input, and output. *J Comp Neurol* **497**, 670-682 (2006).
25. Voogd, J., Schraa-Tam, C.K., van der Geest, J.N. & De Zeeuw, C.I. Visuomotor cerebellum in human and nonhuman primates. *Cerebellum* **11**, 392-410 (2012).
26. van Dorp, S. & De Zeeuw, C.I. Forward Signaling by Unipolar Brush Cells in the Mouse Cerebellum. *Cerebellum* (2015).
27. Sekerkova, G., Watanabe, M., Martina, M. & Mugnaini, E. Differential distribution of phospholipase C beta isoforms and diacylglycerol kinase-beta in rodents cerebella corroborates the division of unipolar brush cells into two major subtypes. *Brain Struct Funct* **219**, 719-749 (2014).
28. Zampini, V., *et al.* Mechanisms and functional roles of glutamatergic synapse diversity in a cerebellar circuit. *Elife* **5**(2016).
29. Neki, A., *et al.* Metabotropic glutamate receptors mGluR2 and mGluR5 are expressed in two non-overlapping populations of Golgi cells in the rat cerebellum. *Neuroscience* **75**, 815-826 (1996).
30. Simat, M., Parpan, F. & Fritschy, J.M. Heterogeneity of glycinergic and gabaergic interneurons in the granule cell layer of mouse cerebellum. *J Comp Neurol* **500**, 71-83 (2007).
31. Ankri, L., *et al.* A novel inhibitory nucleo-cortical circuit controls cerebellar Golgi cell activity. *Elife* **4**(2015).
32. Eyre, M.D. & Nusser, Z. Only a Minority of the Inhibitory Inputs to Cerebellar Golgi Cells Originates from Local GABAergic Cells. *eNeuro* **3**(2016).
33. Langer, T., Fuchs, A.F., Scudder, C.A. & Chubb, M.C. Afferents to the flocculus of the cerebellum in the rhesus macaque as revealed by retrograde transport of horseradish peroxidase. *J Comp Neurol* **235**, 1-25 (1985).
34. Langer, T.P. Basal interstitial nucleus of the cerebellum: cerebellar nucleus related to the flocculus. *J Comp Neurol* **235**, 38-47 (1985).
35. Zeilhofer, H.U., *et al.* Glycinergic neurons expressing enhanced green fluorescent protein in bacterial artificial chromosome transgenic mice. *J Comp Neurol* **482**, 123-141 (2005).
36. Vong, L., *et al.* Leptin action on GABAergic neurons prevents obesity and reduces inhibitory tone to POMC neurons. *Neuron* **71**, 142-154 (2011).
37. Siegers, J.Y., *et al.* Novel avian-origin influenza A (H7N9) virus attachment to the respiratory tract of five animal models. *J Virol* **88**, 4595-4599 (2014).
38. van Riel, D., *et al.* Decrease of virus receptors during highly pathogenic H5N1 virus infection in humans and other mammals. *Am J Pathol* **183**, 1382-1389 (2013).
39. Jaarsma, D., *et al.* Light-microscopic distribution and parasagittal organisation of muscarinic receptors in rabbit cerebellar cortex. *J Chem Neuroanat* **9**, 241-259 (1995).
40. Ruigrok, T.J., Hensbroek, R.A. & Simpson, J.I. Spontaneous activity signatures of morphologically identified interneurons in the vestibulocerebellum. *J Neurosci* **31**, 712-724 (2011).
41. Ruigrok, T.J. Collateralization of climbing and mossy fibers projecting to the nodulus and flocculus of the rat cerebellum. *J Comp Neurol* **466**, 278-298 (2003).
42. Boele, H.J., Koekkoek, S.K., De Zeeuw, C.I. & Ruigrok, T.J. Axonal sprouting and formation of terminals in the adult cerebellum during associative motor learning. *J Neurosci* **33**, 17897-17907 (2013).
43. Paxinos, G. & Franklin, K.B.J. *The mouse brain in stereotaxic coordinates*, (Academic Press, London, 2001).
44. Wang, Q., *et al.* Systematic comparison of adeno-associated virus and biotinylated dextran amine reveals equivalent sensitivity between tracers and novel projection targets in the mouse brain. *J Comp Neurol* **522**, 1989-2012 (2014).
45. Harris, J.A., Oh, S.W. & Zeng, H. Adeno-associated viral vectors for anterograde axonal tracing with fluorescent proteins in nontransgenic and cre driver mice. *Curr Protoc Neurosci* **Chapter 1**, Unit 1 20 21-18 (2012).
46. Ruigrok, T.J., Osse, R.J. & Voogd, J. Organization of inferior olivary projections to the flocculus and ventral paraflocculus of the rat cerebellum. *J Comp Neurol* **316**, 129-150 (1992).
47. Jaarsma, D., Dino, M.R., Cozzari, C. & Mugnaini, E. Cerebellar choline acetyltransferase positive mossy fibres and their granule and unipolar brush cell targets: a model for central cholinergic nicotinic neurotransmission. *J Neurocytol* **25**, 829-842 (1996).

48. Zhang, M.D., *et al.* Comparative anatomical distribution of neuronal calcium-binding protein (NECAB) 1 and -2 in rodent and human spinal cord. *Brain Struct Funct* **221**, 3803-3823 (2016).
 49. Singec, I., *et al.* Neurogranin is expressed by principal cells but not interneurons in the rodent and monkey neocortex and hippocampus. *J Comp Neurol* **479**, 30-42 (2004).
 50. Lein, E.S., *et al.* Genome-wide atlas of gene expression in the adult mouse brain. *Nature* **445**, 168-176 (2007).
 51. Kuijpers, M., *et al.* Amyotrophic lateral sclerosis (ALS)-associated VAPB-P56S inclusions represent an ER quality control compartment. *Acta Neuropathol Commun* **1**, 24 (2013).
 52. Tan, J., Epema, A.H. & Voogd, J. Zonal organization of the flocculovestibular nucleus projection in the rabbit: a combined axonal tracing and acetylcholinesterase histochemical study. *J Comp Neurol* **356**, 51-71 (1995).
 53. Barmack, N.H., Baughman, R.W. & Eckenstein, F.P. Cholinergic innervation of the cerebellum of rat, rabbit, cat, and monkey as revealed by choline acetyltransferase activity and immunohistochemistry. *J Comp Neurol* **317**, 233-249 (1992).
 54. Barmack, N.H., Baughman, R.W., Eckenstein, F.P. & Shojaku, H. Secondary vestibular cholinergic projection to the cerebellum of rabbit and rat as revealed by choline acetyltransferase immunohistochemistry, retrograde and orthograde tracers. *J Comp Neurol* **317**, 250-270 (1992).
 55. Watanabe, D., *et al.* Ablation of cerebellar Golgi cells disrupts synaptic integration involving GABA inhibition and NMDA receptor activation in motor coordination. *Cell* **95**, 17-27 (1998).
 56. Jaarsma, D., *et al.* Metabotropic glutamate receptors are associated with non-synaptic appendages of unipolar brush cells in rat cerebellar cortex and cochlear nuclear complex. *J Neurocytol* **27**, 303-327 (1998).
 57. de Lacalle, S., Hersh, L.B. & Saper, C.B. Cholinergic innervation of the human cerebellum. *J Comp Neurol* **328**, 364-376 (1993).
 58. Jaarsma, D., *et al.* Cholinergic innervation and receptors in the cerebellum. *Prog Brain Res* **114**, 67-96 (1997).
 59. Dugué, G.P., Dumoulin, A., Triller, A. & Dieudonné, S. Target-dependent use of co-released inhibitory transmitters at central synapses. *J Neurosci* **25**, 6490-6498 (2005).
 60. Pietrajtis, K. & Dieudonné, S. Golgi Neurons. in *Handbook of the cerebellum and cerebellar disorders*
- doi: 10.1007/1978-1094-1007-1333-1008_1034 (Springer, 2013).
61. Mapelli, L., Solinas, S. & D'Angelo, E. Integration and regulation of glomerular inhibition in the cerebellar granular layer circuit. *Front Cell Neurosci* **8**, 55 (2014).
 62. Ohishi, H., *et al.* Immunohistochemical localization of metabotropic glutamate receptors, mGluR2 and mGluR3, in rat cerebellar cortex. *Neuron* **13**, 55-66 (1994).
 63. Hioki, H., *et al.* Differential distribution of vesicular glutamate transporters in the rat cerebellar cortex. *Neuroscience* **117**, 1-6 (2003).
 64. Nagao, S., *et al.* Differences of the primate flocculus and ventral paraflocculus in the mossy and climbing fiber input organization. *J Comp Neurol* **382**, 480-498 (1997).
 65. Gonzalo-Ruiz, A., Leichnetz, G.R. & Smith, D.J. Origin of cerebellar projections to the region of the oculomotor complex, medial pontine reticular formation, and superior colliculus in New World monkeys: a retrograde horseradish peroxidase study. *J Comp Neurol* **268**, 508-526 (1988).
 66. Takikawa, Y., Kawagoe, R., Miyashita, N. & Hikosaka, O. Presaccadic omnidirectional burst activity in the basal interstitial nucleus in the monkey cerebellum. *Exp Brain Res* **121**, 442-450 (1998).
 67. Ding, S.L., *et al.* Comprehensive cellular-resolution atlas of the adult human brain. *J Comp Neurol* **524**, 3127-3481 (2016).
 68. Bastianelli, E. Distribution of calcium-binding proteins in the cerebellum. *Cerebellum* **2**, 242-262 (2003).
 69. Singec, I., *et al.* Neurogranin expression by cerebellar neurons in rodents and non-human primates. *J Comp Neurol* **459**, 278-289 (2003).
 70. Geurts, F.J., Timmermans, J., Shigemoto, R. & De Schutter, E. Morphological and neurochemical differentiation of large granular layer interneurons in the adult rat cerebellum. *Neuroscience* **104**, 499-512 (2001).
 71. Guo, C., *et al.* Purkinje Cells Directly Inhibit Granule Cells in Specialized Regions of the Cerebellar Cortex. *Neuron* **91**, 1330-1341 (2016).
 72. Cesana, E., *et al.* Granule cell ascending axon excitatory synapses onto Golgi cells implement a potent feedback circuit in the cerebellar granular layer. *J Neurosci* **33**, 12430-12446 (2013).
 73. Nagao, S., *et al.* Location of efferent terminals of the primate flocculus and ventral paraflocculus revealed by anterograde axonal transport methods. *Neurosci Res* **27**, 257-269 (1997).
 74. De Zeeuw, C.I., Wylie, D.R., Stahl, J.S. & Simpson, J.I. Phase relations of Purkinje cells in the rabbit flocculus during compensatory eye movements. *J Neurophysiol* **74**, 2051-2064 (1995).
 75. Voges, K., *et al.* Mechanisms underlying vestibulo-cerebellar motor learning in mice depend on movement direction. *J Physiol* **595**, 5301-5326 (2017).

Figure legends

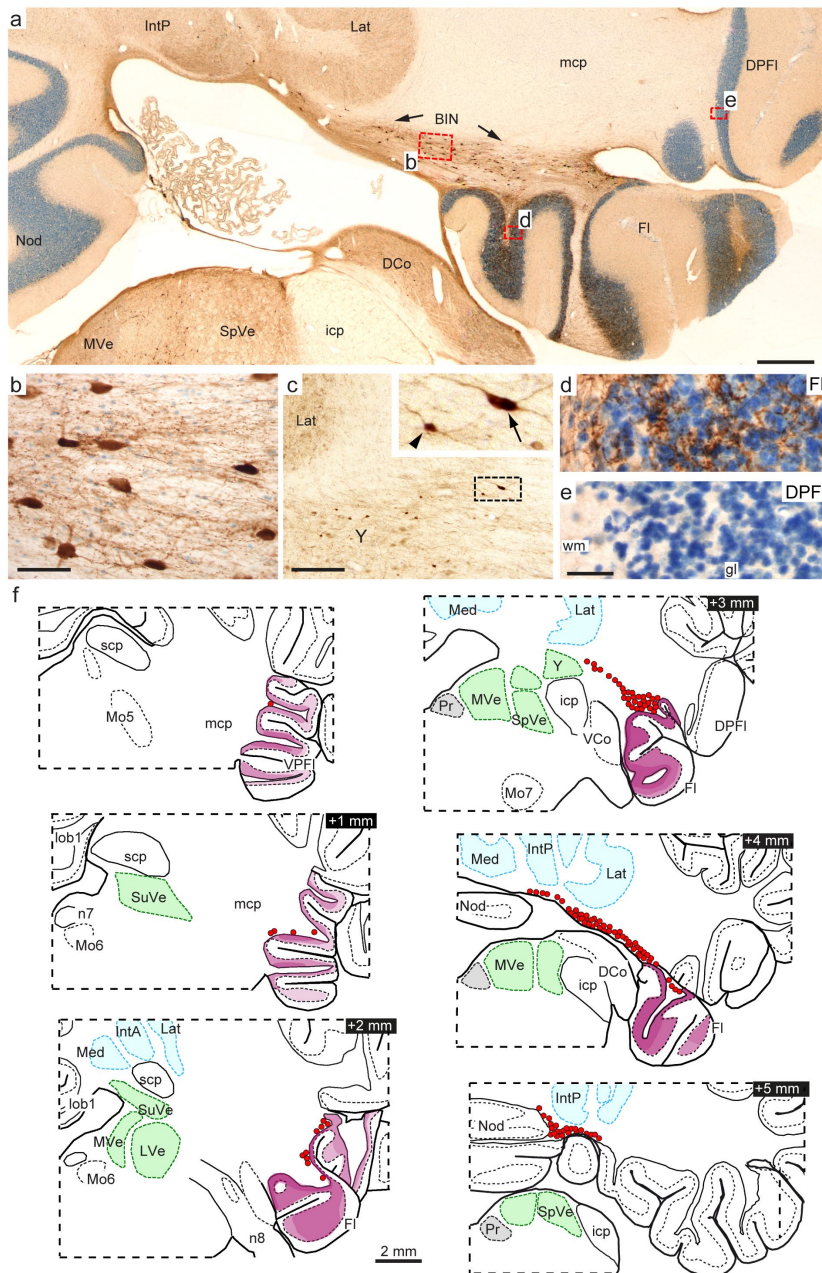


Figure 1. Choline Acetyltransferase (ChAT) immunostaining outlines the basal interstitial nucleus (BIN) in macaque cerebellum

a-e: Low-power (a) and high power (b-e) photomicrographs of ChAT immunoperoxidase diaminobenzidine (DAB) stained coronal sections of Macaque cerebellum illustrating intensely stained BIN neurons in the basal white matter between the flocculus and the cerebellar nuclei (a,b), and ChAT+ beaded fibers in the floccular granule cell layer (a,d). The photomicrograph in c illustrates that ChAT+ BIN neurons (arrow) are considerably larger than ChAT+ neurons in group Y (arrow head). No or minimal ChAT+ fibers occur in the dorsal paraflocculus (DPFI; a,e). Sections are counterstained with thionin (blue).

f: Plots of ChAT+ BIN neurons (red dots) and relative density of ChAT+ beaded fibers (violet staining) in serial coronal macaque cerebellar sections. Cerebellar and vestibular nuclei are indicated in light blue and green, respectively.

Abbreviations: DCo, dorsal cochlear nucleus; DPFI, Dorsal paraflocculus; FI, Flocculus; icp, inferior cerebellar peduncle; IntA, anterior interposed cerebellar nucleus; IntP, posterior interposed nucleus; Lat, lateral cerebellar nucleus; mcp, middle cerebellar peduncle; LVe, lateral vestibular nucleus; MVe, medial vestibular nucleus; Nod, Nodulus; Pr, prepositus hypoglossi; SpVe, spinal vestibular nucleus; SuVe, Superior vestibular nucleus.

Scale bars: a, 500 μ m; c, 200 μ m; b and e, 50 μ m

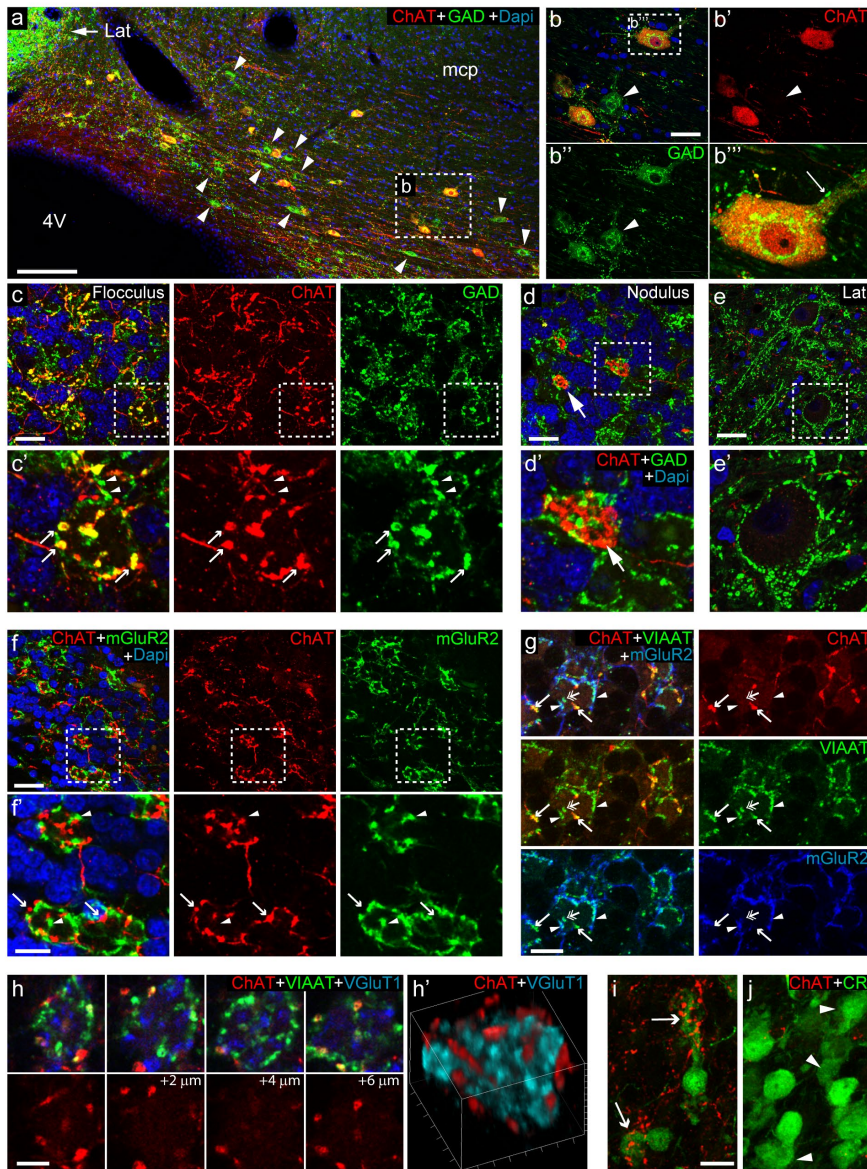


Figure 2. Macaque BIN neurons provide GABAergic input to the granule cell layer of the flocculus

a-e: Double labelling confocal immunofluorescence for ChAT and glutamic acid decarboxylase 65/67 (GAD) shows that ChAT+ neurons in the BIN (*a,b*) and ChAT+ axonal terminals in the granule cell layer of the flocculus (arrows in *c*) are also positive for GAD, while ChAT+ mossy fibers in the granule cell layer of the nodulus are negative for GAD (arrow in *d*). Note in panel *a* and *b*, that the BIN also contains ChAT-GAD+ neurons (arrow heads in *a*, *b*). Also note that both ChAT+ and ChAT- BIN neurons are only sparsely covered by GAD+ nerve terminals (thin arrow in *b''*), which differs from deep cerebellar nuclear neurons whose cell bodies and proximal dendrites are densely innervated by GAD+ synaptic terminals (*e*). Note in *c'* that ChAT+GAD+ boutons (arrows) complement ChAT-GAD+ boutons (arrow heads) in the same glomerulus.

f, g: ChAT/mGluR2 double staining (*f*) and ChAT/mGluR2/VIAAT triple staining (*g*), shows that ChAT+ fibers and boutons (arrows in *f* and *g*) are always mGluR2-, and complement mGluR2+ boutons (arrow heads in *f* and *g*) in glomeruli in the floccular granule cell layer. Both ChAT+ and mGluR2+ boutons stain positive for VIAAT. In *g*, also note the presence of ChAT-mGluR2-VIAAT+ nerve terminals (double-headed arrow).

h: Serial confocal optical sections and 3D-reconstructions of an exemplary mossy fiber ending labeled by VGluT1 that is surrounded by ChAT+VIAAT+ and ChAT-VIAAT+ nerve endings.

i, j: High magnifications of ChAT/calretinin (CR) double staining in the granule cell layer of the ventral paraflocculus showing examples of CR+ UBCs with a substantial number of ChAT+ nerve endings surrounding their brush-like dendritic arbor (arrows in *i*) as well as CR+ UBCs with virtually no ChAT+ nerve endings surrounding the 'brush' (arrow heads in *j*).

Scale bars: *a*, 100 μm ; *b-f*, 25 μm ; *g*, 10 μm ; *h*, 5 μm ; *i*, 20 μm .

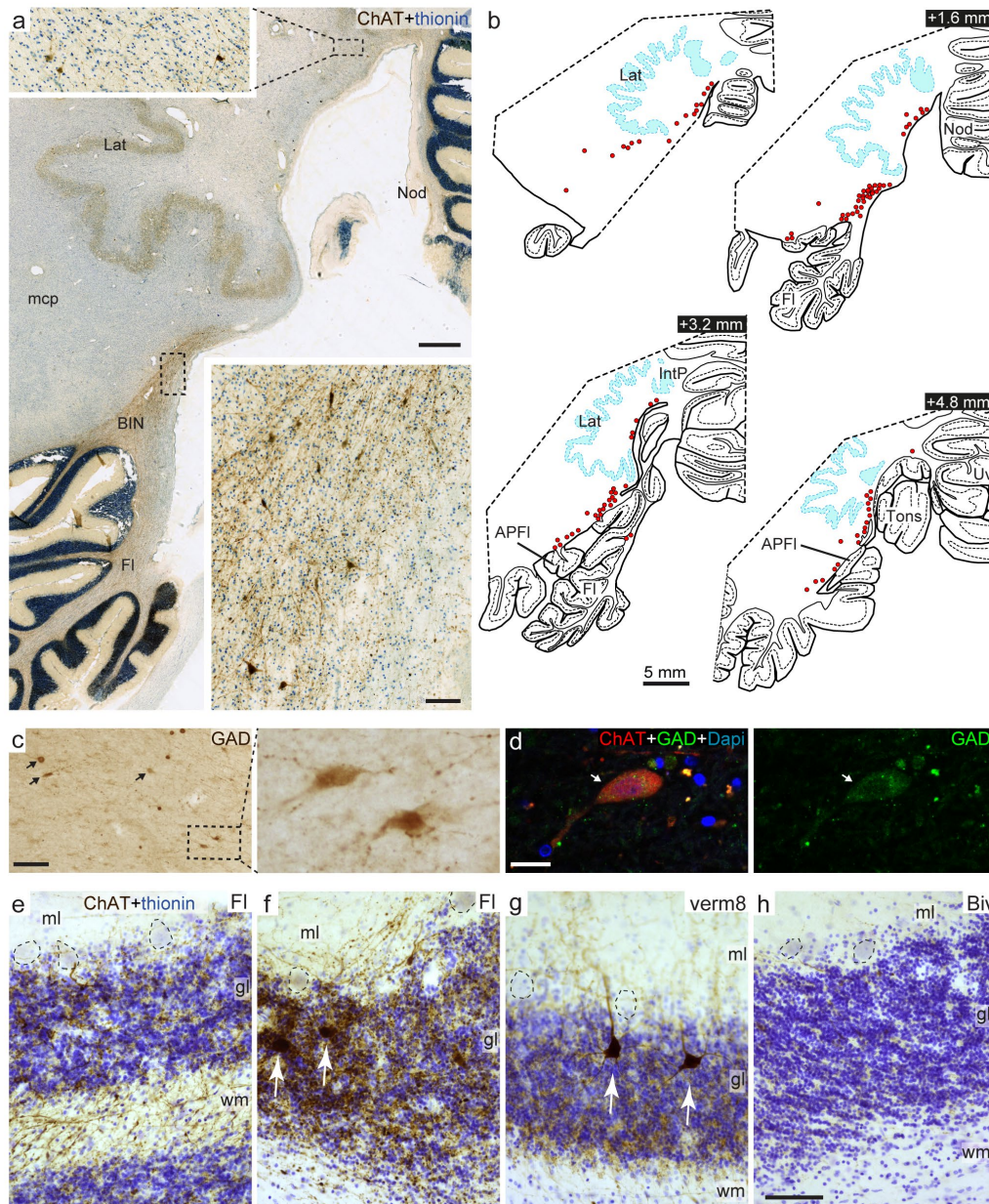


Figure 3. ChAT-staining outlines the BIN in human cerebellum

a: Low- and high-power (inserts) photomicrographs of ChAT immunoperoxidase diaminobenzidine (DAB) stained coronal sections of human cerebellum showing a cluster of ChAT stained neurons in the white matter between the flocculus and the lateral cerebellar nucleus (Lat) that is reminiscent of the BIN in macaque.

b: Plots of ChAT+ neurons in the basal white matter of human cerebellum. ChAT+ neurons are most abundant in the white matter, extending from the ventrolateral aspect of the lateral cerebellar nucleus (Lat) to the peduncles of the flocculus and the accessory paraflocculus (APFI).

c, d: GAD immunoperoxidase-DAB (*c*) and immunofluorescent (*d*) staining of BIN neurons (arrows in *c* and *d*). The BIN neuron shown in *d* (arrow) also is ChAT+.

e-h: ChAT immunoperoxidase-DAB staining reveals variable densities of ChAT+ beaded fibers in the granule cell layer of different lobules that correlate with the presence of ChAT+ Golgi cells: in the flocculus, high densities of ChAT+ fibers occurs in parts of the granule cell layer containing ChAT+ Golgi cells (white arrows in *f, g*), while moderate levels of ChAT+ fibers occur in parts without ChAT+ Golgi cells (*e*). Moderate levels of ChAT+ fibers also occur in lobules with ChAT+ Golgi cells, e.g. lobule 8 of the vermis (*g*). Lobules of the hemispheres with no ChAT+ Golgi cells do not show ChAT+ fibers (*h*, biventral lobule).

Scale bars: *a*, 1 mm (overview) and 100 μ m (insert); *c* and *h*, 100 μ m (also for *e-g*); *d*, 20 μ m.

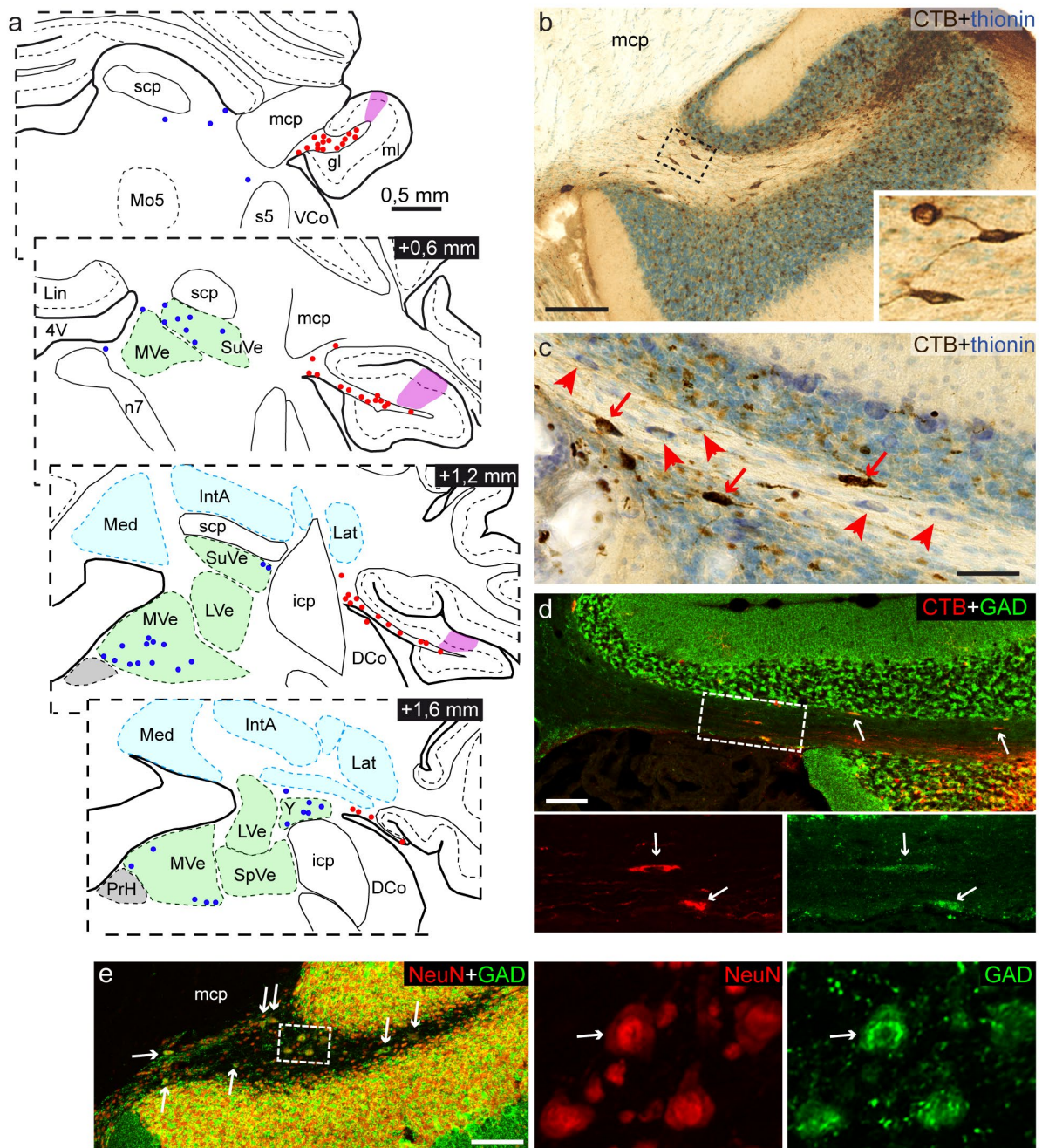


Figure 4. BIN neurons in rat

a-c: Plot (a) and photomicrographs (b, c) of retrogradely cholera toxin β subunit (CTB) labeled BIN neurons (red dots in a; red arrows in c) following a small CTB injection in the flocculus (purple area in a); sections and plots are from rat 836 described in ⁴¹. Note that retrogradely CTB labeled neurons also occur in the vestibular nuclei (blue dots in a). Arrowheads in c point to unlabeled BIN neurons.

d: Double labelling confocal immunofluorescence for GAD and CTB shows that retrogradely CTB labeled BIN neurons (arrows) are GAD+.

e: Double labelling confocal immunofluorescence for GAD and NeuN shows that GAD+ BIN neurons in the rat floccular white matter (arrows) are NeuN+.

Scale bars: b, d and e 100 μ m; c, 50 μ m.

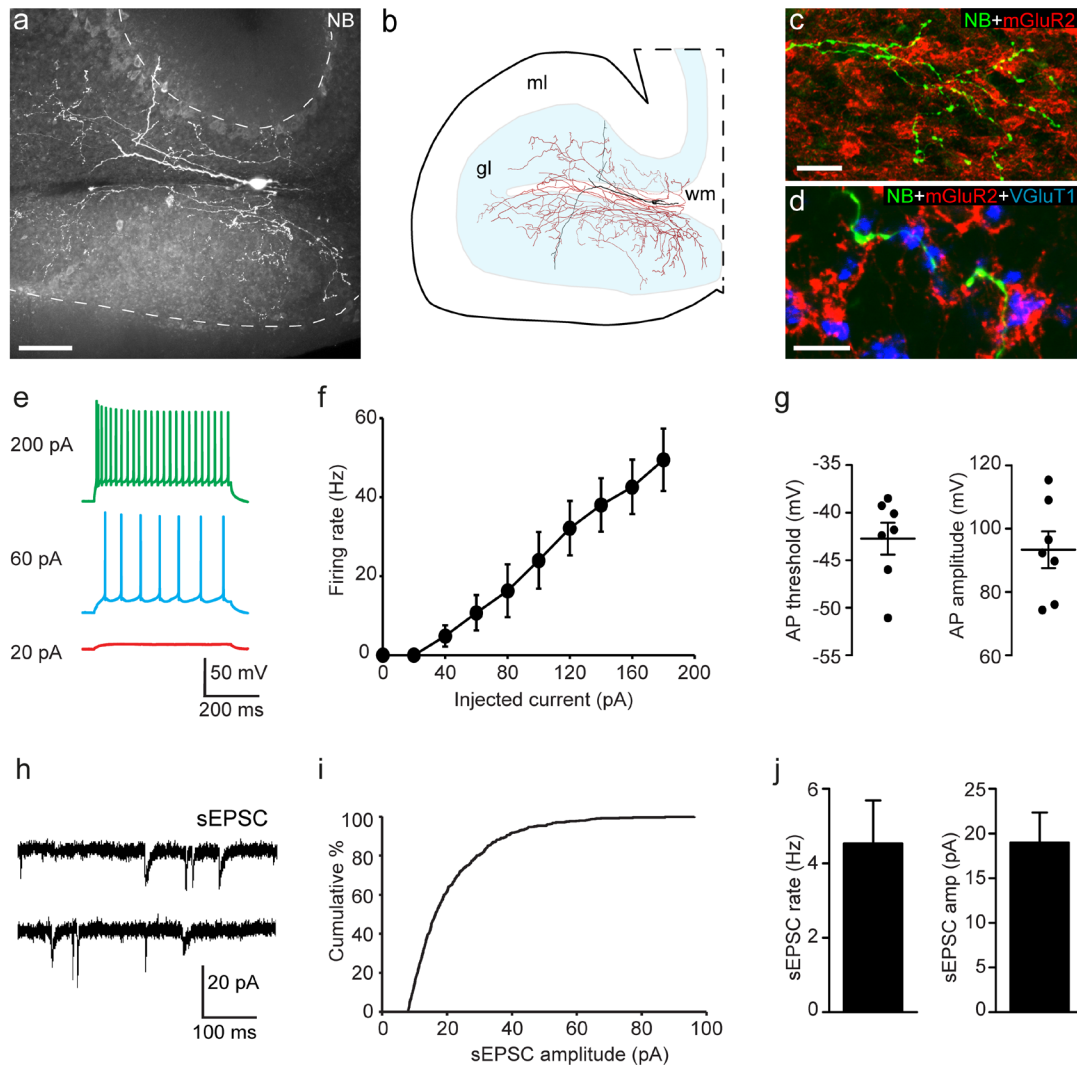


Figure 5. Evoked action potentials and spontaneous EPSC in rat BIN neurons

a-d: Example of a recorded BIN neuron filled with 1% neurobiotin (NB) visualized with A488-streptavidin. NB filling reveals an extensive axonal tree, and dendritic branches that may extend in the granule cell layer. Axonal branches are mGluR2- and contact multiple glomeruli characterized by the presence of VGLUT1+ mossy fiber endings and mGluR2+ Golgi cell axons (c, d). Scale bars: b, 100 μ m; c, 25 μ m; d, 10 μ m.

e: Example traces of subthreshold depolarization of and evoked action potentials with increasing depolarizing current injection.

f: Average firing rate of BIN neurons (mean \pm SE, n=7 cells) as a function of the injected current during the depolarizing step.

g: Action potential threshold and amplitudes (individual values and means \pm SE).

h-j: Example traces (h), cumulative distribution of sEPSC activity from an exemplary BIN neuron (i), and mean \pm SE of sEPSC frequencies and amplitudes (j) of recorded BIN neurons (n=6).

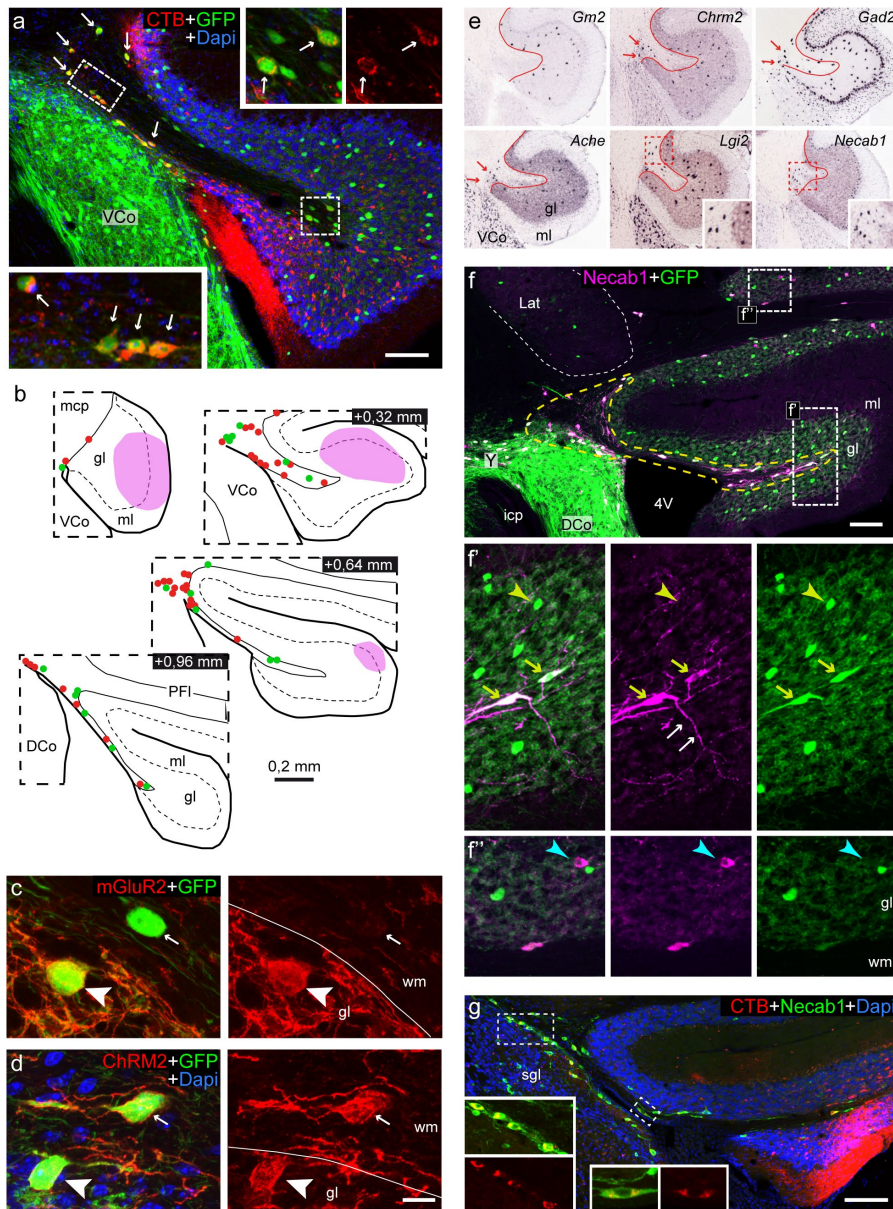


Figure 6. BIN neurons in mouse flocculus identified by retrograde CTB tracing and Necab1 immunostaining

a, b: Double labelling confocal immunofluorescent image (**a**) and plot (**b**) of CTB-labeled BIN neurons (arrows in **a**; red dots in **b**) following CTB injection in the flocculus (purple area in **b** outline the injection area) of GlyT2GFP transgenic mice (**a** is from mouse Gly1; **b** is from mouse Gly4). All retrogradely CTB labeled BIN neurons are also positive for GFP (arrows in **a**). GlyT2-GFP+ BIN neurons that are not positive for CTB are indicated by green dots in **b**. **c, d:** Confocal immunofluorescence of mGluR2 (**c**) and muscarinic M2 receptor (**d**) in the flocculus of a GlyT2GFP transgenic mouse. GlyT2+ Golgi cells in the granule cell layer (gl) stain positive for mGluR2 (arrow heads in **c**) and muscarinic M2 receptor (arrow heads in **d**), while GlyT2GFP BIN neurons are M2+ and mGluR2- (small arrows in **c** and **d**). wm, white matter. **e:** In situ hybridization image from Allan Brain Atlas showing that mGluR2 (*Gm2*) mRNA is expressed in granule cell layer (gl) but not in white matter cells of the flocculus, while muscarinic M2 receptor (*Chrm2*), GAD65 (*Gad2*), AChE and *Lgi2* mRNA occur cells in both the granule cell layer and the white matter (red arrows). *Necab1* mRNA, instead, is expressed in cells in the floccular white matter, but not in the granule cell layer. **f, g:** Confocal images of *Necab1* immunostaining in the flocculus of a GlyT2GFP mouse (**f**), and a non-transgenic mouse receiving a CTB tracer injection in the flocculus (**g**). Intense *Necab1* staining is present in GlyT2GFP+ neurons (yellow arrows in **f**) and CTB-traced BIN neurons (**g**, see inserts). Note in **f'**, that dendrites of some *Necab1*+ BIN neurons may extend in the granule cell layer (white arrows in **f'**). Also note in **f**, a population of *Necab1*+ neurons in the granule cell layer of the para-flocculus (cyan arrow head in **f'**), while no *Necab1*+ neurons occur in the granule cell layer of the flocculus (yellow arrow head in **f** points to a GlyT2GFP+ Golgi cell in the flocculus). Scale bars: **a, f** and **g**, 100 μ m; **d**, 10 μ m.

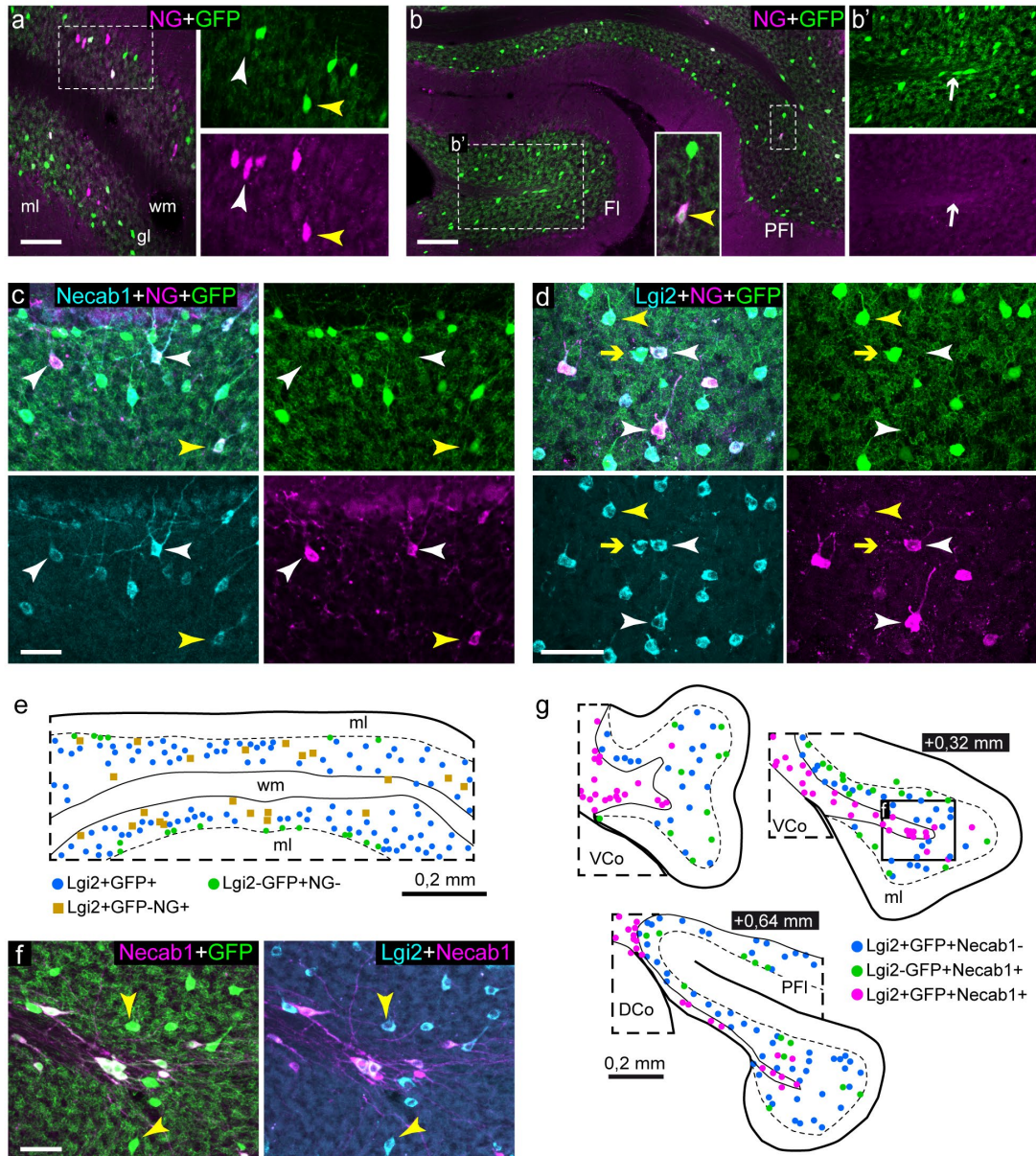


Figure 7. Absence of Necab1+ and Neurogranin+ Golgi cells in mouse flocculus

a,b: Confocal images of neurogranin-immunostaining in GlyT2GFP mouse cerebellar cortex, showing that in lobule 4-5 of the vermis (*a*) neurogranin (NG, rabbit antibody) labelling occurs in GFP- (white arrow head) and GFP+ Golgi cells (yellow arrow head), while in the flocculus (FI in *b*) there are no neurogranin+ Golgi cells. Note in flocculus, that BIN neurons (white arrow in *b'*) do not stain for neurogranin, while sporadic neurogranin+ cells can be observed in the adjacent ventral paraflocculus (PFI, yellow arrow head in insert in *b*).

c: Staining for neurogranin (mouse antibody) and Necab1 in vermis 4-5 of GlyT2GFP mouse illustrates that neurogranin and Necab1 codistribute in GFP- Golgi cells (white arrow heads), and show variable codistribution in GFP+ Golgi cells (e.g. yellow arrow head points to GlyT+neurogranin+Necab1+ cell).

d: Staining for neurogranin (rabbit antibody) and Lgi2 in vermis 4-5 of GlyT2GFP mice shows that Lgi2 is present in neurogranin+GFP- (white arrow heads), neurogranin+GFP+ (yellow arrow heads), and neurogranin-GFP+ Golgi cells (yellow arrow).

e: Plot of vermis 4-5 in coronal section of GlyT2GFP mouse stained for Lgi2 and neurogranin; the plot outlines the distribution of type 1-3 Golgi cells (blue dots, Lgi2+GFP+), type 4 Golgi cells (light brown squares, Lgi2+GFP-NG+) and Lugaro/globular cells (green dots, Lgi2+GFP-NG-). Lgi2+GFP- cells always were also positive for neurogranin.

f,g: Confocal image (*f*) and plot (*g*) illustrating the distribution of Golgi cells (Lgi2+GFP+Necab1-, yellow arrow heads in *f*, blue dots in *g*), Lugaro/globular cells (green dots, Lgi2+GFP-Necab1-), and BIN neurons (magenta dots, Lgi2+GFP+Necab1+) in coronal sections of the flocculus.

Scale bars: *a*, 100 μ m; *b*, 200 μ m; *c*, *d*, *f*, 50 μ m.

Figure 8. BIN neurons innervate granule cell dendrites in glomeruli in mouse flocculus

a-c: Injection of AAV2-CAG-eGFP virus in the white matter and the hilus of the flocculus (*a,b*) results in labelling of BIN neurons and their axons in the floccular granule cell layer (*b,c*). Co-immunostaining for VIAAT shows that GFP+ axons display VIAAT+ varicosities (white boutons, e.g. yellow arrow heads in *c*). Double-labeled GFP+VIAAT+ varicosities are intermingled with GFP-VIAAT+ boutons (magenta boutons, cyan arrow heads in *c*). *d-f:* Transmission electron microscopy of anti-GFP immunoperoxidase-DAB precipitate in the floccular granule cell layer following AAV2-CAG-eGFP infection of BIN neurons. DAB precipitate is associated with presynaptic boutons (outlined by green color coding) that form synapses (red arrows in *d*) with granule cell dendrites (Grd, blue color coding). Post-embedding anti-GABA immunogold-labeling shows that DAB+ axon terminals are also enriched in GABA (*e, f*). Mossy fiber endings and putative Golgi cell axons are coded in yellow and red, respectively.

g,h: Series of optical sections (*g*) and 3-dimensional reconstruction (*h*) of a glomerulus innervated by GFP-labeled BIN axons and labeled for mGluR2, VIAAT and VGluT1. Note that the VGluT1+ mossy fiber rosette is surrounded by GFP+mGluR2-VIAAT+ (small arrows), GFP-mGluR2+VIAAT+ (arrow heads) and single-labeled GFP-mGluR2-VIAAT+ boutons (double-headed arrow).

i: Bar graph showing the area of VIAAT+ nerve endings in floccular granule cell layer that co-distribute with GFP labeled BIN axon endings (green bars) or mGluR2 staining (red bars). Analyzed sections are from 3 mice with AAV2-CAG-GFP virus injections in the BIN showing the highest amount of BIN axonal labeling in the flocculus (mouseV2, mouseV3, mouseV5; see material and methods for details).

j,k: Exemplary confocal images (*j*) and graph (*k*) showing that in the anterior vermis more than 90% of the VIAAT+ axon endings is mGluR2+, whereas in the flocculus the proportion is 60%, as illustrated by the large proportion of single labeled VIAAT+ terminals (green boutons in upper panel in *j*).

l: Cartoon illustrating how BIN axon terminals may complement mGluR2+ Golgi axon terminals in floccular glomeruli.

Scale bars: *b*, 250 μ m; *c*, 5 μ m; *d-f*, 500 nm; *g*, 2 μ m; *j*, 50 μ m.

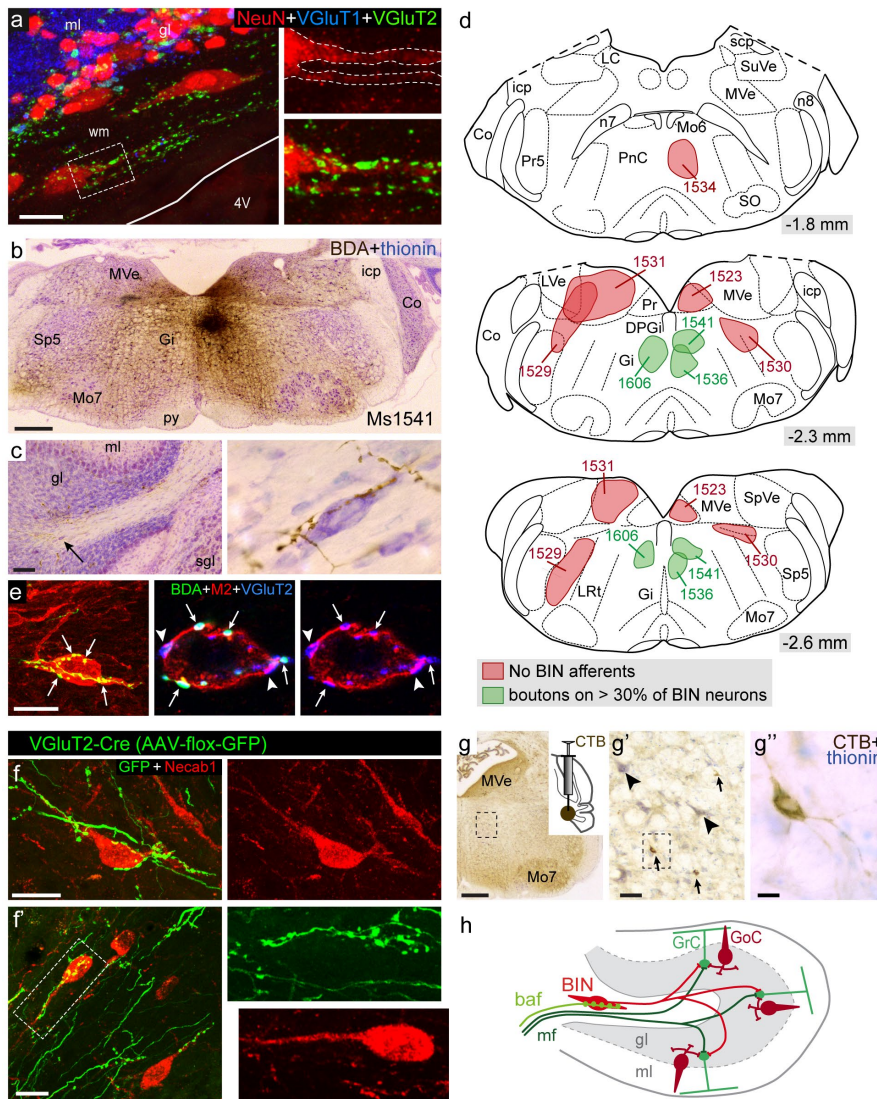


Figure 9. BIN neurons are innervated by VGlut2+ axons arising in the medial medullary reticular formation

a: Confocal image of NeuN/VGlut1/VGlut2 triple staining in rat flocculus showing that cell body and proximal dendrites of BIN neurons are covered by VGlut2+ axon terminals.

b-d: Representative images of injection spot (**b**) and anterogradely-labeled fibers in the floccular white matter (**c**), and map of injection area's of selected BDA (biotinylated dextran amine) anterograde tracing experiments (**d**) showing that injections targeting the gigantocellular reticular nucleus (Gi) in the rostral medullary reticular formation result in labelling of fibers contacting BIN neurons. Injections in surrounding areas (indicated in red) did not result in labeling of fibers innervating BIN neurons, but to variable extent produced labeling of mossy fibers innervating floccular granule cell layer.

e: Maximal projection (left panel, total thickness = 12 μ m) and single optical section (middle and right panel, $z = 1 \mu$ m) illustrating a BDA-labeled fiber from the Gi innervating a BIN neuron (labeled with anti-muscarinic M2 receptor antibody). Arrows in maximal projection and single optical section point to the same nerve endings. Co-staining for VGlut2+ shows that nerve endings from labeled fibers are VGlut2+, and that this cell is innervated by additional VGlut2+ nerve endings from non-labeled fibers (arrow heads).

f: Maximal projections of exemplary BIN neurons identified by (Necab1-immunostaining) innervated by GFP+-beaded fibers following AAV-floxed-GFP injection in the Gi of VGlut2-Cre mouse.

g: Immunoperoxidase-DAB staining of retrogradely labeled medium-sized neurons (arrows in **g'**) in the Gi following CTB injection in hilus of the flocculus. Note that the large Gi neurons (arrow heads) are not labeled for CTB.

h: Schematic representation of BIN neurons and glutamatergic BIN afferent fibers (**baf**) from the Gi in the floccular circuitry.

Scale bars: **a** and **f**, 20 μ m; **b** and **g**, 500 μ m; **c**, 100 μ m; **d** and **g''**, 10 μ m; **g'**, 50 μ m.

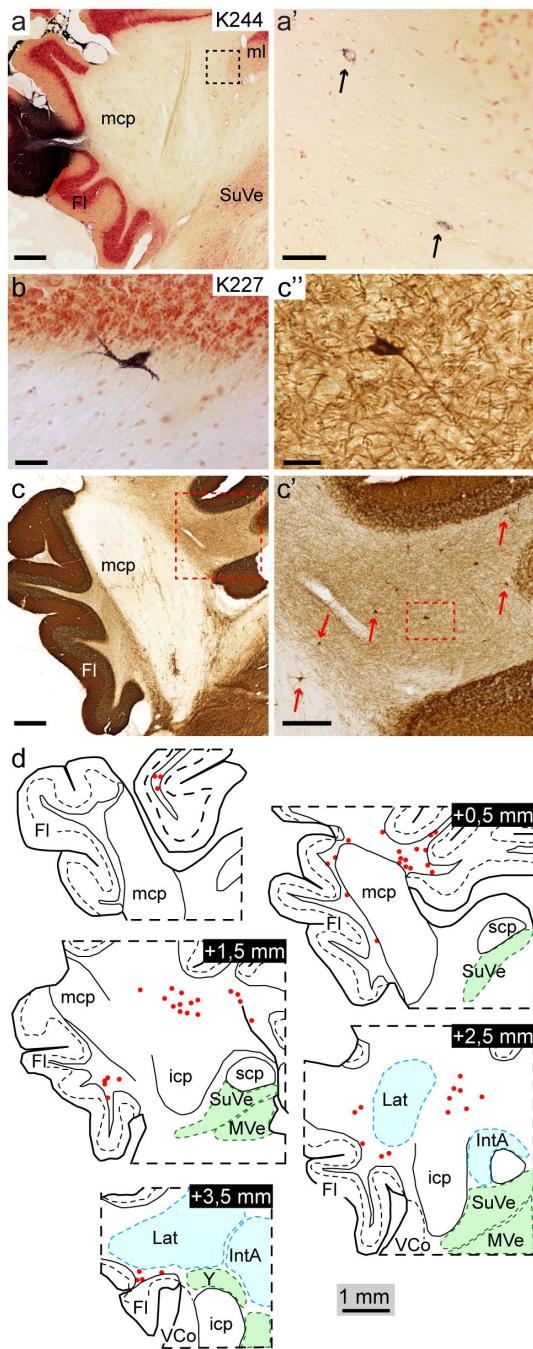


Figure 10. BIN neurons in rabbit

a, b: Low- (a) and high-magnification photomicrographs (a', b) illustrating retrogradely-labeled neurons in the white matter between the medial cerebellar peduncle (mcp) and the anterior vermis (arrows in a', b) following WGA-HRP injection in the rabbit flocculus (a). Images are from experimental animals (K244 and K227) from previously reported experiments⁵².

c, d: GAD-immunoperoxidase staining reveals GAD+ neurons in the white matter medio-caudal of the mcp, while a few GAD+ neurons are present in the floccular white matter lateral of the mcp. In the plot in d, all GAD+ cells in white areas surrounding the mcp are plotted. The distribution and size of GAD+ neurons corresponded to the distribution of WGA-HRP tracing experiments.

Scale bars: a and c, 500 μ m; a', 50 μ m; b and c', 200 μ m.

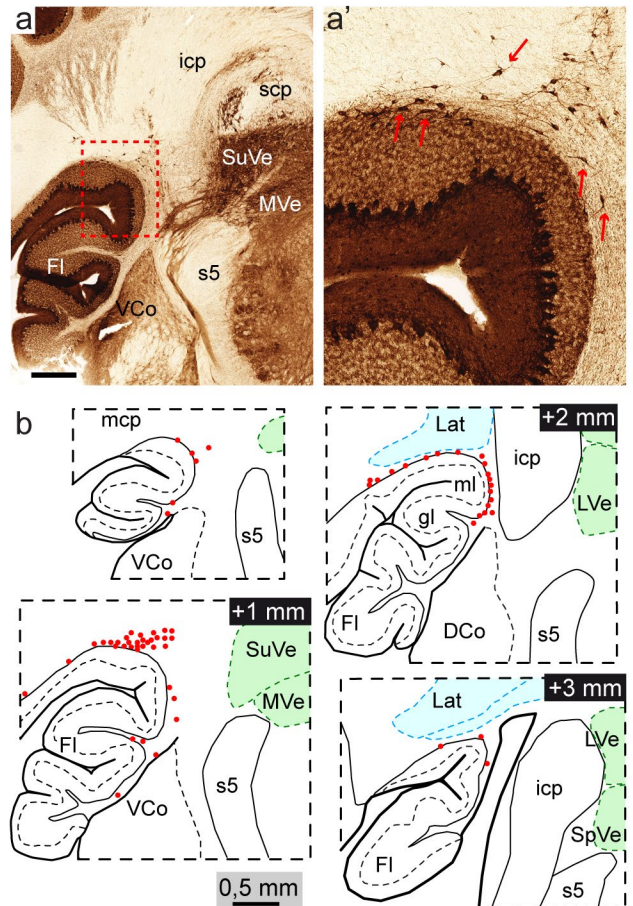


Figure 11. BIN neurons in ferret

Low-(a) and high-magnification (a') images and plots (b) of GAD-immunostaining in ferret flocculus illustrating a cluster of GAD+ neurons (red arrows in a', red dots in b) in the white matter facing the transition zone between the flocculus and the ventral paraflocculus. Scale Bar: a, 500 μ m.

CHAPTER

5.1

Modulating Modulation: Purkinje cell activity in impaired and enhanced compensatory eye movement adaptation

Bin Wu*, Thomas Koudstaal*, Haibo Zhou, Chris I De Zeeuw and Martijn Schonewille#

* these authors contributed equally

In preparation

Abstract

Identifying the neural code underlying the process of learning in the brain is one of the main challenges in neuroscience today. In cerebellar motor learning several plasticity mechanisms have been identified to contribute the adaptation of behavior, but the weight of each contributor and how these processes are integrated in neural code remains unclear. Here we recorded the activity of Purkinje cells, the output neuron of cerebellar cortex, prior to, during and directly following an eye movement training session, comparing the activity in controls to that in conditions of impaired and enhanced learning. In cell-specific mutants with impaired learning, we find that the depth of simple spike modulation is lower during training and had not increased after training, in contrast to that in controls. Conversely, when learning was pharmacologically enhanced, the depth of modulation increase was larger after, but not during, adaptation. The regularity of simple spikes was increased in the impaired mutants, and showed a larger increase under conditions of enhanced learning, suggesting a role for temporal patterns as well. These results constitute the first complete dataset on the Purkinje cell activity related to the induction and the expression of motor learning, and emphasize the relevance of both rate and temporal coding in cerebellar functioning.

Introduction

Learning in the central nervous system requires persistent changes at the cellular level that, when integrated at the network level, produce the acquired response. In cerebellar sensorimotor adaptation this can constitute two distinctly different adaptations: introduction of a novel, conditioned response to an unrelated, existing stimulus, or attuning the size or amplitude of an existing response to altered requirements. Timing-dependent conditioning is typically linked to a decrease in Purkinje cell simple spikes firing rate¹⁻⁴. In contrast, the modification of an existing response can occur in two directions, e.g. by in- or decreasing the size of an arm or eye movement^{1,5,6}. The underlying alterations in Purkinje cell activity for this type of learned modification of behavior is much less understood.

Several decades of intense search for cellular mechanisms, at first largely devoted to long-term depression (LTD) of the parallel fiber to Purkinje cell synapse⁷⁻⁹, have revealed that the majority, if not all, of the synapses in the cerebellar cortex show plasticity^{2,10-12}, and thus could potentially be involved in cerebellar learning. Substantially less is known about the changes of cellular activity in vivo during the cerebellum-dependent trainings and the expression of newly learned behavior. As the Purkinje cell is exclusively responsible for the output of the cerebellar cortex, all adaptive changes of the cortex should be present in its spiking behavior. In eyeblink conditioning the timed blink of the eyelid in response to a light or tone correlates with a timed decrease in simple spike firing in Purkinje cells that are responsive to the unconditioned stimulus, an air-puff to the cornea^{2,8}. A, similarly timing-based, smooth pursuit learning task also requires the depression of simple spike firing⁴.

In parallel to these event- or timing-related learning paradigms, the cerebellum is also required for adjusting the size of a movement, e.g. the size of a leg movement or the amplitude of an eye movement¹³. The alternative nature of these types of learning requires simple spike activity to change in two directions, to facilitate increases and decreases in learning^{6,13}. However, our current understanding of the link between spiking activity and behavior is incomplete; most studies are descriptive, evaluating the correlation in 'control' conditions. Artificially increasing simple or complex spike rate using optogenetic approaches confirmed that Purkinje cells control the size or amplitude of eye movements and that selectively manipulating their activity is sufficient to adapt eye movements¹⁴. Due to the artificial nature, and the absence of simultaneous recordings of Purkinje cell spiking behavior during the induction and expression of learned behavior, the exact spatiotemporal coding of the Purkinje cells, required for the adaptation of behavior, currently remains an enigma.

Here, we follow an alternative approach by comparing Purkinje cell activity before, during and after VOR adaptation under normal conditions to those obtained under conditions of enhanced and of impaired learning. We demonstrate that selectively in relation to an adaptation paradigm, the magnitude of the change in simple spike activity is directly proportional to that of the learned change in eye movement amplitude. In addition, we identify the rate, not the temporal pattern, of simple spike activity as the predominant factor controlling the learning. This bidirectional correlation between simple spike activity and the adapted, but not the baseline, eye movements reveals the near linear correlation between Purkinje cell activity and motor learning.

Results

The cerebellum is an 'online' structure, actively participating in all ongoing movements. To test the possible contribution of Purkinje cell activity to processing of visual and vestibular information, we studied behavioral and cellular responses in control mice in comparison to one mutant mouse model, *L7cre::GABRG2^{lox/lox}* mice, also known as *PC-Δγ2*. *PC-Δγ2* mutants are characterized by the loss of phasic synaptic inhibition from molecular layer interneurons and consequential reduction in excitatory input due to the ablation of the $\gamma 2$ subunit of the GABA_A-receptor in PCs¹⁵. Loss of GABA_A-receptor affects the activity of Purkinje cells and result in impaired VOR adaptation, allowing a direct comparison of the Purkinje cell activities correlating with learning to those that are insufficient to facilitate an adaptation of the behavioral response.

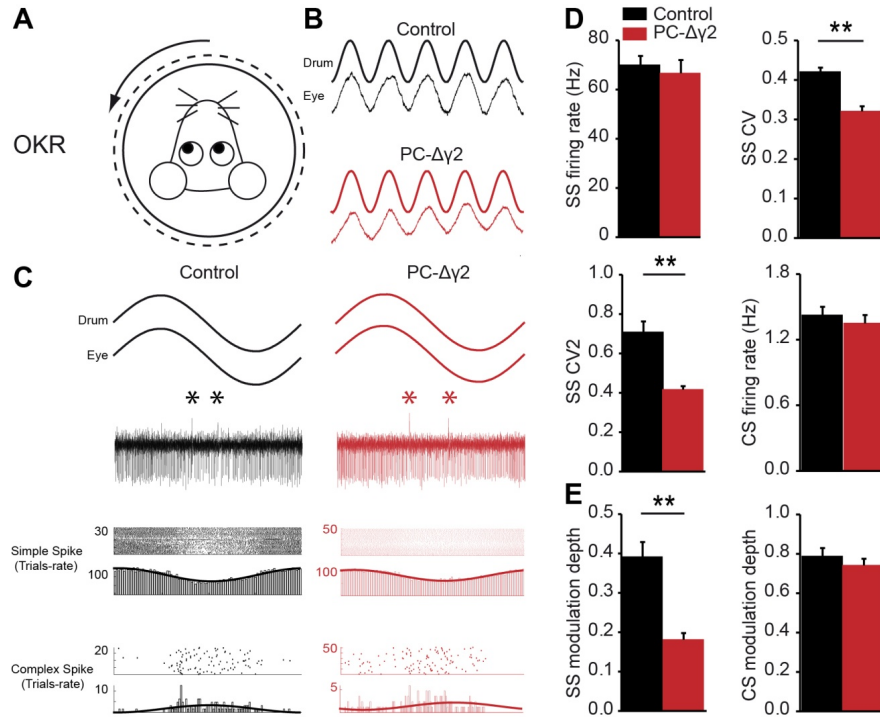


Figure 1. *PC-Δγ2* mice show reduced simple spike modulation depth and increased regularity in response to optokinetic stimulation. A, Schematic drawing of the optokinetic reflex (OKR). B, Example traces of sinusoidal drum stimulation and eye movements of a control (black) and a *PC-Δγ2* (red) mouse. C, Representative traces of vertical-axis (VA) Purkinje cells in response to optokinetic stimulation. Asterisks mark the occurrence of a complex spikes. D, Although both the simple spike and complex spike firing rate did not show difference between control and mutant mice, the simple spikes regularity (CV and CV2) is significantly higher in *PC-Δγ2* mice compared to control group. E, The simple spike modulation depth of *PC-Δγ2* mice is strikingly lower than controls, and the complex spike modulation depth did not differ between the two groups. * $P < 0.05$, ** $P < 0.01$.

Reduced input to Purkinje cells affects sensory stimulation evoked responses.

To do so, we first subjected *PC-Δγ2* and control mice to visual stimulation (OKR) to evoke reflexive responses known as basic compensatory eye movements (Figure 1A, B). Next, we performed extracellular *in vivo* Purkinje cell recordings from single-unit Purkinje cells, identified by the presence of complex spikes and the persistent pause in simple spike following each complex spike (Figure 1C). We included only floccular Purkinje cells that responded optimally to vertical axis stimulation (VA PCs). Average firing rates of simple and complex spikes during OKR were not affected by the mutations, but the impaired inhibitory input caused by mutation did result in more regular simple spikes activity over the entire recording (CV) and also on a spike-to-spike basis (mean CV2, see Methods)(Figure 1D). Complex spike are caused by climbing fibers from the inferior olive, and their activity is generally considered to relate to the error signals driven by retinal slip¹⁶. Spiking probability increases during temporo-nasal, or contraversive, movement of the visual stimulus in controls, and mutants (Figure 1C). The depth of complex spike modulation, the fitted amplitude divided by basal rate of the fitted histogram, did not differ between controls and mutants ($t = 0.795$, $p = 0.430$), suggesting that the mutation had no effect on this error signal (Figure 1E). In *PC-Δγ2* Purkinje cells, the mutation results in an even lower simple spike depth of modulation (Figure 1E, $t = 4.303$, $p < 0.001$). Thus, mutations effectively decreasing the levels of inhibitory input to Purkinje cells lower the depth of modulation during visually-evoked eye movements, either by impairing the range in firing frequencies.

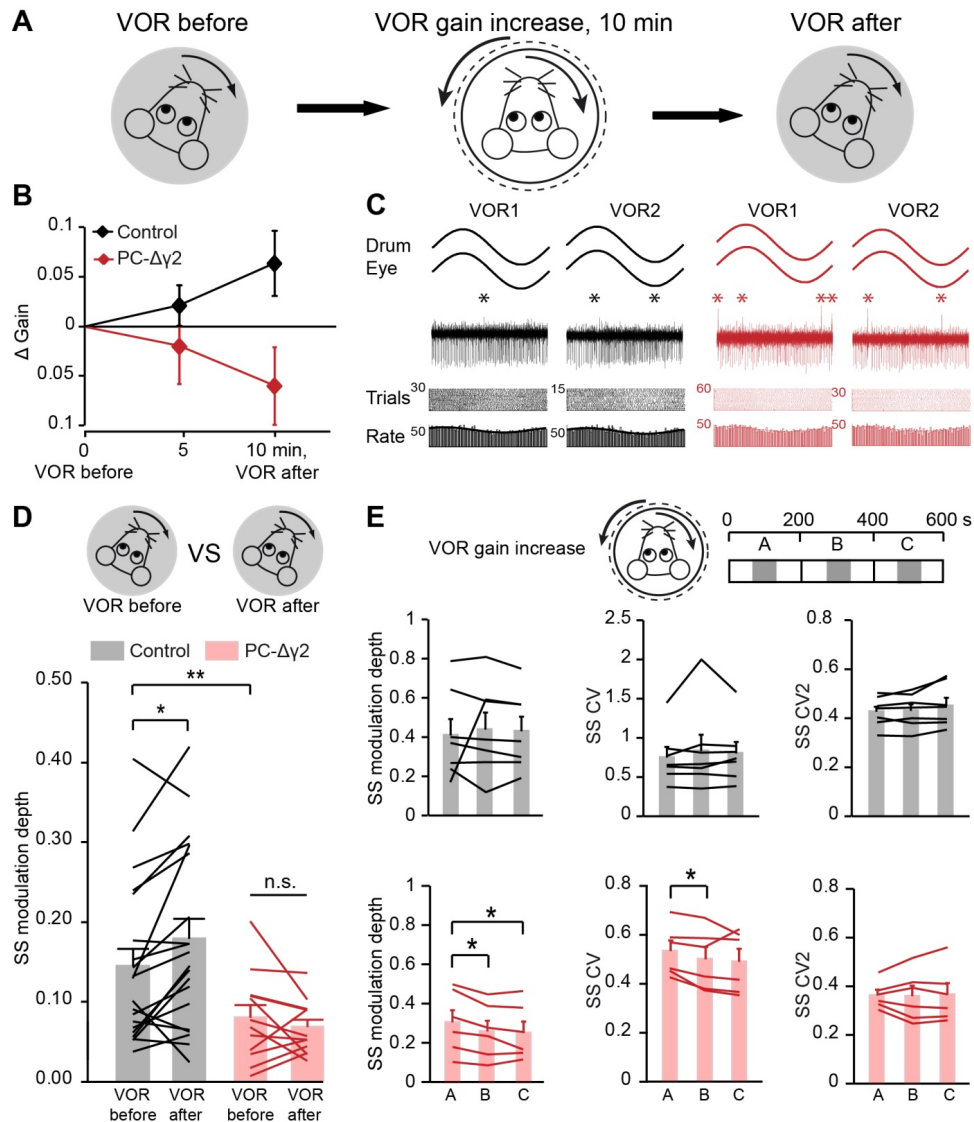


Figure 2. PC- $\Delta\gamma 2$ mice show impaired learning and reduced simple spike modulation depth. A, Schematic drawing depicting the VOR gain increase training paradigm. Purkinje cell activity was recorded before (VOR before, vestibular stimulation), during (VOR gain increase, vestibular and visual stimulation) and after (VOR after, vestibular stimulation) VOR gain increase training. B, Changes in VOR gain between before and after training. C, Representative traces of Purkinje cell activity in response to vestibular stimulation before and after gain increase training (Control: black, PC- $\Delta\gamma 2$: red). D, The simple spike modulation depth was significantly increased in control, but not in PC- $\Delta\gamma 2$ mice. E, Purkinje cell activities during 10 minutes VOR gain increase training (A: 0-200 s, B: 200-400 s, C: 400-600 s). PC- $\Delta\gamma 2$ mice showed reduced simple spike modulation depth and CV during training. * $P < 0.05$, ** $P < 0.01$

Reduced depth of modulation correlates with impaired VOR gain adaptation

To evaluate the role of Purkinje cell activity during a learning paradigm, we subsequently subjected mice to VOR gain increase training. The response to vestibular input can be altered by mismatched visual input, e.g. by rotating the visual input out-of-phase, provoking the mice to make larger eye movements (Figure 2A). We previously showed that motor learning was severely affected in PC- $\Delta\gamma 2$ mice, suggesting that VOR gain increase probably is affected too. We shortened the standard induction protocol, as control mice already show a significant, reproducible increase already after 10 min of gain increase training, and this increased the success rate of continuous Purkinje cell recordings for the complete training session

during combinations of visual and/or vestibular stimulations (Figure 2A). In control mice 10 min of training, in light, had increased the VOR, in dark, larger than that observed in *PC-Δγ2* mice ($t = 2.495$, $p = 0.019$).

Vestibular sensory input alone also results in modulation of Purkinje cells activity, albeit more subtle than during OKR stimulation. As in OKR, the simple spikes activity changes correlate with the direction of the eye movements, with increased activity during ipsiversive motion, reciprocal to complex spike activity (Figure 2C). Compared to the activity of Purkinje cells of control mice, the modulation in cells of *PC-Δγ2* mice was again smaller ($t = 3.305$, $p = 0.002$) (Figure 2D). In control mice, 10 min of mismatched, out-of-phase visual stimulation that increased the VOR gain, also resulted in an increased depth of modulation related to vestibular input. In contrast, 10 min of exposure to the same training protocol did not affect the gain or the depth modulation of VOR in Purkinje cells of *PC-Δγ2* mice.

Based on their reduced depth of modulation during visually evoked OKR, one could imagine that the training stimulation, also in the light, also evokes lower depths of modulation in one of the, or both, mutant lines. Analyzing Purkinje cell activity at three time points during the training confirmed this assumption (Figure 2E). The lower depth of modulation during the training suggest that the reduced inhibitory input to Purkinje cells affects the dynamic range of Purkinje cells, and ultimately hampers the ability of the cerebellum to adapt. Alternatively, or additionally, the spatiotemporal patterns of Purkinje cell activity could also contribute to the acquisition of adapted behavior¹⁷. *PC-Δγ2* mice have an increased regularity of Purkinje cell simple spike intervals during visual stimulation alone^{15,18}, and the temporal pattern of their inhibition can be very relevant to their downstream target neurons¹⁹. However, simple spike regularity did not differ from controls in *PC-Δγ2* mice during the training, and did not change between the VOR before and that after learning (Figure 2E), suggesting it is not related to the expression of learned behavior, but could be relevant for the induction of changes.

In summary, the inability of *PC-Δγ2* mice with reduced Purkinje cell input to adapt correlates with an impaired depth of modulation during the induction of learning. The expression of learning also is restricted in correlation to the depth of Purkinje modulation, suggesting firing rate is here the neural substrate for learning.

T-588 rescues motor learning deficits most effectively in *PC-Δγ2* mutant mice.

The ability to manipulate known cellular mechanisms using genetics or pharmacology is instrumental to developing an understanding of any form of learning. In cerebellar learning, as in most forms of learning, the majority of effective genetic or pharmacological interventions impair the ability to learn^{7,13}. However, manipulations that enhance the learning speed or capabilities could be equally or even more informative. We have previously demonstrated that administration of the substance T-588, a blocker of PF-PC LTD²⁰, does not impair VOR adaptation²¹. Over a shortened, 4-day VOR phase reversal adaptation paradigm, C57BL/6 control mice that received T-588 (10 mg/kg) every day before training adapted significantly faster than controls (Figure 3B). Interestingly, the first day of decrease did not cause any significant differences in gain or phase. In contrast, the phase reversal induction training on the second day resulted in near complete flip of the phase to 180° in mice injected with T-588, a significantly larger change than that observed in controls. Control mice were able to largely reverse their phase over the course of the following days, but at a slower pace, resulting in lower phase and lower gain values. The finding that genetically ablating PF-PD LTD did not enhance, or impair, VOR phase reversal, implicates that the augmenting effects of T-588 are independent of its LTD-blocking capacity. This assumption was confirmed as the phase reversal of *GluR2Δ7* mice, in which LTD has been ablated by truncation of the *GluR2* subunit of the AMPA receptor⁹, was enhanced in a manner similar to that in control mice by the injection of T-588 (Figure 3C). In contrast, in mice with impaired PF-PC LTD and intrinsic plasticity due to Purkinje cell specific deletion of *PP2B*, or calcineurin ('L7-PP2B')⁶, injection of T-588 did not improve phase reversal, except for a small improvement in gain decrease (Figure 3D). The relative absence of improvement in these mice could be interpreted as a sign that the beneficiary effects of T-588 are related to, or even dependent upon, the synaptic or cell intrinsic potentiation of Purkinje cells. This would imply that in *PC-Δγ2* mice, which have no phasic inhibitory input to Purkinje cells, while PF-PC LTP is normal¹⁵,

the impaired VOR phase reversal could benefit from the presence of T-588. This prediction was confirmed, as injection of T-588 in *PC-Δγ2* was able to rescue the VOR phase reversal, to levels comparable to those observed in control mice without T-588 (Figure 3E). In addition to, or contrary to, plasticity mechanisms, impaired depth of simple spike modulation in *PC-Δγ2* mice (Figure 2D) could also be an important factor. In short, the augmenting effects of T-588 on motor learning are independent of PF-PF LTD, but appear to be related to PF-PC LTP and the depth of simple spike modulation. The rapid emergence of the T-588-dependent differences in control mice suggest that T-588 may enhance learning in short-term adaptation experiments too.

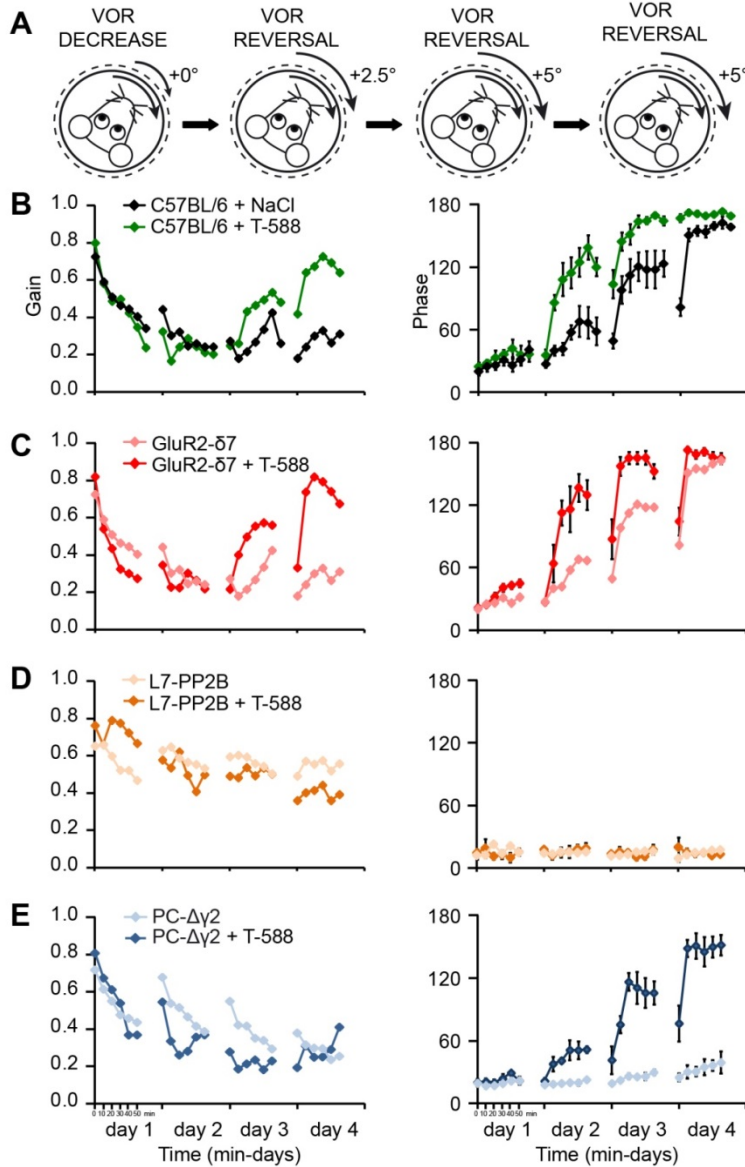


Figure 3. T-588 increases the long-term VOR adaptation. A, Schematic drawing depicting the phase-reversal training paradigm. B, Changes in VOR gain and phase following VOR phase reversal adaptation. Mice injected with T-588 reversed their VOR phase significantly faster than control mice injected with vehicle. C, Even in *GluR2-d7* mutant mice, in which PF-PC LTD is blocked due to a truncation of the related AMPA-receptor subunit, the VOR phase reversal is enhanced, suggesting that the beneficial effects of T-588 are independent of its ability to block LTD. D, T-588 did not affect the VOR phase reversal capabilities of L7-PP2B mice, suggesting that the absence of potentiation prevents the positive effects of T-588. E, The injection of T-588 is able to, at least partially, rescue the

learning deficits in PC- $\Delta\gamma 2$, suggesting that T-588 can compensate for deficits related to modulation depth or regularity.

Pharmacologically augmented learning correlates with changes in Purkinje cell modulation

To test the potential effects on short-term learning, we injected mice with T-588 and subjected them to the same short VOR gain increase training. Here too, the presence of T-588 results in larger adaptive change in control mice (Figure 4A). To identify the underlying cellular changes related to this improved learning behavior, we analyzed Purkinje cells activity in mice injected with T-588. Basic properties such as simple and complex spike firing rates or simple spike regularity were not affected in a group of random floccular and non-floccular Purkinje cells (Figure 4B). Differences became apparent with the introduction of sensory input, as simple spikes, but not complex spikes, in VA PCs had a larger depth of modulation in response to visual input (Figure 4C-D). In addition, Purkinje cells in the presence of T-588 during OKR have a higher CV, but no effect on CV2, suggesting that the higher CV is the result of the strong increase of ~50% in modulation depth.

In short, T-588, known to enhance learning in different VOR adaptation protocols, selectively increases simple spike modulation depth by deepening the troughs.

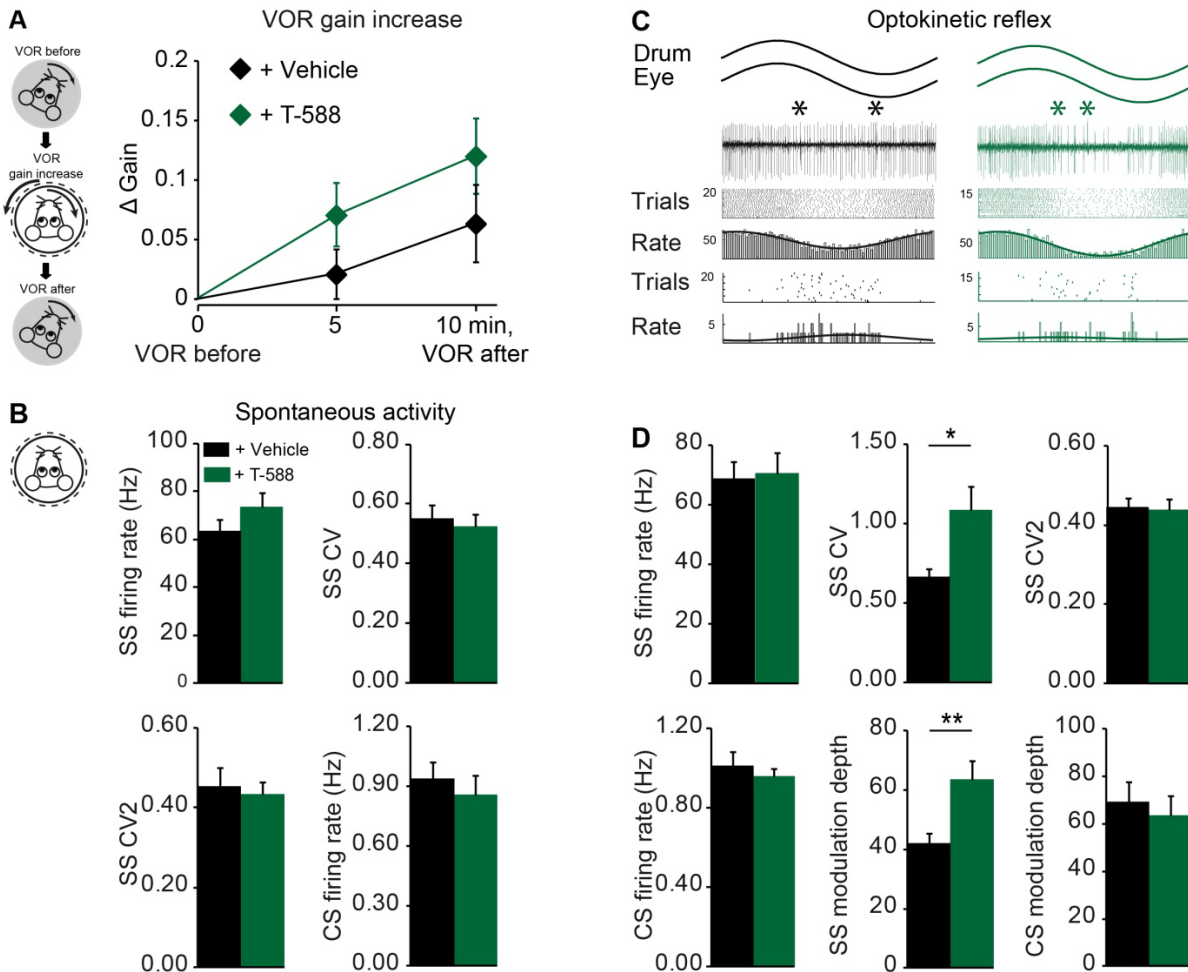


Figure 4, T-588 increases simple spike modulation depth and reduced simple spike regularity in response to optokinetic stimulation. A, T-588 increased the VOR gain. B, The spontaneous activities of purkinje cells, in the absence of sensory input, were not affected by T-588 injection. C, Representative traces of purkinje cell activity in response to optokinetic stimulation (Vehicle: black, T-588: green). D, Simple spike CV and modulation depth, not the firing rate of simple spikes and complex spikes, increased after T-588 injection. * $P < 0.05$, ** $P < 0.01$.

Enhanced learning in VOR gain increase correlates with changes in rate and temporal patterns.

Next, we made use of the opportunity to perform a preliminary analysis of Purkinje cell activity in conditions of normal, impaired and enhanced induction and expression of motor learning, a rare virtue. When subjecting mice to vestibular input, the firing rates and local regularity of the VA Purkinje cells appear not affected by the presence of T-588 (Figure 5A). In contrast, during vestibular input in the dark (VOR) T-588 also causes a deeper modulation of simple spikes (Figure 5B), which is similar to the response to visual stimulation. Interestingly, this deeper modulation was not observed during the training session when visual and vestibular inputs are combined (Figure 5D). As both types of input result an increase in simple spike rate during ipsiversive and decrease during contraversive eye movements, this suggest the possibility of a capping effect in modulation depth. None of the other parameters appeared to be affected either, which could indicate that other phenomena, including e.g. plasticity mechanisms, that are outside our acquisition possibilities create the difference in learning outcome. Purkinje cell activity during VOR, after the induction of gain increase, changed too. Concomitant with the larger increase in gain, the change in depth of modulation is also significantly larger in the presence of T-588 compared to that in controls (Figure 5C, E). In addition to this correlation with a change in rate, the CV and CV2 also increase as result of the learning in the presence of T-588, whereas they are virtually unaltered in controls (Figure 5C).

Overall, despite the absence of a difference during the actual training session, depth of modulation is the parameter that most consistently correlates with the behavioral change after learning. The increase in CV with T-588 can, as in OKR, be explained by the deeper modulation, but the increase in CV2 suggests that the inhibitory input is more pronounced after learning.

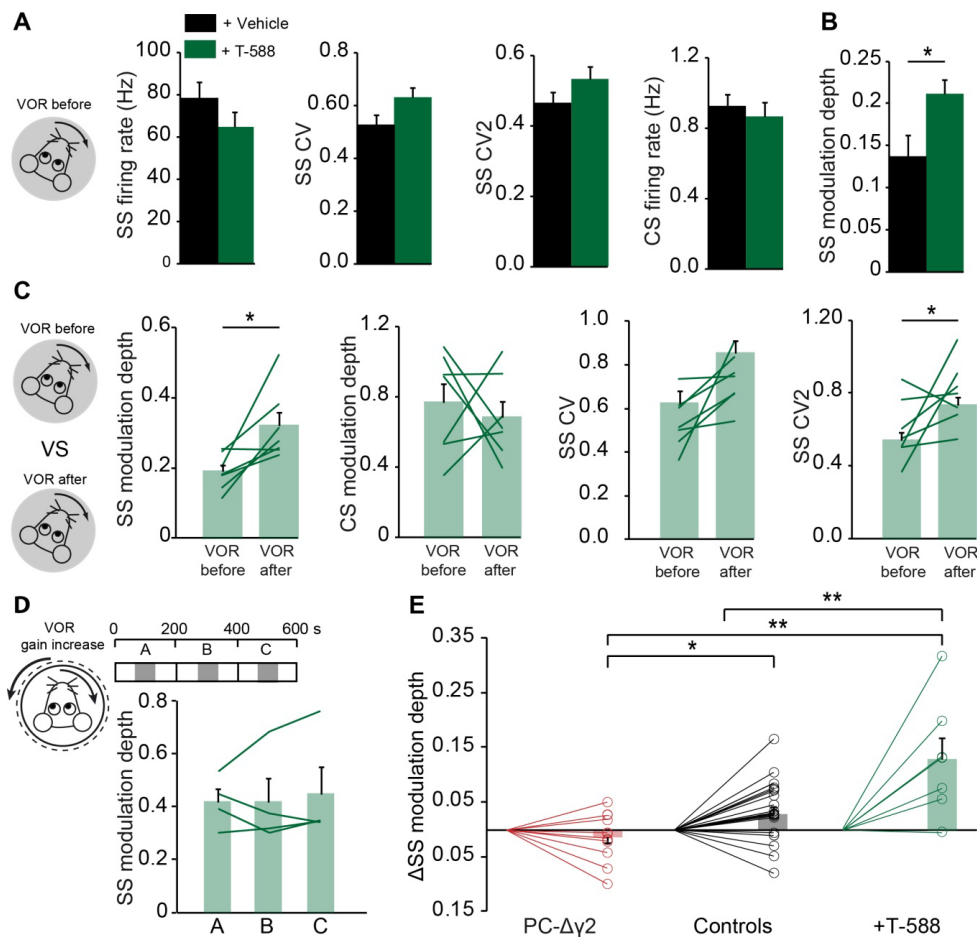


Figure 5, Enhanced learning correlates with increased simple spike modulation depth and reduced simple spike regularity. A, B, T-588 did not change the basic firing properties of purkinje cells, but increased the simple spike modulation depth in response to vestibular stimulation. C, Comparisons Purkinje cell activity before and after VOR gain increase training revealed that T-588 significantly increased the simple spike modulation depth and CV2, whereas complex spike modulation depth was not affected. D, Simple spike modulation depth did not change during VOR gain increase training. E, Changes of simple spike modulation depth in conditions of normal (control), impaired (PC- $\Delta\gamma 2$) and enhanced (+T-588) induction and expression of motor learning. * $P < 0.05$, ** $P < 0.01$.

Discussion

This study is the first to evaluate the Purkinje cell activity that is related to, and arguably responsible for, cerebellar motor learning, under conditions of impaired and enhanced motor learning and under normal circumstances. We show that differences in Purkinje cell simple spike rate and temporal pattern can be present without a direct impact on motor performance, but that there is a consistent correlation between the change in movement amplitude and the change in simple spike depth of modulation. However, a role for the temporal patterns of simple spikes cannot completely be excluded as regularity is increased, by default, in the mutant mice with impaired motor learning, and was decreased after learning in the enhanced VOR response of mice injected with T-588.

The code underlying cerebellar learning.

In recent years several studies have address the question of what cerebellar code, in term of cerebellar zone specific Purkinje cell activity, is related to the induction and expression of motor learning. In eyeblink

conditioning Purkinje cells in the C3 zone gradually develop a suppression of firing rate following the conditioned stimulus, that disappears during extinction². This response is properly timed in that the maximum suppression is timed to precede the onset of the unconditioned stimulus. In compensatory eye movements the exact spike timing, or absence of spikes, may be less important, and simple spikes could have a more gain modulating role¹⁷. Moreover, unidirectional VOR gain increase training is more successful with contraversive vestibular rotation, thus ipsiversive eye movements, and results in a larger increase in, i.e. a potentiation of, simple spike rate compared to before training (Kai Voges, personal communication). In contrast, decrease training reduced the gain of the contraversive VOR, but did not result in significant changes in Purkinje cell activity, suggesting that the changes occurred downstream. These downstream effects putatively still require the activity, e.g. depth of modulation, of VA Purkinje cells to be induced. This concept is supported by the finding that optogenetic stimulation of Purkinje cell simple spikes is sufficient to drive VOR gain increase¹⁴ and would facilitate the integration of information from a population of Purkinje cells, without requiring each of them individually to account for the behavioral change¹. Our finding that the depth of modulation of Purkinje cells correlates with learning ability, both in conditions of enhanced and reduced learning, confirms the essence of the dynamic range of Purkinje cells in cerebellar learning.

The role of plasticity mechanisms in cerebellar learning.

The persistent change in simple spike activity during VOR we observed after the induction of learning, on the other hand, indicates that plasticity occurred upstream of Purkinje cell output. PF-PC LTP would be a likely candidate, since mutant mice lacking this form of plasticity commonly have cerebellar learning deficits^{6,18,22}, but other candidates include e.g. depression or potentiation of inhibitory input²³ or mossy fiber to granule cell LTP¹⁰, which when ablated both also result in learning deficiencies^{11,15,24}. The finding that disruption of PF-PC LTD does not by definition result in cerebellar learning deficits^{20,21}, but cf.²⁵, together with the capabilities of LTD-blocker T-588 to enhance learning and even rescue mutant mice with impaired learning, suggests that PF-PC LTD is redundant for VOR gain adaptation. This may indicate that, at least in cerebellum-dependent gain modulation, the adaptive change responsible for the learned increase in gain is located more in the cerebellum, whereas that for decreases is downstream, putatively in the cerebellar nuclei. Purkinje cells of different cerebellar modules, identified by zebrin expression levels, differ in potential for plasticity mechanisms^{12,26} and basic firing rate of simple and complex spikes²⁷. Perhaps the coding principles found here apply to floccular VA cells and other zebrin-positive modules, but not to zebrin-negative modules, that are more prone to show PF-PC LTD²⁶ and correlate learning with simple spike depression².

To mitigate the consequences of self-motion, most visually-equipped species generate compensatory eye movements, using visual and vestibular sensory input, to minimize retinal slip and stabilize the visual image. Our finding that the capacity for learning bidirectionally correlates with the change in simple spike modulation depth strengthens the link between the activity of Purkinje cells and the adaptive eye response. The persistent change in activity during a 'probe' trial with only vestibular input in the dark after learning indicates that plasticity mechanisms are involved, and that they are located upstream in cerebellar cortical synapses.

Methods

Eye movement recordings

A pedestal with a magnet inside was placed on the mouse head under anesthesia. After a recovery period of > 3 days, the mouse head was fixed to a metal bar with the body restrained in a custom-made holder. During recording, eye movements were elicited by the rotation of the illuminated dotted drum or turntable in light or in the dark, and the pupil position relative to the reference point (corneal reflection) was recorded by infrared camera. After recording, eye movements were calibrated as previously described (martijn, badura). Analysis was performed offline using custom-made Matlab routines, the performances of the eye movements were quantified by calculating gain and phase. Gain represents the

ratio of eye movement velocity to stimulus velocity, and phase indicates the temporal difference between eye movements and stimulus in degrees. Mice were injected with T-588 received 10.0 mg/kg i.p. (Toyama, Japan) dissolved in saline at least 15min before the start of the experiment..

In vivo recordings

Extracellular recordings were performed as previous described (Wulff, Badura). Mice were anesthetized during surgical preparation, an immobilizing construct was placed on their frontal and parietal bones and a craniotomy was made in the left occipital bone, surrounded by a recording chamber. After recovery ≥ 3 days, mice were fixed onto a turntable and purkinje cells were recorded using borosilicate glass pipettes (2.0 mm OD, 1.16 mm ID, Harvard Apparatus, MA, USA). Recordings were obtained from VA purkinje cells (complex spikes have an optimal response to optokinetic stimulation about a vertical axis) in the flocculus (schonewille, JCN). Purkinje cells were recorded during optokinetic stimulation (OKR) at an amplitude of \sim degrees and a frequency of 0.6 Hz, and vestibular stimulation (VOR) at an amplitude of 5 degrees and a frequency of 0.6 Hz. Recordings were analyzed offline using matlab (Neurasmus BV, Rotterdam, The Netherlands, www.neurasmus.com). To obtain PC- $\Delta\gamma 2$ mice (L7cre::gamma2 mice), the Cre/loxP system was used to delete exon 4 of the GABAA receptor $\gamma 2$ subunit gene selectively in Purkinje cells, as described previously¹⁵.

Statistical analyses

All values are shown as mean \pm SEM, comparisons using unpaired student's t-test, unless stated otherwise. Mean CV2 is defined as the mean of $2 \cdot |(ISI)_{n+1} - ISI_n| / (ISI_{n+1} + ISI_n)$. Significant was considered when $p < 0.05$.

References

1. Catz, N., Dicke, P.W. & Thier, P. Cerebellar-dependent motor learning is based on pruning a Purkinje cell population response. *Proc Natl Acad Sci U S A* **105**, 7309-7314 (2008).
2. Jirenhed, D.A., Bengtsson, F. & Hesslow, G. Acquisition, extinction, and reacquisition of a cerebellar cortical memory trace. *J Neurosci* **27**, 2493-2502 (2007).
3. Cao, Y., *et al.* Behavior-related pauses in simple-spike activity of mouse Purkinje cells are linked to spike rate modulation. *J Neurosci* **32**, 8678-8685 (2012).
4. Yang, Y. & Lisberger, S.G. Purkinje-cell plasticity and cerebellar motor learning are graded by complex-spike duration. *Nature* **510**, 529-532 (2014).
5. Ke, M.C., Guo, C.C. & Raymond, J.L. Elimination of climbing fiber instructive signals during motor learning. *Nat Neurosci* **12**, 1171-1179 (2009).
6. Schonewille, M., *et al.* Purkinje cell-specific knockout of the protein phosphatase PP2B impairs potentiation and cerebellar motor learning. *Neuron* **67**, 618-628 (2010).
7. Kashiwabuchi, N., *et al.* Impairment of motor coordination, Purkinje cell synapse formation, and cerebellar long-term depression in GluR delta 2 mutant mice. *Cell* **81**, 245-252 (1995).
8. Koekoek, S.K., *et al.* Cerebellar LTD and learning-dependent timing of conditioned eyelid responses. *Science* **301**, 1736-1739 (2003).
9. Steinberg, J.P., *et al.* Targeted in vivo mutations of the AMPA receptor subunit GluR2 and its interacting protein PICK1 eliminate cerebellar long-term depression. *Neuron* **49**, 845-860 (2006).
10. D'Angelo, E., Rossi, P., Armano, S. & Taglietti, V. Evidence for NMDA and mGlu receptor-dependent long-term potentiation of mossy fiber-granule cell transmission in rat cerebellum. *J Neurophysiol* **81**, 277-287 (1999).
11. Tanaka, S., Kawaguchi, S.Y., Shioi, G. & Hirano, T. Long-term potentiation of inhibitory synaptic transmission onto cerebellar Purkinje neurons contributes to adaptation of vestibulo-ocular reflex. *J Neurosci* **33**, 17209-17220 (2013).
12. Wang, X., Chen, G., Gao, W. & Ebner, T. Long-term potentiation of the responses to parallel fiber stimulation in mouse cerebellar cortex in vivo. *Neuroscience* **162**, 713-722 (2009).
13. Boyden, E.S., *et al.* Selective engagement of plasticity mechanisms for motor memory storage. *Neuron* **51**, 823-834 (2006).
14. Nguyen-Vu, T.D., *et al.* Cerebellar Purkinje cell activity drives motor learning. *Nat Neurosci* **16**, 1734-1736 (2013).
15. Wulff, P., *et al.* Synaptic inhibition of Purkinje cells mediates consolidation of vestibulo-cerebellar motor learning. *Nat Neurosci* **12**, 1042-1049 (2009).
16. Barmack, N.H. & Simpson, J.I. Effects of microlesions of dorsal cap of inferior olive of rabbits on optokinetic and vestibuloocular reflexes. *J Neurophysiol* **43**, 182-206 (1980).
17. De Zeeuw, C.I., *et al.* Spatiotemporal firing patterns in the cerebellum. *Nat Rev Neurosci* **12**, 327-344 (2011).
18. Galliano, E., *et al.* Silencing the majority of cerebellar granule cells uncovers their essential role in motor learning and consolidation. *Cell Rep* **3**, 1239-1251 (2013).
19. Person, A.L. & Raman, I.M. Synchrony and neural coding in cerebellar circuits. *Front Neural Circuits* **6**, 97 (2012).
20. Welsh, J.P., *et al.* Normal motor learning during pharmacological prevention of Purkinje cell long-term depression. *Proc Natl Acad Sci U S A* **102**, 17166-17171 (2005).
21. Schonewille, M., *et al.* Reevaluating the role of LTD in cerebellar motor learning. *Neuron* **70**, 43-50 (2011).
22. Ly, R., *et al.* T-type channel blockade impairs long-term potentiation at the parallel fiber-Purkinje cell synapse and cerebellar learning. *Proc Natl Acad Sci U S A* **110**, 20302-20307 (2013).
23. Jorntell, H. & Ekerot, C.F. Reciprocal bidirectional plasticity of parallel fiber receptive fields in cerebellar Purkinje cells and their afferent interneurons. *Neuron* **34**, 797-806 (2002).
24. Andreescu, C.E., *et al.* Estradiol improves cerebellar memory formation by activating estrogen receptor beta. *J Neurosci* **27**, 10832-10839 (2007).
25. Emi, K., *et al.* Reevaluation of the role of parallel fiber synapses in delay eyeblink conditioning in mice using Cbln1 as a tool. *Front Neural Circuits* **7**, 180 (2013).
26. Wadiche, J.I. & Jahr, C.E. Patterned expression of Purkinje cell glutamate transporters controls synaptic plasticity. *Nat Neurosci* **8**, 1329-1334 (2005).
27. Zhou, H., *et al.* Cerebellar modules operate at different frequencies. *Elife* **3**, e02536 (2014).

CHAPTER

5.2

Mechanisms underlying vestibulo-cerebellar motor learning in mice depend on movement direction

Kai Voges^{1,2}, Bin Wu¹, Laura Post¹, Martijn Schonewille¹ and Chris I. De Zeeuw^{1,3}

¹ Department of Neuroscience, Erasmus University Medical Center, Rotterdam, NL

² SINAPSE, Singapore National University, Singapore

³ Netherlands Institute for Neuroscience, Royal Netherlands Academy of Arts & Sciences Amsterdam, NL

Correspondence: c.dezeeuw@erasmusmc.nl and m.schonewille@erasmusmc.nl

Published on Journal of Physiology (2017)

Abstract

Compensatory eye movements elicited by head rotation, also known as vestibulo-ocular reflex (VOR), can be adapted with the use of visual feedback. The cerebellum is essential for this type of movement adaptation, but its neuronal correlates remain to be elucidated. Here we show that the direction of vestibular input determines the magnitude of eye movement adaptation induced by mismatched visual input in mice, with larger changes during contraversive head rotation. Moreover, the location of the neural correlate of this changed behavior depends on the type of paradigm. Gain-increase paradigms induce increased simple spike (SS) activity in ipsilateral cerebellar Purkinje cells (PC), which is in line with eye movements triggered by optogenetic PC activation. In contrast, gain-decrease paradigms do not induce changes in SS activity, highlighting that the murine vestibulo-cerebellar cortical circuitry is optimally designed to enhance ipsiversive eye movements.

Introduction

As a result of the structure and connections of their receptors, afferents from the vestibular and visual system carry inherently direction-selective information^{1,2}. In principle, this type of information may be relevant for cerebellar motor learning, such as goal-directed adaptation of reaching tasks of the limbs, smooth pursuit eye movements, or compensatory eye movements (CEMs)³⁻⁸. Sensory and motor information required for motor learning are conveyed to the cerebellar cortex through two main afferent systems⁹. These include the mossy fiber system, which modulates simple spike (SS) activity of Purkinje cells (PCs) via parallel fibers (PFs) and interneurons, and the climbing fiber system, which gives rise to the all-or-none complex spike (CS) activity of PCs⁹. The PF to PC synapse as well as the PF to molecular layer interneuron (MLI) synapse and MLI to PC synapse form major sites of cerebellar integration and plasticity^{10,11}, all of which are putatively controlled by the climbing fiber input⁹. Early, postsynaptic long-term depression (LTD) has been suggested as a possible mechanism^{12,13} to adjust the efficacy of these synapses, but it is still under debate to what extent also postsynaptic long-term potentiation (LTP) contributes to a given behavior^{8,14-18}. As spiking activity of the climbing fibers is highly direction-selective¹⁹, the emerging hypothesis is that plasticity mechanisms contributing to learning are direction-selective too. Hence, cerebellar learning, in terms of mechanism and strength, may in principle also depend on the direction of sensory input and/or desired motor output. However, for adaptation of the vestibulo-ocular reflex (VOR), which is one of the most studied cerebellar motor learning tasks²⁰⁻²³, the efficacy of direction-specific learning has not been assessed in detail yet and the quantitative relation between movement direction and adaptation still has to be studied in the same experiments²³⁻²⁵. More specifically, the contribution of both SS and CS activity of PCs to adaptation of the VOR remains enigmatic²⁵⁻²⁹. Based on previous studies in mutants in which various forms of plasticity and/or parts of the cerebellar cortical network are affected^{9,15,16,30,31}, one can make several predictions on potential direction-dependent plasticity mechanisms, even with data that have been collected following sinusoidal stimulations. Deficits in potentiation mechanisms in PCs robustly impair VOR gain-increase, but less so gain-decrease paradigms¹⁵, whereas selective deficits in LTD at the parallel fiber to PC synapse do not appear to lead to obvious changes in any form of VOR adaptation¹⁶. Interestingly, in the related Purkinje cells (vertical-axis type or VA-type, see Methods) increasing SS activity and thus decreasing CS activity is known to correlate with naso-temporal eye movements, during both the VOR and optokinetic reflex (OKR) evoked by visual input³²⁻³⁴. Taken together, this would imply that the strongest training paradigms include those that occur when SS activity of PCs is enhanced and when the climbing fibers are inhibited, i.e. during contraversive head movements^{28,33,35}. Hence, we hypothesize that gain-increase and gain-decrease trainings can both be optimally executed during contraversive head movements and that the levels of increase and decrease of both SS and eye movement gain depend on the level of concomitant climbing fiber activity, with low climbing fiber activity leading to gain-increases and vice versa because of the windows of opportunity set by the synergistic forms of plasticity⁹.

In the present study, we use direction-specific sigmoidal, rather than sinusoidal, visual and vestibular stimuli so as to assess the contribution of individual movement directions in vestibulo-cerebellar learning. By simultaneously monitoring eye movement performance and corresponding PC activity during VOR adaptation, we test our hypothesis that cerebellar learning is direction-dependent. We show that adaptation to the visual stimulus is more pronounced during contraversive head movements, both for gain-increase and gain-decrease VOR adaptation. The learned changes during contraversive head movements are reflected in the activity of PCs when we increase the amplitude of the VOR gain, but not when we decrease it. Finally, optogenetic stimulation of PCs confirms the presence of a quantitative, causal relationship between SS firing, movement direction and amplitude.

Material and methods

Ethical Approval. All experiments were performed under the GGO license no. IG 04-197 and were approved by the Dutch animal ethical committee (DEC, EMC 2572).

Animals. Wildtype mice ($n = 80$; C57bl/6, Harlan) were prepared for eye movement recordings under general inhalation anesthesia (Isoflurane, in 100% O₂; 4% induction, 1.5-2.0% maintenance, Pharmachemie BV) with a magnetic pedestal that was attached to the frontal and parietal bones of the skull with dental cement (Charisma, Heraeus). Mice received buprenorphine (Temgesic, 50µg/kg, i.p., Reckitt Benckiser Pharmaceuticals Ltd.) and carprofen (Rimadyl, 1 mg/kg, i.p., Zoetis) pre- and/or postsurgery for analgesia and prevention of inflammation, respectively. Wild type mice ($n = 30$) from the same supplier were prepared under the same conditions with a magnetic pedestal and a craniotomy in the occipital bone to give access to the cerebellar cortex for extracellular recordings. To protect the brain the dura was left intact, a chamber made out of dental cement (Simplex Rapid, Kemdent) was built around the craniotomy, and closed with ointment (Duratears Z, Alcon Inc) and bone wax (Ethicon W810, Johnson&Johnson Intl). After surgery, mice were allowed to recover for at least 5 days. After experiments animals were first anesthetized as described above and then euthanized by cervical dislocation. For optogenetic experiments, mice expressing Cre recombinase under the Purkinje cell specific L7 promoter (L7Cre)³⁶ were crossed with mice carrying floxed hChR2(H134R)-tdT (Ai27D) to obtain L7-Ai27D animals that express channelrhodopsin-2 H134R fused with TdTomato³⁷ in cerebellar Purkinje cells ($n = 4$; Jackson Laboratories, Bar Harbor, ME, USA).

Stimulation. Vestibular stimulation was delivered through a turntable (diameter 60 cm) with the head of the mouse fixed in the center and its body placed in a custom-made mouse restrainer. For visual stimulation a high-resolution (3800 x 1000 pixels) rear projection system was used. Three standard projectors (D3Series, Vivitek, The Netherlands) projected a blended and warped (Vioso, Presenter) image, consisting of a random dotted pattern (minimum shape size: 2°; colors: black and white) onto a dome shaped screen (radius: 35 cm; azimuth: 240°; elevation: -10 to +60°). Two sinusoidal functions were combined to generate a sigmoidal output for the vestibular stimulus (custom sequencer file, Spike2, CED). The rotation of the table was read out via a potentiometer fixed at the turning axis of the table. Pre-rendered content for the projection system was calibrated with a laser pointer and a webcam mounted on the turntable (custom functions, Matlab 2012a, Mathworks) (Supp Movie 1 and 2).

Mice were familiarized with the experimental setup 3 days prior to experiments by providing visual and vestibular stimulations for 30 minutes. Experiments started with recordings of baseline CEMs – OKR, VVOR and VOR (stimulation amplitudes: 5°, 10°, 15°, 20°, 25°, 30°, with peak velocities 3.8, 7.9, 11.3, 14.6, 18.3 and 22.0°/s) – either in clockwise or counter clockwise direction. VOR gain adaptation experiments started on the next day, beginning with an initial VOR recording. VOR gain-increase and gain-decrease were induced by training mice in blocks (50 repeats, each stimulus cycle is 12 s = 10 min) consisting of out-of-phase or in-phase vestibular and visual input (both at 10° amplitude), respectively, and directly followed by probe trials (20 repeats, 4 min), consisting of VOR recordings in the dark (also at 10° amplitude). This block was repeated 5 or 6 times (i.e. massed training without intervals, total duration 74 or 88 min). Some mice were trained with more than one paradigm, interleaved by at least 7 days recovery period, during which mice were kept in a 12/12 day/night cycle.

VOR gain adaptation experiments combined with electrophysiological recordings started with an initial VOR recording, followed by a block of training sessions (2x10 repeats) and probe trials (1x10 repeats). This block was repeated 3 times (total duration 20 min). In between each experiment mice recovered for at least 24h in a 12/12 day/night cycle. Out of

the 32 cells 4 were stable only till the 3rd probe trial repeat, which was then taken as the last probe trial for further analysis.

Eye movement recordings. Eye movements were recorded and calibrated with a video camera-based system (ETL-200, iScan) as has been described previously³⁸. Three infrared emitters (max. output 600 mW, dispersion angle 7°, peak wavelength 880 nm) were used to illuminate the eye: two from below that were fixed to the table and one from above, which was fixed to the camera and of which the corneal reflection was used as the reference point. To allow mice an unobstructed view onto the screen a hot mirror was mounted between the mouse eye and camera. To achieve natural recording conditions during VOR measurements, we used the contrast-free, Ganzfeld character of the projection screen under ambient light conditions (**Movie S1**). Finally, we also did experiments in which Pilocarpine (Pilocarpine nitrate 2%, Bausch & Lomb) was applied to the recorded eye and experiments in which the recordings were performed in complete darkness, allowing assessment of the impact of the different contexts; these experiments involved successive training paradigms.

Electrophysiology. Glass pipettes (OD 1.5 mm, ID 0.86 mm, borosilicate, Sutter Instruments) were pulled (P-1000, Sutter Instruments) and filled with 2 M NaCl (tip diameter: 2 µm; impedance: 2-4 mΩ). Extracellular recordings were amplified, filtered and sampled (gain: 100; high pass: 30 Hz; low pass: 10 kHz; rate: 50 kHz) (Axon Multiclamp 700B and Digidata 1440A, Molecular Devices). Signals from eye movement recordings, stimuli and PCs were combined (power1401, CED) and stored on hard disc for offline analysis. Pipettes were mounted on a digital 3-axis drive (SM-5, Luigs Neumann) and lowered onto the left paramedian lobule after the dura was removed under light local anesthesia (Xylocaine, AstraZeneca). An angled (-30° azimuth from the rostral-caudal midline; elevation -46°) approach made it possible to reach the flocculus at a depth of 3.5-4.5 mm.

PCs (n = 67 from C57bl6 mice and n = 20 from L7-Ai27 mice) were identified by the presence of simple and complex spikes, and determined to be from a single unit by confirming that each complex spike was followed by a climbing fiber pause. To ensure recordings were made from PCs in floccular vertical-axis zones (visual stimulus rotation axis azimuth: 0°; elevation: 90°)³⁴ the phase locking of CSs was compared between sinusoidal stimulation around the vertical axis and horizontal axis (horizontal axis here refers to the axis at 45° azimuth from the rostral-caudal midline; with an elevation of 0°). If CSs showed strong phase locking while the visual stimulus moved temporo-nasally, the zone was identified as a vertical-axis zone. If phase locking was strongest during upward movement of the stimulus, the zone was identified as a horizontal-axis zone. For the cells that were stable after experiments (n = 16) a tuning curve with sinusoidal rotations in the vertical axis, horizontal axis and an intermediate angle (azimuth: 45°; elevation: 45°) was recorded and the coefficient of synchronization and the z-value were calculated.

Optogenetics. In L7 - Ai27D (see above), an additional small craniotomy in the periotic capsule with a diameter of ~800 µm was performed. To form a cannula that gives access to the caudal floccular complex, the tip of a plastic pipette (5 mm) was placed perpendicular to the bone and fixed with dental cement (Simplex Rapid; Kemdent). After a recovery period of at least 5 days, an optical fibre (200 µm × 5 mm, filter: 470 nm, driver: LEDD1B; Thorlabs, Ely, UK) was lowered between 4 and 5.5 mm into the cannula, and placed on the outside of the paraflocculus, directed towards the flocculus. To mimic eye movements and spiking patterns during visual stimulation, the LED was pulsed over a period of 2.25 s, with increasing frequencies (60, 80, 90, 100 and 120 Hz) and a duty cycle of 50%. Irradiance was varied between 0.12, 0.42, 0.72 and 1.8 mW mm⁻² measured at the electrode tip prior to experiments (Optical power meter 1830-C, with sensor 883-SL; Newport, Irvine, CA, USA).

Analysis. Eye movement position traces were analyzed with a custom plugin for SpikeTrain, a multipurpose *in vivo* analysis tool (Neurasmus BV). Fast eye movement components were detected in the calculated velocity traces and automatically removed from the position and velocity signal. The movement amplitude was calculated by fitting a sigmoidal function to the average eye position and extracting coefficient a from (1):

$$f(t) = \frac{a}{e^{-b*(t-c)}}$$

Gain was calculated as the ratio between stimulus amplitude and eye movement amplitude. Eye movement delay was calculated as the time shift between the velocity peak of the stimulus and the velocity peak of the eye movement. Extracellular recordings were spike sorted with SpikeTrain (Neurasmus BV). Using superparamagnetic clustering SSs and CSs usually split up in two clusters at low temperatures, i.e. $< 0.1^{39}$. Spikes during fast eye movement components were removed in a window of 40 ms prior to, to 80 ms post movement onset. If a stimulus repeat contained movement artifacts or individual eye movements diverging more than 30% from the average this repeat was manually excluded from further analysis. Basic spiking characteristics as firing rate, CV and CV2 were calculated over the whole recording to ensure stable recording conditions (data not shown). Average spiking rates for individual parts of the stimulus were calculated from peristimulus time histograms (bin size for complete stimulus of 12 s: SSs 100 ms, CSs 300 ms; bin size for segments of 4.5 s: SSs 50 ms, CSs 100 ms). Averages of histograms for eye movements and spiking data in figures were smoothed with a running average (span: eye movements 5, SSs 10, CSs 3). Heat maps were derived from the convoluted raster plots (Gaussian filter width/sigma: SSs 400/80, CSs 200/20).

To determine position, velocity and acceleration sensitivity of PC spike modulation, eye movements were fitted to the PSTHs of SS and CS using the formula (2):

$$f(t) = k * f(t) + r * f(\dot{t}) + u * f(\ddot{t}) + c$$

where k gives the position, r the velocity, and u the acceleration dependence. For data following sigmoidal stimulation eye movements were fitted with formula (1) and eye movement data following optogenetic stimulation were linearly fitted. Latencies of peak and trough spike modulation were retrieved from the fitted functions at the maximum or minimum point, respectively.

Histochemistry. After recordings, L7Cre/Ai27D mice were deeply anesthetized with Nembutal and perfused with 75 ml of 4% paraformaldehyde (PFA). The brains were removed from the skull and post-fixed for 1-2 hours in 4% PFA, and stored in 0.1 M PB containing 10% sucrose. After embedding in 10% gelatin and 10% sucrose, blocks were hardened in a solution containing 10% formaldehyde, 30% sucrose for 1-2 hour at room temperature and then stored overnight in 0.1 M PB with 30% sucrose at 4°C. Coronal sections with a thickness of 40 μ m were made with a sliding microtome with cryostat adaptations. For fluorescence the sections were stained with DAPI and mounted on cover slips, dried and covered with vectashield (Vector-H-1000). The expression of Ai27 was determined using a Zeiss LSM700 confocal laser scanning microscope with x10, x20 and x63 (oil immersion) objectives.

Statistics. Eye movement gains in the two directions were compared using a linear mixed model with the trial number as repeated measure, a diagonal covariance matrix and fixed effects for the trial number, the movement direction and uni- or bidirectional stimulation. Although this analysis method also allows for the comparison of mean values in between trials of one group resulting in a p-value for each repeat, here we give only the F and P value over all repeats. Spiking data had an additional repeated measure when spontaneous and stimulus evoked spiking frequencies or the initial and the secondary segment were compared. To compare depth of modulation of spiking data the spontaneous firing frequency was subtracted from the stimulus evoked firing frequency and a linear mixed model was setup, comparable to that for eye movement gains. Significance of correlations was tested with

Spearman's rank correlation coefficient. All statistical analysis was done with SPSS (Version 21, IBM).

Results

To evoke and adapt direction-specific compensatory eye movements we subjected mice to visual and vestibular stimuli around an earth-vertical axis with a sigmoidal position profile. In contrast to sinusoidal stimulation, a sigmoidal stimulus temporally separates the contribution of the individual movement directions and allows us to more directly correlate the spiking activity to eye movements. We recorded eye movements from the left eye and simultaneously recorded single cell activity of PCs (total $n = 87$) from the left flocculus of mice (eye movements only $n = 68$; electrophysiology and eye movements $n = 30$).

Preferred directions for baseline visual compensatory eye movements

We first investigated to what extent normal, un-adapted eye movement reflexes reveal a preference for movement direction (Fig. 1A). Eye movements evoked by sigmoidal horizontal visual stimulation at amplitudes ranging from 5 to 30° (i.e. peak velocities 3.8 to 22.0°/s; $n = 32$ mice) showed a clear direction preference (see Fig. 1B and Supplementary Movie 1). Independent of stimulus amplitude the preferred direction for visually-driven eye movements was the naso-temporal (n-t) direction (i.e. for the optokinetic reflex, OKR, and the visual vestibulo-ocular reflex, VVOR, but not VOR) (Fig. 1C). For the solely visually-driven OKR, gains decreased with increasing stimulus amplitude, yet eye movements in the n-t direction consistently yielded higher gains than those in the opposite direction ($n = 39$, mixed model: $p < 0.001$, $t = 4.81$) (Fig. 1C). Interestingly, the OKR peak velocity was delayed in the n-t direction with respect to that in the t-n direction ($p < 0.001$, $t = 7.05$) (Fig. 1C). Likewise, VVOR gain values showed a preference for n-t movements ($n = 39$, $p < 0.001$, $t = 8.66$) and delays of VVOR peak velocity in the n-t direction were also significantly longer than those in the t-n direction ($p < 0.001$, $t = 8.72$) (Fig. 1C). For the solely vestibularly driven VOR (Fig. 1B and C) gains were not significantly different for the two directions ($n = 31$, $p = 0.10$, $t = 1.64$), but in line with the VVOR data described above VOR delays were shorter for the eye movements in the t-n direction ($p < 0.001$, $t = 6.20$).

To ensure that the preferred direction was independent of the camera position we tested baseline CEMs with extreme camera positions, $\pm 10^\circ$ towards nasal and temporal from the center position. Consistent with the data described above, gains were higher in the n-t direction for visually driven CEM, but not for VOR (Fig. 2A). These eye movement recordings were all obtained from the left eye. To confirm that directional preference is indeed naso-temporal and not a right-left preference, we subsequently also evaluated the direction selectivity in the right eye ($n = 6$) (Fig. 2B). Here, direction-selectivity largely reversed from right to left, to left to right, indicating that the preference is predominantly related to the preference for n-t eye movements (mixed model: VVOR, n vs. t: $p < 0.001$, $t = -2.11$).

Thus, in comparison to sinusoidal stimulation^{26,33}, the visually driven CEMs following sigmoidal stimulation showed similar eye movement-stimulation amplitude relations, with velocity profiles of OKR lagging behind, profiles of VVOR closely tuned to the velocity profile of the stimulus, and VOR velocity profiles leading that of the stimulation. Moreover, and most importantly, both types of visually driven CEMs (i.e. OKR and VVOR) showed higher gain values towards the ipsilateral visual field.

Preferred directions for PC activity

Next, we characterized the correlation of PC activity with different movement directions. To this end, floccular vertical-axis PCs ($n = 27$ cells; 11 mice) were identified by the presence of CSs and SSs (Fig. 3A), the consistent presence of a pause in SSs firing after a CS (i.e. climbing fiber pause), and optimal CS responses during a contraversive visual stimulus around the vertical axis (Fig. 3B and C)^{19,33,34,40}. Vertical-axis PCs had an average baseline SS firing frequency of 63 ± 2 spikes/s at rest (Table 1) (Fig. 4A and B).

Table 1. SS firing rates during baseline compensatory eye movements in the n-t and t-n direction.

Baseline values were calculated from the periods preceding the start of stimulation. Peak and trough rates refer to the maximum and minimum modulation during stimulation, respectively, while depth equals the difference between peak modulation and baseline firing. The 1. seg and 2. seg refer to the first and the second movement direction segment of the stimulus, respectively (for further explanation see).

		n-t			t-n		
		Baseline	Peak/Trough	Depth	Baseline	Peak/Trough	Depth
OKR	Segment1	59 ± 5	88 ± 8	27 ± 3	59 ± 3	35 ± 3	-23 ± 2
	Segment2		49 ± 6	-13 ± 3		69 ± 5	9 ± 4
VVOR	Segment1	59 ± 3	80 ± 7	20 ± 3	62 ± 4	40 ± 4	-22 ± 2
	Segment2		53 ± 4	-9 ± 4		69 ± 6	10 ± 4
VOR	Segment1	66 ± 6	76 ± 7	9 ± 1	74 ± 6	64 ± 8	-9 ± 1
	Segment2		63 ± 5	-3 ± 2		72 ± 5	2 ± 2

The depth of modulation, i.e. the change in spike rate relative to baseline, of SSs was significantly greater during OKR and VVOR than that during VOR (SS depth of modulation OKR vs VOR: $p < 0.001$, $t = -5.346$; VVOR vs VOR: $p = 0.003$, $t = -3.586$), but for all three types of CEMs SS firing rate increased during n-t and decreased during t-n movements of the ipsilateral eye (Fig. 4B and C). Latencies of the maximum change in SS modulation with respect to the maximum change in stimulus velocity were not different for the two movement directions for any type of CEM (SS latency OKR n-t: -0.01 ± 0.09 s, t-n: -0.14 ± 0.09 s; VVOR n-t: 0.02 ± 0.07 s, t-n: -0.13 ± 0.11 s; VOR t-n: -0.07 ± 0.11 s, n-t: -0.16 ± 0.13 s; all $p > 0.2$) and maximum SS modulation generally preceded maximum velocity peak of eye movements (cf. Fig. 1C). Interestingly, for all paradigms, SS modulation during the first segment of the stimulus cycle (colored parts of stimulus traces in figures) was significantly greater than that of the second segment (OKR $p < 0.001$, $t = 9.52$; VVOR $p = 0.001$, $t = 4.34$; VOR $p = 0.042$, $t = -2.18$). Since the first half of the stimulation placed the ipsilateral eye at an eccentric position at the start of the second half of the visual and/or vestibular stimulation, these data suggest that absolute eye position influences PC SS activity, and hence all following data presented here are obtained during the first half of stimulation (Fig. 1B and 4B).

Table 2. CS firing rates during baseline compensatory eye movements in the n-t and t-n direction. Values for baseline, peak and depth were calculated as described in Table 1.

		n-t			t-n		
		Baseline	Peak/Trough	Depth	Baseline	Peak/Trough	Depth
OKR	Segment1	1.4 ± 0.1	1 ± 0.1	-0.4 ± 0.1	1.5 ± 0.2	3.1 ± 0.3	1.5 ± 0.2
	Segment2		2.8 ± 0.2	1.4 ± 0.1		0.7 ± 0.2	-0.7 ± 0.1
VVOR	Segment1	1.4 ± 0.1	0.9 ± 0.2	-0.5 ± 0.1	1.4 ± 0.1	2.8 ± 0.3	1.3 ± 0.1
	Segment2		1.8 ± 0.2	0.6 ± 0.2		0.8 ± 0.2	-0.8 ± 0.1
VOR	Segment1	1.4 ± 0.1	1.5 ± 0.1	0.2 ± 0.1	1.2 ± 0.2	1.01 ± 0.20	-0.2 ± 0.1
	Segment2		1.15 ± 0.03	-0.2 ± 0.1		1.0 ± 0.3	-0.3 ± 0.2

The reciprocal SS and CS activity of vertical-axis PCs during visual and/or vestibular sigmoidal stimulation showed significantly higher levels of modulation during OKR and VVOR than VOR (OKR vs VOR: $p < 0.001$, $t = 4.183$) (Table 2) (Fig. 4C). Interestingly, the depth of

CS modulation during OKR was not significantly different from that during VVOR (n-t: $p = 0.66$, $t = 0.45$; t-n: $p = 0.64$, $t = 0.48$), despite the fact that OKR gains and delays were significantly lower and longer, respectively, than those during VVOR (see Fig. 1C; gain: n-t $p < 0.001$, $t = -23.766$, t-n $p < 0.001$, $t = 4.182$; delay: n-t $p < 0.001$, $t = 7.663$ and t-n $p < 0.001$, $t = -21.841$). Latencies of CS peak modulation in the t-n direction were consistently shorter than in the n-t direction (OKR $p = 0.03$, $t = 2.18$; VVOR $p = 0.03$, $t = -2.21$), in line with the shorter delay in peak velocity of the eye movement (see Fig. 1C). During VOR the CS modulation pattern diverged even more from that of the SSs and revealed a bimodal spiking pattern, consisting of an initial increase followed by a decrease in firing when the ipsilateral eye moved into n-t direction and a reversed pattern in the t-n direction (in 10 out of 16 cells). Together, these data indicate that CS modulation during visuo-vestibular sigmoidal stimulation encodes mainly retinal slip and in addition probably some vestibular and/or motor signals^{33,40}.

Magnitude of VOR gain adaptation depends on movement direction

To test the hypothesis that the strength of gain adaptation depends on the direction of eye movements, we used the sigmoidal stimulus during visuovestibular mismatch training. Animals were trained to increase their VOR gain by rotating the visual stimulus out of phase (180°) with the vestibular stimulus and decrease their VOR gain by rotating both stimuli in phase (0°) ($n = 35$ mice) (Fig. 5A, Supp Movie 2). Interestingly, out of phase trainings with eye movements in the n-t direction, i.e. contraversive vestibular and ipsiversive visual rotation, resulted in a prominent increase of eye movements during probe trials ($n = 11$, Δ -gain: n-t $+0.37 \pm 0.06$; $p = 0.04$, $f = 9.34$), whereas increase trainings with movements in the t-n direction were not successful, with a trend towards gain decrease ($n = 13$, Δ -gain: t-n -0.1 ± 0.02 ; $p = 0.1$, $f = 2.4$; n-t vs. t-n: $p < 0.001$, $t = -11.22$) (Fig. 5B, top). Similar to VOR gain-increase, decrease training was more effective when the visual and vestibular stimulus rotated in phase to suppress eye movements in the n-t direction ($n = 13$, Δ -gain t-n -0.17 ± 0.02) than in the t-n direction ($n = 13$, Δ -gain n-t -0.04 ± 0.03 ; n-t vs. t-n: $p = 0.001$, $t = 3.62$). This effect was not dependent on the presence of visual feedback during the secondary segment of the stimulation (Fig. 6A and B), as the learned responses were similar when mice were subjected to only unidirectional visual training stimulation, with the table rotating back to the starting position in the dark (gain-increase n-t: 0.37 ± 0.08 , t-n: 0.02 ± 0.04 ; $p = 0.079$, $t = 1.761$; gain-decrease n-t: -0.02 ± 0.03 , t-n: -0.17 ± 0.02 ; $p = 0.18$, $t = 1.34$) (Fig. 3B, right). The decrease in gain was not the result of habituation^{41,42}, as “training” stimulation in the dark, without visual input, resulted in a minimal change in gain during n-t movements (Fig. 5B, bottom left, gray curve). This change was different from that in the preferred, contraversive direction ($p < 0.001$, $t = 3.76$), suggesting that habituation is relatively limited for sigmoidal stimulation.

These results demonstrate for the first time that VOR gain adaptation in mice is direction-sensitive in that the adaptation is more pronounced during both increase and decrease trainings during contraversive vestibular input. This implicates that eye movements in the preferred, i.e. naso-temporal, direction are more prone to adapt, while at the same time the contralateral eye does not undergo obvious changes.

Gain-increase training leads to enhancement of SSs

The findings that compensatory eye movements and related SS modulation are both optimal in the n-t direction and that learning visuo-vestibular mismatch tasks is also optimal when the contraversive vestibular stimulus elicits eye movements in the n-t direction point towards preferred plasticity mechanisms that depend on movement direction (i.e. a principal learning direction). Lesions of the flocculus ablate the ability to adapt the VOR^{43,44}, but how floccular PCs contribute to VOR adaptation and how their activity changes during learning is still under

debate. Therefore, we recorded single-unit PC activity during VOR gain adaptation ($n = 32$ cells; 17 mice) (Supp Movie 2).

VOR gain was increased in the identified principal learning direction by contraversive vestibular and ipsiversive visual rotation (10° amplitude each), resulting in n-t movements of the ipsilateral eye, which compensated fully for the stimulus amplitude (eye movement amplitudes ~ 19 - 20°) (middle panel Fig. 7A). In line with what has been previously shown in sinusoidal training paradigms^{28,45}, the SSs showed a substantial increase in firing rate during the initial segments of the individual training cycles, during which the eyes moved into the n-t direction (Fig. 7B). Concomitantly, CS firing rate decreased with a reciprocal pattern. However, displaying close to perfect eye movement compensation, neither the behavioral responses nor the SS or CS spiking patterns changed over successive training sessions ($n = 10$, gain $p = 0.97$, $f = 0.99$; SS $p = 0.9$, $f = 0.3$; CS $p = 0.9$, $f = 0.3$) (Fig. 4A and B, right). In contrast, and as expected, over the successive VOR probe trials eye movement gain steadily and significantly increased ($p = 0.004$, $f = 5.69$) (Fig. 7C). Concomitantly, SS modulation also increased from 8 ± 1 to 20 ± 3 spikes/s ($p = 0.004$, $f = -3.04$), with a peak in modulation at the initial segments of the VOR probe cycle, which predominantly encoded velocity (Fig. 8A and B). During the stationary segment of the stimulus, after the eye had rotated to a temporal position, SS firing maintained a plateau level suggesting encoding of position; this level increased from 71 ± 4 spikes/s in the first trial to 85 ± 5 spikes/s in the last trial (Fig. 7D) ($p = 0.045$, $t = -2.832$). In contrast, CS modulation remained constant not only during training, but also during probe trials (training: $p = 0.91$, $f = 0.299$; probe: $p = 0.98$, $f = 0.51$). During the secondary segment of the training stimulus, i.e. the rotation back to the initial position (Fig. 7B, black parts of stimulus traces) SSs and CSs modulated with the reversed unimodal pattern reflecting conditions during trainings in the non-learning direction (cf. Fig. 5). Purkinje cell recordings during unidirectional increase training (i.e. when the light was turned off during the second segment of the training cycles, see also Fig. 6A) revealed similar results (Fig. 9A-D) ($n = 5$, unidirectional vs. bidirectional: gain $p = 0.11$, $t = 1.62$; SS $p = 0.38$, $t = 0.89$; CS $p = 0.1$, $t = 1.8$), highlighting the facilitatory role of SS activity for gain-increase learning with contraversive head rotation.

Lower VOR gains after decrease training do not correlate with changes in PC simple spike activity

During VOR gain-decrease training in the principal learning direction the contraversive vestibular stimulus was combined with an in-phase visual stimulation (10° amplitude each) so as to suppress eye movements in the n-t direction (Fig. 10A). As could be predicted based on the minimized level of eye movements, SS modulation was largely absent during gain-decrease training sessions, showing a slightly bimodal pattern with no significant difference in SS peak firing rates compared to rest ($n = 11$, SS rest vs. stimulation: $p = 0.746$, $t = -0.325$) (Fig. 10B). Moreover, we observed no significant changes in eye movement gain or SS modulation across the successive training sessions (gain: $p = 0.5$, $f = 0.9$; SS $p = 0.59$, $f = 0.75$) (Fig. 5B). In contrast, during the intermittent probe trials VOR gain values steadily and significantly decreased ($p < 0.001$, $f = 9.82$) (Fig. 10C). However, we found no changes in SS firing during the probe trials over the course of the experiment ($p = 0.92$, $f = 0.17$) (Fig. 10D).

CS modulation during gain-decrease training sessions was also bimodal, but now with a significant peak-to-peak modulation (i.e. initial increase followed by a decrease; $p < 0.001$, $t = 10.521$), closely resembling the pattern of baseline VOR (Fig. 4C, Fig. 10B and Fig. 8B complex spikes during training). During the probe trials CS modulation was unchanged ($p = 0.4$, $f = 1.1$), but the baseline firing frequency showed a significant decrease ($p = 0.025$, $f = 3.76$) (Fig. 10D). This change in CS activity during the probe trials with bidirectional stimulation was also observed during probe trials after unidirectional training sessions with a concomitant change in gain, while SS activity did not change ($n = 6$, mixed model unidirectional: gain $p = 0.003$, $f = 9.257$, SS $p = 0.9$, $f = 0.1$, CS $p = 0.02$, $f = 2.91$) (Fig. 11A-D).

Causality and reversibility support a paradigm-dependent location of neuronal correlates

To find out whether the changes in SS modulation are sufficient to explain the differences in eye movement amplitude during VOR adaptation, we attempted to replicate the responses to a sigmoidal stimulus, using selective optogenetic manipulation of PCs in L7/cre-Ai27 mice in the dark without vestibular stimulation ($n = 20$ cells; 4 mice) (Fig. 12A). Unilateral stimulation of floccular PCs with blue light pulses resulted in SSs and CSs with a normal shape (Fig. 12B and Fig. 13). Increasing stimulus frequency induced concomitantly an increase in SS firing rate and naso-temporal eye movements (Fig. 12C), mimicking those evoked by natural vestibular or visual stimulation. The SS firing rate and pupil position changed proportionally to the light intensity (0.12, 0.42, 0.72, 1.8 mW/mm²) (Fig. 12D). ADD LIGHT CONTROL EXPERIMENT HERE. The change in spike rate per degree of eye movement was significantly higher during optogenetic stimulation than that during VOR adaptation (7 ± 2 vs. 4 ± 3 spikes/s/°, respectively) (2-tailed t-test: $p = 0.02$, $t = 2.52$), possibly reflecting the fact that the basic drive from the primary vestibular afferents to the second-order vestibular neurons is present during VOR adaptation, but not during optogenetic stimulation (Fig. 1A) and/or that natural vestibular stimulation exerts bilateral effects while our optogenetic stimulation was provided unilaterally. In conjunction with the increase in SS activity following natural training stimulation, these data suggest that SS activity can code for gain-increase adaptation contributing to movement-direction selective learning.

Gain increases and gain decreases are reversible when induced with sinusoidal stimulation^{46,47}. Interestingly the reversibility is asymmetric, implicating that the two paradigms depend on different processes⁴⁶, which could in fact be in different locations. Given that here with sigmoidal stimulation SS modulation was increased over consecutive probe trials following VOR gain-increase training, and that there was no significant change in SS activity upon VOR gain-decrease training in the probe trials, one could hypothesize that the learning abilities might ultimately be blocked due to saturation. Alternatively, the gain-decrease training could actively extinguish the changes acquired during gain-increase training, in effect at least in part 'cleaning the sheet' for new trainings. To test this we performed an additional set of behavioral experiments, in which mice ($n = 6$) were first subjected to VOR gain-increase training, immediately followed by a decrease training, both in the principal learning direction. The first block of decrease training ablated the effect of 7 blocks of increase training (total of 98 min), significantly reducing VOR gains to baseline levels (first vs. second probe trial: $p = 0.039$, $t = 2.47$) and below (baseline vs. last decrease probe trial: $p = 0.034$, $t = -2.564$) (Fig. 14A). During the remaining decrease training eye movement gains further decreased, comparable to the effect of VOR gain-decrease training alone (Fig. 5B). To assess SS dynamics during this extinction we next recorded PC activity related to the decrease training ($n = 8$) after the mice had received an increase training (Fig. 14B). While eye movement gains, like before, decreased rapidly after the first decrease training, SS modulation depth declined more gradually from a potentiated peak firing rate back to baseline levels (first vs. second probe: $p = 0.64$, $t = -0.48$; all probes: $p = 0.03$, $f = 3.88$) (Fig. 14B) than could be expected based upon the rapid changes in eye movement gain at the initial stage. This partial discrepancy between behavior and neuronal signals may reflect the differential loci for un-learning VOR gain-increase and learning VOR gain-decrease, which is also suggested by the absence of a change in SS rate following VOR gain-decrease training alone.

Discussion

Directionality is an inherent feature of the compensatory eye movement system and manifests itself in the lateralization of the cerebellum and the mirrored preferred axes of modulation for climbing fiber activity of PCs in the various zones of both flocculi^{34,48}. To test the hypothesis that cerebellar learning depends on movement direction, we investigated to what extent compensatory eye movements and VOR gain-increase and gain-decrease adaptation are

direction-specific. Behavioral results showed that visual input generated a direction-selective difference in eye movement gains and delays, with larger gains and longer delays for eye movements in the naso-temporal (n-t) direction. Learning efficacy was optimal when the vestibular stimulus moved contraversively, which coincides with the preferred n-t movement direction for visually driven compensatory eye movements. In addition, our electrophysiological data showed that SS activity during probe trials could only be correlated with eye movements during VOR gain-increase adaptation in the n-t direction. Moreover, albeit in a reciprocal fashion, CS activity during probe trials was also best correlated with eye movements during VOR gain-decrease adaptation in the same preferred direction (Fig. 15A). Indeed, together these results point towards a principal learning direction for eye movement adaptation.

To the best of our knowledge this is the first study correlating SS and CS activity to eye movement adaptation using sigmoidal trainings and probe trials during complete cycles of learning. This experimental setup allowed quantitative identification of learning rules and direction selectivity for both gain-increase and gain-decrease^{25,27}. Interestingly, gain-increase training was exclusively successful when the visual stimulus moved the eye into the preferred n-t direction, minimizing the activity of the climbing fibers. These data are in line with our working hypothesis that potentiation rather than depression mechanisms drive VOR learning^{15,16,18}, since LTP at the parallel fiber to PC synapse and enhancement of PC intrinsic plasticity are facilitated by a reduction in climbing fiber activity⁹. Importantly, our optogenetic experiments demonstrated that the increase in SS activity is not only necessary but also sufficient to increase the gain (Fig. 12 and Fig. 15B). Likewise, the shorter delays for eye movements in the temporo-nasal (t-n) direction may be related to the rapidly and synchronously activated CSs during contraversive movements, as a lack of olivary gap junctions induces a short delay during such visual compensatory eye movements⁴⁹.

Other forms of plasticity in the cerebellar cortex may also influence SS activity of PCs and thereby gain-increase learning⁹. These include for example those engaging the molecular layer interneurons, which directly control the rate and regularity of SS activity^{9,50}. The inhibitory interneurons as well as the plasticity mechanisms that control their activity are probably also relevant for the inversion of the vestibular signal that occurs between the vestibular organs and the Purkinje cells⁵⁰. Contraversive head rotation decreases activity in the vestibular ganglion neurons, but correlates with an increased firing rate in Purkinje cells (Fig. 1A). Hence, suppression of the inhibitory input, which is indeed facilitated during the absence of climbing fiber activity⁹, may contribute to VOR gain-increase learning, whereas the absence of effects on SS firing rate during gain-decrease training suggests that changes in inhibition in this form of adaptation are absent or nullified by concomitant changes in excitatory input or intrinsic properties. In line with this, mutant mice lacking GABA α 2 receptor subunits at their molecular layer interneuron to PC synapse or mutants lacking the potassium chloride transporter KCC2 specifically in their PCs, both of which suffer from impaired inhibition onto their PC, show virtually normal gain-decrease training, whereas gain-increase learning and phase reversal learning are strongly affected^{9,26,51}. Thus, the changes in SS firing that we observed during gain-increase training may be potentially enhanced by net changes of inputs from both excitatory and inhibitory inputs^{35,52}, but their functional impact during gain-decrease learning appears rather limited.

A dichotomy between gain increase and decrease has been suggested before, but the evidence for the underlying locations and processes is inconclusive^{15,16,18,29,30}. Presumably, plasticity in the vestibular nuclei downstream contributes substantially to gain-decrease learning⁵³⁻⁵⁵. Indeed, the gain-decrease paradigm did not result in persistent changes in SS activity but only in changes in CS activity that may influence plasticity in the vestibular and cerebellar nuclei^{56,57} (Fig. 15A). These data are in line with the observation that mutants, in which the majority of granule cell output is impaired and both LTD and LTP are impaired, can still successfully complete the gain-decrease, but not the gain-increase, paradigm³¹. In addition, plasticity at the level of vestibular nuclei during gain-decrease learning may also explain why gain-increase effects are rather specific for the training

frequency⁵⁸, whereas gain-decrease appears to be more generalized over a wider range of vestibular input frequencies⁵⁹. Finally, the current data are also in line with the behavioral and spike activity phenotypes of various mutants during phase reversal of the VOR, which requires initially an extension of the gain-decrease paradigm followed by an increase in gain, ultimately moving the eye opposite to the natural reflex^{28,60}.

The notion that changes in SS activity of floccular PCs could be directly responsible for the adaptive response during VOR adaptation has been put forward before^{25,61}, as has a contribution of the vestibular nuclei⁶², but here we show for the first time that this activity as well as the level of learning is related to the direction of the eye movement. Optogenetically driven floccular SS activity during contraversive, but not ipsiversive, vestibular input indeed resulted in a higher VOR gain²⁵. In contrast, climbing fiber activation during contraversive head movement had no effect²⁵, arguing against a role for climbing fiber - dependent plasticity during VOR gain-decrease, which is in line with our observations. Kimpo et al.²⁷, on the other hand, observed an effect on PC activity during a gain-increase training paradigm that was supposed to occur during ipsiversive head movements while climbing fibers are activated□. However, eye movement behavior was not recorded during these PC recordings and the current data raise doubt as to whether the gain-increase adaptation fully occurred. It should be noted that, unlike the current study, the majority of previous studies used continuous sinusoidal vestibular input that hampers analysis of direction-specific components and/or that they did not combine behavioral analysis with simultaneous PC recordings.

Our experiments in which we investigated gain-decrease training following gain-increase training, i.e. the decrease in gain occurred following an initial enhancement of SS firing rates (Fig. 15B), revealed that gain-decrease adaptation and changes in SS modulation follow different dynamics, even when both eye movement gain and SS activity are bound to decrease. While the gain had already dropped to baseline levels after one training session, SS modulation gradually declined over several training sessions, but never dropped below baseline, once more indicating that the locus for VOR gain-decrease learning resides partly somewhere downstream of PC output. Nevertheless, proper PC activity may also be required for successful VOR gain-decrease training, as it is impaired after flocculectomy⁴¹.

It is interesting to note that other laterally eyed animals such as zebrafish show a similar pronounced asymmetry in directional sensitivity of their optic system⁶³. Moreover, even though direction-selectivity remains to be investigated at a more detailed level, several findings point towards similar mechanisms in frontal eyed animals. For example in non-human and human primates, unidirectional rotations around the vertical axis also resulted in asymmetric gain changes towards the adapted, but not un-adapted side^{23,24}. Rotations around the horizontal axis in humans appear to have a direction-specific preference for downward movements⁶⁴⁻⁶⁶ that may coincide with increased SS activity in floccular horizontal-axis zones^{21,67}. It would be interesting to find out to what extent floccular PC activity is also concomitantly and selectively enhanced in frontal eyed animals during ipsiversive eye movements. If this correlation holds throughout all vertebrate species, one might hypothesize that such control systems provide evolutionary advantageous control over explorations of the ipsilateral visual field and concomitantly ipsilateral motor control, such as limb movements. After all, with such a configuration the cerebral cortical control systems involved, i.e. frontal eye fields, primary and secondary visual cortices as well as the cortical areas involved in limb control, all develop on the same side of the brain, offering optimal opportunities for integration from a neuro-anatomical point of view.

The asymmetry in learning mechanisms for different directions might depend partly on the different types of cerebellar zones involved. PCs in floccular zones are predominantly, if not exclusively, zebrin-positive and thus have a relatively low SS firing rate^{14,68,69}. Thereby, they are probably more prone to be potentiated by their parallel fiber input⁷⁰. In contrast, PCs in the zebrin-negative zones, such as those controlling eyeblink conditioning⁷¹, have relatively high SS firing rates and are probably more prone to be suppressed^{72,73}. Interestingly, in cerebellum-dependent eyeblink conditioning the learning related changes that occur in PCs are indeed in the opposite direction, i.e. SS firing is suppressed in a time-locked fashion to the

conditioned eyeblink response⁷³⁻⁷⁵. Together these studies and the current results suggest that potentiation and suppression of SS activity could be module-dependent, as a general feature intrinsic to cerebellar functioning⁷⁶.

References

- 1 Ezure, K. & Sasaki, S. Frequency-response analysis of vestibular-induced neck reflex in cat. I. Characteristics of neural transmission from horizontal semicircular canal to neck motoneurons. *J Neurophysiol.* 1978; 41, 445-58.
- 2 Lopez-Barneo, J., Darlot, C., Berthoz, A. *et al.* Neuronal activity in prepositus nucleus correlated with eye movement in the alert cat. *J Neurophysiol.* 1982; 47, 329-52.
- 3 Robinson, D. A. Adaptive gain control of vestibuloocular reflex by the cerebellum. *J Neurophysiol.* 1976; 39, 954-69.
- 4 Distler, C. & Hoffmann, K. P. Development of the optokinetic response in macaques: a comparison with cat and man. *Ann N Y Acad Sci.* 2003; 1004, 10-8.
- 5 Smith, M. A. & Shadmehr, R. Intact ability to learn internal models of arm dynamics in Huntington's disease but not cerebellar degeneration. *J Neurophysiol.* 2005; 93, 2809-21.
- 6 Tseng, Y. W., Diedrichsen, J., Krakauer, J. W. *et al.* Sensory prediction errors drive cerebellum-dependent adaptation of reaching. *J Neurophysiol.* 2007; 98, 54-62.
- 7 Cahill, H. & Nathans, J. The optokinetic reflex as a tool for quantitative analyses of nervous system function in mice: application to genetic and drug-induced variation. *PLoS One.* 2008; 3, e2055.
- 8 Medina, J. F. & Lisberger, S. G. Links from complex spikes to local plasticity and motor learning in the cerebellum of awake-behaving monkeys. *Nat Neurosci.* 2008; 11, 1185-92.
- 9 Gao, Z., van Beugen, B. J. & De Zeeuw, C. I. Distributed synergistic plasticity and cerebellar learning. *Nat Rev Neurosci.* 2012; 13, 619-35.
- 10 Lev-Ram, V., Wong, S. T., Storm, D. R. *et al.* A new form of cerebellar long-term potentiation is postsynaptic and depends on nitric oxide but not cAMP. *Proc Natl Acad Sci U S A.* 2002; 99, 8389-93.
- 11 Coesmans, M., Weber, J. T., De Zeeuw, C. I. *et al.* Bidirectional parallel fiber plasticity in the cerebellum under climbing fiber control. *Neuron.* 2004; 44, 691-700.
- 12 Ito, M. Cerebellar control of the vestibulo-ocular reflex--around the flocculus hypothesis. *Annu Rev Neurosci.* 1982; 5, 275-96.
- 13 Ito, M. & Kano, M. Long-lasting depression of parallel fiber-Purkinje cell transmission induced by conjunctive stimulation of parallel fibers and climbing fibers in the cerebellar cortex. *Neurosci Lett.* 1982; 33, 253-8.
- 14 Hansel, C., de Jeu, M., Belmeguenai, A. *et al.* alphaCaMKII Is essential for cerebellar LTD and motor learning. *Neuron.* 2006; 51, 835-43.
- 15 Schonewille, M., Belmeguenai, A., Koekkoek, S. K. *et al.* Purkinje cell-specific knockout of the protein phosphatase PP2B impairs potentiation and cerebellar motor learning. *Neuron.* 2010; 67, 618-28.
- 16 Schonewille, M., Gao, Z., Boele, H. J. *et al.* Reevaluating the role of LTD in cerebellar motor learning. *Neuron.* 2011; 70, 43-50.
- 17 Peter, S., Ten Brinke, M. M., Stedehouder, J. *et al.* Dysfunctional cerebellar Purkinje cells contribute to autism-like behaviour in Shank2-deficient mice. *Nat Commun.* 2016; 7, 12627.
- 18 Gutierrez-Castellanos, N., Da Silva-Matos, C. M., Zhou, K. *et al.* Motor Learning Requires Purkinje Cell Synaptic Potentiation through Activation of AMPA-Receptor Subunit GluA3. *Neuron.* 2017; 93, 409-24.
- 19 Simpson, J. I. & Alley, K. E. Visual climbing fiber input to rabbit vestibulo-cerebellum: a source of direction-specific information. *Brain Res.* 1974; 82, 302-8.
- 20 Lisberger, S. G. & Fuchs, A. F. Role of primate flocculus during rapid behavioral modification of vestibuloocular reflex. II. Mossy fiber firing patterns during horizontal head rotation and eye movement. *J Neurophysiol.* 1978; 41, 764-77.
- 21 Hirata, Y. & Highstein, S. M. Analysis of the discharge pattern of floccular Purkinje cells in relation to vertical head and eye movement in the squirrel monkey. *Prog Brain Res.* 2000; 124, 221-32.
- 22 Ito, M. Cerebellar circuitry as a neuronal machine. *Prog Neurobiol.* 2006; 78, 272-303.
- 23 Ushio, M., Minor, L. B., Della Santina, C. C. *et al.* Unidirectional rotations produce asymmetric changes in horizontal VOR gain before and after unilateral labyrinthectomy in macaques. *Exp Brain Res.* 2011; 210, 651-60.
- 24 Migliaccio, A. A. & Schubert, M. C. Unilateral adaptation of the human angular vestibulo-ocular reflex. *J Assoc Res Otolaryngol.* 2013; 14, 29-36.
- 25 Nguyen-Vu, T. D., Kimpo, R. R., Rinaldi, J. M. *et al.* Cerebellar Purkinje cell activity drives motor learning. *Nat Neurosci.* 2013; 16, 1734-6.
- 26 Wulff, P., Schonewille, M., Renzi, M. *et al.* Synaptic inhibition of Purkinje cells mediates consolidation of vestibulo-cerebellar motor learning. *Nat Neurosci.* 2009; 12, 1042-9.
- 27 Kimpo, R. R., Rinaldi, J. M., Kim, C. K. *et al.* Gating of neural error signals during motor learning. *Elife.* 2014; 3, e02076.

- 28 Badura, A., Clopath, C., Schonewille, M. *et al.* Modeled changes of cerebellar activity in mutant mice
are predictive of their learning impairments. *Sci Rep.* 2016; 6, 36131.
- 29 Titley, H. K. & Hansel, C. Asymmetries in Cerebellar Plasticity and Motor Learning. *Cerebellum.* 2016;
15, 87-92.
- 30 Boyden, E. S., Katoh, A., Pyle, J. L. *et al.* Selective engagement of plasticity mechanisms for motor
memory storage. *Neuron.* 2006; 51, 823-34.
- 31 Galliano, E., Gao, Z., Schonewille, M. *et al.* Silencing the majority of cerebellar granule cells uncovers
their essential role in motor learning and consolidation. *Cell Rep.* 2013; 3, 1239-51.
- 32 Graf, W., Simpson, J. I. & Leonard, C. S. Spatial organization of visual messages of the rabbit's
cerebellar flocculus. II. Complex and simple spike responses of Purkinje cells. *J Neurophysiol.* 1988; 60,
2091-121.
- 33 De Zeeuw, C. I., Wylie, D. R., Stahl, J. S. *et al.* Phase relations of Purkinje cells in the rabbit flocculus
during compensatory eye movements. *J Neurophysiol.* 1995; 74, 2051-64.
- 34 Schonewille, M., Luo, C., Ruigrok, T. J. *et al.* Zonal organization of the mouse flocculus: physiology,
input, and output. *J Comp Neurol.* 2006; 497, 670-82.
- 35 Badura, A., Schonewille, M., Voges, K. *et al.* Climbing fiber input shapes reciprocity of Purkinje cell
firing. *Neuron.* 2013; 78, 700-13.
- 36 Barski, J. J., Dethleffsen, K. & Meyer, M. Cre recombinase expression in cerebellar Purkinje cells.
Genesis. 2000; 28, 93-8.
- 37 Madisen, L., Mao, T., Koch, H. *et al.* A toolbox of Cre-dependent optogenetic transgenic mice for light-
induced activation and silencing. *Nat Neurosci.* 2012; 15, 793-802.
- 38 Stahl, J. S., van Alphen, A. M. & De Zeeuw, C. I. A comparison of video and magnetic search coil
recordings of mouse eye movements. *J Neurosci Methods.* 2000; 99, 101-10.
- 39 Quiroga, R. Q., Nadasdy, Z. & Ben-Shaul, Y. Unsupervised spike detection and sorting with wavelets
and superparamagnetic clustering. *Neural Comput.* 2004; 16, 1661-87.
- 40 Winkelman, B. H., Belton, T., Suh, M. *et al.* Nonvisual complex spike signals in the rabbit cerebellar
flocculus. *J Neurosci.* 2014; 34, 3218-30.
- 41 Nagao, S. Effects of vestibulocerebellar lesions upon dynamic characteristics and adaptation of
vestibulo-ocular and optokinetic responses in pigmented rabbits. *Exp Brain Res.* 1983; 53, 36-46.
- 42 Gutierrez-Castellanos, N., Winkelman, B. H., Tolosa-Rodriguez, L. *et al.* Impact of aging on long-term
ocular reflex adaptation. *Neurobiol Aging.* 2013; 34, 2784-92.
- 43 Kassardjian, C. D., Tan, Y. F., Chung, J. Y. *et al.* The site of a motor memory shifts with consolidation. *J
Neurosci.* 2005; 25, 7979-85.
- 44 Shutoh, F., Ohki, M., Kitazawa, H. *et al.* Memory trace of motor learning shifts transsynaptically from
cerebellar cortex to nuclei for consolidation. *Neuroscience.* 2006; 139, 767-77.
- 45 Raymond, J. L. & Lisberger, S. G. Neural learning rules for the vestibulo-ocular reflex. *J Neurosci.*
1998; 18, 9112-29.
- 46 Boyden, E. S., Katoh, A. & Raymond, J. L. Cerebellum-dependent learning: the role of multiple
plasticity mechanisms. *Annu Rev Neurosci.* 2004; 27, 581-609.
- 47 Broussard, D. M., Titley, H. K., Antflick, J. *et al.* Motor learning in the VOR: the cerebellar component.
Exp Brain Res. 2011; 210, 451-63.
- 48 Wylie, D. R., De Zeeuw, C. I., DiGiorgi, P. L. *et al.* Projections of individual Purkinje cells of identified
zones in the ventral nodulus to the vestibular and cerebellar nuclei in the rabbit. *J Comp Neurol.* 1994;
349, 448-63.
- 49 Kistler, W. M., De Jeu, M. T., Elgersma, Y. *et al.* Analysis of Cx36 knockout does not support tenet that
olivary gap junctions are required for complex spike synchronization and normal motor performance.
Ann N Y Acad Sci. 2002; 978, 391-404.
- 50 Miyashita, Y. & Nagao, S. Contribution of cerebellar intracortical inhibition to Purkinje cell response
during vestibulo-ocular reflex of alert rabbits. *J Physiol.* 1984; 351, 251-62.
- 51 Seja, P., Schonewille, M., Spitzmaul, G. *et al.* Raising cytosolic Cl⁻ in cerebellar granule cells affects
their excitability and vestibulo-ocular learning. *EMBO J.* 2012; 31, 1217-30.
- 52 Barmack, N. H. & Yakhnitsa, V. Modulated discharge of Purkinje and stellate cells persists after
unilateral loss of vestibular primary afferent mossy fibers in mice. *J Neurophysiol.* 2013; 110, 2257-74.
- 53 Gittis, A. H. & du Lac, S. Intrinsic and synaptic plasticity in the vestibular system. *Curr Opin Neurobiol.*
2006; 16, 385-90.
- 54 McElvain, L. E., Bagnall, M. W., Sakatos, A. *et al.* Bidirectional plasticity gated by hyperpolarization
controls the gain of postsynaptic firing responses at central vestibular nerve synapses. *Neuron.* 2010; 68,
763-75.
- 55 Jamali, M., Chacron, M. J. & Cullen, K. E. Self-motion evokes precise spike timing in the primate
vestibular system. *Nat Commun.* 2016; 7, 13229.

- 56 Pugh, J. R. & Raman, I. M. Potentiation of mossy fiber EPSCs in the cerebellar nuclei by NMDA
receptor activation followed by postinhibitory rebound current. *Neuron*. 2006; 51, 113-23.
- 57 De Zeeuw, C. I., Hoebeek, F. E., Bosman, L. W. *et al.* Spatiotemporal firing patterns in the cerebellum.
Nat Rev Neurosci. 2011; 12, 327-44.
- 58 Lisberger, S. G., Miles, F. A. & Optican, L. M. Frequency-selective adaptation: evidence for channels in
the vestibulo-ocular reflex? *J Neurosci*. 1983; 3, 1234-44.
- 59 Kimpo, R. R., Boyden, E. S., Katoh, A. *et al.* Distinct patterns of stimulus generalization of increases
and decreases in VOR gain. *J Neurophysiol*. 2005; 94, 3092-100.
- 60 Clopath, C., Badura, A., De Zeeuw, C. I. *et al.* A cerebellar learning model of vestibulo-ocular reflex
adaptation in wild-type and mutant mice. *J Neurosci*. 2014; 34, 7203-15.
- 61 Blazquez, P. M., Hirata, Y., Heiney, S. A. *et al.* Cerebellar signatures of vestibulo-ocular reflex motor
learning. *J Neurosci*. 2003; 23, 9742-51.
- 62 Lisberger, S. G. Neural basis for motor learning in the vestibuloocular reflex of primates. III.
Computational and behavioral analysis of the sites of learning. *J Neurophysiol*. 1994; 72, 974-98.
- 63 Feierstein, C. E., Portugues, R. & Orger, M. B. Seeing the whole picture: A comprehensive imaging
approach to functional mapping of circuits in behaving zebrafish. *Neuroscience*. 2015; 296, 26-38.
- 64 Akao, T., Kumakura, Y., Kurkin, S. *et al.* Directional asymmetry in vertical smooth-pursuit and
cancellation of the vertical vestibulo-ocular reflex in juvenile monkeys. *Exp Brain Res*. 2007; 182, 469-
78.
- 65 Bonnet, C., Hanuska, J., Rusz, J. *et al.* Horizontal and vertical eye movement metrics: what is important?
Clin Neurophysiol. 2013; 124, 2216-29.
- 66 Ke, S. R., Lam, J., Pai, D. K. *et al.* Directional asymmetries in human smooth pursuit eye movements.
Invest Ophthalmol Vis Sci. 2013; 54, 4409-21.
- 67 Hirata, Y. & Highstein, S. M. Plasticity of the vertical VOR: a system identification approach to
localizing the adaptive sites. *Ann N Y Acad Sci*. 2002; 978, 480-95.
- 68 Fujita, H., Aoki, H., Ajioka, I. *et al.* Detailed expression pattern of aldolase C (Aldoc) in the cerebellum,
retina and other areas of the CNS studied in Aldoc-Venus knock-in mice. *PLoS One*. 2014; 9, e86679.
- 69 Zhou, H., Lin, Z., Voges, K. *et al.* Cerebellar modules operate at different frequencies. *Elife*. 2014; 3,
e02536.
- 70 Wang, X., Chen, G., Gao, W. *et al.* Parasagittally aligned, mGluR1-dependent patches are evoked at long
latencies by parallel fiber stimulation in the mouse cerebellar cortex in vivo. *J Neurophysiol*. 2011; 105,
1732-46.
- 71 Mostofi, A., Holtzman, T., Grout, A. S. *et al.* Electrophysiological localization of eyeblink-related
microzones in rabbit cerebellar cortex. *J Neurosci*. 2010; 30, 8920-34.
- 72 Wadiche, J. I. & Jahr, C. E. Patterned expression of Purkinje cell glutamate transporters controls synaptic
plasticity. *Nat Neurosci*. 2005; 8, 1329-34.
- 73 ten Brinke, M. M., Boele, H. J., Spanke, J. K. *et al.* Evolving Models of Pavlovian Conditioning:
Cerebellar Cortical Dynamics in Awake Behaving Mice. *Cell Rep*. 2015; 13, 1977-88.
- 74 Jirenhed, D. A., Bengtsson, F. & Hesslow, G. Acquisition, extinction, and reacquisition of a cerebellar
cortical memory trace. *J Neurosci*. 2007; 27, 2493-502.
- 75 Wetmore, D. Z., Jirenhed, D. A., Rasmussen, A. *et al.* Bidirectional plasticity of Purkinje cells matches
temporal features of learning. *J Neurosci*. 2014; 34, 1731-7.
- 76 De Zeeuw, C. I. & Ten Brinke, M. M. Motor Learning and the Cerebellum. *Cold Spring Harb Perspect
Biol*. 2015; 7, a021683.

Legends

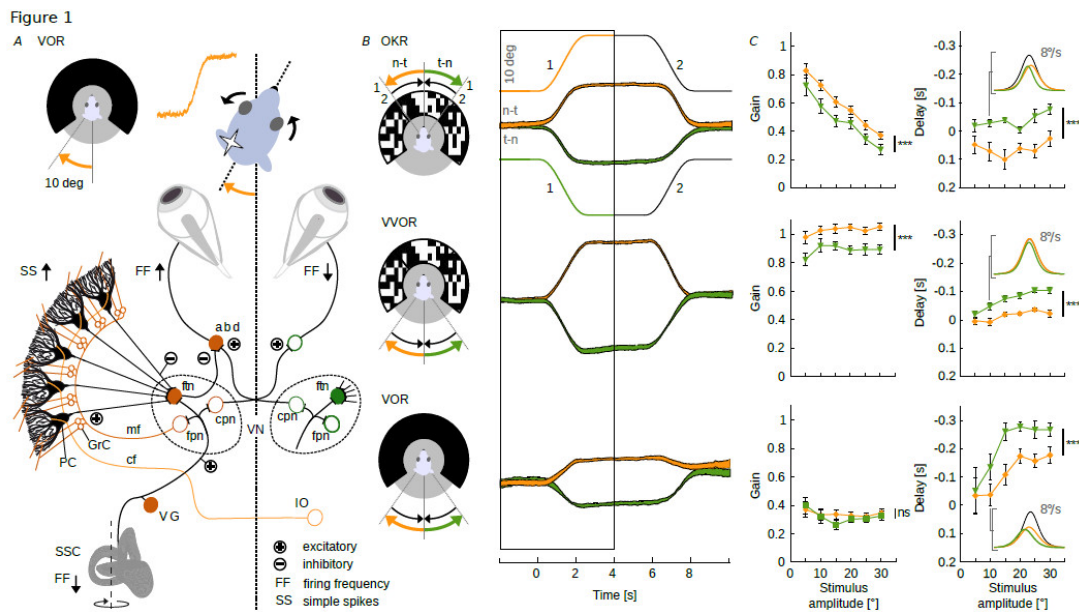


Figure 1. Baseline compensatory eye movements have a preferred direction.

A, Rotating a head-fixed mouse in the dark in contraversive direction with respect to the recording side will evoke a compensatory eye movement into naso-temporal direction towards the ipsilateral visual field (top) via a three-neuron arc in the brainstem (bottom, filled orange symbols). Sensory information from the semi-circular canals (SCC), transferred by the vestibular ganglion cells (VG), reaches the vestibular nuclei (VN). Excitatory inputs drive flocculus projection neurons (fjn), flocculus target neurons (ftn) and commissural projection neurons (cpn). The PCs in the flocculus, which receive their input from the VN via mossy fibers (mf) to the granule cells (GrC) and after processing in the molecular layer, provide an inhibitory input to the VN, which in turn inhibit ipsilateral abducens neurons (abd); thus through a process of disinhibition PCs are expected to eventually facilitate a naso-temporal eye movement. The climbing fibers (cf) of the inferior olive (IO) provide the error signal to the contralateral PCs. **B**, CEMs following direction-selective stimulation. Icons (left) display eye movement (n-t orange, t-n green) and stimulus direction (arrow heads) for the visual (arrows top) and the vestibular (arrows bottom) stimulus. Numbers at the icon for OKR indicate the first and second stimulus segment. Note that visual stimulation evokes CEMs in the same direction as the stimulus, whereas vestibular stimulation-evoked movements are opposite to the direction of the stimulus. Right, stimulus (thin lines) and average eye movement traces recorded at a stimulation amplitude of 10° for naso-temporal (n-t) and temporo-nasal (t-n) eye movements. Analysis of eye movement was performed during the initial segment (black box, number 1). **C**, Gains of average eye movements (left) were significantly larger in the n-t direction (n=20) than in the t-n (n=19) direction for the visually driven OKR and VVOR, but not for the VOR over stimulation amplitudes ranging from 5 to 30° (peak velocities 3.8 to 22.0°/s). Delays (right) for the t-n direction were leading (i.e. have a more negative delay than) those of the other direction. Insets show example velocity profiles of n-t and t-n movements following 10° stimulation (black lines). Data are represented as mean ± SEM; population data (B middle panels) represent ± SEM.

Figure 2

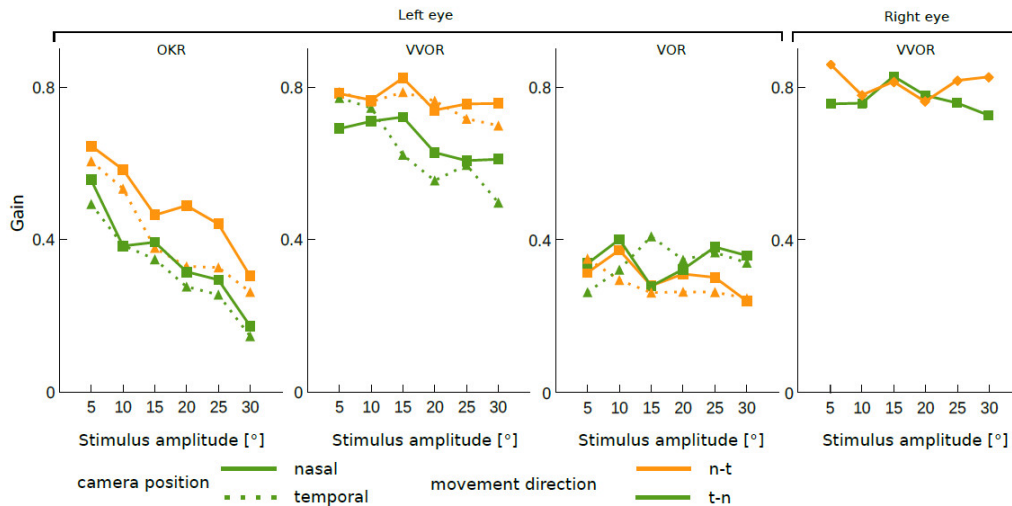


Figure 2. Relation eye movement gain, preferred direction, and camera position.

To rule out the possibility that camera position relative to the eye might have resulted in asymmetric recording conditions, eye movements were measured at two additional camera positions, i.e. at $+10^\circ$ and -10° from the usual position. Independent of camera position, eye movements during visual stimulation were larger in the n-t direction. Moreover, here too gains did not show any direction dependence during vestibular stimulation in the dark, further assuring that differences in preferred direction are not related to the camera position. Data are shown as mean values.

Figure 3

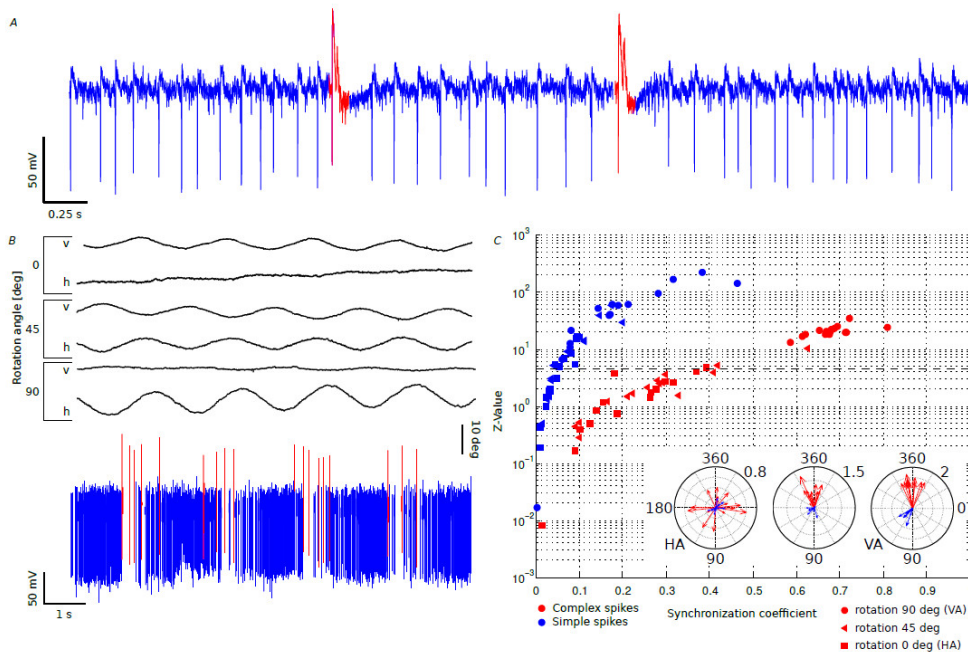


Figure 3. Identification of vertical-axis floccular PCs.

A, *In vivo* extracellular recordings were obtained from cerebellar PCs during visual and/or vestibular stimulation in awake mice. Recordings were identified as a single unit by the consistent presence of a pause in SSs (blue) following each CS (red). B, Traces show examples of vertical axis (VA) and horizontal axis (HA) eye movements following visual stimulation around three different rotational axes (from top to bottom: HA, intermediate and VA). To separate VA-responsive PCs from HA-responsive

and non-floccular PCs the activity of PCs in response to each stimulus was recorded and SSs (blue) and CSs (red) were identified (bottom). C, PCs showing significant ($p < 0.001$ for z-values > 4.6) synchronization with VA but not HA stimulus were identified with the use of circular statistics and used for further analysis. Insets: polar plots show a strong phase relation and depth of modulation for SSs and CSs during VA stimulation (right) but less so during intermediate or vertical axis stimulation (middle and left inset, respectively).

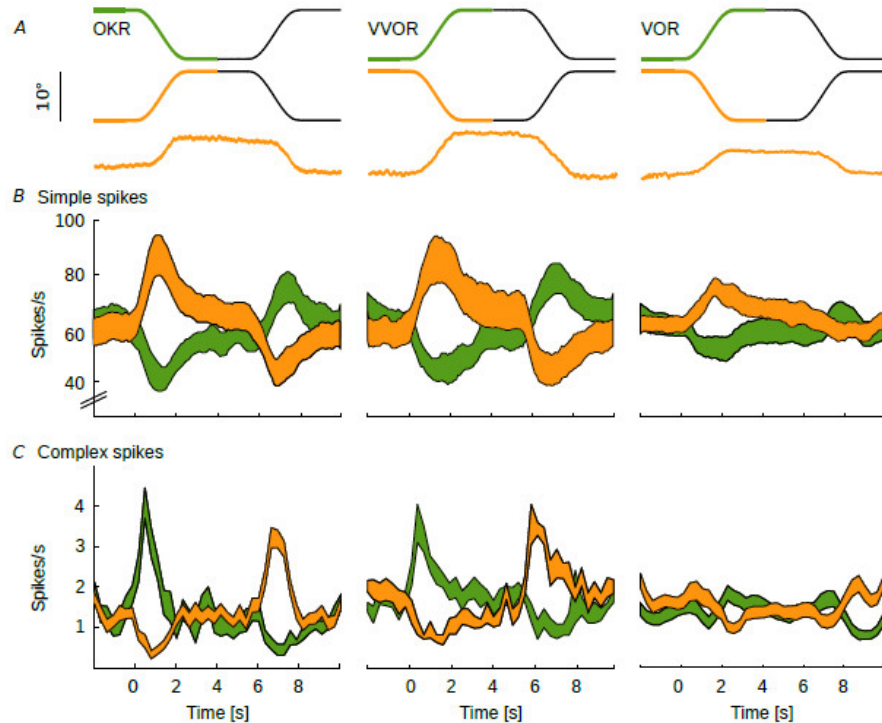


Figure 4. PCs spiking patterns reflect the direction of movement.

A, Stimulus traces in the two movement directions (top, n-t orange, t-n green) and example eye movement traces (bottom, n-t direction). Note that data are sorted according to eye movement, rather than stimulus, direction. B and C, Average SS and CS firing during base line CEMs measured at a stimulation amplitude of 10° . PCs (total of 27) showed an increase or decrease of SS firing and the reciprocal CS pattern for the n-t and t-n direction, respectively. B, The SS firing pattern in one direction was a mirror image of the spiking pattern in the other direction in terms of depth of modulation and latency to peak modulation. C, Visually driven CS modulated stronger in the t-n direction with a bigger lead of peak modulation as compared to the n-t direction; the CSs during stimulation in t-n direction may explain why eye movement delays were shorter in this direction. CS activity during VOR showed a bimodal pattern with an initial increase followed by a decrease in the n-t and vice versa for the t-n direction. Data are represented as mean \pm SEM; population data (B and C) represent \pm SEM.

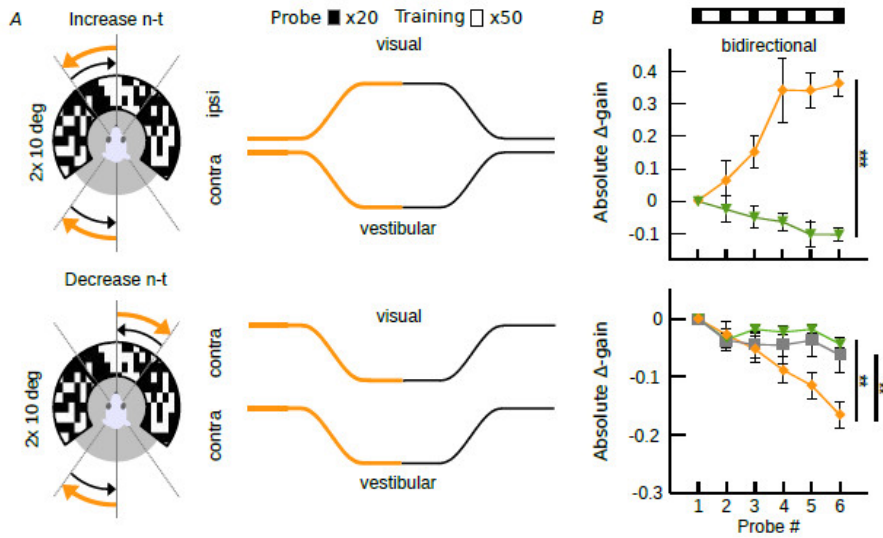


Figure 5. VOR gain-increase and gain-decrease training have a principal learning direction.

A, Scheme of stimulation during gain-increase (vestibular and visual stimulus out-of-phase, top) and gain-decrease training (vestibular and visual stimulus in-phase, bottom). Icons depict stimulation (left) and stimulus traces (right) during training sessions with contraversive vestibular stimulation (n-t, orange, cf. Fig. 6A for unidirectional ipsiversive stimulation); during probe trials mice received vestibular stimulation in the dark in the respective direction. B, Changes in eye movement gain were measured during VOR probe trials (black boxes; 20 repeats = 4 min, top), caused by five gain-increase ($n = 24$; starting gain: 0.35 ± 0.02) (top panels) or gain-decrease ($n = 26$; starting gain: 0.35 ± 0.03) (bottom panels) training sessions (white boxes; 50 repeats = 10 min; total: $6 \times 4 \text{ mins} + 5 \times 10 \text{ mins} = 74 \text{ mins}$). Learning effect depended on the direction of stimulation, with significantly better learning in trainings based on contraversive (n-t, orange) than with ipsiversive (t-n, green) vestibular stimulation. Note that this difference was independent of whether the visual stimulus was presented bidirectionally, i.e. present during both ipsi- and contraversive vestibular input, or unidirectional, when the visual stimulus was presented only during the first segment of the vestibular stimulus, i.e. only during either ipsi- or contraversive input (Fig. 6). VOR habituation in the learning direction (gray line, bottom left), i.e. contraversive head rotations, is significantly different from VOR decrease in the same direction. Data are represented as mean \pm SEM.

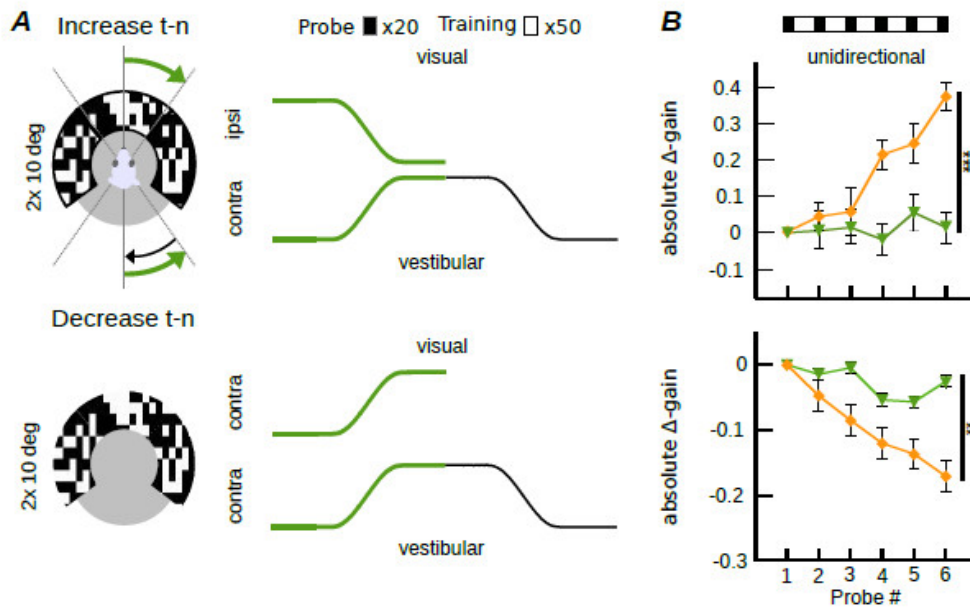


Figure 6. Unidirectional VOR gain adaptation.

A, Schemes showing how we provided unidirectional stimulation during gain-increase (vestibular and visual stimulus out-of-phase, top) and gain-decrease training (vestibular and visual stimulus in-phase, bottom). Icons depict visual and vestibular stimulation (left) and stimulus traces (right) during training sessions with ipsiversive vestibular stimulation (t-n, green); during probe trials mice received vestibular stimulation in the dark in the respective direction. *B*, Changes in eye movement gain were measured during VOR probe trials (black boxes; 20 repeats = 4 min, top); these changes were induced by five gain-increase (top panels) or gain-decrease (bottom panels) training sessions (white boxes; 50 repeats = 10 min; total time 74 min (6x4mins+5x10mins)). As during bidirectional stimulation, the learning effect depended on the direction of stimulation, with significantly better learning in trainings based on contraversive (n-t, orange) than with ipsiversive (t-n, green) vestibular stimulation.

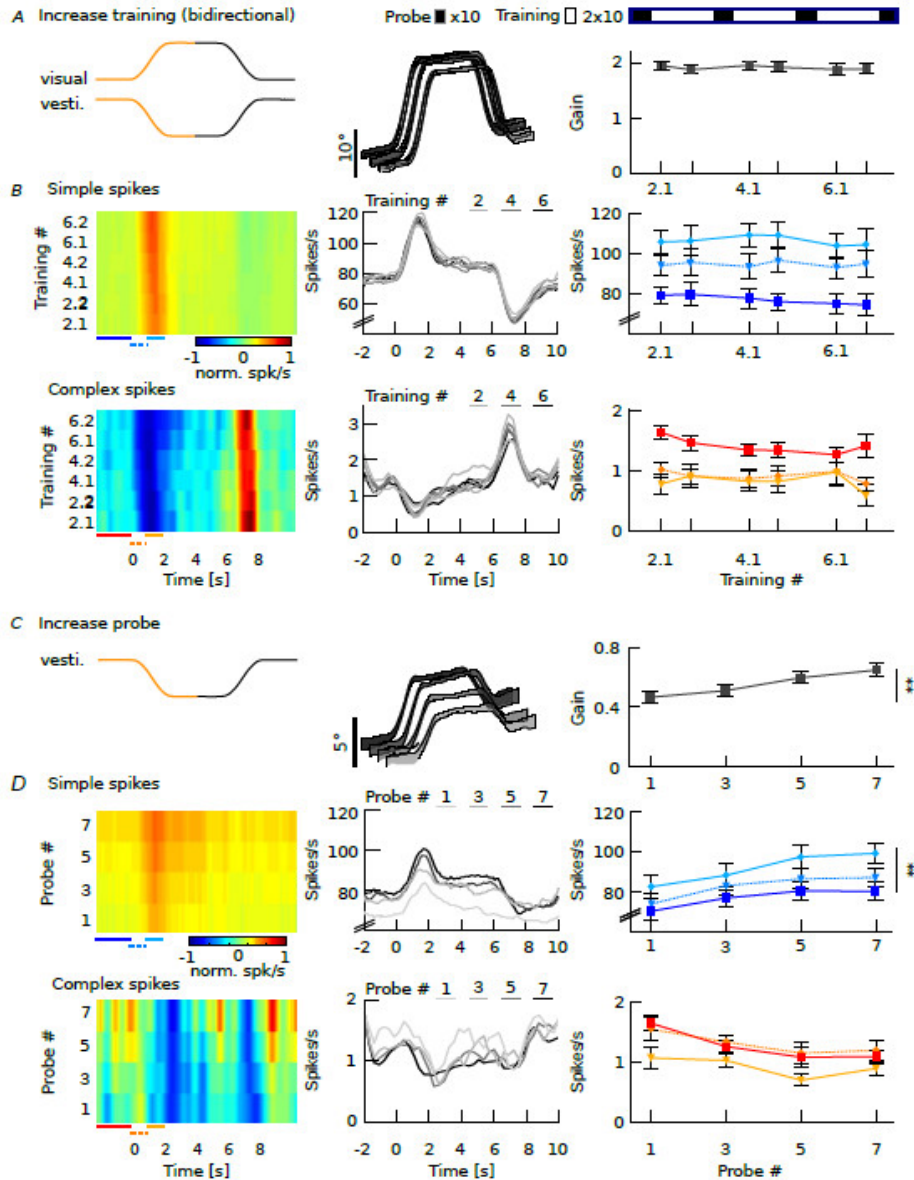


Figure 7. VOR gain-increase correlates with increased SS activity in probe trials.

A, VOR gain-increase training was induced by simultaneous visual and vestibular stimulations moving in opposite directions. After an initial VOR baseline measurement including 10 stimulus cycles of 12 s each (2 min), we recorded from each cell during 3 consecutive training blocks (total duration 20 min). Each of these training blocks consisted of 2 visuovestibular mismatch training sessions and each session included 10 stimulus cycles (i.e. 2 x 2 min) and 1 VOR probe session including 10 stimulus cycles (i.e. 1 x 2 min). Only repeats with stable spiking activity were used for analysis. From the start of the gain-increase training the eye movements of the mice compensated close to optimally for the combined amplitude of the visual and vestibular stimulation and the gains during this visuovestibular mismatch stimulation did not change significantly over time (middle panel). Schematic drawing at the top right illustrates the order of 10 VOR probe trials in the dark (black boxes) and 20 visuovestibular training trials (white boxes) for 3 consecutive blocks. B, Heat maps of normalized SS and CS responses of an example PC during the training trials qualitatively (left) and average firing rates of all cells for each training block quantitatively (middle) representing unimodal and reciprocal SS and CS firing rates. Absolute firing rates (right) were determined for three intervals during the first segment of stimulation as indicated by colored lines below heatmaps of relative firing rate (left): The baseline before the stimulus (solid lines, SS dark blue and CS red) compared to the accelerating and decelerating half of the stimulus

(dotted and solid line, SS light blue and CS light red, respectively). SS and CS activity were stable over the subsequent training sessions. C, As a result of the increase training sessions, eye movement amplitude in the probe trials (i.e. during vestibular stimulation in the dark only) increased from starting gains of ~ 0.4 to ~ 0.7 (right). D, Similar to B, but for probe trials. While CS activity was not affected, SS firing rate increased significantly, particularly during the decelerating phase of the initial segment and during the stationary segment of the stimulus, over the course of the training sessions (right). Data are represented as mean \pm SEM; eye movement population data (middle panels) represent \pm SEM and spiking data are mean values.

Figure 8

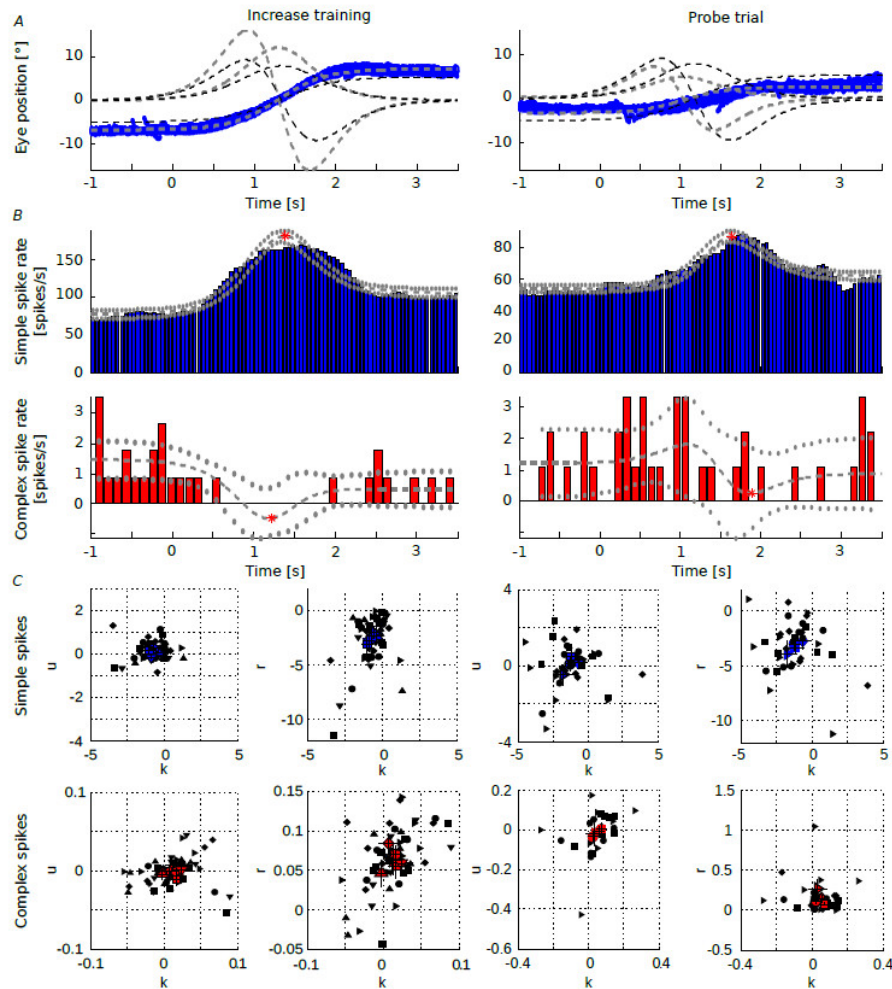


Figure 8. Regression of VA PC responses during increase training.

A, Position, velocity and acceleration profiles of the initial segment of a sigmoidal vestibular stimulation (black) and the corresponding averaged eye movement responses of a single mouse (gray) during increase training (left) and during the first probe trial (right). Note that during the increase training (left panel) the added visual stimulation results in compensatory eye movements that are larger than that of the vestibular stimulus alone (right panel). B, Corresponding averaged SS (blue) and CS (red) activity profiles of a VA Purkinje cell during these initial segments of the training and probe trial; data were fitted using an inverse dynamics model of the eye movements (gray) (Materials & Methods formula 2). C, Results of all recorded PCs for position (k), velocity (r) and acceleration (u) components of SSs (top row) and CSs (bottom) during increase training (left) and probe trials (right). Data are represented as mean \pm SEM.

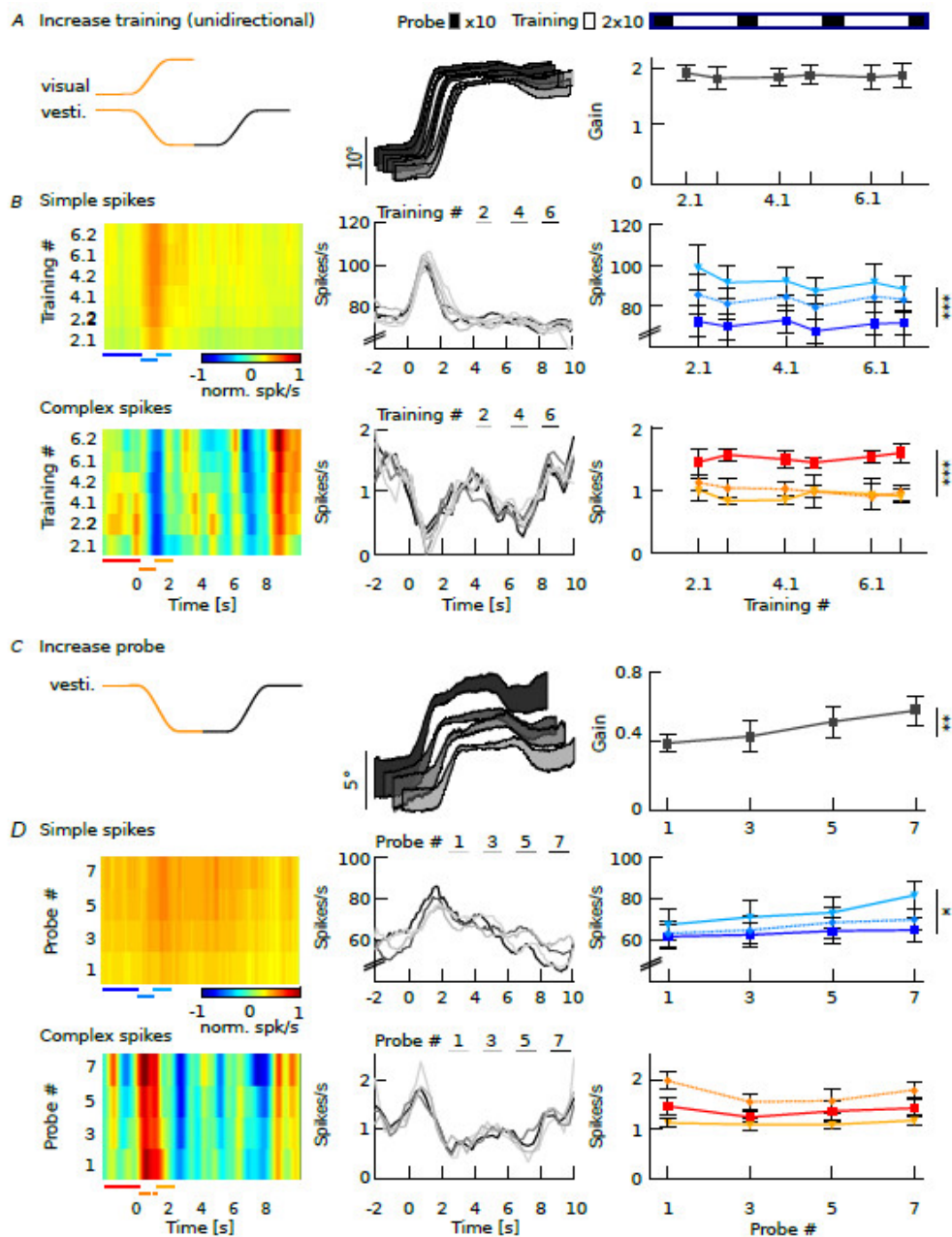


Figure 9. Eye movements and PC modulation during training and probe trials following unidirectional training.

A, Stimulus and average eye movements during unidirectional increase training, which consisted of visual and vestibular stimuli moving in opposite directions during the initial segment of the stimulus and the vestibular stimulus rotating back without the visual stimulus present during the second segment (left). Eye movements compensated for the combined amplitude of the stimuli during the initial segment (middle) and gains did not change over time (right). B, Heat map of normalized SS and CS responses of a representative PC (left) and average firing rates for each training block (middle). Absolute firing rates (right) were determined for three intervals during the first segment of stimulation as indicated by colored lines below heat-maps of relative firing rate (left): The baseline before the stimulus (solid lines, SS dark blue and CS red) compared to the accelerating and decelerating half of the stimulus (dotted and solid line, SS light blue and CS light red, respectively). Note that a significant modulation was only present during the initial segment. C, Stimulus and average eye movements during probe trials. In probe trials,

when the vestibular stimulus was delivered in the dark (left), eye movement amplitude significantly increased over the training sessions (middle, right). D, SS and CS responses of the same cell as in B (left) and on average for all cells (right) show that SS activity increases during vestibular stimulation over the course of gain-increase learning. Spike data on the left are mean values. Eye movement population data in the middle panels and spike data on the right represent mean \pm SEM.

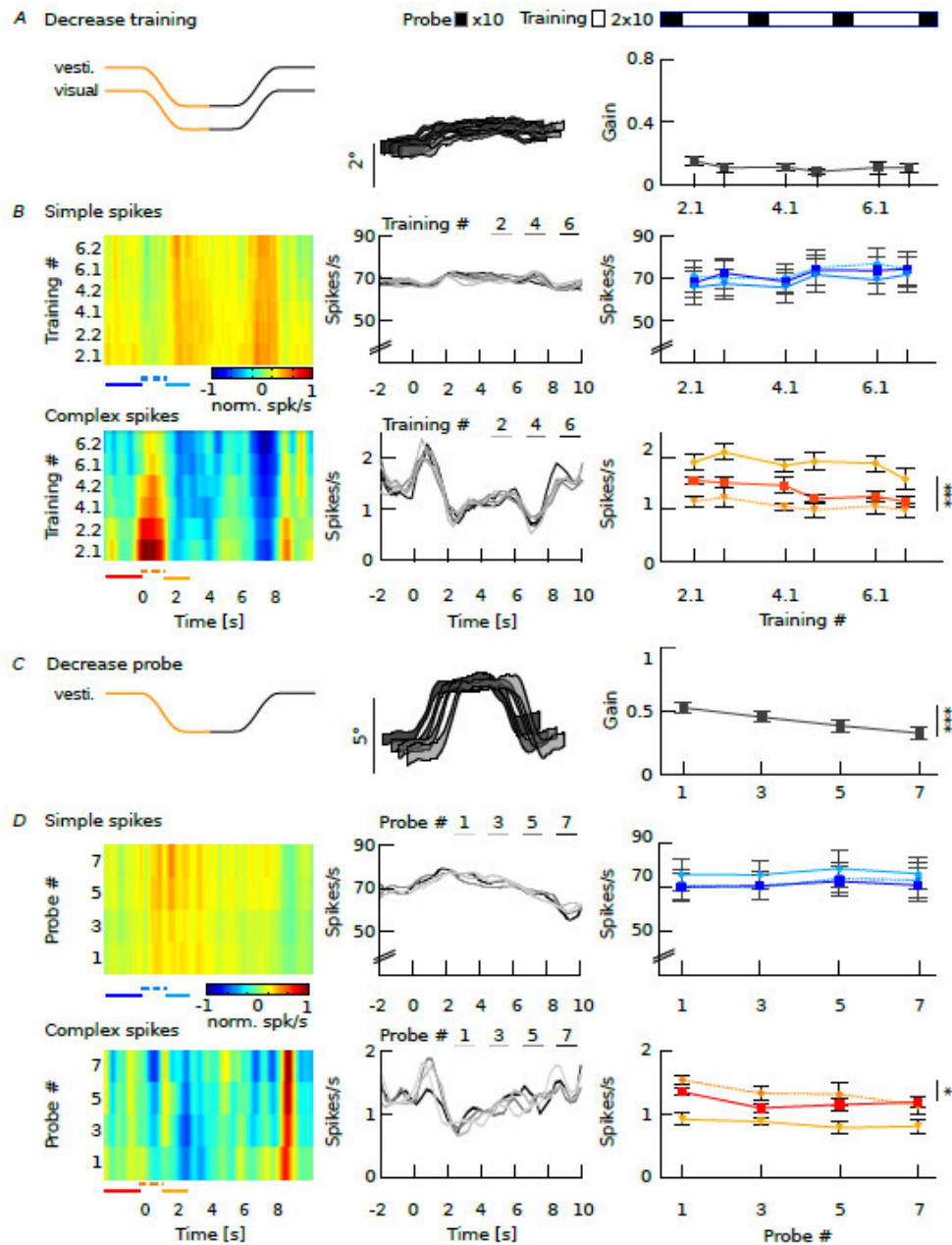


Figure 10. VOR gain-decrease affects CS activity during training sessions.

A, VOR gain-decrease training was induced by simultaneous visual and vestibular stimulations that move in-phase (left panel), which resulted in minimized eye movements (middle panel) that did not change in gain over time (right panel). Order of VOR probe trials (black boxes lasting 8 minutes) and training sessions (white boxes lasting 12 minutes) is illustrated above the line plots. B, SS and CS activity, on average, did not change during the decrease training sessions. Insets in middle panels show graphical fit of the acceleration profile of the stimulus onto the bimodal average SS and CS modulation during the initial segment of the stimulus. Absolute firing rates (right) were determined for three intervals

during the first segment of stimulation as indicated by colored lines below heatmaps of relative firing rate (left): The baseline before the stimulus (solid lines, SS dark blue and CS red) compared to the accelerating and decelerating half of the stimulus (dotted and solid line, SS light blue and CS light red, respectively). C, Vestibular stimulus and average eye movements during probe trials in the dark (left panel). Eye movement amplitude decreased over subsequent training sessions (middle panel), with gains starting from ~ 0.4 and significantly decreasing to ~ 0.26 (right panel). D, Same PC as in B (left panels) and group averages (middle panels) showing that gain-decrease was reflected in CS activity, but not in SS activity (right panels). Spike data on the left are mean values. Eye movement population data in the middle panels and spike data on the right represent mean \pm SEM.

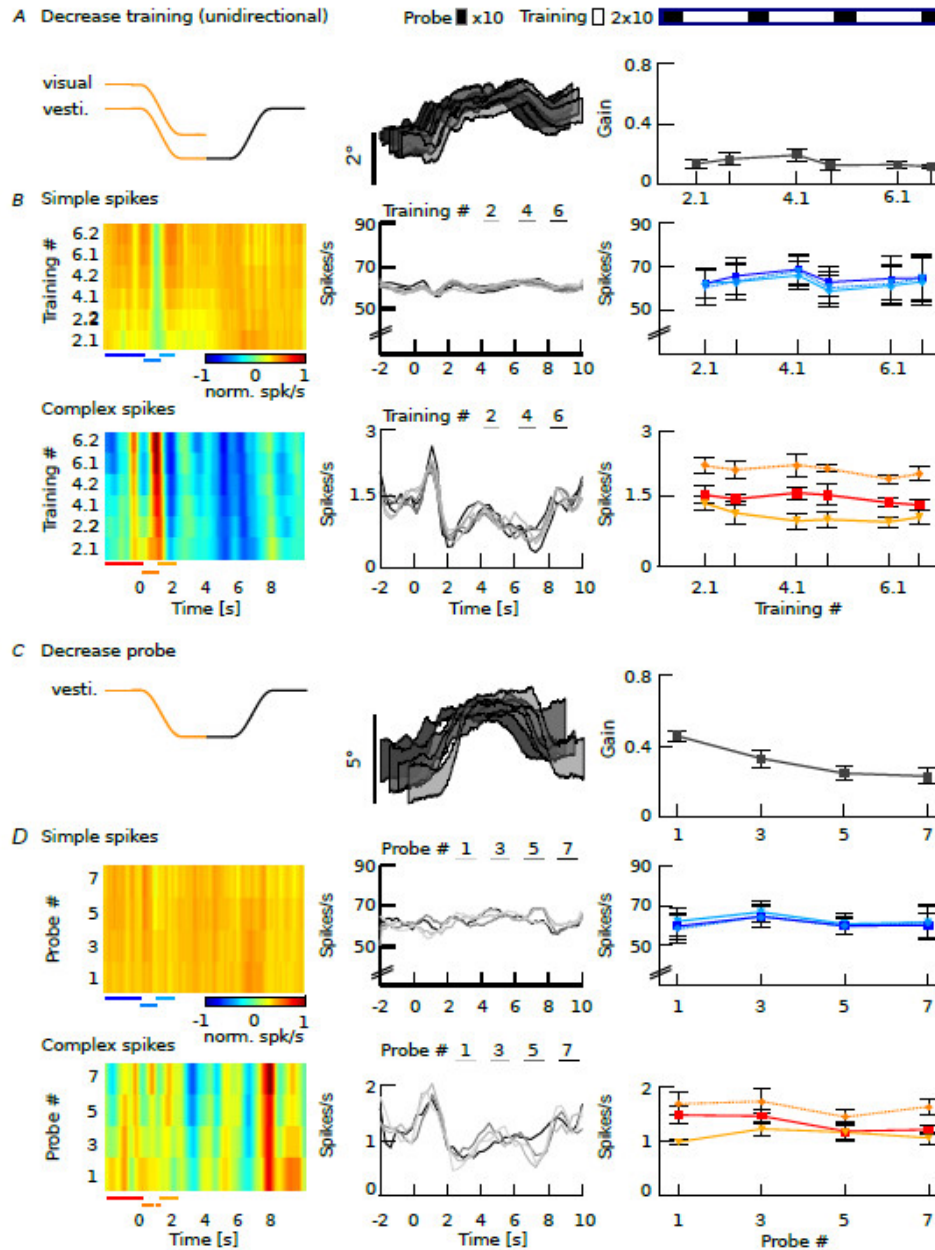


Figure 11. Eye movements and PC modulation during training and probe trials following unidirectional decrease training.

A, Stimulus and average eye movements during unidirectional decrease training consisting of visual and vestibular stimuli moving in phase during the initial segment of the stimulus and the vestibular stimulus rotating back without the visual stimulus present during the second segment (left). Eye movements were

minimized as a result of the stimuli during the initial segment (middle) and these gains did not change over time (right). B, Heat map of normalized SS and CS responses of a representative PC (left) and average firing rates for each training block (middle). Absolute firing rates (right) were determined for three intervals during the first segment of stimulation as indicated by colored lines below heatmaps of relative firing rate (left): The baseline before the stimulus (solid lines, SS dark blue and CS red) compared to the accelerating and decelerating half of the stimulus (dotted and solid line, SS light blue and CS light red, respectively). SS responses were largely absent, whereas CSs showed a similar bimodal pattern as seen in bidirectional training (Fig. 10). C, Stimulus and average eye movements during probe trials. In probe trials, when the vestibular stimulus is delivered in the dark (left), eye movement amplitude significantly decreased over the training sessions (middle, right). D, SS and CS responses of the same cell as in B (left); on average the cells (middle, right) show no changes in SS or CS activity over time. Eye movement population data in the middle panels and spike data on the right represent mean \pm SEM.

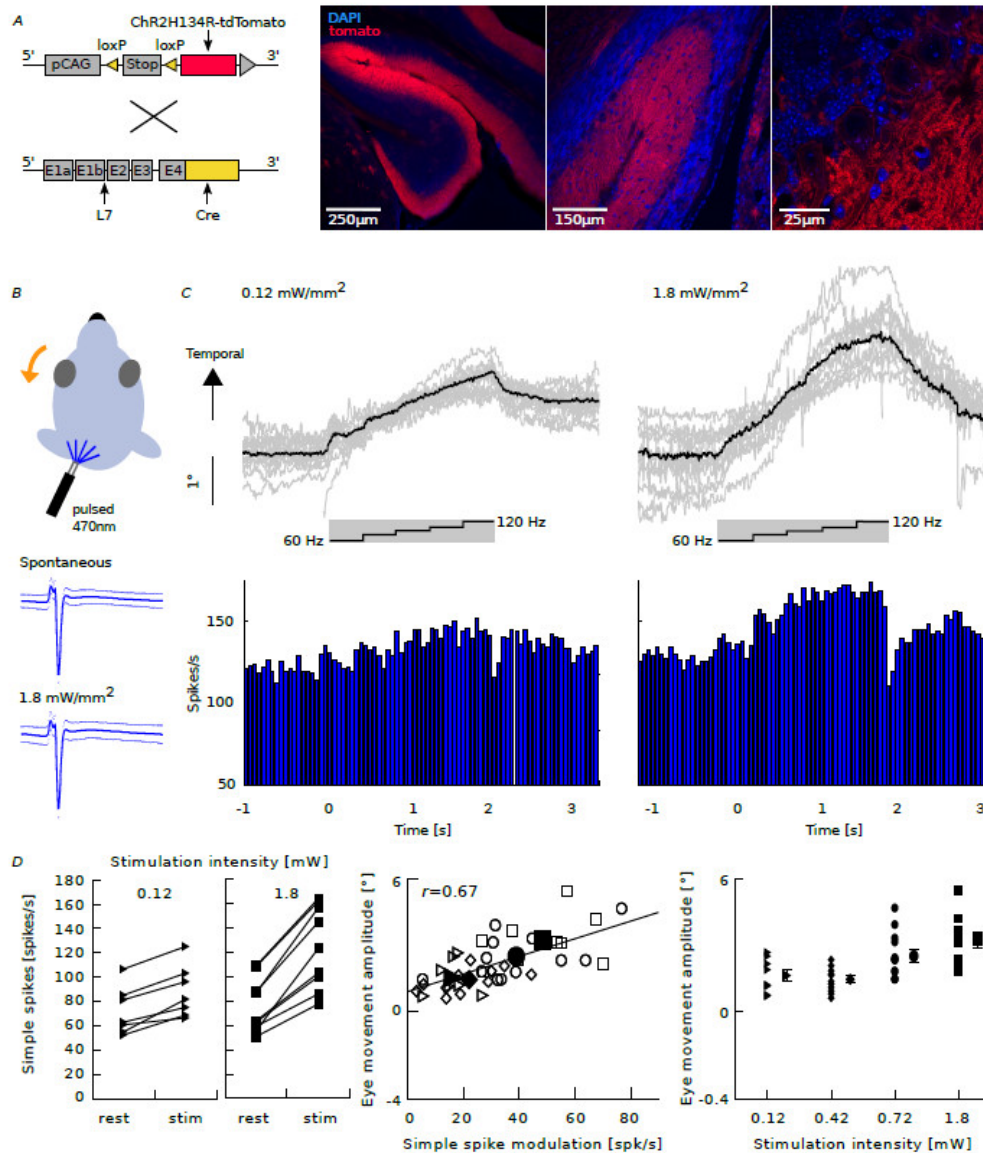


Figure 12. Interactions between SS activity and direction and amplitude of eye movements.
A, Purkinje cell-specific Cre (L7-Cre) and Cre-recombinase-dependent channelrhodopsin expressing (Ai27D) mice were crossed to generate mice in which the firing activity of Purkinje cells can be increased by a light stimulus (left). Confocal images of sagittal cerebellar slices of the flocculus-parafloccular complex showed reliable expression of channelrhodopsin (red) in PCs. Blue indicates

DAPI staining. *B*, Selective optogenetic stimulation of PCs in the flocculus with blue light (pulsed 470nm; five steps: 60, 80, 90, 100, 120 Hz for 400 ms each) resulted in temporal eye movements (top). SS shapes did not differ between spontaneous and evoked activity (bottom). *C*, Example eye movement traces (top, $n = 10$, black line = average) following repeated optogenetic stimulation (gray box) mimicking the naturally evoked response, raster plot (middle) and PSTH (bottom) of the SS response due to low (left) and high (right) light intensities (Fig. 13 for CS). *D*, Increasing intensities resulted in increases in SS firing rates of individual cells (left) and accompanying ipsiversive eye movements (right). Optogenetically evoked changes in SS firing correlate with changes in eye movements (middle) in terms of direction and eye movement per spike, indicating a causal relationship (triangles, diamonds, circles and squares indicate 0.12, 0.42, 0.72 and 1.8 mW/mm², respectively, filled symbols represent mean values). Note that optogenetic stimulation also evoked eye movements in the vertical plane (Fig. 13).

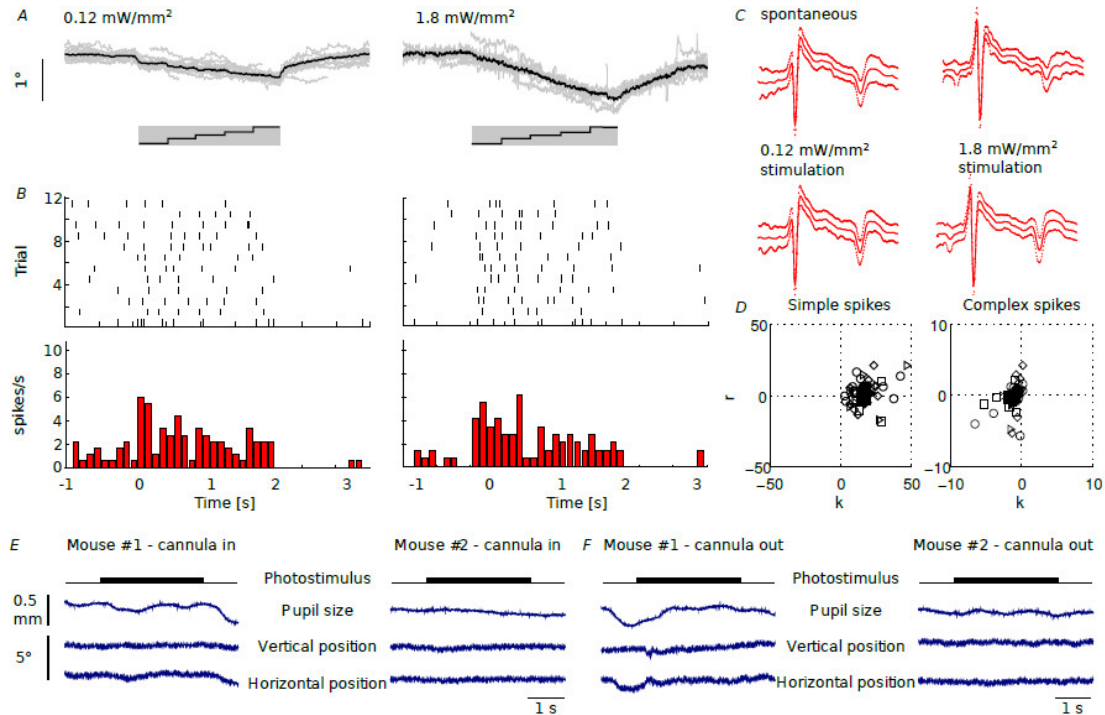


Figure 13. Optogenetic stimulation of floccular PCs and corresponding eye movements.

A, Examples of horizontal (middle) eye movements evoked by stimulation traces (bottom) at different light intensities. Stimulation traces consisted of light pulses with increasing frequencies (60, 80, 90, 100, 120 Hz; 50% duty cycle; 450 ms duration each). Eye movements increased in amplitude with increasing light intensity and were typically diagonal, consisting of a temporal and ventral component. *B*, Raster plots and PSTHs of CS activity corresponding to the eye movements in *A*. *C*, Average CS shapes and 95% confidence interval of the cell in *B* during stimulation and interstimulus intervals. Shapes of the two spike types were not different during these periods, suggesting that the optogenetically evoked CSs are electrophysiologically similar to spontaneous CSs (for SS cf. Fig. 6B). *D*, Linear regression of the eye movement onto PC cell firing showed a strong correlation with the position component (k) for the four light intensities of both SS and CS firing (0.12 mW, position k : SS = 19.7 ± 4.9 , CS = -1.2 ± 0.5 , velocity r : SS = 1.2 ± 2.2 , CS = -0.9 ± 0.3 ; 1.8 mW, position k : SS = 16.5 ± 2.6 , CS = -1.6 ± 0.5 , velocity r : SS = -2 ± 1.5 , CS = -0.5 ± 0.2). Using a linear fit of the eye movements the constant velocity term represents the offset of spiking, whereas the acceleration term was zero and did not contribute.

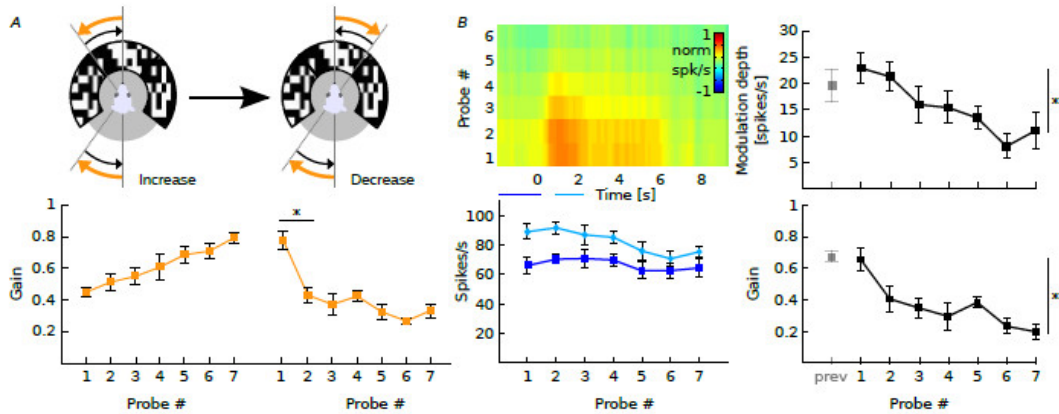


Figure 14. Neuronal correlates for VOR adaptation involve the cerebellar cortex and targets downstream of PCs.

A, VOR gain-decrease training can reverse adapted changes in eye movement gain due to increase training. Icons (top) depict the paired paradigm. Note the sharp drop in gain after the first decrease training block (bottom). Data from behavioral experiments. B, Heat map of simple spike activity of an example cell (left top) showing that the increase in SS firing after gain-increase training returns to near baseline levels during decrease training (compare to Fig. 4D and Fig. 5D). Averaged firing rates of all recorded cells ($n = 8$) prior to (dark blue) and during (light blue) stimulation (left bottom). Eye movement gains, as in A, decreased with an initial fast drop followed by a slower decrease (right bottom), whereas the depth of simple spike modulation (right top) returned more gradually to baseline levels (gray data point indicating depth of modulation after increase training, cf. Fig. 7D). Data are represented as mean \pm SEM.

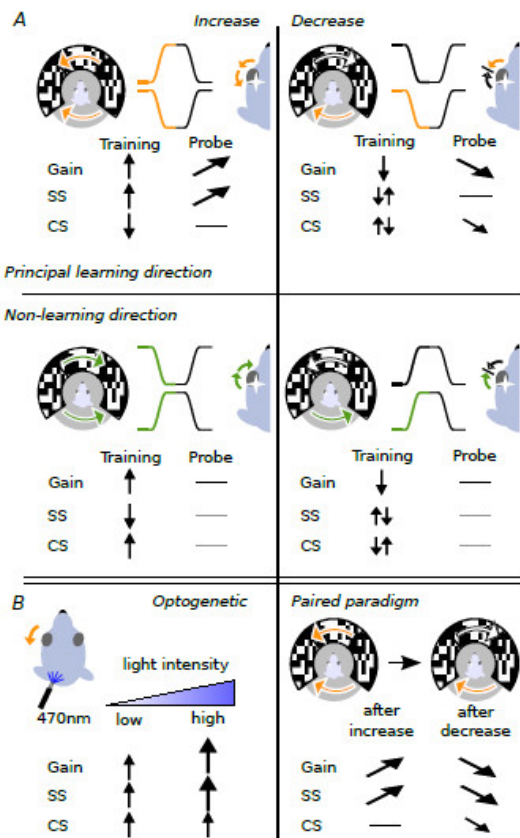


Figure 15. VOR adaptation and its neural correlates are paradigm and direction specific.

A, VOR adaptation and related spiking changes during gain-increase (left) and gain-decrease (right) adaptation paradigms in the principal (top) and non-learning (bottom) direction. The gain of the VOR evoked by contraversive rotation could be adapted, increased or decreased, whereas that evoked by ipsiversive rotation could not. During gain-increase training in the principal learning direction simple spike and complex spike rates increased and decreased, respectively, and the simple spike firing rate during probe trials after training increased significantly, in line with the VOR gain. Conversely, complex spike and simple spike modulation during gain-decrease training was more complex, revealing a bimodal CS pattern during training and a CS reduction during the probe trials, whereas simple spike rates did not change over time in probe trials. B, Ipsilateral optogenetic stimulation and simultaneous recordings of PCs in the flocculus evoked an increase in SS and CS firing and naso-temporal eye movements. Increasing light intensities led to increasing PC activity and eye movement amplitudes, effectively simulating the behavioral and neuronal changes observed due to visuovestibular mismatch, gain-increase training (left). A paired paradigm showed that simple spike activity potentiated by gain-increase training, unlike that in naïve mice, can be actively suppressed by gain-decrease training. This discrepancy and the rapid drop in eye movement gain compared to the gradual decrease in simple spike activity point towards the potential involvement of downstream areas in the decrease of eye movement gain, e.g. the vestibular nuclei.

Supplementary Movie Legends

Supplementary Movie 1. Recording conditions during baseline compensatory eye movements.

Visual and vestibular stimulation as well as eye movements and PC recordings are shown for OKR, VVOR and VOR. Note that for the purpose of the movie the light conditions were changed. Under experimental conditions there were no other light sources than the projection system.

Supplementary Movie 2. Recording conditions during VOR decrease and increase training.

Combined visual and vestibular stimulation for gain-decrease and gain-increase training. Probe trials were executed as can be seen from Supplementary Movie 1 during VOR. Note that for the purpose of the movie the light conditions were changed. Under experimental conditions there were no other light sources than the projection system.

CHAPTER

6.1

Cerebellar development contributes to compensatory eye movement behavioral and adaptive functionality

Bin Wu¹, Laura Post, Chris De Zeeuw^{1,2} and Martijn Schonewille^{1*}

¹ Department of Neuroscience, Erasmus Medical Center, 3015CN, Rotterdam, the Netherlands

² Netherlands Institute for Neuroscience, Royal Dutch Academy for Arts and Sciences, 1105 CA, Amsterdam, the Netherlands

* Correspondence: Martijn Schonewille

Abstract

Cerebellar development is thought to play a crucial role in the emergence of many forms of motor behaviors and learning, but ontogenetic changes in cerebellar activity during learning have not been investigated thoroughly. Here, we examined the effects of cerebellar developmental changes on compensatory eye movement baseline reflexes and plasticity by using Purkinje cell specific deletion of Protein phosphatase 2B mouse line (L7-PP2B^{KO} mice). We found that acute blockade of PP2B partially affected the vestibulo-ocular reflex (VOR) adaptation but not the reflex itself. Whereas chronic deletion of PP2B induced by tamoxifen in adult mice affected all kinds of plasticity and optokinetic reflex (OKR), but not VOR. Moreover, juvenile L7-PP2B^{KO} mice showed progressive PP2B deletion and behavioral impairments in an age-related manner. Together, our results provide authentic evidence that development might play an important role in the initiation of eye movement baseline reflex and adaptations. Notably, cerebellar development contributes to the initial set-point of VOR in the juvenile phase, which is unable to be reset after maturation of the cerebellum. Our findings shed light on understanding the development as well as its contributions to cerebellar dependent reflexes and motor learning.

In preparation

Introduction

The cerebellum, considered as a neuronal machine, plays a crucial role in the motor controls as well as their adaptation by determining how to perform accurate and correct movements^{1,2}. The primary cerebellar cyto-architecture that is the process of neurogenesis and wiring assembly during which cerebellar circuits and functions are established, is set during early development³. Early cerebellar damage is often associated with worse outcomes than that in adulthood, indicating a developmental role in the later cerebellar function⁴. Since it is highly conserved in phylogenesis, develops late in neuro-ontogeny, has a relatively simple anatomical structure, and entails versatile behavioral functions⁵⁻⁸, the cerebellum is considered as a prime model system for investigating the interactions between development and motor control as well as learning^{9,10}. Recently, increasing attention has been drawn on the cerebellar development and associated developmental disorders^{4,11,12}. While there is a wealth of knowledge on the development of motor behavior in human infants, children, and adolescents¹³⁻¹⁶, pre-clinical animal investigations have fallen behind on the study of the emergence of behavioral motifs across postnatal development. Accordingly, whether ontogenetic changes in cerebellar activity affect motor behavior or learning in rodents is still an open question. In this scenario, we speculate that the disruption of cerebellar function early in development, could not only have profound influences on the structure and function of the regions that it connects with, but also lead to abnormal behavioral magnifications at later stages.

To quantitatively evaluate the influence of postnatal development across the entire span, a sophisticated and specific functional cerebellar behavior is necessary. A prime example of such behaviors is the compensatory eye movements¹⁷, a group of reflexes including vestibule-ocular reflex (VOR) and optokinetic response (OKR) under the control of the cerebellar flocculus. VOR helps to maintain a stable image of the visual world on the retina during head movements by providing opposite movement of the eyes. OKR serves to stabilize a moving image on the retina by moving the eyes in the same direction with head movements. Both of them are plastic¹⁸⁻²⁰, for example, the amplitude of these reflexes can be adaptively adjusted whenever there is a visual image slip across the retina, thereby ensuring image stability throughout life, and if necessary, reestablishes the reflexes after damage. More specifically, in response to the altered visual environments, the VOR is able to increase or decrease its gain (eye velocity/head velocity), and even reverse its phase (eye to stimulus in degrees). Compensatory eye movement reflexes and their adaptations have many favorable attributes as a test of cerebellar function. They can be induced repeatedly with minimal fatigue, and produce an electronic record that is readily and objectively quantifiable.

In light of the concurrent development of the cerebellar size and structure, it is not equivalent to directly compare the behavioral changes across ages. Therefore, we shift our focus on calmodulin-activated protein phosphatase 2B (calcineurin or PP2B), which has been reported to play a role in acting as a molecular switch regulating the phosphorylation state of AMPA receptors. Previous study showed that adult Purkinje cell specific PP2B knockout (L7-PP2B^{KO}) mice exhibited severe deficits in both baseline reflexes and plasticity²¹. In this context, this mouse line provides a novel perspective to probe whether there is a developmental commitment in the establishment of innate motor behaviors.

In this study, by using comparative behavioral analysis in L7-PP2B^{KO} mice across various ages, we sought out to examine the effects of cerebellar development on compensatory eye movement baseline reflexes and plasticity. Our work highlights the developmental role during adaptive cerebellar function, and links the interactions between development and motor learning, thus helping for a better understanding and management of neurodevelopmental disorders.

Materials and Methods

Animals

For all experiments, we used adult male and female mice with a C57Bl/6 background that were, unless stated otherwise, individually housed, had food *ad libitum* and were on a 12:12 light/dark cycle. In all experiments the experimenters were blind to mouse genotypes. All experiments were approved by the Dutch Ethical Committee for animal experiments and were in accordance with the Institutional Animal Care and Use Committee. L7-PP2B^{KO} mice with PC-specific knockout of PP2B were used previously²¹.

Antibodies and peptides

The following primary antibodies and blocking peptide were used in the experiments: rabbit anti-PP2B (polyclonal, raised against the peptide with residues 450-500 of the human PP2BA protein, Genscript USA Inc.), which was used as blocking peptide. Rabbit anti-PP2B (polyclonal PPP3R1, proteintech) was used for immunostaining.

Immunohistochemistry

Anesthetized mice were perfused with 4% paraformaldehyde in 0.12M phosphate buffer (PB). Brains were taken out and post-fixed for 1 h in 4% PFA at room temperature, then transferred in 10% sucrose overnight at 4°C. The next day, the solution was changed for 30% sucrose and left overnight at 4°C. Non-embedded brains were sectioned either sagittally or transversally at 40µm thickness with freezing microtome. Free-floating sections were rinsed with 0.1M PB and incubated 2h in 10mM sodium citrate at 80°C for 2 h, for antigen retrieval. For immuno-fluorescence, sections were rinsed with 0.1M PB, followed by 30 minutes in Phosphate Buffered saline (PBS). Sections were incubated 90 minutes at room temperature in a solution of PBS/0.5% Triton-X100/10% normal horse serum to block nonspecific protein-binding sites, and incubated 48 h at 4°C in a solution of PBS/0.4% Triton-X100/2% normal horse serum, with primary antibodies as follows: Aldolase C (1:500, goat polyclonal, SC-12065), Calbindin (1:7000, mouse monoclonal, Sigma, #C9848), and PP2B (1:500, rabbit polyclonal, proteintech). After rinsing in PBS, sections were incubated 2 h at room temperature in PBS/0.4% Triton-X100/2% normal horse serum solution with secondary antibodies coupled with Alexa488, Cy3 or Cy5 (Jackson ImmunoResearch), at a concentration of 1:200. Sections were mounted on coverslip in chrome alum (gelatin/chromate) and covered with Mowiol (Polysciences Inc.). For Light Microscopy section were pre-treated for endogenous peroxidase activity blocking with 3% H₂O₂ in PBS, then rinsed for 30 minutes in PBS, incubated 90 minutes in a solution of PBS/0.5% Triton-X100/10% normal horse serum to block nonspecific

protein-binding sites, followed by the primary antibody incubation as described before. After 48 h, sections were rinsed in PBS and incubated 2h at room temperature in PBS/0.4% Triton-X100/10% normal horse serum solution with HRP coupled secondary antibodies (Jackson ImmunoResearch), at a concentration of 1:200. Sections were rinsed with 0.1M PB and incubated in diaminobenzidine (DAB, 75 mg/100ml) for 10 minutes. Sections were mounted on glasses in chrome alum (gelatin/chromate), dried with successive Ethanol steps, incubated in Xylene and covered with Permount mounting medium (Fisher Chemical). Images were acquired with an upright LSM 700 confocal microscope (Zeiss) for fluorescent microscopy.

Western blot

Cerebellar tissue from subjects was dissected and immediately frozen in liquid nitrogen. Samples were homogenized with a Dounce homogenizer in lysis buffer containing 50 mM Tris-HCl pH 8, 150 mM NaCl, 1% Triton X-100, 0.5% sodium deoxycholate, 0.1% SDS and protease inhibitor cocktail. Protein concentrations were measured using Pierce BCA protein assay kit (Thermo Fisher). Samples were denatured and proteins were separated by SDS-PAGE in Criterion™ TGX Stain-Free™ Gels (Bio-Rad), and transferred onto nitrocellulose membranes with the Trans-Blot® Turbo™ Blotting System (Bio-Rad). Membranes were blocked with 5% BSA (Sigma-Aldrich) in TBST (20mM Tris-HCl pH7.5, 150mM NaCl and 0.1%, Tween20) for 1 h and probed with the primary antibodies and secondary antibodies subsequently. Membranes were scanned by Odyssey Imager (LI-COR Biosciences) and quantified using Image Studio Lite (LI-COR Biosciences).

Stereotaxic injection

Two weeks prior to eye movement measurements, we performed stereotaxic injection of AAV2-CAG-eGFP virus carrying either PP2B peptides or scramble in the bilateral flocculi following a lateral-dorso-ventral direct approach (1 mm depth; 100-150 nl, UNC viral core, titres $1.0-1.2 \times 10^{13}$ vg ml⁻¹). After injection, the pipette was left in place for > 10 min before being slowly withdraw. All the process was done under isoflurane (4% induction, 1.5-2% maintenance) anesthesia.

Compensatory eye movement recordings

We subjected alert L7-PP2B^{KO} mice to compensatory eye movement recordings which were described in detail previously²¹. In short, mice were equipped with a pedestal under general anesthesia with isoflurane/O₂. After a 2-3 days of recovery, mice were head-fixed with the body loosely restrained in a custom-made restrainer and placed in the center of a turntable (diameter: 63 cm) in the experimental set-up. A round screen (diameter 60 cm) with a random dotted pattern ('drum') surrounded the mouse during the experiment. Compensatory eye movements were induced by sinusoidal rotation of the drum in light (OKR), rotation of the table in the dark (VOR) or the rotation of the table in the light (visually enhanced VOR, VVOR) with an amplitude of 5° at 0.1-1 Hz. Motor performance in response to these stimulations was evaluated by calculating the gain (eye velocity/stimulus velocity) and phase (eye to stimulus in degrees) of the response. Motor learning was studied by subjecting mice to mismatched visual and vestibular input. Rotating the drum (visual) and table (vestibular) simultaneously, in phase

at 0.6 Hz (both with an amplitude of 5°, 5 x 10 min) in the light will induce an increase of the gain of the VOR (in the dark). Subsequently, VOR Phase reversal was tested by continuing the next days (day 2-5, keeping mice in the dark in between experiments) with in phase stimulation, but now with drum amplitudes of 7.5° (days 2) and 10° (days 3, 4, and 5), while the amplitude of the turntable remained 5°. This resulted, over days of training, in the reversal of the VOR direction, from a normal compensatory rightward eye movement (in the dark), when the head turns left, to a reversed response with a leftward eye movement, when the head moves left. At the end of the VOR phase reversal training the OKR was probed again and compared to the OKR before training, to examine OKR gain increase. VOR gain increase was evoked by subjecting mice to out of phase drum and table stimulation at 1.0 Hz (both with an amplitude of 1.6°). A CCD camera was fixed to the turntable in order to monitor the eyes of the mice. Eye movements were recorded with eye-tracking software (ETL-200, ISCAN systems, Burlington, NA, USA). For eye illumination during the experiments, two infrared emitters (output 600 mW, dispersion angle 7°, peak wavelength 880 nm) were fixed to the table and a third emitter, which produced the tracked corneal reflection, was mounted to the camera and aligned horizontally with the optical axis of the camera. Eye movements were calibrated by moving the camera left-right (peak-to-peak 20°) during periods that the eye did not move²². Gain and phase values of eye movements were calculated using custom-made Matlab routines (MathWorks).

Statistics

All values are shown as mean ± SEM. For combined analysis of multiple sections, ANOVA for repeated measures was used to analyze eye movement. All statistical analyses were performed using SPSS 20.0 software. Data was considered statistically significant if $P < 0.05$. * $P < 0.05$, ** $P < 0.01$, *** $P < 0.001$.

Results

Acute blocking of PP2B partially affects the adaptation of VOR but not the reflex itself

Given that chronic deletion of PP2B in L7-PP2B^{KO} mice affects both baseline reflexes and plasticity, what is the effect of acute block? If its effect is equivalent to chronic, one would expect similar eye movements deficits in acute pharmacological inhibition of PP2B. To this end, we administered FK506, a selective PP2B inhibitor^{23,24} (10 mg/kg, i.p.) to L7-PP2B^{KO} wildtype littermate mice (n=8), and saline vehicle to L7-PP2B^{KO} mutant mice (n=6) as well as wildtype mice (n=7) respectively, 15mins prior to eye movement measurements (**Figure 2A**). Essentially, the pharmacological inhibition of PP2B by FK506 showed a similar hyper-phosphorylation of Ser778 in Dynamin1 to that of genetic deletion of PP2B^{25,26}, indicating a comparable blockage of the enzymatic activity of PP2B (**Figure 2A**). Consequently, the wildtype groups injected with FK506 and vehicle-only had a comparable motor performance during both baseline optokinetic reflex (OKR, $p=1$, repeated measure ANOVA with Bonferroni correction) VOR ($p=1$), whereas the mutant group injected with vehicle exhibited significant deficits in the baseline eye movements gain of the OKR ($p=0.01$) and VOR ($p=0.01$) across different frequencies (**Figure 2B-C**). Intriguingly, although FK506

wildtype group and vehicle-only wildtype group learned equally well in gain-decrease paradigm ($p=1$, **Figure 2D**), there was a significant impairment between the two in VOR phase-reversal training over 5 consecutive days ($p<0.001$, **Figure 2F**). As expected, L7-PP2B^{KO} mutant mice injected with vehicle were unable to learn both of this learning paradigms ($p<0.001$, **Figure 2D-F**). Thus, acute pharmacological blocking the enzymatic function of PP2B only partially affects VOR adaptation, while leaving all the reflexes intact.

Disrupting the binding of PP2B with other proteins does not affect baseline or plasticity of compensatory eye movements

Since PP2B contribute to the maintenance of PSD integrity and synaptic function²⁷, it may control synaptic functions not only via its enzymatic activity, but may also through a mechanism independent thereof, i.e. scaffolding structural function. We therefore set out to investigate whether the structural role of PP2B contributes to eye movement behaviors or not. To disrupt the interaction between PP2B and metabotropic glutamate receptor 1 (mGluR1) complex in vivo, we synthesized peptides that covered the entire length of PP2B, including three mGluR1-binding domains, and scramble sequence as a control. Subsequently, we bilaterally injected AAV virus containing flexed either PP2B peptides or scramble constructs into the bilateral flocculi of adult L7-PP2B^{KO} wildtype mice (**Figure 3A**). We found that neither OKR ($p=0.732$) or VOR ($p=0.103$) differed significantly between peptide-inhibition group ($n=6$) and scramble control group ($n=7$) (**Figure 3B-C**). Also, gain-decrease learning ($p=0.717$) and five days phase reversal adaptation ($p=0.736$) were comparable between the two groups (**Figure 3E-F**). These results implied that the non-enzymatic role of PP2B may be not involved in the baseline performance and adaptive plasticity.

Taken the results of acute blocking of PP2B by FK506 and peptide together, the function of regulating protein dephosphorylation as well as non-enzymatic scaffolding structure is unlikely to account for the whole behavioral deficiencies of baseline performance and plasticity. Thus, an explanation extending beyond acute deletion of PP2B, such as chronic influence of deletion, may be required.

Chronic deletion of PP2B after development completion affects OKR and VOR adaptations, but not VOR baseline performance

To determine whether chronic PP2B deletion affects the behavior of compensatory eye movements, we crossed the *loxP*-flanked PP2B mice with tamoxifen-dependent L7^{Cre-ERT2} to generate conditional L7-PP2B^{KO} mice (**Figure 4A**). Specifically, we applied tamoxifen to both L7^{Cre-ERT2};*CNB1*^{fl/fl} mice ($n=12$) and L7^{-/-};*CNB1*^{fl/fl} mice ($n=13$), and vehicle-only to L7^{Cre-ERT2};*CNB1*^{fl/fl} mice ($n=10$). If the deficits of eye movement baseline reflexes and plasticity are completely or in part of developmental origin, we should observe no or less changes in conditional L7-PP2B^{KO} adult mice after tamoxifen injections (injected after maturation). Indeed, there were no significant differences only in VOR performance among these three groups ($p=0.375$, **Figure 4C**), indicating that a developmental factor putatively contributes to the emergence of VOR. However, the other reflex such as OKR, and learning including gain-increase, gain-decrease as well as phase reversal, did show significant changes between L7^{Cre-ERT2};*CNB1*^{fl/fl} mice and L7^{-/-};*CNB1*^{fl/fl} mice after tamoxifen injection (OKR, $p=0.02$; Gain-increase, $p=0.047$; Gain-decrease, $p=0.001$; Phase reversal in day 4,

$p < 0.001$; repeated measure ANOVA with Bonferroni correction) (**Figure 4B** and **4D-F**, red and black lines). As expected, $L7^{Cre-ERT2/-}; CNB1^{fl/fl}$ mice injected either tamoxifen or vehicle did not differ in OKR and VOR adaptations (**Figure 4B** and **4D-F**, blue and black lines). It should be noted that 4 weeks after tamoxifen treatment, $L7^{Cre-ERT2/-}; CNB1^{fl/fl}$ mice had shown a virtually ablation of PP2B in PCs (**Figure 4G**), whereas there was no visible deletion in either $L7^{-/-}; CNB1^{fl/fl}$ mice injected with tamoxifen (**Figure 4H**) or $L7^{Cre-ERT2/-}; CNB1^{fl/fl}$ mice injected with vehicle (**Figure 4I**).

It seems that chronic PP2B deletion after cerebellar maturation is able to reset the appearance of OKR and plasticity; however, it is insufficient to affect VOR baseline performance, especially when compared to that of $L7$ -PP2B^{KO} mice (dotted line in **Figure 4C**). In this context, the concomitant questions are: where does the change in VOR come from? Is it a developmental effect?

PP2B deprivation and behavioral deficits in $L7$ -PP2B^{KO} mice progressively aggravate along with the cerebellar development

To answer above questions, we first examined the expression level of PP2B protein in the flocculus of $L7$ -PP2B^{KO} mice on various days at the juvenile age of postnatal (P) 14, 18, 20 and 24 days, respectively. Compared with the consistent existence of calbindin, PP2B showed a dynamic expression. Specifically, as early as age of P14 when mice started to open the eyes, a small proportion (roughly less than 20%) of Purkinje cells initiated the process of PP2B deletion (**Figure 5A**); at P18, the proportion of Purkinje cells with deleted PP2B became larger (nearly 50%, **Figure 5B**); notably, from P20 or P24 onwards, the Purkinje cells with PP2B deletion had already got access to the level of adult $L7$ -PP2B^{KO} mice (over 90%, **Figure 5C-D**).

Next, we investigated the measurement of compensatory eye movements in juvenile $L7$ -PP2B^{KO} mice at various age of P18-20, P26-30 and adulthood, respectively. At P18-20, $L7$ -PP2B^{KO} mice showed comparable baseline performance of OKR and VOR, as well as VOR gain-increasing learning, when compared with their littermate controls (KO, n=8-9; WT, n=10-11; OKR, $p=0.965$; VOR, $p=0.461$; Gain-increase, $p=0.636$, repeated measure ANOVA, **Figure 6A-C**). Note that PP2B deletion had almost reached a saturation level at this stage, yet it still did not affect the compensatory eye movements, indicating a developmental commitment. By contrast, $L7$ -PP2B^{KO} mice at P26-30 showed significant impairments in OKR (KO, n=10; WT, n=13; $p=0.001$), VOR (KO, n=8; WT, n=9; $p=0.047$) and phase reversal (KO, n=10; WT, n=11; $p < 0.001$) (**Figure 6A-B** and **6E**), and an affected gain-decrease learning in spite of non-statistic difference (KO, n=9; WT, n=8; $p=0.052$; **Figure 6D**). Likewise, adult group (the dataset was used previously²¹, here are shown in dotted lines), also showed significant but even more evident deficits than the mice of P26-30, across all the baseline performance and plasticity (KO, N=8-15; WT, n=8-23; all $p < 0.001$ except gain-decrease $p=0.002$, repeated measure ANOVA, **Figure 6A-E**). It is also noteworthy that juvenile mice (P26-30) exhibited a faster learning capability than adult mice in the 4 days phase reversal training (**Figure 6E**). Together, these findings offer authentic evidence that development might play an important role in the initiation of eye movement baseline reflexes as well as adaptations. Especially, cerebellar development appears to commit the onset of VOR functionality at the age of postnatal 3-4 weeks.

Discussion

In the present study, we found that acute blockage of PP2B enzymatically or structurally were not able to affect the baseline reflexes of compensatory eye movements, whereas chronic inducible PP2B ablation in adult mice could selectively affect OKR and VOR adaptations, but not VOR baseline performance. Moreover, at variance with the devoid of PP2B expression, juvenile L7-PP2B^{KO} mice at the age of P18-20 showed normal baseline performances as well as plasticity, compared with wildtype controls; subsequently, as the cerebellum developing, PP2B knockout mice at the age of P26-30 began to exhibit comparable impairments in OKR, VOR and VOR phase reversal with their adult mutant counterparts (see summary in **Figure 7**). Together, by interference of PP2B, our findings suggest that cerebellar development indeed contributes to the functional onset and progressive amelioration of compensatory eye movements.

The cerebellum provides an excellent platform to decipher ontogenetic steps for circuit assembly and the onset and maturation of gaze-stabilizing reflexes as well as adaptations. It has been reported that there are two processes assure adequate compensatory eye movements throughout life²⁸⁻³⁰: first, the congenital reflexes need to develop, until they are identical to those observed in adults. Thereafter, an adaptive, plastic process maintains this normal performance by calibrating the response to reduce visual field motion during head perturbations. Consistent with these two processes, our results found that as early as P18-20, Purkinje cell specific PP2B knockout mice exhibited normal eye movement performance and learning; one week later at age of P26-30, the deficiency in OKR and VOR gradually showed up, but VOR adaptation (gain-decrease) was still comparable with controls. Based on these findings, we postulate that the third to fourth postnatal weeks are the critical phases for the priming and refinement of OKR and VOR baseline performance as well as their adaptations. Notably, chronic ablation of PP2B induced by tamoxifen could not replicate the behavioral deficit selectively in VOR performance, indicating the requirement of development in the early stage. That is to say, the early phase (third-fourth postnatal weeks) is essential for the initiation of the VOR functionality, which is unable to reset in the later stages once the cerebellum becomes mature.

Why does the onset and fine-tuning of the compensatory eye movements take place at the third-fourth postnatal weeks? Given that eye opening occurs at postnatal 14-15 days in mice³¹, one possible reason may be attributed to the development of the visual pathway. It has been reported that early visual experience could influence the manifestation of VOR^{32,33}, thus we postulate that the maturation of visual pathways in the early phase is important to fashion neural structures mediating the VOR. An alternative explanation is the morphological ontogenesis of the cerebellum, which is regarded as cerebellum-intrinsic and not activity-dependent. The cerebellum undergoes its major growth in the third month and infant stage in humans, and the first 2 weeks after birth in mice, primarily due to expansion of granule cell progenitors^{34,35}. Studies in ferrets reveal concrete series of time courses: Purkinje cells are dispersed into a monolayer by P9, the formation of folia decreases abruptly at around P20, and the external granular layer peaks in thickness at around P22³⁶. It is suggested that although Purkinje cell subtype organization starts as early as embryonic stage, it is supposed to play a key role in instructing postnatal circuit wiring¹¹. In newborn rodents, Purkinje cells are

initially innervated by multiple climbing fibers with similar strengths in the first postnatal week, but from P9 to P17, climbing fibers successively undergo functional differentiation, dendritic translocation and elimination^{37,38}. Moreover, *in vivo* electrophysiological study in anesthetized and awake mice found that the firing rate of complex spike increased sharply at 3 weeks of age, whereas the firing rate of simple spike gradually increased until 4 weeks of age³⁹, which matches up with onset timing of the behavioral phenotypes in the current study.

During postnatal development, chemo- and activity-dependent mechanisms may also play a role in the set-point of eye movements. It is hypothesized that molecular mechanisms initially guide the basic ontogenetic wiring into a “crude” topographic map, whereas cerebellum-dependent activity is required to sculpt a “fine” map, establishing the spatio-temporal specificity of the reflex control¹¹. Therefore, one may argue that there is a possibility that PP2B, as a genetic cue, contributes to the development of eye movement control. However, we observed that the deletion of PP2B started at least from P14, and promptly reached the level similar to that of adult knockout mice as early as P20, which was at odds with the normal behaviors at the same age. Furthermore, acute blockage of PP2B only partially affected VOR phase reversal, while other types of adaptations and baseline reflexes were intact. Therefore, PP2B itself is hardly involved in the developing process of compensatory eye movements.

Given that cerebellar development is more protracted than other brain regions⁸, it appears to be more vulnerable and take higher risks of genetic or environmental disruptions, which putatively leads to abnormal motor behavioral magnifications. That is probably why many developmental disorders, such as autism, attention deficit hyperactivity disorder and developmental dyslexia and so on, have common cerebellar deficiencies^{4,9,11,12}. Since childhood movement disorders may progress to much worse forms in adulthood, it is important to elucidate how cerebellar development contributes motor controls in a systematic and comprehensive manner. Although tons of human studies have been performed to explore the developmental role of the cerebellum in eye movements^{13-15,40}, rodent studies are overtly lacking. By directly examining the relationship between cerebellar development and compensatory eye movement behavioral and adaptive functionality, our study found that developmental changes of the cerebellar assembly have significant implications for motor behaviors and adaptive learning at later stages; and the early phase of third and fourth postnatal weeks seem particularly critical for the development of normal function in mice.

To our knowledge, this is the first quantitative and comparative study that performed across various young stages of mouse regarding to compensatory eye movements. It is likely to have noticeable implications for the understanding and management of neurodevelopmental disorders. Future cerebellar functional studies could focus on whether other motor behaviors also change over postnatal development and how they might change when cerebellar development is altered due to neonatal perturbation or genetic factors.

References

- 1 Ito, M. Historical review of the significance of the cerebellum and the role of Purkinje cells in motor learning. *Ann N Y Acad Sci.* 2002; 978, 273-88.
- 2 De Zeeuw, C. I. & Yeo, C. H. Time and tide in cerebellar memory formation. *Curr Opin Neurobiol.* 2005; 15, 667-74.
- 3 Marzban, H., Del Bigio, M. R., Alizadeh, J. *et al.* Cellular commitment in the developing cerebellum. *Front Cell Neurosci.* 2014; 8, 450.
- 4 Wang, S. S., Kloth, A. D. & Badura, A. The cerebellum, sensitive periods, and autism. *Neuron.* 2014; 83, 518-32.
- 5 Larsell, O. The morphogenesis and adult pattern of the lobules and fissures of the cerebellum of the white rat. *J Comp Neurol.* 1952; 97, 281-356.
- 6 Hatten, M. E. & Heintz, N. Mechanisms of neural patterning and specification in the developing cerebellum. *Annu Rev Neurosci.* 1995; 18, 385-408.
- 7 Sillitoe, R. V., Marzban, H., Larouche, M. *et al.* Conservation of the architecture of the anterior lobe vermis of the cerebellum across mammalian species. *Prog Brain Res.* 2005; 148, 283-97.
- 8 Bayer, S. A., Altman, J., Russo, R. J. *et al.* Timetables of neurogenesis in the human brain based on experimentally determined patterns in the rat. *Neurotoxicology.* 1993; 14, 83-144.
- 9 Manto, M. U. & Jissendi, P. Cerebellum: links between development, developmental disorders and motor learning. *Front Neuroanat.* 2012; 6, 1.
- 10 Martinez, S. The cerebellum: from development to structural complexity and motor learning. *Front Neuroanat.* 2014; 8, 118.
- 11 Leto, K., Arancillo, M., Becker, E. B. *et al.* Consensus Paper: Cerebellar Development. *Cerebellum.* 2016; 15, 789-828.
- 12 Wang, R., Tan, J., Guo, J. *et al.* Aberrant Development and Synaptic Transmission of Cerebellar Cortex in a VPA Induced Mouse Autism Model. *Front Cell Neurosci.* 2018; 12, 500.
- 13 Charpiot, A., Tringali, S., Ionescu, E. *et al.* Vestibulo-ocular reflex and balance maturation in healthy children aged from six to twelve years. *Audiol Neurootol.* 2010; 15, 203-10.
- 14 Finocchio, D. V., Preston, K. L. & Fuchs, A. F. Infant eye movements: quantification of the vestibulo-ocular reflex and visual-vestibular interactions. *Vision Res.* 1991; 31, 1717-30.
- 15 Alahyane, N., Lemoine-Lardennois, C., Tailhefer, C. *et al.* Development and learning of saccadic eye movements in 7- to 42-month-old children. *J Vis.* 2016; 16, 6.
- 16 Roucoux, A., Culee, C. & Roucoux, M. Development of fixation and pursuit eye movements in human infants. *Behav Brain Res.* 1983; 10, 133-9.
- 17 Stahl, J. S. Using eye movements to assess brain function in mice. *Vision Res.* 2004; 44, 3401-10.
- 18 Faulstich, B. M., Onori, K. A. & du Lac, S. Comparison of plasticity and development of mouse optokinetic and vestibulo-ocular reflexes suggests differential gain control mechanisms. *Vision Res.* 2004; 44, 3419-27.
- 19 Katoh, A., Kitazawa, H., Itohara, S. *et al.* Dynamic characteristics and adaptability of mouse vestibulo-ocular and optokinetic response eye movements and the role of the flocculo-olivary system revealed by chemical lesions. *Proc Natl Acad Sci U S A.* 1998; 95, 7705-10.
- 20 Miles, F. A. & Lisberger, S. G. Plasticity in the vestibulo-ocular reflex: a new hypothesis. *Annu Rev Neurosci.* 1981; 4, 273-99.
- 21 Schonewille, M., Belmeguenai, A., Koekkoek, S. K. *et al.* Purkinje cell-specific knockout of the protein phosphatase PP2B impairs potentiation and cerebellar motor learning. *Neuron.* 2010; 67, 618-28.
- 22 Stahl, J. S. Using eye movements to assess brain function in mice. *Vision Res.* 2004; 44, 3401-10.
- 23 Butcher, S. P., Henshall, D. C., Teramura, Y. *et al.* Neuroprotective actions of FK506 in experimental stroke: in vivo evidence against an antiexcitotoxic mechanism. *J Neurosci.* 1997; 17, 6939-46.
- 24 Pardo, R., Colin, E., Regulier, E. *et al.* Inhibition of calcineurin by FK506 protects against polyglutamine-huntingtin toxicity through an increase of huntingtin phosphorylation at S421. *J Neurosci.* 2006; 26, 1635-45.
- 25 Clayton, E. L., Anggono, V., Smillie, K. J. *et al.* The phospho-dependent dynamin-syndapin interaction triggers activity-dependent bulk endocytosis of synaptic vesicles. *J Neurosci.* 2009; 29, 7706-17.
- 26 Cottrell, J. R., Levenson, J. M., Kim, S. H. *et al.* Working memory impairment in calcineurin knock-out mice is associated with alterations in synaptic vesicle cycling and disruption of high-frequency synaptic and network activity in prefrontal cortex. *J Neurosci.* 2013; 33, 10938-49.
- 27 Kuno, T., Mukai, H., Ito, A. *et al.* Distinct cellular expression of calcineurin A alpha and A beta in rat brain. *J Neurochem.* 1992; 58, 1643-51.
- 28 Eviatar, L., Miranda, S., Eviatar, A. *et al.* Development of nystagmus in response to vestibular stimulation in infants. *Ann Neurol.* 1979; 5, 508-14.
- 29 Gauthier, G. M. & Robinson, D. A. Adaptation of the human vestibuloocular reflex to magnifying lenses. *Brain Res.* 1975; 92, 331-5.

- 30 Sherman, K. R. & Keller, E. L. Vestibulo-ocular reflexes of adventitiously and congenitally blind adults. *Invest Ophthalmol Vis Sci.* 1986; 27, 1154-9.
- 31 Ko, H., Cossell, L., Baragli, C. *et al.* The emergence of functional microcircuits in visual cortex. *Nature.* 2013; 496, 96-100.
- 32 Weissman, B. M., DiScenna, A. O. & Leigh, R. J. Maturation of the vestibulo-ocular reflex in normal infants during the first 2 months of life. *Neurology.* 1989; 39, 534-8.
- 33 Goode, C. T., Maney, D. L., Rubel, E. W. *et al.* Visual influences on the development and recovery of the vestibuloocular reflex in the chicken. *J Neurophysiol.* 2001; 85, 1119-28.
- 34 Rakic, P. & Sidman, R. L. Histogenesis of cortical layers in human cerebellum, particularly the lamina dissecans. *J Comp Neurol.* 1970; 139, 473-500.
- 35 Dobbing, J. & Sands, J. Quantitative growth and development of human brain. *Arch Dis Child.* 1973; 48, 757-67.
- 36 Christensson, M., Broman, J. & Garwicz, M. Time course of cerebellar morphological development in postnatal ferrets: ontogenetic and comparative perspectives. *J Comp Neurol.* 2007; 501, 916-30.
- 37 Hashimoto, K. & Kano, M. Synapse elimination in the developing cerebellum. *Cell Mol Life Sci.* 2013; 70, 4667-80.
- 38 Watanabe, M. & Kano, M. Climbing fiber synapse elimination in cerebellar Purkinje cells. *Eur J Neurosci.* 2011; 34, 1697-710.
- 39 Arancillo, M., White, J. J., Lin, T. *et al.* In vivo analysis of Purkinje cell firing properties during postnatal mouse development. *J Neurophysiol.* 2015; 113, 578-91.
- 40 Krishna, O., Helo, A., Rama, P. *et al.* Gaze distribution analysis and saliency prediction across age groups. *PLoS One.* 2018; 13, e0193149.

Figure and Legend

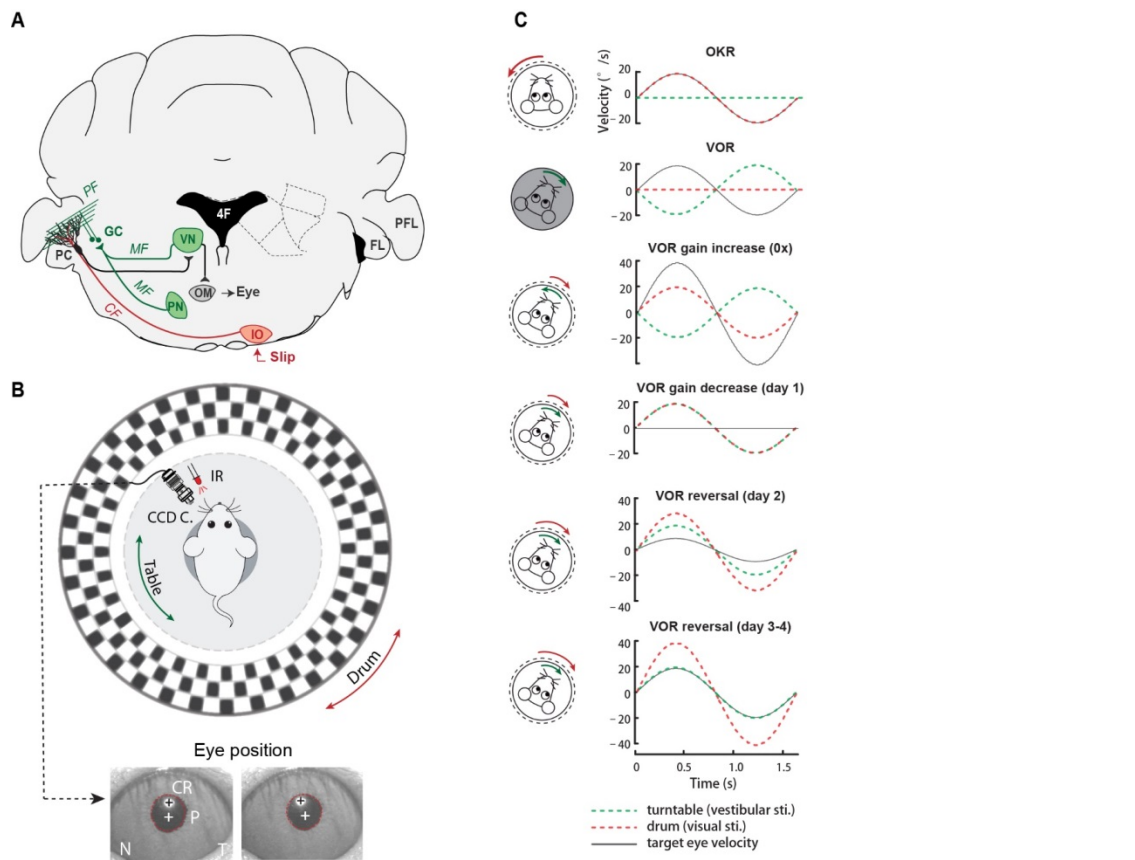


Figure 1 | Schematic illustration of compensatory eye movement behavioral paradigms

A, Cerebellar circuitry controlling compensatory eye movements and their adaptation. PCs in the flocculus (FL) receive vestibular and visual input via the mossy fiber (MF) - parallel fiber (PF) system (green) and climbing fiber input (CF, red) from the inferior olive (IO), indicating retinal slip. These two inputs converge on PCs, which influence eye movements via the vestibular nuclei (VN) and the oculomotor (OM) neurons. PN, pontine nuclei; GC, granule cell. **B**, Eye movement recording setup. Mice are head-fixed in the center of a turntable for vestibular stimulation and surrounded by a random dotted pattern ('drum') for visual stimulation. A CCD camera was used for infrared (IR) video-tracking of the left eye. Bottom, examples of nasal (N) and temporal (T) eye positions. Red circles, pupil fit; black cross, corneal reflection (CR); white cross, pupil center. **C**, Graphical explanation of the trajectory relationship among turntable (equivalent to vestibular stimulation, green dashed line), drum (equivalent to visual stimulation, red dashed line) and target eye trace (black line) in different compensatory eye movement baseline and adaptive behavioral paradigms at an amplitude of 5° and frequency of 0.6 Hz.

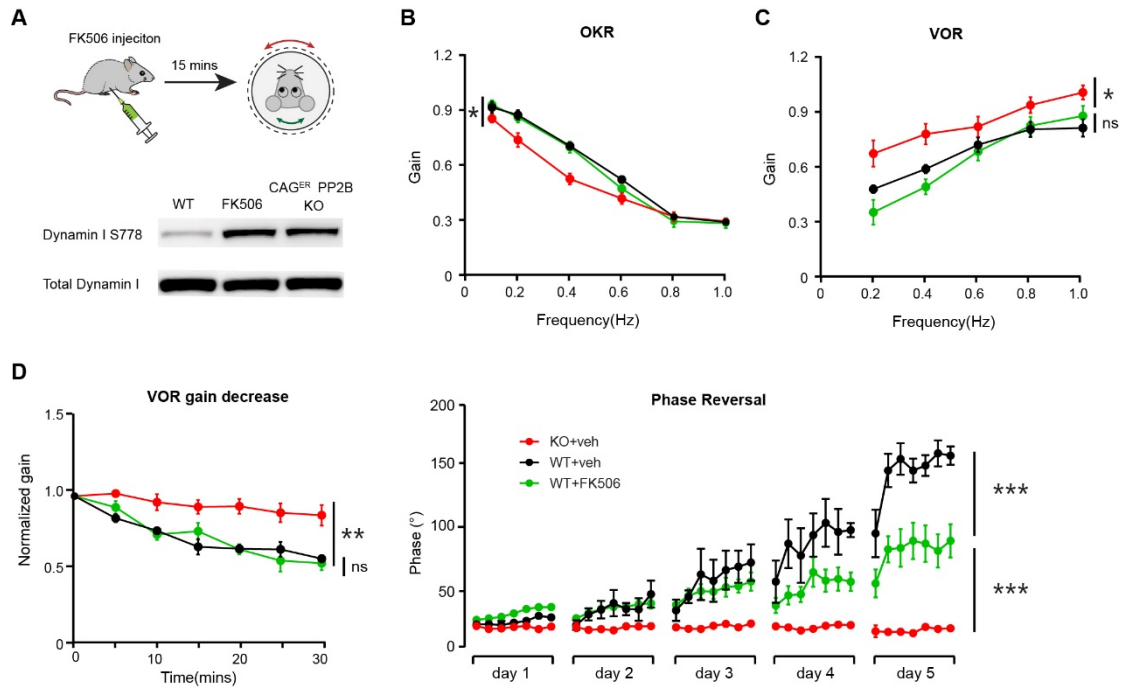


Figure 2 | Effects of acute pharmacological blocking of PP2B on compensatory eye movements

A, Top, schematic strategy of eye movement recording with FK506 injection. Bottom, western blot for validating FK506 inhibition efficiency, cortices tissues were collected from the mice after the behavioral experiments. **B-E**, Compensatory eye movement measurements during the optokinetic reflex (**B**), vestibulo-ocular reflex (**C**), gain-decrease learning (**D**) and phase reversal in consecutive 5 days (**E**) in L7-PP2B^{KO} wildtype littermate mice injected with FK506 (green, n=8), L7-PP2B^{KO} mutant mice (red, n=6) injected with vehicle as well as wildtype mice injected with vehicle (black, n=7). Data are represented as mean \pm SEM.

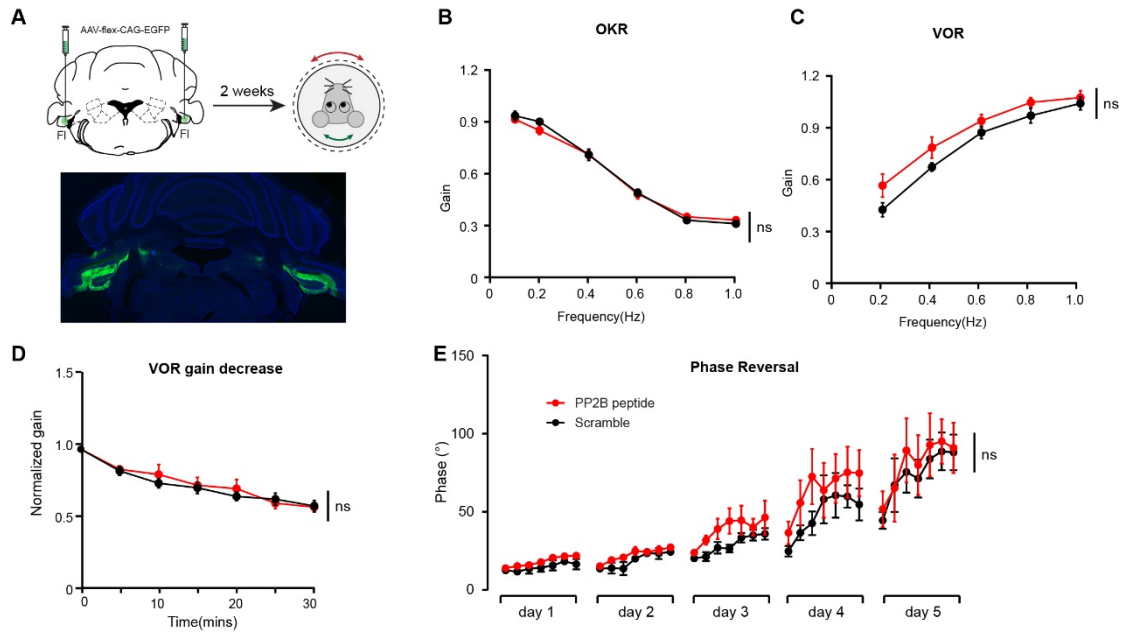


Figure 3 | Effects of acute inhibition of PP2B by peptides on compensatory eye movements

A, Top, schematic illustration of bilateral injections of AAVs into flocculus and concomitant eye movement measurements in two weeks. Bottom, Example of successful injections of AAV in bilateral flocculi (labeled with CAG-EGFP). **B-E**, Compensatory eye movement measurements during OKR (**B**), VOR (**C**), gain-decrease learning (**D**) and phase reversal in consecutive 5 days (**E**) in L7-PP2B^{KO} wildtype mice injected AAV virus containing flexed either PP2B peptides (red, n=6) or scramble constructs (black, n=7). Data are represented as mean ± SEM

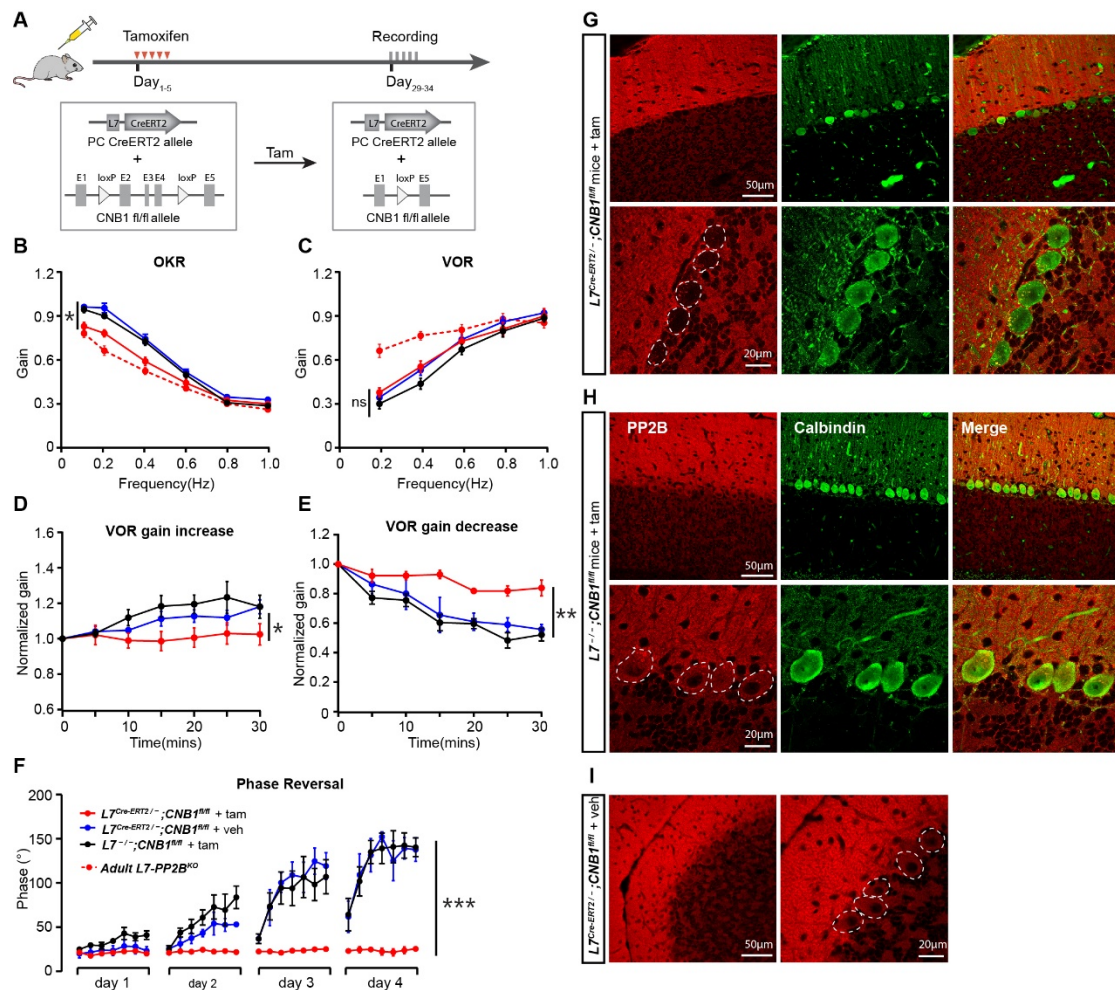


Figure 4 | Tamoxifen-induced chronic ablation of PP2B in adult mice

A, Generation of a Purkinje cell specific PP2B deletion triggered by tamoxifen. **B-F**, Compensatory eye movement measurements during OKR (B), VOR (C), gain-increase learning (D), gain-decrease learning (E) and phase reversal in consecutive 4 days (F) in *L7^{Cre-ERT2}^{-/-};CNB1^{fl/fl}* mice (red, n=12) and *L7^{-/-};CNB1^{fl/fl}* mice (black, n=13) by tamoxifen injection, and *L7^{Cre-ERT2}^{-/-};CNB1^{fl/fl}* mice injected with vehicle-only (blue, n=10). Dotted lines are referred to as adult group. Data are represented as mean \pm SEM. **G-I**, Corresponding immunofluorescent images of each groups. White dotted lines indicate the somata of Purkinje cells.

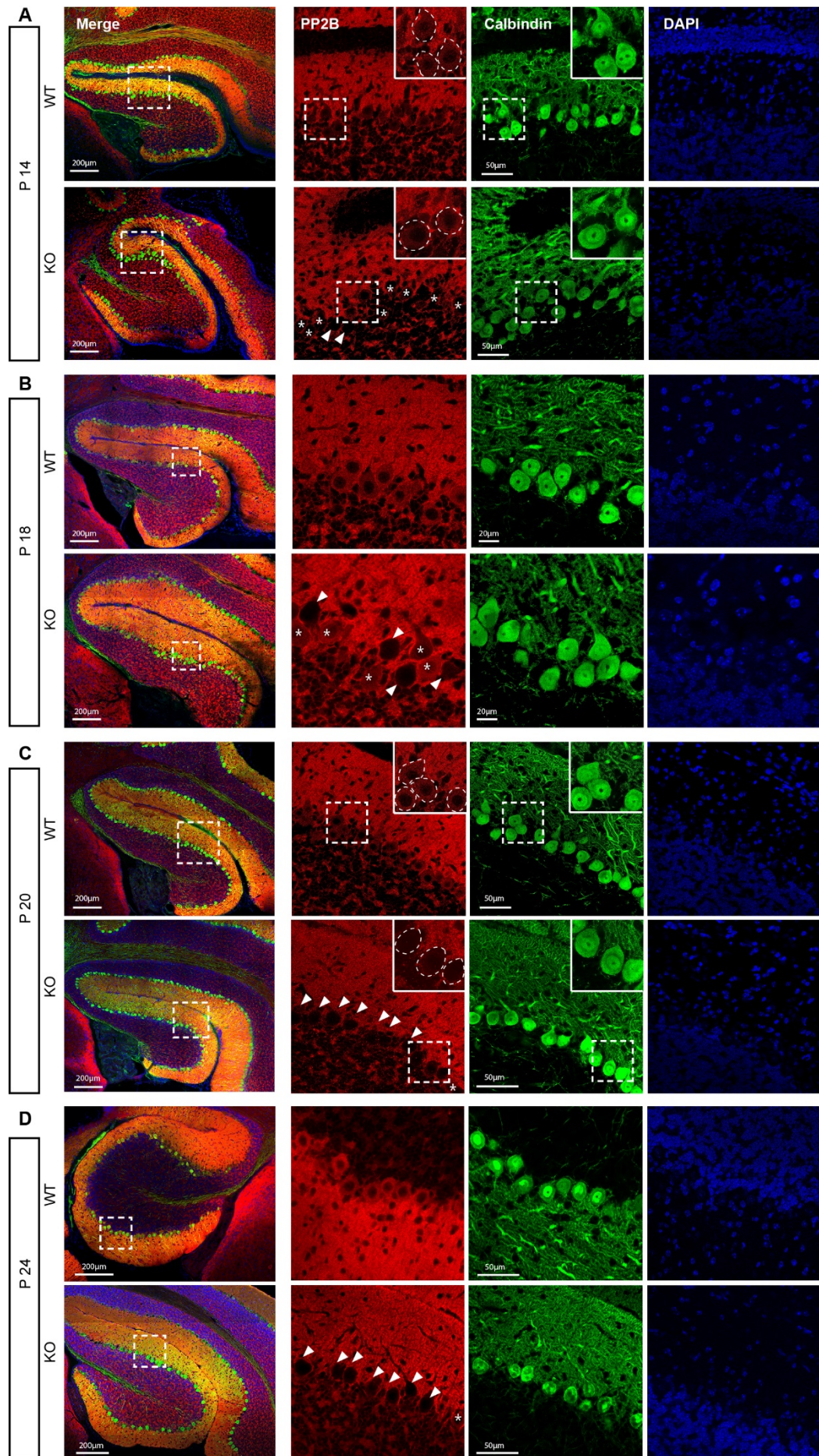


Figure 5 | Expression of PP2B in the developing L7-PP2B^{KO} mice

Immunofluorescent images of PP2B expression in the flocculus of L7-PP2B^{KO} mice at the juvenile ages of postnatal (P) 14 (A), 18 (B), 20 (C) and 24 (D) days. Leftmost lane, overview staining of flocculi; framed areas are magnified on the right three lanes (red, PP2B; green, calbindin; blue, DAPI). White dotted lines indicate the somata of Purkinje cells. White triangles indicate Purkinje cell somata with the absence of PP2B, white asterisks indicate Purkinje cell somata with the presence of PP2B.

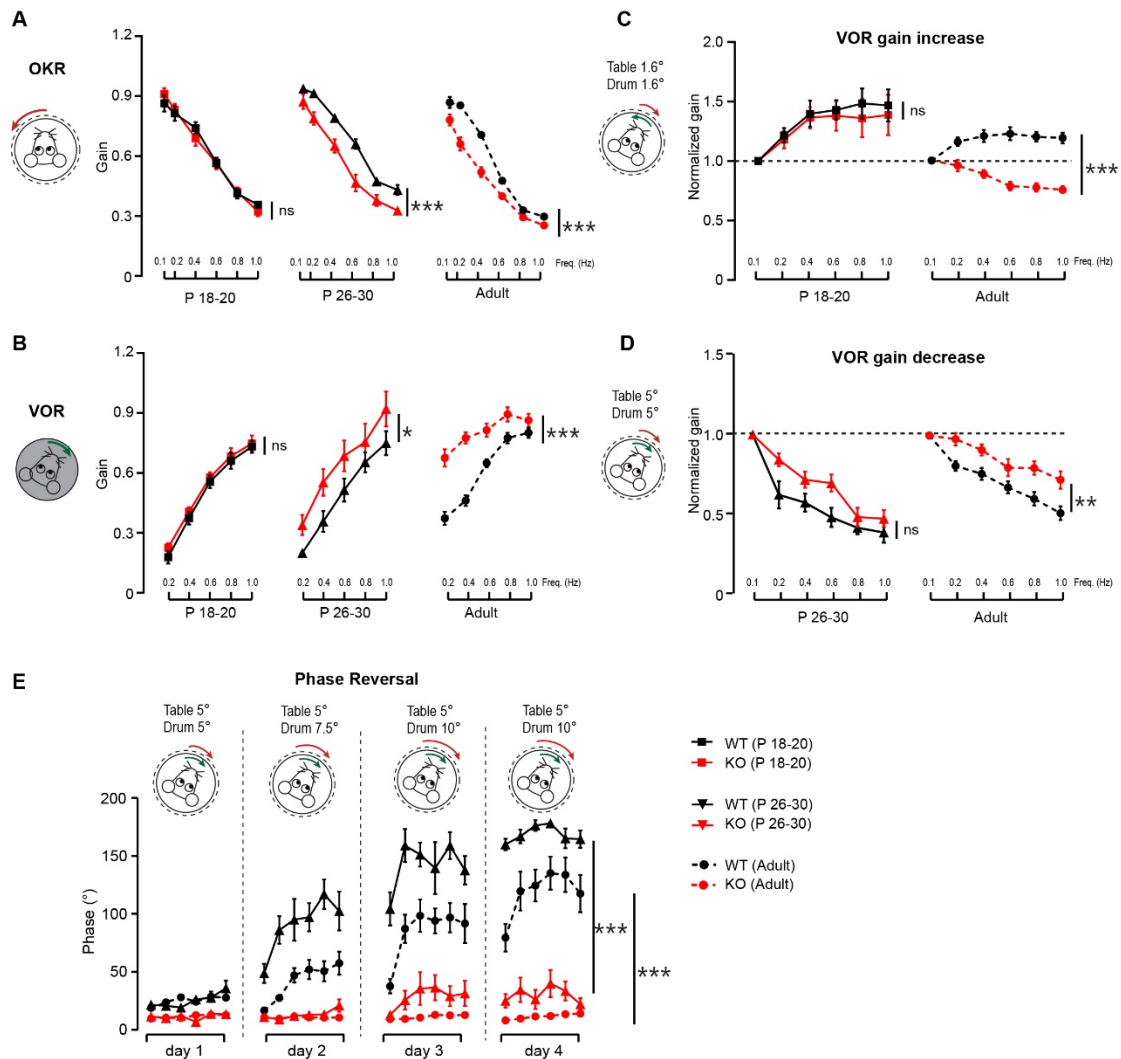
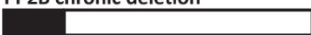


Figure 6 | L7-PP2B^{KO} mice show progressive behavioral impairments in an age-related manner

Compensatory eye movement measurements of OKR (A), VOR (B), gain-increase learning (C), gain-decrease learning (D) and phase reversal in consecutive 4 days (E) in L7-PP2B^{KO} mice at various age of P18-20 (squared lines), P26-30 (triangular lines) and adulthood (dotted lines). Wildtype group are shown in black; mutant group are shown in red; data are represented as mean ± SEM.

PP2B manipulation \ behavior	OKR	VOR	Gain-increase	Gain-decrease	Phase reversal
PP2B chronic deletion 	×	×	×	×	×
PP2B acute deletion 	✓	✓	—	✓	×
PP2B chronic deletion after development completion 	×	✓	×	×	×
PP2B deletion in developing juvenile mice					
 P18-20	✓	✓	✓	—	✓
 P26-30	×	×	—	✓	×

 Presence
 Absence
 not affected
 affected
 not available

Figure 7 | Summary of the impacts of various PP2B genetic manipulation strategies on compensatory eye movements

Supplemental tables | Behavioral statistics (repeated measures ANOVA) for various PP2B interference groups

Table 1. WT injected with FK506 group

Paradigms	Mice # (1/2/3)	Comparisons	P-value
OKR	7/6/8	1-2	0.042
		1-3	1
		2-3	0.093
VOR	7/6/8	1-2	0.055
		1-3	1
		2-3	0.013
VOR gain decrease	7/6/8	1-2	0.002
		1-3	1
		2-3	0.002
Phase reversal (Day 5)	7/6/8	1-2	< 0.001
		1-3	< 0.001
		2-3	0.001

Bonferroni correction for multiple comparisons. 1: WT+veh; 2: KO+veh; 3: WT+FK506

Table 2. WT injected with pp2b-peptide group

Paradigms	Mice # (1/2)	F-value	P-value
OKR	6/7	0.124	0.732
VOR	6/7	3.16	0.103
VOR gain decrease	6/7	0.138	0.717
Phase reversal (Day 5)	6/7	0.120	0.736

1: WT + PP2B peptide; 2: WT + scramble

Table 3. L7-PP2B^{CKO} (tamoxifen inducible) group

Paradigms	Mice # (1/2/3)	Comparisons	P-value
OKR	12/10/13	1-2	0.564
		1-3	0.020
		2-3	0.001
VOR	12/10/13	1-2	0.216
		1-3	0.375
		2-3	1.00
VOR gain increase	7/8/9	1-2	1
		1-3	0.047
		2-3	0.303
VOR gain decrease	6/4/6	1-2	1.00
		1-3	0.001
		2-3	0.018
Phase reversal (Day 4)	6/4/6	1-2	1.00
		1-3	< 0.001
		2-3	< 0.001

Bonferroni correction for multiple comparisons .

- 1: L7^{-/-};CNB1^{fl/fl} mice + tam;
- 2: L7^{Cre-ERT2/-};CNB1^{fl/fl} mice + veh;
3. L7^{Cre-ERT2/-};CNB1^{fl/fl} mice + tam

Table 4. P18-20 cohort

Paradigms	Mice # (WT/MUT)	F-value	P-value
OKR	11/9	0.002	0.965
VOR	11/8	0.568	0.461
VOR gain increase	10/9	0.232	0.636
VOR gain decrease	-	-	-
Phase reversal	-	-	-

Table 5. P26-28 cohort

Paradigms	Mice # (WT/MUT)	F-value	P-value
OKR	13/10	14.7	0.001
VOR	9/8	4.69	0.047
VOR gain increase	-	-	-
VOR gain decrease	8/9	4.51	0.052
Phase reversal (Day 4)	11/10	375	< 0.001

Table 6. Adult cohort

Paradigms	Mice # (WT/MUT)	F-value	P-value
OKR	23/15	32.5	< 0.001
VOR	23/14	29.2	< 0.001
VOR gain increase	13/10	57.2	< 0.001
VOR gain decrease	13/13	12.0	0.002
Phase reversal (Day 4)	8/8	65.4	< 0.001

CHAPTER

6.2

Interactions of protein phosphatase 2B with PSD-proteins support synaptic integrity and cerebellar learning

Zhanmin Lin¹, Bin Wu¹, Maarten Paul², Ka Wan Li³, Yao Yao⁴, Ihor Smal⁴, Martina Proietti Onori¹, Hana Hasanbegovic¹, Karel Bezstarosti⁵, Jeroen Demmers⁵, Adriaan Houtsmuller², Erik Meijering⁴, Freek Hoebeek¹, Martijn Schonewille¹, August B Smit^{3#}, Zhenyu Gao^{1#*} and Chris I. De Zeeuw^{1,5}

¹ Department of Neuroscience, Erasmus MC, Rotterdam, The Netherlands.

² Optical Imaging Center, Erasmus MC, Rotterdam, The Netherlands.

³ Department of Molecular and Cellular Neurobiology, Center for Neurogenomics and Cognitive Research, VU University Amsterdam, Amsterdam, The Netherlands.

⁴ Center for Proteomics, Erasmus MC, Rotterdam, The Netherlands.

⁵ Netherlands Institute for Neuroscience, KNAW, Amsterdam, The Netherlands.

Correspondence to A.B.S. guus.smit@vu.nl or Z.G. z.gao@erasmusmc.nl

* Lead contact to Z.G. z.gao@erasmusmc.nl

In preparation

Abstract

Protein phosphatase 2B (PP2B) is critical for synaptic plasticity and learning. Yet, the precise molecular mechanisms by which PP2B controls these processes remain largely unclear. Following mass-spectrometry of synaptosomes and co-immunoprecipitation experiments we identified structural proteins and receptor subunits that directly interact with PP2B at postsynaptic densities (PSDs) of cerebellar Purkinje cells. Deleting PP2B in Purkinje cells resulted in significant downregulation of PSD proteins without affecting the phosphorylation state on average. The impaired synaptic nanoclusters of these proteins were restored by re-expression of PP2B, partly independent of its phosphatase activity. Likewise, the mobility of surface glutamate receptors and the level of motor learning were at least partly controlled by a non-enzymatic function of PP2B. Thus, we identified a novel mechanism by which PP2B controls the integrity of PF-PC synapses, and propose a combined phosphatase and structural role of PP2B in governing synaptic function and learning.

Introduction

The maintenance and modulation of synaptic transmission is critical for virtually all brain functions, varying from online control of perception and action up to long-term processes, such as memory formation and retrieval. One of the main cellular mechanisms by which neurons control synaptic efficacy is to dynamically set the phosphorylation state of synaptic proteins¹. Phosphorylation is achieved by activation of protein kinases, such as PKA, PKC and CaMKII², whereas dephosphorylation is accomplished by protein phosphatases (Hunter, 1995; Mulkey et al., 1994; Shi, 2009). Phosphoprotein phosphatase 2B (PP2B, calcineurin), which predominantly dephosphorylates proteins on Ser and Thr residues (Stemmer and Klee, 1991), accounts for up to 1% of the total protein in mammalian neurons and is enriched in synapses^{3,4}.

PP2B phosphatase activity is triggered by binding of the Ca²⁺/calmodulin complex^{5,6}, which leads to dephosphorylation of synaptic and cytoplasmic proteins in a Ca²⁺-dependent manner. Upon Ca²⁺ influx, activated PP2B is often in direct competition with protein kinases PKA and CaMKII, which can provide a complex phosphorylation/dephosphorylation signature of proteins³. Thereby, the Ca²⁺ concentration can determine the state of phosphorylation and dephosphorylation of synaptic proteins and change their functional status. For example, the phosphorylation state of AMPA receptors determines to what extent they will be subject to exocytosis or endocytosis⁷. Such a Ca²⁺-dependent dynamic switch of the phosphorylation state of AMPA receptors has been postulated to determine the threshold and direction for the induction of long-term plasticity, i.e., controlling the level of long-term potentiation (LTP) or long-term depression (LTD) (also referred to as the Bienenstock-Cooper-Munro plasticity rule⁸). Indeed, it has been shown that PP2B directly regulates the dephosphorylation of Ser845 of GluR1 by binding to scaffold protein AKAP150⁹⁻¹¹. The phosphorylation state of GluR1 Ser845 in turn can regulate receptor insertion and removal from the membrane, underlying LTP and LTD induction, respectively. Consequently, various forms of procedural and declarative memory formation have been shown to depend on proper functioning of PP2B¹²⁻¹⁴.

Interestingly, over the past decade CaMKII has been shown to operate not only as an enzyme, i.e., a kinase, but also as a structural synaptic protein^{2,15}. For example, the presence of kinase-dead CaMKII is sufficient for normal short-term presynaptic plasticity and activity-dependent proteasome redistribution in hippocampal neurons, indicating its kinase activity is not essential for these functions¹⁶⁻¹⁸. Given the prominent enrichment of PP2B in the synapse⁴, we set out to test the hypothesis that PP2B may control, like CaMKII, synaptic functions not only via its enzymatic activity, but also through a mechanism independent thereof. Our data show that blocking the enzymatic function of PP2B only partially affects adaptation of the vestibulo-ocular reflex (VOR), whereas ablation of PP2B in Purkinje cells completely blocks this form of motor learning. Accordingly, at the parallel fiber to Purkinje cell (PF-PC) synapse PP2B interacts with Shank2 and binds directly to Homer3 and mGluR1, all of which are prominently distributed at the postsynaptic density (PSD), and these proteins remain prominently present at the synapse as long as PP2B is present, even in its phospho-dead form. In addition, we demonstrate a crucial role of PP2B in controlling surface mobility of glutamatergic receptors at the PF-PC synapse, and distribution of its PSD proteins. Moreover, our data suggest that phospho-dead PP2B contributes to VOR learning. Together, our data show that PP2B does not only operate as an enzyme, but also serves a critical role in controlling PSD structure, highlighting a dual function of PP2B in governing synaptic plasticity and learning.

Results

Selective inhibition of phosphatase activity of PP2B partially impairs cerebellar learning

Cell-type specific knockout of PP2B in cerebellar Purkinje cells (L7-PP2B KO mice) has been shown to result in marked cerebellar learning deficits, including that of adaptation of the VOR¹⁹. We first evaluated whether these deficits were solely caused by loss of phosphatase activity during learning. If so, we should expect to observe similar impairments when the phosphatase activity of PP2B is pharmacologically inhibited. To this end WT mice (n=8) were systemically injected with the selective PP2B inhibitor, FK506^{20,21} (10 mg/kg, i.p.), for the 5 consecutive days during which they were subjected to the eye movement measurements.

Levels of eye movement performance and learning were assessed, and compared with those in L7-PP2B KO mice (n=7), as well as in WT controls (n=7) that received injections with the vehicle. The groups injected with FK506 and vehicle-only had a comparable motor performance during both baseline optokinetic reflex (OKR, $p = 0.9$), baseline VOR ($p = 0.50$) and VOR in the light (VVOR, $p = 0.95$) (**Figs. 1A-C**). In contrast, genetic deletion of PP2B in Purkinje cells exhibited small but significant deficits in the baseline eye movements amplitudes of the OKR ($p = 0.01$) and VOR in the dark ($p = 0.01$) across different frequencies, whereas motor performance during VVOR was similar across the three groups (**Figs. 1A-C**). We subsequently probed the level of cerebellar learning in these mice with a visuo-vestibular gain-decrease training paradigm (Schonewille et al., 2010). Whereas the groups injected with FK506 and vehicle-only learned equally well in this gain-decrease paradigm ($p > 0.99$), L7-PP2B KO mice were unable to learn the same paradigm ($p = 0.0003$, **Fig. 1D**). Subsequent VOR phase-reversal training over 5 consecutive days caused a prominent reversal of eye movement direction in the animals injected with vehicle-only and some learning in the animals injected with FK506, but failed to induce phase-reversal in the L7-PP2B KO mice ($p < 0.0001$, **Fig. 1E**). Thus, although chronic pharmacological inhibition of the enzymatic function of PP2B resulted in a deficit in the phase-reversal learning, the level of learning was still significantly better than that in the L7-PP2B KO mice ($p < 0.0001$, **Fig. 1E**). Given that pharmacological inhibition of PP2B by FK506 and genetic deletion of PP2B are likely to induce a comparable blockage of the enzymatic activity of PP2B, since both result in a similar hyperphosphorylation of Ser778 in Dynamin1 (**Fig. S1**, see methods)^{22,23}, the differences in behavioral learning between the animals injected with FK506 and the L7-PP2B KO mice require an explanation that extends beyond enzymatic control of PP2B. We therefore set out to investigate to what extent PP2B may also exert functions other than regulating protein dephosphorylation.

Multiple PP2B interacting proteins are down-regulated in the L7-PP2B KO mice

To clarify the effects of genetic deletion of PP2B at the level of protein composition in the PF to PC synapse, which is supposed to be one of the main sites for mediating VOR learning²⁴, we used a quantitative iTRAQ proteomic analysis (see **methods**) of the molecular layer of both L7-PP2B KO and A6-PP2B KO mice, in which PP2B was selectively ablated from PCs and granule cells (GCs), respectively^{19,25}. Given that granule cells provide the PFs to the PCs, with this approach we were able to compare the protein composition of a P2 + microsome fraction in which PP2B was selectively deleted from the pre- or postsynaptic compartment of the PF-PC synapse (**Fig. 2A**). Quantitative iTRAQ analysis of the synaptic protein composition of the L7-PP2B mice revealed a lower abundance of seven proteins (**Fig. 2A**), including two postsynaptic receptors (mGluR1, Grid2) and five well-studied PSD proteins (Homer3, Shank1, Shank2, α CaMKII and Shisa6). Due to the stringent rules we applied to the iTRAQ analysis (see **methods**), these results are likely to underestimate the overall alterations in the synapse. The changes in protein levels were subsequently validated by immunoblotting of the L7-PP2B vs. WT PF-PC synaptosome samples and verified in three independent experiments. Indeed, here we confirmed the alterations of the 7 proteins mentioned above. Additional immunoblotting for β CaMKII, GluR2 and GluR3 (but not GluR1) showed lower levels in the L7-PP2B mice (**Fig. 2B-D**). None of these proteins were significantly down-regulated in the A6-PP2B KO mice (**Suppl Table a6PP2B iTRAQ**). Interestingly, the iTRAQ analysis of the A6-PP2B KO mice showed altered expression of, for example, the presynaptic Synapsin1/2, VAMP2, and TMEM163 (**Fig. 2A; Suppl Table a6PP2B iTRAQ**), thus differentiating the impact of PP2B deletion in controlling the synaptic protein levels at the postsynaptic side from that at the presynaptic side of PF-PC synapses.

These results raise the question to what extent the lower protein levels in the L7-PP2B KO mice can be explained by an altered level of phosphorylation of these proteins. We therefore compared the level of synaptic phospho-peptides between the L7-PP2B KO and their WT littermates (see **methods**). The majority of PSD proteins showed no significant change (<50% fold change) following PC-specific ablation of PP2B, but we found a significantly ($p < 0.001$) elevated phosphorylation level for several sites of Shank1, Shank2, pcp2 and Cacna1g (**Fig. 2E; Suppl. Table Phospho-proteomics**). The phosphorylation state of other proteins that we established with lower levels in the L7-PP2B KO, i.e., Homer3, mGluR1, α CaMKII, β CaMKII and Grid2, was not changed (**Fig 2E-F**). These data indicate that

PP2B may regulate the level of various PSD proteins without affecting their phosphorylation level on average.

PP2B stably and directly interacts with multiple PSD proteins

To explore how PP2B deletion could affect the synaptic protein levels at the PF-PC synapse, we used antibodies specifically against PP2B to capture the stable PP2B interactors from the synaptic membrane fraction and we subsequently determined their identity using high resolution liquid chromatography/mass spectrometry (LC-MS/MS) (workflow **Fig. 3A**; see also methods). Of all proteins detected with this immuno-precipitation (i.e., all P2-fragments) 79 were considered as stable PP2B interactors, which could be divided into 5 partially overlapping groups following Ingenuity Pathway Analysis (**Fig. 3B**; **Supp Table cerebellum IP combined**). These included receptors (group 1: e.g., mGluR1, and Grid2), calcium-related proteins (group 2: e.g., calmodulin, β CaMKII, and calcium-dependent ATPases), enzymes (group 3: e.g., Dynamin, PLPPR4 and DLAT), transporters (group 4: e.g., HSP3, SYT and 14-3-3(3)), and structural proteins (group 5: e.g., Homer3, Shank1/2 and Actin). These results indicate that PP2B interacts with multiple functional groups in PF-PC synapses.

As PP2B deletion appeared to affect the level of seven proteins specifically and these proteins were found in the PP2B IP, we investigated whether PP2B directly interacts with each of these proteins or through a common protein²⁶. We separately co-expressed PP2B with some of the candidate PSD proteins in HEK293 cells and tested their binding using immuno-precipitation experiments. Because native PP2B is also present in HEK293 cells, exogenous CNA was labeled with a flag tag. Based on the LC-MS/MS results, we chose to co-express Homer3, mGluR1, Grid2, Shank1, Shank2, α CaMKII, and β CaMKII individually with CNA subunits. All tested PSD proteins apart from Shank2 were confirmed to directly and stably bind to the CNA subunit of PP2B (**Fig. 3D**). These results illustrate a direct protein-protein binding between PP2B and these interactors.

To further investigate the composition of PP2B containing protein complexes in their native binding states, we performed blue-native PAGE(BN)-LC-MS/MS analysis on the PP2B immuno-precipitated samples of the PF-PC synapses²⁷. PP2B containing complexes were separated by mass on a blue-native gel and subsequently divided into 30 slices. Each slice was processed and analyzed for protein content by mass spectrometry separately (workflow **Fig. 3A lower panel**). The PP2B subunits, CNA and CNB, were present in the BN-gel throughout all molecular weights, demonstrating the mass diversity of PP2B containing complexes (**Fig. 3C**). However, two prominent peaks were observed in the CNA and CNB distribution, one at ~60 kDa and one at ~480 kDa, which represent the majority of PP2B protein in complexes. Calmodulin tightly migrated with the lower molecular weight form of PP2B. mGluR1 migrates with the higher MW complex of PP2B. Other PP2B interactors such as Shank1, Homer 3, Grid2, α CaMKII, and β CaMKII were all detected in the very large molecular weight protein complexes in which the amount of PP2B protein is low. Together these data demonstrate two major different PP2B containing complexes at the PF-PC synapse, and the presence of minor large molecular weight PP2B-PSD protein complexes in PF-PC synapses.

dSTORM reveals how PP2B affects distribution of PSD interactors

We then examined whether PP2B has any role in controlling the distribution of its PSD interactors at the nanoscopic level. We utilized direct stochastic optical reconstruction microscopy (dSTORM) to resolve the fine structures of these proteins in the synapse and PSD (Dani et al., 2010; Huang et al., 2010). Five PP2B interacting proteins, including Shank1, Shank2, Grid2, Homer3 and mGluR1, were labeled in cultured cerebellar PCs, and the geometry of their localization in PF-PC synapses were quantified (**Fig. 4A-C**). Clusters containing Homer3 and mGluR1 were smaller in PCs derived from L7-PP2B KO mice than in those from WTs (**Fig. 4B, C**). Instead, the cluster sizes of Shank1, Shank2 and Grid2 were increased in the PP2B KO PCs (**Fig. 4B, C**). We next asked to what extent these alterations were induced by a lack of phosphatase activity. Thereto, WT PCs were cultured in the presence of FK506 (2 μ M) to acutely (30 min; referred to as FKA) or chronically (18 days; referred to as FKL) inhibit the phosphatase activity of PP2B. Acute inhibition of PP2B had no effect on the size of clusters of these PSD proteins (**Fig. 4B**). In contrast, chronic PP2B inhibition significantly decreased ($p < 0.0001$) and increased ($p < 0.0001$) the size of the

clusters of Homer3 and Grid2, respectively. Importantly, chronic PP2B inhibition did not change the cluster sizes of Shank1, Shank2 and mGluR1, distinct from the phenotypes of L7-PP2B KO PCs. These results further support a dual role of PP2B, exerting both a phosphatase and structural function in maintaining PSD integrity at the nanoscopic level.

To find out to what extent the role of PP2B in the formation of the PSD nano-clusters is essential, we sought to rescue the changes of nano-clusters by re-expressing PP2B in the KO Purkinje cells. Re-expressing native PP2B reinstated the size of clusters of all 5 synaptic proteins not the case for shank1 (**Fig. 4C**). Importantly, when we re-expressed a PP2B variant that lacks phosphatase activity (phospho-dead PP2B 151A^{28,29}) in PP2B KO cells, the nano-cluster distributions of Homer3, mGluR1, and Shank2 were restored to WT levels (**Fig. 4C**). These data illustrate a stringent PP2B-dependent regulation of PSD proteins and indicate that the synaptic distribution of Homer3, mGluR1 and Shank2 can be regulated by PP2B in a phosphatase-independent manner (**Fig. 4D**).

Glutamate receptors mobility is influenced by PP2B

Since the surface expression of AMPA receptors is regulated by their phosphorylation state, it is possible that a lack of PP2B phosphatase activity will alter the surface expression of AMPA receptors. Indeed, we observed a consistent increase in the size of surface GluR2 in FKA and FKL treated PCs as well as in PCs derived from L7-PP2B KO mice (**Fig. S4A**). Concurrently, an enhanced miniature EPSC amplitude was observed in the PCs of three groups in which the phosphatase activity was reduced (**Fig. S4B, C**), suggests a phosphatase-dependent elevation of functional AMPA receptors at their PF-PC synapses, which may reflect a form of homeostatic compensation for the lack of LTP.

The function of glutamatergic receptors at synapses is affected not only by the total surface expression, but also by their lateral mobility^{30,31}. We next conducted a set of experiments to examine how the mobility of glutamate receptors were affected by pharmacological or genetic inhibition of PP2B in cultured PCs (**Fig. 5A**). Single molecule tracking was performed for the ionotropic glutamatergic receptor subunits, GluR1, GluR2, and the metabotropic receptor mGluR1, i.e., three of the main receptor subunits present in PCs³². The overall mobility of these glutamate receptors was similar to the ones observed in cultured hippocampal neurons (**Fig. 5**)³³. Acute and chronic inhibition of PP2B phosphatase activity in wild type PCs with FK506 (i.e., the FKA and FKL groups) did not significantly alter the receptor mobility of mGluR1, GluR1 or GluR2 ($p = 1$) (**Fig. 5B-D**). Compared with the receptor mobility to the WT groups, L7-PP2B KO PCs had a significantly smaller mobile fraction for all three receptors ($p < 0.0001$, $p = 0.0003$, $p < 0.0001$; for mGluR1, GluR1, GluR2, respectively, Mann-Whitney test) (**Fig. 5B-D**). Notably, the receptor mobility in the FKA and that in the FKL group were generally higher than that in the L7-PP2B KO group, indicating that the presumptive structural function of PP2B may also affect the mobility of these receptors. We next tested whether re-expressing PP2B in the L7-PP2B KO PCs could rescue the deficits in receptor mobility. While re-expressing WT PP2B successfully rescued the mobility deficits of all three receptors (see KOR group in **Fig. 5**), none of them were rescued by reintroducing the phosphor-dead 151A PP2B variant (**Fig. 5B-D**). These results indicate that as far as receptor mobility control is concerned, the structural function of PP2B cannot act completely independent from its phosphatase function.

Motor learning can be partially rescued by PP2B expression in Purkinje cells

Given the major contribution of PP2B to the maintenance of PSD integrity and synaptic function, we wondered whether motor performance and learning could be improved by reinstating PP2B into the cerebellum. To test this hypothesis, we bilaterally injected AAV virus containing flexed native PP2B or phosphor-dead 151A mutant PP2B constructs (WT or H151A; **Fig. 6A**) into the flocculi of adult L7-PP2B KO mice, which resulted in a PC-specific re-expression of PP2B in approximately 50% of the cells (**Fig. 6B**). L7cre mice injected with AAV-flex-mCherry were used as control for behavioral performance. We first tested the baseline performance of these mice during OKR, VOR, and VVOR. Re-expressing either native or 151A mutant PP2B into the flocculi restored the VOR, OKR and VVOR performance to control level (**Fig. 6C-E**). These mice were subsequently tested with the gain-down training paradigm. The L7-PP2B KO mice with re-expression of native PP2B showed a partial, yet

significant improvement in the gain-decrease paradigm ($p = 0.006$, **Fig. 6F**). Furthermore, both types of rescue (KOR and 151A) mice showed a partial and significant improvement ($p = 0.00027$ and 0.038 , respectively) in the phase-reversal paradigm (**Fig. 6G**). However, in both cases the enzymatic impact of PP2B was also evident in that there was a significant difference ($p = 0.013$ and 0.011 , for gain-decrease and phase-reversal, respectively) between the re-expression of the complete PP2B and expression of the phosphor-dead 151A mutant PP2B (**Figs. 6F, G**). Together with the phosphatase inhibition experiments (**Fig. 1**), these data indicate that PP2B facilitates compensatory eye movement learning through both its enzymatic function and the non-enzymatic role it may serve to structurally maintain and control the PF-PC PSD.

Discussion

In this study we explored the role of PP2B, one of the most abundant phosphatases in the brain, in maintaining PSD structure and function thereof in cerebellar learning. We show that genetic deletion of PP2B causes more severe learning deficits than pharmacological inhibition of PP2B phosphatase activity can explain. Following deletion of PP2B from Purkinje cells various of the key PSD proteins show markedly lower expression, most of which are not associated with an altered state of phosphorylation. Proteomic analysis reveals the same group of PSD proteins, highlighting that they may act as stable interactors directly binding to PP2B. Upon removal of PP2B in cultured PCs, the size of nano-clusters of each of these PSD proteins is significantly altered. Moreover, the size of the nano-clusters of Homer3, mGluR1 and Shank2 could be rescued by expressing PP2B with or without its phosphatase activity. In contrast, the surface AMPA receptor level and the lateral mobility of AMPA and mGluR1 receptors partly depend on the phosphatase activity of PP2B. While re-expression of PP2B with or without its phosphatase activity is sufficient to improve the baseline performance in compensatory eye movement paradigms, proper cerebellar motor learning was warranted only with re-expressing fully functional PP2B, requiring both the phosphatase and structural domains. These results show for the first time that PP2B does not only act as a phosphatase but also as a structural protein, together facilitating maintenance of synaptic function and behavioral learning.

Synaptic plasticity at the PF-PC synapses has long been postulated to be the most suited candidate for cerebellar learning³⁴⁻³⁶. Inspired by this idea, large collection of studies were designed to address this question by genetically manipulating one of the enzymes involved in synaptic plasticity, such as protein kinase PKC^{37,38}, cGKI, CaMKIV³⁹, α/β CaMKII^{7,40}, as well as protein phosphatase PP2B¹⁹. These manipulations shed light on the relation between cerebellar learning and synaptic plasticity at the PF-PC synapse. However, it remained to be determined whether the impaired ability of phosphorylated/dephosphorylated AMPA receptors forms the sole cause of the cerebellar learning deficits observed in these mutants. Indeed, our previous study showed that the cerebellar learning was unaffected when the pick1 mediated, Ser880 phosphorylation dependent endocytosis of AMPA receptors, and hence the LTD at PF-PC synapses was blocked⁴¹. In line with this notion, we now show that unlike the genetic deletion of PP2B in Purkinje cells, pharmacological inhibition of PP2B enzymatic function did not affect baseline performance of compensatory eye movement and only partially affected gain-down and phase-reversal learning. Since systemic injection of FK506 was as potent in inhibiting PP2B enzymatic activity as the genetic deletion, this limited behavioral effect is most likely the consequence of structural alterations following deletion of PP2B. Thus, considering that neither the dendritic arborization nor the dendritic spine density of PCs is altered in young adult L7-PP2B KO mice¹⁹, the level of motor learning in L7-PP2B KO mice can probably partly be explained by structural alterations occurring at the PSD of their PF-PC synapses.

Our iTRAQ and subsequent quantitative western blot experiments confirmed the alterations of PSD protein composition in L7-PP2B KO mice. We identified a significant down regulation of several proteins in the PF-PC synapses. Interestingly enough, these are all well studied key PSD-enriched proteins (Homer3, Shank1/2, CaMKII, Shisa6) and associated glutamatergic receptor subunits and receptors (GluR2, mGluR1, Grid2). Given the rather stringent selection criteria we used in this study, we cannot exclude the possibility that more PSD proteins are also up/down regulated in L7-PP2B KO mice. We did not observe any

alteration of presynaptic proteins in the L7-PP2B KO mice, in sharp contrast with the down regulation of presynaptic proteins after deleting PP2B from presynaptic granule cells. This result indicates the protein downregulation is strictly contained in the postsynaptic compartment of PF-PC synapses, without inducing any concurrent change at the presynaptic site. More interestingly, the phosphorylation level of these PSD proteins remain unaltered for PSD proteins (but Shank1 and Shank2), indicating the equilibrium of protein phosphorylation of these PSD proteins are not exclusively dependent on the presence of PP2B, or at least could be well compensated by other phosphatases in the L7-PP2B KO mice.

The PSD proteins lower expressed in the L7-PP2B KO mice are identified to stably interact with PP2B and form large molecular weight complex at the PF-PC synapses. This is consistent with previous studies that these PSD proteins are clustered as large protein complex, such as the Homer/Shank/mGluR^{38,42} and mGluR1/Shank/Grid2⁴³ complexes. These PSD protein complexes play crucial roles in controlling synaptic function and plasticity. Homer3 as the predominant isoform in Purkinje cells, is phosphorylated by CaMKII. In the non-phosphorylated state, Homer localizes to the postsynaptic density (PSD)⁴⁴ and by binding to mGluR1 with ER-associated ITPR1 receptors³², homer can regulate intracellular calcium⁴⁵. In hippocampus, knocking out Homer1 impairs LTP⁴⁶. In cerebellum, Shank2, Grid2, CaMKII and mGluR1 are all crucial for LTD induction at the PF-PC synapses^{43,47}. We found that the nano-clustering of these PSD proteins were altered in the PP2B KO Purkinje cells, and reintroducing PP2B back to Purkinje cells fully recovered the nano-clustering of all the PSD proteins tested. Thus by direct interaction with these PSD proteins, PP2B could function as either a reversible coupler to selectively crosslink several PSD complexes, or to be selectively inserted in different loci of the PSD complex to dephosphorylate specific proteins, for instance the synaptic receptors. Our result is not in line with that a normal PF-PC LTD was found in the L7-PP2B KO mice¹⁹. It is possible that down-regulating multiple proteins in the LTD pathway by PP2B could have a different end result on plasticity. Alternatively, a PP2B related LTD deficit could be seen when different plasticity induction protocol is used⁴⁸.

Recent studies convincingly illustrate the importance of lateral mobility in mediating glutamatergic synaptic function^{31,33}. The lateral mobility of AMPA and mGluR1 receptors were severely impaired in the PP2B KO Purkinje cells. This is consistent with the leading theory that lateral mobility of AMPA receptors is controlled by its phosphorylation level. Here we observed a significant enhanced movements of surface GluR2 containing receptors as well as an increased synaptic transmission after pharmacological and genetic inhibition of PP2B activity. We postulate that apart from impaired synaptic plasticity, impaired AMPA receptor mobility also contribute to the learning deficits observed in these mice. Possibly, the deficits in PSD complex contribute to the impaired AMPA receptor mobility. It has been shown that surface receptors mobility is tightly controlled by several PSD proteins, including homer, stargazin and PSD95. Thus both the reduction of total protein concentration and the altered nano-cluster distribution of these PSD proteins could affect the mobility of AMPA and mGluR1 receptors.

PP2B has long been considered to function only as a phosphatase. Current study provides evidence for a novel structural role of PP2B in maintaining the PSD complex integrity. Our proteomics data indicate that the reduction of PSD proteins in the L7-PP2B KO mice is not correlated with the hyperphosphorylation of these proteins. Possibly, removing PP2B from PSD complex resulted in instable complex formation which lead to protein degradation. This suggests that PP2B could also function as a scaffolding protein to maintain the integrity of PSD complex. Indeed, the impaired nano-cluster distribution of homer3 and mGluR1 of PP2B KO Purkinje cells were restored after expressing a phosphatase dead PP2B variant 151A. A similar enzymatic independent role in controlling synaptic plasticity has been previous reported for the CaMKII at the CA3-CA1 synapses of hippocampus. Using targeted mouse mutants and pharmacologic inhibition of α CaMKII, Hojjati and colleagues demonstrated that the α CaMKII protein, but not its activation, autophosphorylation or its ability to phosphorylate synapsin I, is required for normal short-term presynaptic plasticity at hippocampal CA3-CA1 synapses¹⁷. In contrast to the structural function of PP2B in the PSD complex, the lateral mobility of glutamatergic receptor could not be rescued by phosphatase dead PP2B. It is possible that the lateral mobility is strictly regulated by the PP2B phosphatase function. However, pharmacological inhibition of PP2B had smaller effects on lateral mobility, than the phosphatase dead PP2B. More likely, the lateral mobility relies on both the phosphatase activity of PP2B and its structural supports to a fully functional PSD complex. Since we were unable to rescue the nano-cluster distribution of key PSD proteins such as shank1 and

shank2 with phosphatase dead PP2B, a compromised PSD complex might not be sufficient to support a proper receptor function.

It is intriguing that by re-expressing native PP2B, we were able to rescue all the deficits in L7-PP2B KO mice, ranging from PSD protein distribution to cerebellar learning. This argues against the possibility that genetic deletion of PP2B causes irreversible developmental deficits in Purkinje cells and cerebellar circuits. Rather, it is likely that PP2B is constantly required for proper synaptic function and motor learning. While expressing PP2B in nearly half of the floccular Purkinje cells was sufficient to restore baseline performance and partially rescue motor learning, it is conceivable that restoring PP2B activity in all Purkinje cell could to large extent, if not completely, rescue the learning deficits. Since PP2B malfunction has been indicated in various neurological disorders, our findings open a door to future targeted gene therapy towards these patients.

References

- 1 Feng, W. & Zhang, M. Organization and dynamics of PDZ-domain-related supramodules in the postsynaptic density. *Nat Rev Neurosci.* 2009; 10, 87-99.
- 2 Hell, J. W. CaMKII: claiming center stage in postsynaptic function and organization. *Neuron.* 2014; 81, 249-65.
- 3 Stemmer, P. & Klee, C. B. Serine/threonine phosphatases in the nervous system. *Curr Opin Neurobiol.* 1991; 1, 53-64.
- 4 Kuno, T., Mukai, H., Ito, A. *et al.* Distinct cellular expression of calcineurin A alpha and A beta in rat brain. *J Neurochem.* 1992; 58, 1643-51.
- 5 Mansuy, I. M. & Shenolikar, S. Protein serine/threonine phosphatases in neuronal plasticity and disorders of learning and memory. *Trends Neurosci.* 2006; 29, 679-86.
- 6 Shi, Y. Serine/threonine phosphatases: mechanism through structure. *Cell.* 2009; 139, 468-84.
- 7 Jorntell, H. & Hansel, C. Synaptic memories upside down: bidirectional plasticity at cerebellar parallel fiber-Purkinje cell synapses. *Neuron.* 2006; 52, 227-38.
- 8 Bienenstock, E. L., Cooper, L. N. & Munro, P. W. Theory for the development of neuron selectivity: orientation specificity and binocular interaction in visual cortex. *J Neurosci.* 1982; 2, 32-48.
- 9 Bhattacharyya, S., Biou, V., Xu, W. *et al.* A critical role for PSD-95/AKAP interactions in endocytosis of synaptic AMPA receptors. *Nat Neurosci.* 2009; 12, 172-81.
- 10 Jurado, S., Biou, V. & Malenka, R. C. A calcineurin/AKAP complex is required for NMDA receptor-dependent long-term depression. *Nat Neurosci.* 2010; 13, 1053-5.
- 11 Sanderson, J. L., Gorski, J. A., Gibson, E. S. *et al.* AKAP150-anchored calcineurin regulates synaptic plasticity by limiting synaptic incorporation of Ca²⁺-permeable AMPA receptors. *J Neurosci.* 2012; 32, 15036-52.
- 12 Malleret, G., Haditsch, U., Genoux, D. *et al.* Inducible and reversible enhancement of learning, memory, and long-term potentiation by genetic inhibition of calcineurin. *Cell.* 2001; 104, 675-86.
- 13 Zeng, H., Chattarji, S., Barbarosie, M. *et al.* Forebrain-specific calcineurin knockout selectively impairs bidirectional synaptic plasticity and working/episodic-like memory. *Cell.* 2001; 107, 617-29.
- 14 Mansuy, I. M. Calcineurin in memory and bidirectional plasticity. *Biochem Biophys Res Commun.* 2003; 311, 1195-208.
- 15 Shen, K., Teruel, M. N., Subramanian, K. *et al.* CaMKIIbeta functions as an F-actin targeting module that localizes CaMKIIalpha/beta heterooligomers to dendritic spines. *Neuron.* 1998; 21, 593-606.
- 16 Tabata, T., Sawada, S., Araki, K. *et al.* A reliable method for culture of dissociated mouse cerebellar cells enriched for Purkinje neurons. *J Neurosci Methods.* 2000; 104, 45-53.
- 17 Hojjati, M. R., van Woerden, G. M., Tyler, W. J. *et al.* Kinase activity is not required for alphaCaMKII-dependent presynaptic plasticity at CA3-CA1 synapses. *Nat Neurosci.* 2007; 10, 1125-7.
- 18 Bingol, B., Wang, C. F., Arnott, D. *et al.* Autophosphorylated CaMKIIalpha acts as a scaffold to recruit proteasomes to dendritic spines. *Cell.* 2010; 140, 567-78.
- 19 Schonewille, M., Belmeguenai, A., Koekkoek, S. K. *et al.* Purkinje cell-specific knockout of the protein phosphatase PP2B impairs potentiation and cerebellar motor learning. *Neuron.* 2010; 67, 618-28.
- 20 Butcher, S. P., Henshall, D. C., Teramura, Y. *et al.* Neuroprotective actions of FK506 in experimental stroke: in vivo evidence against an antiexcitotoxic mechanism. *J Neurosci.* 1997; 17, 6939-46.
- 21 Pardo, R., Colin, E., Regulier, E. *et al.* Inhibition of calcineurin by FK506 protects against polyglutamine-huntingtin toxicity through an increase of huntingtin phosphorylation at S421. *J Neurosci.* 2006; 26, 1635-45.
- 22 Clayton, E. L., Anggono, V., Smillie, K. J. *et al.* The phospho-dependent dynamin-syndapin interaction triggers activity-dependent bulk endocytosis of synaptic vesicles. *J Neurosci.* 2009; 29, 7706-17.

- 23 Cottrell, J. R., Levenson, J. M., Kim, S. H. *et al.* Working memory impairment in calcineurin knock-out mice is associated with alterations in synaptic vesicle cycling and disruption of high-frequency synaptic and network activity in prefrontal cortex. *J Neurosci.* 2013; 33, 10938-49.
- 24 De Zeeuw, C. I. & Ten Brinke, M. M. Motor Learning and the Cerebellum. *Cold Spring Harb Perspect Biol.* 2015; 7, a021683.
- 25 Galliano, E., Gao, Z., Schonewille, M. *et al.* Silencing the majority of cerebellar granule cells uncovers their essential role in motor learning and consolidation. *Cell Rep.* 2013; 3, 1239-51.
- 26 Baumgartel, K. & Mansuy, I. M. Neural functions of calcineurin in synaptic plasticity and memory. *Learn Mem.* 2012; 19, 375-84.
- 27 Wittig, I., Braun, H. P. & Schagger, H. Blue native PAGE. *Nat Protoc.* 2006; 1, 418-28.
- 28 Baksh, S., DeCaprio, J. A. & Burakoff, S. J. Calcineurin regulation of the mammalian G0/G1 checkpoint element, cyclin dependent kinase 4. *Oncogene.* 2000; 19, 2820-7.
- 29 Oliveria, S. F., Dittmer, P. J., Youn, D. H. *et al.* Localized calcineurin confers Ca²⁺-dependent inactivation on neuronal L-type Ca²⁺ channels. *J Neurosci.* 2012; 32, 15328-37.
- 30 Heine, M., Groc, L., Frischknecht, R. *et al.* Surface mobility of postsynaptic AMPARs tunes synaptic transmission. *Science.* 2008; 320, 201-5.
- 31 Penn, A. C., Zhang, C. L., Georges, F. *et al.* Hippocampal LTP and contextual learning require surface diffusion of AMPA receptors. *Nature.* 2017; 549, 384-8.
- 32 Tu, J. C., Xiao, B., Yuan, J. P. *et al.* Homer binds a novel proline-rich motif and links group 1 metabotropic glutamate receptors with IP3 receptors. *Neuron.* 1998; 21, 717-26.
- 33 Constals, A., Penn, A. C., Compans, B. *et al.* Glutamate-induced AMPA receptor desensitization increases their mobility and modulates short-term plasticity through unbinding from Stargazin. *Neuron.* 2015; 85, 787-803.
- 34 Marr, D. A theory of cerebellar cortex. *J Physiol.* 1969; 202, 437-70.
- 35 Albus, J. S. A theory of cerebellar function. *Math. Biosci.* 1971; 10, 25-61.
- 36 Ito, M. Historical review of the significance of the cerebellum and the role of Purkinje cells in motor learning. *Ann N Y Acad Sci.* 2002; 978, 273-88.
- 37 De Zeeuw, C. I., Hansel, C., Bian, F. *et al.* Expression of a protein kinase C inhibitor in Purkinje cells blocks cerebellar LTD and adaptation of the vestibulo-ocular reflex. *Neuron.* 1998; 20, 495-508.
- 38 Xia, J., Chung, H. J., Wihler, C. *et al.* Cerebellar long-term depression requires PKC-regulated interactions between GluR2/3 and PDZ domain-containing proteins. *Neuron.* 2000; 28, 499-510.
- 39 Boyden, E. S., Katoh, A., Pyle, J. L. *et al.* Selective engagement of plasticity mechanisms for motor memory storage. *Neuron.* 2006; 51, 823-34.
- 40 van Woerden, G. M., Hoebeek, F. E., Gao, Z. *et al.* betaCaMKII controls the direction of plasticity at parallel fiber-Purkinje cell synapses. *Nat Neurosci.* 2009; 12, 823-5.
- 41 Schonewille, M., Gao, Z., Boele, H. J. *et al.* Reevaluating the role of LTD in cerebellar motor learning. *Neuron.* 2011; 70, 43-50.
- 42 Xiao, B., Tu, J. C., Petralia, R. S. *et al.* Homer regulates the association of group 1 metabotropic glutamate receptors with multivalent complexes of homer-related, synaptic proteins. *Neuron.* 1998; 21, 707-16.
- 43 Uemura, T., Mori, H. & Mishina, M. Direct interaction of GluRdelta2 with Shank scaffold proteins in cerebellar Purkinje cells. *Mol Cell Neurosci.* 2004; 26, 330-41.
- 44 Hayashi, M. K., Tang, C., Verpelli, C. *et al.* The postsynaptic density proteins Homer and Shank form a polymeric network structure. *Cell.* 2009; 137, 159-71.
- 45 Xiao, B., Tu, J. C. & Worley, P. F. Homer: a link between neural activity and glutamate receptor function. *Curr Opin Neurobiol.* 2000; 10, 370-4.
- 46 Gerstein, H., O'Riordan, K., Osting, S. *et al.* Rescue of synaptic plasticity and spatial learning deficits in the hippocampus of Homer1 knockout mice by recombinant Adeno-associated viral gene delivery of Homer1c. *Neurobiol Learn Mem.* 2012; 97, 17-29.
- 47 Peter, S., Ten Brinke, M. M., Stedehouder, J. *et al.* Dysfunctional cerebellar Purkinje cells contribute to autism-like behaviour in Shank2-deficient mice. *Nat Commun.* 2016; 7, 12627.
- 48 Fujiwara, A., Kakizawa, S. & Iino, M. Induction of cerebellar long-term depression requires activation of calcineurin in Purkinje cells. *Neuropharmacology.* 2007; 52, 1663-70.

Figure legends

Figure 1

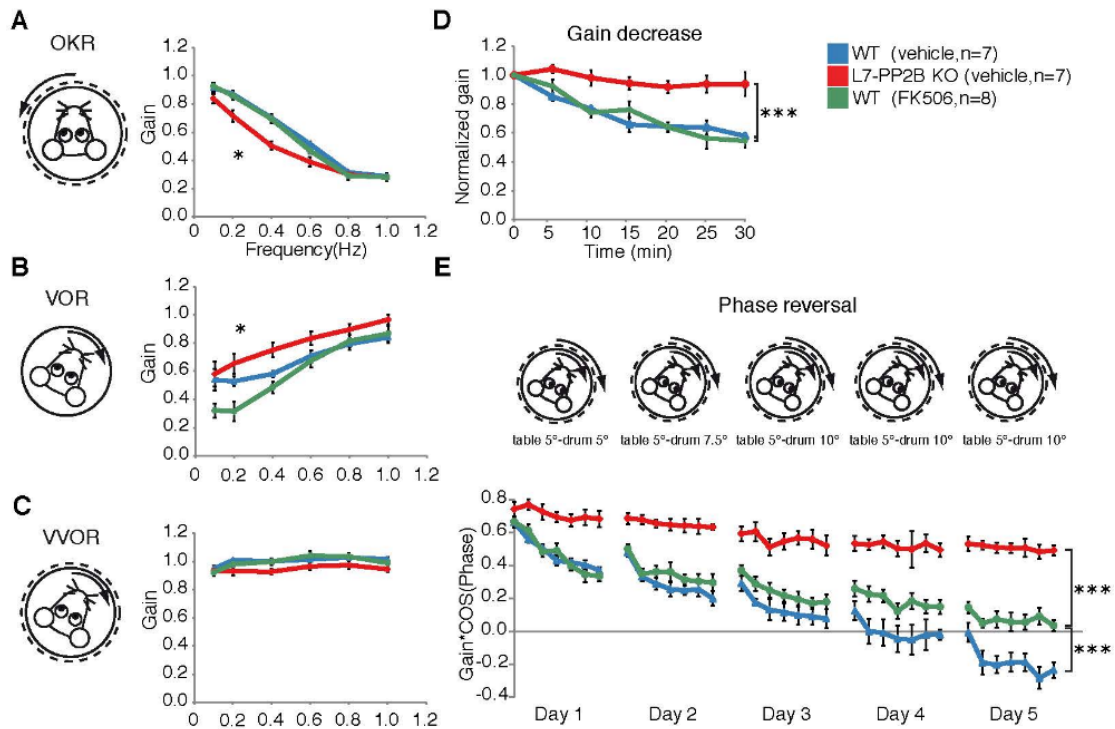


Figure 1. Selective inhibition of phosphatase activity of PP2B could not fully reproduce the phenotype of the L7-PP2B KO.

(A) Motor performance during the optokinetic reflex revealed no aberrations in the FK-506 injected group (i.e. group in which phosphatase function of PP2B was specifically inhibited) compared to controls and L7-PP2B KOs. Error bars indicate \pm SEM.

(B) Same as (A), but for the vestibular reflex (VOR) without light;

(C) Same as (A), but for the vestibulo-ocular reflex in the light (VVOR);

(D) Short term learning paradigm of gain decrease. Error bars indicate \pm SEM.

(E) Long term learning paradigm of 5 days phase reversal eye movement. Y-axis indicates the value of (gain*cos(phase)). Phase reversal learning in the FK-506 injected group is impaired compared to controls, but is better than that of L7-PP2B KO mice, indicating that apart from its functions as a phosphatase, PP2B also has a structural role. Error bars indicate \pm SEM.

Figure 2

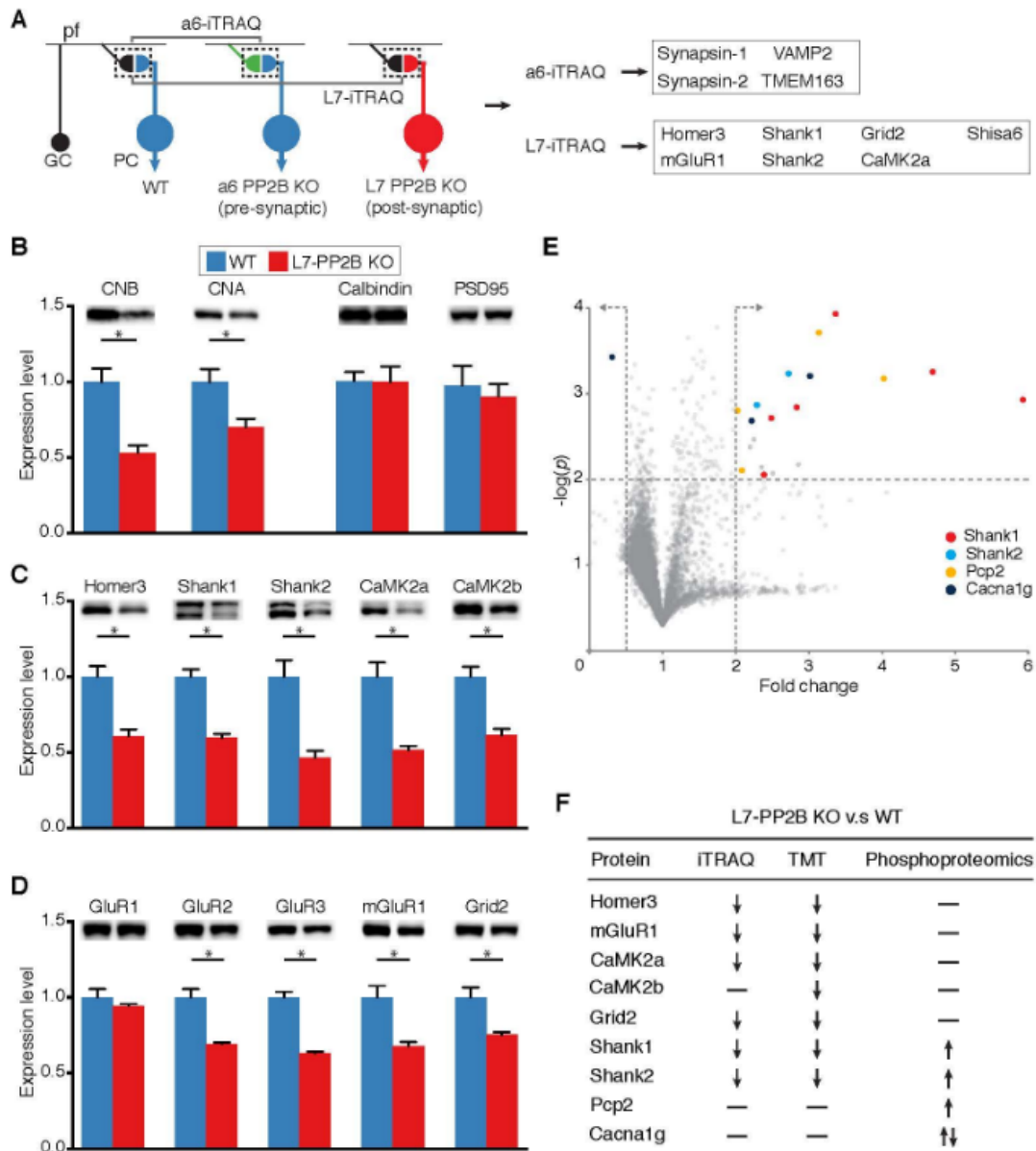


Figure 2. Specific pre- and post-synaptic knockout of PP2B in PF-PC synapses resulted in down-regulation of pre- and post-synaptic proteins, respectively.

(A) Left: Scheme of cerebellar cortex circuitry and iTRAQ experimental setup; **Right:** List of significantly down-regulated proteins in L7-PP2B (post-synaptic KO) and a6-PP2B (pre-synaptic KO) synaptosomes identified by 8-plex iTRAQ ($n=4:4$ mice per run, repeated twice);

(B, C, D) Western blot result of L7-PP2B KO and WT littermates synaptosomes ($n=6:6$ mice, 10-12 wk old). **(B)** CNB and CNA confirmed successful KO of PP2B; Calbindin and PSD95 signals show that the number of Purkinje cells and synapses are not affected by knocking out PP2B, respectively ($p=0.9009$, $p=0.2413$, unpaired parametric t -test). **(C)** Multiple PSD-proteins are down-regulated in L7-PP2B KO. **(D)** At the receptors level, except for GluR1, glutamate receptor subunits are significantly down-regulated in L7-PP2B KO. Error bars indicate \pm SEM.

(E) Phospho-proteomic results revealed changed protein/phosphor-sites in L7-PP2B mice (P2, 10-plex TMT, 5: 5 comparisons, each pair consisted of 2:1 male:female mice, 10-12 wk old). Phospho-proteomics volcano plot. The X-axis and Y-axis indicated fold-change and $\log(p$ -value) respectively, the red area indicated fold change > 2 while $p < 0.01$. By comparing WT and L7-PP2B mice P2 fractions, only 1 site from Cacna1g is less-phosphorylated in L7-PP2B mice, while a number of proteins/sites are more-phosphorylated, such as Shank1, Shank2, pcp2 etc.

(F) Summarized comparison of changed proteins between iTRAQ, TMT and phospho-proteomics experiments.

Figure 3

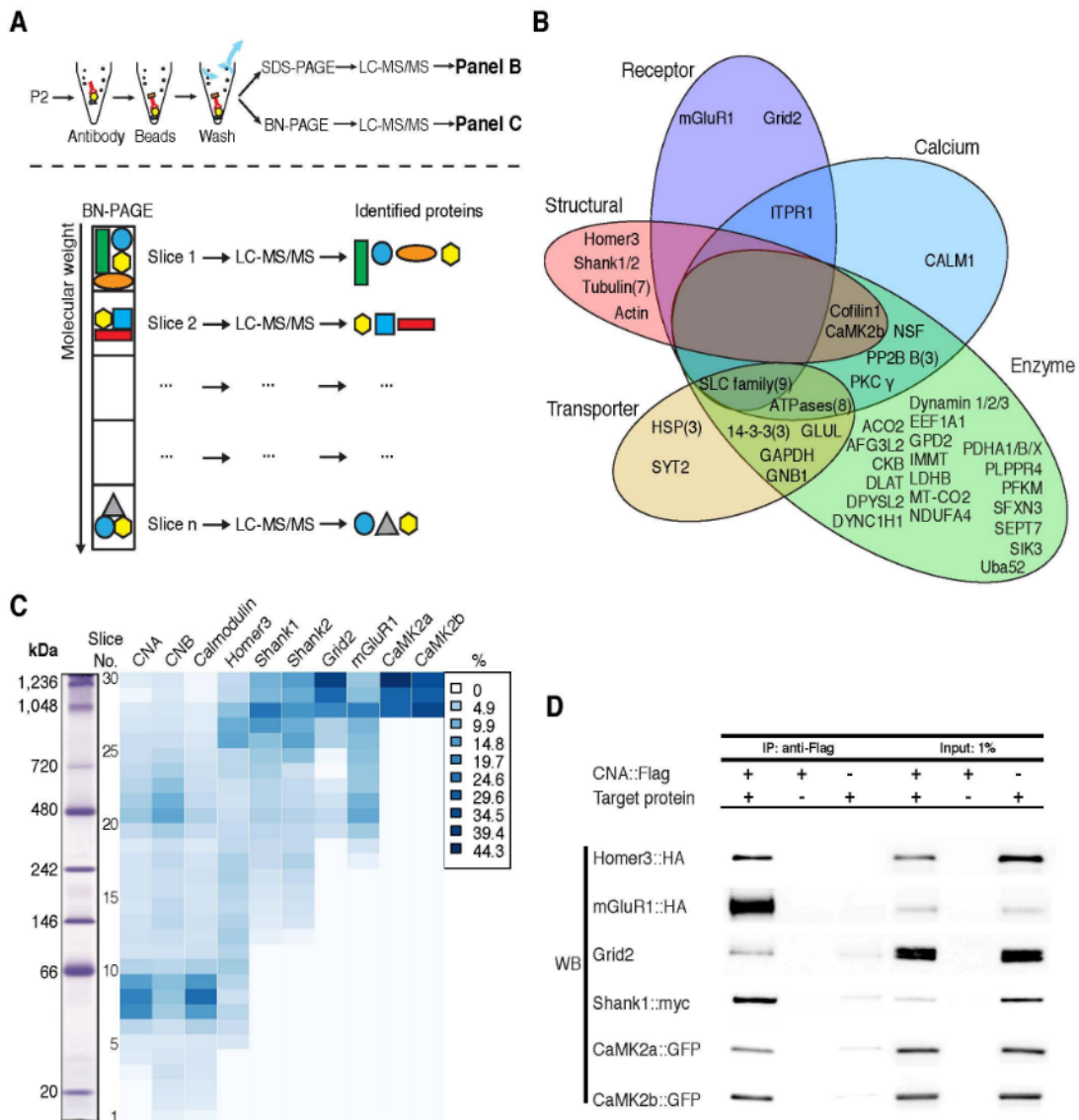


Figure 3. PP2B stably and directly interacts with multiple PSD-proteins.

(A) Illustration of IP-MS/MS workflow. Top panel: Immunoprecipitation-MS/MS for cerebellar PP2B in WT mice P2 fractions. Lower panel: Scheme of IP-BN (blue native)-PAGE-MS/MS.

(B) IP-MS/MS result. Proteins identified as PP2B interactors followed criteria that they were identified as “True interactor” in IP with 2 PP2B antibodies, and for least twice for each antibody (See Method, and Supp table cerebellum_IP_combined_overlapped). Proteins are manually grouped by their known functions, the number in the brackets indicates the number of proteins belongs to that protein family, and the only protein from the IP-MS/MS result not included in the graph is the C1QC protein.

(C) The result of IP/BN-PAGE/MS from WT cerebellar P2 fractions. Different proteins are presented in columns, fractions are presented in rows, and colors are coded with normalized iBAQ value in percentage. Note CNA, CNB and calmodulin are well co-localized. The interactors of CNA, including CaMK2, Homer3, Shank1, Shank2, Grid2 and mGluR1 are enriched in the high-molecular weight fractions, also CaMK2a and Homer3 also form multiple complexes with CNA in various molecular weight range.

(D) HEK293 cell Co-IP experiments showed direct interactors. Homer3, mGluR1, Shank1, CaMK2b showed strong enrichments in CNA co-expression compared to their controls (CNA over-expression or target protein expression only). Grid2 and CaMK2a showed moderate enrichments.

Figure 4

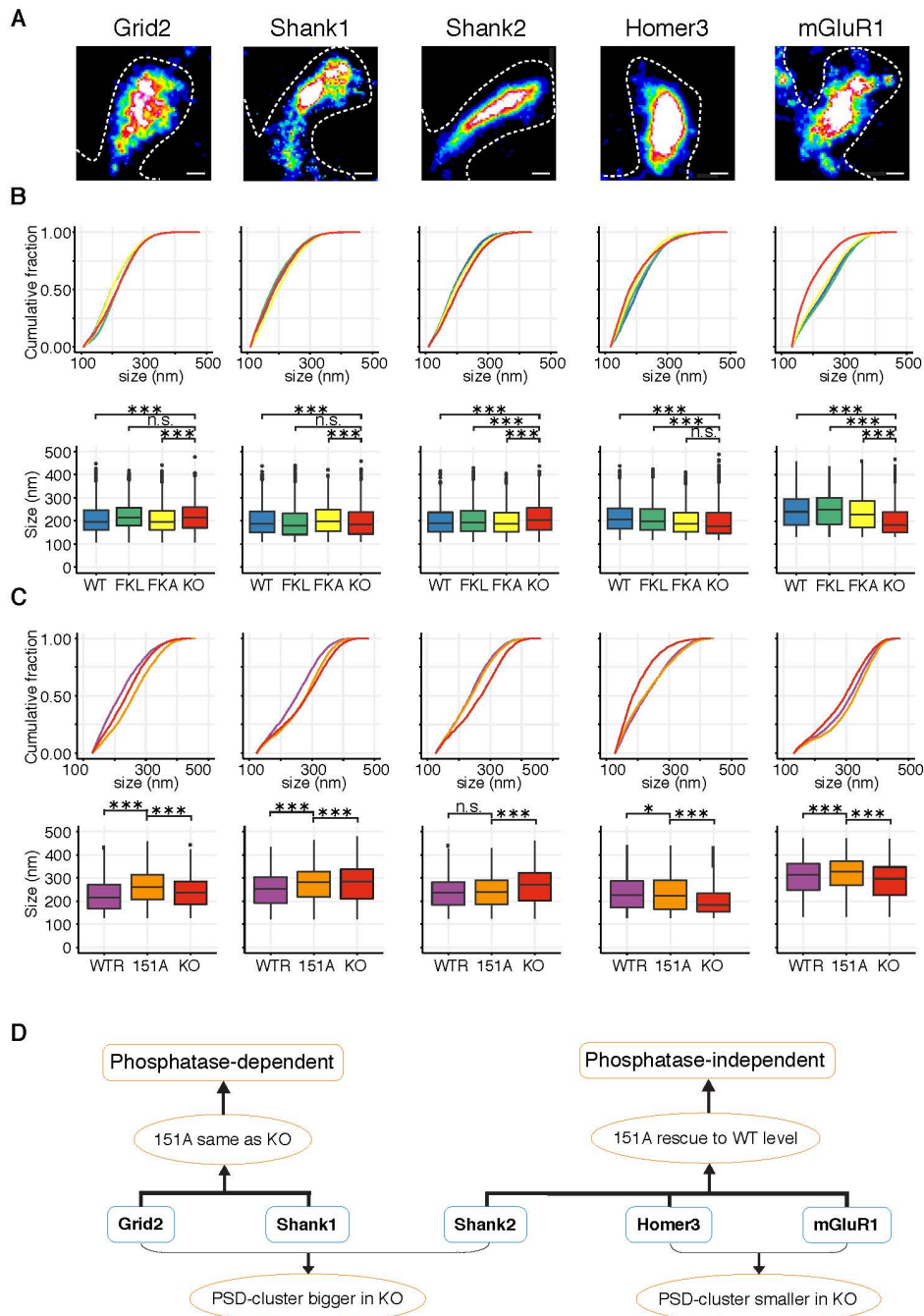


Fig. 4 dSTORM results revealed PP2B PSD-interactors nano-cluster size regulated by PP2B via phosphatase-dependent and phosphatase-independent manners.

(A) Example of dSTORM images of cultured Purkinje cells' spines immunostained with PP2B PSD-interactors, scale bars are 100 μ m.

(B) Top panel is the cumulative plot, and lower panel is the boxplot. WT, pharmacologically long-term and short-term blockage of PP2B by FK-506 (FKL and FKA), and KO were compared.

(C) Top panel is the cumulative plot, and lower panel is the boxplot. Comparisons of WT-PP2B rescue in KO (WTR), phosphor-dead expression in KO (151A) and KO.

(D) Summarized result for **(D)**, the nano-cluster sizes of Homer3, mGluR1 are smaller in PP2B KO, while Shank2, Shank1, and Grid2 showed bigger nano-cluster size in PP2B KO. Moreover, nano-cluster of Homer3, mGluR1 and Shank2 can be rescued to WT level under expression of phosphor-dead PP2B in KO cells, indicated their regulation by PP2B via phosphatase-independent manner; nano-cluster size of Shank1 and Grid2 are depends on PP2B activity, as the phosphor-dead expression lead to same level as KO.

Figure 5

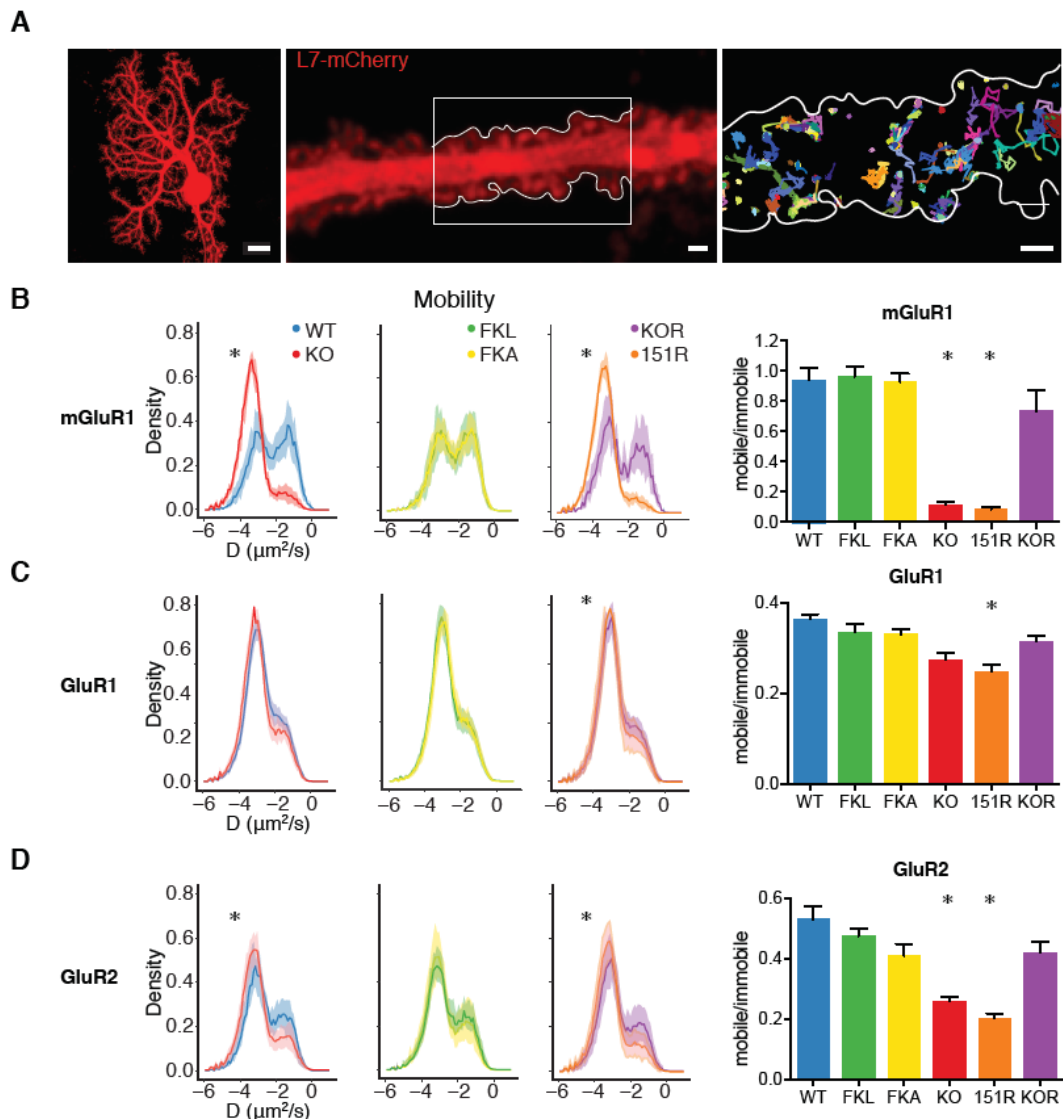


Figure 5. Glutamate receptors are less mobile in PP2B KO Single molecule tracking of surface mGluR1, GluR1 and GluR2 on Purkinje cells primary culture.

(A) Example of a cultured Purkinje cells (DIV21, left panel, scale bar is 10 μm); Example of a tracking mask of Purkinje cell dendrite visualized by transfection of L7-mCherry to a cultured Purkinje cell (middle panel, scale bar is 1 μm); Example of surface GluR2 tracks from the middle panel (right panel, scale bar is 1 μm);

(B) The surface mGluR1 tracking results under different conditions, which is the summarized in the rightest panel. mGluR1 in WT Purkinje cells are more mobile than the PP2B KO ones. Shades and error bars indicate $\pm\text{SEM}$. Noted while the expression of WT PP2B in KO cells rescued the mobility, while the expression of phosphor-dead PP2B in KO cells lead to same level of mobility as PP2B KOs.

(C) Same as C, but for surface GluR2.

(D) Same as D, but for surface GluR1.

Figure 6

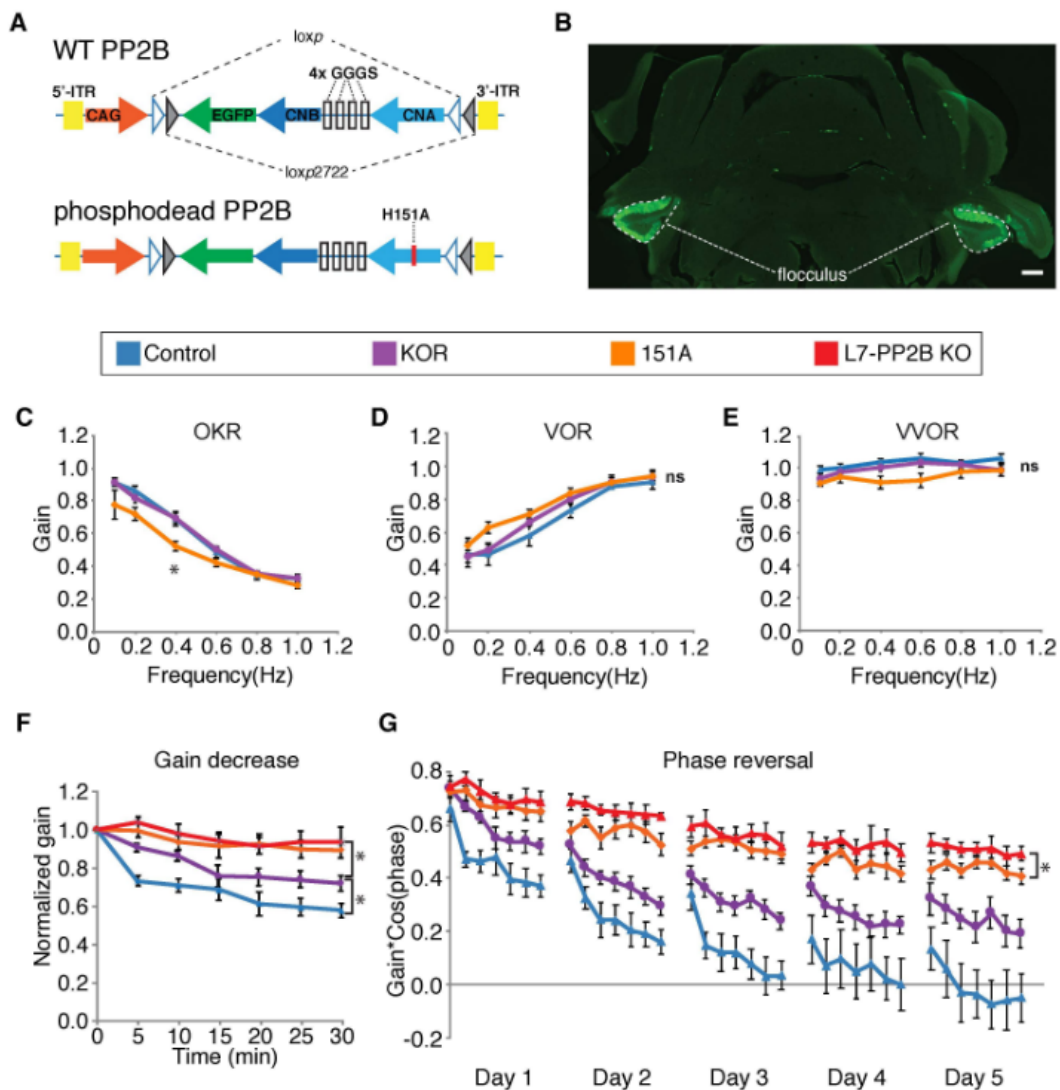


Figure 6. Expression of phospho-dead PP2B could not rescue motor learning deficit in L7-PP2B KOs.

(A) Scheme of the Cre-dependent WT-PP2B and phospho-dead PP2B AAVs. The phospho-dead PP2B is introduced by a single amino-acid mutation of CNA, H151A.

(B) Example of bilateral injections of AAV into flocculus. Lower panel shows the experimental groups: control (WT littermates injected with CAG-EGFP, $n=9$ mice); WTR (L7-PP2B KOs re-expressed with WT-PP2B showed in **(A)**, $n=11$ mice); 151A (L7-PP2B KOs injected with phospho-dead PP2B showed in **(A)**, $n=12$ mice); and L7-PP2B KO ($n=7$ mice, adapted from Fig. 1).

(C) Motor performance during the optokinetic reflex revealed no aberrations in the 151A group (i.e. group in which phosphatase function of PP2B was abolished and the structural function of PP2B were kept) compared to the other two groups (ANOVA with Bonferroni correction, $p = 0.028$).

(D) Same as **(C)**, but for the vestibular reflex (VOR) without light;

(E) Same as **(C)**, but for the vestibulo-ocular reflex in the light (VVOR);

(F) Short term learning paradigm of gain decrease (ANOVA with Bonferroni correction, $p < 0.001$; 151A vs. WTR: $p = 0.006$; control vs. WTR: $p = 0.013$).

(G) Long term learning paradigm of 5 days phase reversal eye movement. Y-axis indicates the value of ($\text{gain} \cdot \cos(\text{phase})$). Phase reversal comparison for the last two days showed both control mice injected with GFP and L7-PP2B mice injected with WT-PP2B learned, both the 151A and KO groups are impaired, although the difference indicate the 151A groups learned better than the KO (compared with the last two days learning, unpaired t-test, $p = 0.038$).



Figure S1. After the behavioral experiments, the cortices of the mice were tested for FK-506 inhibition efficiency. All error bars indicate \pm SEM.

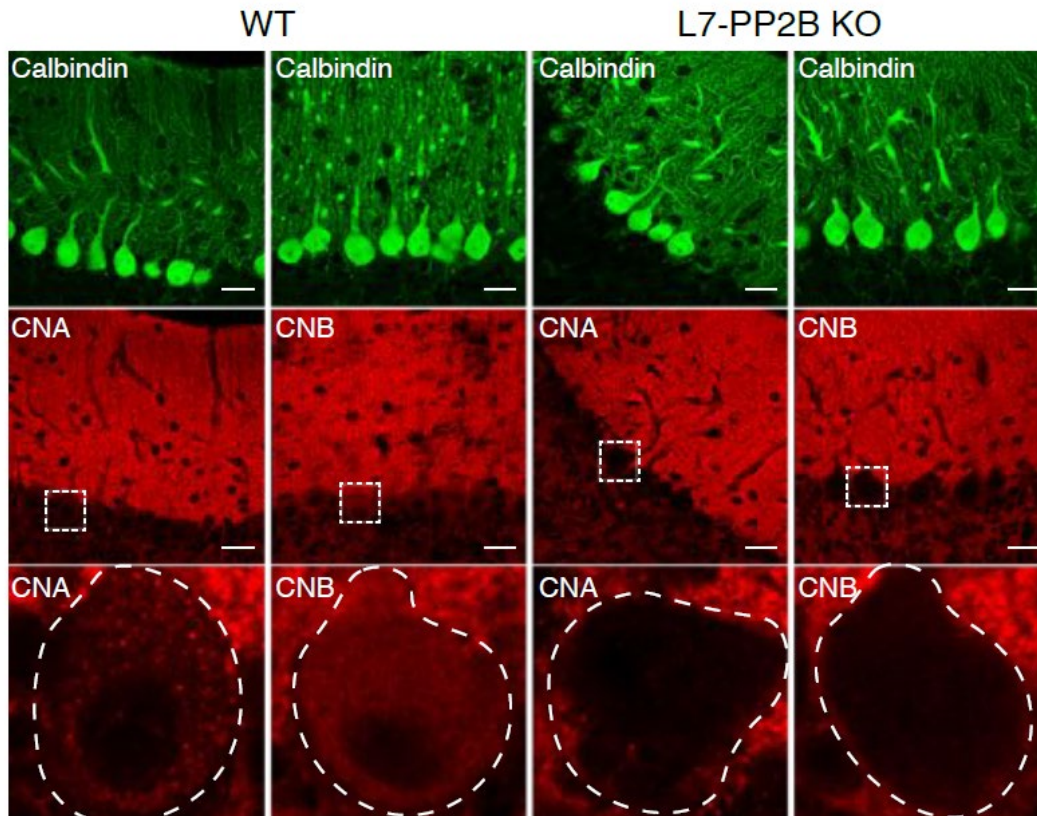


Figure S2. L7-PP2B KO mice is devoid of both CNB and CNA. The morphology of Purkinje cells in the L7-PP2B mice shown by a Purkinje cell marker Calbindin (left panel). Both CNB and CNA are absent in the Purkinje cells of the L7-PP2B mice (middle and right panels, right panels are the zoom-in for the middle panels, $n=2:2$ mice). Scale bars are 100 μ m.

Fig. S3, related to Fig. 2

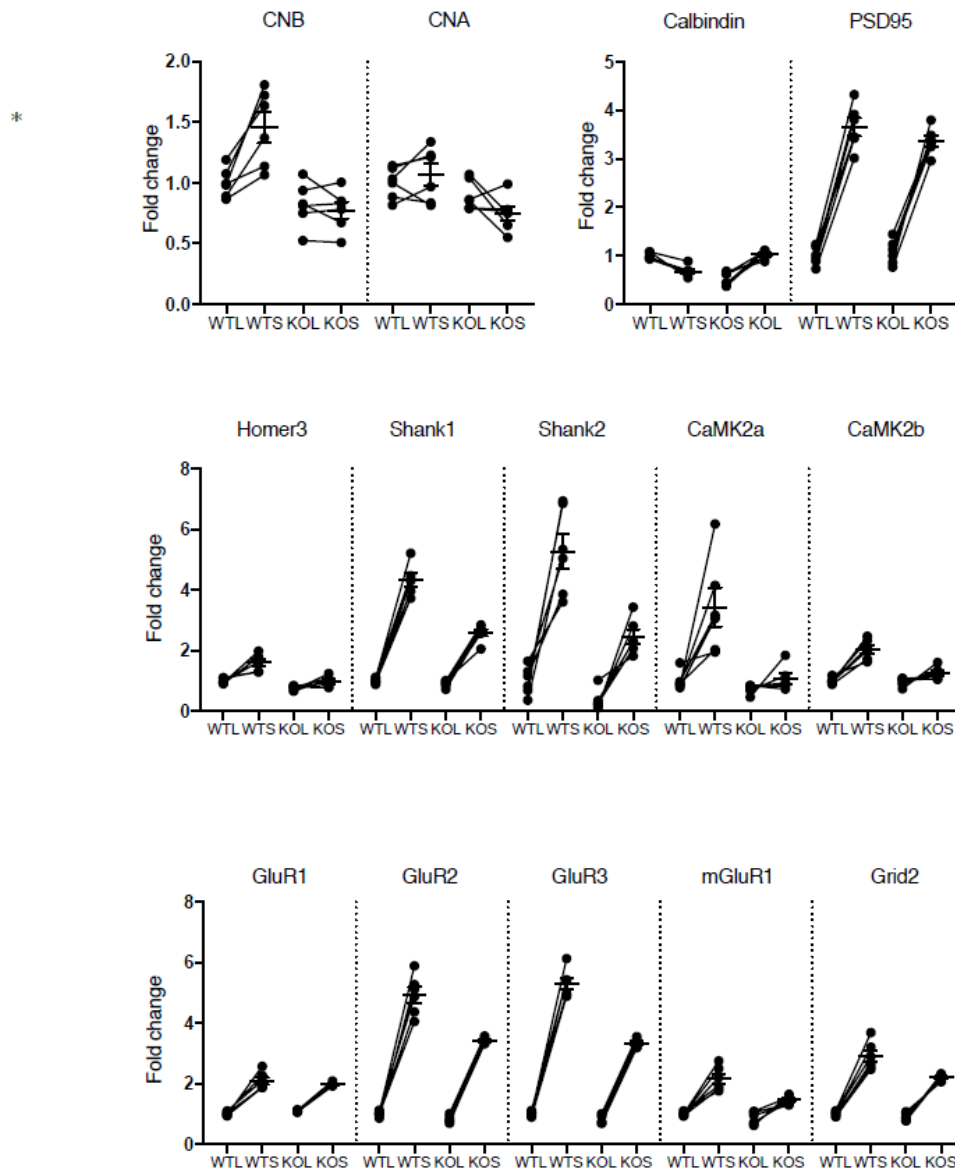


Figure S3. Fold changes of target protein after synaptosome preparations in L7-PP2B KO and WTs.

Fig. S4, related to Fig. 4

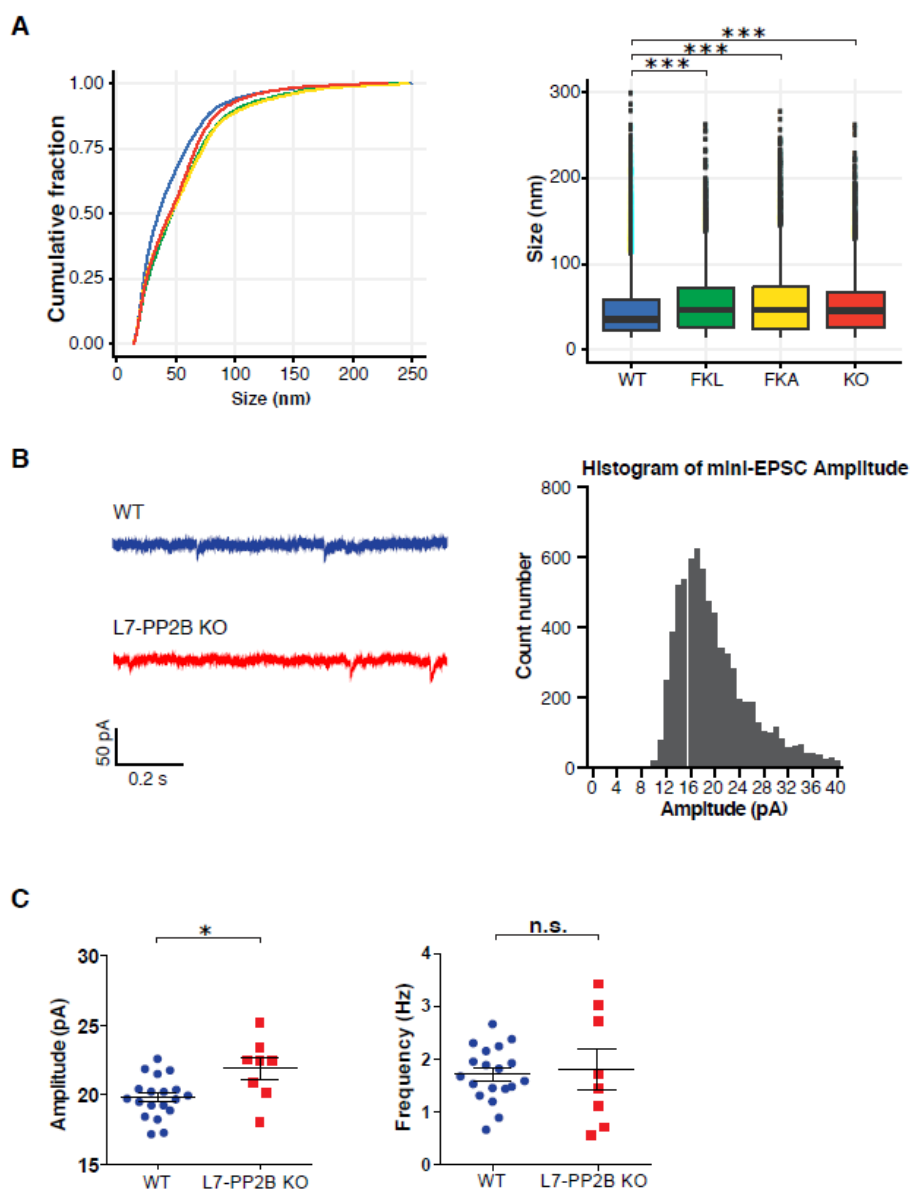


Figure S4. Surface GluR2 regulation by PP2B.

(A) Left: Cumulative plot of surface GluR2 nano-cluster size affected by pharmacological blockage or KO of PP2B. Right: the boxplot of (A) showed that blockage or KO of PP2B increased surface GluR2 nano-cluster size.

(B) Left: example traces of mini-EPSC recording. Right: histogram of mini-EPSC amplitude from all recordings, bin size = 1 pA.

(C) The amplitude of mini-EPSC is increased in the L7-PP2B KO (Mann-Whitney test, $p = 0.019$, $n = 19:8$ cells (WT:KO)), but not the frequency (Mann-Whitney test, $p = 0.979$).

Fig. S5, related to Fig. 5

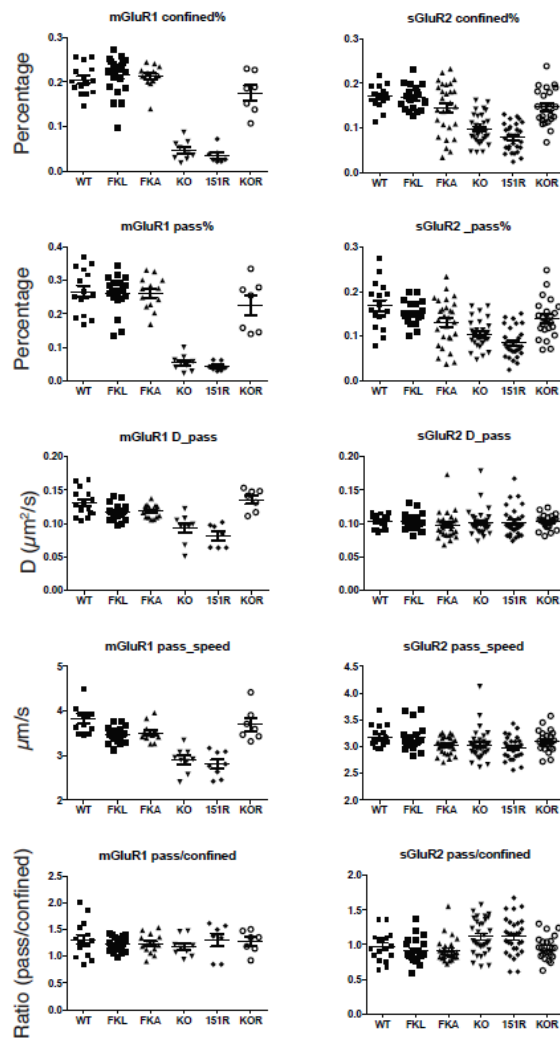


Figure S5. Sub-divided mobile fractions of single molecule glutamate receptors tracking. The trend among different groups for mGluR1 and GluR2 are similar to the mobile groups. Noted different trends between mGluR1 and GluR2 indicates they have interactions with protein complexes with different molecular weight (see Fig. 2C), and their sensitivity to the PP2B enzymatic activity.

Fig. S6, related to Fig. 6

Infection percentage and phase reversal performance

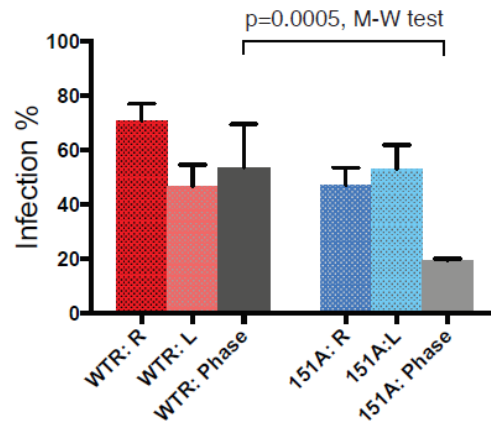


Figure S6. Infection rate from right and left flocculus, and their learning performance as shown in Fig. 6C. The overall infection rate is not different between WTR and 151A groups (Mann-Whitney test $p = 0.331$)

Methods

Animals

We used L7-PP2B mice with PC-specific knockout of PP2B (Schonewille et al., 2010). We created the GC-specific PP2B knockout by crossing the *floxed-PP2B* mice and the *a6-Cre* mice. Male mice of the following genotypes were used for the experiments: homozygous/+ (referred to as L7-PP2B or A6-PP2B) and homozygous/-, wild-type/+ and wild-type/- (littermate controls). Mice were decapitated at 10-12 weeks and the cerebella were quickly dissected and stored at -80 °C until further use.

Unless stated otherwise, all mice were of the *C57/Bl6* background.

Immunoprecipitation

We carried out the IP experiments in 2 conditions, (a) IP experiments using an anti-PP2B antibody, and (b) control experiments containing empty beads without primary antibodies.

Antibodies and peptides—The following primary antibodies and blocking peptide were used in the experiments: rabbit anti-PP2B (polyclonal, raised against the peptide with residues 450-500 of the human PP2BA protein, Genscript USA Inc.), the latter of which was also used as IP blocking peptide. Mouse anti-PP2B (monoclonal raised against amino acids 312-521 of the PP2B catalytic A α subunit, Santa Cruz.)

Preparation of P2+Microsome fraction — For each IP, 4 cerebella were homogenized in a 15 ml glass potter containing ice-cold homogenization buffer (0.32 M sucrose, 5 mM HEPES, EDTA-free protease inhibitor (Roche Applied Science), pH7.4) at 900 RPM with 12 up and down strokes of the piston. The lysate was centrifuged at 1000 g, 4°C, for 10 min to remove the cell debris and nuclei. The supernatant was centrifuged at 100,000 g, 4°C for 120 min. After ultracentrifugation, the pellet and microsomes (P2 + M) were resuspended with 25 mM HEPES buffer (pH 7.4, protease inhibitor). The protein concentration was determined by Bradford measurement (Bio-Rad) and adjusted to 10 μ g/ μ L.

Extraction of protein complexes—To solubilize proteins and protein complexes, 5 mg P2+M was mixed with a sample volume of extraction buffer (25mM HEPES, 150 mM NaCl, 2% DDM, pH 7.4) and incubated on a rotator at 4°C for 60 min, then centrifuged at 20,000g, 4°C for 20 min. The supernatant was collected and the pellet was resuspended in the extraction buffer (25mM HEPES, 150 mM NaCl, 1% DDM, pH 7.4) and incubated and centrifuged as before. After that, the supernatant was pooled with the previously collected supernatant and centrifuged at 20,000g, 4°C for 20 min. The supernatant containing the extracted proteins and protein complexes was used for further IP experiments.

Blue Native PAGE—blue native PAGE (Wittig et al., 2006) was performed using the Novex® NativePAGE™ Bis-Tris Gel System (Invitrogen) according to the manufacturer's protocol. Briefly, 75 μ g DDM extracted sample diluted to 100 μ L was centrifuged at 134,000 g, 4°C for 30 min. 14 μ L of the supernatant was mixed with 2 μ L BN sample buffer, and 10 μ L of which was added with 0.5 μ L 5% G-250 and centrifuged at 20,000 g, 4°C for 20 min. 20 μ L supernatant was loaded on a 3-12% Bis-Tris gel for the first dimension, non-denaturing PAGE. After running the gel was cut and subjected to the second dimension of SDS-PAGE and analyzed with the PP2B antibody (1:1000, Genscript). The MS/MS spectra obtained from each gel slice were searched against the mouse database with MaxQuant version 1.5.2.8. To accurately quantify and determine protein distribution across the BN-gel, peptides were manually curated using Skyline. For peak picking a selection of most abundant and unique peptides for the proteins of interest was made. Next, the m/z and retention time at which a given peptide was identified by MaxQuant was used to select the correct MS1 peak area. This was done for each slice separately, using the same precursor, m/z and retention time. Peptide abundance was summed per protein per slice and divided by the maximum intensity value observed for the protein across the gel. This data is shown in a heatmap as relative abundance.

Immunoprecipitation—After extraction of the protein complexes, 10 μ g antibody was added and incubated overnight on a rotator at 4°C. 40 μ L Protein A&G agarose beads (Santa Cruz) were washed for 4 times with wash buffer (25mM HEPES, 150 mM NaCl, 0.1% DDM, pH 7.4) and added to the sample. As a control the extract was incubated with the beads without

antibody. For a peptide blocking experiment, the extract was incubated with 10 µg antibody in the presence of 20 µg peptide antigen. After 1h incubation on a rotator at 4°C, the sample was washed for 4 times with the wash buffer. SDS-PAGE loading buffer was added to the sample and boiled at 95°C for 3 min. 5µL 30% acrylamide per sample was added to each sample to facilitate the identification of cysteine containing peptides. The proteins were separated on a 10% gel by an SDS-PAGE system (Bio-Rad) followed by In-Gel Digestion.

After SDS-PAGE, the gel was fixed in a sufficient amount of fixation buffer (50% Ethanol, 3% Phosphoric Acid) for at least 1 h and washed with Milli-Q water for 4 ×15 min; and stained with Coomassie blue G-250 for 2 h and washed with water for 4 ×15 min. The stacking gel was removed and the separation gel was cut into 5 pieces according to the protein marker (30, 45, 60, 120 kDa) to reduce sample complexity and to facilitate the subsequent MS analysis. The gel pieces were separately transferred into a 1.5 ml Eppendorf tube and destained. The destaining was performed by adding 500 µL of 50 mM NH₄HCO₃ / 50% acetonitrile to the gel fragments and vortexing for 20 min. The solution was removed and discarded. 500 µL 100% acetonitrile was added and vortexed for 20 min. The solution was removed and discarded. 200 µL 50 mM NH₄HCO₃ was added and incubated for 5 min at RT. 200 µL of acetonitrile was added and the sample was incubated overnight allowing complete destaining. The solution was discarded and 500 µL 100% acetonitrile was added and vortexed for 20 min, after which the solution was discarded and the gel fragments were dried in a SpeedVac for 30 min.

In-gel digestion—The in-gel digestion was performed by adding 160-180 µL trypsin solution (6.7 µg/ml, sequence grade; Promega) containing 50 mM NH₄HCO₃ and incubation at 37 °C overnight. After digestion, the solution containing the tryptic peptides was collected and the remaining peptides in the tube were extracted by adding and removing 50 mM NH₄HCO₃ / 50% acetonitrile twice. This solution was pooled and dried in the SpeedVac and stored at -20°C. Immediately before LC-MS/MS analysis, the sample was re-dissolved in 15 µL 0.1 M HAc and centrifuged at 20,000g for 15 min. The supernatant containing peptides was transferred to an MS tube and analyzed with LC-MS/MS.

LC-MS/MS analysis—The peptides were injected into the loop of an Eksogent nano LC-ultra 1D plus HPLC system equipped with a C18 column (200-mm homemade Altima C18 analytical column, 100 µm ID 3 µm particle size). Peptides were separated using a linear gradient of 5 % solvent A (0.1 % acidic acid, 5 % Acetonitrile) and 45 % solvent B (0.1 % acidic acid, 80 % Acetonitrile) in 50 min. The LC system was directly coupled in-line with an LTQ-Orbitrap Velos instrument (Thermo Fisher Scientific). The LTQ-Orbitrap was set to data-dependent mode to switch automatically between MS and MS/MS. MS spectra range from 330 till 2000 m/z can be acquired in the Orbitrap at an FWHM resolution of 30,000 after accumulation to 500,000 in the linear ion trap with one microscan. The five most abundant precursor ions were selected for fragmentation by CID with an isolation width of 2 DA. CID was performed in the linear ion trap after accumulation to 50,000 with 1 microscan.

Protein Identification—MS/MS spectra were searched against a mouse database (IPI_v.3.79) with ProteinPilot™ software (version 3.0; Applied Biosystems; MDS Sciex) using the Paragon™ algorithm (version 3.0.0.0; Shilov et al.) as the search engine. The search parameters were set to cysteine modification by acrylamide and digest done with trypsin. The detected protein threshold (unused protscore (confidence)) in the software was set to 0.05 to achieve 10% confidence, and identified proteins were grouped to minimize redundancy.

The extracted protein complex was analyzed with LC-MS/MS analysis, which generated a large list of proteins. The MS/MS raw data were analyzed by Protein Pilot to translate MS2 spectra into peptides (sequence), which were then mapped against a database to map them to proteins. Subsequently, from this large amount of IP data IgG, trypsin and Keratin proteins clusters were excluded since these are obviously contaminants. In this experiment, we included the “unused” values generated from the software ProteinPilot as a semi-quantitative means for relative comparison (Klemmer et al., 2009). Tryptic peptides shared by multiple proteins were assigned to the winner protein. Only proteins of which unique peptides were found, were taken along. Proteins not meeting these requirements were excluded from further analysis. The remaining protein data set was loaded into Ingenuity Pathway Analysis (IPA), which created a protein network. All interconnections made by IPA were based on “known direct interactions”.

IP-LC/MS/MS analysis criteria—Two 2 PPP3CA antibodies was used to find the interactors of PP2B: 1. Antibody#165, rabbit poly-colonial from Genscript, 4 times independent experiment replicates; 2. Antibody#292, mouse mono-colonial from Santa Cruz, 3 times independent experiment replicates. The controls are IP without antibody, with beads, run along the experiment groups.

The protein identified in Miguel's script as True Interactor ("T") in both antibodies, and at least 2 times from each antibody. The value is the log₂ fold change between this experiment and the control group (REF).

iTRAQ

Synaptic Membrane Preparation—Synaptic membranes from predominantly glutamatergic synapses were isolated from 10-12 wk *a6-PP2B*, *L7-PP2B* and WT mice as described previously (Li et al., 2007; Klychnikov et al., n.d.). A short overview of the experimental setup is presented in Fig. 3a. In brief, for each sample, cerebellum from one mouse was homogenized as described in *Preparation of P2+M* section. The lysate was centrifuged at 1000 g, 4 °C, for 10 min. The supernatant was loaded on top of a sucrose step gradient consisting of 0.85 M and 1.2 M sucrose. After ultracentrifugation at 100,000 g, 4 °C for 2 h, the synaptosome fraction at the interface of 0.85/1.2 M sucrose was collected, diluted six times with 5 mM HEPES buffer (pH 7.4), and centrifuged at 80,000 g, 4 °C for 40 min. The pellet was resuspended with 200 μ L 5 mM HEPES buffer (pH 7.4). Protein concentration was determined by Bradford (Bio-Rad) and adjusted to 0.75 μ g/ μ L, then confirmed by running on a 10 % Stain-free SDS-PAGE system. All the buffer contains phosphatase inhibitor cocktails 2 and 3 (Sigma). The obtained synaptic membranes were subjected to trypsin digestion and iTRAQ reagent tagging.

Protein Digestion and iTRAQ Labeling—In three independent 8-plex iTRAQ experiments we compared WT samples (n=8) with *L7-PP2B* KO samples (n=8)(two sets) and WT (n=5) with *a6-PP2B* KO (n=3)(one set). The digestion and iTRAQ labeling of proteins in synaptic membrane fractions have been described in previous studies (Li et al., 2007; Klychnikov et al., n.d.). In short, for each sample, 75 μ g of dried synaptic membranes were resuspended in 28 μ L of 0.5 M Triethylammonium bicarbonate buffer (Sigma) (pH 8.5), containing 0.85 % RapiGest (Waters Corp.). A 2- μ L cleavage reagent (iTRAQ reagent kit, AB Sciex) was added and incubated at 55 °C for 1 h, after which 1 μ L of Cys blocking reagent (iTRAQ reagent kit, AB Sciex) was added and samples were vortexed for 10 min. Subsequently, 5 μ g of trypsin (sequencing grade, Promega) was added and incubated 2 h at 55 °C. The tryptic peptides were then tagged with iTRAQ reagents. After incubation for 3 h, the samples were pooled and acidified with 10% trifluoroacetic acid to pH 2.5–3. After 1 h, the sample was centrifuged, and the supernatant was dried in a SpeedVac. In each iTRAQ experiment, tissue from 4 WT and 4 KO were isolated (blinded for the experimenter) and tagged with 113 Da, 114 Da, 115 Da, 116 Da, 117 Da, 118 Da, 119 Da, and 121 Da reagents.

Two-dimensional Liquid Chromatography—The dried iTRAQ labeled sample was dissolved in 200 μ L of loading buffer (20% acetonitrile, 10 mM KH₂PO₄, pH 2.9), whereas 200 μ L was injected into a strong cation exchange column (2.1 \times 150-mm PolySMLFOETHYL A column, PolyLC Inc.). Peptides were eluted with a linear gradient of 0 – 500 mM KCl in 20% acetonitrile, 10 mM KH₂PO₄ (pH 2.9), over 25 min at a flow rate of 200 μ L/min. Fractions were collected at 1-min intervals and dried in a SpeedVac. SCX fractions were redissolved in 20 μ L of 0.1% TFA, and fractionated by C18 nano-liquid chromatography (standard 2D-LC procedure).

MALDI-MS/MS—The sample was analyzed on an ABI 5800 proteomics analyzer (AB Sciex). Peptide collision-induced dissociation was performed at 1 kV; the collision gas was air. MS/MS spectra were each collected from 1500 laser shots. Peptides with the signal-to-noise ratio > 50 at the MS mode were selected for an MS/MS experiment; a maximum of 20 MS/MS was allowed per spot. The precursor mass window was 200 relatives to resolution (full width at half maximum).

iTRAQ Protein Identification and Quantitation — To annotate spectra, Mascot (Matrix Science) searches were performed against the SwissProt database (release Nov. 2011) and

the larger but more redundant National Center for Biotechnology Information (NCBI) database (release Nov. 2011) using the GPS Explorer (AB Sciex version 3.6). MS/MS spectra were searched against mouse databases with trypsin specificity and fixed iTRAQ modifications at lysine residues and N-termini of the peptides. Mass tolerance was 150 ppm for precursor ions and 0.5 Da for fragment ions; one missed cleavage was allowed. The false discovery rate (percentage) for peptide identification was calculated using a randomized database. Protein redundancy in the result files was removed by clustering the precursor protein sequences at a threshold of 90% sequence similarity over 85% of the sequence length (Blastclust, version 20041205). Subsequently, all peptides were matched against the protein clusters; those that were matched to more than one protein cluster were not considered for protein identification and quantification, leaving only “unique” peptides in the analysis. Only proteins identified with at least two peptides with a confidence interval $\geq 95\%$ (AB Sciex CI, percentage) were considered identified, and of these proteins, only those with three or more quantifiable peptides in both iTRAQ experiments were included in subsequent quantitative analyses. Peak areas for each iTRAQ signature peak (m/z 113.1, 114.1, 115.1, 116.1, 117.1, 118.1, 119.1, 121.1) were obtained and corrected according to the manufacturers’ instructions to account for the differences in the isotopic overlap.

To compensate for the possible variations in the starting amounts of the samples, the individual peak areas of each iTRAQ signature peak were \log_2 -transformed and normalized to the total peak area of the signature peak. Peptides with iTRAQ signature peaks of less than 2000 were not considered for quantification. Within each experiment, for each peptide, the peak area in each sample was mean-centered. Protein averages were calculated from these mean-centered peak areas of multiple peptides. Finally, the eight mutants and eight WT protein means of both experiments were used to calculate the average difference between WT and *L7-PP2B* KO mice. To assess whether this difference had occurred by chance due to the multiple testing problem or could be deemed significant, we calculated the permutation-derived false discovery rate (q-value) using the Excel plug-in of the Significance Analysis of Microarrays (SAM) program (Roxas and Li, 2008; Tusher et al., n.d.). The settings for the SAM program were: two class unpaired, \log_2 -scaled, t-statistic, 1000 permutations, automatic estimation of s_0 factor, and 10 *k-nearest* neighbors.

Phosphoproteomics

Protein extraction and digestion—Cerebellar P2 from 2 males and 1 female mouse were pooled to ensure enough yield of phospho-peptides after enrichment. Protein concentrations were measured using the BCA assay (Thermo Scientific). Proteins were extracted by acetone precipitation at -20°C overnight. Samples were centrifuged at 8,000 g for 10 min at 4°C . The acetone was removed and the pellet allowed to dry. The protein pellet (~4 mg protein) was dissolved in 1 ml 50 mM Tris/HCl (pH 8.2), 0.5 % SDC and proteins were digested with LysC (1:200 enzyme: protein ratio) for 4 h at 37°C . Next, trypsin was added (1:100 enzyme: protein ratio) and the digestion proceeded overnight at 30°C . Digests were acidified with 50 μL 10 % formic acid (FA) and centrifuged at 8,000 g for 10 min at 4°C to remove the precipitated SDC. The supernatant was transferred to a new centrifuge tube. The digests were purified with C18 solid phase extraction (Sep-Pak, Waters), lyophilized and stored at -20°C .

Phosphopeptide enrichment—Phosphopeptide enrichment proceeded with some modifications to the method of Kettenbach *et al.* (Kettenbach, A. N.; Gerber, S. A. (2011) *Anal. Chem.* 83: 7635–7644). 4 mg lyophilized peptide digest was dissolved in 1 ml 50 % acetonitrile (ACN), 2 M Lactic acid with 6 mg TiO_2 beads (GL Sciences) and incubated on a rotator at room temperature (RT) for 2 h. Beads were washed twice with 2 M lactic acid / 50 % ACN and once with 4% FA in 50 % ACN. Phospho-peptides were eluted twice with 150 μL of 50 mM K_2HPO_4 , 1% pyrrolidine, acidified with 90 μL of 10 % FA and stored at -20°C .

Tandem Mass Tagging labeling—Isobaric labeling of the enriched phosphopeptides was performed using the 10-plex tandem mass tag (TMT) reagents (Thermo Fisher Scientific) with some modifications to the method of Böhm *et al.* (*J. Proteome Res.* 2015, 14, 2500–2510). Phosphopeptides were loaded onto 20 mg C18 cartridges prepared in-house. The C18 cartridges were washed once with 1 ml 0.1% TFA and two times with 1 mL of 50 mM KH_2PO_4 (pH 4.5). TMT reagents (0.8 mg) were dissolved in 10 μL of dry ACN and diluted with 200 μL 50 mM KH_2PO_4 . This TMT solution was immediately loaded onto the column and labeling on column proceeded for 1 h at RT. Each of the 10 samples was labeled with a different TMT tag.

After labeling the column was washed twice with 1 ml 2 % ACN / 0.2 % formic acid and the labeled peptides were eluted with 1 ml 50 % ACN. TMT labeled samples were pooled and lyophilized.

High-pH and reversed phase HPLC—TMT labeled phospho-peptides were subjected to offline orthogonal high-pH and reverse phase fractionation. TMT labeled phospho-peptides were solubilized in 0.1 % TFA and loaded onto a 20 mg PLRP-S cartridge made in-house. The cartridge was washed once with 1 ml 0.1 % TFA and three times with 1 ml milliQ water. The peptides were eluted step-wise from the column with 0 %, 5 %, 10 %, 15 %, 25 % and 40 % ACN / 10 mM ammonium formate (pH 10). The 6 fractions were dried by vacuum centrifugation and each fraction was reconstituted with 2 % ACN / 0.2 % FA for nanoLC-MS/MS analysis.

Orbitrap Lumos parameters—Mass spectra were acquired on an Orbitrap Lumos (Thermo) coupled to an EASY-nLC 1200 system (Thermo). Peptides were separated on an in-house packed 75 μm inner diameter column containing 50 cm Waters CSH130 resin (3.5 μm , 130 \AA , Waters) with a gradient consisting of 2–20 % ACN, 0.1 % FA over 150 min at 300 nl/ min. The column was kept at 50 $^{\circ}\text{C}$ in a NanoLC oven - MPI design (MS Wil GmbH). For all experiments, the instrument was operated in the data-dependent acquisition (DDA) mode. MS1 spectra were collected at a resolution of 120,000 with an automated gain control (AGC) target of $2\text{E}5$ and a max injection time of 50 ms. The most intense ions were selected for MS/MS, top speed method 3 seconds cycle time. Precursors were filtered according to charge state (2-7), and monoisotopic peak assignment. Previously interrogated precursors were dynamically excluded for 70 seconds. Peptide precursors were isolated with a quadrupole mass filter set to a width of 0.7 Th. When applying the MS3 method, ion trap MS2 spectra were collected at an AGC of $5\text{E}4$, max injection time of 50 ms and CID collision energy of 35 %. For Orbitrap MS3 spectra, the operation resolution was 60,000 with an AGC setting of $1\text{E}5$ and a max injection time of 120 ms. The HCD collision energy was set to 65 % to ensure maximal TMT reporter ion yield. Synchronous precursor selection (SPS) was enabled at all times to include up to 10 MS2 fragment ions in the MS3 scan.

Data analysis—Peak lists were automatically created from raw data files using the Proteome Discoverer 2.1 (Thermo) software. The Mascot search algorithm (version 2.2, MatrixScience) was used for searching spectra against the UniProt database (taxonomy: *Mus musculus*, version December 2016). The peptide tolerance was set to 10 ppm and the fragment ion tolerance was set to 0.6 Da. A maximum number of 2 missed cleavages were allowed. TMT tags on peptide N-termini/ lysine residues (+229.162932 Da) and carbamidomethylation of cysteine residues (+57.02146 Da) were set as static modifications, while methionine oxidation (+15.99492 Da) and serine, threonine and tyrosine phosphorylation (+79.96633 Da) were set as variable modifications. The target FDR for both PSMs and peptides was set to 0.01. Only peptides marked 'high confidence' were taken into account for further analysis. Proteins were marked with 'high confidence' when they fulfilled the requirement for an FDR = 0.01. The co-isolation threshold was set to 75 % and the minimum signal-to-noise ratio to 10. For TMT quantification, a 0.01 Th window centered on the theoretical m/z value of each reporter ion was queried for the nearest signal intensity. Reporter ion intensities were adjusted to correct for the isotopic impurities of the different TMT reagents (according to the manufacturer's specifications).

Cell culture

Purkinje cells were isolated from E17-E19 mice embryos following a method previous described (Tabata et al., 2000) with slight modifications. Briefly, the cerebella were dissected in ice-cold HBSS supplemented with 20 $\mu\text{g}/\text{ml}$ Gentamicin (both from Life Technologies), then incubated with 10 U/ml Papain (Sigma) and 2.5 U/ml DNase I (Roche) and 4 mM MgCl_2 (Sigma) at 33 $^{\circ}\text{C}$ for 20 min. The cerebella were titrated in HBSS with 2.5 U/ml DNase I and 4 mM MgCl_2 and were filtered with 200 μm Nylon mesh (Millipore). After washing twice in HBSS the cells were plated on pre-cleaned, poly-ornithine (500 $\mu\text{g}/\text{ml}$, Sigma) coated 1.5H glass-bottomed slide (Ibidi) at the density of 1.2×10^6 cells/ cm^2 . For tracking experiments the cells were transfected before plating with L7-mCherry or -GFP (a gift from Dr. XXX) using Nucleofector 4D (Lonza) according to manufacturer's protocol. The culture medium contained PNBm neural basal medium (Lonza), GS21 neural supplement (1:50, Globalstem), 5 $\mu\text{g}/\text{ml}$ Gentamicin and 2 mM Glutamax (Life Technologies), half-volume of the medium was

changed once a week and the day before the experiment.

dSTORM

The cerebellar culture was fixed with 4% PFA/ 4% sucrose in PBS on DIV 21 at room temperature for 10 min, washed 3 times with PBS containing 10mM Tris-PBS (pH 7.4). Slides were blocked in 10% horse serum with 0.1% Triton-X100 (Sigma) for 1 hour at room temperature (for surface GluR2 staining, TX-100 was excluded), then incubated with primary antibodies at 4°C overnight. After washing with DPBS for 3×5min, the secondary antibodies (6.7 ug/mL, ThermoFisher or Jackson Laboratory) were added and incubated for 1h at room temperature. Then slides were washed with DPBS for 3×5min, post-fixed with 4 % PFA at RT for 10 min, washed 3 times with Tris-PBS and stored at 4°C with 1: 15K diluted 0.1 µm TetraSpeck™ Microspheres (ThermoFisher). Samples were used within 2 wks. During imaging, no free-floating fluorophore was observed. The analysis was done with custom-written scripts in R. Briefly the spine (ROI) was picked objectively with Fiji, the imported localizations files were analyzed blindly with DBSCAN (Ref.). After removal of background, the sizes of nano-clusters were plotted in R (ggplot2).

Live cell imaging

The single particle tracking experiments were done on DIV 21-23, with a Zeiss Elyra PS1 microscopy, imaging solution containing (in mM): 135 NaCl, 3 KCl, 2 CaCl₂, 2 MgCl₂, 20 and 10 HEPES, (pH 7.25) at 37 °C. First, the targeted Purkinje cell was identified by the expression of L7-XFP and cell morphology, and a confocal Z-stack was obtained for later reference. The imaging started immediately after adding the primary antibody directly labeled with Alexa488/ATTO488/ATTO594. The images were obtained by an EMCCD (Andor) at 30 Hz for 5000 frames. For analysis, the appropriate confocal image was used to align with the time-lapse images and to generate the Region of Interest (ROI), the tracking within the ROI was done in Fiji (<https://www.ncbi.nlm.nih.gov/pubmed/22743772?dopt=Abstract>) using an SOS plugin (<https://www.ncbi.nlm.nih.gov/pubmed/28324611>). Tracks shorter than 10 frames were excluded from analysis.

CHAPTER

6.3

AMPA protein Shisa6 is essential for Purkinje cell synaptic potentiation and motor learning

Saša Peter^{1,6}, Bastiaan H.A. Urbanus^{1,6}, Remco V. Klaassen^{2,6}, Bin Wu¹, Henk-Jan Boele¹, Sameha Azizi¹, Johan A. Slotman³, Adriaan B. Houtsmuller³, Martijn Schonewille¹, Freek E. Hoebeek^{1,5}, Sabine Spijker², August B. Smit^{2,*} & Chris I. De Zeeuw^{1,4,*}

¹ Department of Neuroscience, Erasmus MC, 3000 DR, Rotterdam, The Netherlands

² Department of Molecular and Cellular neurobiology, Center for Neurogenomics and Cognitive Research, VU University Amsterdam, 1081 HV Amsterdam, The Netherlands

³ Optical imaging center, Department of Pathology, Erasmus MC, 3000 DR Rotterdam, The Netherlands

⁴ Netherlands Institute for Neuroscience, 1105 CA, Amsterdam, The Netherlands

⁵ NIDOD Department, Brain Center Rudolf Magnus, Wilhelmina Children's Hospital, UMC Utrecht, The Netherlands

⁶ Co-first authors

*Correspondence: c.dezeeuw@erasmusmc.nl, guus.smit@vu.nl

Submitted

Abstract

The majority of fast excitatory postsynaptic currents in the brain are gated through AMPA-type glutamate receptors, the kinetics and trafficking of which can be modulated by auxiliary proteins. It is unclear whether and how auxiliary proteins can modulate synaptic function to contribute to procedural memory formation. Here, we report that Purkinje cells express the auxiliary protein Shisa6 (CKAMP52). Shisa6 co-localizes with glutamate receptor GluA2 and interacts with the non-AMPA glutamate receptor GluD2. Absence of *Shisa6* affects basal excitatory transmission, deactivation of AMPA-receptors, as well as induction of long-term potentiation (LTP). Moreover, mice harbouring a Purkinje cell-specific knockout of *Shisa6*, i.e. *Shisa6*^{L7 KO}, show a reduction in their simple spike activity *in vivo*, as well as severe impairments in motor coordination tasks including ErasmusLadder, phase reversal learning of the vestibulo-ocular reflex, and eyeblink conditioning. These results indicate that Shisa6 is crucial for Purkinje cell AMPA-receptor function, synaptic plasticity, and cerebellar motor learning.

Introduction

Repetitive postsynaptic depolarization through activation of AMPA-type glutamate receptors (AMPA-Rs) is one of the main mechanisms to adjust synaptic weights in the brain. AMPA-R-driven depolarization can trigger a range of voltage-dependent processes, including Ca^{2+} -influx through voltage-dependent channels and activated NMDA-receptors, which in turn induces modulation of AMPA currents¹. This form of synaptic plasticity has garnered great interest over the past decades, as it is considered a fundamental cellular mechanism underlying memory formation^{2,3}. Different types of auxiliary proteins have been shown to modulate trafficking, mobility and gating properties of AMPARs, each of which may shape cell and/or brain region specific types of plasticity and AMPAR-modifying molecular pathways⁴. Shisa proteins can affect mobility (Shisa6) and gating properties of AMPARs (Shisa6, -7 and -9), such as receptor deactivation and desensitization in the hippocampus⁴⁻¹⁰. Also, Shisa9 (CKAMP44) has been shown to be responsible for the distinctive short-term depression in dorsal lateral geniculate nucleus synapses by reducing the rate of recovery from desensitization¹¹.

In this study, we investigated whether the formation of procedural memories requires Shisa6-dependent modification of AMPARs. The cerebellum is crucial in procedural memory formation and is equipped with a wide spectrum of plasticity types that are hypothesized to work in a synergistic fashion¹². Cerebellar plasticity can be studied in well-defined behavioural learning paradigms, such as VOR adaptation and Pavlovian eyeblink conditioning. Various cell-specific promoters allow precise genetic manipulations, through which this unique brain structure has provided important insights into the cellular mechanisms of motor learning in general. For example, experiments using the granule cell-specific GABA_A-receptor subunit $\alpha 6$ promoter¹³ or the Purkinje cell (PC)-specific L7 promoter^{14,15} have confirmed that synaptic plasticity at the parallel fibre (PF) to PC synapse is essential for cerebellum-dependent motor learning. Since many of these cerebellar forms of plasticity also included potentiation or depression of AMPAR currents¹⁴⁻¹⁹, we here aim to uncover how Shisa6 affects synaptic transmission in the cerebellar cortex, and consequently cerebellar motor learning. We found that Shisa6 is prominently expressed by PCs and that PC-specific ablation of *Shisa6* (*Shisa6*^{L7 KO}) affects the function of the PF to PC synapse in that they have increased deactivation of AMPAR-mediated excitatory postsynaptic currents (EPSCs), impaired PF to PC baseline excitatory input as well as LTP. These impairments are supported by our findings that Shisa6 interacts with AMPAR subunits and GluD2 and that AMPAR subunits are downregulated in the absence of Shisa6 while GluD2 is upregulated. Moreover, *Shisa6*^{L7 KO} mice show both lower simple spike (SS) firing of their PCs and impaired motor learning, highlighting a critical role of AMPAR auxiliary proteins in procedural memory formation.

Results

Increased AMPAR deactivation and reduced frequency of PF to PC mediated EPSCs in *Shisa6*^{L7 KO} mice.

mRNA expression levels visualized by *in situ* hybridization²⁰ indicate that of the major brain-expressed Shisa family members, only *Shisa6* is expressed in cerebellar PCs. Using immunohistochemistry, we showed that the Shisa6 protein is expressed in PCs of control mice and absent in PCs of *Shisa6*^{L7 KO} mice (Fig.1a, Supplementary Fig. 1a). Given the co-localization of Shisa6 with GluA2 in the hippocampus⁷, we next investigated to what extent this apposition also occurs in the cerebellum. Using 3D structural illumination microscopy (3D-SIM) we found that Shisa6 also co-localizes with GluA2 subunits in the molecular layer (ML) of the cerebellum (Fig. 1b). To uncover the role of Shisa6 in the ML we recorded miniature excitatory postsynaptic currents (mEPSCs) in PCs of *Shisa6*^{L7 KO} (Fig. 1c). The mEPSCs in *Shisa6*^{L7 KO} PCs had a decreased rise time (Fig. 1d, $p < 0.001$) and a decreased decay time compared to the control (Fig. 1e, $p < 0.001$), indicating that Shisa6 has a role in deactivation of AMPARs, which is in line with effects observed in mEPSCs of hippocampal pyramidal cells⁷. However, unlike that of the hippocampal pyramidal cells lacking Shisa6, the frequency distribution of mEPSCs in PCs of *Shisa6*^{L7 KO} mice indicated a large reduction in the total number of events (Fig. 1f), which was found to be significantly different (Fig. 1g, $p < 0.001$). However, the median amplitude of mEPSCs was not different in *Shisa6*^{L7 KO} mice (Fig. 1h, $p = 0.28$). Even though we did not find direct evidence for reduced mEPSC amplitudes we considered the possibility that lower mEPSC amplitudes could disappear in the noise floor of our recordings. We

therefore also recorded spontaneous EPSCs (sEPSCs) and increased the experimental temperature in order to facilitate larger amplitudes and more frequent EPSCs (Supplementary Fig. 1b). The sEPSC rise time (Supplementary Fig. 1c, $p = 0.55$) was not different between the groups. The decay time was confirmed to be lower (Supplementary Fig. 1d, $p = 0.005$) in addition to a large reduction in the number of EPSCs (Supplementary Fig. 1e), which was found to be significantly different (Supplementary Fig. 1f, $p = 0.005$). In contrast to mEPSCs the larger median amplitudes of sEPSCs were found to be significantly lower in the absence of Shisa6 (Supplementary Fig. 1g, $p = 0.002$). A plausible explanation for the absence of such difference in the relatively small mEPSCs is that lower amplitudes could be obscured by the noise floor.

To further explore the hypothesis of reduced PF to PC synaptic functionality, we evoked excitatory synaptic input by stimulating PFs with varying stimulation intensities (Fig. 1i). The excitatory postsynaptic response at the PF to PC synapse was highly reduced in *Shisa6*^{L7 KO} (Fig. 1j, $p < 0.001$ for each stimulation amplitude). In contrast, PF paired-pulse facilitation was normal (Fig. 1k, $p = 0.86$). When exploring the possibility of impaired postsynaptic inhibitory responses in the PC, we found that spontaneous inhibitory postsynaptic currents (sIPSCs) did not differ in their rise time (Supplementary Fig. 1h, i, $p = 0.50$), decay time (Supplementary Fig. 1j, $p = 0.23$), frequency (Supplementary Fig. 1k, $p = 0.32$) or amplitude (Supplementary Fig. 1l, $p = 0.63$). From these results, we conclude that Shisa6 is specifically involved in the facilitation of functional PF to PC excitation and AMPAR activation and deactivation at the PF to PC synapse.

Cerebellar Shisa6 interacts with both AMPA and Delta-2 type glutamate receptors.

As the impact of deletion of *Shisa6* on mEPSC and sEPSC frequency at PCs differed from those at hippocampal CA1 pyramidal cells⁷, we next investigated to what extent the cerebellar interaction profile of Shisa6 was distinct from that found in the hippocampus. First, we immunoprecipitated cerebellar Shisa6 protein complexes from the n-Dodecyl-beta-D-Maltoside-extracted crude synaptic membrane fraction and subjected these to mass spectrometric (MS) analysis (Fig. 2a, Supplementary File 1). As anticipated, AMPAR subunits GluA1-3 (*Gria1-3*) were highly enriched in cerebellar Shisa6 complexes, yet surprisingly, so was the cerebellum-specific glutamate receptor Delta2 (GluD2; *Grid2*). GluD2 has been reported to have a profound effect on postsynaptic AMPAR levels at PC synapses²¹ and to play an essential role in coordinating PF to PC plasticity^{22,23}. We confirmed the interaction between Shisa6 (Flag-Shisa6) and GluD2 by co-expression in recombinant HEK293 cells, followed by immunoprecipitation using a Flag-specific antibody (Fig. 2b). Immunoblot analysis confirmed that Shisa6 can directly bind GluD2, and that the interaction as such does not depend on co-association with AMPAR subunits. Finally, we investigated whether GluA2 and GluD2 co-associate within the same native Shisa6 sub-complexes by means of immuno-depletion IP (Fig. 2c). Native cerebellar GluA2 complexes were removed from the crude synaptic lysate by means of immunoprecipitation (depletion with empty beads as control), yielding the “input after depletion” fraction. Subsequently, Shisa6 complexes were immunoprecipitated from this depleted input and analysed for their GluA2 and GluD2 content. Near full depletion of GluA2 was confirmed (beads-depleted: set to 100%, Anti-GluA2-depleted, $p < 0.001$), yet little reduction was observed in the level of Shisa6-associated GluD2 (beads-depleted: set to 100%, anti-GluA2-depleted, $p = 0.31$). We therefore conclude that native Shisa6-GluD2 binding does not depend on co-association with GluA2 and predominantly constitutes a separate protein subcomplex. Shisa6 appears to have a distinct cerebellar interaction profile, which includes an independent association with AMPA- and Delta-2 type glutamate receptors.

Shisa6 deletion results in AMPAR downregulation and GluD2 upregulation.

Since Shisa6 associates with both AMPA- and GluD2-type glutamate receptors, and given that mEPSC frequency and sEPSC frequency and amplitude at PC synapses was reduced upon deletion of *Shisa6*, we next investigated how the absence of *Shisa6* affected synaptic protein levels. To this end we first extracted all proteins from the crude synaptic membrane fraction of eight WT and *Shisa6*^{null} mice and subjected these to sequential window acquisition of all theoretical fragment ion spectra (SWATH) MS analysis (Fig. 3a, b, Supplementary Fig. 2a and Supplementary File 2). The resulting proteome encompassed 3,043 proteins with highly reproducible quantification (Supplementary Fig. 2c, CV = 0.064). In line with the reduced sEPSC amplitude in *Shisa6*^{null} mice we observed a significant downregulation of both synaptic GluA3 (*Gria3*) ($p < 0.001$) and GluA2 (*Gria2*) ($p < 0.001$), whereas GluA1 (*Gria1*) levels did not change significantly ($p = 0.026$; cut-off value of 0.01). Interestingly, the opposite effect was observed for the GluD2 receptor (*Grid2*), which was upregulated under *Shisa6* KO conditions ($p < 0.001$). As Shisa6 strongly interacts with GluD2, and the GluD2 levels were upregulated in the absence of Shisa6 in the *Shisa6*^{L7 KO}, we next investigated the impact on synapse number and synaptic morphology in PCs using electron microscopy (Fig. 3c). The

number of PSDs was unaffected in *Shisa6*^{L7KO} (Fig. 3d, e, $p = 0.65$). Similarly, the length of the PSD was not affected (Fig. 3f, g, $p = 0.51$). Finally, we did not observe changes in the protein composition of the postsynaptic density (PSD), as indicated by the unmodified expression of PSD marker proteins, e.g., Shank1, PSD95 (*Dlg4*), Homer3 and CamK2B (Supplementary Fig. 2b). In short, absence of *Shisa6* does not affect composition, length or number of PSDs in PCs, but removal of *Shisa6* enhances synaptic GluA2 levels, while reducing the number of GluA2- and GluA3-containing AMPAR receptors.

Impaired LTP, but not LTD, in PCs of *Shisa6*^{L7KO} mice.

Given that auxiliary subunits of AMPARs, of which *Shisa6* is one, have previously been shown to affect excitatory current potentiation^{4,24}, we hypothesized that PC synaptic plasticity might be affected in the *Shisa6*^{L7KO}. Using high frequency stimulation (Fig. 4a) we were able to induce LTP in PCs of control mice (Fig. 4b, $p = 0.027$), but not of *Shisa6*^{L7KO} (Fig. 4b, $p = 0.54$). Considering the lower synaptic GluA3 expression in *Shisa6*^{L7KO} and the importance of GluA3 higher conductance for PF to PC LTP¹⁵ we tested the hypothesis that the inability to induce LTP in the *Shisa6*^{L7KO} was dependent on GluA3 increased conductance (Fig. 4c). For this purpose, we applied forskolin (FSK), which induces increased GluA3 conductance mediated LTP, and observed a typical potentiation in both the control (Fig. 4d, $p = 0.033$) and the *Shisa6*^{L7KO} (Fig. 4d, $p < 0.001$). Considering the increased synaptic GluA2 in *Shisa6*^{L7KO} and its importance for LTD²⁵ we also evaluated long-term depression (LTD) using the classical 1 Hz protocol of climbing fibre (CF) activation together with PF stimulation (Fig. 4e) and found that LTD could be induced in PCs of both control (Fig. 4f, $p = 0.025$) and *Shisa6*^{L7KO} mice (Fig. 4f, $p = 0.008$). In addition, we looked at CF responses *ex vivo* during development and found no evidences for impaired CF elimination in the *Shisa6*^{L7KO}, arguing against the possibility of abnormal CF innervation due to a developmental phenotype (Supplementary Fig. 5e, $p = 0.57$). Together, these results indicate that a lack of *Shisa6* impairs LTP induction at the PF to PC synapse, whereas LTD and CF development appear unaffected.

***Shisa6*^{L7KO} mice show impaired motor performance and learning.**

To explore behavioural phenotypes in the *Shisa6*^{L7KO}, we assessed a number of basic cerebellum-dependent motor behaviours. Baseline motor performance, as tested with a rotarod, showed that *Shisa6*^{L7KO} mice fall earlier from the rotating wheel (Fig. 5a, b, day 1-4, 40 rpm, $p = 0.044$; day 5, 80 rpm, $p = 0.008$). This was not due to altered grip force, because this was unaffected (Supplementary Fig. 3a, $p = 0.28$). On the balance beam, used to evaluate gross movement coordination on a small diameter rod, we found no significant impairment in the *Shisa6*^{L7KO} (Supplementary Fig. 3b; for 6 mm rod, $p = 0.24$; for 12 mm rod, $p = 0.22$). However, when we evaluated the walking patterns on the pressure-sensitive rungs of the ErasmusLadder, we observed a significantly increased number of missteps in the *Shisa6*^{L7KO} (Fig. 5a, c; $p = 0.004$), indicating impaired motor coordination²⁶.

Next, we analysed compensatory eye movements, commonly used to assess the cerebellar contribution to motor performance and procedural learning^{13,27}. Examination of the visually driven optokinetic reflex (OKR) indicated that both its amplitude (Fig. 5d; $p = 0.012$) and phase (Fig. 5e; $p = 0.008$) with respect to those of the stimulus were reduced in *Shisa6*^{L7KO} mice. When testing the vestibulo-ocular reflex in the dark (VOR), which is driven by head motion, we found that the gain of the amplitude was increased in *Shisa6*^{L7KO} mice (Fig. 5f, $p = 0.044$), whereas the phase was not (Fig. 5g, $p = 0.15$). Using the visually guided VOR (VVOR) paradigm, in which the optokinetic and vestibulo-ocular reflex work together, we found no differences in gain (Fig. 5h, $p = 0.36$) or phase (Fig. 5i, $p = 0.69$), indicating that the increase in VOR gain allowed the *Shisa6*^{L7KO} mice to compensate for their impairments in optokinetic control under normal conditions in which the light is present. These data are in line with previous recordings in *Lurcher* mice, which lack PCs²⁸, highlighting that ablation of *Shisa6* selectively from PCs is sufficiently detrimental to mimic cerebellar functional deficits that occur when PCs are lost.

Given that excitatory input and plasticity at the PF to PC synapse is dysfunctional in *Shisa6*^{L7KO} mice, we hypothesized that cerebellum-dependent motor learning might also be affected. To test this hypothesis, we first subjected the *Shisa6*^{L7KO} and control mice to visuo-vestibular mismatch training (Fig. 6a). This sensitive five-day training paradigm first aims to decrease the gain and then to reverse the phase of the VOR from the direction opposite to the vestibular input (indicated as 0°) to an eye movement that is in the same direction as the vestibular input (phase >90°). During training the visual stimulus rotated in-phase with the vestibular stimulus; on the first day both stimuli rotated at 5° amplitude, effectively causing a decrease of VOR gain, while on the next four training days the visual stimulus amplitude increased first to 7.5° (day 2) and subsequently to 10° (days 3-5) so as to gradually induce a reversal of VOR phase. In between sessions the mice were kept in the dark.

Analysis of the first day showed that *Shisa6*^{L7KO} mice have impaired VOR gain-decrease learning (Fig. 6b; $p < 0.001$), a sign of severe motor learning impairment^{14,29}. Indeed, whereas control mice demonstrated the ability to reverse the phase of their VOR, *Shisa6*^{L7KO} mice did not (Fig. 6c; $p = 0.002$). This interpretation was further confirmed when we analysed the eye movements made by the *Shisa6*^{L7KO} mice during the training in the light condition. *Shisa6*^{L7KO} mice were unable to adapt their VOR, and also impaired in tracking the visual training stimulus during the training (Supplementary Fig. Sb; $p < 0.001$).

We next subjected the mice to a Pavlovian eyeblink conditioning paradigm, using a light pulse as a conditioning stimulus (CS) and a corneal air puff as an unconditioned stimulus (US)³⁰ (Fig. 6d). *Shisa6*^{L7KO} mice had both a significantly lower CR amplitude and a significantly lower percentage of successful CRs (Fig. 6d-f; CR amplitude, $p = 0.006$; CR percentage, $p = 0.004$). Together, the compensatory eye movement and eye-blink conditioning paradigms reveal that *Shisa6* expression in cerebellar PCs is relevant for both baseline motor performance and cerebellum-dependent motor learning.

Lower spike output and enhanced regularity of PC firing in *Shisa6*^{L7KO} mice.

The phenotypes in excitatory synaptic transmission and related motor coordination impairments induced by PC-specific ablation of *Shisa6* have relatively large effect sizes. However, the connection between *ex vivo* physiological abnormalities and behaviour is not directly apparent. To bridge this gap we analysed SS and complex spike (CS) firing frequencies and firing regularity (CV2) of PCs *in vivo*. To align our results with VOR adaptation and eyeblink conditioning while taking the baseline specifics of the mediating cerebellar zones into consideration^{30,31}, we recorded Purkinje cell activity from both anterior (Fig. 7a) and posterior (Fig. 7d) lobules in awake mice. The SS firing rate of PCs was significantly lower in *Shisa6*^{L7KO} mice in both the anterior (Fig. 7b; $p = 0.009$) and posterior lobules (Fig. 7e; $p = 0.003$). In addition, there was an increase in the regularity of SS firing in PCs of the anterior lobe (i.e., a significant decrease in the co-efficient for adjacent intervals, CV2; $p < 0.001$; Fig. 7c), while the regularity of SS firing in the posterior lobe was not significantly affected (Supplementary Fig. 7f; $p = 0.14$). The firing rate (Supplementary Fig. 5a; $p = 0.40$) and regularity of CSs (Supplementary Fig. 5b; $p = 0.10$) were both unaffected, neither in the anterior lobes, nor the posterior lobes (Supplementary Fig. 5c, d; both $p = 0.16$).

To exclude the possibility that loss of *Shisa6* impairs firing rates *in vivo* through effects on intrinsic mechanisms for the generation of SSs in PCs, we injected currents of varying strengths into the PC soma *ex vivo* (Supplementary Fig. 6a). We found no change in the number of spikes generated in the *Shisa6*^{L7KO} (Supplementary Fig. 6b; $p = 0.79$). In fact, blocking all afferent input and measuring the pacemaker activity of PCs with cell-attached recordings *ex vivo* revealed no differences in firing frequency or CV2, neither in the anterior lobe (for frequency $p = 0.29$; for CV2 $p = 0.60$; Supplementary Fig. 6c-e), nor in the posterior lobe (for frequency $p = 0.64$; for CV2 $p = 0.33$; Supplementary Fig. 6f-h). We conclude that there are no major deficiencies in the ability of PCs to generate SSs in *Shisa6*^{L7KO} mice, suggesting that *Shisa6* has an important role in the proper integration of synaptic excitatory inputs that are required to control the frequency and regularity of SS firing of PCs in awake behaving animals.

Discussion

Here, we provide the first evidence for a role of *Shisa6* auxiliary AMPAR subunits in cerebellar PF to PC synaptic function and motor coordination. We report the co-localization of the auxiliary AMPAR subunit *Shisa6* with GluA2 in PCs, and a direct interaction with the AMPAR subunits GluA1–3 and non-AMPA glutamate receptor subunit GluD2. Mice with PC-specific deletion of *Shisa6* showed strongly reduced PF to PC basal excitatory postsynaptic transmission, impaired LTP and reduced SS activity *in vivo*. Moreover, ablation of *Shisa6* in PCs resulted in impaired motor performance as well as severely affected procedural learning. Together, these findings indicate a crucial role for *Shisa6* in the physiology of PF to PC synapses and cerebellum-dependent motor behaviour.

Several auxiliary subunits have thus far been shown to affect AMPAR conductance, kinetics and localization⁴. The first mouse line to spur interest in auxiliary subunits was the severely ataxic stargazin mouse mutant, in which a lack of the Transmembrane AMPAR Regulatory Protein TARP γ -2 (i.e., stargazin) resulted in absence of excitatory transmission at the mossy fibre to granule cell synapse^{32,33}. TARP γ -2 as well as other more recent family members have been shown to control both trafficking and kinetic profiles of AMPARs^{4,34,35}. Specific and partially overlapping modulating

effects have also been found to occur in the Shisa family of auxiliary AMPAR subunits. For instance, in the hippocampus the first identified member of the Shisa family, Shisa9 (CKAMP44), was shown to cause fast and strong desensitization of AMPARs currents^{9,11}, whereas Shisa6 was reported to decrease the rates of deactivation and desensitization of AMPARs⁷.

We report that Shisa6 co-localizes with GluA2 in PCs and that its absence from PCs results in decreased decay times of their mEPSCs and sEPSCs, in line with previously reported data on Shisa6 at AMPARs in the hippocampus⁷. In addition, we find that the frequency of mEPSCs and frequency and amplitudes of sEPSCs in PCs are both lower in *Shisa6*^{L7 KO} mice and that the amplitude of their EPSCs evoked by PF stimulation is also reduced. The latter findings stand in marked contrast to what was observed in the hippocampus, as deletion of *Shisa6* in hippocampal pyramidal neurons did not affect the EPSC frequency or amplitude at CA3/CA1 synapses⁷. To elucidate the mechanism involved in the reduction of excitation at the PF to PC synapse, we first set out to identify Shisa6 interacting proteins in PC synaptosomes. Here, we identified interactions between Shisa6 and AMPAR subunits GluA1–3 as well as GluD2. When we further explored the abundance of synaptic proteins in the absence of *Shisa6*, we found that levels of GluA2 and GluA3 were decreased, whereas GluD2 was increased.

Given these interactions and the impact of *Shisa6* deletion, at least two main postsynaptic physiological factors may contribute to the reduced EPSC frequency and amplitudes observed in this study. First, there is a decrease of active postsynaptic AMPARs, as indicated by the downregulation of AMPAR subunits, GluA2 and GluA3; their reductions may both directly affect EPSC amplitudes^{15,36}. Second, considering that Shisa6 traps AMPARs by interacting with PSD-95 in the hippocampus, abnormal localization of AMPARs in the PSD could also contribute to deficits in synaptic potentiation at different time scales, which has been shown to directly impact desensitization of the AMPARs³⁷. Given that we did not find any major ultrastructural deficit at the postsynaptic density of PF to PC synapses, it appears that these two potential contributions can be played out at a molecular and cell-physiological level without morphological aberrations.

Dynamic changes in the number and sensitivity of AMPARs are thought to be part of the central mechanism that facilitates different types of learning^{2,15,38}. Work on molecular targets involved in plasticity mechanisms at the PF to PC synapse has revealed different molecules involved in AMPAR modulation, including GluD2, phosphatases, kinases, scaffolding proteins, and the GluA3 subunit^{14-16,29,39-41}. When assessing the role of Shisa6 in long-term synaptic plasticity we found an impaired induction of LTP in PCs of *Shisa6*^{L7 KO} mice, whereas LTD could still be induced. Interestingly, recent findings indicate that induction of LTP at the PF to PC synapse can be facilitated through increases in GluA3 open-channel probability and that this increase is inducible with forskolin¹⁵. By applying forskolin we effectively induced LTP in both groups, thus indicating that the GluA3 receptors that are present at the level of the synapse can be modulated to increase their conductance. This experiment reveals the possibility that the normal PF dependent LTP induction is not sufficient in order to trigger GluA3 conductance increase dependent LTP in the absence of Shisa6. Because PF to PC synapses are typically activated by sensory learning-mediated bursts of granule cell activity⁴², which in turn can drive Ca²⁺ T-type channel-dependent LTP⁴³, it is plausible that impaired LTP induction in *Shisa6*^{L7 KO} is partly a result of faster AMPAR deactivation and thus less postsynaptic depolarization than would be needed for Ca²⁺-dependent LTP induction. In addition, the higher expression of synaptic GluD2 could facilitate a prolonged state of depression at the post synaptic site, thus suppressing potentiation²⁵. In contrast, LTD is dependent on large CF depolarization-induced influx of Ca²⁺ and consequently the removal of AMPARs from the membrane^{44,45}. This form of CF dependant synaptic plasticity was not directly affected by the absence of Shisa6, which is in line with the findings that multiple CF innervation was eliminated during development at a normal pace and that CS spike frequency and regularity in awake behaving adult *Shisa6*^{L7 KO} mice were also normal. Thus, Shisa6 appears to affect both basal neurotransmission as well as LTP at the PF to PC synapse, without affecting CF transmission or LTD induced by CF activity.

Even though Shisa6 was found to strongly interact with both AMPAR subunits GluA1–3 and GluD2, the type and consequences of these interactions appear to be diverse as highlighted by their respective down- and upregulation in the *Shisa6*^{L7 KO} mice. Given that GluD2 may also directly affect the level and function of AMPARs²¹, it is plausible that *Shisa6* in fact may serve a homeostatic function, aiming to properly balance the concentration and localization of both receptors via differential control. The upregulation of GluD2 could further restrict the number of active AMPARs at the PF to PC synapse, as deletion of *GluD2* is known to lead to higher expression of AMPARs at PF to PC synapses²¹. Indeed, the absence of GluD2 in different KO models has revealed its function in

PF to PC AMPAR composition, morphology as well as LTD^{21-23,46,47}. Thus, in the presence of *Shisa6* the PF to PC synapse has a mechanism in place to keep the AMPARs properly in place at the right dosage, via both upregulating AMPARs and downregulating GluD2. As *Shisa6* did not directly affect the efficacy of the CF to PC synapse, the CFs could guide LTD induction via systems control mechanisms tuned to the procedural demands, while local homeostasis is independently guarded by synaptic scaffolding proteins like *Shisa6*. In principle, the local changes in level of GluD2 could also have signalled pre-synaptic changes, as GluD2 is also involved in presynaptic function and glutamate release⁴⁸. However, we found no evidence for morphological abnormalities at PF to PC synapses under the condition of increased GluD2 levels and we found no abnormalities in the paired pulse facilitation paradigms, a phenotype that has previously been detected in the absence of GluD2⁴⁸. Thus, in contrast to *Shisa6* in the hippocampus, which lacks GluD2, *Shisa6* in the cerebellum appears to differentially regulate AMPARs and GluD2, possibly to elicit homeostatic mechanisms that serve to maintain excitability at an optimal level.

Shisa6^{L7 KO} mice have strong impairments in motor performance as indicated by the deficiencies identified in baseline OKR and VOR, as well as on the Rotarod and ErasmusLadder. In addition, we found strong motor learning deficits as shown by the VOR phase reversal and classical eye blink conditioning paradigm. Physiological abnormalities, in addition to synaptic LTP, are further revealed using *in vivo* single unit recordings of PCs where we show that the firing frequency as well as irregularity of SSs is lower. In a similar way that excitatory input at the PF to PC synapse can affect SS regularity, changes in the inhibitory input from molecular layer interneurons may also affect regularity of SSs^{16,49}. However, given the absence of changes in frequency or amplitude of the sIPSCs of PCs in the absence of *Shisa6*, we think changes in inhibition are unlikely to contribute to the changes in SS regularity in *Shisa6*^{L7 KO} mice.

Cerebellar mouse mutants in which synaptic plasticity is selectively impaired often suffer from impaired motor learning, but much less frequently from motor performance deficits^{12,16,50}. Here, we show that the absence of *Shisa6* results in both motor performance impairments and motor learning deficits and that these behavioural abnormalities coincide with PC deficits in basal synaptic excitatory transmission, LTP induction as well as *in vivo* spike output and regularity of firing. By now, many studies have reported that regularity of SS firing and its modulation through synaptic input play crucial roles in motor learning^{16,49,51-54}. One way by which the reduced frequency and regularity of SS firing in PCs of the *Shisa6*^{L7 KO} mice may contribute to the behavioural phenotypes is by impaired spatiotemporal coding of sensory information⁵⁰. To our knowledge, this is the first report on the effects of auxiliary subunit-mediated AMPAR deactivation on LTP and spike frequency modulation in the cerebellum, coupled to strong baseline performance and learning phenotypes. Together, these results provide novel insight into the roles that auxiliary AMPAR subunits can play in the long-term modulation of synaptic currents, neuronal excitability, and as a consequence, motor coordination.

Materials and Methods

Further information and requests for resources and reagents should be directed to Chris I. De Zeeuw (c.dezeeuw@erasmusmc.nl). For the *Shisa6* mouse line please contact Sabine Spijker (s.spijker@vu.nl).

Experimental models

Experiments and analyses were performed with the experimenters blinded to the genotype. Both males and females were used for all experiments and all mice were randomly allocated to an experimental group. All mice were individually housed from the age of P21 with food and water available *ad libitum* and in 12:12 h light/dark cycles. All experiments were approved by local (DEC) and national ethical committees. Adult mice aged 4 to 24 weeks old were used for the behavioural assays, *in vivo* physiology and immunoprecipitation and SWATH protocol. Mice used were *Shisa6*^{L7 KO} and their littermate controls all bred on a mixed C57BL6/Nhsd and C57BL6/J background. The *Shisa6*^{L7 KO} model was generated by crossing Purkinje specific L7(Pcp2)-Cre mice⁵⁵ with *Shisa6*^{tm1a2(Caliper)CNCR-VUA}⁷. Genotyping was performed on postnatal day (P)7–10 using primers Rz742, Rz804 and Rz803. Using a previously described PCR method⁷, we found that the *Shisa6*^{L7 KO} littermates contained a relatively large number of germline deletions always affecting one allele. For the immunoprecipitation and SWATH protocols we used *Shisa6*^{null} mice and their WT litter mates. In

the current manuscript, all mice denoted as control are *Shisa6*^{L7 HET} (i.e., heterozygous whole-body deletion), whereas the *Shisa6*^{L7 KO} is a full KO for PCs and has heterozygous whole-body deletion. All experiments were conducted in line with the European guidelines for care and use of laboratory animals (Council Directive 86/609/EEC). The individual experimental protocols were approved by the Animal Experiment Committee (EDC) of the ErasmusMC.

DNA expression constructs

The full-length coding DNA for mouse GluD2 (*Grid2*) was obtained from Genecopoeia (Mm02855; Rockville, MD, USA) as shuttle-clone and subsequently Gateway-cloned (Invitrogen; Waltham, MA, USA) into the pTRCGw-IRES2-EGFP vector⁷. FLAG-Shisa6-pTRCGw-IRES2-EGFP as described previously⁷.

Immunoprecipitation and mass spectrometry of mouse cerebellar Shisa6 protein-complexes

Immunoprecipitation using anti-Shisa6 antibody was performed on the n-Dodecyl-beta-Maltoside (DDM) extracted crude synaptic membrane fraction, prepared from the cerebellar tissue of WT and *Shisa6*^{null} mice, as described previously for the hippocampus (Klaassen et al., 2016). Eluted proteins were fractionated by SDS-PAGE, subjected to in-gel tryptic digestion, and analysed on a TripleTOF 5600+ mass spectrometer (Sciex, Framingham, MA, USA) operating in information-dependent acquisition (IDA) mode, as described previously⁷.

TripleTOF 5600+ data was imported into MaxQuant (version 1.6.1.0) (Cox and Mann, 2008) and searched against the Uniprot mouse reference proteome (April 2018 release; including canonical and additional sequences). Methionine oxidation and N-terminal acetylation were selected as variable modifications, and propionamide set as fixed cysteine modification. For both peptide and protein identification the false discovery rate was set to 0.01. Match between runs was enabled with a match time window of 0.7 min and alignment time window of 20 min. MaxLFQ normalization was enabled with a LFQ minimal ratio count of 1. Remaining parameters were left to default, with proteingroup identification requiring a minimum of 1 razor + unique peptide. The filtering and statistical analysis of the Maxquant results was performed in Perseus (version 1.6.2.1)^{56,57}. in the following order: (1) Importing the Maxquant *proteinGroups.txt* file into Perseus; (2) Removal of "Reverse", "Potential contaminant", and "Only identified by site" proteingroups; (3) Log2 transformation of all LFQ intensity values; (4) Removal of proteingroups in which any WT value was derived "By matching", (5) Removal of proteingroups with less than three valid Log2 LFQ intensity values in the WT group; (6) Imputation of missing values (7.7% of the KO population) from a normal distribution (width 0.3, down shift 1.8, whole matrix) (7) Performing a Student's T-test (S0=0.5) followed by permutation-based FDR analysis on the Log2 LFQ intensity values (FDR=0.01, 2500 permutations).

Immunoprecipitation of mouse cerebellar Shisa6 protein-complexes after immuno-depletion of GluA2

All extraction, binding and washing steps were performed at 4 °C with ice-cold buffers. GluA2 antibody was added to DDM-extracted crude synaptic membranes and incubated O/N. The antibody-GluA2 complexes were subsequently cleared from the lysate by addition of protein A/G agarose beads (Santa Cruz, sc-2003; Dallas, TX, USA). Shisa6 antibody was added to the "GluA2-depleted" lysate, incubated O/N and immobilized on protein A/G agarose beads. The beads were washed four times with wash buffer (0.1% DDM, 150 mM NaCl, 25 mM HEPES pH7.4) and eluted with Laemmli sample buffer.

HEK293 cell culture and transfection

HEK293 cells (ATCC; Manassas, VA, USA) were cultured for a maximum of 20 passages in DMEM medium (Gibco, Life Technologies; Waltham, MA, USA) supplemented with 10% FBS (Invitrogen; Waltham, MA, USA) and 1% Penicillin-Streptomycin (Gibco, Life Technologies; Waltham, MA, USA). Cells were plated in 10 cm dishes 16-24 hours prior to transfection, and 50-60% confluent at the time of transfection. HEK293 cells were transfected with plasmid DNA (5ug) encoding GluD2 alone or in combination with flag-Shisa6 using Polyethylenimine (PEI) (25 kDa linear, Polysciences; Hirschberg an der Bergstrasse, Germany) and incubated for 42-48 hr.

Co-precipitation from HEK293 cells

All lysis, washing and centrifugation steps were performed at 4 °C with ice-cold buffers. HEK293 cells were washed once with PBS, resuspended in lysis buffer (1% Triton X-100, 150 mM NaCl, 25 mM HEPES (pH 7.4), supplemented with EDTA-free Complete protease inhibitor (Roche, Basel, Switzerland), and incubated for 1 hr with 10 RPM end-over-end mixing. The supernatant was cleared of debris by two consecutive 20 minute centrifugation steps at 20,000x g. Anti-flag antibody was added to the supernatant, incubated O/N, and immobilized on Protein A/G agarose beads. The beads were washed four times with lysis buffer and eluted with Laemmli sample buffer.

Immunoblot analysis

Protein samples were dissolved in Laemmli sample-buffer, heated to 96 °C for 5 minutes, and loaded onto a 4–15% Criterion TGX Stain-Free gel (Bio-Rad, Temse, Belgium) along with Precision Plus protein standard (Bio-Rad, Temse, Belgium). The gel-separated proteins were imaged with the Gel-Doc EZ system (Bio-Rad, Temse, Belgium), transferred O/N onto PVDF membrane (Bio-Rad; Temse, Belgium) and probed with various antibodies (see 'Antibodies' section). Scans were acquired with the Odyssey Fc system (Li-Cor, Lincoln, NE, USA), and adjusted and quantified using Image Studio Lite 5.2.5 software (Li-Cor, Lincoln, NE, USA).

Sample preparation for SWATH MS analysis

Crude synaptic membranes were prepared from the cerebellum of Shisa6 WT and Shisa6^{null} mice as described previous⁷, with the addition of PhosSTOP phosphatase inhibitors (Roche, Basel, Switzerland) to the homogenisation buffer. Proteins were extracted and digested according to the filter-aided sample preparation (FASP) protocol⁵⁸ with some adaptations. Proteins were extracted and reduced by incubation with SDS-lysis buffer (final concentration of 1 ug protein/μl, 2% SDS, 100 mM Tris-HCl (pH 8.5) and 2.5 mM Tris(2-carboxyethyl)phosphine-HCl (TCEP)) for 1 hr at 56 °C with 1100 RPM mixing. Next, proteins were alkylated by addition of methyl methanethiosulfonate (MMTS; final concentration of 5 mM) for 10 minutes at RT. The protein lysate was diluted to 0.5% SDS with Urea buffer (8 M Urea, 100 mM Tris-HCL (pH 8.5)), centrifuged at 20000g for 2 minutes at 20 °C, and 100 μl was loaded onto a Microcon Ultracel PL-30 filter (Merck Millipore, Darmstadt, Germany). The filters were centrifuged at 12000g for 10 minutes at 20 °C and subsequently washed five times with 100 μl Urea buffer and four times with 100 μl 50 mM NH₄HCO₃ (identical centrifugation settings). After washing, Trypsin/LysC Mix (Promega, Leiden, The Netherlands) was added to the filters at an enzyme to protein ratio of 1 to 25, and incubated O/N at 37 °C within a humidified chamber. Digested peptides were collected from the filter by elution with 50 mM NH₄HCO₃ and acidified to a final concentration of 0.5% trifluoroacetic acid (TFA). Finally, the eluted peptides were desalted using an Oasis HLB 96-well μelution plate (Waters, Milford, MA, USA) following the manufacturer's guidelines and using 0.1% TFA and 80% acetonitril + 0.1% TFA as binding and elution buffers, respectively.

In order to prepare an experiment-specific spectral library, an additional four FASP preparations were performed on lysate pooled equally from all Shisa6 WT mice. Two samples were purified directly by Oasis HLB desalting, with the remaining two samples pooled and fractionated using the high pH reversed-phase peptide fractionation kit (Pierce, Thermo Scientific, Waltham, MA, USA) according to the manufacturer's instructions.

Micro-LC and information-dependent acquisition MS of spectral library fractions

Peptides were analyzed by micro LC MS/MS using an Ultimate 3000 LC system (Dionex, Thermo Scientific, Waltham, MA, USA) coupled to the TripleTOF 5600+ mass spectrometer. Dried peptide samples were redissolved in 5% acetonitril + 0.1% formic acid (FA), supplemented with iRT calibration peptides (Biognosys, Zurich, Switzerland) and loaded onto a 5 mm PepMap100 C18 precolumn (300 μm i.d., 5 μm particle size (Dionex, Thermo Scientific, Waltham, MA, USA). Separation was achieved on a 150 mm ChromXP C18 column (300 μm i.d., 3 μm particle size (Sciex)) using a linear aqueous-organic gradient of 5%-18% acetonitrile (+0.1% FA) in 88 minutes, 25% at 98 minutes, 40% at 108 minutes and 90% at 110 minutes, using a flow rate of 5 μL/minute. Eluting peptides were electro-sprayed directly into the TripleTOF MS operated in IDA mode. One full scan consisted of a single full profile MS scan (150 ms, m/z 350 to 1250 and charge state +2 to +5), followed by MS/MS analysis of the top 25 most intense precursor ions (150ms, m/z 200 to 1800, charge state +2 to +5, high sensitivity mode and precursor ion count/s > 150). Dynamic exclusion was set to 16 seconds. Ions were fragmented using rolling collision energy with an energy spread of 5eV.

Micro-LC and SWATH MS

The LC setup and settings were identical to those described for the IDA MS of spectral library fractions. SWATH measurement consisted of a full precursor ion scan (150 ms, m/z 350–1250) followed by sequential precursor isolation windows of 8 Da across the mass range of m/z 450–770 with 1 Da overlap (80 ms). Total cycle time was around 3.2 seconds, providing 8–9 data points across a typical peptide. The collision energy for each window was determined by the appropriate collision energy for a 2+ ion, centered upon the window with a spread of 15 eV.

Analysis of spectral library IDA MS results

The spectral library files were imported into MaxQuant (version 1.6.1.0)⁵⁹ and searched against the Uniprot mouse reference proteome (April 2018 release; including canonical and additional sequences) supplemented with the Biognosys iRT FASTA database. Methionine oxidation and N-terminal acetylation were selected as variable modifications, and MMTS modification of cysteine set as fixed modification. For both peptide and protein identification the false discovery rate was set to 0.01. Remaining parameters were left to default. The spectral library was made from the MaxQuant *msms.txt* file using Spectronaut (version 11.0.15038.23)⁶⁰. Imported peptides were filtered for a Q-value threshold of <0.01 with all other settings left to default.

SWATH data processing and statistical analysis

The peptide abundances were extracted from the raw SWATH data by Spectronaut (version 11.0.15038.23), using default BGS factory settings. Next, Spectronaut performed across-run normalization based on total peak areas. Peptide abundances were exported from Spectronaut as a report and further processed using the R language for statistical computation⁶¹. Each unique precursor was considered a peptide (e.g., the same peptide sequence observed with distinct modifications or charge was considered a distinct peptide). The Spectronaut fragment group Q-values were used to select for high confidence peptides, with the following filter settings: Peptides must have a Q-value smaller than, or equal to, 10^{-4} in at least seven out of eight replicas within at least one group. Protein abundances were calculated at the gene level by summation of the normalized peak area of their respective peptides. Peptides that matched to multiple genes in the spectral library were compiled into separate groups with unique sets of genes. Next, the protein abundance matrix was Loess normalized using the *normalizeCyclicLoess* function from the limma R package (Smyth et al., 2005), which was set to 'fast' and iterations were set to 10. Finally, the normalized protein abundances were imported into Perseus (version 1.6.2.1) for statistical analysis. All data was Log2 transformed and differential expression between the groups was assessed by Student's T-test (S0=0) followed by permutation-based FDR analysis (FDR = 0.05, 2500 permutations).

Electron microscopy

Adult mice were transcardially perfused with fixative 4% PFA (EM grade) 1% Glutaaraldehyde (EM grade) in 0.12 M sodiumcacodylaat (NaCac). The brains were removed and put in 4% PFA at 4 °C overnight. The following day 100 µm sagittal slices were cut using a Vibratome (VT1000S, Leica, The Netherlands). The slices were then washed, in order: 3 times 10 min in 0.1 M NaCac, 2 hours 4 °C in 2% Osmium Tetroxide + 0.1 M NaCac + 1.5% K3Fe(CN)6, then 3 times 10 min in 0.1 M NaCac. Finally, 3 times 10 min MilliQ wash. The slices were then bathed in ISO 3696 Type 1 ultrapure water (MilliQ) overnight. The next day, slices were washed again, and dehydrated in order: 10 min MilliQ, 10 min 50% EtOH, 60 min 1% Uranyl Acetate/50% EtOH, 10 min 70% EtOH, 5 min 80% EtOH, 5 min 90% EtOH, 5 min 96% EtOH, 5 min 100% EtOH, 2 times 8 min Dimethoxypropane (DMP), 2 hours DMP: Durcupan 1 (Fluka) (1:1), 2 hours DMP: Durcupan 1 (1:3). The following day this was continued: 2 hours D1 (50 °C), 2 hours Durcupan 2 (Fluka) (50 °C) and then polymerized 3 nights at 60 °C. Ultrathin sections (60 nm) were cut using an ultramicrotome (Ultracut UCT, Leica) and contrasted with 6% uranyl acetate in MilliQ and lead citrate staining, sections from controls and *Shisa6*^{L7KO} mice were examined using an electron microscope (Philips CM100). For ultrastructural PSD analysis, spine synapses have been selected from proximal and distal molecular layer from lobule 3 and lobule 10. PSDs were manually counted and their length was quantified using Fiji software.

Immunohistochemistry

Mouse brains were snap-frozen after removal without perfusion. Tissue was sectioned at 10 µm using a cryostat at -20 °C and a knife temperature of -14 °C. Sections were air-dried on superfrost glass and stored at -80 °C. For staining, sections were defrosted at room temperature (RT) for 60 min and subsequently washed with -20 °C Clarks liquid (75 mL EtOH + 25 mL HAc) for 10 min followed by 3 times 10 min of PBS wash. Sections were incubated for 120 min in blocking solution (PBS + 0.3% Triton X-100 + 4% NGS) at RT and washed 3 times in PBS for 10 min. Following a 60-min incubation

in 5% BSA (in PBS) at RT and subsequent PBS washing, sections were incubated in SA5193 antibody (1:1000, dissolved in 2% bovine-serum albumin) and anti-GluA2 antibody (1:200) overnight at 4 °C. The sections were then washed for 3 times 10 min in PBS followed by 120 min of fluorescent antibody staining (1:200, Streptavidin-Cy3) in 2% BSA at RT. After the fluorescent antibody staining, a wash of 3 times 10 min of PBS was followed by 2 times 10 min wash with PB. The sections were then put in DAPI (200 μ L in 50 mL 0.1 M PB) for 10 min. This was concluded by 2 times 10 min PB wash. Following PBS washing, the sections were thionin-stained and permount-covered using standard protocols. Images were taken using an upright confocal microscope (LSM 700, Zeiss, Oberkochen, Germany).

3D-SIM imaging and analysis

3D-SIM images were acquired using a Zeiss Elyra ps.1 microscope, fitted with bp 420-480, bp 495 – 575, bp 570 – 650 and lp 655 emission filters. Five rotations and five shifts of the illumination pattern were used to acquire raw images. A 3D volume was imaged using a z-stack with an interval of 110 nm. Raw images were reconstructed into high resolution images using the Zeiss ZEN software on the default settings (segmentation of zeroth, first and second order were set on 100,100 and 83 respectively, where 100 is maximum filtering, the generalised Wiener filter with a regularization of 10^{-6} was used to filter noise, images were baseline cut to remove negative values).

Images were analysed using ImageJ in the FIJI framework⁶². The number of distinct synapses in which co-localization was observed were determined using the maxima of individual Shisa6 and GluA2 spots in a single field of view at the centre of the 3D imaged volume. If Shisa6 spots were at a distance closer than 120 nm, they were defined as co-localizing.

Ex vivo electrophysiology

Following decapitation of mice under isoflurane anaesthesia, the cerebellum was removed, and moved into an ice-cold 'slicing medium'. The slicing medium contained (in mM) 240 sucrose, 2.5 KCL, 1.25 Na_2HPO_4 , 2 MgSO_4 , 1 CaCl_2 , 26 NaHCO_3 and 10 D-Glucose and was carbogenated continuously (95% O_2 and 5% CO_2). Sagittal slices, 250 μm thick, of the cerebellar vermis were cut using a vibrotome (VT1200S, Leica) and put in carbogenated artificial cerebrospinal fluid (ACSF) containing (in mM): 124 NaCl, 2.5 KCL, 1.25 Na_2HPO_4 , 2 MgSO_4 , 2 CaCl_2 , 26 NaHCO_3 and 15 D-Glucose. Slices were incubated for at least 1 hour at 34 ± 1 °C before the start of the experiment. Slice physiology was done at 34 ± 1 °C unless otherwise specified in the methods section. Recordings were done in the presence of 100 μM picrotoxin, except for the spontaneous inhibitory postsynaptic current (sIPSC) recordings. Whole-cell patch clamp recordings and cell-attached recordings were performed with EPC9 and EPC10-USB amplifiers (HEKA Electronics, Lambrecht, Germany) using Pulse and Patchmaster software (HEKA Electronics). Recordings were excluded if the series (R_s) or input resistances (R_i) changed by >15% during the experiment, which was determined using a hyperpolarizing voltage step relative to the -65 mV holding potential. Analysis of the spontaneous inhibitory postsynaptic currents (sIPSC) and mEPSC and sEPSC event frequencies, amplitudes, 10 – 90% rise times, and decay times (τ) was done using Mini-analysis software (Synaptosoft) and Python. Analysis of the AP threshold (defined by a slope of >20 mV/ms), AHP amplitude, decay time (τ), spike count, and seal tests in intrinsic excitability experiments was performed exclusively on the first AP elicited by a depolarizing current injection. All electrophysiological recordings were analysed using Clampfit (Molecular Devices). Spontaneous spiking rates in cell-attached experiments were analysed using Clampfit, after filtering the data with a 1.5 kHz low-pass filter and calculating the derivative of the original signal.

For whole-cell recordings PCs were visualized using upright microscopes (Axioskop 2 FS and Axio Examiner.D1, Carl Zeiss Microscopy GmbH, Jena, Germany) equipped with a 40x objective. Recording electrodes (3–5 M Ω , 1.65 mm outside diameter (OD) and 1.11 mm interior diameter (ID), World Precision Instruments, Sarasota, FL, USA) were prepared using a P-97 micropipette puller (Sutter Instruments, Novato, CA, USA), and filled with an intracellular solution containing (mM): 120 K-Gluconate, 9 KCL, 10 KOH, 4 NaCl, 10 HEPES, 28.5 Sucrose, 4 Na_2ATP , 0.4 Na_3GTP (pH 7.25 – 7.35 with an osmolarity of 295 ± 5). Note that we adjusted the osmolarity using sucrose. sIPSCs were recorded in the presence of NBQX disodium salt hydrate and APV (Sigma-Aldrich, Missouri, United States), using an intracellular solution containing (mM): 150 CsCl, 1.5 MgCl_2 , 0.5 EGTA, 4 Na_2ATP , 0.4 Na_3GTP , 10 HEPES, 5 QX-314 (pH 7.25 – 7.35 with an osmolarity of 295 ± 5). sEPSCs were recorded at -75 mV using an intracellular solution containing (in mM): 130 CsMeSO₄, 4 $\text{MgCl}_2 \cdot 6\text{H}_2\text{O}$, 0.2 EGTA, 10 HEPES, 4 Na_2ATP , 0.4 Na_3GTP , 10 phosphocreatine-disodium, 1 QX-314 (pH 7.25-

7.35, osmolarity 295±5). The same internal solution was used for the CF elimination experiments. Cslow and Rseries compensation were used for both sIPSC and sEPSC recordings, in order to improve the accuracy of measurements of the event kinetics. For extracellular stimulation of PFs, patch electrodes were filled with ACSF and positioned in the upper third of the molecular layer lateral to the soma of the patched PC. For afferent PF stimulation protocols intensities were varied between 3 – 15 µA, with 3 µA increments for the experiments involving evaluation of stimulation strength to PC EPSC amplitude. For PF–PC transmission, we used various inter-stimulus intervals (50 – 200 ms).

For CF stimulation, similar electrodes (filled with ACSF) were positioned near the patched PC soma in the surrounding granule layer. We selected those recordings in which CF stimuli elicited clear all-or-none responses and lacked the co-activation of PC axons (identifiable by antidromic APs) for further analysis. For CF elimination, experimental tissue was prepared in a similar way. We systematically scanned the granule cell layer to elicit CF responses and recorded PC responses at –20 mV holding potential to prevent voltage escape during the CF-evoked EPSCs.

The synaptic plasticity protocols for inducing LTP and long-term depression (LTD) were applied to lobules 5/6 and conducted as described previously¹⁶. In short, for synaptic plasticity all recordings were done in voltage-clamp, except for the tetanus, which consisted of 8 pulses of PF-stimulation at 100 Hz for 5 min (21 ± 1 °C, LTP) or single-pulsed PF + CF stimulation (5 ms interval) at 1 Hz for 5 min (34 ± 1 °C, LTD). We evaluated the synaptic plasticity by the change in PF-EPSC (baseline at 0.05 Hz) relative to the mean value calculated during the last 5 min pre-tetanus. For the FSK dependent LTP induction we used a concentration of 50 µM.

Cell-attached (CA) recordings were made using similar patch pipettes as in the previously described experiments, and using ACSF as an internal solution. Recordings were made in voltage clamp mode in lobules I-III and lobule X of the vermal cerebellum to allow a comparison between anterior and posterior activity, respectively. Spontaneous spiking rates were recorded in the presence of PTX, NBQX and APV, in order to eliminate synaptic input. Intrinsic excitability was measured using sequential current injections in current clamp mode. Cells were held at a holding current equivalent to a –65 mV holding potential, and injected with 500 ms long current pulses ranging from –100 pA to +1000 pA, relative to the holding current, in 100 pA increments (5 s inter-sweep interval).

***In vivo* electrophysiology**

In vivo recordings were performed as recently described³¹. In short, an immobilizing pedestal was fixed on the skull (see for details the section on “compensatory eye movements” below) and a craniotomy (Ø 1 mm) was performed on the occipital bone under general anesthesia with an isoflurane/O₂ mixture (5% induction, 1.5 – 2.0% maintenance). The craniotomy was protected by a recording chamber made with Charisma (Heraeus Kulzer, Germany) and closed with bone wax. After 3 days of recovery mice were head-fixed to a head bar and the body was restrained in a custom-made tube for electrophysiological recordings. PCs were recorded from vermal lobules I–III (pitch angle: –40°) and X (pitch angle: –65°) using borosilicate glass pipettes (OD 1.5 mm, ID 0.86 mm, Sutter Instruments, USA) mounted on a digital 3-axis drive (SM-5, Luigs & Neumann, Germany). PCs were identified by the presence of simple and complex spikes, and determined to be from a single unit by confirming that each complex spike was followed by a CF pause. All *in vivo* recordings were recorded amplified, filtered and digitized (Axon Multiclamp 700B, CED Power1401) and were analysed offline using Spiketrain (Neurasmus BV, Rotterdam, The Netherlands, www.neurasmus.com), running under MatLab (Mathworks, MA, USA). For each cell the firing rate, CV and mean CV2 were determined for simple and complex spikes, as well as the CF pause. The CV is calculated by dividing the s.d. by the mean of the interspike intervals, whereas CV2 is calculated as $2 \times \frac{|ISI_{n+1} - ISI_n|}{(ISI_{n+1} + ISI_n)}$. Both are measures for the regularity of the firing, with CV reflecting that of the entire recording and mean CV2 that of adjacent intervals, making the latter a measure of regularity on small timescales. The CF pause is determined as the duration between a complex spike and the first following simple spike.

Compensatory eye movements

Mice between 6 and 12 weeks of age were prepared for head-restrained recordings of compensatory eye movements. These types of recordings have been described in detail previously¹⁴. In order to head restrain the mice during the eye movement task a small pedestal was attached using optibond primer and adhesive (Kerr, Bioggio, Switzerland) under isoflurane anaesthesia (induction with 4% and

maintained at 1.5% concentration). After a recovery period of two to three days the mouse head was restrained by fixation with screws on the pedestal at the experimental setup. A round screen with a random dotted pattern (the drum) surrounded the mouse during the experiment. The optokinetic reflex (OKR), vestibulo-ocular reflex (VOR) and the light guided vestibulo-ocular reflex (VVOR) were induced using a sinusoidal rotation of the drum (OKR) in light, rotation of the table in the dark (VOR) or the rotation of the table and drum (VVOR) in the light. The motor behaviour was assessed by rotating the table and/or drum at 0.1 to 1 Hz with a fixed 5° amplitude. In order to evaluate motor learning, a mismatch between visual and vestibular input was created. Rotating both the visual and vestibular stimuli in phase (at the same amplitude) induced a decrease of gain; rotating the drum at greater amplitude relative to the table induced the so-called phase reversal of the VOR (day 1, 5°; day 2, 7.5°; day 3 – 4, 10°). Both training protocols were induced at 0.6 Hz with table rotation amplitude of 5°. For eye illumination during the experiments two table fixed infrared emitters (output 600 mW, dispersion angle 7°, peak wavelength 880 nm) and a third emitter, which produced the tracked corneal reflection (CR), were mounted to the camera and aligned horizontally with the optical axis of the camera. The movements of the eyes were recorded with eye-tracking software (ETL-200, ISCAN systems, Burlington, NA, USA). Gain and phase values of eye movements were calculated using Matlab (MathWorks Inc, City, Country).

Eyeblink conditioning

Shisa6^{L7 KO} mice and control mice were anesthetized with an isoflurane/oxygen mixture (5% for induction, 1.5 – 2% for maintenance). After a local scalp injection of bupivacaine hydrochloride (2.5 mg/ml, Bupivacaine Actavis) we made a sagittal scalp incision of 2 – 3 cm length. Next, we carefully removed the exposed periosteum and further scratched the skull using an etchant gel (Kerr, Bioggio, Switzerland). After this, we placed a construct allowing head-fixation using Optibond primer and adhesive (Kerr, Bioggio, Switzerland) and Charisma (Heraeus Kulzer, Armonk, NY, USA). After surgery, mice had 3 – 5 days to recover.

All behavioural experiments were conducted using head-fixed mice that were placed on top of a cylindrical treadmill on which they were allowed to walk freely. The treadmill consisted of a foam roller (diameter 15 cm, width 12 cm; Exervo, TeraNova EVA) with a horizontal metal rod through the axis that was connected with a ball bearing construction to two solid vertical metal poles. A horizontal messing bar was fixated to the same vertical poles at 3-5 cm above the treadmill. Mice were head-fixed to this bar using 1 screw and 2 pins, thereby ensuring perfect head-fixation. This entire setup was placed in a sound- and light-isolating chamber. National Instruments (NI-PXI) processors were used to control experimental parameters and to acquire the eyelid position signal. Eyelid movements were recorded with the magnetic distance measurement technique (MDMT), which makes use of an NVE GMR magnetometer, positioned above the upper left eyelid, that measures movements of a minuscule magnet (1.5 x 0.7 x 0.5 mm) that is placed on the lower eyelid of the animal with superglue (cyanoacrylate). This way, MDMT allows high spatio-temporal detection of eyeblink kinematics⁶³. The unconditioned stimulus (US) consisted of a weak air-puff applied to the eye (30 psi, 10 ms duration), which was controlled by an API MPPI-3 pressure injector, and delivered via a 27.5 gauge needle that was perpendicularly positioned at 0.5 – 1 cm from the centre of the left cornea. Prior to training the experimenter always carefully inspected whether the needle opening was positioned exactly perpendicular to the center of the mouse's cornea so that the air puff would hit the cornea and not too much the surrounding areas and would thus elicit reliable reflexive eyeblinks. The conditional stimulus (CS) was a green LED light (CS duration 260 ms, LED diameter 5 mm) placed 10 cm in front of the mouse's head. Because we performed our experiments in almost complete darkness this small LED light was a salient stimulus, which could be easily detected by both eyes. The training consisted of 2 daily habituation sessions, 1 baseline measurement and 6 daily acquisition sessions. During the habituation sessions, mice were placed in the setup for 30 – 45 min, during which the air puff needle (for US delivery) and green LED (for CS delivery) were positioned properly but no stimuli were presented. On the day of acquisition session 1, each animal first received 20 CS-only trials as a baseline measure, to establish that the CS did not elicit any reflexive eyelid closure. During each daily acquisition session, animals received 200 paired CS-US trials and 20 CS only trials. The interval between the onset of CS and that of US was set at 250 ms. Because of the inherent delay in the delivery of air puff of 14 ms, we triggered the air puff at 236 ms after CS onset so that it would hit the cornea exactly at 250 ms after CS onset. The inter-trial interval was set according to the following constraints: at least 10 seconds had to elapse, the eyelid had to be open below a predetermined threshold, and eyelid position had to be stable for at least 1 s for a trial to begin. During all training sessions, the experimenter carefully inspected threshold and stability parameters and adjusted them if

necessary. All experiments were performed at approximately the same time of day by the same experimenter.

Individual eyeblink traces were analysed automatically with custom computer software (LabVIEW or MATLAB) in a five-step process. First, trials with significant activity in the 500 ms pre-CS period were regarded as invalid for further analysis. Second, trials were normalized by aligning the 500 ms pre-CS baselines and calculating the averaged UR amplitude in Volts per session. The voltage corresponding with a full closure was further used in the analysis of the eyeblink traces as the 100% value reflecting full eyelid closure (± 1 mm movement), and other values like CR amplitude were expressed relative to this 100% value. Third, in valid normalized CS-only trials, eyelid movements larger than 5% of the 500 ms pre-CS period and with a latency to CR onset between 10 – 250 ms and a latency to CR peak of 25 – 500 ms (both relative to CS onset) were considered as conditioned responses (CRs). Fourth, based on this trial-by-trial analysis we calculated for each session per mouse (1) the percentage of eyeblink CRs, (2) the averaged amplitude in the CS-US interval (based on all valid trials and not thus only for trials in which a CR was present), and (3) timing parameters such as latency to CR onset and latency to CR peak time relative to CS onset (based on only these trials wherein a CR is present). Fifth, we calculated group averages (*Shisa6*^{L7KO} vs. controls) for the same parameters (1 – 3) and determined statistically significant differences using Repeated Measures ANOVA. Data was considered statistically significant if $p < 0.05$.

Griptest

The strength of the mice was determined using a grip test. By placing the forepaws of a grid attached to a force gauge (BIOSEB, Chaville, France) and steadily pulling the mice by the tail. The grip strength was defined as the maximum weight pulled before releasing the grid. The test was performed over the course of four consecutive days.

Rotarod

Mice were trained to walk on the accelerating Rotarod (Ugo Basile, Comerio Varese, Italy). The Rotarod consisted of a cylinder with a diameter of 3 cm. The starting speed of the Rotarod was 3 rotations per minute (rpm) and was set to a maximum of 40 r.p.m. in 270 s. The maximum walking time on the rotarod was 300 s. Latency to fall was recorded on the moment the mouse fell down or clang to the rod for three turns. This experiment consisted of four days with four daily turns on the Rotarod. On the fifth day there was an additional trial set to 80 r.p.m. The interval between each turn was 1 h.

Balance Beam

The Balance Beam is a small rod with a diameter of 12 or 6 mm. The Balance Beam was elevated for 43 cm with two steel rods at both ends. The home cage of the animal was placed at the end of the rod. Mice were placed on the beam and had to walk from one end of the beam to the other end where their home cage was located. The length of this trajectory was 80 cm. We measured the time it took for the mice to cross the beam. In addition, we analysed video material to inspect if the mice presented with misstep behaviour.

ErasmusLadder

Mice were tested on ErasmusLadder (Noldus, Wageningen, NL). The ErasmusLadder is a fully automated system consisting of a horizontal ladder between two shelter boxes. It has 37 rungs on each side of the ladder and all the rungs are attached to custom-made pressure sensors that are continuously monitored²⁶. In the current study, mice were tested in 5 daily sessions, during which mice were trained to walk between two shelter boxes for 50 trials each day. Step length and step time were defined as the distance and time between two consecutive touches from the right front limb, respectively.

Statistics

All statistical analyses were performed using SPSS, Python, R or Graphpad Prism. Data in the figures is presented as mean \pm SEM. Sample sizes (n) are present in all Figure legends. The p-values are indicated in the results section. Mean \pm SD, Brown-Forsythe tests for homogeneity of variances, type of statistical analysis, test-statistics and exact p-values are reported in Supplementary Tables 1-7. Extensive statistics related to Figure 2 and Figure 3 are reported in Supplementary Files 1 and 2. All statistical analyses of the SWATH data were performed on Log2-transformed data (see

Supplementary File 2). Non-parametric analysis of longitudinal factorial data was performed using the nparLD package for R⁶⁴.

References

1. Greer, P.L. & Greenberg, M.E. From synapse to nucleus: calcium-dependent gene transcription in the control of synapse development and function. *Neuron* 59, 846-860 (2008).
2. Nabavi, S., *et al.* Engineering a memory with LTD and LTP. *Nature* 511, 348-352 (2014).
3. Bliss, T.V. & Lomo, T. Long-lasting potentiation of synaptic transmission in the dentate area of the anaesthetized rabbit following stimulation of the perforant path. *J Physiol* 232, 331-356 (1973).
4. Greger, I.H., Watson, J.F. & Cull-Candy, S.G. Structural and Functional Architecture of AMPA-Type Glutamate Receptors and Their Auxiliary Proteins. *Neuron* 94, 713-730 (2017).
5. Pei, J. & Grishin, N.V. Unexpected diversity in Shisa-like proteins suggests the importance of their roles as transmembrane adaptors. *Cell Signal* 24, 758-769 (2012).
6. Huettner, J.E. TARPs and AMPA Receptors: Function Follows Form. *Neuron* 93, 989-991 (2017).
7. Klaassen, R.V., *et al.* Shisa6 traps AMPA receptors at postsynaptic sites and prevents their desensitization during synaptic activity. *Nat Commun* 7, 10682 (2016).
8. Farrow, P., *et al.* Auxiliary subunits of the CKAMP family differentially modulate AMPA receptor properties. *Elife* 4, e09693 (2015).
9. von Engelhardt, J., *et al.* CKAMP44: a brain-specific protein attenuating short-term synaptic plasticity in the dentate gyrus. *Science* 327, 1518-1522 (2010).
10. Schmitz, L.J.M., *et al.* The AMPA receptor-associated protein Shisa7 regulates hippocampal synaptic function and contextual memory. *Elife* 6(2017).
11. Chen, X., *et al.* CKAMP44 modulates integration of visual inputs in the lateral geniculate nucleus. *Nat Commun* 9, 261 (2018).
12. Gao, Z., van Beugen, B.J. & De Zeeuw, C.I. Distributed synergistic plasticity and cerebellar learning. *Nature reviews. Neuroscience* 13, 619-635 (2012).
13. Galliano, E., *et al.* Silencing the majority of cerebellar granule cells uncovers their essential role in motor learning and consolidation. *Cell reports* 3, 1239-1251 (2013).
14. Schonewille, M., *et al.* Purkinje cell-specific knockout of the protein phosphatase PP2B impairs potentiation and cerebellar motor learning. *Neuron* 67, 618-628 (2010).
15. Gutierrez-Castellanos, N., *et al.* Motor Learning Requires Purkinje Cell Synaptic Potentiation through Activation of AMPA-Receptor Subunit GluA3. *Neuron* 93, 409-424 (2017).
16. Peter, S., *et al.* Dysfunctional cerebellar Purkinje cells contribute to autism-like behaviour in Shank2-deficient mice. *Nat Commun* 7, 12627 (2016).

17. Takamiya, K., Mao, L., Hugarir, R.L. & Linden, D.J. The glutamate receptor-interacting protein family of GluR2-binding proteins is required for long-term synaptic depression expression in cerebellar Purkinje cells. *J Neurosci* 28, 5752-5755 (2008).
18. Suvrathan, A. & Raymond, J.L. Depressed by Learning-Heterogeneity of the Plasticity Rules at Parallel Fiber Synapses onto Purkinje Cells. *Cerebellum* (2018).
19. Suvrathan, A., Payne, H.L. & Raymond, J.L. Timing Rules for Synaptic Plasticity Matched to Behavioral Function. *Neuron* 92, 959-967 (2016).
20. Lein, E.S., *et al.* Genome-wide atlas of gene expression in the adult mouse brain. *Nature* 445, 168-176 (2007).
21. Yamasaki, M., *et al.* Glutamate receptor delta2 is essential for input pathway-dependent regulation of synaptic AMPAR contents in cerebellar Purkinje cells. *J Neurosci* 31, 3362-3374 (2011).
22. Kakegawa, W., Kohda, K. & Yuzaki, M. The delta2 'ionotropic' glutamate receptor functions as a non-ionotropic receptor to control cerebellar synaptic plasticity. *J Physiol* 584, 89-96 (2007).
23. Kohda, K., Kakegawa, W. & Yuzaki, M. Unlocking the secrets of the delta2 glutamate receptor: A gatekeeper for synaptic plasticity in the cerebellum. *Commun Integr Biol* 6, e26466 (2013).
24. MacLean, D.M., *et al.* Stargazin promotes closure of the AMPA receptor ligand-binding domain. *J Gen Physiol* 144, 503-512 (2014).
25. Kakegawa, W., *et al.* D-serine regulates cerebellar LTD and motor coordination through the delta2 glutamate receptor. *Nat Neurosci* 14, 603-611 (2011).
26. Vinueza Veloz, M.F., *et al.* Cerebellar control of gait and interlimb coordination. *Brain Structure and Function* 220, 3513-3536 (2015).
27. Gonshor, A. & Jones, G.M. Extreme vestibulo-ocular adaptation induced by prolonged optical reversal of vision. *J Physiol* 256, 381-414 (1976).
28. Van Alphen, A.M., Schepers, T., Luo, C. & De Zeeuw, C.I. Motor performance and motor learning in Lurcher mice. *Ann N Y Acad Sci* 978, 413-424 (2002).
29. Hansel, C., *et al.* alphaCaMKII Is essential for cerebellar LTD and motor learning. *Neuron* 51, 835-843 (2006).
30. ten Brinke, M.M., *et al.* Evolving Models of Pavlovian Conditioning: Cerebellar Cortical Dynamics in Awake Behaving Mice. *Cell Rep* 13, 1977-1988 (2015).
31. Zhou, H., *et al.* Differential Purkinje cell simple spike activity and pausing behavior related to cerebellar modules. *J Neurophysiol* 113, 2524-2536 (2015).
32. Hashimoto, K., *et al.* Impairment of AMPA receptor function in cerebellar granule cells of ataxic mutant mouse stargazer. *J Neurosci* 19, 6027-6036 (1999).
33. Chen, L., *et al.* Stargazin regulates synaptic targeting of AMPA receptors by two distinct mechanisms. *Nature* 408, 936-943 (2000).
34. Tomita, S., *et al.* Stargazin modulates AMPA receptor gating and trafficking by distinct domains. *Nature* 435, 1052-1058 (2005).

35. Yamazaki, M., *et al.* Relative contribution of TARPs gamma-2 and gamma-7 to cerebellar excitatory synaptic transmission and motor behavior. *Proc Natl Acad Sci U S A* 112, E371-379 (2015).
36. Lu, W., *et al.* Subunit composition of synaptic AMPA receptors revealed by a single-cell genetic approach. *Neuron* 62, 254-268 (2009).
37. Heine, M., *et al.* Surface mobility of postsynaptic AMPARs tunes synaptic transmission. *Science* 320, 201-205 (2008).
38. Makino, H. & Malinow, R. Compartmentalized versus global synaptic plasticity on dendrites controlled by experience. *Neuron* 72, 1001-1011 (2011).
39. De Zeeuw, C.I., *et al.* Expression of a protein kinase C inhibitor in Purkinje cells blocks cerebellar LTD and adaptation of the vestibulo-ocular reflex. *Neuron* 20, 495-508 (1998).
40. Ito, M. & Karachot, L. Protein kinases and phosphatase inhibitors mediating long-term desensitization of glutamate receptors in cerebellar Purkinje cells. *Neurosci Res* 14, 27-38 (1992).
41. Nomura, T., *et al.* Cerebellar long-term depression requires dephosphorylation of TARP in Purkinje cells. *Eur J Neurosci* 35, 402-410 (2012).
42. van Beugen, B.J., *et al.* High frequency burst firing of granule cells ensures transmission at the parallel fiber to purkinje cell synapse at the cost of temporal coding. *Front Neural Circuits* 7, 95 (2013).
43. Ly, R., *et al.* T-type channel blockade impairs long-term potentiation at the parallel fiber-Purkinje cell synapse and cerebellar learning. *Proc Natl Acad Sci U S A* 110, 20302-20307 (2013).
44. Weber, J.T., De Zeeuw, C.I., Linden, D.J. & Hansel, C. Long-term depression of climbing fiber-evoked calcium transients in Purkinje cell dendrites. *Proc Natl Acad Sci U S A* 100, 2878-2883 (2003).
45. Linden, D.J. The expression of cerebellar LTD in culture is not associated with changes in AMPA-receptor kinetics, agonist affinity, or unitary conductance. *Proc Natl Acad Sci U S A* 98, 14066-14071 (2001).
46. Hirano, T., Kasono, K., Araki, K. & Mishina, M. Suppression of LTD in cultured Purkinje cells deficient in the glutamate receptor delta 2 subunit. *Neuroreport* 6, 524-526 (1995).
47. Ichikawa, R., Sakimura, K. & Watanabe, M. GluD2 Endows Parallel Fiber-Purkinje Cell Synapses with a High Regenerative Capacity. *J Neurosci* 36, 4846-4858 (2016).
48. Yamashita, M., Kawaguchi, S.Y. & Hirano, T. Contribution of postsynaptic GluD2 to presynaptic R-type Ca(2+) channel function, glutamate release and long-term potentiation at parallel fiber to Purkinje cell synapses. *Cerebellum* 12, 657-666 (2013).
49. Wulff, P., *et al.* Synaptic inhibition of Purkinje cells mediates consolidation of vestibulo-cerebellar motor learning. *Nat Neurosci* 12, 1042-1049 (2009).
50. De Zeeuw, C.I., *et al.* Spatiotemporal firing patterns in the cerebellum. *Nat Rev Neurosci* 12, 327-344 (2011).
51. Hoebeek, F.E., *et al.* Increased noise level of purkinje cell activities minimizes impact of their modulation during sensorimotor control. *Neuron* 45, 953-965 (2005).

52. Walter, J.T., *et al.* Decreases in the precision of Purkinje cell pacemaking cause cerebellar dysfunction and ataxia. *Nat Neurosci* 9, 389-397 (2006).
53. Nguyen-Vu, T.D., *et al.* Cerebellar Purkinje cell activity drives motor learning. *Nat Neurosci* 16, 1734-1736 (2013).
54. Jirenhed, D.A., Bengtsson, F. & Hesslow, G. Acquisition, extinction, and reacquisition of a cerebellar cortical memory trace. *J Neurosci* 27, 2493-2502 (2007).
55. Barski, J.J., Dethleffsen, K. & Meyer, M. Cre recombinase expression in cerebellar Purkinje cells. *Genesis* 28, 93-98. (2000).
56. Tyanova, S., Temu, T. & Cox, J. The MaxQuant computational platform for mass spectrometry-based shotgun proteomics. *Nat Protoc* 11, 2301-2319 (2016).
57. Geyer, P.E., *et al.* Proteomics reveals the effects of sustained weight loss on the human plasma proteome. *Mol Syst Biol* 12, 901 (2016).
58. Wisniewski, J.R., Zougman, A., Nagaraj, N. & Mann, M. Universal sample preparation method for proteome analysis. *Nat Methods* 6, 359-362 (2009).
59. Cox, J. & Mann, M. MaxQuant enables high peptide identification rates, individualized p.p.b.-range mass accuracies and proteome-wide protein quantification. *Nat Biotechnol* 26, 1367-1372 (2008).
60. Bruderer, R., *et al.* Extending the limits of quantitative proteome profiling with data-independent acquisition and application to acetaminophen-treated three-dimensional liver microtissues. *Mol Cell Proteomics* 14, 1400-1410 (2015).
61. Team, R.C. R: A language and environment for statistical computing. (2013).
62. Schindelin, J., *et al.* Fiji: an open-source platform for biological-image analysis. *Nat Methods* 9, 676-682 (2012).
63. Koekkoek, S.K., *et al.* Monitoring kinetic and frequency-domain properties of eyelid responses in mice with magnetic distance measurement technique. *J Neurophysiol* 88, 2124-2133 (2002).
64. Noguchi, K., Gel, Y.R., Brunner, E. & Konietzschke, F. nparLD: an R software package for the nonparametric analysis of longitudinal data in factorial experiments. *Journal of Statistical Software* 50(2012).

Figure legends

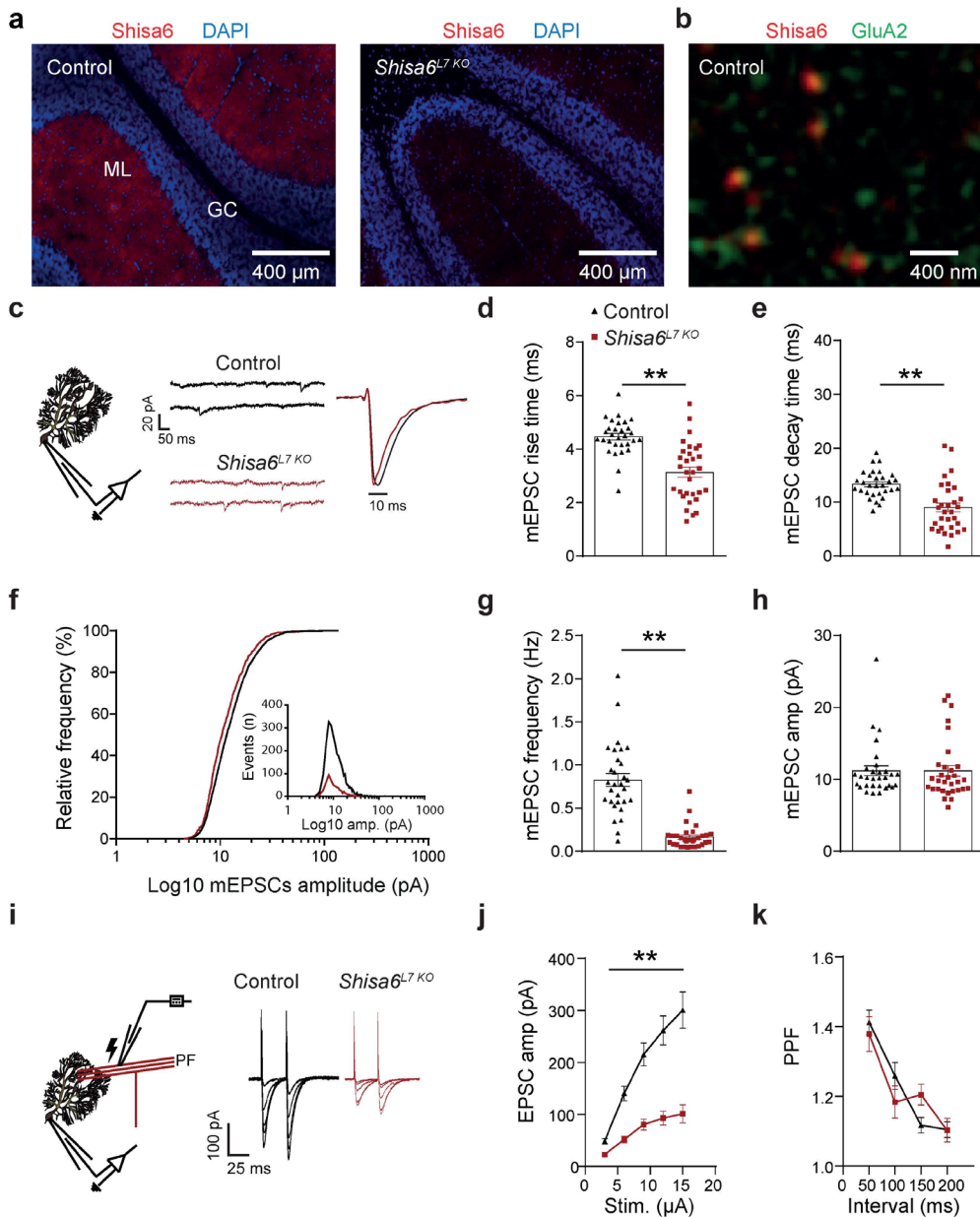


Figure 1

Figure 1. Purkinje cell-specific KO of Shisa6 has lowered PF to PC excitatory input. (a) Representative confocal images of control and Shisa6^{L7KO} mice show Shisa6 expression in the ML of PCs. For split-channel images, see Supplementary Fig. 1a. (b) SIM imaging in control mice shows colocalization of Shisa6 (red) and GluA2 (green) in the PC ML. (c) Whole-cell patch clamp recording configuration of mEPSCs including raw traces and normalized to amplitude averaged control and Shisa6^{L7KO} mEPSC. (d, e) mEPSC rise times and mEPSC decay times are significantly faster in the Shisa6^{L7KO} in comparison to controls (control: 30 cells / 4 animals; Shisa6^{L7KO}: 31 cells / 4 animals). (f) mEPSCs in Shisa6^{L7KO} PCs indicate lower frequency, but comparable amplitude. (g, h) This difference is significantly lower for mEPSC frequency while the median amplitude does not appear to be different (control: 30 cells / 4 animals; KO: 31 cells / 4 animals). (i) Sample traces of evoked EPSCs generated by stimulating afferent PFs with increasing stimulation strengths. (j, k) Evoked EPSCs were consistently of lower amplitude in the Shisa6^{L7KO} whereas the paired pulse facilitation ratio was unaffected (control: 21 – 25 cells/6 animals; Shisa6^{L7KO}: 25 – 27 cells/7 animals). Data are represented as mean \pm SEM, significance indicated by * = $p < 0.05$, ** = $p < 0.01$, see Supplementary Table 1 for statistics.

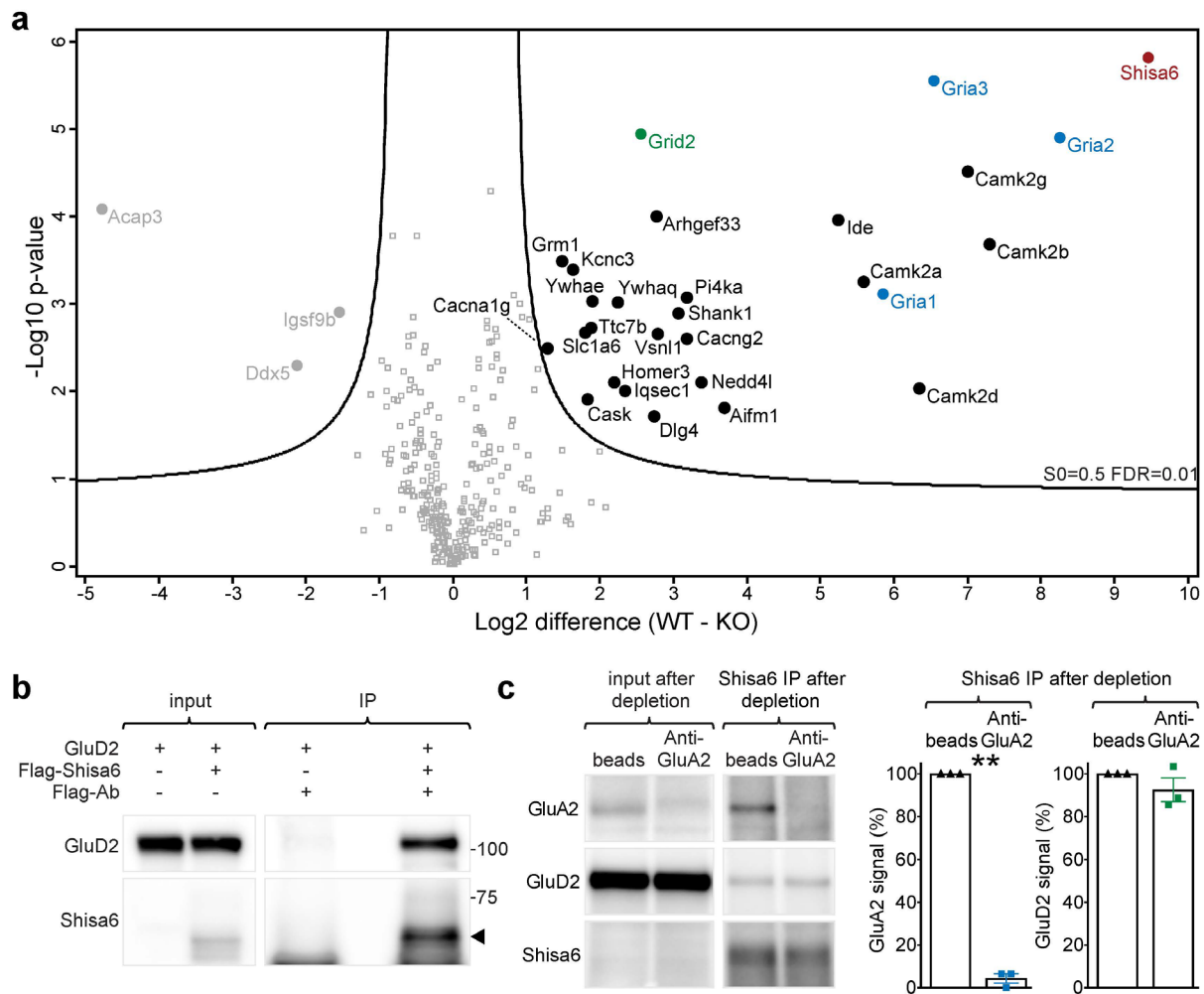


Figure 2

Figure 2. Cerebellar Shisa6 interacts with both AMPA- and Delta-2-type glutamate receptors. (a) Native Shisa6 complexes were immunoprecipitated from the cerebellum of Shisa6 WT and Shisa6^{null} mice (DDM-extracted crude synaptic membranes; n = 3 IPs per genotype) and subjected to mass spectrometric analysis. Significantly enriched proteins are represented by closed circle symbols and labelled by gene name (Student's t-test with permutation-based FDR analysis; S0 = 0.5, FDR = 0.01). Additional information, including protein identification and quantification, statistical analysis, data distribution, and the full list of proteins is provided in Supplementary File 1. (b) GluD2 directly binds to flag-Shisa6 as shown by co-precipitation from HEK293 cells using a Flag-specific antibody. (c) Native Shisa6-GluD2 association is independent of GluA2, as revealed by immuno-depletion IP. GluA2 complexes were removed from the DDM-extracted crude synaptic membrane lysate by immunoprecipitation using an anti-GluA2 antibody (empty beads as control), yielding the "input after depletion" fraction. Shisa6 complexes were immunoprecipitated from this depleted input and their GluA2 and GluD2 content quantified. Shown on the left is an example experiment, with the averaged results of three replicates on the right. Data are represented as mean ± SEM, where significance is indicated by ** = p < 0.01, see Supplementary Table 2 for statistics.

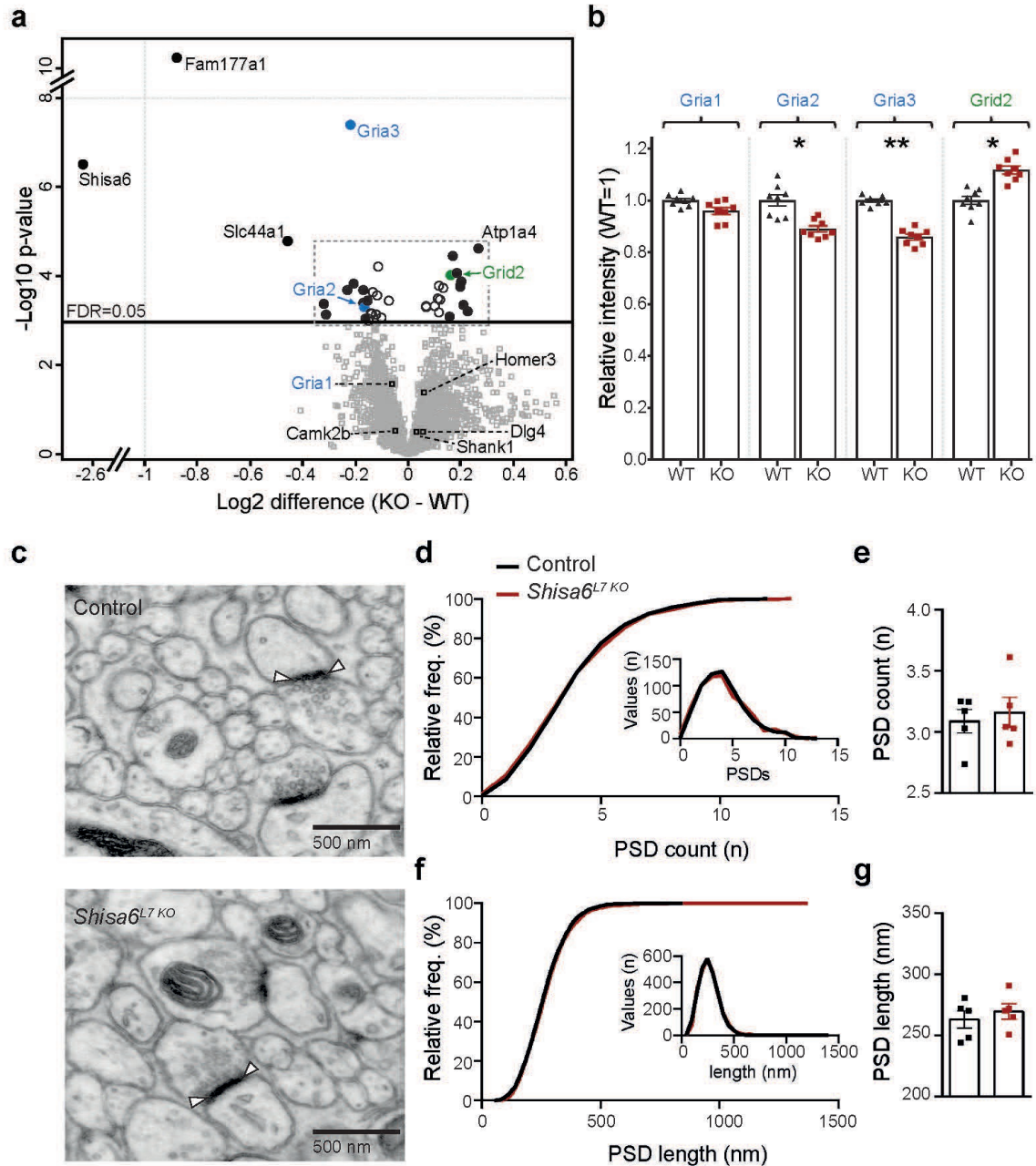


Figure 3. Shisa6 deletion alters synaptic glutamate receptor levels without affecting PSD length or count. (a) Comparison of the cerebellar synaptic proteome of WT and *Shisa6*^{null} mice, as acquired by label free SWATH-MS measurement. Proteins with a significant difference between the mice are represented by circle symbols and labelled by gene name (Student t-test with permutation-based FDR correction, FDR ≤ 0.05); filled circles indicate proteins with a fold-change greater than 10%. AMPAR subunits GluA2 (*Gria2*) and GluA3 (*Gria3*) are significantly downregulated upon *Shisa6* deletion, whereas GluD2 (*Grid2*) reveals an increased expression in the absence of *Shisa6*. See Supplementary Fig. 2 for a more detailed overview of the proteins at the centre of the volcano plot, and Supplementary File 2 for a full list of proteins. (b) Detailed comparison of GluA and GluD2 regulation after setting the mean WT intensity to 1. (c) Examples of EM pictures including PF to PC synapses and their PSDs. (d) Cumulative frequency plot (histogram inset) of all sampled EM pictures indicating no population difference in PSD count (control: 640 images/5 mice; *Shisa6*^{L7 KO}: 640 images/5 mice). (e) Average PSD count per animal did not differ between the groups. (f) Cumulative frequency plot (histogram inset) of all sampled PSDs indicating no population difference in PSD length (control: 2629 PSDs/5 mice; *Shisa6*^{L7 KO}: 2629 PSDs/5 mice). (g) Average PSD length per animal did not differ between the groups. Data are represented as individual replicates and by the mean ± SEM; significance is indicated by * = $q < 0.05$, ** = $q < 0.01$, see Supplementary Table 3 for statistics.

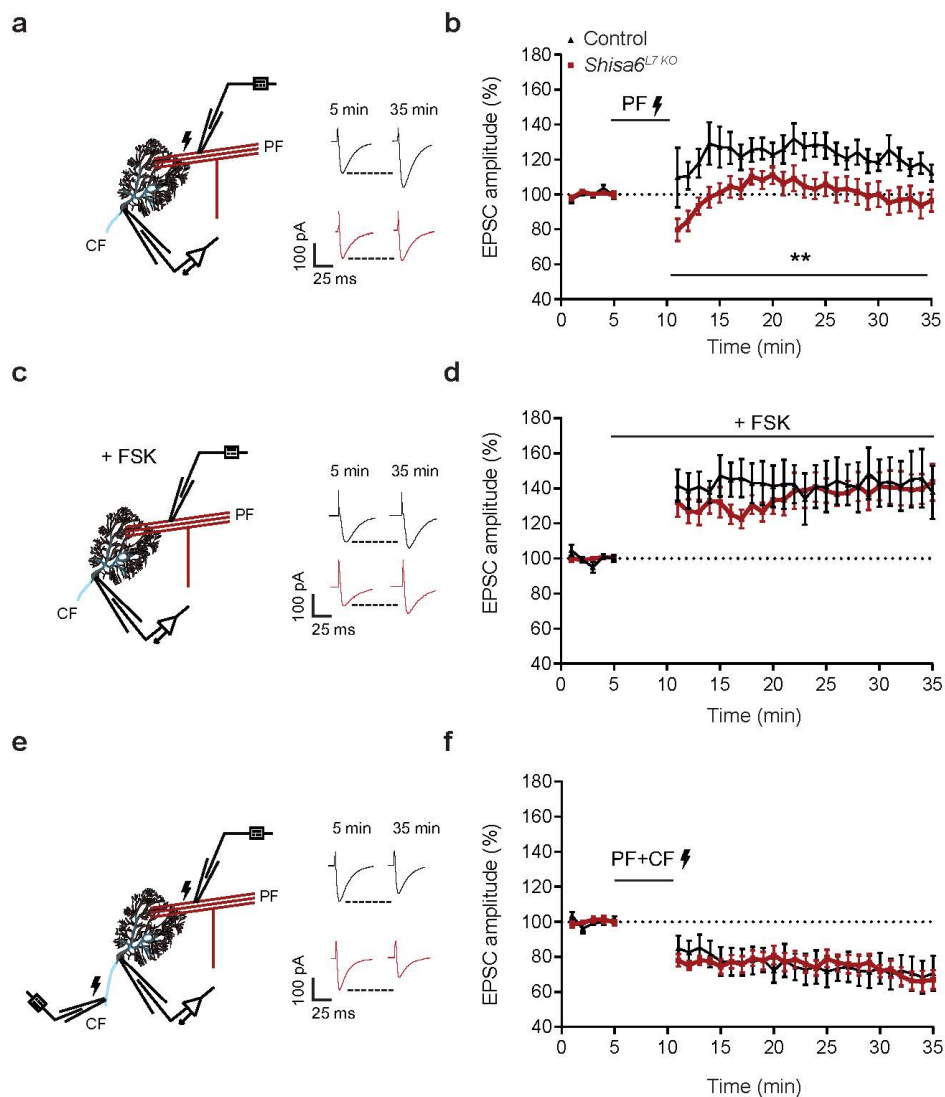


Figure 4

Figure 4. Shisa6 affects LTP, but not LTD at the PF-PC synapse. (a) Recording configuration for PF-PC stimulation and PC voltage clamp in LTP experiments including sample traces. (b) LTP at the PF-PC synapse was induced in control animals after a 5-minute induction protocol, whereas LTP was absent in the *Shisa6*^{L7KO} (control 7 cells/4 mice; *Shisa6*^{L7KO}: 9 cells/5 mice). (c) LTP configuration for induction of LTP with FSK. (d) LTP at the PF-PC synapse was similarly induced in both groups after FSK application (control 7 cells/4 mice; *Shisa6*^{L7KO}: 9 cells/5 mice). (e) Recording configuration for PF-PC LTD including sample traces. PFs are stimulated in the distal ML, whereas the CF is stimulated close to the soma. (f) LTD was successfully induced in both control and *Shisa6*^{L7KO} animals after a 5-minute induction of conjunctive CF and PF stimulation (control: 7 cells/5 mice; *Shisa6*^{L7KO}: 7 cells/5 mice). For both LTP and LTD, the pre-induction data is based on the mean of the last 5 minutes of the baseline recording. Post-induction data is the mean of minutes 20-25 of the post-induction recording. Data are represented as mean \pm SEM; significance is indicated by * = $p < 0.05$, ** = $p < 0.01$, see Supplementary Table 4 for statistics.

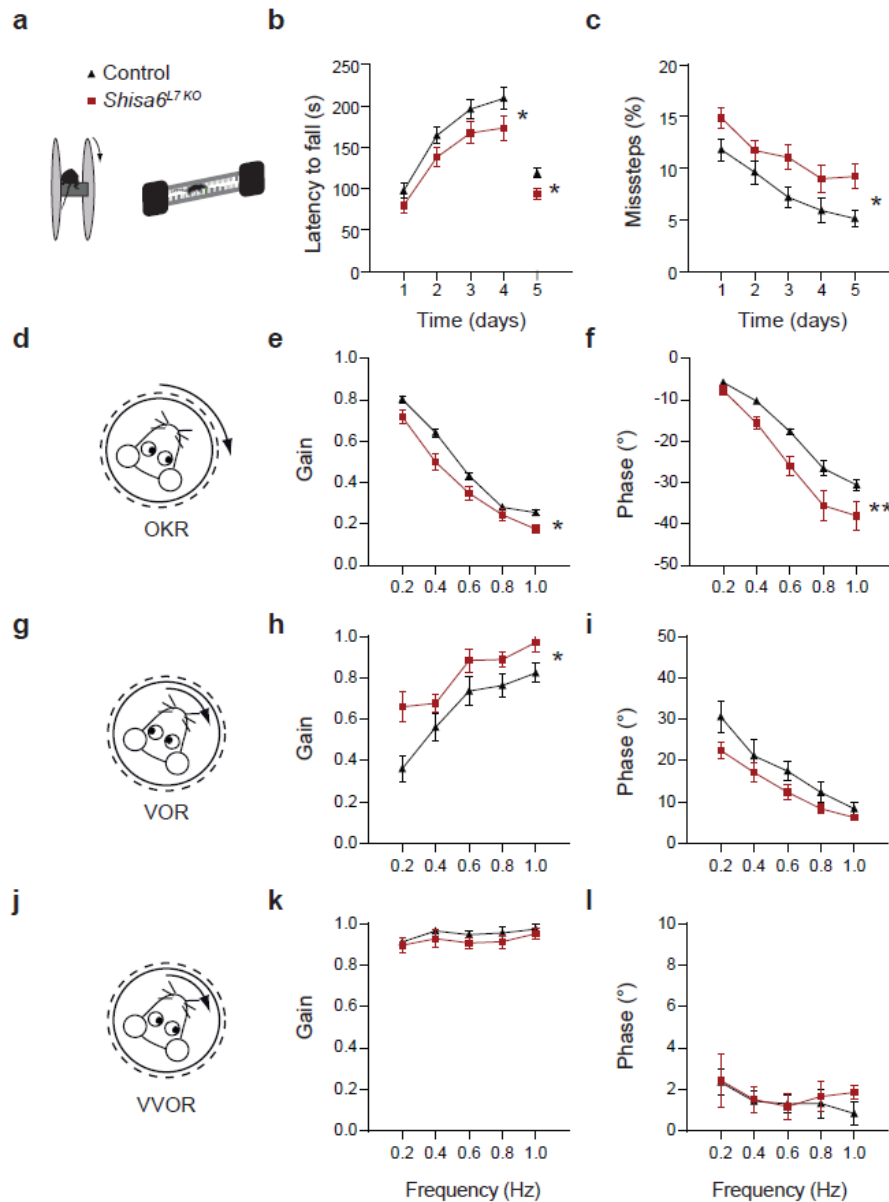


Figure 5

Figure 5. *Shisa6^{L7 KO}* mice show impaired motor performance. See also Supplementary Fig. 3 for additional behaviour paradigms. (a, b) The baseline motor performance investigated on the rotarod indicated that *Shisa6^{L7 KO}* mice tend to have a shorter latency to fall from the rotating wheel (control: 17 mice; *Shisa6^{L7 KO}*: 16 mice). (a, c) Walking patterns on the ErasmusLadder indicate impaired motor coordination as revealed by an increased number of missteps in the *Shisa6^{L7 KO}* (control: 10 mice; *Shisa6^{L7 KO}*: 9 mice). (d-f) Motor performance of the optokinetic reflex (OKR), evaluated with a drum that rotates horizontally around the mouse at a fixed amplitude of 5° and with increasing frequencies, was impaired in both gain and phase for the *Shisa6^{L7 KO}* mice (control: 7 mice; *Shisa6^{L7 KO}*: 6 mice). (g-i) Vestibulo-ocular reflex (VOR) performance, where vestibular input in the dark induces compensatory eye movements, was significantly higher for VOR gain in the *Shisa6^{L7 KO}* (control: 7 mice; *Shisa6^{L7 KO}*: 6 mice). (j-l) Baseline visually-enhanced VOR (VVOR) performance, utilizing both the vestibular and optokinetic modalities, was unaffected in the *Shisa6^{L7 KO}* mice (control: 7 mice; *Shisa6^{L7 KO}*: 6 mice). Data are represented as mean ± SEM; significance is indicated by * = $p < 0.05$, ** = $p < 0.01$, see Supplementary Table 5 for statistics.

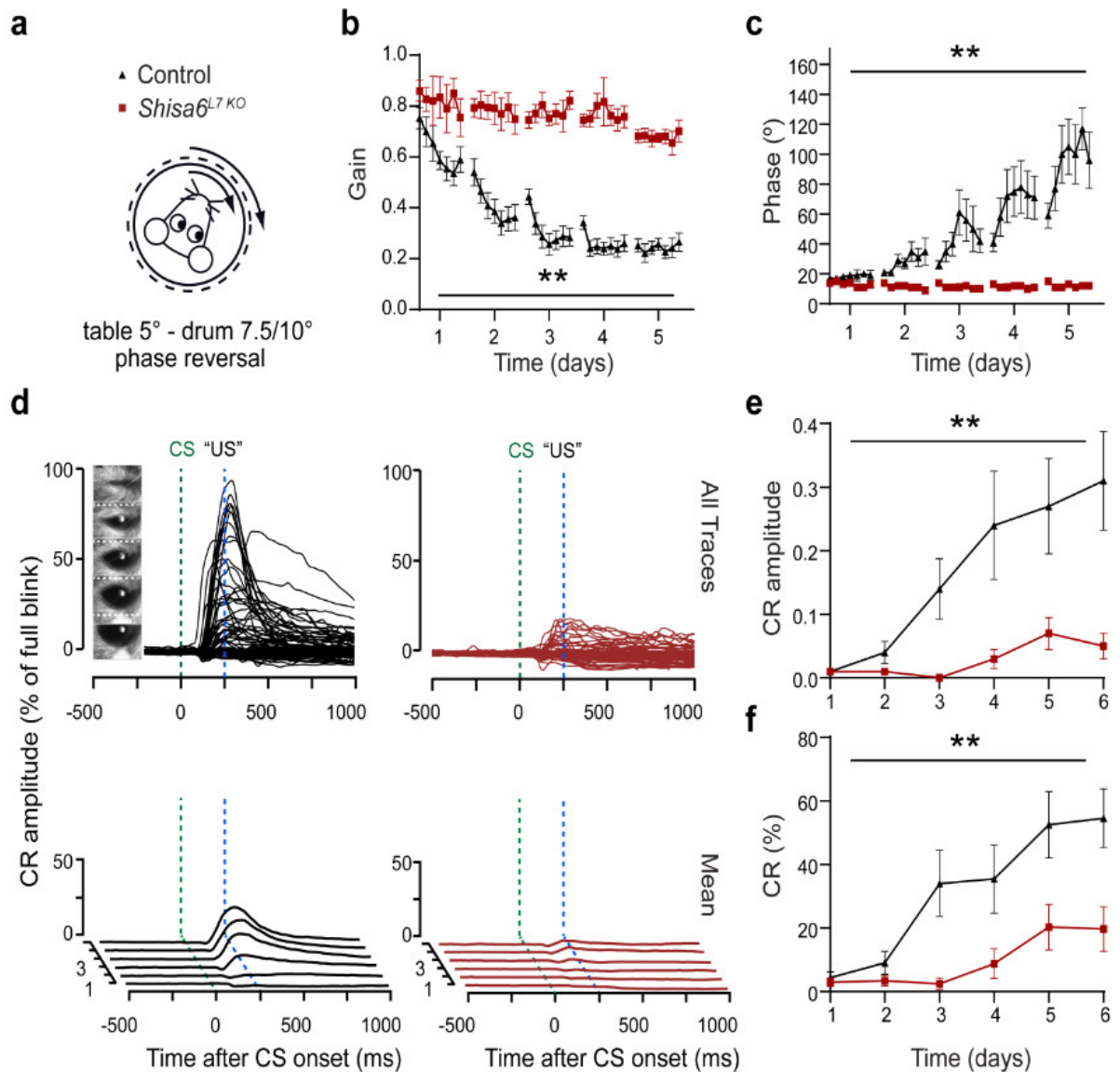


Figure 6

Figure 6. *Shisa6*^{L7 KO} mice show impaired motor learning. (a) After phase reversal training, induced by mismatching visual and vestibular input, mice were tested in the dark for learned responses. (b, c) The *Shisa6*^{L7 KO} mice showed severe impairments in phase reversal adaptation, evidenced by a lack of gain and phase changes over days, whereas control mice showed a reduction in gain and an increase in phase (control: 7 mice; *Shisa6*^{L7 KO}: 6 mice). See also Supplementary Fig. 4 for the average training (in light) gain and phase per day. (d) Experimental setup for the eyeblink conditioning where a 260 ms LED light was used as the conditioned stimulus (CS), and a corneal air puff as the unconditioned stimulus (US). Post-training testing was done using only the CS. Top: the eyelid responses for all individual trials. Bottom: the average eyeblink amplitude for each of the six sessions. (e) The average CR amplitude (threshold: eyelid movement at least 10% of a full blink) for eyelid movements in the 500 ms centred on the US was significantly lower in the *Shisa6*^{L7 KO} mice compared to the controls (control: 16 mice; *Shisa6*^{L7 KO}: 16 mice). (f) The percentage of CR responses over sessions. The *Shisa6*^{L7 KO} mice showed significantly fewer responses than the control over time, indicative of impaired learning (control: 16 mice; *Shisa6*^{L7 KO}: 16 mice). Data are represented as mean \pm SEM; significance is indicated by * = $p < 0.05$, ** = $p < 0.01$, see Supplementary Table 6 for statistics.

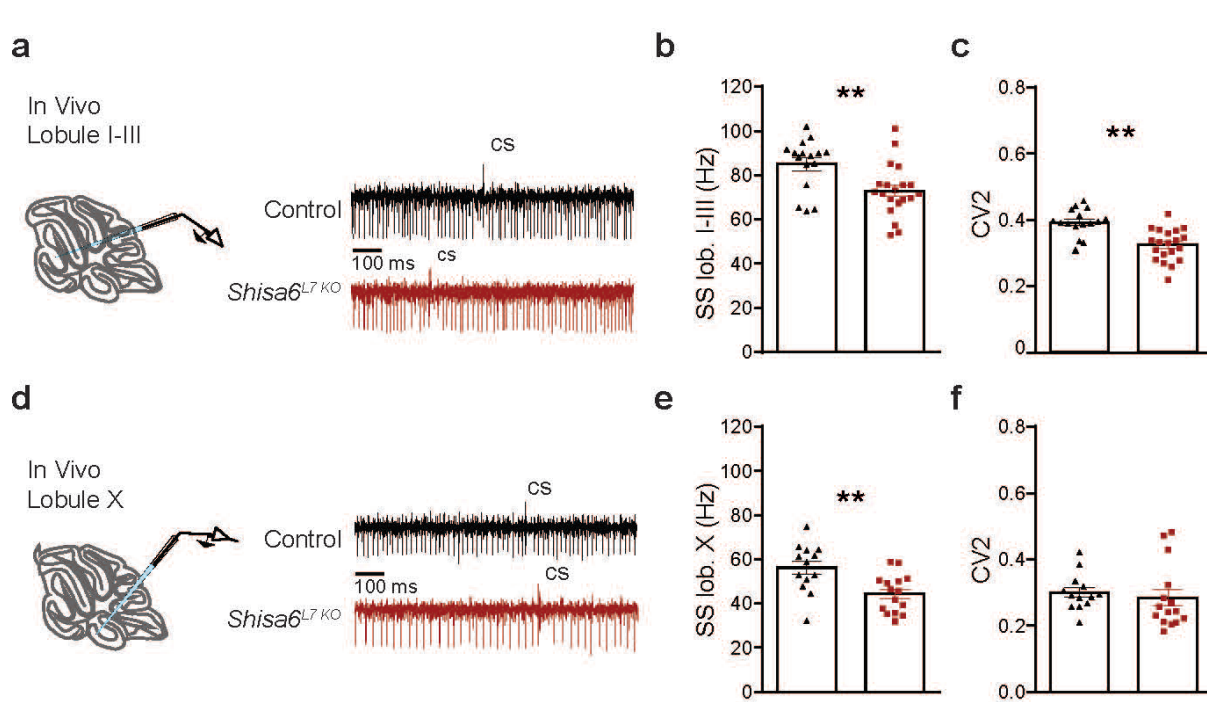
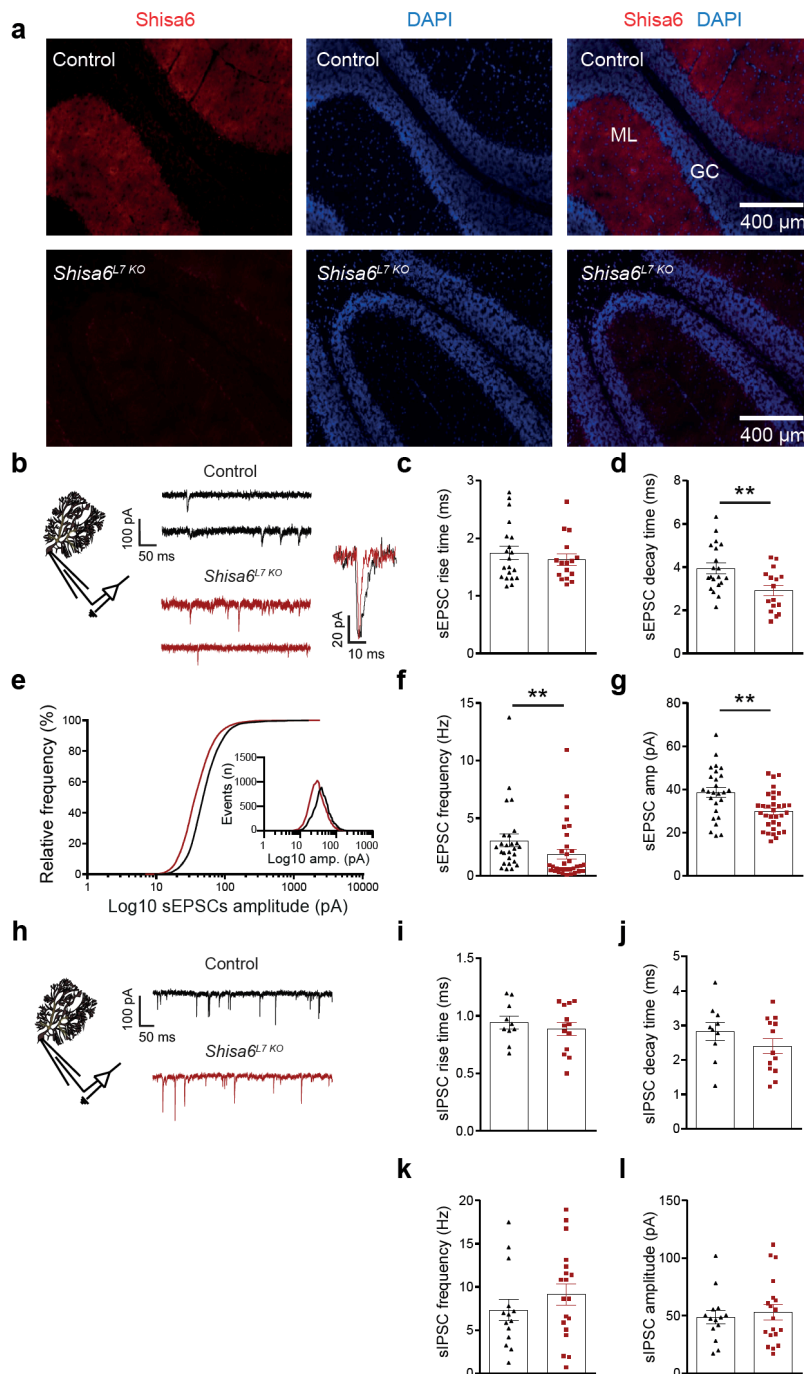
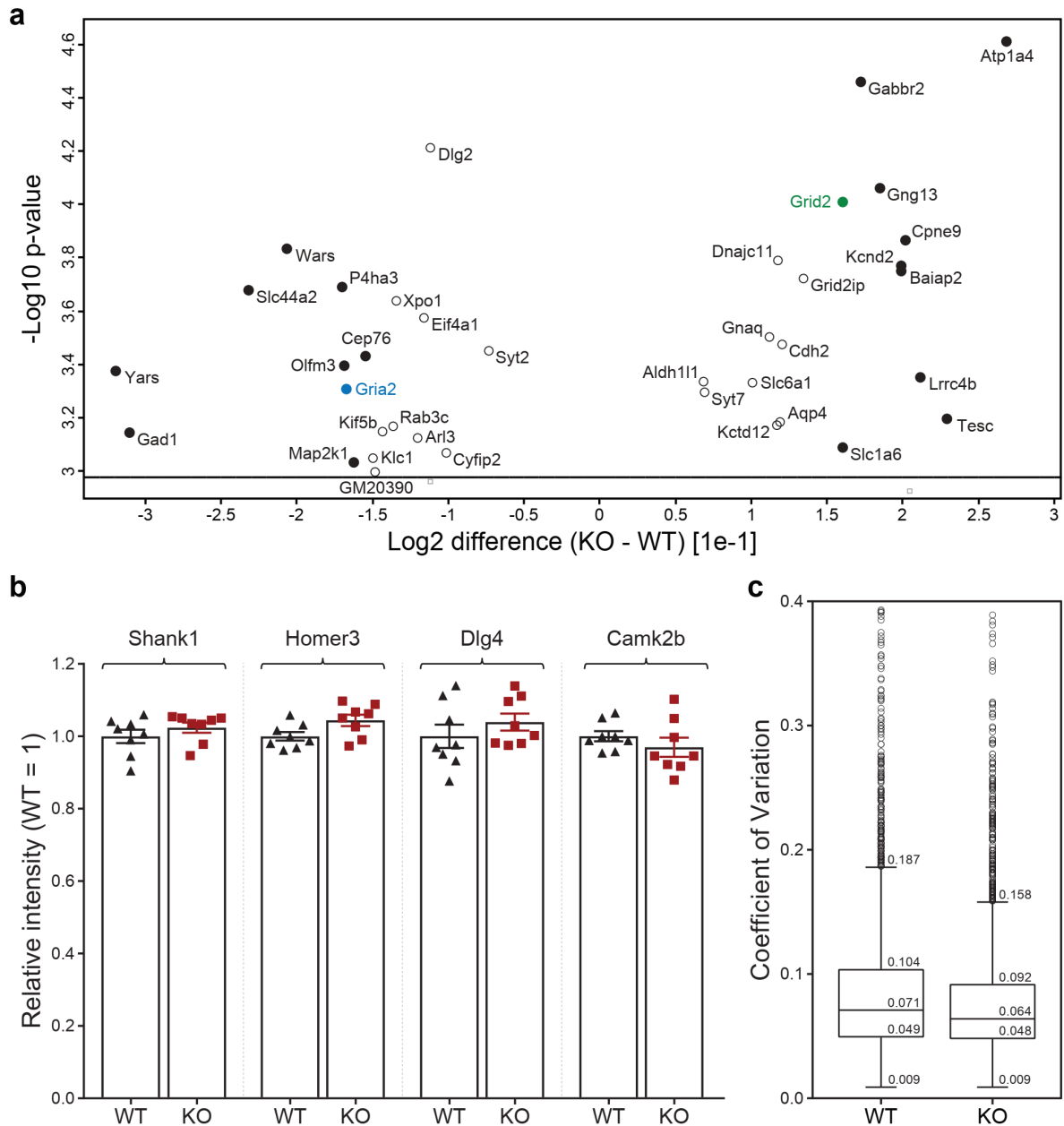


Figure 7

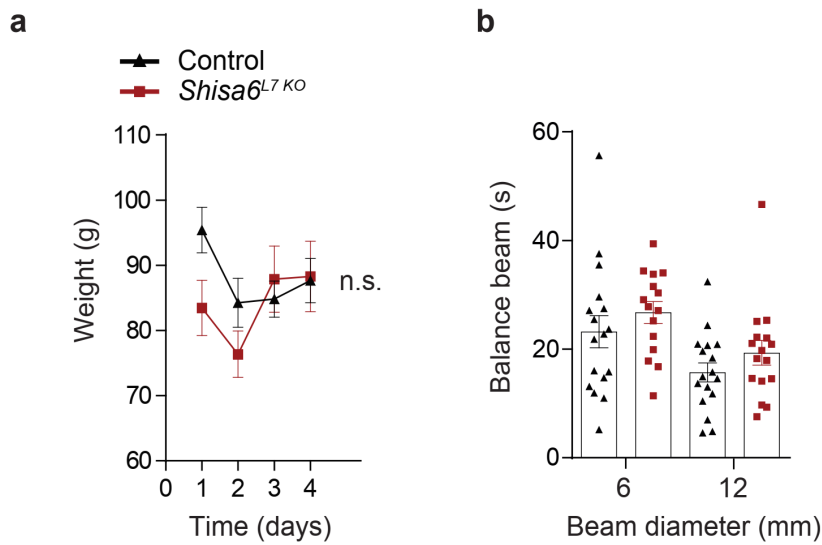
Figure 7. *Shisa6*^{L7 KO} mice show reduced simple-spike (SS) frequencies, and increased SS regularity in vivo. (a) Left: Recording configuration for anterior (lobule I-III) in vivo recordings. Right: example excitatory recordings from the anterior cerebellum. Note the complex spikes (CS), and subsequent SS pause. (b, c) SS frequency in lobules I-III was significantly lower in the *Shisa6*^{L7 KO}. Moreover, a significant difference in the CV2 was found between the two groups, indicating that the SS regularity was increased in the *Shisa6*^{L7 KO} (control: 16 cells/3 mice; *Shisa6*^{L7 KO}: 20 cells/3 mice). (d) Recording configuration for posterior (lobule X) in vivo recordings, as in A. (e, f) SS frequency was lowered in the *Shisa6*^{L7 KO} mice, whereas spike regularity was unaffected (control: 13 cells/3 mice; *Shisa6*^{L7 KO}: 15 cells/3 mice). Data are represented as mean ± SEM; significance is indicated by * = $p < 0.05$, ** = $p < 0.01$, see Supplementary Table 7 for statistics. See also Supplementary Fig. 5 and 6 for complex spike parameters and intrinsic excitability measurements, respectively.



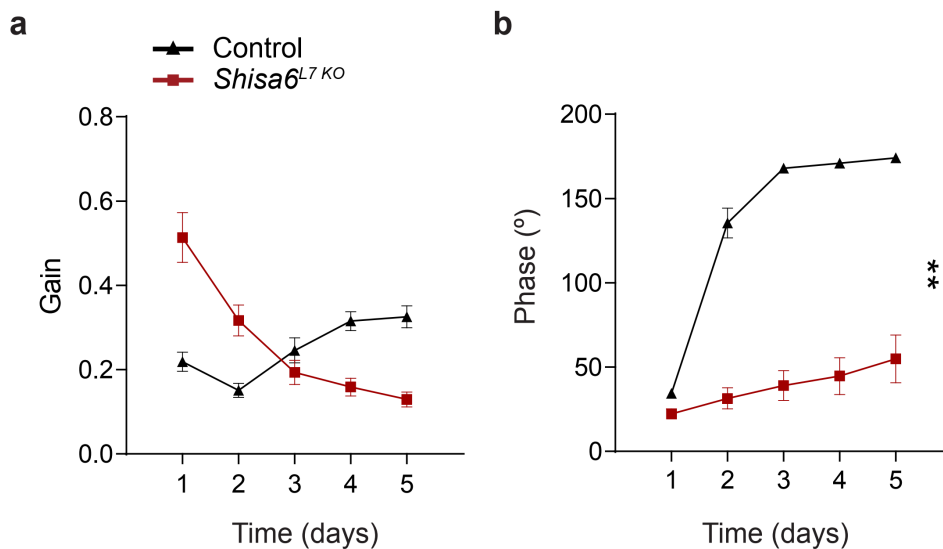
Supplementary Figure 1. Related to Figure 1, sEPSCs confirm mEPSCs data and reveal difference in amplitude while inhibition measured by sIPSCs does not seem to be altered. (a) Representative confocal images of the cerebellar cortex of both control and *Shisa6*^{L7 KO} littermates, showing strong expression of *Shisa6* predominantly in the ML, and absence of *Shisa6* in the *Shisa6*^{L7 KO} mice. (b) sEPSCs raw example traces. (c, d) sEPSC rise times are unaffected whereas sEPSC decay times are significantly faster in the *Shisa6*^{L7 KO} in comparison to controls (control: 20 cells/4 animals; *Shisa6*^{L7 KO}: 16 cells; 5 animals). (e) sEPSCs in *Shisa6*^{L7 KO} PCs show consistently lower amplitudes, as evidenced by the cumulative relative frequency. Inset: histogram of all sEPSCs, similarly showing a leftward shift in sEPSC amplitude. (f, g) Comparison of the sEPSC frequency in the control and the *Shisa6*^{L7 KO} animals indicates a significant reduction in the mutants' sEPSC number. In addition *Shisa6*^{L7 KO} PCs exhibit significantly lower median sEPSC amplitudes (control: 26 cells/4 animals; KO: 33 cells/7 animals). (h) sIPSCs raw example traces. (i, j) The absence of *Shisa6* does not affect sIPSC kinetics, evidenced by the equivalent rise and decay times for both groups (control: 10 cells/3 mice; *Shisa6*^{L7 KO}: 13 cells/3 mice). (k, l) sIPSC frequency and median amplitude are similarly unaffected by the absence of *Shisa6* (control: 14 cells/3 mice; *Shisa6*^{L7 KO}: 19 cells/5 mice). Data are represented as mean \pm SEM; significance is indicated by * = $p < 0.05$, ** = $p < 0.01$.



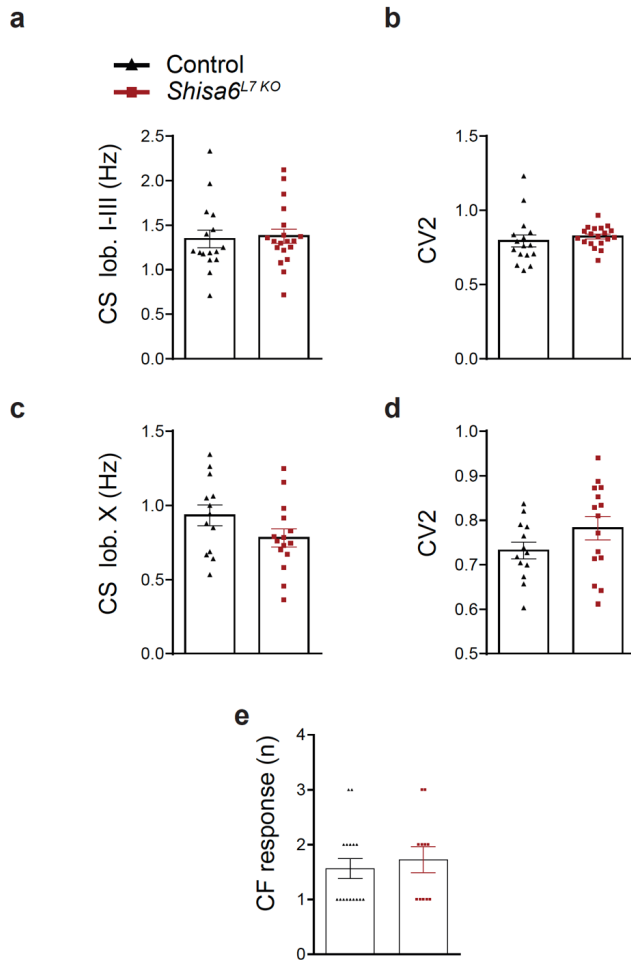
Supplementary Figure 2. Related to Figure 3, proteins showing increased and decreased expression in the absence of *Shisa6*. A group of core PSD proteins is unaffected. (a) A more detailed view of the significantly differentially expressed proteins in the *Shisa6*^{null} as described in Figure 3a. Open circles are proteins with a fold-change below 10%; filled circles are proteins with a fold-change above 10%. (b) Four PSD-localized proteins, as identified by SWATH MS analysis, are unaffected by the absence of *Shisa6*. (c) The median Coefficient of Variation (CoV) of 3142 quantified protein groups for the *Shisa6* WT and *Shisa6*^{null} replicas was 7.1% and 6.4%, respectively. Thereby demonstrating excellent reproducibility (data presented as Tukey boxed plot).



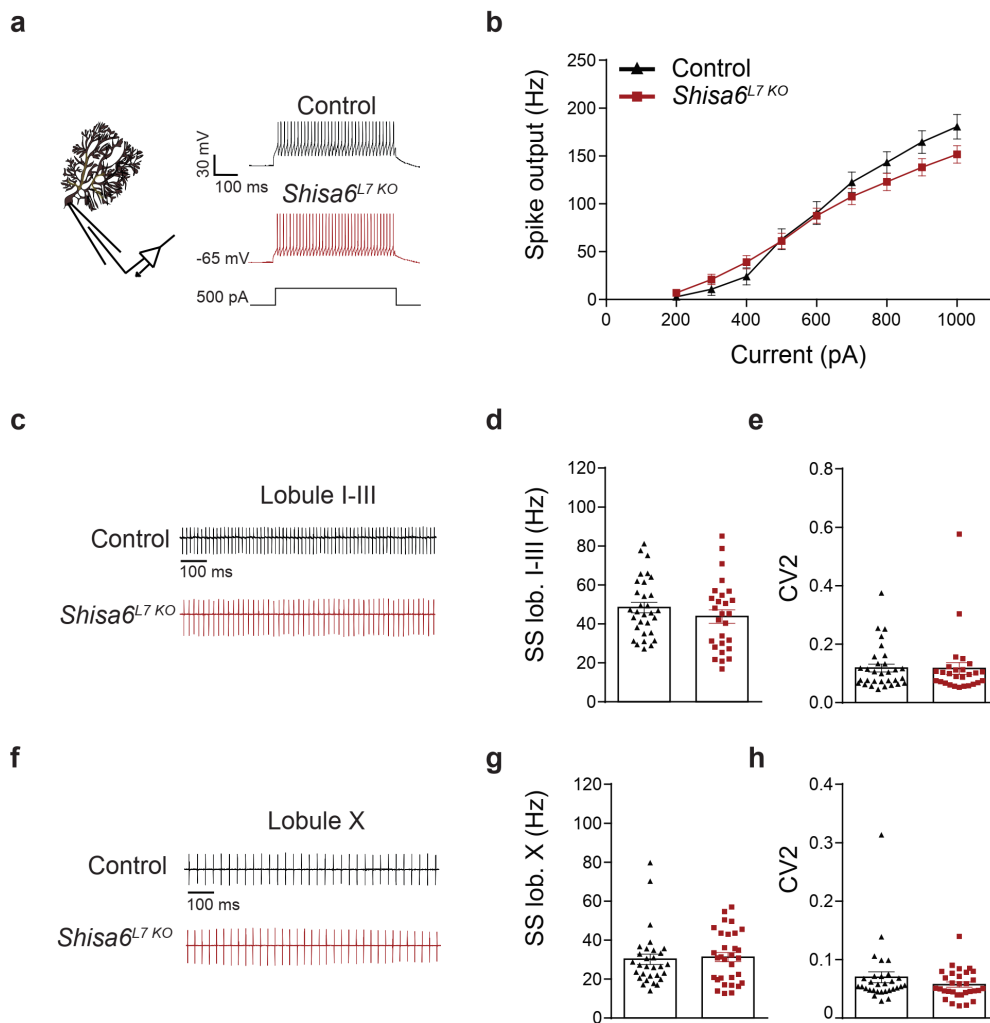
Supplementary Figure 3. Related to Figure 5, no difference was found in the grip force and balance beam paradigms for the *Shisa6*^{L7 KO} mice. (a) The grip force was not significantly different across 5 days of testing between the two groups (control: 17 mice; *Shisa6*^{L7 KO}: 14 mice). (b) The balance beam test did not show any significant performance difference between the two groups (control: 17 mice; *Shisa6*^{L7 KO}: 16 mice). Data are represented as mean \pm SEM; significance is indicated by * = $p < 0.05$, ** = $p < 0.01$.



Supplementary Figure 4. Related to Figure 6, averages of eye movements per day during training (in the light). (a, b) The *Shisa6*^{L7 KO} mice have extreme difficulties in the tracking of the visual stimulus during phase reversal training, which is clear from both the amplitude (gain) as well as the timing (phase) of the eye movements. (control: 7 mice; *Shisa6*^{L7 KO}: 6 mice). Data are represented as mean \pm SEM; significance is indicated by * = $p < 0.05$, ** = $p < 0.01$.



Supplementary Figure 5. Related to Figure 7, complex spike (CS) parameters in vivo and climbing fibre (CF) developmental elimination ex vivo were unaffected in *Shisa6*^{L7 KO} mice. (a, b) CS frequency and regularity in the anterior lobules were unaltered in *Shisa6*^{L7 KO} mice (control: 16 cells/3 mice; *Shisa6*^{L7 KO}: 20 cells/3 mice). (c, d) Similarly, the CS frequency and regularity are unaffected in the posterior lobule X in the *Shisa6*^{L7 KO} mice (control: 13 cells/3 mice; *Shisa6*^{L7 KO}: 15 cells/3 mice). (e) Climbing fibre elimination in young mice was not different in the *Shisa6*^{L7 KO} mice compared to controls (control: 16 cells/3 mice; *Shisa6*^{L7 KO}: 11 cells/3 mice). Data are represented as mean \pm SEM.



Supplementary Figure 6. Related to Figure 7, intrinsic excitability as measured by current injections in current clamp recordings and ex vivo cell-attached recordings of spontaneous simple-spikes (SS), was unaffected in the *Shisa6*^{L7 KO} mice. (a) Recording configuration for whole cell patch clamp recording of PCs. Right: sample spike train after a 500 ms, 500 pA current injection in current clamp. (b) Spiking frequency as a measure of intrinsic excitability, evoked by current injections from 200 to 1000 pA, in 100 pA increments. No difference was observed between the control and *Shisa6*^{L7 KO} mice (control: 26 cells/4 mice; *Shisa6*^{L7 KO}: 31 cells/3 mice). (c) Example traces of ex vivo cell-attached recordings in PC in the anterior lobules. (d, e) Neither the SS frequency, nor the SS regularity were not affected in the *Shisa6*^{L7 KO} animals (control: 31 cells/4 mice; *Shisa6*^{L7 KO}: 27 cells/4 animals). (f) Example traces from ex vivo cell-attached recordings in lobule X. (g, h). As in the anterior lobules, SS frequency and regularity were unaffected in the *Shisa6*^{L7 KO} animals (control: 30 cells/4 mice; *Shisa6*^{L7 KO}: 31 cells/4 mice). Data are represented as mean ± SEM.

CHAPTER

7

Dysfunctional cerebellar Purkinje cells contribute to autism-like behaviour in Shank2-deficient mice

Saša Peter^{1,2,7,*}, Michiel M. ten Brinke^{2,7}, Jeffrey Stedehouder³, Claudia M. Reinelt⁴, Bin Wu², Haibo Zhou², Kuikui Zhou², Henk-Jan Boele², Steven A. Kushner³, Min Goo Lee⁵, Michael J. Schmeisser^{4,6}, Tobias M. Boeckers⁴, Martijn Schonewille², Freek E. Hoebeek² and Chris I. De Zeeuw^{1,2,*}

¹ Netherlands Institute for Neuroscience, 1105 CA, Amsterdam, Netherlands

² Department of Neuroscience, Erasmus MC, 3000 DR, Rotterdam, Netherlands

³ Department of Psychiatry, Erasmus MC, 3000 DR, Rotterdam, Netherlands

⁴ Institute for Anatomy and Cell Biology, 89081 Ulm, Germany

⁵ Yonsei University College of Medicine, 120-752 Seoul, Korea

⁶ Department of Neurology, 89081 Ulm, Germany

⁷ Co-first authors

* Correspondence: c.dezeeuw@erasmusmc.nl, s.peter@nin.knaw.nl

Published on Nature communications (2016)

Abstract

Loss-of-function mutations in the gene encoding the postsynaptic scaffolding protein *SHANK2* are a highly penetrant cause of autism spectrum disorders (ASD) including cerebellum-related motor problems. Recent studies have implicated cerebellar pathology in etiology of ASD. Here, we evaluate the possibility that cerebellar Purkinje cells represent a critical locus of ASD pathophysiology in *Shank2*-related ASD. Absence of *Shank2* impairs both Purkinje cell intrinsic plasticity and induction of long-term potentiation at the parallel fiber to Purkinje cell synapse. Moreover, inhibitory input onto Purkinje cells is significantly enhanced, most prominently in the posterior lobe where simple spike regularity is most affected. Using Purkinje cell-specific *Shank2*-knockouts, we replicate alterations of simple spike regularity *in vivo* and establish cerebellar-dependence of ASD-like behavioural phenotypes in motor learning and social interaction. These data highlight the importance of *Shank2* for Purkinje cell function, and support a model by which cerebellar pathology is prominent in certain forms of ASD.

Introduction

Autism spectrum disorders (ASD) are neurodevelopmental disease entities primarily defined by deficits in social interaction and repetitive behaviour¹. In addition, individuals with autism often suffer from motor skill deficiencies², many of which manifest early in the disease³. The aetiology of ASD is complex with reported pathophysiological alterations encompassing multiple brain regions, including the cerebellum¹. Cerebellum-related motor symptoms of ASD patients have been observed by impairments in eyeblink conditioning^{4,5}, eye movement abnormalities^{6,7}, general motor learning deficits^{8,9} as well as balance and postural difficulties^{10,11}. Patients with cerebellar lesions emerging later in development are often diagnosed with cerebellar cognitive affective syndrome, a condition characterized by deficits in language, executive function and impaired emotions which overlaps considerably with symptoms in ASD¹². Anatomical evidence for cerebellar involvement in ASD includes a decrease in the number of Purkinje cells (PCs) by post-mortem brain histopathological examination^{13,14} and functional connectivity between the cerebellum, and frontoparietal and sensorimotor regions in resting-state fMRI studies of ASD¹⁵. Moreover, the cerebellum is among the most prominent brain regions demonstrating high co-expression of ASD-associated genes¹⁶.

Emerging data indicate that neurodevelopmental disorders including ASD result from dysfunctional synaptic networks^{17,18}. The postsynaptic density (PSD) in particular represents a critically important proteomic hub for a considerable proportion of neurodevelopmental disease-causing mutations, including ASD¹⁹. A prominent example is the Shank family of postsynaptic scaffolding proteins, which has gained wide attention because of their strong link to ASD²⁰⁻²⁴. To date, two studies have independently reported generating *Shank2* knockout (KO) mice with ASD-like behaviour and abnormal hippocampal processing^{25,26}. However, in addition to the forebrain, *Shank2* is also highly expressed in cerebellar PCs^{27,28}. Moreover, patients with *Shank2*-related ASD exhibit motor impairments consistent with cerebellar dysfunction²⁹. However, the causal influence of cerebellar dysfunction on *Shank2*-related ASD has never been established.

We therefore used both global germ-line *Shank2* knock-out (KO; *Shank2*^{-/-}) and PC-specific *Shank2* KO (*L7-Shank2*^{-/-}) mouse models to investigate the causal influence of *Shank2* on cerebellar function and ASD-related behaviours. Notably, *Shank2*^{-/-} mice have impairments in plasticity at the parallel fiber (PF) to PC synapse, increased inhibitory input onto PCs, and significant irregularities in PC simple spike activity. Moreover, *L7-Shank2*^{-/-} mice show deficits in social interaction and exhibit task-specific repetitive behaviour. Together, these results provide novel insight into the pathophysiological mechanisms by which *Shank2* mutations cause impairments in cerebellar function that may contribute to ASD.

Results

Reduction of functional cerebellar AMPAR in *Shank2*^{-/-} mice

A divergent role of the *Shank2* scaffolding protein has been hypothesized for PSD function and cellular morphology³⁰. To evaluate the morphology of *Shank2*-deficient postsynaptic specializations along PC dendrites, we quantified the structural characteristics of dendritic spines and PSDs in the distal molecular layer of global *Shank2*^{-/-} mice using Golgi-Cox staining of PC dendrites and electron microscopy (**Fig. 1**). Neither spine density (WT: 1.93±0.74 spines/μm dendrite; *Shank2*^{-/-}: 1.82±0.67 spines/μm dendrite; P=0.2, Mann-Whitney U-test (MWU-test, see Supplementary Table 1 for additional statistics), nor the length (WT: 1.34±0.77 μm; *Shank2*^{-/-}: 1.32±0.50 μm; P=0.4, MWU-test) or width of individual spines (WT: 0.72±0.45 μm; *Shank2*^{-/-}: 0.71±0.32 μm; P=0.9, MWU-test) was significantly affected (**Fig. 1a**). In addition, the length (WT: 313.3±97.1 nm; *Shank2*^{-/-}: 305.3±96.2 nm; P=0.3) and thickness of PSDs (WT: 26.2±6.0 nm; *Shank2*^{-/-}: 26.0±5.3 nm; P=0.9) were similar between genotypes (**Fig. 1b,c**). In contrast, biochemical analysis of cerebellar synaptosomes indicated that global *Shank2*^{-/-} mice have lowered expression of AMPA receptor subunits GluA1 (WT: 1.00±0.37; *Shank2*^{-/-}: 0.63±0.23; P=0.041) (**Fig. 1d, Supplementary Fig. 1**) and GluA2 (WT: 1.00±0.32; *Shank2*^{-/-}: 0.58±0.11; P=0.014). In addition, we looked into the ASD pathology related cell adhesion molecule neuroligin 3 (Nlgn3), which has been shown to interact with Shank proteins¹⁹, but found no significant difference in its expression (WT: 1.00±0.37; *Shank2*^{-/-}: 0.84±0.33; P=0.4). Together, these findings indicate that *Shank2* is not crucial for the morphological differentiation of PC dendritic spines and PSDs, but instead may play an important role in the maintenance of cerebellar GluA1 and GluA2 levels.

Normal baseline excitability in *Shank2*^{-/-} Purkinje cells

Considering that we found a reduction of cerebellar AMPA receptor expression in global *Shank2*^{-/-} mice, we next examined neurotransmission at the PF-PC synapse using *ex vivo* whole-cell recordings (at 21±1°C) (**Fig. 2a**). PF-PC EPSCs, which were obtained in WT and *Shank2*^{-/-} under comparable conditions (holding current: WT: -389±102 pA; *Shank2*^{-/-}: -388±114 pA, P=1; PC input resistance: WT: 67.2±16.8 MΩ; *Shank2*^{-/-}: 69.1±12.4 MΩ; P=0.8; **Fig. 2b,c**), revealed no significant differences in rise time (WT: 2.1±0.7 ms; *Shank2*^{-/-}: 1.7±0.6 ms; P=0.2) or decay time (WT: 9.7±0.8 ms; *Shank2*^{-/-}: 9.3±0.3 ms; P=0.3) (**Fig. 2d,e**). Moreover, evoking PF-EPSCs using stimulation currents varying from 3 to 15 μA resulted in similar event amplitudes (P=0.9, repeated-measures ANOVA) (**Fig. 2f,g**) and applying inter-stimulus intervals varying from 50 to 200 ms evoked comparable levels of paired-pulse facilitation (P=0.2, repeated-measures ANOVA) (**Fig. 2h**), indicating that baseline PF-PC synaptic transmission is unaltered by the lack of *Shank2*. Next, we evaluated whether the loss of *Shank2* affected neurotransmission at the climbing fiber (CF) to PC synapse. CF stimulation induced PC complex spikes in WT and *Shank2*^{-/-}. These waveforms showed no significant differences in the amplitude of the initial Na⁺-spike (WT: 51.8±6.4 mV; *Shank2*^{-/-}: 48.5±5.9 mV, P=0.3) and in the number of subsequent Ca²⁺-spikelets (WT: 1.6±0.5; *Shank2*^{-/-}: 2.0±0.7; P=0.2) or the amplitude of Ca²⁺-spikelets (WT: 31.8±11.9 mV; *Shank2*^{-/-}: 33.9±6.4 mV, P=0.7) (**Supplementary Fig. 2a-c**). Moreover, at P9-10 virtually all PCs of both WT and *Shank2*^{-/-} were innervated by multiple CFs, while at P25-35 all converted into mono-innervation (number of CF responses P9-10: WT: 2.0±0.5; *Shank2*^{-/-}: 2.3±0.5; P=0.2; P25-35: WT: 1.0±0.0; *Shank2*^{-/-}: 1.0±0.0; P=1, MWU-test) (**Supplementary Fig. 2d,e**). Finally, the characteristic paired-pulse depression of CF-PC synaptic transmission showed no differences throughout the tested developmental stages (P9-10: WT: 0.59±0.14; *Shank2*^{-/-}: 0.54±0.11; P=0.5; P25-35: WT: 0.75±0.11; *Shank2*^{-/-}: 0.77±0.1; P=0.6) (**Supplementary Fig. 2f,g**), together indicating that the CF to PC input in *Shank2*^{-/-} mice is not only normal in its baseline characteristics but also with respect to developmental elimination³¹.

To examine PC kinetics, we evoked action potentials (APs) using depolarizing current steps at near-physiological temperature (33±1°C) (**Fig. 2i**). Evoked APs showed comparable thresholds (WT: -51.4±3.9 mV; *Shank2*^{-/-}: -51.0±3.5 mV; P=0.8), amplitudes (WT: 39.8±5.8 mV; *Shank2*^{-/-}: 35.9±5.8 mV; P=0.1) and half-widths (WT: 0.29±0.02 ms; *Shank2*^{-/-}: 0.30±0.03 ms; P=0.7), as well as after-hyperpolarization amplitudes (WT: 6.5±1.6 mV; *Shank2*^{-/-}: 7.5±1.7 mV; P=0.2) (**Fig. 2j-m**). In addition, PC intrinsic excitability was normal³² in that current step injections of increasing amplitude resulted in a linear current-to-firing frequency relationship (P=0.1, repeated-measures ANOVA) (**Fig. 2n,o**) with a similar slope (WT: 16.2±2.2 Hz; *Shank2*^{-/-}: 16.1±2.3 Hz; P=1.0) (**Fig. 2o**). Together, these findings indicate that both the baseline transmission at PC excitatory synapses and PC intrinsic excitability remain intact in global *Shank2*^{-/-} mice.

Increased sIPSCs and spiking irregularity in *Shank2*^{-/-} PCs

To investigate inhibition of PCs in global *Shank2*^{-/-} mice, we recorded spontaneous inhibitory postsynaptic currents (sIPSCs). Since PC activity can be related to the presence or absence of the glycolytic enzyme aldolase-c (referred to as zebrin)³³, we recorded from the predominantly zebrin-negative anterior lobules I-V as well as the predominantly zebrin-positive posterior lobule X of the cerebellar cortex (**Fig. 3a,b**). In both regions, we observed an increase in the frequency (lobules I-V: WT: 8.3±5.9 Hz; *Shank2*^{-/-}: 12.2±5.4 Hz; P=0.0295; lobule X: WT: 14.2±7.0 Hz; *Shank2*^{-/-}: 21.5±8.8 Hz; P=0.0079) (**Fig. 3c,e**), but not in the amplitude (for lobules I-V, WT: 53.2±24.4 pA; *Shank2*^{-/-}: 65.2±29.5 pA; P=0.1; for lobule X, WT: 58.9±19.0 pA; *Shank2*^{-/-}: 64.0±24.7 pA; P=0.5), of sIPSCs (**Fig. 3d,f**). Importantly, *Shank2*^{-/-} sIPSC frequency was higher in lobule X than in the anterior lobe (P=0.0002). Given that inhibition decreases the firing frequency of PCs, but increases their irregularity^{34,35}, we hypothesized that the increased frequency of sIPSCs in *Shank2*^{-/-} would translate into an overall decrease of *in vivo* simple spike (SS) activity but with an increased irregularity (**Fig. 3g,h**). The global *Shank2*^{-/-} mice did indeed exhibit a decrease in firing frequency in lobules I-V (WT: 88.2±18.7 Hz; *Shank2*^{-/-}: 76.3±11.8 Hz; P=0.0096) (**Fig. 3i**), but notably not in lobule X (WT: 52.6±12.7 Hz; *Shank2*^{-/-}: 50.3±12.9 Hz; P=0.6) (**Fig. 3i**). Conversely, and consistent with the relative magnitude of the change in sIPSC frequency, the irregularity of PC SS firing was increased in lobule X (CV: WT, 0.30±0.08; *Shank2*^{-/-}, 0.38±0.09, P=0.0086; CV2: WT, 0.29±0.07; *Shank2*^{-/-}, 0.40±0.11, P=0.0003), but not in lobules I-V (CV: WT, 0.48±0.06; *Shank2*^{-/-}, 0.49±0.12, P=0.7; CV2: WT, 0.45±0.04; *Shank2*^{-/-}, 0.48±0.08, P=0.1) (**Fig. 3j-n**). The complex spike frequency and the pause in SS firing following each complex spike was similar between global *Shank2*^{-/-} mice and their WT littermates in both the anterior (WT: frequency 1.28±0.29 Hz; pause 9.11±1.98 ms; *Shank2*^{-/-}: 1.32±0.24 Hz; 10±2.9 ms; P=0.7 and P=0.2, respectively) and posterior lobules (WT: frequency 0.67±0.19 Hz; pause 19.7±5.5

ms; *Shank2*^{-/-}: frequency 0.84±0.37 Hz; pause 17.61±5.29 ms; P=0.1 and P=0.2, respectively) (**Supplementary Fig. 3**). Thus, in the absence of *Shank2*, the zebrin-positive lobule X selectively exhibits a highly irregular pattern of PC simple spike firing, which is consistent with a relative increase of inhibitory input onto lobule X PCs.

Impaired synaptic and intrinsic plasticity in *Shank2*^{-/-} PCs

Given that *Shank2* functions as a PSD scaffolding protein of postsynaptic receptors^{17,30} for which we observed decreased expression of both GluA1 and GluA2 in cerebellar synaptosomes of *Shank2*^{-/-} mice (**Fig. 1**), we reasoned that PC synaptic plasticity might also be affected^{25,26}. Induction of long-term potentiation (LTP) (33±1°C; 1 Hz, 5 min PF-tetanus) (**Fig. 4a**) reliably increased PF-EPSC amplitudes in WT PCs (121.1±19.8% at t=40 min; P=0.003, repeated-measures ANOVA), but not in those of global *Shank2*^{-/-} mice (91.8±14.2% at t=40; P=0.3, repeated-measures ANOVA) (**Fig. 4b**). In contrast, both WT and global *Shank2*^{-/-} mice exhibited robust long-term depression (LTD) of PF-EPSCs following co-activation (1 Hz) of PFs and CFs (WT: 71.4±14.9%; P<0.0001; *Shank2*^{-/-}: 76.9±14.6%; P=0.0009, repeated-measures ANOVA) (**Fig. 4c,d**). Since LTP has been reported to facilitate adaptation of intrinsic properties, driving spike activity³², we next examined PC intrinsic plasticity before and after PF-LTP induction (**Fig. 4e**). Whereas WT mice readily demonstrated a potentiation of intrinsic excitability (139.7±21.3% at t=40 min; P=0.005, repeated-measures ANOVA), intrinsic plasticity was markedly impaired in global *Shank2*^{-/-} mice (104.6±22.2% at t=40 min; P=0.5, repeated-measures ANOVA) (**Fig. 4f**). These results suggest that *Shank2* is a critical modulator of both synaptic and intrinsic plasticity in Purkinje cells.

Expression of *Shank2* in *L7-Shank2*^{-/-} mice

To explore the behavioural impact of the lack of *Shank2* in PCs, we generated a PC-specific knockout of *Shank2* (see methods section) using the floxed version of the *Shank2*^{-/-} mutants²⁵ and the L7-vector³². Immunocytochemical analysis with the SA5193 rabbit primary *Shank2* antibody^{25,36} confirmed that *Shank2*^{-/-} was specifically deleted in PCs in the PC-specific *L7-Shank2*^{-/-} mice, but not in WT littermates, whereas it was ubiquitously deleted in the global *Shank2*^{-/-} (**Fig. 5**). Importantly, PC-specific deletion of *Shank2* had no discernible impact on cellular zebrin identity, or on the zonal patterns of zebrin staining across cerebellar modules (**Supplementary Fig. 4**).

Impaired motor learning in *L7-Shank2*^{-/-} mice

Given the variety of electrophysiological aberrations in PCs in the global *Shank2*^{-/-}, we next examined motor behavior in the PC-specific *L7-Shank2*^{-/-} mice. Unlike the hyperactivity exhibited by global *Shank2*^{-/-} mice in an open field^{25,26}, mice with PC-specific deletion of *Shank2* exhibited no evidence of hyperactivity in the open field test compared to their WT littermates (velocity: WT: 12.28±2.79 cm/s; *L7-Shank2*^{-/-}: 13.24±2.61 cm/s; P=0.3; distance moved: WT: 7.37±1.68 m; *L7-Shank2*^{-/-}: 7.94±1.57 m; P=0.3) (**Supplementary Fig. 5a,b**). The lack of hyperactivity was confirmed using the PhenoTyper Box (Noldus), in which free exploration was quantified over a 30 min-period in a homecage-like environment (velocity: WT: 6.7±1.1 cm/s; *L7-Shank2*^{-/-}: 6.3±1.3 cm/s; P=0.5, distance moved: WT: 384.6±68.8 cm; *L7-Shank2*^{-/-}: 371.7±79.7 cm; P=0.5, repeated-measures ANOVA) (**Supplementary Fig. 5c,d**). Moreover, during the ErasmusLadder test³⁷ motor performance was similar between genotypes, including the efficiency and timing of steps (2nd day efficiency, WT: 33.1±20.0%; *L7-Shank2*^{-/-}: 47.1±15.4 cm; P=0.3; 2nd day timing: WT: 359.2±84.2 ms; *L7-Shank2*^{-/-}: 330.7±49.4 ms; P=0.8, repeated-measures ANOVA) (**Supplementary Fig. 5e,f**). Finally, the amplitude (gain) and timing (phase) of baseline optokinetic (OKR) (OKR gain, P=0.6, OKR phase, P=0.9, repeated-measure ANOVA) and vestibulo-ocular reflexes (VOR) (VOR gain, P=0.4, VOR phase, P=0.2, repeated-measure ANOVA) were also similar (**Supplementary Fig. 5g-j**), further highlighting that motor performance is normal in *L7-Shank2*^{-/-} mutants.

In contrast, motor learning was consistently affected in a variety of cerebellar motor learning tasks (**Fig. 6**). Using a conditioning task within the ErasmusLadder, in which mice were presented with a tone preceding the elevation of an obstructive rung at a 200 ms interval³⁷, *L7-Shank2*^{-/-} mice were unable to successfully avoid the obstacle (*L7-Shank2*^{-/-} versus WT: P=0.018, repeated-measures ANOVA) (**Fig. 6a,b**). Furthermore, *L7-Shank2*^{-/-} mice failed to acquire the normal increase in VOR gain (*L7-Shank2*^{-/-} versus WT: P=0.006, repeated-measures ANOVA) or shift in VOR phase (2nd day; P=0.047, 3rd P=0.0013, 4th P<0.0001, 5th P=0.0003, repeated-measures ANOVA) following visuovestibular mismatch training³⁸ (**Fig. 6c-f**). Finally, *L7-Shank2*^{-/-} mice exhibited a significant impairment of Pavlovian eyeblink-conditioning³⁹ using a light pulse as the conditioning stimulus (CS) and a corneal air puff as the unconditioned stimulus at a 250 ms interval (conditioned response or CR

rate: $P=0.0013$; CR amplitude: $P=0.0009$; repeated-measures ANOVA) (**Fig. 6g-i**). These findings indicate that *L7-Shank2*^{-/-} mice have normal baseline motor performance, but prominent impairments in motor learning.

Irregular *in vivo* PC simple spikes in *L7-Shank2*^{-/-} mice

To investigate whether the changes in electrophysiological properties observed in PCs of the global *Shank2*^{-/-} mice may contribute to the behavioural phenotypes observed, we tested to what extent the changes in simple spike activity also occurred in the *L7-Shank2*^{-/-} mice. We first recorded extracellular single units *in vivo* from the largely zebrin-negative lobules I-V (**Fig. 7a-d**) and the predominantly zebrin-positive lobules IX-X (**Fig. 7e-h**). Importantly, the recordings in the *L7-Shank2*^{-/-} mice fully reproduced the increases in CV (WT, 0.35 ± 0.07 ; *L7-Shank2*^{-/-}, 0.49 ± 0.09 ; $P<0.0001$) and CV2 (WT, 0.36 ± 0.06 ; *L7-Shank2*^{-/-}, 0.47 ± 0.06 ; $P<0.0001$) (**Fig. 7g,h**) that were found in the posterior lobules of the global *Shank2*^{-/-} (**Fig. 3i-n**), confirming the higher SS irregularity. In addition, the *L7-Shank2*^{-/-} mice also showed signs of SS irregularity in the anterior lobules in that their CV2 was also significantly increased (WT, 0.43 ± 0.04 ; *L7-Shank2*^{-/-}, 0.47 ± 0.04 ; $P=0.0092$) (**Fig. 7c,d**). The *L7-Shank2*^{-/-} SS mice activity did not show higher firing frequencies in either the anterior (WT: 104.4 ± 25.8 Hz; *L7-Shank2*^{-/-}: 101.2 ± 19.7 Hz; $P=0.6$) or posterior (WT: 70.9 ± 19.5 Hz; *L7-Shank2*^{-/-}: 76.3 ± 23.4 Hz; $P=0.4$) lobules (**Fig. 7b,f**). Finally, we also recorded SS activity of PCs in the flocculus of the vestibulocerebellum, because they are known to directly control VOR adaptation³⁴ (**Fig. 7i-l**). In PCs that were identified to be related to VOR-adaptation by their response to motion around the vertical axis in space, we again found a significant increase in SS irregularity (CV: WT, 0.39 ± 0.07 ; *L7-Shank2*^{-/-}, 0.53 ± 0.08 ; $P<0.0001$; CV2: WT, 0.39 ± 0.07 ; *L7-Shank2*^{-/-}, 0.52 ± 0.08 ; $P<0.0001$), while their overall firing frequency was unaffected (WT: 68.2 ± 15.0 Hz; *L7-Shank2*^{-/-}: 69.6 ± 18.8 Hz; $P=0.8$) (**Fig. 7j-l**). Moreover, *L7-Shank2*^{-/-} showed a bigger difference with WT in SS irregularity in the posterior lobules (40.0% and 30.6% higher CV and CV2, respectively) compared to that in the anterior lobules (4.4% and 9.3% higher CV and CV2, respectively). No significant differences were observed in the duration of the complex spike-induced simple spike pause or the complex spike firing frequency in any of the recorded lobules ($P>0.2$ in all cases) (**Supplementary Fig. 6**). Together, *L7-Shank2*^{-/-} mice demonstrate the critical importance of *Shank2* in PCs for maintaining SS regularity.

Reduced cognitive functioning in *L7-Shank2*^{-/-} mice

We next examined social and repetitive ASD-like behaviours in the PC-specific *L7-Shank2*^{-/-} mice. The three-chamber social interaction task is a widely used social interaction paradigm for evaluating ASD-like behaviour in mouse models of autism^{25,26}. WT mice exhibited a normal preference for the chamber in which the stranger mouse (S1) was present, compared to the empty chamber ($P=0.0002$, MWU-test) (**Fig. 8a**). In contrast, *L7-Shank2*^{-/-} mice had no preference for either S1 or the empty chamber ($P=0.7$, MWU-test) (**Fig. 8b**). Comparing the preference index (stranger-empty) between WT and *L7-Shank2*^{-/-} mice revealed a significantly decreased preference of *L7-Shank2*^{-/-} mice for the stranger mouse ($P=0.0213$) (**Fig. 8c**), indicating their social interaction deficits. With the introduction of a second stranger in the previously empty chamber, WT mice again demonstrated an increased preference for the novel stranger (S2), this time compared to the familiar mouse (S1) ($P=0.0001$, MWU-test) (**Fig. 8d**), whereas *L7-Shank2*^{-/-} mice showed no preference for either the familiar or the novel stranger mice ($P=0.1$, MWU-test) (**Fig. 8e**). Comparing the preference index (S2-S1) between WT and *L7-Shank2*^{-/-} confirmed the impairment of social interaction in *L7-Shank2*^{-/-} mice ($P=0.0136$) (**Fig. 8f**). Because of previously reported compulsive grooming²⁵ and jumping²⁶ in global *Shank2*^{-/-} mice, we next examined repetitive behaviour. We observed no significant differences between WT and *L7-Shank2*^{-/-} mice in the percentage of buried marbles in the marble-burying task ($P=1.0$) (**Fig. 8g**) or in the duration of grooming over a 15 min-period ($P=0.054$) (**Fig. 8h**). However, the *L7-Shank2*^{-/-} mice did show an increase of repetitive behaviour in the T-maze through an increased perseveration, highlighting a reduction in cognitive flexibility ($P=0.0023$, MWU-test) (**Fig. 8i**). Finally, we observed no significant difference in anxiety ($P=0.7$, χ^2 -test) or olfactory sensitivity ($P=0.6$) of *L7-Shank2*^{-/-} mice that could have potentially biased the social behaviour assessments (**Supplementary Fig. 7**). Together, these results indicate that *L7-Shank2*^{-/-} mice exhibit ASD-like social impairments and task-specific repetitive behaviour.

Discussion

Severe loss-of-function mutations in *SHANK2* have been firmly established as conferring a high genetic risk for ASD and intellectual disability^{20,22,29}. Children with disruptive *SHANK2* mutations

exhibit motor impairments, language delay and cerebellar dysfunction including dysmetria and dysdiadochokinesis²⁹. Considering the increasing evidence for cerebellar involvement in ASD⁴⁰, we investigated anatomical, molecular and physiological consequences of global *Shank2* ablation in the cerebellum. In addition, we analyzed *L7-Shank2*^{-/-} mice with cerebellar PC-specific deletion of *Shank2* to evaluate the extent to which the ASD-related behavioural findings in global *Shank2*^{-/-} mice can be attributed to cerebellar dysfunction.

In recent years, several genetic mouse models for ASD have been used for the study of cerebellar abnormalities. The first study to implement a Purkinje cell-specific model related to ASD involved the deletion of FMR1, the fragile X mental retardation 1 protein⁴¹. In this study, the authors reported eye-blink abnormalities and increased LTD in both global and Purkinje cell-specific deletion of FMR1. Furthermore, global Nlgn3-KO mutants exhibited deficits in cerebellum-related motor performance as assessed by the ErasmusLadder⁴². A more recent model examining the 15q11-13 duplication ASD syndrome demonstrated impaired cerebellar synaptic plasticity and motor learning deficits as assessed by eye-blink conditioning⁴³. Perhaps the most definitive study implicating cerebellar dysfunction as etiologic for ASD-like behaviour involved a Purkinje cell-specific deletion of *Tsc1*⁴⁴. This study was the first to demonstrate that Purkinje cell-specific deletion of an ASD-associated gene results in ASD-like behaviour. Finally, a very recent study using multiple mouse models of syndromic ASD found a consistent pattern of impaired sensorimotor integration⁴⁵. These studies have established the foundation by which the cerebellar synaptic pathophysiology underlying ASD can be mechanistically investigated¹⁸.

Given the general importance of *Shank2* in the regulation of neuronal plasticity^{25,26}, we investigated both synaptic and intrinsic plasticity of cerebellar Purkinje cells (**Fig. 4**). Our results indicate that *Shank2* is crucial for PF-PC LTP, but not LTD. Additionally, we show that *Shank2* is important for intrinsic plasticity of neuronal excitability⁴⁶. In contrast to a recent study of the 15q11-13 duplication ASD syndrome in which PC synaptic plasticity deficits were limited to LTD⁴³, our results now highlight LTP impairments as a candidate mechanism underlying the cerebellar pathophysiology of ASD. *Shank2* is a dedicated scaffolding protein, which has a major role in the regulation of glutamate receptor integration, synaptic transmission and plasticity^{17,47}. Future molecular and functional studies will have to elucidate the exact mechanisms by which *Shank2* mediates plasticity in the Purkinje cell, but it may well include a suboptimal integration of GluR subunits as the expression levels of GluA1 and GluA2 were both reduced in the *Shank2*^{-/-} mice. Since GluR subunit levels were analysed in synaptosomes from whole cerebella, it remains to be further investigated to what extent these changes are limited to the PF to PC synapse.

Because of the cerebellar physiological impairments and the previously reported motor hyperactivity in *Shank2*^{-/-} mice^{25,26}, we examined activity levels during both baseline exploration and motor learning. To our surprise we did not find motor performance abnormalities in the PC-specific *L7-Shank2*^{-/-} mice during various assessments including five separate locomotion and eye movement tests (**Supplementary Fig. 2**). However, we did observe substantial impairments of cerebellar motor learning including conditioning of locomotion and eyeblink responses as well as adaptation of compensatory eye movements (**Fig. 6**). It might seem counterintuitive that baseline motor performance can be intact while the capacity for motor learning is reduced, but this combination has been observed in many different mutant lines over the last few decades⁴⁸. Most likely, it reflects the indispensable role of PC plasticity for the acquisition of new behaviours within relatively short periods of time as occurs during the experimental training paradigms (i.e. in the order of hours) and the ability of the motor performance control system to compensate upstream and/or downstream of the affected synapse when prolonged adaptation periods are available as occurs during postnatal development (i.e. in the order of weeks)⁴⁹. The potential causality of the identified electrophysiological abnormalities as underlying the motor learning impairments is strengthened by our independent findings in another Purkinje cell-specific mouse mutant (*L7-PP2B*^{-/-}), in which also both synaptic LTP and intrinsic plasticity were affected³². Together, these phenotypes point towards a PC-dependent contribution to the behavioural motor impairments frequently observed in ASD.

In addition to changes in plasticity, we also found that inhibition of PCs was enhanced in the global *Shank2*^{-/-} mutants. Since reduced inhibition of PCs increases regularity of SS activity³⁴, we hypothesized that PCs of the global *Shank2*^{-/-} mutants should have a higher level of irregularity of SS firing (**Fig. 3**). Indeed, this hypothesis was not only consistent with the *in vivo* extracellular recordings in lobule X of the global *Shank2*^{-/-}, but also confirmed in three different areas (Lobules I-V, Lobules IX-X and the flocculus) of the *L7-Shank2*^{-/-} mice (**Fig. 7**). Moreover, this correlation was also in line with

the fact that the differences in sIPSCs, CV and CV2 had bigger effect sizes in the posterior lobules than the anterior lobules.

The increased frequency of inhibition in the global *Shank2*^{-/-} did not occur concomitantly with increased amplitude of sIPSCs postsynaptically at PCs, indicating that the observed effect could be of pre-synaptic origin. The PC irregularity in the *L7-Shank2*^{-/-} would then have to originate from a pre-synaptic effect of the postsynaptic absence of *Shank2*. Indeed, recent evidence indicates the possibility of Shank-mediated transsynaptic signalling through transmembrane proteins affecting both post and pre-synaptic processes important for vesicle release probability⁵⁰. This type of transsynaptic signalling could manipulate the inhibitory input to PCs either directly or indirectly, e.g. through altered glutamate spillover from the climbing fiber to Purkinje cell synapse⁵¹. Future research aimed at pinpointing the sites relevant to the effects described above should thus focus not only on Purkinje cell specific mouse mutants, but also on those in which their afferents are specifically affected^{52,53}. In doing so, important consideration in studies implementing cell-specific deletions should be given to germline analyses, given the sensitivity of the *L7-cre*^{44,54} and *Shank2* lines (Supplementary Table 1)^{55,56}.

We observed a significant decrease in SS frequency in the anterior lobules of global *Shank2*^{-/-} mice, but not in their posterior lobules, nor in the anterior or posterior lobules of *L7-Shank2*^{-/-} mice. We believe that this inconsistency may reflect the fact that the spontaneous SS firing frequency of PCs is probably largely due to their intrinsic properties rather than the synaptic efficacy of their inhibitory or excitatory inputs³³. Indeed, blocking inhibitory or excitatory synaptic input to PCs by deleting their GABA-A-gamma2 receptor-subunits or abolishing voltage gated calcium channels at their parallel fiber input primarily affects the regularity of SS firing, rather than their firing frequency^{34,53}. Thus, the consistent irregularity of SS in PCs, particularly in the posterior lobe, of the *Shank2*^{-/-} mutants underlines the putative importance of precise SS regularity for behavioural output⁴⁸. Although abnormalities in the anterior and posterior lobules have both been proposed as relevant sites of cerebellar pathology in ASD⁵⁷, our converging data obtained in the posterior lobe suggest that the mechanisms governing the regularity of SS firing reveal a common biological vulnerability in the etiology of ASD.

Here, we report impaired social and task specific repetitive behaviour due to the Purkinje cell-specific deletion of *Shank2* (**Fig. 8**). This result is particularly interesting as, to our knowledge, it is the first Purkinje cell-specific mouse model for a non-syndromic form of autism in which ASD-like behaviour has been established. The impaired social behaviour, late-onset ataxia and reduced excitability of Purkinje cells previously observed in *L7-Tsc1* mice⁴⁴ were due to the absence of a protein that inhibits mTOR signalling through which the translation of a wide variety of proteins is regulated. In contrast, we here show that disruption of the synapse through the absence of a single postsynaptic scaffolding protein in the Purkinje cell is sufficient to show impaired ASD-related motor learning and social behavioural impairments. In addition to the social impairments, we found signs of enhanced repetitive behaviour in the T-maze paradigm, but not the marble burying task or grooming tasks. Since the T-maze task reveals the level of cognitive inflexibility following decision making over consecutive trials rather than the level of repetitious behaviour dominated by high-frequency motor activity that characterizes the other two tasks and that may well be confounded by deficits in cerebellar motor learning, these results highlight the importance of the Purkinje cell synaptic function for ASD beyond the classically ascribed motor-related behaviour.

One of the main challenges remaining is to mechanistically explain the contribution of impaired Purkinje cell physiology to the observed ASD behavioural phenotypes. As previously mentioned, the Shank family of postsynaptic scaffolding proteins has many different interacting proteins in the postsynaptic density through which they could contribute to the functional establishment of regulatory mechanisms for plasticity. The translational challenge from synapse to behaviour brings about two main questions: How does an impaired Purkinje cell mediate ASD-related behaviour? And how might Purkinje cell impairments lead to abnormal brain function beyond the cerebellum with regards to neurodevelopmental critical periods? The first question has been extensively addressed by the accumulating evidence regarding the contribution of ASD-related cerebellar dysfunction to impaired motor learning, as apparent from the eye movement adaptation, ErasmusLadder, and eyeblink conditioning findings examined here and by other investigators⁴⁵. It is indeed possible that the increased inhibition and irregularity of SS firing, in addition to impaired cerebellar plasticity mechanisms, may contribute to social and repetitive behaviour-related phenotypes in ASD. We believe that the answer to how the cerebellum can essentially contribute to socially impaired behaviour could reside in various mechanisms. The idea that disruption of a certain

brain area during development could affect the development and consequently the function of other inter-connected areas, also termed developmental diaschisis, has recently been put forward as a prime mechanism for the cerebellum in its ability to influence other cortical areas in critical developmental periods⁵⁸. In the future, the latter hypothesis can for example be tested with Purkinje cell specific *Shank2* ablation at different stages during development using inducible mouse models, as has recently been employed for other ASD-related genes^{24,59}. These experiments will help to further elucidate the mechanisms by which differential genes, such as *Shank2*, regulate cerebellar function and ultimately ASD-like behaviour.

Methods

Experiments and analyses were performed with the experimenters blinded to the genotype. Mice used were global germ-line *Shank2*^{-/-} and their littermate WT all bred on a mixed C57BL6/N and C57BL6/J background. The generation of these mice has previously been described in detail^{25,26}. The *L7-Shank2*^{-/-} was generated by crossing Purkinje specific L7(Pcp2)-Cre⁵⁴ with *Shank2*^{flxd/flxd}²⁵. Genotyping was performed on postnatal day (P)7-10 using primers 1700 S (TCCATGGTT TCGCGAGAGCG), 1842 AS (TCCCTATTGGGACGCAGTGG) and 2394 AS (CAGCATCATGACAATGTCTCCA). For all experiments we used mice from both genders, unless indicated otherwise. The mice were individually housed with food and water available *ad libitum* and in 12:12 hrs light/dark cycles. All experiments were approved by local and national ethical committees.

Primary antibodies

The anti-*Shank2* SA5193 antibody has been characterized previously²⁵ the following antibodies were from commercial suppliers: anti-GluA1 (Cat. No. 182 003), anti-GluA2 (Cat. No. 182 103), anti-Nlgn3 (Cat. No. 129 113) (all Synaptic Systems, Goettingen, Germany), anti-β3-Tubulin (Cat. No. MRB-435P) (Covance, Brussels, Belgium) and Aldolase C (Cat. No. 12065) (Santa Cruz, Dallas, U.S.A.)

Golgi stainings

Adult mouse cerebella were dissected and prepared using the FD Rapid GolgiStain Kit (NeuroTechnologies, Vilnius, Lithuania). Serial coronal sections of 150 μm were collected from WT and global *Shank2*^{-/-} mice and Z-stack images were taken using an upright Axioscope (Carl Zeiss, Jena, Germany). Distal dendrites of Purkinje cells were traced for spine analysis.

Electron microscopy

Adult mice were transcardially perfused with fixative (2 % paraformaldehyde, 2.5 % glutaraldehyde, 1 % saccharose in 0.1 M cacodylate buffer, pH 7.3) and their cerebella were dissected and post-fixed overnight at 4 °C. After dehydration and staining with 2 % uranyl acetate, the material was embedded in epoxy resin. Ultrathin sections were cut using an ultramicrotome (Ultracut UCT, Leica). After lead citrate staining, sections from WT and global *Shank2*^{-/-} mice were examined using an electron microscope (JEM 1400 TEM, Jeol). For ultrastructural PSD analysis, spine synapses have been selected in the distal molecular layer where the parallel fiber-Purkinje cell (PF-PC) contacts greatly outnumber other types of synapses.

Biochemistry

Adult mouse cerebella were homogenized on ice in HEPES-buffered sucrose (320 mM sucrose, 5 mM HEPES, pH 7.4) containing protease inhibitor mixture (Roche, Mannheim, Germany). The homogenate was centrifuged (1.000 x g, 4 °C) to remove cell debris and nuclei. The supernatant was further centrifuged (12.000 x g, 4 °C) to obtain a pellet containing the cerebellar synaptosomes. Equal amounts of 10-20 μg protein per lane were separated by SDS-polyacrylamide gel electrophoresis and blotted onto polyvinylidene fluoride membranes using standard protocols. After incubation with primary antibodies (1:1.000 for anti-Shank1, anti-GluA1, anti-GluA2, anti Nlgn3; 1:10.000 for anti-β3-Tubulin), immunoreactivity was visualized on X-ray film (GE Healthcare, Freiburg, Germany) using HRP-conjugated secondary antibodies (Dako; Hamburg, Germany) and the SuperSignal detection system (Thermo Scientific). For quantification, the films were scanned, the grey value of each band was analysed by ImageJ (National Institutes of Health, Bethesda, MD, USA) and normalized to the grey value of β3-Tubulin.

Immunohistochemistry

Mouse brains were snap-frozen after removal without perfusion. Tissue was sectioned at 7 μm using a cryostat at -20°C and a knife temperature of -14°C . Sections were air-dried on superfrost glass and stored at -80°C . For staining sections were defrosted at room temperature (RT) for 60 min and subsequently washed with -20°C MeOH for 3 min followed by 3X 10 min of PBS wash. To permeabilize membranes, sections were incubated for 60 min in 0.5% Triton X-100 in PBS at RT and washed 3X in PBS for 10 min. Following a 60 min incubation in 5% BSA (in PBS) at RT and subsequent PBS washing, sections were incubated in SA5193 antibody (1:1000, dissolved in 2% bovine-serum albumin, see ³⁶) O/N at 4°C . The sections were then washed for 3X 10 minutes in PBS followed by 120 min of fluorescent antibody staining (1:200, Donkey anti goat-Cy3) in 2% BSA at RT. After the fluorescent antibody a wash of 3X 10 min of PBS was followed by 2X 10 min wash with PB. The sections were then put for 10 min in DAPI (200 μl in 50 ml 0.1 M PB). This was concluded by a 2x 10 min PB wash. For Zebrin (Adolase C) we used a different approach after the defrosting of sections at RT. These slices were washed with 10 min 4% PFA followed by 20 min of methanol and subsequently by 2 min PBS and 30 min 100 ml PBS (with 2 ml 30% H_2O_2 + 0.8 ml sodium azide). Here after a wash of 2 min PBS and 2X 2 min in PBS (with 1 L PBS, 5 g protifar and 1.5 g glycine, sections were incubated in the primary antibody for Adolase C (1:1000; Santa Cruz, Dallas, U.S.A., Cat. No. 12065) O/N at 4°C . The sections were then washed for 3X 10 minutes in PBS followed by 90 min of fluorescent antibody staining (1:200, donkey anti goat-Cy3; The Jackson Laboratory, Sacramento, U.S.A., Cat. No 705-165-147) in 2% BSA at RT. After the fluorescent antibody a wash of 3X 10 min of PBS was followed by 2X 10 min wash with PB. The sections were then put for 10 min in DAPI (ThermoFisher Scientific, Waltham, U.S.A., Cat. No. D3571; 200 μl in 50 ml 0.1 M PB). This was concluded by a 2X 10 min PB wash. Following PBS washing, the sections were thionin-stained and permount-covered using standard protocols. All immunohistological stainings have successfully been replicated on multiple occasions.

Ex vivo electrophysiology

Following decapitation of mice under isoflurane anaesthesia, the cerebellum was removed into an ice-cold 'slicing medium', containing (in mM) 240 sucrose, 2.5 KCL, 1.25 Na_2HPO_4 , 2 MgSO_4 , 1 CaCl_2 , 26 NaHCO_3 and 10 D-Glucose, that was carbogenated continuously (95% O_2 and 5% CO_2). Sagittal slices, 250 μm thick, of the cerebellar vermis were cut using a vibrotome (VT1200S, Leica) and put in carbogenated artificial cerebrospinal fluid (ACSF) containing (in mM): 124 NaCl, 5 KCL, 1.25 Na_2HPO_4 , 2 MgSO_4 , 2 CaCl_2 , 26 NaHCO_3 and 20 D-Glucose, for at least one hour at $34\pm 1^{\circ}\text{C}$ before the start of the experiment. Slice physiology was done at room temperature $21\pm 1^{\circ}\text{C}$ or $33\pm 1^{\circ}\text{C}$ as indicated in the results section and in the presence of 100 μM picrotoxin except for the sIPSCs recordings. Whole-cell patch clamp recording were performed with an EPC9 amplifier (HEKA Electronics, Lambrecht, Germany). Recordings were excluded if the series (Rs) or input resistances (Ri) changed by more than 15% during the experiment, which was determined using a hyperpolarizing voltage step relative to the -65 mV holding potential. Data analysis (rise times (10-90% for EPSC and action potentials)), decay time (τ) for EPSC and IPSC amplitudes, action potential threshold (identified by steepest slope in membrane potential prior to action potential) and AHP amplitude (minimal membrane potential relative to the action potential threshold)) was performed using Clampfit software (Molecular Devices).

For whole-cell recordings Purkinje cells (PCs) were visualized using an upright microscope (Axioskop 2 FS, Carl Zeiss) equipped with a 40X objective. Recording electrodes (3-5 M Ω , 1.65 mm OD and 1.11 mm ID, World Precision Instruments, Sarasota, FL, USA) were filled with an intracellular solution containing (mM): 120 K-Gluconate, 9 KCL, 10 KOH, 4 NaCL, 10 HEPES, 28.5 Sucrose, 4 Na_2ATP , 0.4 Na_3GTP (pH 7.25-7.35 with an osmolarity of 295 ± 5). Note that we adjusted the osmolarity using sucrose ^{46,60}. For the recording of sIPSCs we used an intracellular solution containing (mM): 150 CsCl, 1.5 MgCl_2 , 0.5 EGTA, 4 Na_2ATP , 0.4 Na_3GTP , 10 HEPES, 5 QX314 (pH 7.25-7.35 with an osmolarity of 295 ± 5). For extracellular stimulation of parallel fibers (PFs), similar patch electrodes were filled with ACSF and positioned in the upper third of the molecular layer lateral to the patched Purkinje cell. The stimulation intensity was set to evoke an EPSC of 300 ± 50 pA (typically 3-6 μA stimulation intensity). For PF-PC transmission we used various inter-stimulus intervals (50-200 ms) (see Fig. 2). For recordings of spontaneously occurring IPSCs (sIPSCs) we used the previously mentioned K^+ -based internal and recorded their occurrence during at least 120 s.

For climbing fiber stimulation similar electrodes (filled with ACSF) were positioned near the patched Purkinje cell soma in the surrounding granule layer. We selected those recordings in which climbing fiber stimuli elicited clear all-or-none responses and lacked the co-activation of Purkinje cell

axons (identifiable by backpropagating action potentials) for further analysis. For CF elimination experimental tissue was prepared in a similar way for all age groups. We systematically scanned the granule cell layer to elicit CF responses and recorded PC responses (using an intracellular solution containing (in mM): 115 CsMeO₃, 20 CsCl, 2.5 MgCl₂, 10 HEPES, 0.6 EGTA, 4 Na₂ATP, 0.4 Na₃GTP, 10 Na-phosphocreatine) at -20 mV holding potential to prevent voltage escape during the CF-responses. For CF-PC transmission we evaluated the paired pulse ratio at 50 ms stimulus interval. To evaluate the complex spike waveforms we analysed the amplitude of the Na⁺-spike and the amplitude of the first Ca²⁺-spikelet evoked during the LTD-tetanus⁶¹. Current clamp recordings were corrected off-line for the calculated liquid junction potential (-10.2 mV).

The synaptic (LTP, LTD) and intrinsic plasticity protocols were recorded from lobules 5/6 and conducted as described previously^{32,46}. In short, for synaptic plasticity all recordings were done in voltage-clamp, except for the tetanus, which consisted of single-pulsed PF-stimulation at 1 Hz for 5 min (LTP) or single-pulsed PF + single-pulsed CF stimulation (5 ms interval) at 1 Hz for 5 min (LTD). We evaluated the synaptic plasticity by the change in PF-EPSC (presented at 0.05 Hz) relative to the mean value calculated during the last 5 min pre-tetanus. For intrinsic plasticity we utilized the PF-LTP tetanus (but without bias currents, i.e., I=0 pA) and evaluated the impact on the number of action potentials evoked by 300 pA current injections during 500 ms (presented at 0.05 Hz).

Extracellular Purkinje cell recordings

In vivo recordings were performed as recently described³³. An immobilizing pedestal was fixed on the skull and a craniotomy (Ø 3 mm) was performed on the occipital bone. After recovery of 5 days, mice were head-fixed and body restrained for recordings. Single unit recording was identified by the presence of a short simple spike pause (>6 ms) after each complex spike. Purkinje cells were recorded from vermal lobules I-V and X using single barrel (2.0 mm OD, 1.16 mm ID, Harvard Apparatus, MA, USA) and double barrel (theta septum, 1.5 OD, 1.02 ID; World Precision Instruments) borosilicate glass pipettes. *In vivo* recordings were analysed offline using Spiketrain (Neurasmus BV, Rotterdam, The Netherlands, www.neurasmus.com) and custom scripts in MatLab (Mathworks, Natick, MA, USA). The CV is calculated by dividing the SD by the mean of the interspike intervals, whereas CV2 is calculated as $2 * |IS|_{n+1} - |IS|_n| / (|IS|_{n+1} + |IS|_n)$.

Compensatory eye movements

Mice between 8 and 10 weeks of age were prepared for head-restrained recordings of compensatory eye movements. These types of recordings have been described in detail previously³². In order to head restrain the mice during the eye movement task, a small pedestal was attached using Optibond primer and adhesive (Kerr, Bioggio, Switzerland) under isoflurane anaesthesia in O₂ (induction with 4% and maintained at 1.5% concentration). After a recovery period of two to three days, mice were head-restrained by fixation using the pedestal in the experimental setup. A round screen with a random dotted pattern ('drum') surrounded the mouse during the experiment. The optokinetic reflex (OKR), vestibulo-ocular reflex (VOR) and the light-guided vestibulo-ocular reflex (VVOR) were induced using a sinusoidal rotation of the drum in light (OKR), rotation of the table in the dark (VOR) or the rotation of the table (VVOR) in the light. The motor behaviour was assessed by rotating the table and/or drum at 0.1 to 1 Hz with a fixed 5° amplitude. In order to evaluate motor learning, a mismatch between visual and vestibular input was created. Rotating both the visual and vestibular stimuli in phase (at the same amplitude) induced a decrease of gain; rotating the drum at greater amplitude relative to the table induced the so-called phase reversal of the VOR (day 1, 5° phase difference; day 2, 7.5°; day 3-4, 10°). Rotating the visual and vestibular stimuli out of phase (at the same amplitude) induced the VOR gain increase. All training protocols were induced at 0.6 Hz with table rotation amplitude of 5°. For eye illumination during the experiments two table-fixed infrared emitters (output 600 mW, dispersion angle 7°, peak wavelength 880 nm) and a third emitter, which produced the tracked corneal reflection (CR), were mounted to the camera and aligned horizontally with the optical axis of the camera. Eye movements were recorded with eye-tracking software (ETL-200, ISCAN systems, Burlington, NA, USA). Gain and phase values of eye movements were calculated using MatLab (MathWorks).

Eyeblink conditioning

Mice of 12-15 weeks of age were prepared for head-restrained eyeblink conditioning³⁹. In short, a small brass pedestal was attached to the skull using Optibond primer and adhesive (Kerr) and Charisma (Heraeus Kulzer, Armonk, NY, USA), under isoflurane anaesthesia. Three to five days after

surgery, mice were habituated during two short (30-45 min) sessions on two days in a sound- and light-isolating chamber which houses the eyeblink set up. During these sessions mice were head-fixed and suspended over a foam cylindrical treadmill. While no stimuli were presented, a 27.5 gauge needle through which US air-puffs are delivered was positioned at 5 mm from the center of the left cornea, a green LED (\varnothing 5 mm) that delivers the CS was placed 5 cm in front of the mouse, and an GMR magnetometer (NVE, Eden Prairie, MN, USA) was fixed above the left eye. During five subsequent acquisition training days, this sensor measured the distance of a miniscule magnet (1.5x0.7x0.5 mm) that was placed on the left lower eyelid with high accuracy, while 200 paired trials were presented, usually spaced 10 ± 2 s apart, plus the time needed for a sporadic unstable eyelid to stabilize in open position. Each paired trial consisted of a 280 ms green LED CS, co-terminating with a 30 ms airpuff (30 psi, through an MPPI-3 pressure injector; ASI, Eugene, OR, USA). All experiments were performed at approximately the same time of day by the same experimenter. Individual eyeblink traces were analyzed using custom LabVIEW (National Instruments, Austin, TX, USA) or MATLAB (Mathworks, Natick, MA, USA) scripts. Trials with significant activity in a 500 ms pre-CS baseline period were regarded as invalid for further analysis. Valid trials were aligned by making the mean of their baseline activity zero, and the average amplitude of all post-US unconditioned blink responses was used to denote 100% eyelid closure. From this, the average eyelid closure as a percentage from baseline to full closure at the end of the CS-US interval was calculated over all valid trials. To calculate percentage of CRs, trials were judged to contain a CR if the eye closed for more than 5% between 50-250 ms after CS and the CR reached its peak after 100 ms.

ErasmusLadder

The ErasmusLadder (Noldus, Wageningen, Netherlands) is a fully automated system consisting of a horizontal ladder between two shelter boxes. It has 37 rungs on each side, spaced 15 mm apart, and attached to custom-made pressure sensors that are continuously monitored. In order to create a left-right alternating pattern, even rungs on one side and odd rungs on the other side are elevated by 6 mm. Prototype testing revealed that optimum forepaw displacement for mice is about 6 cm in a single step at medium high velocity, which is the distance between 3 consecutive elevated rungs and is defined as efficient step in the text (for more details, see ³⁷). It is clear from previous studies that mice improve their walking efficiency over training sessions by increasing the number of efficient steps relative to steps of lower sizes ³⁷. In the current study, mice (male, 15-18 weeks old) were tested in 6 daily sessions consisting of 2 unperturbed sessions, 1 session with a fixed obstacle in the middle of the ladder and 3 perturbed sessions. During the first three sessions, mice were trained to walk between two shelter boxes for 50 trials each day. In the perturbed sessions, a sudden appearance of a rising rung on the right side of the mouse was used as the unconditional stimulus (US). A 15 kHz tone was used as the conditional stimulus (CS) and preceded the US by 200 ms in CS-US paired trials. CS-only trials and paired trials were randomly distributed among 50 trials. There were twice as many paired trials as CS-only trials. Step length and step time were defined as the distance and time between two consecutive touches from the right front limb. To estimate motor adaptation in CS-only trials, we calculated step speed (step length/step time) using only the steps within 1 s before and 1 s after the CS. The speed ratio during conditioning was defined as the speed post-CS divided by the speed pre-CS.

General behavioural analyses

Behavioural experiments were performed using *L7-Shank2^{-/-}* and WT littermate controls aged 8-16 weeks during the light period of their diurnal cycle. The mice used in the general behavioural experiments described here underwent multiple tests.

For the PhenoTyper test, mice were placed in a homecage-like apparatus (Noldus) with *ad libitum* access to food and water, and left to explore for 30 minutes. Locomotion was recorded using the automated software Noldus Ethovision XT 11 and distance and speed were calculated.

For the open field test, mice were placed in a novel circular, brightly-lit 110-cm-diameter open arena for 10 min. Locomotion was recorded using the automated software Noldus Ethovision XT 11 and total distance travelled, as well as average speed were calculated. During analysis the arena was subdivided in three concentric zones named the inner (25 cm), middle (15 cm) and outer zone (15 cm), and percentage of time in each zone was calculated.

For the three-chamber social interaction test, age and gender-matched WT target subjects (Stranger 1 and 2) were habituated for 5 consecutive days before beginning of testing by being placed inside round metal-wired cages. On the test day, experimental mice were placed in the central chamber of a clear Plexiglas box (60 x 35 cm) divided into three interconnected chambers. After habituation for 5 min. an unfamiliar mouse (Stranger 1; S1) was introduced into a wire cage in one of

the side-chambers and an empty wire cage in the other side-chamber. The dividers were then raised and the test mouse was allowed to freely explore all three chambers over a 5-minute session. Next, the mouse remained in the chamber with stranger 1 for an additional 5-minute session. Subsequently, a novel stranger mouse (Stranger 2; S2) was placed in the previously empty wire cage and again the test mouse was left to explore for 5 min. Time spent in each chamber, as well as overall locomotion, was calculated using the automated software Noldus Ethovision XT 11. Preference indices were calculated by subtracting the time spent with the empty wire cage from the time spent with stranger 1 ($S1 - E$), and subtracting the time spent with stranger 1 from time spent with stranger 2 ($S2 - S1$).

For the T-maze spontaneous alternation test, mice were placed at the base of a T-maze (arm length 50 cm) and were given the choice to freely explore either the right or left arm of the maze for 10 consecutive trials. A choice was assumed to be made when mice stepped into an arm with all four paws. At that moment the gate to that arm was closed and the animal was allowed to explore the arm for 5 s. Then, the mouse was gently placed back at the base of the T-maze for the next trial. When the mouse chose a similar arm at two consecutive trials, this was scored as number of repeats, indicative of repetitive behaviour.

For the grooming test, mice were removed from their homecage, received a single puff of water spray and placed in clean transparent cages (15 x 15 x 20 cm) under bright light for 15 min. Behaviour was recorded with a high-speed camera (30Hz full frame rate), and time spent grooming was scored by two independent raters. All types of grooming – paw licking, nose and head self-grooming, body grooming, leg grooming and tail/genital grooming – were scored.

For the marble burying test, Makrolon cages (50 x 26 x 18 cm) were filled with 4 cm of bedding material and 20 glass marbles, which were arranged in an equidistant 4 x 5 grid. Animals were given access to the marbles for 30 min. Marbles 100% covered by bedding were scored as buried and marbles covered partially contributed 50% to the total score.

For the olfactory test, a piece (1.25 g) of cookie was put into the subject's cage each day for three consecutive days, and checked for complete consumption the following day. For 24 hrs before the test phase, mice were completely food-deprived. Subjects were placed in a clean Makrolon cage (50 x 26 x 18 cm) with 4 cm of clean bedding, and allowed to habituate for 5 min. Then, a piece of cookie (1.25 g) was hidden in a random corner in the cage at 1 cm depth. Latency to find the cookie was recorded for a maximum of 15 mins (900 s).

Data analysis

In the text, mean \pm SD values are presented, in the figures SEM-values are reported, and p-values smaller than 0.05 are considered significantly different. Two-sided Student's *t*-tests were performed, unless stated otherwise. For a complete representation of the data we have included a detailed overview of all statistics in Supplementary Table 1. Additionally, since the L7-Cre line was shown to reveal germline deletions (see also [44]) and since the potential impact of cerebellar Purkinje cells on general cognitive tests is widely debated^{62,63}, we have checked for heterozygous germline deletions in our L7-Shank2 mice and statistically excluded the possibility they could have influenced our conclusions on the non-cerebellar paradigms (Supplementary Table 1).

Data Availability

In addition to our supplementary data file, which contains data points that support the findings of this study, data sets are available from the corresponding authors upon request.

Acknowledgements

We thank M. Rutteman, L. Post E. Haasdijk, A.C. Ypelaar, R. de Avila Freire, Laurens W.J. Bosman, B.H.A. Urbanus, J. van Dongen, P. Bacilio, K. Knape, R. Zienecker and N. Beth for their technical assistance and N. Rahmati, S. Gornati, O.H.J. Eelkman Rooda, C.B. Schäfer and A. Plauška for discussions; and the Dutch Organisation for Medical Sciences (ZonMw), NWO (ALW), Neuro-Basic, ERC-Advanced and ERC-POC for their financial support to S.A.K., M.S., F.E.H. and C.I.D.Z. This work was further supported by the Innovative Medicines Initiative Joint Undertaking under grant agreement n° 115300, resources of which are composed of financial contribution from the European Union's Seventh Framework Programme (FP7/2007-2013) and EFPIA companies' in kind contribution (to T.M.B.), the Deutsche Forschungsgemeinschaft (DFG SFB1149 to T.M.B.), the Baustein program of Ulm University (L.SBN.0081 to M.J.S.) and the 2013R1A3A2042197 grant from the National Research Foundation, the Ministry of Science, ICT & Future Planning, Republic of Korea (to M.G.L.).

Author contributions

S.P. wrote the manuscript, designed, performed and analysed the *ex vivo* electrophysiological recordings, eye movement adaptations and ASD related behaviours. M.M.B contributed to major revision steps of the manuscript. C.M.R. performed and analysed Golgi stainings and electron microscopy. M.M.B., H.Z., and B.W. designed, performed and analysed the *in vivo* electrophysiological recordings. K.Z. designed, performed and analysed the ErasmusLadder experiments. J.S. analysed, designed and supported in the ASD related behaviour experiments. H.J.B. and M.M.B. designed and analysed the eye blink experiments. M.G.L., M.J.S. and T.M.B. provided global *Shank2*^{-/-} mice; M.J.S. and T.M.B. the *Shank2*^{flox/flox} mice and contributed to critical revisions of the manuscript. S.A.K., M.S., F.E.H., and C.I.D.Z. provided major revisions to the manuscript and guided the project. All authors discussed the results and implications and commented on the manuscript. The authors declare no competing financial or non-financial interests.

References

1. Chen, J.A., *et al.* The Emerging Picture of Autism Spectrum Disorder: Genetics and Pathology. *Annual Review of Pathology: Mechanisms of Disease* 10, 111-144 (2015).
2. Kanner, L. Autistic disturbances of affective contact. *Nervous child* 2, 217-250 (1943).
3. Zwaigenbaum, L., Bryson, S. & Garon, N. Early identification of autism spectrum disorders. *Behavioural brain research* 251, 133-146 (2013).
4. Sears, L.L., Finn, P.R. & Steinmetz, J.E. Abnormal classical eye-blink conditioning in autism. *Journal of autism and developmental disorders* 24, 737-751 (1994).
5. Oristaglio, J., *et al.* Children with autism spectrum disorders show abnormal conditioned response timing on delay, but not trace, eyeblink conditioning. *Neuroscience* 248, 708-718 (2013).
6. Takarae, Y., *et al.* Pursuit eye movement deficits in autism. *Brain* 127, 2584-2594 (2004).
7. Schmitt, L.M., Cook, E.H., Sweeney, J.A. & Mosconi, M.W. Saccadic eye movement abnormalities in autism spectrum disorder indicate dysfunctions in cerebellum and brainstem. *Molecular autism* 5, 47 (2014).
8. Marko, M.K., *et al.* Behavioural and neural basis of anomalous motor learning in children with autism. *Brain* 138, 784-797 (2015).
9. Mostofsky, S.H., Goldberg, M.C., Landa, R.J. & Denckla, M.B. Evidence for a deficit in procedural learning in children and adolescents with autism: implications for cerebellar contribution. *Journal of the International Neuropsychological Society* 6, 752-759 (2000).
10. Memari, A.H., Ghanouni, P., Shayestehfar, M. & Ghaheri, B. Postural control impairments in individuals with autism spectrum disorder: a critical review of current literature. *Asian journal of sports medicine* 5(2014).
11. Stins, J.F., *et al.* Attentional and sensory contributions to postural sway in children with autism spectrum disorder. *Gait & Posture* (2015).
12. Schmahmann, J.D. The role of the cerebellum in cognition and emotion: personal reflections since 1982 on the dysmetria of thought hypothesis, and its historical evolution from theory to therapy. *Neuropsychology review* 20, 236-260 (2010).
13. Allen, G. The cerebellum in autism. *Clinical Neuropsychiatry* 2, 321-337 (2005).
14. Bailey, A., *et al.* A clinicopathological study of autism. *Brain* 121, 889-905 (1998).
15. Stoodley, C.J. Distinct regions of the cerebellum show gray matter decreases in autism, ADHD, and developmental dyslexia. *Frontiers in systems neuroscience* 8(2014).
16. Menashe, I., *et al.* Co-expression profiling of autism genes in the mouse brain. *PLoS computational biology* 9, e1003128 (2013).
17. Grabrucker, A.M., Schmeisser, M.J., Schoen, M. & Boeckers, T.M. Postsynaptic ProSAP/Shank scaffolds in the cross-hair of synaptopathies. *Trends in cell biology* 21, 594-603 (2011).
18. Zoghbi, H.Y. & Bear, M.F. Synaptic dysfunction in neurodevelopmental disorders associated with autism and intellectual disabilities. *Cold Spring Harbor perspectives in biology* 4, a009886 (2012).
19. Bourgeron, T. From the genetic architecture to synaptic plasticity in autism spectrum disorder. *Nature Reviews Neuroscience* 16, 551-563 (2015).
20. Leblond, C.S., *et al.* Genetic and functional analyses of SHANK2 mutations suggest a multiple hit model of autism spectrum disorders. *PLoS Genet* 8, e1002521 (2012).
21. Durand, C.M., *et al.* Mutations in the gene encoding the synaptic scaffolding protein SHANK3 are associated with autism spectrum disorders. *Nat Genet* 39, 25-27 (2007).
22. Berkel, S., *et al.* Mutations in the SHANK2 synaptic scaffolding gene in autism spectrum disorder and mental retardation. *Nature genetics* 42, 489-491 (2010).
23. Sato, D., *et al.* SHANK1 Deletions in Males with Autism Spectrum Disorder. *Am J Hum Genet* 90, 879-887 (2012).
24. Mei, Y., *et al.* Adult restoration of Shank3 expression rescues selective autistic-like phenotypes. *Nature* 530, 481-484 (2016).
25. Schmeisser, M.J., *et al.* Autistic-like behaviours and hyperactivity in mice lacking ProSAP1/Shank2. *Nature* 486, 256-260 (2012).
26. Won, H., *et al.* Autistic-like social behaviour in Shank2-mutant mice improved by restoring NMDA receptor function. *Nature* 486, 261-265 (2012).
27. Böckers, T.M., *et al.* Differential expression and dendritic transcript localization of Shank family members: identification of a dendritic targeting element in the 3' untranslated region of Shank1 mRNA. *Molecular and Cellular Neuroscience* 26, 182-190 (2004).
28. Boeckers, T.M., *et al.* Proline-rich synapse-associated proteins ProSAP1 and ProSAP2 interact with synaptic proteins of the SAPAP/GKAP family. *Biochemical and biophysical research communications* 264, 247-252 (1999).

29. Leblond, C.S., *et al.* Meta-analysis of SHANK mutations in autism spectrum disorders: a gradient of severity in cognitive impairments. *PLoS genetics* 10, e1004580 (2014).
30. Sala, C., *et al.* Shank synaptic scaffold proteins: keys to understanding the pathogenesis of autism and other synaptic disorders. *Journal of neurochemistry* (2015).
31. Hashimoto, K. & Kano, M. Functional differentiation of multiple climbing fiber inputs during synapse elimination in the developing cerebellum. *Neuron* 38, 785-796 (2003).
32. Schonewille, M., *et al.* Purkinje cell-specific knockout of the protein phosphatase PP2B impairs potentiation and cerebellar motor learning. *Neuron* 67, 618-628 (2010).
33. Zhou, H., *et al.* Cerebellar modules operate at different frequencies. *eLife*, e02536-e02536 (2014).
34. Wulff, P., *et al.* Synaptic inhibition of Purkinje cells mediates consolidation of vestibulo-cerebellar motor learning. *Nature neuroscience* 12, 1042-1049 (2009).
35. Häusser, M. & Clark, B.A. Tonic synaptic inhibition modulates neuronal output pattern and spatiotemporal synaptic integration. *Neuron* 19, 665-678 (1997).
36. Boeckers, T.M., *et al.* Proline-rich synapse-associated protein-1/cortactin binding protein 1 (ProSAP1/CortBP1) is a PDZ-domain protein highly enriched in the postsynaptic density. *The Journal of neuroscience* 19, 6506-6518 (1999).
37. Veloz, M.F.V., *et al.* Cerebellar control of gait and interlimb coordination. *Brain Structure and Function*, 1-24 (2014).
38. De Zeeuw, C.I. & Ten Brinke, M.M. Motor Learning and the Cerebellum. *Cold Spring Harbor perspectives in biology* 7, a021683 (2015).
39. ten Brinke, M.M., *et al.* Evolving Models of Pavlovian Conditioning: Cerebellar Cortical Dynamics in Awake Behaving Mice. *Cell Rep* 13, 1977-1988 (2015).
40. Becker, E.B. & Stoodley, C.J. Autism spectrum disorder and the cerebellum. *International review of neurobiology* 113, 1 (2013).
41. Koekkoek, S.K.E., *et al.* Deletion of FMR1 in Purkinje cells enhances parallel fiber LTD, enlarges spines, and attenuates cerebellar eyelid conditioning in Fragile X syndrome. *Neuron* 47, 339-352 (2005).
42. Baudouin, S.J., *et al.* Shared synaptic pathophysiology in syndromic and nonsyndromic rodent models of autism. *Science* 338, 128-132 (2012).
43. Piochon, C., *et al.* Cerebellar plasticity and motor learning deficits in a copy-number variation mouse model of autism. *Nature communications* 5(2014).
44. Tsai, P.T., *et al.* Autistic-like behaviour and cerebellar dysfunction in Purkinje cell Tsc1 mutant mice. *Nature* 488, 647-651 (2012).
45. Kloth, A.D., *et al.* Cerebellar associative sensory learning defects in five mouse autism models. *eLife* 4, e06085 (2015).
46. Belmeguenai, A., *et al.* Intrinsic plasticity complements long-term potentiation in parallel fiber input gain control in cerebellar Purkinje cells. *The Journal of neuroscience* 30, 13630-13643 (2010).
47. Jiang, Y.-h. & Ehlers, M.D. Modeling Autism by< i> SHANK</i> Gene Mutations in Mice. *Neuron* 78, 8-27 (2013).
48. De Zeeuw, C.I., *et al.* Spatiotemporal firing patterns in the cerebellum. *Nature Reviews Neuroscience* 12, 327-344 (2011).
49. van Alphen, A.M. & De Zeeuw, C.I. Cerebellar LTD facilitates but is not essential for long-term adaptation of the vestibulo-ocular reflex. *Eur J Neurosci* 16, 486-490 (2002).
50. Arons, M.H., *et al.* Autism-associated mutations in ProSAP2/Shank3 impair synaptic transmission and neurexin-neurologin-mediated transsynaptic signaling. *J Neurosci* 32, 14966-14978 (2012).
51. Szapiro, G. & Barbour, B. Multiple climbing fibers signal to molecular layer interneurons exclusively via glutamate spillover. *Nat Neurosci* 10, 735-742 (2007).
52. Badura, A., *et al.* Climbing fiber input shapes reciprocity of Purkinje cell firing. *Neuron* 78, 700-713 (2013).
53. Galliano, E., *et al.* Silencing the majority of cerebellar granule cells uncovers their essential role in motor learning and consolidation. *Cell reports* 3, 1239-1251 (2013).
54. Barski, J.J., Dethleffsen, K. & Meyer, M. Cre recombinase expression in cerebellar Purkinje cells. *genesis* 28, 93-98 (2000).
55. Schmidt-Supprian, M. & Rajewsky, K. Vagaries of conditional gene targeting. *Nat Immunol* 8, 665-668 (2007).
56. Kobayashi, Y. & Hensch, T.K. Germline recombination by conditional gene targeting with Parvalbumin-Cre lines. *Front Neural Circuits* 7, 168 (2013).
57. Mosconi, M.W., *et al.* The role of cerebellar circuitry alterations in the pathophysiology of autism spectrum disorders. *Front Neurosci* 9, 296 (2015).
58. Wang, S.S.H., Kloth, A.D. & Badura, A. The cerebellum, sensitive periods, and autism. *Neuron* 83, 518-532 (2014).
59. Silva-Santos, S., *et al.* Ube3a reinstatement identifies distinct developmental windows in a murine Angelman syndrome model. *J Clin Invest* 125, 2069-2076 (2015).
60. Coesmans, M., Weber, J.T., De Zeeuw, C.I. & Hansel, C. Bidirectional parallel fiber plasticity in the cerebellum under climbing fiber control. *Neuron* 44, 691-700 (2004).
61. van Woerden, G.M., *et al.* betaCaMKII controls the direction of plasticity at parallel fiber-Purkinje cell synapses. *Nat Neurosci* 12, 823-825 (2009).
62. Galliano, E., *et al.* Synaptic transmission and plasticity at inputs to murine cerebellar Purkinje cells are largely dispensable for standard nonmotor tasks. *J Neurosci* 33, 12599-12618 (2013).
63. Rochefort, C., *et al.* Cerebellum shapes hippocampal spatial code. *Science* 334, 385-389 (2011).

Figure Legends

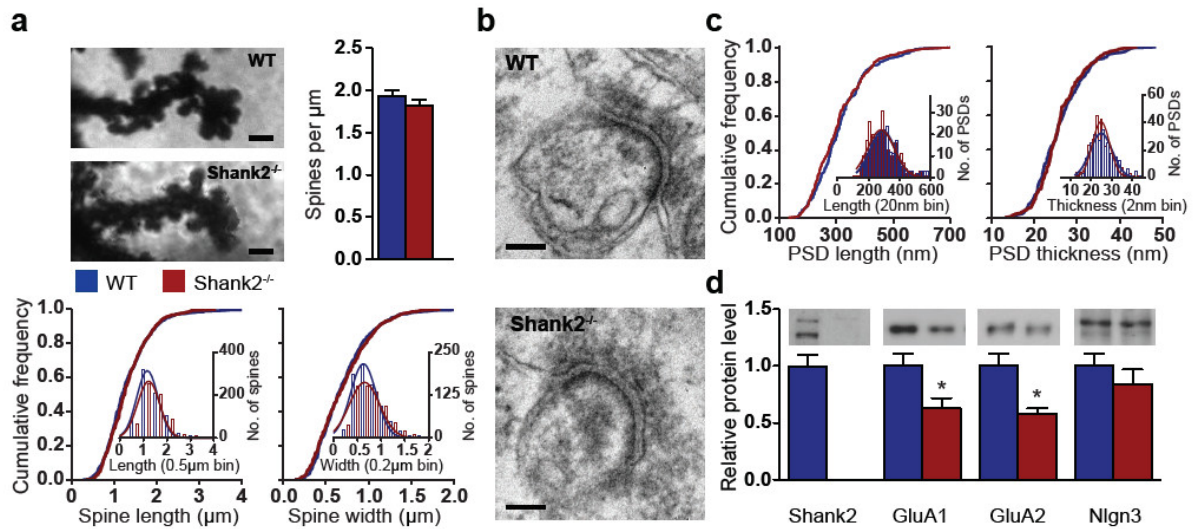


Figure 1. Reduction of AMPA receptor subunits in *Shank2*^{-/-} cerebellar synaptosomes, but no changes in spine and PSD morphology in the distal molecular layer (DML). (a) Representative images (Golgi-Cox staining) of distal Purkinje cell dendrites in the DML, quantification of spine density (WT, $n=97/4$, dendrites/mice; *Shank2*^{-/-}, $n=89/4$, $P=0.2$, MWU-test) and cumulative frequency plots of spine length ($P=0.4$, MWU-test) and thickness ($P=1$, MWU-test) in WT ($n=748/4$ spines/mice) and *Shank2*^{-/-} mice ($n=639/4$) as indicated. Scale bar: 1 μm . (b,c) Representative images (electron microscopy) of spine synapses in the DML and cumulative frequency plots of PSD length (WT, $n=226/4$, PSDs/mice; *Shank2*^{-/-}, $n=243/4$, $P=0.3$) and thickness (WT, $n=223/4$; *Shank2*^{-/-}, $n=233/4$, $P=0.9$) as indicated. Scale bar: 100 nm. (d) Biochemical analysis of *Shank2* (WT, $n=12$ synaptosomes; *Shank2*^{-/-}, $n=6$), *GluA1* (WT, $n=12$ synaptosomes; *Shank2*^{-/-}, $n=6$, $P=0.041$) *GluA2* (WT, $n=11$; *Shank2*^{-/-}, $n=5$, $P=0.014$), and *Nlgn3* (WT, $n=12$; *Shank2*^{-/-}, $n=6$, $P=0.4$) in cerebellar synaptosomes from WT and *Shank2*^{-/-} mice as indicated. Data in bar graphs are presented as mean \pm SEM; single asterisks indicates $p < 0.05$. Two-sided *t*-tests were used, unless stated otherwise.

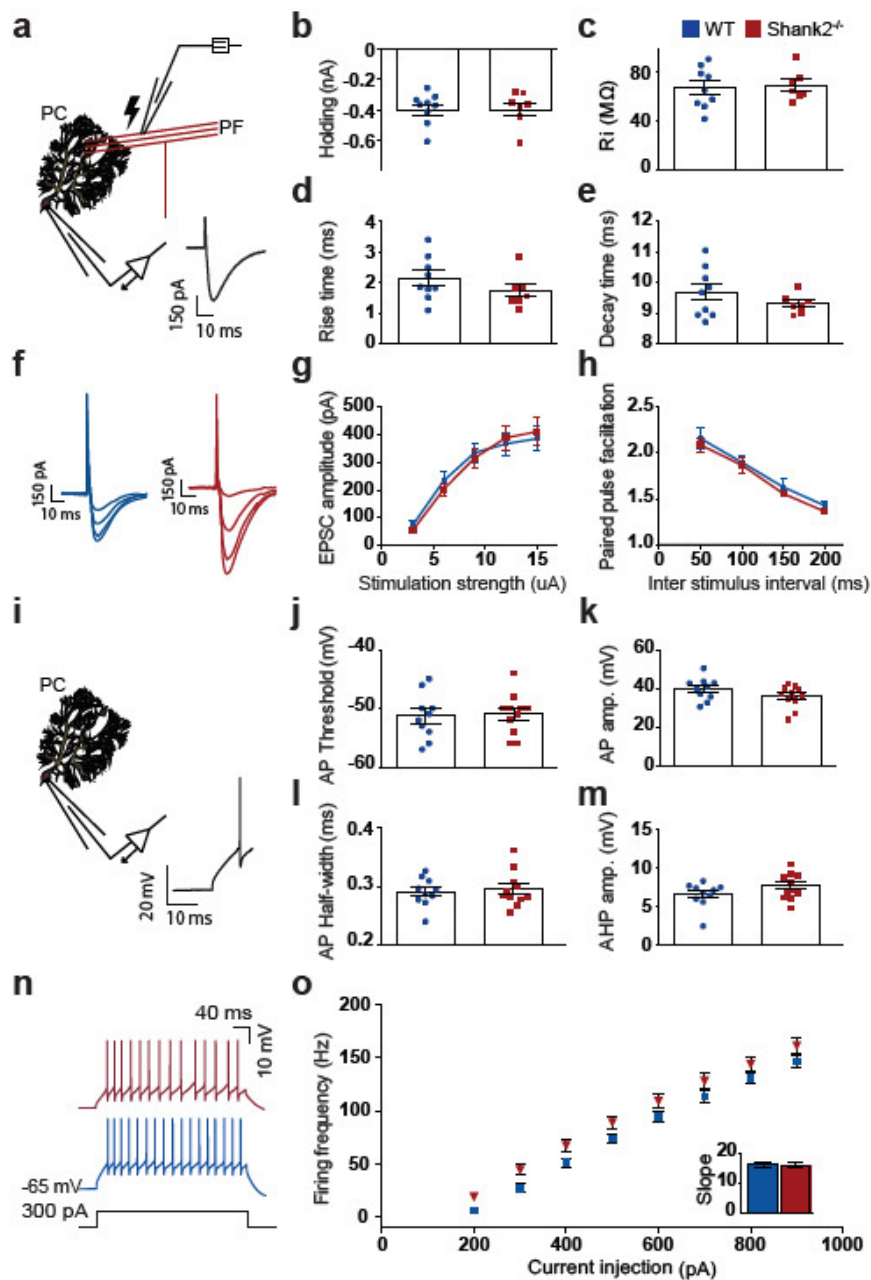


Figure 2. No changes in excited synaptic and intrinsic properties in *Shank2*^{-/-} Purkinje cells ex vivo. (a) Recording configuration for voltage clamp recordings of PF-PC synaptic transmission. Inset: an example PF-EPSC. (b-e) With comparable holding current (at -65mV) ($P=1$) and input resistance (R_i) ($P=0.8$), PC EPSC rise time ($P=0.2$) and EPSC decay time ($P=0.3$) are not different between WT ($n=9/6$, cells/animals) and *Shank2*^{-/-} ($n=7/6$). (f) Example EPSCs in response to 3, 6, 9, 12, and 15 μ A stimulation. (g,h) Varying stimulation strength ($P=0.9$, repeated-measures ANOVA) and inter-stimulus interval ($P=0.2$, repeated-measures ANOVA) evoked comparable EPSC amplitude or facilitation (WT, $n=11/3$; *Shank2*^{-/-} 15/3). (i) Recording configuration for whole cell recording. Inset: an example action potential. (j-m) Action potential threshold ($P=0.8$), amplitude ($P=0.1$), half-width ($P=0.7$), and afterhyperpolarization ($P=0.2$) were not different (WT, $n=10/6$; *Shank2*^{-/-}, $n=11/6$). (n) Example traces of intrinsic Purkinje cell excitability as apparent from action potential firing evoked by 300 pA current injections. (o) No difference in evoked firing frequency relative to various levels of current injections (WT, $n=10/5$; *Shank2*^{-/-}, $n=11/5$, $P=0.1$, repeated-measures ANOVA). Inset barplot shows average slope of firing rate per current step ($P=1$). Data are represented as mean \pm SEM. Two-sided t-tests were used, unless stated otherwise.

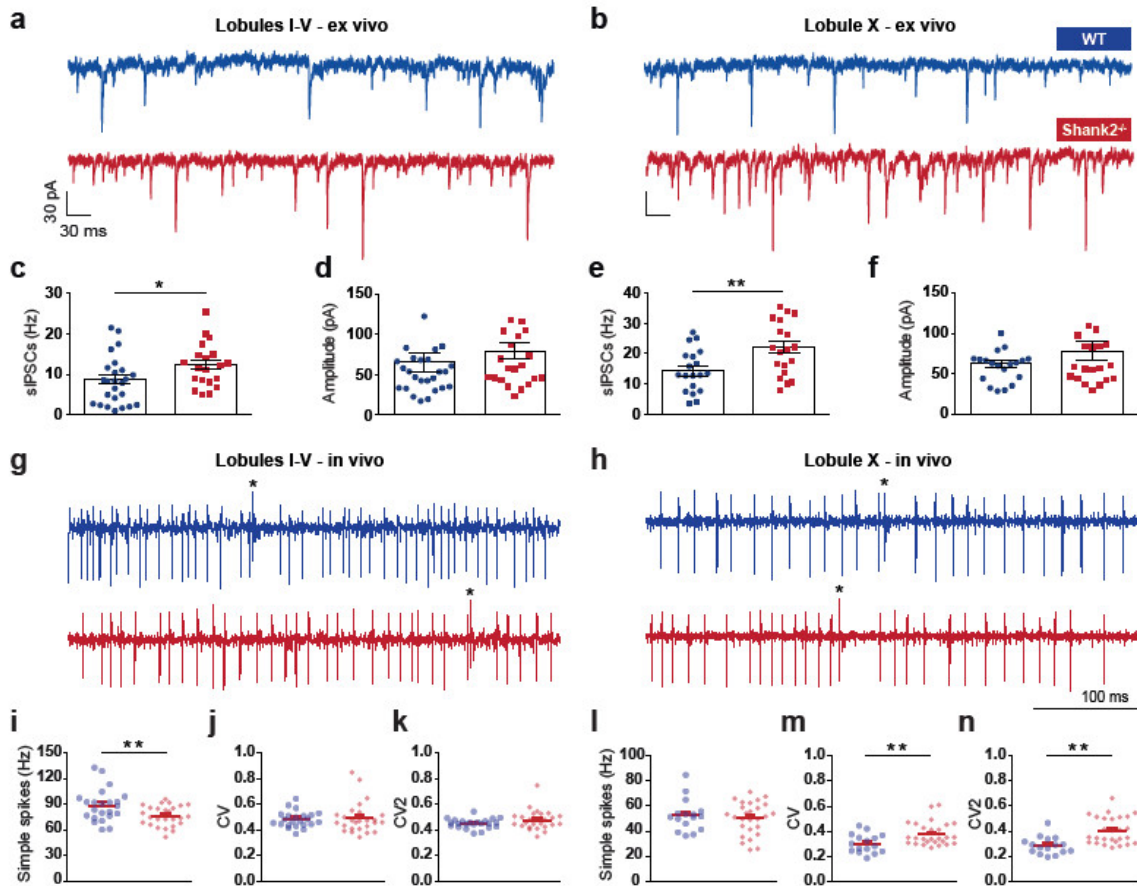


Figure 3. Increased spontaneous inhibitory events and higher simple spike irregularity in *Shank2*^{-/-} Purkinje cells. (a, b) Example of spontaneous firing inhibitory post synaptic currents (sIPSCs) in lobules I-V and X. (c, e) A higher frequency of sIPSCs is found in both anterior (I-V) ($P=0.0295$) and posterior (X) lobules ($P=0.0079$) in *Shank2*^{-/-} PCs (anterior: WT, $n=25/3$, cells/animals; *Shank2*^{-/-}, $n=20/3$; posterior: WT, $n=19/3$; *Shank2*^{-/-}, $n=19/3$). (d, f) There were no significant differences in sIPSC amplitudes anteriorly ($P=0.1$) or posteriorly ($P=0.5$). (g, h) Extracellular traces of PCs recorded in anterior (left) and posterior (right) lobules in the cerebellum, in WT and *Shank2*^{-/-}. Asterisks denote complex spikes. (i, j, k) Simple spike (SS) firing frequency was significantly lower ($P=0.0096$) in *Shank2*^{-/-} ($n=26/3$) compared to wildtype ($n = 23/3$), whereas the coefficient of variation (CV) ($P=0.7$) and CV2 ($P=0.1$) did not differ. (l, m, n) In posterior lobule X, while SS firing frequency was similar ($P=0.6$), CV ($P=0.0086$) and CV2 ($P=0.0003$) were significantly higher in *Shank2*^{-/-} ($n=27/3$) compared to WT ($n = 16/3$). Data are represented as mean \pm SEM. Single and double asterisks indicate $P<0.05$ and $P<0.01$, respectively. Two-sided *t*-tests were used, unless stated otherwise.

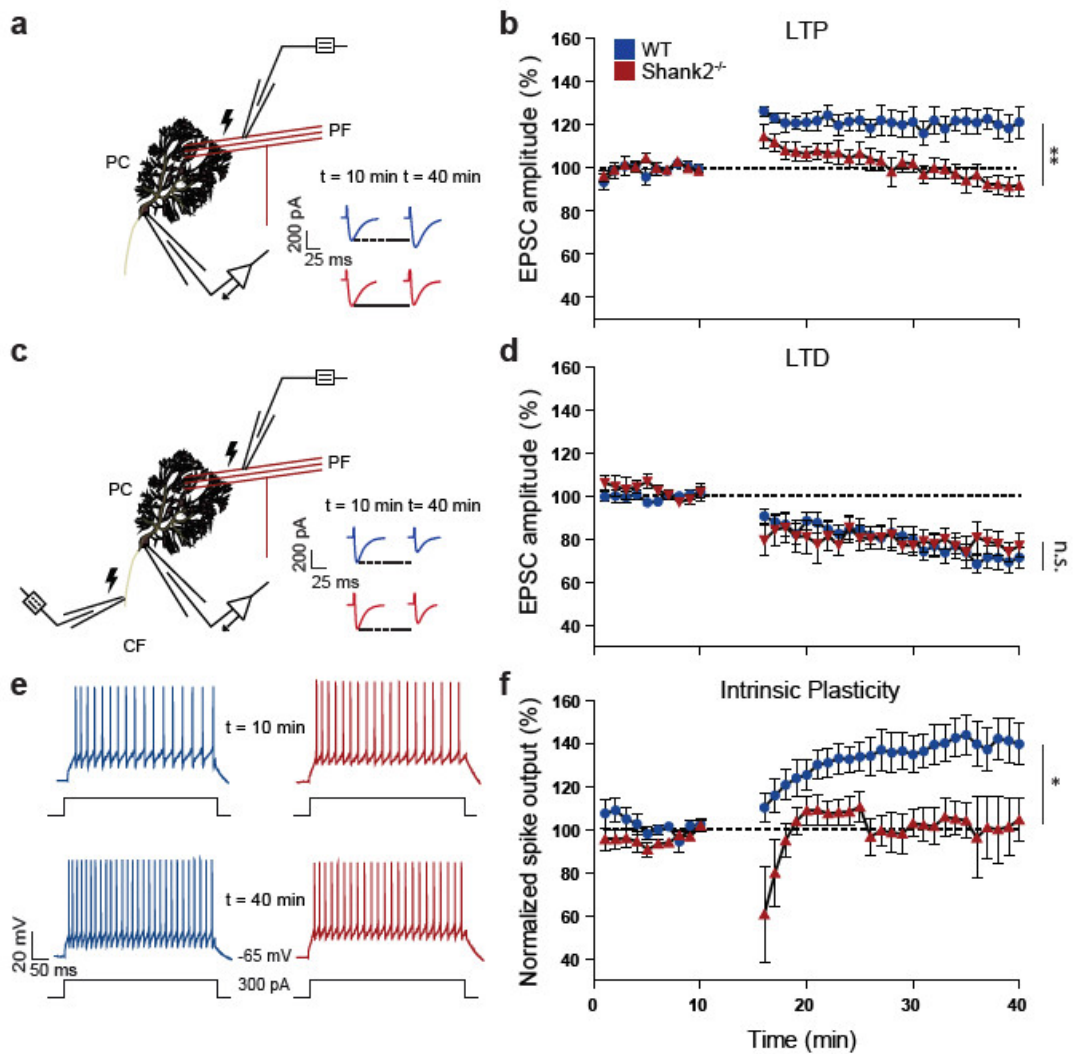


Figure 4. Impaired synaptic and intrinsic plasticity in *Shank2*^{-/-} ex vivo. (a) Recording configuration for PF-LTP experiments. Inset: example of 5 averaged EPSCs for WT (blue) and *Shank2*^{-/-} (red) before LTP induction (at 10 minutes) and after LTP induction (at 40 min). (b) LTP experiment with 5 min PF stimulation at 1Hz inducing LTP in WTs ($n=7/6$, cells/animals, $P=0.0027$) but not in *Shank2*^{-/-} PCs ($n=12/6$, $P=0.3$), which is reflected in the difference between genotypes ($P=0.0066$). (c) Recording configuration for PF-LTD experiments. Inset: example traces as in a. (d) LTD is induced in both WT ($n=9/6$, $P<0.0001$) and *Shank2*^{-/-} ($n=7/6$, $P=0.0009$) PCs, to a similar degree ($P=1$). (e) Example of traces for intrinsic plasticity with current injections of 300 pA. (f) LTP induction protocol induced enhanced spike output in WT PCs ($n=5/4$, $P=0.0053$), but not in *Shank2*^{-/-} PCs ($n=5/4$, $P=0.5$), as reflected in their difference ($P=0.0201$). Data are represented as mean \pm SEM. Single and double asterisks indicate $P<0.05$ and $P<0.01$, respectively. All tests were repeated-measures ANOVAs.

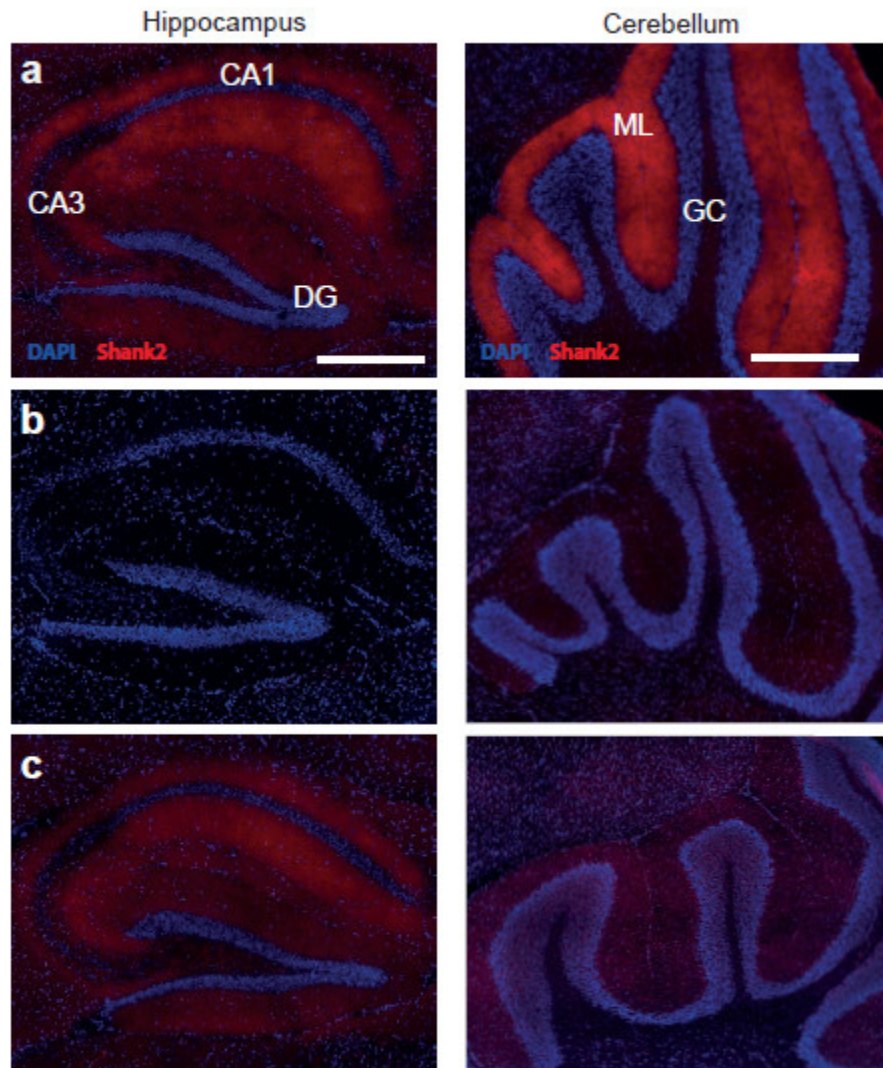


Figure 5. Immunohistological staining of the Shank2 protein in $Shank2^{-/-}$ and $L7-Shank2^{-/-}$ hippocampus and cerebellum. (a) Sagittal cryosection of hippocampal Shank2 (red) and nucleus staining (DAPI; blue) in a WT (left) $L7-Shank2^{-/-}$. Scale bar: 500 μm . Sagittal cryosection of cerebellar Shank2 staining (right). Scale bar: 200 μm . (b) Staining for Shank2 in the hippocampus and cerebellum of the global $Shank2^{-/-}$ shows absence of expression. (c) The $L7-Shank2^{-/-}$ shows expression in the hippocampus, but not in the molecular layer of the cerebellum.

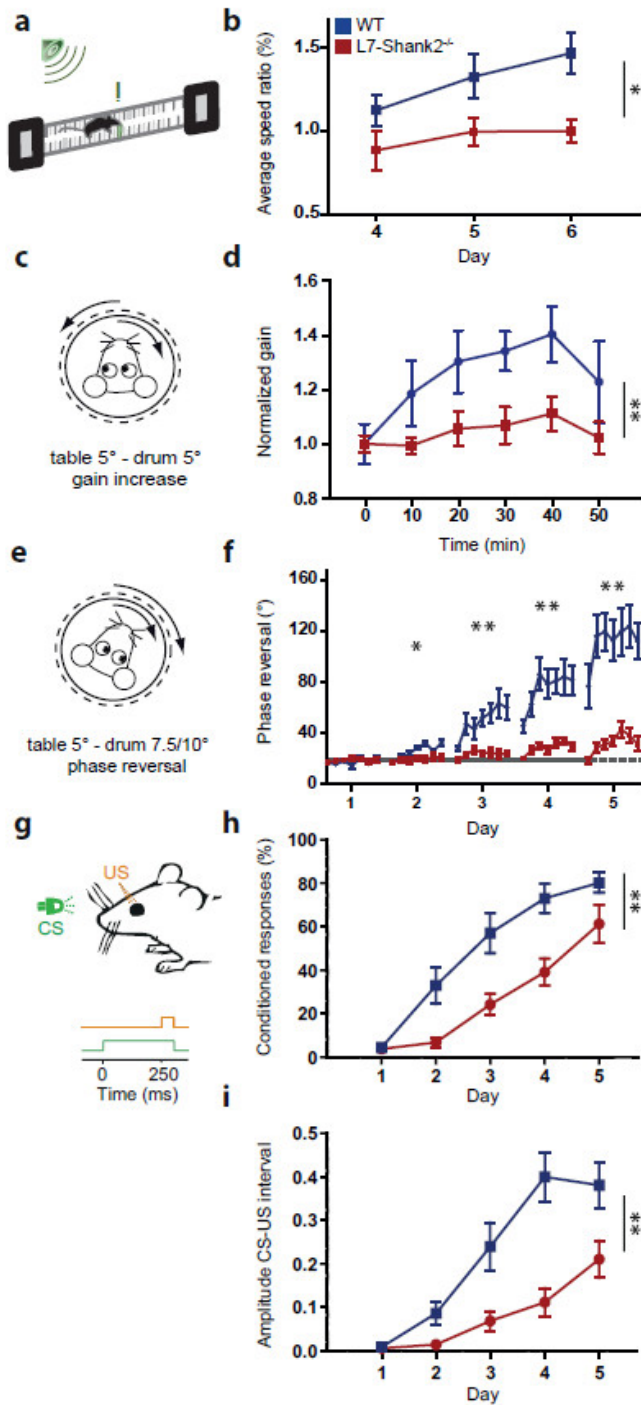


Figure 6. L7-Shank2^{-/-} mice show impaired motor learning. (a, b) After three days of training, WT (n=9) but not L7-Shank2^{-/-} mice (n=6) ($P=0.018$) learned to increase their speed during a conditioned ErasmusLadder test using tone-cued rung displacements. (c, d) In vestibulo-ocular reflex (VOR) gain increase training, L7-Shank2^{-/-} mice (n=8) were not able to adapt their gain like WT mice did (n=7) ($P=0.006$). (e, f) L7-Shank2^{-/-} mutants (n=9) did not adapt their VOR phase following a reversal training paradigm, whereas WT (n=9) did (2nd day, $P=0.047$; 3rd, $P=0.0013$; 4th, $P<0.0001$; 5th, $P=0.0003$). (g, h, i) Impaired percentage ($P=0.0013$) and amplitude ($P=0.0009$) of conditioned responses (CRs) in L7-Shank2^{-/-} mice (n=10) compared to WT (n=11) in an eyeblink conditioning paradigm (200 paired trials daily). Data are represented as mean \pm SEM. Single and double asterisks indicate $P<0.05$ and $P<0.01$, respectively. All tests were repeated-measures ANOVAs.

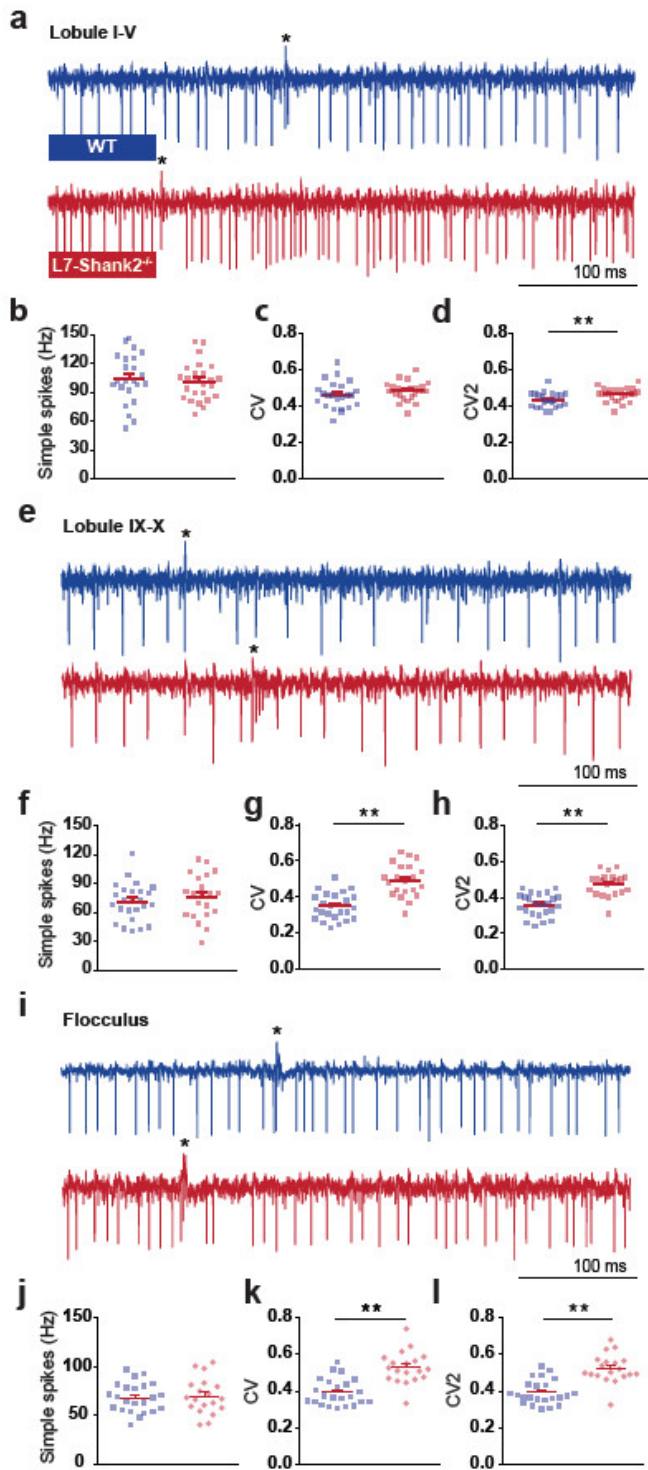


Figure 7. *In vivo* simple spike firing characteristics in L7-Shank2^{-/-} Purkinje cells. (a) Extracellular PC traces recorded from anterior lobules (I-V) in WT (top) and L7-Shank2^{-/-} (bottom) mice. (b,c,d) Firing characteristics in the anterior lobules reveal a difference in CV2 ($P=0.0092$) between L7-Shank2^{-/-} ($n=25/3$, cells/animals) and WT ($n=23/3$). (e) Example PC traces from posterior lobules (IX-X). (f,g,h) PCs from the posterior cerebellum in L7-Shank2^{-/-} ($n=21/3$) showed significantly higher CV ($P<0.0001$) and CV2 ($P<0.0001$) values compared to WT ($n=25/3$). (i) Example PC traces from posteriorly located flocculus, which is responsible for VOR learning. (j,k,l) Again, L7-Shank2^{-/-} ($n=19/2$) shows significantly higher CV ($P<0.0001$) and CV2 ($P<0.0001$) values than WT ($n=23/2$). Double asterisks denote $P<0.01$. All tests were two-sided *t*-tests.

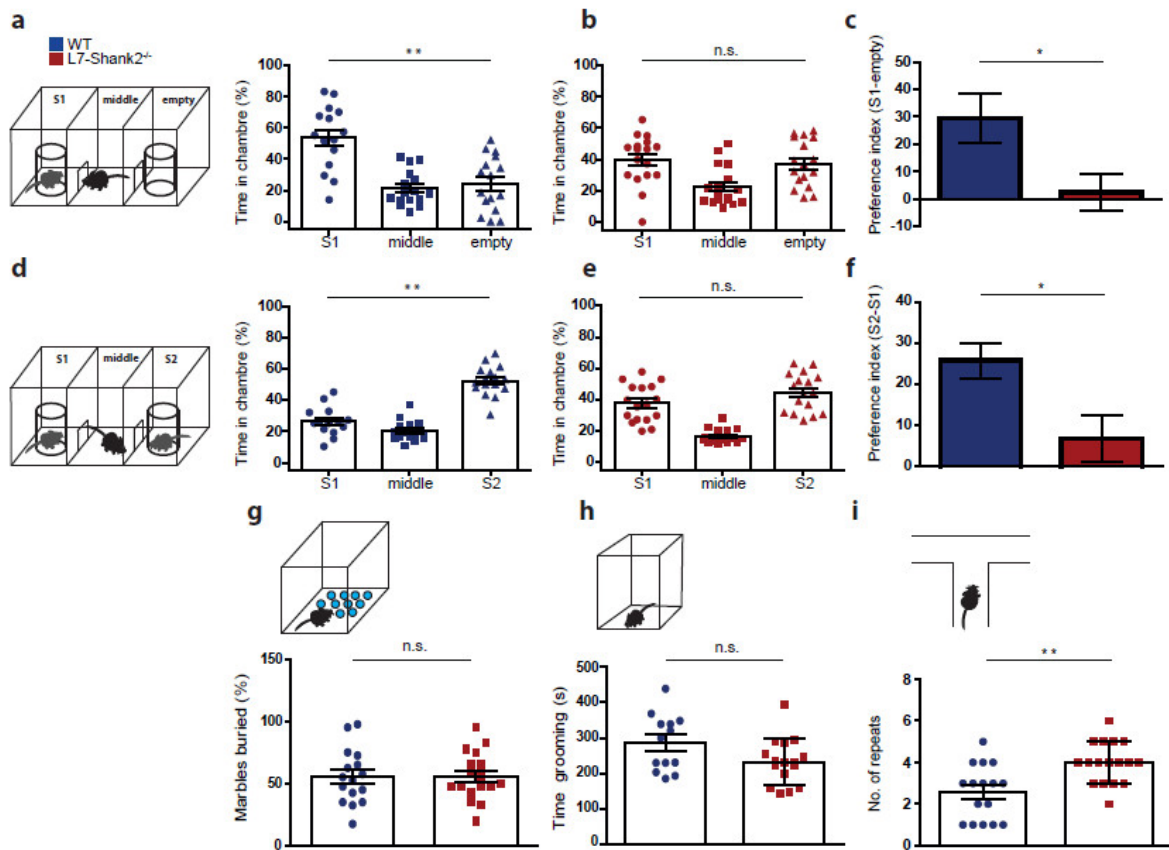


Figure 8. *L7-Shank2^{-/-}* mice show social impairment and signs of task-specific repetitive behaviour. (a) Three-chamber social interaction evaluated by relative time spent in each chamber. WT ($n=16$) prefer to spend time in the room with the stranger 1 mouse (S1), compared to the empty room ($P=0.0002$, MWU-test). (b) This was not the case for *L7-Shank2^{-/-}* ($n=17$) mice ($P=0.7$, MWU-test). (c) The preference index (S1-empty) confirms the difference between genotypes ($P=0.021$). (d) Following the introduction of a second stranger (S2), WT ($n=16$) prefer to spend time in the chamber with S2 compared to that with S1 ($P=0.0001$, MWU-test). (e) The *L7-Shank2^{-/-}* mice ($n=17$) did not show a preference for newly introduced S2 ($P=0.1$, MWU-test). (f) The S1-S2 preference index indicates that WT prefer S2 more than *L7-Shank2^{-/-}* do ($P=0.013$). (g) No difference was found in a marble burying task indicative of anxious and/or repetitive behaviour (WT, $n=16$; *L7-Shank2^{-/-}*, $n=17$, $P=1.0$). (h) *L7-Shank2^{-/-}* ($n=16$) seemed to trend towards less grooming than WT ($n=13$) ($P=0.054$). (i) T-maze paradigm showed less consecutive alternations in *L7-Shank2^{-/-}* ($n=17$) compared to WT ($n=16$) ($P=0.0023$, MWU-test) indicating repetitive decision-making. Data are presented as mean \pm SEM. Single and double asterisks indicate $P<0.05$ and $P<0.01$, respectively. Two-sided t-tests were used, unless stated otherwise.

CHAPTER

8

Discussion

Research in a nutshell

The cerebellum is a powerful processing as well as adaptive neural machine that we use to improve our performance in a multitude of tasks.

Among many components of the cerebellum, the vestibulocerebellum, is the oldest part and occupies the major portion of the primitive cerebellum, as described in **Chapter 1**. It is very important for our everyday life by virtue of providing information about our self-motion and spatial orientation relative to the world, which is required for ensuring gaze stability, balance and postural control.

Using the vestibulocerebellum as model systems, this thesis focusses on unravelling the complex cellular and circuit mechanisms underpinning simple and skilled motor behaviours. By employing a multi-level cellular and systems neuroscience approach combining *in vivo* and *in vitro* electrophysiology, two-photon imaging, viral-based manipulation techniques and quantitative behavioral paradigms, such as eye movement adaptation and eyeblink conditioning, we aimed to generate new insights into the neural computations that underlie cerebellar-dependent motor control and motor learning. (**Chapter 2, 3, 5**)

Experimentally-based knowledge about neural networks in the cerebellum has also become increasingly more detailed. Physiologically, it has been shown previously that the PCs firing activity is correlated to the expression of zebrin and we found that this differentiation is mediated by TRPC3 channels (**Chapter 3**). Anatomically, BIN cells have been added to the neural wiring diagram of the floccular cortical network, albeit that their functional roles are still unclear (**Chapter 4**). Also, more and more proteins have been identified to be important to motor behaviors and learning, i.e. PP2B and Shisa6 (**Chapter 6**).

Beyond motor control, the cerebellum may be involved in processes as diverse as emotion, speech, working memory and social behavior. In this thesis, we found that genetic deletion of Shank2, a human risk gene for ASD, exclusively in Purkinje cells affected their activity and induced autism-like behavior (**Chapter 7**).

Cerebellar uniformity and heterogeneity

The cerebellar cortex is generally assumed to have a uniform cytoarchitecture with regard to cell types and their connectivity. It consists of three stereotyped layers: the molecular layer, the Purkinje cell layer and the granular cell layer, which further contain seven main neuronal cell types across all the lobules: Purkinje cells (PCs), granule cells, Golgi cells, Lugaro cells, unipolar brush cells, basket cells and stellate cells. As the sole output of the cortex, Purkinje cells are considered to be the most important neurons among these. They are located in a monolayer and have an extensive fan-like dendritic tree projecting into the molecular layer, where they receive input from two major types of excitatory fibers, climbing fibers and parallel fibers. Purkinje cell axons make inhibitory synaptic contact with the cerebellar nuclei neurons. In turn, these neurons form most of the output from the cerebellum, providing connections to a wide range of other CNS structures to control and adjust a wide range of movement features include timing^{1,2}, amplitude^{3,4} and coordination⁵ as well as cognitive processes⁶. It was originally thought that the neural computation was the same throughout the cerebellum and

that regional differences in function were to a large extent due to differences in input and output connectivity⁷. However, this pluriformity of behavioral features does not match with the homogeneity of the structure and cyto-architecture of the cerebellum. How is the homogeneously organized cerebellum able to control the different features it control? A widely held assumption is that the same neural computation is performed throughout a uniform circuitry in the adult mammalian cerebellar cortex, and differences in function can be explained primarily by distinct patterns of input and output connectivity. However, accumulating evidence from anatomy, genetics and physiology suggest this is not the whole picture.

Why Zebrin-identity?

Recently, cellular heterogeneity has been proposed to be the driver of differentiation in the behavior of individual cells that operate within a larger ensemble⁸. It has been uncovered that the PCs can be divided into two main groups with a distinct firing behavior^{9,10}. One group, consisting of PCs that are positive for the glycolytic enzyme aldolase C, also referred to as zebrin II^{11,12}, shows relatively low simple spike firing rates, whereas the PCs in the other group that form zebrin-negative zones, fire at higher rates⁹. The symmetric pattern of alternating zebrin-positive (Z+) and zebrin-negative (Z-) bands of PCs is highly conserved in all vertebrate classes, varying from birds and mice up to primates including humans¹³⁻¹⁸. Cerebellar modules are closed loop circuits consisting of interconnections between specific sub-regions of the inferior olive, cerebellar cortex and cerebellar nuclei. Interestingly, zebrin is capable to demarcate olivocerebellar modules, anatomically defined operational units each consisting of a closed loop between the inferior olive, parasagittal bands of the cerebellar cortex and the cerebellar nuclei^{19,20}.

Following zebrin, other proteins with a similar or complementary striped expression pattern were identified, of which some are linked to synaptic input or spiking activity, including: excitatory amino acid transporter 4 (EAAT4)²¹⁻²³, metabotropic glutamate receptor 1b (mGluR1b)^{22,24}, inositol-3-phosphate receptor 1 (IP3R1)²⁵, PLC β 4²⁶, PKC δ ²⁷, NCS1²⁸ and GABAB2^{29,30}. EAAT4 is expressed in Z+ PCs where it reduces glutamate spill-over, and thereby can attenuate the induction of long-term depression of parallel fiber to PC synapses (PF-PC LTD)²². Inversely, only Z- PCs express mGluR1b and PLC β 4; mGluR1 is required for correct climbing fiber elimination and for PF-PC LTD, as it is activated by spill-over glutamate³¹, and loss of PLC β 4, as the downstream mediator of mGluR1, has similar effects³². The isoform mGluR1a, which unlike mGluR1b is not expressed in any pattern, is considered to be responsible for these effects³³.

Why TRPC3?

The proteins of transient receptor potential cation channel (TRPC) family, which are calcium-permeable upon activation by phospholipase C or diacylglycerol, are widely expressed in the brain and critically involved in the development and maintenance of synaptic transmission³⁴⁻³⁷. Of these, TRPC1 and TRPC3 are prominently expressed in the cerebellum, but TRPC3 is most abundant in PCs³⁴. It is suggested that TRPC3 could mediate the slow excitatory postsynaptic potential following activation of mGluR1b^{24,33,37}.

In **Chapter 3**, we demonstrated that zebrin-negative PCs show a relatively high expression of TRPC3, which has a dominant impact on its electrophysiological features.

Indeed, gain-of-function and loss-of-function mutations in the gene encoding for TRPC3 selectively affected activity in the zebrin-negative modules. Also, we show that adaptation of compensatory eye movements, which is controlled by Z+-modules in the vestibulocerebellum^{9,38}, is not affected by the loss of TRPC3 function, whereas the learning rate during eyeblink conditioning, which is linked to the Z- modules^{39,40}, is decreased after PC-specific ablation of TRPC3, highlighting the behavioral relevance of firing rate modulation by TRPC3. Together, TRPC3 appears to be a key player in the molecular machinery responsible for differential control over PC activity and function.

Although our current study has its main focus on the differential contribution of TRPC3 at the cell and systems physiological level, it is tempting to speculate how the loss of TRPC3 in PCs results in an eyeblink conditioning phenotype without affecting VOR adaptation. The reduction in firing rate of zebrin-negative PCs may directly contribute to the impaired conditioning. The suppression of simple spike firing that correlates with the conditioned response could be occluded by the lower resting rate in L7-TPRC3^{KO} mice. Alternatively, PF-PC LTD could play a role as it is in line with the simple spike suppression and blocking TRPC3 function completely abolishes this form of LTD⁴¹. However, genetically ablating PF-PC LTD did not affect the ability to perform eyeblink conditioning successfully⁴², arguing against an exclusive role for this form of plasticity. Schreurs and colleagues demonstrated that intrinsic excitability is increased after eyeblink conditioning⁴³. A third option could be that TRPC3 also affects the adaptive increase of excitability, intrinsic plasticity, which is calcium-activated potassium channel function dependent⁴⁴, and thereby delays the expression of a conditioned blink response. All three options would not necessarily affect VOR adaptation and could contribute to the deficits in eyeblink conditioning, but given the relatively mild phenotype, one or two could be sufficient.

Why two processing systems?

So far, a clear picture come to emerge that slower movements, such as compensatory eye and head movements, are controlled by zebrin-positive modules operating at lower firing rate and using rate coding downstream, whereas faster movements, such as eyeblink responses or limb activity during locomotion, may depend on zebrin-negative modules operating at higher firing rate and fast rebound activity in the cerebellar nuclei^{2,45}. In other words, zebrin-positive modules readily allow for potentiation mechanisms via rate coding, while zebrin-negative modules easily allow for suppression mechanisms by temporal coding using rebound bursting.

In this regard, a more conceptual question can be brought about: why are there, at least, two different types of PCs or two information processing systems?

An appealing hypothesis is that zebrin-negative and zebrin-positive bands control two muscles with opposing functions, e.g. a flexor and an extensor. However, trans-synaptic retrograde tracing using rabies virus from antagonist muscles demonstrated that although 3rd order labeling can be found in different parasagittal strips of PCs, there is no apparent division in zebrin-negative and zebrin-positive strips⁴⁶. A second possibility would be that individual muscles are controlled by either only zebrin-negative or zebrin-positive strips, or a combination of both, when needed. In the vestibulocerebellum of the pigeon, each movement direction is controlled by a set of zebrin-negative and zebrin-positive bands¹³. In this configuration each PC within the set, or separately, would then serve a distinct function, for which it is optimized

by gene expression patterns. This dissociation of function could entail e.g. timing versus coordination⁴⁷ or moving versus holding still⁴⁸, although none of these distinctions have been linked to specific zebrin-identified modules. Thirdly, it may be the net polarity of the connectivity downstream of the cerebellar nuclei up to the motor neurons or the cerebral cortical neurons that determines the demand(s) of the module(s) involved⁴⁹. Module-specific driver lines would greatly aid to answer these questions, but are currently not available. Lastly, given that the most characteristic feature of all functions of the cerebellum is its ability to control timing at a high resolution, we would speculate that the higher firing rate renders the system become timing-sensitive and responds promptly, thereby avoiding dangerous and improving survival rate. This condition can be considered as a pulled string maintained at a high energy level that can be released on command and evoke very fast effects when needed, such as to protect one's eye with an eyeblink when a dangerous event is approaching.

Together, it is likely that proper cerebellar function is based on the presence of (at least) two *modi operandi* that offer a rich repertoire to acquire and control sensorimotor processes.

Revisiting the sites for VOR adaptation

The VOR, operating on basis of the vestibulocerebellum, is an adaptive control system that self-calibrates motor commands to achieve compensatory eye movements. It is mediated by a three-neuron-arc pathway: vestibular ganglion, vestibular nuclei and extraocular premotor neurons, but also independent on the cerebellum. In order to maintain a proper reflex throughout life, the VOR needs to be continuously adapted. This adaptive capability has been extensively investigated as a model of neural plasticity and considerable controversy has arisen concerning the specific neural site at which plastic modifications take place. Masao Ito first proposed the, still widespread believed, "flocculus hypothesis"⁵⁰, on the basis of the classic Marr-Albus theory^{51,52}. In his framework, Ito postulated that the parallel fiber-Purkinje cell synapse in the flocculus is the site of VOR adaptation, and the underlying mechanism is, what is known as, cerebellar LTD. In 1981, however, Miles and Lisberger proposed a different view - "vestibular nuclei hypothesis", which argue that when there is a visual-vestibular mismatch, floccular Purkinje cells outputs encoding the error signal, induce plastic changes in the level of FTNs in the vestibular nuclei, so that the vestibular nuclei instead of the flocculus, is the exclusive locus for VOR adaptive modifications. Over the years, as the evidence from electrophysiological experiments cumulated, Lisberger further modified "vestibular nuclei hypothesis" to "multisite hypothesis" that VOR motor learning lie in both the flocculus as well as the brain stem⁵³. However, none of them seem to perfectly be consistent with experimental data.

In **Chapter 5.2**, we designed an alternative experiment to probe this question based on a sigmoidal, rather than sinusoidal, combination of visual and vestibular stimuli which could optimally isolate the responses of Purkinje cells to a specific direction. We found convincing evidence showing that adaptation to the visual stimulus is more pronounced during contraversive head movements with respect to the recording side, which coincides with the preferred naso-temporal direction of eye movements driven visually. Moreover, the learned changes in gain-increase VOR adaptation were quantitatively reflected in the potentiated

activity of Purkinje cell simple spike, whereas there was no change in Purkinje cell responses after VOR gain decrease. Thus, we deduced that the locus of neural correlates for VOR adaptation is paradigm specific. In this scenario, we propose a modified viewpoint of the multisite hypothesis that gain-increase learning-related changes reside in the flocculus whereas gain-decrease learning is located in vestibular nucleus (**Chapter 1.2**). Specifically, VOR gain-increase learning is accomplished in the floccular complex by potentiation of Purkinje cell simple spike firing, whereas gain-decrease learning is induced by attenuation of the synaptic efficacy between primary vestibular afferents and their postsynaptic interneurons in the medial vestibular nuclei. In addition, we postulate that gain-increase learning is a feedback loop represented by the eye velocity signal originating from the inferior olive, whereas gain-decrease learning is likely to be a feedforward loop, both of which occur probably through an ever-updating internal model.

Cerebellar development and its role in eye movement control

The cerebellum is probably a prime model for the study of neurogenesis and circuit assembly^{54,55}. Indeed, cerebellar circuitry is highly conserved in phylogenesis, and modular and stereotyped from the morphological standpoint, thus providing a structure of choice to investigate the relationships between regional developmental defects and learning⁵⁶⁻⁵⁹. It has been reported that the functional establishment of cerebellar circuits, which involves in successive waves of progenitors proliferation and migration, imitate during early embryonic development⁶⁰, and marked morphological changes still occur after birth⁶¹ (see concrete developmental timelines for human and rodent in **Figure 2**). Importantly, early-term damage to the developing cerebellum is often associated with worse outcomes than that in adulthood⁶², indicating a developmental role in the later cerebellar function⁶³. Currently, it is a common view that many neurodevelopmental disorders are associated with cerebellar deficits⁶³⁻⁶⁵.

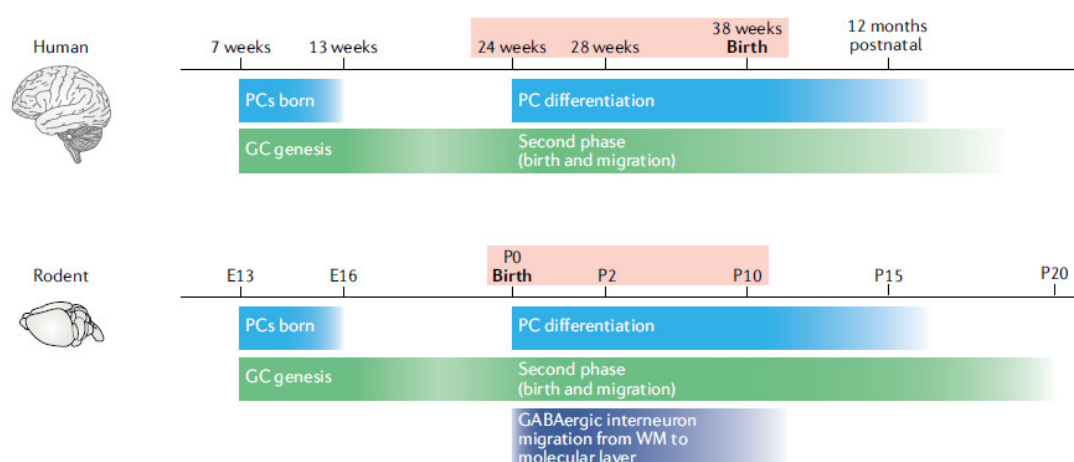


Figure 1. Human and rodent cerebellar developmental timelines. When the human and rodent timelines are aligned on the basis of major cellular and/or developmental events in the cerebellum, in humans the window of vulnerability to injury (indicated by pink shading) is mostly late gestational, whereas in preclinical rodent models it is mostly postnatal. Figure from (Sathyanesan A et al, 2019)⁶¹

Interestingly, Purkinje cell subtype specification likely takes place when Purkinje cells undergo terminal mitosis between E10 and E13⁶⁶. Birthdating studies have identified two distinct PC populations: an early-born cohort (E10-E11.5) destined to become zebrin-positive and a late-born cohort (E11.5-E13) destined to become zebrin-negative^{67,68}. This subtype organization is thought to play a key role in instructing circuit wiring into topographic maps⁶⁴. However, one critical question is when and how does the structural evolution turn into functional properties in the cerebellum?

Deciphering the ontogenetic establishment of cerebellar behavioral functions poses particular requirements to the experimental paradigm. Most important is the accessibility of experimental animals at the developmental stage of behavior onset as well as the possibility to apply methods to quantify the respective behavior and even to do electrophysiological recording of the neuronal firing activity. Compensatory eye movements, a group of reflexes including vestibule-ocular reflex (VOR) and optokinetic response (OKR) under the control of the cerebellar flocculus, are mostly well suited for such studies⁶⁹. It has been reported that there are two processes assure adequate compensatory eye movements throughout life⁷⁰⁻⁷²: first, the congenital reflexes need to develop, until they are identical to those observed in adults. Thereafter, an adaptive, plastic process maintains this normal performance by calibrating the response to reduce visual field motion during head perturbations. These events are essentially complete after embryogenesis in precocial animals, whereas some functional components mature only postnatally⁷³. In fact, according to behavioral experiments, VOR seems to reach an adult level until 3 months of life in human⁷⁴, but data in rodent are largely missing.

In **Chapter 6.1** we report that as early as P18-20, Purkinje cell specific PP2B knockout mice exhibited normal eye movement performance and learning; one week later at age of P26-30, the deficiency in OKR and VOR gradually showed up, but VOR gain-decrease adaptation was still comparable with controls. Based on these findings, we postulate that the third to fourth postnatal weeks are the critical phases for the priming and refinement of OKR and VOR baseline performance as well as their adaptations. Notably, chronic ablation of PP2B induced by tamoxifen could not replicate the behavioral deficit selectively in VOR performance, indicating the requirement of development in the early stage. That is to say, the early phase (third-fourth postnatal weeks) is essential for the initiation of the VOR functionality, which is unable to reset in the later stages once the cerebellum becomes mature.

During postnatal development, chemo- and activity-dependent mechanisms may also play a role in the set-point of eye movements. It is hypothesized that molecular mechanisms initially guide the basic ontogenetic wiring into a “crude” topographic map, whereas cerebellum-dependent activity is required to sculpt a “fine” map, establishing the spatio-temporal specificity of the reflex control⁶⁴. Given that cerebellar development is more protracted than other brain regions⁵⁹, it appears to be more vulnerable and take higher risks of genetic or environmental disruptions, which putatively leads to abnormal motor behavioral magnifications. That is probably why many developmental disorders, such as autism, attention deficit hyperactivity disorder and developmental dyslexia and so on, have common cerebellar deficiencies^{54,63-65}. Taken together, the study on cerebellar development and its role in eye movement control, is likely to have noticeable implications for the understanding the neural

basis of neurodevelopment and associated diseases.

Understanding the principles of motor learning

In about 40 years, the Marr-Albus-Ito theory for cerebellar motor learning has prevailed through the scientific community, which deems the role of PF-PC LTD as the main mechanism underlying motor learning. Following this theory, Miles and Lisberger raised an alternative theory in 1981. Subsequently, Fujita in 1982 proposed an adaptive filter theory. However, none of them seem to perfectly be in line with experimental data. For example, specific impairment of PF-PC LTD does not cause motor learning deficits^{42,75}, suggesting LTD may not be the sole mechanism underlying motor learning. Fortunately, with new techniques developing during the last two decades, our knowledge of the molecular mechanism underlying synaptic plasticity has increased considerably, which has challenge the above canonical theories⁷⁵, several points should be kept in mind to a better understanding of motor learning. I will list five of them below.

First, the neural activity in cerebellum is way more complex than we thought. Anatomically, in the human cerebellum, information from 200 million mossy fiber inputs is expanded to 40 billion granule cells, whose parallel fiber outputs then converge onto 15 million Purkinje cells⁷⁶. The spontaneous activities of Purkinje cells are shaped by cortical, vestibular and sensory information relayed by over 150,000 excitatory and inhibitory synaptic inputs⁷⁷, intriguingly, they output down to a group of no more than 100,000 deep nuclear cells. It is reported that a single Purkinje cell is estimated to innervate approximately 30-40 DCN neurons and in turn, each DCN neuron, receives projections from about 600-900 Purkinje cells⁷⁸. Thus, to dissect the contributions of different cerebellar components to a learned behavior, it is reasonable to consider network-level interplay as the physiological basis for cerebellar learning, rather than merely focusing on separate cell level or singular plasticity mechanism.

Second, conventionally, neural coding contains two forms: rate coding and temporal coding. Rate coding has been commonly defined as a neural code in which stimulus attributes are encoded by the number of spikes occurring during a time window whose length is determined by the stimulus timescale; whereas temporal coding has been defined as a neural code in which stimulus attributes are encoded by the precise timing of spikes within the same time window^{79,80}. Meanwhile, **Chapter 5.1** we found that the depth of modulation of Purkinje cells correlates with learning ability, both in conditions of enhanced and reduced learning, expanding the knowledge of the neural coding.

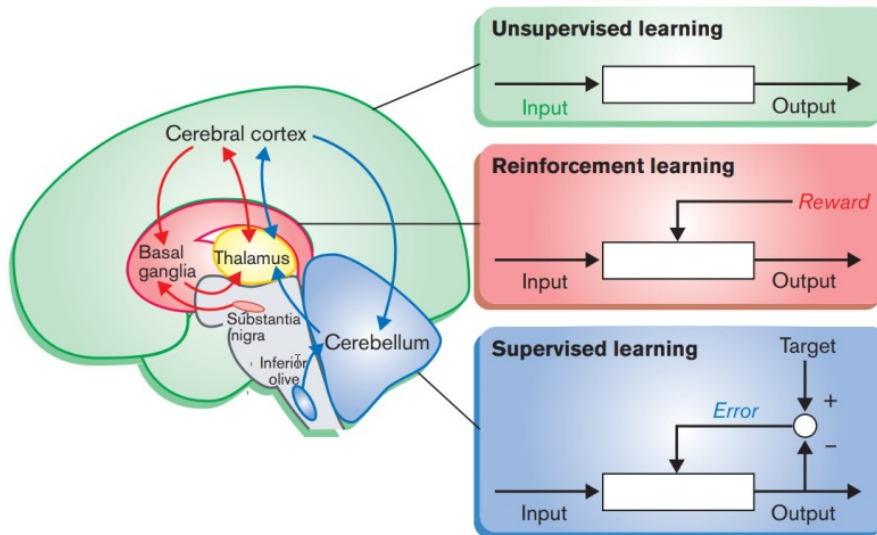


Figure 2. Specialization of various brain areas for different types of learning. The cerebellum is specialized for supervised learning, which is guided by the error signal encoded in the climbing fiber input from the inferior olive. The basal ganglia are specialized for reinforcement learning, which is guided by the reward signal encoded in the dopaminergic input from the substantia nigra. The cerebral cortex is specialized for unsupervised learning, which is guided by the statistical properties of the input signal itself, but may also be regulated by the ascending neuromodulatory inputs. Figure from (Doya et al. 2000)⁸¹

Third, different types of learning are specialized in various brain areas. In the whole brain level, theoretical models of learning in different parts of the brain suggest that the cerebellum, the basal ganglia, and the cerebral cortex are specialized for different types of learning⁸¹ (**Figure 2**). Within the cerebellum, a microcomplex has been conceived as a modular unit of cerebellar neuronal circuits. It incorporates a microzone of the cerebellar cortex and a small group of cerebellar and/or vestibular nuclear neurons that are attached to a small group of inferior olive (IO) neurons and that of parvocellular red nuclear neurons. Such a microcomplex is equipped with two types of memory (cortical and nuclear), which have complementary roles in learning. Specifically, **Chapter 3**, zebrin-positive zones, such as those controlling adaptation of the VOR, appear to predominantly form their memories by potentiation mechanisms and express their memories via rate coding, whereas zebrin-negative zones, such as those controlling eyeblink conditioning, appear to predominantly form their memories by suppression mechanisms and express their memories in part by temporal coding using rebound bursting⁴⁵.

Fourth, a compelling hypothesis of procedural learning is that the cerebellum acquires and stores internal models. Specifically, the highly organized three-layered neuronal networks like a simple perceptron, which is based on the design of neuronal circuits, have been proposed as an internal model of the cerebellum that is capable of spatial and temporal pattern recognition. With the internal model, the cerebellum can be expected to simulate a controlled object or its inverse⁸². In light of this point, in **Chapter 1.2**, we postulate that gain-increase learning is a feedback loop represented by the eye velocity signal originating from the inferior olive, whereas gain-decrease learning is likely to be a feedforward loop, both of which occur probably through an ever-updating internal model.

Lastly, single plasticity cannot fully explain the consequences of motor behaviors and

learning. LTD and LTP have been shown to be symmetric correlates of each other in vitro,⁸³⁻⁸⁵ whereas different cerebellar motor learning paradigms have been shown to be asymmetric and not equally reversible⁸⁶. Now the common conclusion is that distributed plasticity synergistically underlies motor learning⁸⁷. But how can both cerebellar LTD and LTP participate in one behavior, i.e., increasing the gain of the VOR? One possibility is that during learning, LTP first comes into play to increase the active synapses and the number of signals available, and then LTD prunes these into an optimal configuration.

Beyond movements: cerebellar non-motor functions

The cerebellum canonically plays a crucial role in the motor controls and learning by determining how to perform accurate and correct movements. However, the past decade has seen an increasing awareness of its role in non-motor functions⁸⁸⁻⁹⁰, which are reflected in the higher cognitive function defects that accompany motor dysfunction following cerebellar damage⁶. It is reported that congenital deficits, particularly in vermal agenesis, lead to later communicative and affective relevant disorders⁹¹. Furthermore, series of studies reveal that cerebellar-specific disruptions lead to autistic spectrum disorder (ASD) related behaviors^{63,92-95}. Intriguingly, recent studies even show that the cerebellum is involved in the rewarding^{96,97} and planning⁹⁸. It is suggested that the cerebellum participates in higher order brain function probably via its extensive connections with subthalamic nucleus, red nucleus, amygdala and prefrontal cortex⁹⁹⁻¹⁰¹ and other unknown brain areas (see the scheme in **Figure 3**).

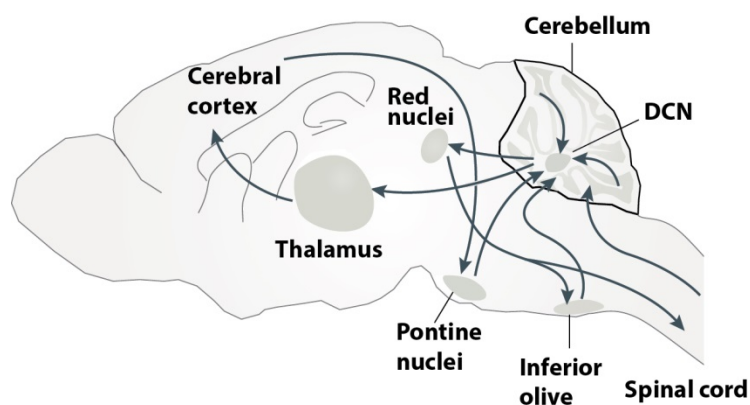


Figure 3. General scheme of cerebellar connections in the mouse. Main inputs contain the spinal cord, inferior olive and pontine nuclei. Main outputs consist of connections from cerebellar nuclei which gather the information of cerebellar cortex, to the cerebral cortex via the thalamus, and to spinal cord through red nuclei. Adapted from (Sathyanesan A et al, 2019)⁶¹

Consistent with the above-mentioned studies, our work in **Chapter 7** found that Purkinje cell-specific deletion of *Shank2*, which encodes postsynaptic scaffolding proteins, resulted in impaired social and task specific repetitive behavior. Previous study in L7-Tsc1 mice reported impaired social behavior, late-onset ataxia and reduced excitability of Purkinje cells, due to the absence of a protein that inhibits mTOR signaling pathway⁹². In contrast, we did not observe clear morphological deficits in the cerebellum of *Shank2* knockout mice. Instead, these mice

exhibited reduced AMPAR, increased IPSC frequency, impaired LTP and irregularity of simple spike firing in Purkinje cells. It is indeed possible that these alterations may contribute to social and repetitive behavior-related phenotypes in ASD. Our finding suggests that disruption of the synapse through the absence of a single postsynaptic scaffolding protein in the Purkinje cell is sufficient to lead to ASD-related behavior, highlighting the significance of the cerebellum for mental function beyond the classically ascribed motor-related behavior. Recently, as previously mentioned, it is hypothesized that the disruption of a certain brain area during development could affect the development and consequently the function of other inter-connected areas. Thus, both development and network-level interplay should be taken into account in further studies.

Future directions

It is the organ of brain, which is responsible for all our thoughts, perceptions and actions, that makes each individual unique. A grand challenge in neuroscience is to understand how the cerebellum processes multisensory information and encodes neural commands in order to generate appropriate behavioral responses. As this domain is undergoing faster changes than ever before, there are many more questions could be brought about following the ones raised in the previous chapters. I will emphasize four perspectives as follows.

To begin with, in this time of increasing appreciation for the heterogeneity within particular Purkinje cell types, the advancement of unraveling the encoding scheme underlying the diverse cerebellar functionality is more and more approaching. Current evidence suggests that TRPC3 is required for the cellular heterogeneity that introduces distinct physiological properties in an otherwise homogeneous population of Purkinje cells, thereby conjuring functional heterogeneity in cerebellar sensorimotor integration (**Chapter 3**). Following up with TRPC3, many concomitant questions can be put forward. For instance, how does TRPC3 participate in the variety of encoding schemes of cerebellar motor learning, wherein impaired eyeblink conditioning and normal VOR adaptation? What is the molecular pathway downstream of TRPC3 cascade? To what extent does TRPC3 influence the differentiation between zebrin-positive and zebrin-negative modules? Interestingly, several other proteins in the cascade connecting mGluR1-independent pathways are expressed in bands that are either similar or complementary to zebrin, as well as a number of proteins that have no known connection to it. Future work needs to identify all the proteins that have a differential expression between modules and determine their contribution, by using tag-labeled proteomic techniques, i.e. iTRAQ. In addition, except for Purkinje cells, the zebrin-identified modularity is possibly presented in other components. Recent studies have shown that mossy fibers carrying efferent motor copies and others carrying proprioceptive information can converge onto a single granule cell¹⁰², and in the vestibulocerebellum the mossy fiber inputs have distinct biophysical signatures¹⁰³. Therefore, future study on the activity of granule cells *in vivo* between modules is essentially needed. A challenging but more informative approach is *in vivo* patch-clamp recording of granule cells while the animal is engaged in a behavioral or learning paradigm in order to directly monitor the dynamic changes.

Moreover, another major focus in this field is how the cerebellum adapts motor behaviors

in response to the internal and external environments^{104,105}. We have shown that modulation depth in Purkinje cell, which is likely to be a novel representation of neuronal coding, in combination with spatial and temporal tuning of firing activity, accommodates VOR adaptations dependent on directionality and localization (**Chapter 5**). It becomes more and more clear that even the apparent simple behavioral action such as vestibulo-ocular reflex engages in intricate endeavors. Rather, these findings were gathered in the vestibulocerebellar system, whether they are readily applied to other domains is still an open question. Further efforts are required to proceed along the hierarchical levels of motor control, from reflexes to locomotion or coordination, automatic and voluntary motor actions, and the ultimate cognitive functions. It is obvious that clarifying such issues at both the cellular level for analyzing single neurons and the system level would help for advancing understanding of how neural circuits in our brain truly work.

Thirdly, despite the neurobiological basis of neurodevelopment and associated diseases is still not widely recognized, it is a common view that many neurodevelopmental disorders are associated with cerebellar deficits. We report that cerebellar development contributes to compensatory eye movement behavioral and adaptive functionality (**Chapter 6**). But the morphogenetic and molecular mechanisms taking place during cerebellar development are not known. Further study should focus on characterizing the dynamic changes during either natural or disturbed cerebellar development, and especially those dictate the generation, migration, and differentiation of neurons. Advances today in experimental embryology, genetic engineering, neuroimaging and single cell sequencing techniques render the possibility to approach the analysis of molecular mechanisms underlying the ontogenesis of the cerebellum. In addition, to further determine the contribution of certain type of neurons, i.e. Purkinje cells, to development, we can take advantage of optogenetic approach. By turning neurons 'on' and 'off', we will be able to manipulate behavioral alterations, thereby bridging the gap between behavioral analysis and circuit perturbations on a millisecond timescale. Further, physiological changes during development should also be taken into consideration. Simultaneous measurement of neuronal activity using optrode or silicon array recordings will facilitate to tackle the question that how changes in neuronal firing activities contribute to the cerebellar functions on a system-level.

Last but not least, the cerebellum is now thought to encode an unexpected level of functional diversity, accordingly, a growing appreciation and accompanying questions emerge in terms of cerebellar non-motor functions, especially for ASD. We report impaired social and task specific repetitive behavior due to Purkinje cell-specific deletion of Shank2 (**Chapter 7**). As discussed previously, the Shank family of postsynaptic scaffolding proteins harbors many different interacting proteins in the postsynaptic density through which they could subserve the functional regulation of synaptic plasticity. The main challenge remaining is to mechanistically explain the contribution of impaired Purkinje cell physiology to the observed ASD behavioral phenotypes. Alternatively, how does an impaired Purkinje cell mediate ASD-related behavior? In addition, since ASD is regarded as a neurodevelopmental disease, the concomitant questions would be: whether there is a critical or sensitive period during which Purkinje cell impairments lead to ASD-related behavior, and if so, to what extent does acute and developmental effects of impaired Purkinje cells contribute to the non-motor autistic symptomatology? To resolve these questions, Purkinje cell-specific Shank2 ablation should be

initiated at different stages during development by using spatially and temporally controlled approaches in the future study.

In the last decade, neuroscience spawned quantitative datasets of unprecedented breadth and depth. Besides those traditional approaches in terms of anatomy, immunology, electrophysiology and optogenetics, many new advanced technologies are constantly springing up due to interdisciplinary integration, such as CRISPR/Cas9 based gene editing¹⁰⁶, single cell RNA sequencing¹⁰⁷, electrocorticography decoding (ECoG) or brain-computer interfaces¹⁰⁸, large-scale population neuronal recording¹⁰⁹, high-speed and spatially precise optical tools monitoring neuronal activity in freely-behaving¹¹⁰ and so on. We believe that with so many technological advances, in combination with the development of big-data analysis and artificial intelligence, breakthroughs in the cerebellar domain are on the immediate horizon. In the near future, we will not only come to a much deeper appreciation for the biological mechanisms underlying cerebellar function, but also open new avenues to treat neurological diseases such as movement disorders, ataxia, epilepsy, intellectual disability, autism spectrum disorder, and so forth.

References

- 1 Markram, H., Lubke, J., Frotscher, M. *et al.* Regulation of synaptic efficacy by coincidence of postsynaptic APs and EPSPs. *Science*. 1997; 275, 213-5.
- 2 De Zeeuw, C. I., Hoebeek, F. E., Bosman, L. W. *et al.* Spatiotemporal firing patterns in the cerebellum. *Nat Rev Neurosci*. 2011; 12, 327-44.
- 3 Schonewille, M., Luo, C., Ruigrok, T. J. *et al.* Zonal organization of the mouse flocculus: physiology, input, and output. *J Comp Neurol*. 2006; 497, 670-82.
- 4 Lisberger, S. G. Internal models of eye movement in the floccular complex of the monkey cerebellum. *Neuroscience*. 2009; 162, 763-76.
- 5 Manni, E. & Petrosini, L. A century of cerebellar somatotopy: a debated representation. *Nat Rev Neurosci*. 2004; 5, 241-9.
- 6 Schmahmann, J. D. & Sherman, J. C. The cerebellar cognitive affective syndrome. *Brain*. 1998; 121 (Pt 4), 561-79.
- 7 Cerminara, N. L., Lang, E. J., Sillitoe, R. V. *et al.* Redefining the cerebellar cortex as an assembly of non-uniform Purkinje cell microcircuits. *Nat Rev Neurosci*. 2015; 16, 79-93.
- 8 Altschuler, S. J. & Wu, L. F. Cellular heterogeneity: do differences make a difference? *Cell*. 2010; 141, 559-63.
- 9 Zhou, H., Lin, Z., Voges, K. *et al.* Cerebellar modules operate at different frequencies. *Elife*. 2014; 3, e02536.
- 10 Xiao, J., Cerminara, N. L., Kotsurovskyy, Y. *et al.* Systematic regional variations in Purkinje cell spiking patterns. *PLoS One*. 2014; 9, e105633.
- 11 Brochu, G., Maler, L. & Hawkes, R. Zebrin II: a polypeptide antigen expressed selectively by Purkinje cells reveals compartments in rat and fish cerebellum. *J Comp Neurol*. 1990; 291, 538-52.
- 12 Ahn, A. H., Dziennis, S., Hawkes, R. *et al.* The cloning of zebrin II reveals its identity with aldolase C. *Development*. 1994; 120, 2081-90.
- 13 Graham, D. J. & Wylie, D. R. Zebrin-immunopositive and -immunonegative stripe pairs represent functional units in the pigeon vestibulocerebellum. *J Neurosci*. 2012; 32, 12769-79.
- 14 Marzban, H. & Hawkes, R. On the architecture of the posterior zone of the cerebellum. *Cerebellum*. 2011; 10, 422-34.
- 15 Apps, R. & Hawkes, R. Cerebellar cortical organization: a one-map hypothesis. *Nat Rev Neurosci*. 2009; 10, 670-81.
- 16 Caffè, A. R., Vonschantz, M., Szel, A. *et al.* Distribution of Purkinje Cell-Specific Zebrin-II Aldolase-C Immunoreactivity in the Mouse, Rat, Rabbit, and Human Retina. *Journal of Comparative Neurology*. 1994; 348, 291-7.
- 17 Sillitoe, R. V., Marzban, H., Larouche, M. *et al.* Conservation of the architecture of the anterior lobe vermis of the cerebellum across mammalian species. 2005; 148, 283-97.
- 18 Buono, P., D'Armiento, E. P., Terzi, G. *et al.* Differential distribution of aldolase A and C in the human central nervous system. *J Neurocytol*. 2001; 30, 957-65.
- 19 Ruigrok, T. J. Ins and outs of cerebellar modules. *Cerebellum*. 2011; 10, 464-74.

- 20 Sugihara, I. & Quay, P. N. Identification of aldolase C compartments in the mouse cerebellar cortex by olivocerebellar labeling. *J Comp Neurol.* 2007; 500, 1076-92.
- 21 Gincel, D., Regan, M. R., Jin, L. *et al.* Analysis of cerebellar Purkinje cells using EAAT4 glutamate transporter promoter reporter in mice generated via bacterial artificial chromosome-mediated transgenesis. *Exp Neurol.* 2007; 203, 205-12.
- 22 Wadiche, J. I. & Jahr, C. E. Patterned expression of Purkinje cell glutamate transporters controls synaptic plasticity. *Nat Neurosci.* 2005; 8, 1329-34.
- 23 Dehnes, Y., Chaudhry, F. A., Ullensvang, K. *et al.* The glutamate transporter EAAT4 in rat cerebellar Purkinje cells: a glutamate-gated chloride channel concentrated near the synapse in parts of the dendritic membrane facing astroglia. *J Neurosci.* 1998; 18, 3606-19.
- 24 Mateos, J. M., Osorio, A., Azkue, J. J. *et al.* Parasagittal compartmentalization of the metabotropic glutamate receptor mGluR1b in the cerebellar cortex. *Eur J Anat.* 2001; 5, 15-21.
- 25 Furutama, D., Morita, N., Takano, R. *et al.* Expression of the IP3R1 promoter-driven nls-lacZ transgene in Purkinje cell parasagittal arrays of developing mouse cerebellum. *J Neurosci Res.* 2010; 88, 2810-25.
- 26 Sarna, J. R., Marzban, H., Watanabe, M. *et al.* Complementary stripes of phospholipase Cbeta3 and Cbeta4 expression by Purkinje cell subsets in the mouse cerebellum. *J Comp Neurol.* 2006; 496, 303-13.
- 27 Barmack, N. H., Qian, Z. & Yoshimura, J. Regional and cellular distribution of protein kinase C in rat cerebellar Purkinje cells. *J Comp Neurol.* 2000; 427, 235-54.
- 28 Jinno, S., Jeromin, A., Roder, J. *et al.* Compartmentation of the mouse cerebellar cortex by neuronal calcium sensor-1. *J Comp Neurol.* 2003; 458, 412-24.
- 29 Fritschy, J. M., Meskenaite, V., Weinmann, O. *et al.* GABAB-receptor splice variants GB1a and GB1b in rat brain: developmental regulation, cellular distribution and extrasynaptic localization. *Eur J Neurosci.* 1999; 11, 761-8.
- 30 Chung, S. H., Kim, C. T. & Hawkes, R. Compartmentation of GABA B receptor2 expression in the mouse cerebellar cortex. *Cerebellum.* 2008; 7, 295-303.
- 31 Aiba, A., Kano, M., Chen, C. *et al.* Deficient cerebellar long-term depression and impaired motor learning in mGluR1 mutant mice. *Cell.* 1994; 79, 377-88.
- 32 Miyata, M., Finch, E. A., Khiroug, L. *et al.* Local calcium release in dendritic spines required for long-term synaptic depression. *Neuron.* 2000; 28, 233-44.
- 33 Ohtani, Y., Miyata, M., Hashimoto, K. *et al.* The synaptic targeting of mGluR1 by its carboxyl-terminal domain is crucial for cerebellar function. *J Neurosci.* 2014; 34, 2702-12.
- 34 Hartmann, J., Dragicevic, E., Adelsberger, H. *et al.* TRPC3 channels are required for synaptic transmission and motor coordination. *Neuron.* 2008; 59, 392-8.
- 35 Sun, Y., Sukumaran, P., Bandyopadhyay, B. C. *et al.* Physiological Function and Characterization of TRPCs in Neurons. *Cells.* 2014; 3, 455-75.
- 36 Becker, E. B. The Moonwalker mouse: new insights into TRPC3 function, cerebellar development, and ataxia. *Cerebellum.* 2014; 13, 628-36.
- 37 Hartmann, J., Henning, H. A. & Konnerth, A. mGluR1/TRPC3-mediated Synaptic Transmission and Calcium Signaling in Mammalian Central Neurons. *Cold Spring Harb Perspect Biol.* 2011; 3.
- 38 Sanchez, M., Sillitoe, R. V., Attwell, P. J. *et al.* Compartmentation of the rabbit cerebellar cortex. *J Comp Neurol.* 2002; 444, 159-73.
- 39 Mostofi, A., Holtzman, T., Grout, A. S. *et al.* Electrophysiological localization of eyeblink-related microzones in rabbit cerebellar cortex. *J Neurosci.* 2010; 30, 8920-34.
- 40 Hesslow, G. Inhibition of classically conditioned eyeblink responses by stimulation of the cerebellar cortex in the decerebrate cat. *J Physiol.* 1994; 476, 245-56.
- 41 Kim, S. J. TRPC3 channel underlies cerebellar long-term depression. *Cerebellum.* 2013; 12, 334-7.
- 42 Schonewille, M., Gao, Z., Boele, H. J. *et al.* Reevaluating the role of LTD in cerebellar motor learning. *Neuron.* 2011; 70, 43-50.
- 43 Schreurs, B. G., Tomsic, D., Gusev, P. A. *et al.* Dendritic excitability microzones and occluded long-term depression after classical conditioning of the rabbit's nictitating membrane response. *J Neurophysiol.* 1997; 77, 86-92.
- 44 Ohtsuki, G., Piochon, C., Adelman, J. P. *et al.* SK2 channel modulation contributes to compartment-specific dendritic plasticity in cerebellar Purkinje cells. *Neuron.* 2012; 75, 108-20.
- 45 De Zeeuw, C. I. & Ten Brinke, M. M. Motor Learning and the Cerebellum. *Cold Spring Harb Perspect Biol.* 2015; 7, a021683.
- 46 Ruigrok, T. J., Pijpers, A., Goedknegt-Sabel, E. *et al.* Multiple cerebellar zones are involved in the control of individual muscles: a retrograde transneuronal tracing study with rabies virus in the rat. *Eur J Neurosci.* 2008; 28, 181-200.
- 47 Diedrichsen, J., Criscimagna-Hemminger, S. E. & Shadmehr, R. Dissociating timing and coordination as functions of the cerebellum. *J Neurosci.* 2007; 27, 6291-301.
- 48 Shadmehr, R. Distinct neural circuits for control of movement vs. holding still. *J Neurophysiol.* 2017; 117, 1431-60.

49 De Zeeuw, C. I. & Ten Brinke, M. M. Motor Learning and the Cerebellum. *CSHP Biol.* 2015; 7, a021683.

50 Ito, M. Neural design of the cerebellar motor control system. *Brain Res.* 1972; 40, 81-4.

51 Marr, D. A theory of cerebellar cortex. *J Physiol.* 1969; 202, 437-70.

52 Albus, J. S. A theory of cerebellar function. *Math. Biosci.* 1971; 10, 25-61.

53 Lisberger, S. G., Pavelko, T. A. & Broussard, D. M. Neural basis for motor learning in the vestibuloocular reflex of primates. I. Changes in the responses of brain stem neurons. *J Neurophysiol.* 1994; 72, 928-53.

54 Manto, M. U. & Jissendi, P. Cerebellum: links between development, developmental disorders and motor learning. *Front Neuroanat.* 2012; 6, 1.

55 Martinez, S. The cerebellum: from development to structural complexity and motor learning. *Front Neuroanat.* 2014; 8, 118.

56 Larsell, O. The morphogenesis and adult pattern of the lobules and fissures of the cerebellum of the white rat. *J Comp Neurol.* 1952; 97, 281-356.

57 Hatten, M. E. & Heintz, N. Mechanisms of neural patterning and specification in the developing cerebellum. *Annu Rev Neurosci.* 1995; 18, 385-408.

58 Sillitoe, R. V., Marzban, H., Larouche, M. *et al.* Conservation of the architecture of the anterior lobe vermis of the cerebellum across mammalian species. *Prog Brain Res.* 2005; 148, 283-97.

59 Bayer, S. A., Altman, J., Russo, R. J. *et al.* Timetables of neurogenesis in the human brain based on experimentally determined patterns in the rat. *Neurotoxicology.* 1993; 14, 83-144.

60 Marzban, H., Del Bigio, M. R., Alizadeh, J. *et al.* Cellular commitment in the developing cerebellum. *Front Cell Neurosci.* 2014; 8, 450.

61 Sathyanesan, A., Zhou, J., Scafidi, J. *et al.* Emerging connections between cerebellar development, behaviour and complex brain disorders. *Nat Rev Neurosci.* 2019; 20, 298-313.

62 Limperopoulos, C., Bassan, H., Gauvreau, K. *et al.* Does cerebellar injury in premature infants contribute to the high prevalence of long-term cognitive, learning, and behavioral disability in survivors? *Pediatrics.* 2007; 120, 584-93.

63 Wang, S. S., Kloth, A. D. & Badura, A. The cerebellum, sensitive periods, and autism. *Neuron.* 2014; 83, 518-32.

64 Leto, K., Arancillo, M., Becker, E. B. *et al.* Consensus Paper: Cerebellar Development. *Cerebellum.* 2016; 15, 789-828.

65 Wang, R., Tan, J., Guo, J. *et al.* Aberrant Development and Synaptic Transmission of Cerebellar Cortex in a VPA Induced Mouse Autism Model. *Front Cell Neurosci.* 2018; 12, 500.

66 Miale, I. L. & Sidman, R. L. An autoradiographic analysis of histogenesis in the mouse cerebellum. *Exp Neurol.* 1961; 4, 277-96.

67 Hoshino, M., Nakamura, S., Mori, K. *et al.* Ptf1a, a bHLH transcriptional gene, defines GABAergic neuronal fates in cerebellum. *Neuron.* 2005; 47, 201-13.

68 Hashimoto, M. & Mikoshiba, K. Mediolateral compartmentalization of the cerebellum is determined on the "birth date" of Purkinje cells. *J Neurosci.* 2003; 23, 11342-51.

69 Stahl, J. S. Using eye movements to assess brain function in mice. *Vision Res.* 2004; 44, 3401-10.

70 Eviatar, L., Miranda, S., Eviatar, A. *et al.* Development of nystagmus in response to vestibular stimulation in infants. *Ann Neurol.* 1979; 5, 508-14.

71 Gauthier, G. M. & Robinson, D. A. Adaptation of the human vestibuloocular reflex to magnifying lenses. *Brain Res.* 1975; 92, 331-5.

72 Sherman, K. R. & Keller, E. L. Vestibulo-ocular reflexes of adventitiously and congenitally blind adults. *Invest Ophthalmol Vis Sci.* 1986; 27, 1154-9.

73 Straka, H. Ontogenetic rules and constraints of vestibulo-ocular reflex development. *Curr Opin Neurobiol.* 2010; 20, 689-95.

74 Eviatar, L. & Eviatar, A. Neurovestibular examination of infants and children. *Adv Otorhinolaryngol.* 1978; 23, 169-91.

75 Galliano, E. & De Zeeuw, C. I. Questioning the cerebellar doctrine. *Prog Brain Res.* 2014; 210, 59-77.

76 Llinas RR, Walton KD & EJ, L. The Synaptic Organization of the Brain, 5th edition. Shepherd GM (ed.) (Oxford University Press). *Ch. 7 Cerebellum.* 2004, 271-309.

77 Hausser, M. & Clark, B. A. Tonic synaptic inhibition modulates neuronal output pattern and spatiotemporal synaptic integration. *Neuron.* 1997; 19, 665-78.

78 Baumel, Y., Jacobson, G. A. & Cohen, D. Implications of functional anatomy on information processing in the deep cerebellar nuclei. *Front Cell Neurosci.* 2009; 3, 14.

79 Aldworth, Z. N., Dimitrov, A. G., Cummins, G. I. *et al.* Temporal encoding in a nervous system. *PLoS Comput Biol.* 2011; 7, e1002041.

80 Theunissen, F. & Miller, J. P. Temporal encoding in nervous systems: a rigorous definition. *J Comput Neurosci.* 1995; 2, 149-62.

81 Doya, K. Complementary roles of basal ganglia and cerebellum in learning and motor control. *Curr Opin Neurobiol.* 2000; 10, 732-9.

82 Wolpert, D. M., Miall, R. C. & Kawato, M. Internal models in the cerebellum. *Trends Cogn Sci.* 1998; 2, 338-47.

83 Titley, H. K. & Hansel, C. Asymmetries in Cerebellar Plasticity and Motor Learning. *Cerebellum*. 2016; 15, 87-92.

84 Coesmans, M., Weber, J. T., De Zeeuw, C. I. *et al.* Bidirectional parallel fiber plasticity in the cerebellum under climbing fiber control. *Neuron*. 2004; 44, 691-700.

85 Lev-Ram, V., Mehta, S. B., Kleinfeld, D. *et al.* Reversing cerebellar long-term depression. *Proc Natl Acad Sci U S A*. 2003; 100, 15989-93.

86 Boyden, E. S., Katoh, A. & Raymond, J. L. Cerebellum-dependent learning: the role of multiple plasticity mechanisms. *Annu Rev Neurosci*. 2004; 27, 581-609.

87 Gao, Z., van Beugen, B. J. & De Zeeuw, C. I. Distributed synergistic plasticity and cerebellar learning. *Nat Rev Neurosci*. 2012; 13, 619-35.

88 Schmahmann, J. D. The role of the cerebellum in cognition and emotion: personal reflections since 1982 on the dysmetria of thought hypothesis, and its historical evolution from theory to therapy. *Neuropsychol Rev*. 2010; 20, 236-60.

89 Marien, P., Ackermann, H., Adamaszek, M. *et al.* Consensus paper: Language and the cerebellum: an ongoing enigma. *Cerebellum*. 2014; 13, 386-410.

90 Baumann, O., Borra, R. J., Bower, J. M. *et al.* Consensus paper: the role of the cerebellum in perceptual processes. *Cerebellum*. 2015; 14, 197-220.

91 Tavano, A., Grasso, R., Gagliardi, C. *et al.* Disorders of cognitive and affective development in cerebellar malformations. *Brain*. 2007; 130, 2646-60.

92 Tsai, P. T., Hull, C., Chu, Y. *et al.* Autistic-like behaviour and cerebellar dysfunction in Purkinje cell Tsc1 mutant mice. *Nature*. 2012; 488, 647-51.

93 Hagerman, R., Hoem, G. & Hagerman, P. Fragile X and autism: Intertwined at the molecular level leading to targeted treatments. *Mol Autism*. 2010; 1, 12.

94 Badura, A., Verpeut, J. L., Metzger, J. W. *et al.* Normal cognitive and social development require posterior cerebellar activity. *Elife*. 2018; 7.

95 Stoodley, C. J., D'Mello, A. M., Ellegood, J. *et al.* Altered cerebellar connectivity in autism and cerebellar-mediated rescue of autism-related behaviors in mice. *Nat Neurosci*. 2017; 20, 1744-51.

96 Wagner, M. J., Kim, T. H., Savall, J. *et al.* Cerebellar granule cells encode the expectation of reward. *Nature*. 2017; 544, 96-100.

97 Carta, I., Chen, C. H., Schott, A. L. *et al.* Cerebellar modulation of the reward circuitry and social behavior. *Science*. 2019; 363.

98 Gao, Z., Davis, C., Thomas, A. M. *et al.* A cortico-cerebellar loop for motor planning. *Nature*. 2018; 563, 113-6.

99 Proville, R. D., Spolidoro, M., Guyon, N. *et al.* Cerebellum involvement in cortical sensorimotor circuits for the control of voluntary movements. *Nat Neurosci*. 2014; 17, 1233-9.

100 Bostan, A. C., Dum, R. P. & Strick, P. L. The basal ganglia communicate with the cerebellum. *Proc Natl Acad Sci U S A*. 2010; 107, 8452-6.

101 Farley, S. J., Radley, J. J. & Freeman, J. H. Amygdala Modulation of Cerebellar Learning. *J Neurosci*. 2016; 36, 2190-201.

102 Huang, C. C., Sugino, K., Shima, Y. *et al.* Convergence of pontine and proprioceptive streams onto multimodal cerebellar granule cells. *Elife*. 2013; 2, e00400.

103 Chabrol, F. P., Arenz, A., Wiechert, M. T. *et al.* Synaptic diversity enables temporal coding of coincident multisensory inputs in single neurons. *Nat Neurosci*. 2015; 18, 718-27.

104 Shadmehr, R., Smith, M. A. & Krakauer, J. W. Error correction, sensory prediction, and adaptation in motor control. *Annu Rev Neurosci*. 2010; 33, 89-108.

105 Huberdeau, D. M., Krakauer, J. W. & Haith, A. M. Dual-process decomposition in human sensorimotor adaptation. *Curr Opin Neurobiol*. 2015; 33, 71-7.

106 Hsu, P. D., Lander, E. S. & Zhang, F. Development and applications of CRISPR-Cas9 for genome engineering. *Cell*. 2014; 157, 1262-78.

107 Carter, R. A., Bihannic, L., Rosencrance, C. *et al.* A Single-Cell Transcriptional Atlas of the Developing Murine Cerebellum. *Curr Biol*. 2018; 28, 2910-20 e2.

108 Anumanchipalli, G. K., Chartier, J. & Chang, E. F. Speech synthesis from neural decoding of spoken sentences. *Nature*. 2019; 568, 493-8.

109 Jun, J. J., Steinmetz, N. A., Siegle, J. H. *et al.* Fully integrated silicon probes for high-density recording of neural activity. *Nature*. 2017; 551, 232-6.

110 Packer, A. M., Russell, L. E., Dagleish, H. W. *et al.* Simultaneous all-optical manipulation and recording of neural circuit activity with cellular resolution in vivo. *Nat Methods*. 2015; 12, 140-6.

Summary

This dissertation uses the vestibulocerebellar system to unravel the neural basis of accurate behavioral responses, adaptable motor learning and even non-motor functionalities. To this end, I have revealed cellular and synaptic mechanisms that underlie appropriate neuronal coding and sensorimotor integration and how these errors in this coding results in motor (learning) deficits and disease.

In **Chapter 1.2**, we reviewed the anatomical and physiological characteristics of the components of the VOR circuit, and proposed that the two types of VOR adaptation are mediated via different pathways and encoded at different loci: gain-increase learning is accomplished in the floccular complex whereas gain-decrease learning is induced in the vestibular nucleus. This concept provides a novel insight in where and how specific form of motor learning helps us deal with the outside world.

In **Chapter 2**, we addressed a sophisticated approach of targeted recording electrophysiological activity *in vivo* in the cerebellum in awake animals. We focused on analyzing the activity of two populations of Purkinje cells discriminated by zebrin. By driving the expression of a fluorescent marker with the promotor of one of the differentiating genes, the presence of a fluorescence signal could be used to recognize and approach Purkinje cells, while specific features of the signal can be used as a marker to identify the two subpopulations.

In **Chapter 3**, to decipher the relevance of zebrin-identified heterogeneity in Purkinje cells, we tested the function of TRPC3 by using mouse genetics and electrophysiology *in vitro* and *in vivo*. We found that TRPC3 predominantly had an impact on the firing activity of zebrin-negative Purkinje cells. More importantly, it could selectively affect the eyeblink conditioning which is zebrin-negative associated. These findings suggest that TRPC3 contributes to the cellular heterogeneity in that it introduces distinct physiological properties in the sub-population of Purkinje cells, thus conjuring functional heterogeneity in cerebellar sensorimotor integration.

In **Chapter 4**, we clarify the anatomical and histological characteristics of the basal interstitial nucleus neurons. We demonstrate that they are GABAergic and glycinergic and receive a relevant and unique excitatory input from the medio-rostral medullary reticular formation. As a putatively novel inhibitory afferent system, this type of neurons may play an essential role in the proper conversion of mossy fiber activity into Purkinje cell firing in the flocculus.

In **Chapter 5**, we focus on the relationship between Purkinje cell activity and behavior of the mouse. **Chapter 5.1** reveals that the magnitude of the change in Purkinje cells simple spike activity correlates with learning ability, both in conditions of enhanced and reduced learning. This study emphasizes the relevance of both rate and temporal coding in cerebellar functioning and expands the knowledge of the neuronal coding. **Chapter 5.2** shows that directionality has behavioral and neuronal correlates. Specifically, the direction of vestibular

input determines the efficiency of eye movement adaptation in mice, with larger changes during contraversive head rotation and, more importantly, that gain-increase paradigms induce increased simple spike activity in ipsilateral cerebellar Purkinje cells.

In **Chapter 6**, we focus on the roles of synaptic proteins in motor learning and cerebellar development. By genetic manipulation of PP2B, **Chapter 6.1** aims to evaluate the developmental contribution to the initiation of eye movement baseline reflex and adaptations. Notably, cerebellar development contributes to the initial set-point of VOR in the juvenile phase, which is unable to be reset after maturation of the cerebellum. **Chapter 6.2** identifies the molecular mechanisms by which PP2B controls the integrity of PF-PC synapses and proposed a combined phosphatase and structural role of PP2B in governing synaptic function and learning. **Chapter 6.3** showed that Shisa6 is crucial for Purkinje cell AMPA-receptor function, synaptic plasticity, and cerebellar motor learning.

In **Chapter 7**, we extend the research beyond the motor domain. Through *in vivo* and *in vitro* electrophysiology on mice lacking the autism-related Shank2 gene, we found impairments in Purkinje cell intrinsic plasticity, LTP induction at the parallel fiber to Purkinje cell synapse, and simple spike regularity in predominantly zebrin-positive Purkinje cells. Purkinje cell-specific Shank2-mutants showed deficits in motor learning and even impaired social behavior, highlighting the importance of cerebellar pathology in the generation of autism spectrum disorder.

Samenvatting

Dit proefschrift gebruikt het vestibulocerebellaire systeem om de neuronale basis te ontrafelen van correct motorisch gedrag, motorisch leren en zelfs niet-motorische functies. Hiertoe heb ik de cellulaire en synaptische mechanismen onderzocht die ten grondslag liggen aan de juiste neuronale codering en sensorimotorische integratie en hoe fouten in deze codering resulteren in motorische (leer)problemen en aandoeningen.

In **hoofdstuk 1.2** hebben we de anatomische en fysiologische kenmerken van de componenten van het circuit dat ten grondslag ligt aan de vestibulo-oculaire reflex (VOR) besproken en voorgesteld dat de twee typen VOR-adaptatie via verschillende routes en op verschillende loci worden gecodeerd: gain-increase leren wordt bewerkstelligd in het flocculaire complex terwijl gain-decrease leren wordt geïnduceerd in de vestibulaire kern. Dit concept geeft een nieuw inzicht in waar en hoe specifieke vormen van motorisch leren tot expressie komen als reactie op de buitenwereld.

In **Hoofdstuk 2** hebben we een verfijnde aanpak van gerichte elektrofysiologische afleidingen in vivo in het cerebellum bij wakkere dieren behandeld. We concentreerden ons op het analyseren van de activiteit van twee populaties van Purkinje-cellen die onderscheiden werden op basis van de expressie van zebrin. Door de expressie van een fluorescente marker aan te sturen met de promotor van een van de genen met een vergelijkbare expressie als zebrin, kan de aanwezigheid van een fluorescentiesignaal worden gebruikt om Purkinje-cellen te herkennen en te benaderen, terwijl de sterkte van het signaal kan worden gebruikt als een marker om de subpopulaties te identificeren.

In **Hoofdstuk 3** hebben we de functie van TRPC3 getest door middel van muismodellen waarin TRPC3 genetisch gemoduleerd is, in combinatie met elektrofysiologie in vitro en in vivo, om de relevantie van de zebrin-geïdentificeerde heterogeniteit in Purkinje-cellen te ontcijferen. We vonden dat TRPC3 voornamelijk een invloed had op de vuuractiviteit van zebrin-negatieve Purkinje-cellen. Daarnaast hebben we aangetoond dat het selectief de eyeblink-conditionering beïnvloedt, waarvan we weten dat deze afhankelijk is van zebrin-negatieve Purkinje-cellen. Deze bevindingen suggereren dat TRPC3 bijdraagt aan de cellulaire heterogeniteit doordat het andere fysiologische eigenschappen introduceert in de zebrin-negatieve subpopulatie van Purkinje-cellen, waarmee er functionele heterogeniteit wordt veroorzaakt in cerebellaire sensorimotorische integratie.

In **Hoofdstuk 4** verduidelijken we de anatomische en histologische kenmerken van de basale interstitiële kernneuronen. Deze neuronen zijn GABAergisch en glycinergisch en ontvangen een unieke exciterende input van de medio-rostrale medullaire reticulair formatie. Dit type neuron vormt een nieuw inhiberend systeem, dat mogelijk een essentiële rol speelt in de omzetting van mossel activiteit naar Purkinje cel vuurgedrag in de flocculus.

In **Hoofdstuk 5** concentreren we ons op de relatie tussen de activiteit van Purkinje cellen en

het gedrag van de muis. **Hoofdstuk 5.1** laat zien dat de grootte van de verandering in de Purkinje cellen simple spike activiteit correleert met het leervermogen, zowel in omstandigheden van verbeterd als verminderd leren. Deze studie benadrukt de relevantie van zowel codering in vuurfrequentie als regelmaat van het vuren bij het functioneren van de kleine hersenen en vergroot daarmee onze kennis van de neuronale codering. **Hoofdstuk 5.2** laat ten eerste zien dat de richting van bewegingen gedrags- en neuronale asymmetrisch is. In het bijzonder bepaalt de richting van de vestibulaire input de efficiëntie van oogbewegingsaanpassing bij muizen, met grotere veranderingen tijdens koprotatie in tegengestelde richting (weg van het bestudeerde oog). Bovendien is vastgesteld dat VOR gain increase training leidt tot een toename in simple spike-activiteit van Purkinje-cellen aan de ipsilaterale kant van de kleine hersenen.

In **Hoofdstuk 6** concentreren we ons op de rol van synaptische eiwitten in motorisch leren en de ontwikkeling van kleine hersenen. Door genetische manipulatie van PP2B, geeft **hoofdstuk 6.1** bewijs dat ontwikkeling een belangrijke rol zou kunnen spelen bij het vaststellen van het basale niveau van reflex sterkte. Hierin laten we zien dat tijdens de ontwikkeling van de kleine hersenen in de vroege ontwikkelingsfase het initiële setpoint van VOR wordt bepaald, en dat dit niet kan worden gereset na rijping van het cerebellum. **Hoofdstuk 6.2** identificeert de moleculaire mechanismen waarmee PP2B de integriteit van PF-PC-synapsen regelt en toont aan dat PP2B zowel een enzymatische rol als een structurele rol heeft het controleren van de functie van de synaps en het leren. **Hoofdstuk 6.3** toont aan dat Shisa6 cruciaal is voor de functie van AMPA receptoren in Purkinje cellen, voor synaptische plasticiteit en daarmee voor cerebellum-afhankelijke motorische leerprocessen.

In **hoofdstuk 7** breiden we het onderzoek uit buiten het motorische domein. Door in vivo en in vitro elektrofysiologische afleidingen te doen op muizen zonder het autisme-gerelateerde Shank2-gen, vonden we stoornissen in de intrinsieke plasticiteit van Purkinje-cellen, LTP-inductie bij de synapse van de Purkinje cel en de regelmatigheid van simple spikes, overwegend in zebrin-positieve Purkinje cellen. Purkinje cel specifieke Shank2-mutanten vertoonden gebreken in motorisch leren en maar ook afwijkingen in sociaal gedrag, wat het belang van cerebellaire pathologie bij de generatie van autismespectrumstoornis ondersteunt.

Curriculum Vitae

Personal details

Name: Bin Wu (吴斌)
Birthdate: February 26, 1986
Birthplace: Qingdao, Shandong province, China
Nationality: Chinese

Education

2014 – 2019 PhD in Neuroscience, Erasmus MC, Dept. of Neuroscience, Rotterdam, Netherlands
2010 – 2013 Master in Neurology, Shanghai Jiaotong University, School of medicine, China
2005 – 2010 Bachelor in Medicine, Wenzhou Medical University, China

Social experience

2015 – 2019 Committee Chinese Association of Life science in the Netherlands (CALN)
2016 – 2017 Committee PhD students organization of Erasmus MC (Promeras)
2016 – 2017 Committee Graduate School Neurosciences Amsterdam Rotterdam (ONWAR)

Awards

2013 Outstanding Graduates of Shanghai Jiao Tong University
2013 China Scholarship Council (CSC) Scholarship

PhD Portfolio

Name of PhD student	Bin Wu
Erasmus MC Department	Department of Neuroscience
PhD period	2014 - 2019
Promotor	Prof. Dr. C.I. De Zeeuw
Co-promotor	Dr. Martijn Schonewille

PhD training

General courses

2018	Programming in Matlab
2018	Bio Conductor Workshop
2017	The NGS in DNA diagnostics course
2016	Scientific English writing
2016	Basic course on R
2016	Workshop on Microsoft Excel 2010: Advanced
2016	Workshop on Photoshop and Illustrator CS6 for PhD-students
2015	OIC Course Functional Imaging and Super Resolution

Specific courses

2014	Neurodevelopment
2014	Neurological disorders
2014	Molecular and cellular mechanisms underlying plasticity and behavior
2014	Cognitive neuroscience
2014	Psychiatric disorders
2014	Molecular neurobiology workshop

Posters

2019	EMBO symposium, Heidelberg, Germany <i>"TRPC3 is essential for functional heterogeneity of cerebellar Purkinje cells"</i>
2017	Society for Neuroscience Meeting, Washington DC, US <i>"Heterogeneity of cerebellar Purkinje cells differentially determines spiking activity and motor learning"</i>
2016	Annual PhD-meeting of ONWAR, Zeist, NL <i>"Modulating Modulation: Purkinje cell activity in impaired and enhanced compensatory eye movement adaptation"</i>

Presentations

2019	Flash talk in EMBL neuroscience symposium, Heidelberg, Germany
2014-2018	Labtalk presentation at Department of Neuroscience, Erasmus MC (4x)

Teaching

2014-2018	Assisting with <i>in vivo</i> electrophysiology workshops for neuroscience master students
2014-2018	Assisting with <i>in vivo</i> electrophysiology workshops for ONWAR PhD students

Academic memberships

2016-2019	Dutch Neurofederation, the Netherlands
2017-2018	Society for Neuroscience (SfN), United States
2016-2017	Federation of European Neuroscience Societies (FENS), European Union

Conferences

2019	EMBL: Probing Neural Dynamics with Behavioural Genetics, Heidelberg, Germany
2017	48 th Society for Neuroscience Meeting, Washington DC, United States
2017	Procedural Learning Summer School, Amsterdam, the Netherlands
2016	Annual PhD-meeting of ONWAR, Zeist, the Netherlands
2016	10 th FENS Forum of Neuroscience, Copenhagen, Denmark

List of Publications

1. **Bin Wu**, Chris De Zeeuw, Martijn Schonewille. A new perspective on vestibulo-ocular reflex adaptation. (*Chapter 1.2, in preparation*)
2. **Bin Wu**, Chris De Zeeuw, Martijn Schonewille. Vestibulo-ocular reflex adaptations are differentially encoded in divergent sites. (*Chapter 5.3, in preparation*)
3. **Bin Wu**, Laura Post, Chris De Zeeuw, Martijn Schonewille. Cerebellar development contributes to compensatory eye movement behavioral and adaptive functionality. (*Chapter 6.1, in preparation*)
4. **Wu B***, Koudstaal T*, Zhou H, De Zeeuw CI, Schonewille M. Modulating Modulation: Purkinje cell activity in impaired and enhanced compensatory eye movement adaptation. (*Chapter 5.1, in preparation*)
5. Lin Z, **Wu B**, Paul M, Li K, Proietti Onori M, Hasanbegovic H, Houtsmuller A, Hoebeek FE, Schonewille M, Gao Z, Smit AB, De Zeeuw CI. Interactions of Calcineurin with PSD-proteins modulate AMPA receptor trafficking in Purkinje cells. (*Chapter 6.2, in preparation*)
6. **Bin Wu**, Francois G.C. Blot, Aaron B. Wong, Catarina Osorio, Youri Adolfs, R.Jeroen Pasterkamp, Jana Hartmann, Esther B. E. Becker, Henk-Jan Boele, Chris De Zeeuw, Martijn Schonewille. TRPC3 is essential for functional heterogeneity of cerebellar Purkinje cells. (*Chapter 3, under review in Elife*)
7. Peter S, Urbanus B, Klaassen KV, **Wu B**, Boele HJ, Azizi S, Slotman J, Houtsmuller AB, Schonewille M, Hoebeek FE, Spijker S, Smit AB, De Zeeuw CI. AMPAR protein Shisa6 is essential for Purkinje cell synaptic potentiation and motor learning. (*Chapter 6.3, submitted*)
8. **Wu B**, Schonewille M. Targeted electrophysiological recordings in vivo in the mouse cerebellum. Extracellular recording approaches. Humana Press, New York. 2018, 19-37. (*Chapter 2*)
9. Jaarsma D, Blot F, **Wu B**, Subariam M, Voogd J, Ruigrok T, Gao Z, Schonewille M, De Zeeuw CI. The basal interstitial nucleus (BIN) of the cerebellum provides diffuse ascending inhibitory input to the floccular granule cell layer. J Comp Neurol. 2018 Jun 26. doi: 10.1002/cne.24479. (*Chapter 3*)
10. Voges K, **Wu B**, Post L, Schonewille M, De Zeeuw CI. Cerebellar learning mechanisms in mice depend on movement direction. Journal of Physiology. 2017, 595(15):5301-5326. (*Chapter 5.2*)
11. Peter S, Ten Brinke MM, Stedehouder J, Reinelt CM, **Wu B**, Zhou H, Zhou K, Boele HJ, Kushner SA, Lee MG, Schmeisser MJ, Boeckers TM, Schonewille M, Hoebeek FE, De Zeeuw CI. Dysfunctional cerebellar Purkinje cells contribute to autism-like behaviour in Shank2-deficient mice. Nature Communications. 2016, 7: 12627. (*Chapter 7*)